Quantum microwave sources from inelastic Cooper pair tunneling

Ambroise Peugeot

université PARIS-SACLAY

Quantum microwave sources from inelastic Cooper pair tunneling

Thèse de doctorat de l'université Paris-Saclay

École doctorale n° 564, Physique en Ile-de-France (PIF)
Spécialité de doctorat: Physique
Unité de recherche : Université Paris-Saclay, CEA, CNRS, SPEC
91191, Gif-sur-Yvette, France
Référent : Faculté des sciences d'Orsay

Thèse présentée et soutenue en visioconférence totale, le 15 juin 2020, par

Ambroise PEUGEOT

Composition du Jury

Jacqueline BLOCH Directrice de recherche, C2N (CNRS/Université Paris-Saclay)	Présidente
Benjamin HUARD Professeur, ENS de Lyon	Rapporteur & Examinateur
Xavier WAINTAL Directeur de recherche, HDR, PHELIQS (CEA/Université Grenoble Alpes)	Rapporteur & Examinateur
Nicolas ROCH Chargé de recherche, Institut Néel (CNRS)	Examinateur
Nicolas TREPS Professeur, LKB (CNRS/Université Pierre et Marie Curie)	Examinateur
Fabien PORTIER Chargé de recherche, SPEC (CEA/CNRS)	Directeur de thèse
Anne ANTHORE Chargée de recherche, C2N (CNRS/Université Paris-Saclay)	Invitée
Jean-Jacques GREFFET Directeur de recherche, Laboratoire Charles Fabry (CNRS/Institut d'Optique)	Invité

Thèse de doctorat

NNT : 2020UPASS093

Remerciements

De très nombreuses personnes m'ont aidé et soutenu tout au long de mon travail de thèse, que ce soit par leur excellence scientifique, leurs avis éclairés sur la physique et le monde en général, leur bonté et générosité, ou bien simplement par leur bonne humeur en toutes circonstances. Il serait trop long de détailler tout ce que je dois à chacun d'entre vous, aussi espéré-je que la sincérité des prochaines lignes compensera leur concision, et surtout que personne ne m'en voudra si par malheur j'oublie de le citer nommément.

Merci tout d'abord à Jacqueline Bloch, Benjamin Huard, Xavier Waintal, Nicolas Roch, Nicolas Treps, Anne Anthore et Jean-Jacques Greffet d'avoir accepté de composer mon jury de thèse, malgré les multiples changements et reports dûs à la situation particulière que nous traversions. Bien que très conscient de l'importance solennelle de l'évènement je ne me suis jamais senti intimidé au cours de la soutenance, et cela grâce à votre bienveillance et votre compréhension.

Merci à François Daviaud ainsi qu'aux autres membres de la direction du SPEC de m'avoir permis de réaliser ma thèse au sein de cet extraordinaire laboratoire. Merci au personnel administratif et technique pour leur très efficace support, sans lequel je pense que les labos de physique ne tourneraient pas aussi bien !

Merci aux membres du Groupe Nano-Electronique, qui constituent une des équipes les plus dynamiques et hautes en couleur que j'aie jamais connues. Merci en particulier à Patrice Roche qui trouvait toujours le temps de m'écouter malgré son agenda bien chargé, ainsi qu'à Marc Westig, Carles Altimiras et Iouri Moukharski qui m'ont accueilli au sein de l'équipe "Photons" et fait profiter de leur savoir et leur expérience ô combien précieux. Merci énormément aux autres thésards et aux post-docs du groupe, dont la camaraderie et la bonne humeur ont rendu ces années de thèse beaucoup plus agréables. Merci enfin à Patrice Jacques, dont la rigueur et l'habilité technique m'ont toujours impressionné - et parfois sauvé la mise lorsque la manip faisait des siennes !

Merci aussi aux membres du Groupe Quantronique, qui constituait ma "deuxième maison" au SPEC. C'est une chance incroyable de pouvoir apprendre aux côtés de chercheurs aussi talentueux que pétris d'humanité. Merci en particulier à Daniel Estève à qui revient la paternité du projet "Micro-ondes quantiques" et qui était toujours très fier des résultats de son bébé. Merci aussi à Denis Vion qui a souvent mouillé la chemise pour me débloquer sur des sujets aussi variés que la nanofabrication, les mesures micro-ondes, les simulations Sonnet ou même la bonne tenue d'un cahier de manip. Tu as fixé pour moi un modèle de travail et d'intégrité scientifique que j'espère pouvoir un jour approcher.

I would like to thank very much Simon Dambach, Björn Kubala, Ciprian Padurariu and Joachim Ankerhold from Universität Ulm who collaborated with us, providing deep

theoretical insights and valuable numerical simulations to our experiments. It was always a pleasure to discuss with you and to welcome you in Saclay, and I still hope that I could visit you in Ulm one day. Many thanks also to Juha Leppäkangas (now in Chalmers) who contributed greatly to the understanding of our entanglement experiment, even though he initially predicted the impossibility to observe any sign of quantum squeezing!

Merci à toutes les personnes que j'ai croisées lors d'écoles d'été et de conférence, qui m'ont marqué par leur esprit brillant, la profondeur de leur réflexion et par leur sympathie. La recherche fondamentale est un domaine ardu, et il est plus que précieux d'appartenir à une communauté où l'excellence ne cède qu'à l'humanité et la camaraderie.

Merci à ma famille et à mes proches, qui m'ont toujours soutenu malgré l'étrangeté de la voie que j'ai choisi de suivre et les contraintes qui l'accompagnent. Merci évidemment à Aneta, qui a toujours été là pour moi et qui a accepté que je fasse de l'ombre à notre mariage en programmant ma soutenance de thèse quinze jours avant.

J'aurais aimé pouvoir remercier une dernière fois Fabien Portier, qui a été la colonne vertébrale de mes années de thèse et de ma carrière naissante de physicien. Mon travail lui est bien entendu entièrement dédié, mais il me semble que c'est bien peu de choses en regard de tout ce qu'il m'aura apporté et appris. Ne trouvant les mots pour exprimer l'étendue de ma reconnaissance, je dirais simplement qu'en plus du mentor scientifique incomparable qu'il a été pour moi, Fabien a été pour tous ceux qui le connaissaient un modèle d'humanité, d'amitié, d'humour et de culture, et enfin de bienveillance.

Merci pour tout.

Contents

Chapter 1

General introduction: quantum coherence with a dissipative, out-of-equilibrium conductor

In this work, we study the coherent interaction of a dc-biased Josephson junction (JJ) with the modes of its electromagnetic environment. We show that when carefully engineering this environment, a JJ can provide a bright source of quantum microwave radiation.

A first description of the Josephson junction

The starting point of our work is the Josephson junction, which is a tunnel junction between two superconducting electrodes (Fig.1.1). In a normal state tunnel junction, electrons can cross the insulating layer thanks to the tunnel effect, giving rise to an electrical current I. A tunnel junction is a quantum coherent conductor, in the sense that the phase of charge carriers is preserved during their transmission through the barrier.

In the superconducting state, electrons pair to form the so called Cooper pairs. These Cooper pairs undergo a phase transition analogous to the Bose-Einstein condensation, and can be described by a macroscopic wavefunction. Cooper pairs can also tunnel through the barrier, carrying a charge 2e. Their tunneling gives rise to the Josephson current $I = I_0 \sin(\phi)$ [1]. Here ϕ is the difference of the phases of the two superconducting condensates in each electrode, while I_0 is a phenomenological quantity called the critical current of the junction.

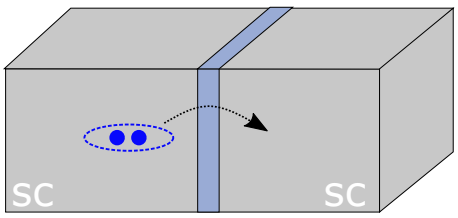

Figure 1.1: Schematic drawing of a JJ between two superconducting (sc) electrodes (in grey). The transport of current through the junction at low energy can be described as the tunneling of Cooper pairs through the insulating barrier (slate blue layer).

The phase difference ϕ is itself proportional to the integral of the voltage V across the junction, so that $\dot{\phi} = \frac{2e}{\hbar}V$. This phase is thus akin to a magnetic flux.

The Josephson equation can be rewritten to link the derivative of the current I to the voltage drop V, with: $\frac{dI}{dt} = I_0 \cos(\phi)\frac{2e}{\hbar}V$, or equivalently $V = \frac{\hbar/2e}{I_0 \cos(\phi)}\frac{dI}{dt}$. The JJ can thus be seen as a non-linear inductance $L_J(\phi) = \frac{\hbar/2e}{I_0 \cos(\phi)}$, while being intrinsically dissipationless [2]. Due to their unique properties, JJs are ubiquitous in two *a priori* very different fields of research: quantum information science and mesoscopic transport.

Josephson junctions in Quantum Information devices

When a JJ is embedded in a circuit, its non-linearity can be exploited to implement a given functionality, just as for any electrical component. JJs are in particular crucial in the field of Quantum Information, as their coherence properties and absence of intrinsic dissipation make them suitable for the manipulation of quantum signals.

As an example a circuit can be built where a JJ behaves in a given frequency band as a negative impedance, so that it amplifies the incoming signals in that band. This Josephson amplifier can be engineered to work at the quantum limit, in the sense that it only adds to the amplified signals the minimum amount of noise required by quantum mechanics [3][4][5]. Other types of quantum-limited devices can be built around JJs, such as frequency converters [6][7], or single-photon detectors [8][9][10].

The non-linear response of JJs is also used to engineer effective two-level systems, known as artificial atoms or qubits. One of the simplest ones is the dipole formed by a single JJ in parallel with a capacitance. This device implements an anharmonic LC resonator. Transitions between the ground state and first excited state of this oscillator can be selectively addressed, making it effectively a two-level system.

JJ-based qubits can couple electrically to superconducting microwave resonators, which host modes of the electromagnetic field [11]. Their field of study is called circuit-QED, as it was inspired by cavity-QED experiments with real atoms in cavities. Circuit-QED allow probing the light-matter interaction, in settings where the natural coupling strength of QED can be tweaked to engineer novel effects [12].

Furthermore, superconducting qubits are a potential platform for the dawning field of quantum computing, which motivates a great number of theoretical proposals for increasingly complex experiments (Fig.1.2). The experimental effort to implement these experiments aims notably at increasing the coherence lifetime of these artificial atoms, as well as the fidelity of the logical gates acting on them.

These various examples illustrate how quantum coherence can be harnessed by using JJs as non-linear dissipationless electrical dipoles. The success of these experiments rely notably on the careful decoupling of the JJ from the uncontrolled degrees of freedom in their environment. In these conditions the microscopic inner workings of the junction can mostly be ignored, and it may be considered solely through the quantum engineer point of view [13].

In contrast to this situation, in this work we will carry out experiments where the junction is galvanically connected to a biasing circuit. Put under a dc voltage bias, the junction

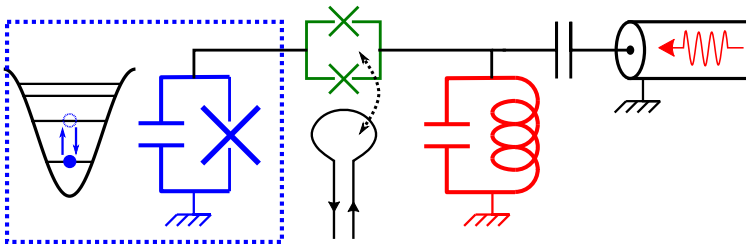

Figure 1.2: Example of a superconducting circuit where various JJs (crosses) are used to manipulate quantum information. A JJ in parallel with a capacitance (in blue) forms an anharmonic oscillator. This qubit can be selectively coupled to an electrical resonator (in red) through a Superconducting QUantum Interference Device (in green), whose admittance can be quickly varied by threading a magnetic flux through the loop (green arrow).

should be considered as a link between two electronic reservoirs kept out of equilibrium, allowing for the flow of a dissipative dc current. This setting connects superconducting circuits with an older field of research, the physics of coherent conductors.

Quantum transport in the mesoscopic regime

A coherent conductor is an electrical conductor small enough for the phase of the electrons wavefunction to be preserved during their transmission. Electric transport through these systems should then be described by the scattering of electronic waves in the sample, opening the possibility for quantum interferences.

Early experiments in quantum electrical transport focused on evidencing electronic interference effects on the most easily accessible observables, such as the dc electrical conductance. Coherent transport has been studied in a wide variety of mesoscopic conductors: Josephson junctions, but also normal tunnel junctions between two metallic electrodes, p-n junctions in semi-conductors, more exotic junctions where the barrier layer is itself semiconducting, magnetic, or displaying a strong spin-orbit interaction, 2D electron gases that can be patterned to yield quantum dots or quantum point contacts...

The results of these experiments are well understood within the so-called Landauer-Büttiker (LB) approach, where charge transfer through quantum conductors is probabilistic [14][15][16]. Due to charge granularity, this probabilistic character induces current noise of purely quantum origin. The observation of this shot noise was one of the most prominent experimental confirmations of the LB approach [17][18].

Later experiments include the application of an ac voltage bias. If the frequency ω of the ac bias is high enough so that $\hbar\omega$ exceeds the thermal energy k_BT, singularities appear in the low frequency noise power $S_{II}(0) = \langle I^2\rangle - \langle I\rangle^2$ at voltage $V = k\hbar\omega/e$. This is an indication of photo-assisted tunneling, where the transmission of an electron through the sample is accompanied by the absorption of k quanta of energy $\hbar\omega$ [19][20][21].

From current noise to microwave radiation

The current noise at finite frequency $S_{II}(\omega) = \int \langle I(t)I(t+\tau)\rangle e^{i\omega\tau}dt$ is a more intricate quantity, which also yields precious information on the system under study [16]. On general grounds current fluctuations through the conductor can be picked up by the

electromagnetic modes of the environment, where they are dissipated as an *emission power* (Fig.1.3). If this environment is not in the vacuum state, it can also emit energy into the conductor through this mechanism. $S_{II}(\omega)$ is then related to the emission and/or absorption of light by the conductor.

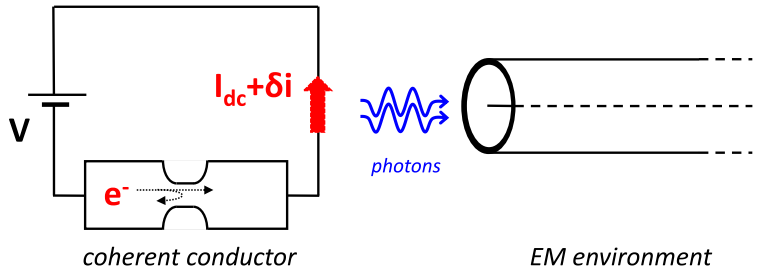

Figure 1.3: Schematic model of a coherent conductor (represented here as a constriction in an electron waveguide) put out of equilibrium by a dc voltage bias V. The current I flowing through the circuit consists of a dc part I_{dc}, due to the irreversible transfer of charges through the conductor, and of a fluctuating part δI with spectral density $S_{II}(\omega)$, due e.g to the granularity of charge for shot-noise. This current noise can be picked up by modes in the electromagnetic environment, resulting in the emission of photons by the conductor.

The *shot-noise* due to single-charge tunneling through an out-of-equilibrium tunnel junction [22] is the most simple example of this kind of radiation. Due to the very low transmission probability through the tunnel barrier, each tunnel event is random, and uncorrelated with the previous and following ones. The current I resulting from this large number of independent events presents fluctuations that can be characterized by the noise spectral density $S_{II}(\omega)$.

Suppose that we connect an impedance $Z(\omega)$ at zero temperature in parallel with a voltage-biased junction, in order to pick up this current noise and measure its value. In a simple microscopic picture, electrons tunneling elastically from the source electrode to the other one end up with an excess energy eV, which is dissipated in the sink reservoir. The part of this energy which is dissipated in $Z(\omega)$ can be interpreted as the emission of photons $\hbar\omega$ from the tunnel junction into the environment. Most importantly, as each tunneling electron carries an energy which is at most eV, it can never emit photons at frequency higher than $eV/\hbar$, resulting in $S_{II}(\omega > 2eV/\hbar) = 0$ [16][23].

This simple result connects the properties of microscopic charges to a macroscopic observable: the Joule power dissipated in an external impedance. It also links charge transport through a conductor to the emission of light in its environment, i.e highlights the link between electronics and optics in quantum coherent conductors.

The QED of coherent conductors

We have given a simplified description of how the JJ is considered both in circuit-QED and in mesoscopic transport: either as a non-linear electrical dipole used to engineer quantum information processing, or as a coherent conductor hosting microscopic processes. In both fields the interaction of JJs with the electromagnetic field is also studied, but once again with very different points of view.

In circuit-QED, classically coherent microwave light is commonly used to prepare a system in a given quantum state, or to read-out this state after manipulation. The weak signals

emitted by the quantum system are often phase-locked with the initial driving field, so that they can be detected in a coherent way through e.g homodyne detection. The field emitted by a quantum device may also consist of quantum light, i.e states of light that cannot be described by classical optics: propagating single-photons, cavity Fock states, squeezed vacuum states... with applications in quantum information processing. In all these cases, it is very obvious that light should be considered as a **signal**, i.e a coherent wave whose detection requires a phase reference.

By contrast, in the early mesoscopic transport experiments we have presented light is seen as electrical noise, with no special care accorded to its coherence properties. In photo-assisted transport, there is no direct link between the state of light being shined on the conductor and the observables of the system. In the case of shot-noise radiation, the only observable that can be predicted by a scattering theory of electron transport is the spectral density of the emitted light $S_P(\omega) = 2Re[Z(\omega)]S_{II}(\omega)$. The properties of the light itself, such as it statistics or the existence of any form of quantum coherence, are generally not considered, as it would require a much more complex theoretical machinery. In the absence of coherence, light exchanged between a conductor and modes of its environment is considered as a **noise** instead of a signal.

The unification of these two points of view, that would result in a consistent picture of the interaction between quantum light and a conductor's microscopic degrees of freedom, is the focus point of the **Quantum Electro-Dynamics of conductors**. In this approach, one can start by considering a coherent conductor, possibly out of equilibrium, and study the interaction between charges and light. Including a description of the quantum state of light reveals the coherence properties of this interaction. In particular it has been shown that **dissipative transport** through the conductor can result in the creation of **non-classical light states** [24][25][26][27][28]. It was also recently suggested that the coupling between a cavity and a dissipative quantum conductor may be used to produce cat states of the electromagnetic field [29].

In the example of shot-noise radiation, one may wonder if the properties of fermionic particles are imprinted onto the radiated light, due to the microscopic coupling mechanism behind this light-matter interaction. In the simple case of a dc-biased tunnel junction, the emission of light occurs upon the incoherent relaxation of charges in the reservoirs. As the photons are created randomly and independently, the statistics of the emitted photons is that of thermal radiation, i.e a classical state of light.

However for more exotic conductors such as quantum point contacts, it has been predicted that the Fermi statistics of the electrons may be imprinted unto the photons, leading to the creation of strongly non-classical light with sub-Poissonian statistics [24]. The experimental test of this prediction is the subject of ongoing research, requiring challenging technological development [30].

In the work presented here, we focus on the quantum properties of light emitted by a simple type of conductor through a mechanism closely related to shot-noise emission: the inelastic tunneling of charges through a dc-biased Josephson junction.

Light emission in the environment of a conductor and inelastic tunneling

In the simple picture of shot-noise emission we gave earlier, we started by describing the emission of current noise by the conductor, then explained how this noise can be picked up by modes of its environment. These modes play a passive role, in the sense that they only act as a sink where the electrostatic energy of the charges can be dumped. However as a coupling always go both ways, there should be a counter-action of the environment onto the conductor.

Let us examine more closely the mechanism of this coupling in the case of a normal tunnel junction. After a single electron has tunneled, the charge of each electrode changes suddenly by $\pm e$. This displacement of the charge state of the system can be described by the shift operator $e^{i\chi}$, with χ the electron phase difference across the junction. This phase is set by $\chi(t) = \frac{e}{\hbar}\int^t V(t')dt'$, with V the voltage drop across the junction.

A perfectly constant dc voltage would lead to elastic tunneling of the charges. However in a more complete picture we must consider the voltage fluctuations coming from the environment of the junction, described as an impedance $Z(\omega)$. Even if this environment is at zero temperature, it still displays vacuum fluctuations, with a spectral density $S_{VV}(\omega) = 2Re[Z(\omega)]\hbar\omega$.

These finite frequency voltage fluctuations can prompt inelastic mechanisms, where the charges tunnel inelastically while emitting or absorbing photons from the environment. The energy needed to create (absorb) these photons is extracted from (given to) the bias voltage source itself, so that the junction acts as a kind of dc/ac converter. The radiated light populates the modes of the environment, bringing them out of equilibrium and hence modifying the value of their voltage fluctuations. This brings the questions of under which conditions this inelastic mechanism exist, and how it modifies the transport properties of the junction.

These questions were tackled for the first time in the early Nineties, with the development of the so-called $P(E)$ theory [31]. This perturbative treatment of the tunneling Hamiltonian assumes that the emission/absorption rates of photons are low enough, so that the environment stays close to thermal equilibrium. Then the value of the voltage fluctuations are simply set by the thermal occupation and characteristic impedances of the environment modes. If they have a large occupation, the probabilities of photon emission and absorption are nearly equal, so that both forward and backward inelastic tunneling occur with similar rates and the total current through the junction is not modified. On the other hand if the environment modes are empty, they can only absorb photons, opening up new channels for dissipative transport through the junction (Fig.1.4).

These inelastic emission processes have a significant impact on the transfer of charges through the conductor when the environment impedance $Re[Z(\omega)]$ cannot be neglected compared to the quantum of impedance $R_K = h/e^2 \simeq 25.8$ kΩ. As the electromagnetic environment of a tunnel junction is typically of the order of the vacuum impedance $Z_0 = \sqrt{\frac{\mu_0}{\epsilon_0}} \simeq 377\ \Omega$, the contribution of inelastic tunneling is generally much smaller than direct elastic processes, both in the dc current and in the current noise.

Inelastic effects are much more prominent in superconducting JJ. At a bias voltage smaller than the superconducting gap $2\Delta/e$, no quasiparticles can flow through the junction. Inelastic processes involving the environment modes are thus the only means by which a

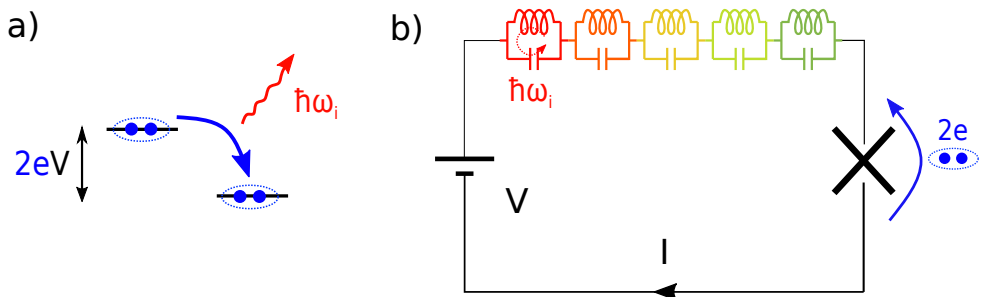

Figure 1.4: a) Schematic picture of a Cooper pair inelastically tunneling through a dc-biased junction while emitting a photon of energy $\hbar\omega_i = 2eV$. b) The energy to create a photon in a mode of the environment (depicted here as a collection of LC oscillators) is extracted from the voltage source V.

dc-biased JJ can allow the flow of a dc current[1]. This is a simple example of a mechanism in which the environment of a coherent conductor significantly modifies its transport properties.

Inelastic Cooper-pair tunneling: from dissipative transport to quantum light emission

The first experimental tests of the $P(E)$ theory in the superconducting case thus focused on the dc transport through the junction. A 1994 experiment by Holst and coworkers [32] was the first one to prove that inelastic Cooper-pair tunneling (ICPT) could be enhanced by tailoring the environment of a JJ, engineering resonances in $Re[Z(\omega)]$ at microwave frequencies. A dissipative current $\bar{I}$ was measured for values of bias voltage V below the gap voltage. The $\bar{I}(V)$ curve of the sample was well reproduced by simulations based on the $P(E)$ theory and the impedance $Re[Z(\omega)](\omega)$ of the circuit in series with the junction. In particular peaks in the $\bar{I}(V)$ curve are associated with the emission of photons in the modes at the environment at frequency $2eV/\hbar$, in processes where the whole electrostatic energy $2eV$ provided by the voltage source upon the tunneling of a single charge $2e$ is converted into photons (Fig.1.5).

Progress in the field of microwave engineering and measurement allowed for the direct detection of this emitted light in a second pioneering experiment in 2011 [33]. The "bright side" of inelastic Cooper-pair tunneling was unambiguously proven, with the measurement of photon emission rates coinciding with the Cooper-pair tunneling rates on the single-photon $\bar{I}(V)$ resonances. This experiment also proved the existence of *multi-photon* processes, where the energy $2eV$ is shared among multiple photons created at the same time (Fig.1.6).

The positive results of this experiment and novel techniques for detecting the emitted light prompted the proposal of new experiments, where the statistics of the photons themselves would be measured. These experiments aimed at broadening the field of Josephson photonics, going beyond the reach of the $P(E)$ theory by studying the state of the emitted light itself, in settings where the emitted photons can modify the state of the environment and act back onto the dc transport.

[1]Note also that for JJ, $Re[Z(\omega)]$ has to be compared to the superconducting quantum of impedance $R_Q = R_K/4$, so that inelastic processes are easier to trigger compared to the normal case.

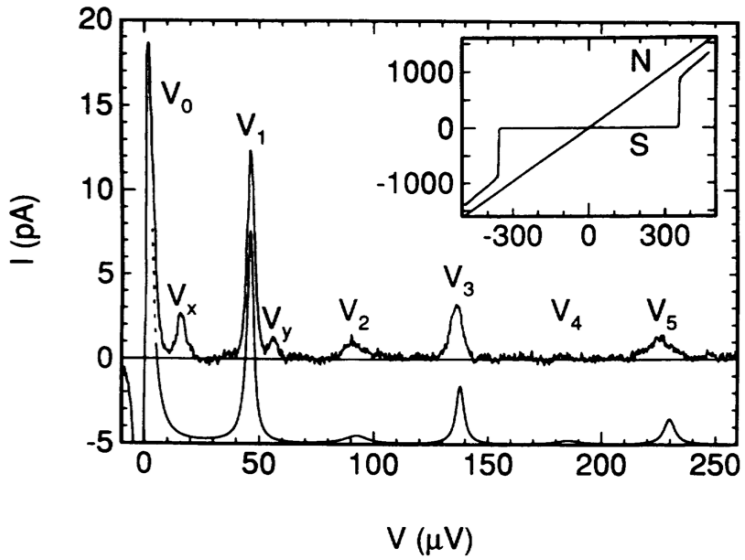

Figure 1.5: Experimental I(V) measured in [32]. A dc current is measured below the gap voltage $2\Delta/2$, due to inelastic Cooper pair tunneling processes. Each peak at bias voltage V_i is associated to the emission of light in a resonance of the environment at frequency $2eV_i/\hbar\omega$, in processes where one photon is created for each transferred Cooper pair.

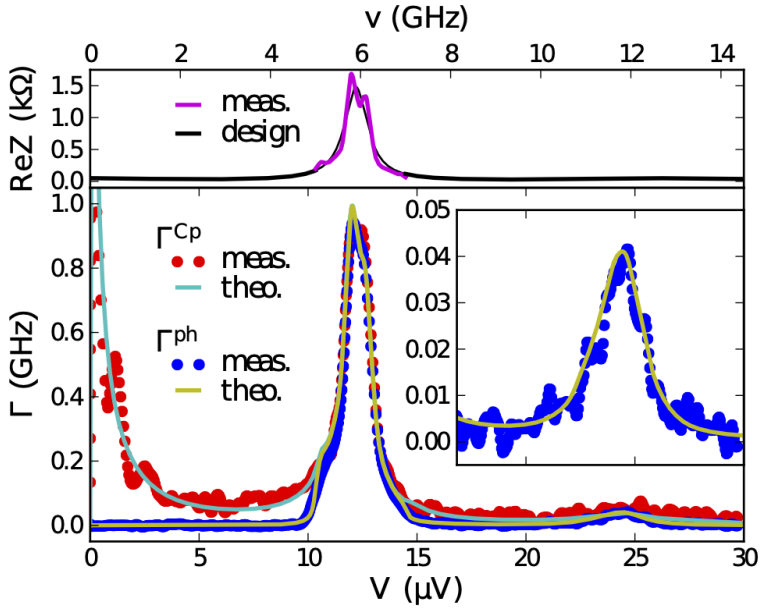

Figure 1.6: Results of the experiment described in [33], where both the Cooper pair tunneling rate Γ_{Cp} and the photon emission rate Γ_{ph} in a mode at $\omega_r/2\pi$ =6 GHz were measured. On the 1-photon resonance $2eV = \hbar\omega_r$, Γ_{Cp} and Γ_{ph} coincide. On the 2-photon resonance $2eV = 2\hbar\omega_r$, the emission power at ω_r is detected, indicating 2-photon processes (inset).

In this work we present two experiments that we carried out to investigate two complementary aspects of this physics: the **strong-coupling** of a JJ to a single microwave mode and the emission of **entangled photons** by ICPT.

Strong-coupling of a JJ to a single mode

One of the main assumptions of the $P(E)$ theory is that the modes of the environment are only weakly perturbed by the inelastic photon creation processes. A sufficient criterion for this condition to hold is that the stationary population of the modes, resulting from the balance between photon creation and the modes intrinsic losses, stays close to its equilibrium value $\bar{n} = n_B(T) = (e^{\frac{\hbar\omega}{k_B T}} - 1)^{-1}$.

This condition on the stationary state of the modes ensures that the dc current and photon emission rates are correctly predicted by the $P(E)$ theory, as the excess population due to ICPT does not modify the tunneling probability. However, in an instantaneous picture, right after one photon has been created the mode can be greatly displaced from its equilibrium state, in particular if it was initially in the vacuum state. If the mode is strongly coupled to the junction, this sudden change of its occupation modifies deeply the instantaneous voltage fluctuations, impacting the Cooper pair tunneling rate.

This back-action of the emitted light on the photon creation rate can lead to non-trivial dynamics of the system. It is however not obvious if the resulting state of light displays non-classical statistics: even if the voltage ZPF which prompt the photon emission are by nature quantum, the vacuum state itself is quasi-classical. A more complete treatment reveals that the stationary state of the modes depends crucially on their coupling strength to the junction.

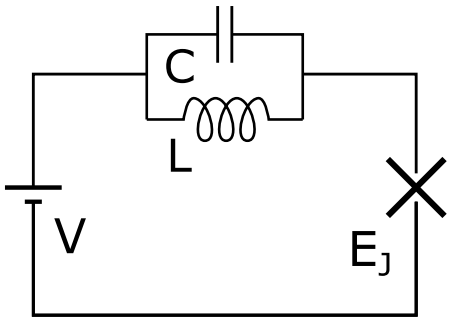

Figure 1.7: A LC resonator hosting a single mode of radiation is put in series with a dc bias source and a JJ. The two dipoles are coupled: inelastic tunneling across the junction can be prompted by the voltage fluctuations in the resonator. At the same time the tunnel current through the junction is directly injected into the oscillator, creating excitations in the mode.

In a simple circuit including a JJ and a single mode at frequency ω_r (represented by a LC oscillator in figure 1.7 with $\omega_r = \sqrt{LC}^{-1}$), the dimensionless constant characterizing their coupling is $r = \frac{\pi Z_c}{R_Q}$, with $Z_c = \sqrt{\frac{L}{C}}$ the characteristic impedance of the mode. In the strong coupling regime $r \sim 1$, the voltage ZPF $\Delta V = \sqrt{r}\frac{\hbar\omega_r}{2e}$ are of the same amplitude as the dc voltage V on the single-photon resonance $2eV = \hbar\omega_r$, where one photon is created for each tunneling Cooper pair.

The strong coupling regime is predicted to yield two observable effects on the system [34]. First, even in the limit of a vanishing population of the mode, the tunneling rate is impacted by its ZPF. This reduction of the tunneling probability appears in the Josephson energy E_J of the junction, which is renormalized by the phase fluctuations of the mode down to $E_J^* = E_J e^{-\frac{r}{2}}$.

Second, for low tunneling rates, corresponding to a weak driving of the mode such that its population $\bar{n}$ stays low, non-classical properties are predicted for the emitted light, which should display both antibunching and sub-Poissonian statistics. Both can be characterized by the second order coherence function of the light $g^{(2)}(\tau) = (1 - \frac{r}{2}e^{-\kappa|\tau|})^2$, with κ the resonator leak rate. This effect arises from the coherent back-action of the field in the resonator onto the junction. The presence of a first photon in the mode reduces the probability to create a second one, leading to anti-correlations in the photon flux emitted by the resonator (Fig.1.8).

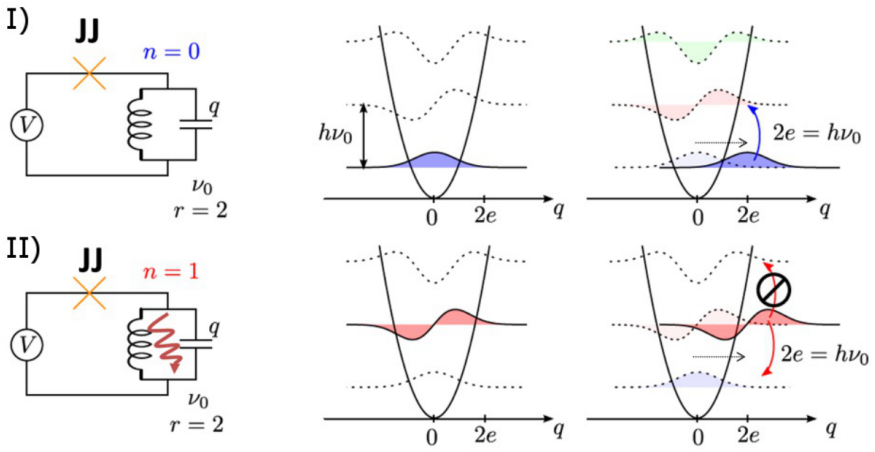

Figure 1.8: Photon blockade mechanism in a mode strongly coupled to a JJ with $r = 2$. After a single Cooper pair has tunneled, the mode ends up in its first excited state, with a wavefunction displaced in charge space by $q = 2e$. This displaced wavefunction does not overlap with the next excited state, so that the creation of a second photon is forbidden.

For high enough impedance of the resonator such that $r \sim 2$, this simple circuit implements a **single-photon source**. From a practical point of view, the simplicity of the antibunching mechanism, which requires only to tune the bias voltage to $V = \frac{\hbar\omega_r}{2e}$ and the impedance to $Z_c = \frac{2R_Q}{\pi} \simeq 4$ kΩ, could make it suited for applications where high rates of microwave single photons are required. On the fundamental point of view, this device illustrates the extent of **dissipation engineering**, an approach to quantum experiments where dissipation is a ressource instead of a detrimental phenomenon.

The design of an experiment in the strong coupling regime was the research project of Chloé Rolland, during her PhD stay in our team in 2014-2016 [35]. She managed to design and fabricate a sample including a microwave mode with impedance $Z_c \simeq 2$ kΩ, strongly coupled with a flux tunable SQUID with $r \simeq 1$ (Fig.1.9). Using the microwave equivalent of a Hanbury Brown-Twiss interferometer, she made preliminary measurements of the statistics of the emitted photons in the low driving regime, indicating antibunching. However the detection setup suffered from spurious parasitic couplings between the measurement lines, which added a considerable noise to the measurements.

This PhD thesis presents our efforts to develop a novel type of *linear detection setup*, allowing not only for the measurement of the power radiated by the sample, but also of the quadratures of these signals. By combining these quadratures in a judicious way, we are able to reject the parasitic background noise due to spurious microwave coupling of the lines, increasing greatly our accuracy in the measurement of correlation functions of the signals. We could thus better confirm the measurement of antibunching of the

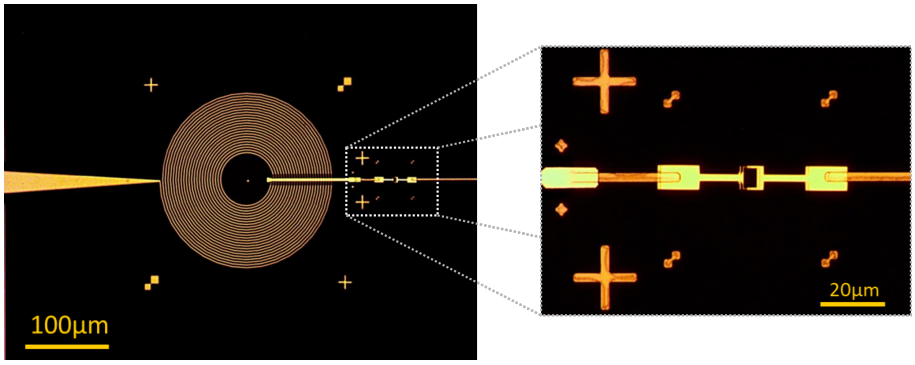

Figure 1.9: Micrography of the sample fabricated by Chloé Rolland during her PhD. The microfrabricated coil (left part) implements a resonator in the strong-coupling regime with a SQUID-like tunable JJ (inset), with $r \simeq 1$.

photons emitted by the sample (Fig.1.10), studying the transition to classical light as the population of the mode is increased [36].

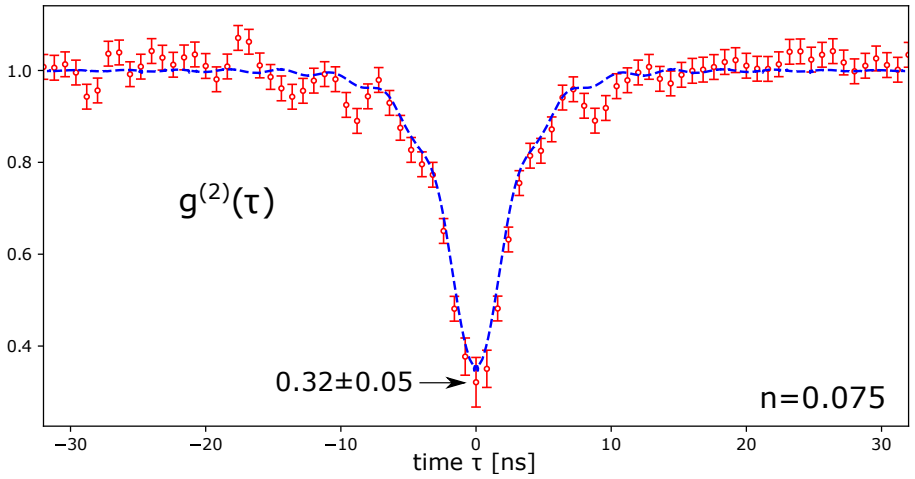

Figure 1.10: Second order coherence function of the photons emitted by the strong-coupling sample at low occupation number $n = 0.075$ of the resonator. The value $g^{(2)}(0) = 0.32$ proves the sub-Poissonian statistics of the photon, at an emission rate $\Gamma \simeq 60$ Mphotons/s.

Our linear detection setup also grants us a much better resolution on the spectral properties of the light emitted by the junction, both in ICPT regime as well as for bias voltages larger than the gap voltage $2\Delta/e$, where the junction behaves as a source of shot-noise. Combining these measurements with a simple modelling of the embedding circuit of the sample, we are able to characterize carefully the environment, measuring its impedance $Re[Z(\omega)]$ and the population of its modes. We could thus check a prediction of the $P(E)$ theory, namely that the effective Josephson energy of the junction E_J^* is reduced by the equilibrium phase fluctuations of all the modes in its environment, from the rf range up to microwave frequencies.

Beyond photon statistics, our detection setup allows us to measure arbitrary correlation functions of the photons emitted by a sample. We used it in a different experiment to prove the entanglement of light emitted by ICPT at two different frequencies.

Entangled beams emitted by inelastic tunneling

The results from figure 1.6 show that when the bias voltage V on a JJ satisfies $2eV = \hbar(\omega_a+\omega_b)$, with ω_a and ω_b the frequencies of resonances in the environment of the junction, a dc current can flow, through inelastic processes where for each tunneling Cooper pair a pair of photons is created, with one photon in each resonance (Fig.1.11).

This process is reminiscent of parametric down-conversion in quantum optics, where one photon is absorbed from a "pump" mode at $\omega_p = \omega_a + \omega_b$ and coherently converted into a pair of photons at ω_a and ω_b via a non-linear interaction. Depending on the form of this interaction, the created photon pair can be in an entangled state, sharing a non-local degree of freedom (e.g a total spin equal to zero), while local measurements on a single photon from the pair yield incoherent results (e.g a random spin value). Such pair state are typically used in Bell tests of non-locality in quantum physics.

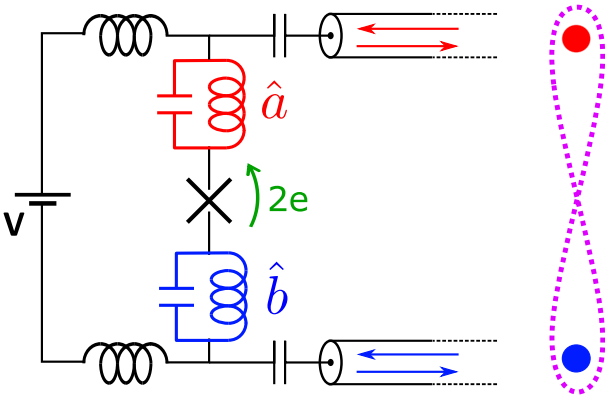

Figure 1.11: Two resonators at frequencies ω_a, ω_b are connected to a dc-biased JJ. When $2eV = \hbar\omega_a+\hbar\omega_b$, entangled photon pairs are created upon the tunneling of Cooper pairs .

Entanglement of microwave beams of light by a Josephson device has already proven that parametric down conversion can be achieved in a circuit-QED setting [37]. The non-local observable in this experiment is the sum of the phases of the two fields, which leads to two-mode squeezing of their quadratures. This result proves that the non-linearity of a Josephson device can be used to engineer a coherent two-mode drive. Nevertheless, it is non obvious whether or not the photon pairs created by inelastic tunneling display such non-classical properties. Indeed the ICPT mechanism has no direct equivalent in optics, as here the role of the coherent pump mode is played by the many-body superconducting states of the two electrodes.

The coherence of this macroscopic electronic system lies in the phase of the superconducting ground state. This phase coherence should in principle be inherited by the photon pairs created by ICPT. In a galvanically connected junction, the time evolution of the phase difference $\hat{\phi}$ is set by the value of the voltage bias V across the junction. In the simple circuits we have been discussing so far, the dc part of the voltage drives a linear increase of this phase with: $\frac{d\hat{\phi}(t)}{dt} = \frac{2eV}{\hbar}$, while the finite frequency voltage fluctuations from the environment modes prompt the inelastic photon emission processes. In a more realistic setting, the junction is also coupled to a continuum of low frequency modes, from dc to at least $k_BT/\hbar \simeq 2\pi \times 400$ MHz at $T = 20$ mK. These modes are in a thermal state with a high occupation number, so that they add random noise to the voltage bias.

This low frequency noise yields a random dephasing of the superconducting phase difference, which displays a very limited coherence time of at most a few hundreds of nanoseconds. It thus seems that this dissipative system can never yield quantum coherence effects. However we have been able to prove that a judicious choice of observables could prove the entanglement of the microwave light emitted by ICPT, even in the absence of a stationary phase reference, provided the environment of the junction is carefully controlled.

We build our experiment on a previous one realized by Olivier Parlavecchio during his PhD stay in our team in 2011-2014 [38] (Fig.1.12). In this first experiment, a JJ is placed in series with two microwave resonators, implementing modes at 5.1 GHz and 7 GHz. The impedance of these resonators is low enough so that the modes are only weakly coupled to the junction with $r \ll 1$, so that their occupation do not perturb tunneling rates. On the photon-pair resonance $2eV = h \times 12.1$ Ghz, the leaking microwave powers measured at the output of the two modes show non-classical correlations, indicating that the photons are indeed created by pairs. This result validates the pair creation mechanism, and prove that the two resonators are coherently driven by the junction [39].

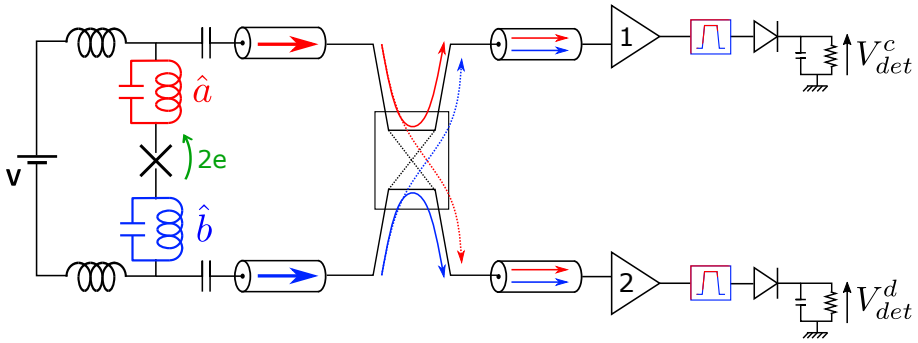

Figure 1.12: Schematic representation of the setup used in to probe the non-classical statistics of photon pairs emitted by a JJ. The microwave power leaking at the output of the two modes (red and blue) is detected at room temperature after amplification and being split over a HBT-type setup.

This experiment relies on the fact that photon flux correlations measured at the output of the resonators are directly linked to photon numbers inside the cavities. The connection between propagating modes and the cavity modes can be expressed using the input-output formalism. In this spirit, it was finally understood that non-local phase correlations between the cavity fields would be imprinted in the outgoing photons. Thus, even if the phase difference across the junction is prone to local noise and display a limited coherence time, the emitted light can conserve its 2-photon coherence as it propagates away from the sample.

The phase correlations of the photons emitted at two different frequencies can be characterized by the violation of a classical inequality on 2-photon correlation functions, which provides an *entanglement witness*. In an experimental setup similar to 1.12, we have been able to detect this entanglement by using our linear detection setup (Fig.1.13). We confirmed this simple picture of the entanglement of the propagating fields, according to which the photons stay entangled if they leave the resonators faster that the dephasing rate at the junction.

As this dephasing rate stems from low frequency voltage, it is not intrinsic to the sample itself, but rather to its embedding circuit. We confirmed that the dephasing rate was indeed limited by the value of the equilibrium thermal voltage noise on the junction, by

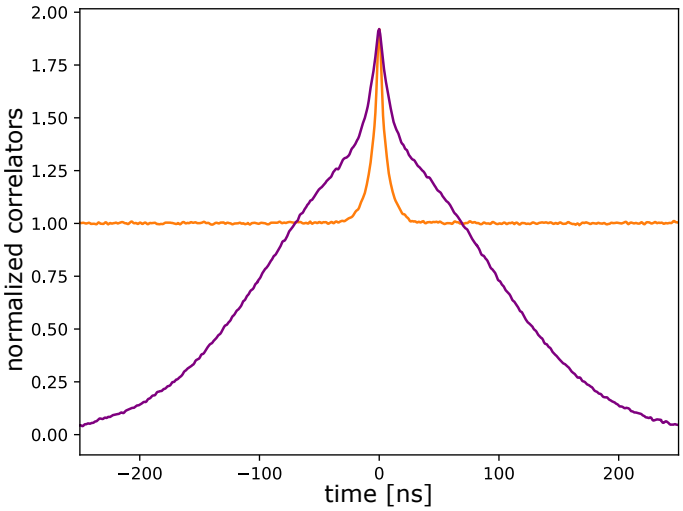

Figure 1.13: 2-photon correlators proving the entanglement of the emitted fields. For separable fields the phase correlation function (purple) is always smaller than the population correlator (orange).

actively heating or cooling down these modes (Fig.1.14). This heating/cooling mechanism is based on ICPT through the very same junction that is creating the entangled photons. This last result proves that a dissipative, open quantum system, actively coupled to a bath in a deeply classical state, can still create observable entanglement. The cooling mechanism itself could be extended to bring quantum devices to their ground state, or perform the spectroscopy of mesoscopic systems at rf frequencies.

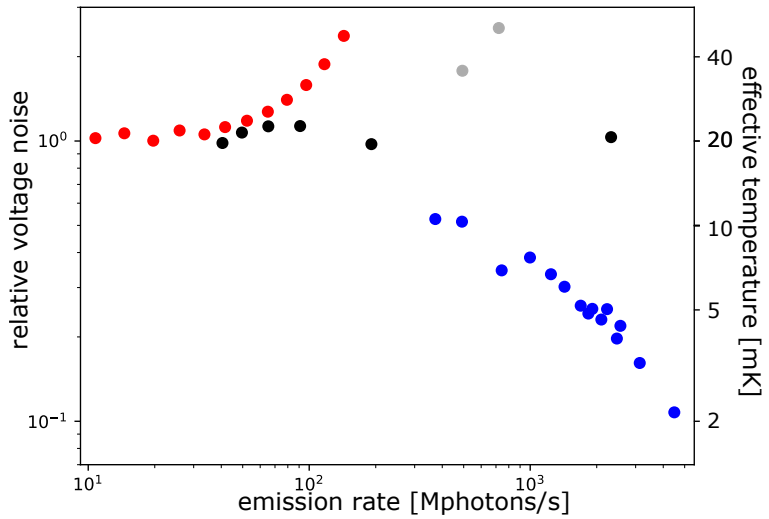

Figure 1.14: Relative voltage noise as a function of the tunneling rates for different bias settings. The junction can be used to either heat up (red dots) or cool down (blue dots) the low frequency modes of its environment, increasing/reducing their voltage noise. This interaction can also be turned off to yield a non-interacting regime (black dots).

Conclusions, on-going experiments and perspectives

In this PhD work, we explore how the concepts and tools of quantum optics can be adapted in a mesoscopic setting to yield a novel type of quantum light sources.

In our experiments we consider a dc-biased JJ, which is an out-of-equilibrium, open quantum system interacting with the modes of its electromagnetic environment from dc up to $2eV/\hbar \sim$ a few GHz. We study how to model the interaction with these modes, which display very different time scales and equilibrium populations. We describe how the high frequency modes, implemented by microwave resonators, act like cavities in the vacuum state driven by inelastic transport through the junction, while the low frequency thermal modes act like a source of random voltage noise, dephasing this drive on a slow timescale.

We study two different kinds of samples, one with a single mode in the strong coupling regime $r \simeq 1$ and another one where two modes at different frequencies couple to the same junction. In each experiment, we fully characterize the environment of the sample, using the emission properties of the junction in different regimes of bias voltage and Josephson energy. We then measure correlation functions to prove the non-classical properties of the light emitted by ICPT, studying the transition to a classical light source at high emission rates.

In the strong coupling experiment, we prove the single-photon character of the light emitted at low driving by measuring the antibunching of the photons, with a second order coherence $g^{(2)}(0) = 0.32 < 1$, the value for classical states. This experiment does not rely on any phase coherence of the emitted photons. However we prove how our phase-sensitive detection setup increases the accuracy of the measurement, by rejection of the parasitic background of thermal noise from the amplification chain. We also quantitatively measure the renormalization of the Josephson energy of the junction by the ZPF of the modes in its environment.

In the two-mode experiment, we detect the entanglement of the emitted photons by proving their 2-photon phase coherence. We interpret this entanglement in the frame of two-mode squeezing, and relate the phase correlations of the emitted fields to the dynamics of the superconducting phase of the junction. We study the deviation to a pure two-mode squeezer due to the finite impedance of the modes, which leads to a back-action of the emitted photons onto the junction. We study how this back-action yields increasingly classical statistics of the fields at high emission rates. We prove that the dephasing rate at the junction, which yields the finite phase coherence time of the entangled beams, originates from the low frequency voltage noise of the bias setup. We then increase the value of the maximum rate at which we still detect entanglement by cooling down these modes, hence reducing their voltage noise. This active cooling mechanism is based on low frequency noise absorption by the junction itself through ICPT.

The results of these two experiments prove that a dc-biased JJ can be a versatile **source of microwave quantum light**, even though it is coupled to a continuum of modes with very high thermal occupation. The strong coupling experiment highlights the impact of ZPF fluctuations from the environment on the drive implemented by the junction, which can lead to the creation of strongly non-Gaussian states of light. In the two-mode entanglement experiment, this non-Gaussianity reduces the fidelity of the light

state compared to a pure two-mode squeezed state. However this non-Gaussianity could be advantageous for the creation of strongly non-classical light, which could be used in quantum information protocols.

We also contributed to the design of other experiments, that have not been realized yet. The first one follows a proposal to implement an autonomous Fock-state stabilizer, using a junction coupled to two modes, of which one is in the strong-coupling regime $r = 2$. We developed a design for a sample that would implement a flux tunable microwave resonator, allowing to reach this strong coupling condition. We also conducted a preliminary sideband cooling experiment, aiming to cool down a rf mode down to its its quantum ground state by ICPT. These experiments would allow going further than the realization of sources of quantum light, towards the manipulation of quantum states.

In future experiments we may try to stick closer to circuit-QED settings, by e.g adding coherent microwave tones to phase-lock the emitted signals and remove the problems yielded by the absence of a stationary phase reference. This kind of ICPT device would then benefit from the intrinsic rejection of any Kerr terms in the system Hamiltonian, which make it more suited for high photon number applications.

It may also be interesting to depart frankly from circuit-QED and explore a parameter space forbidden to typical superconducting circuits. As an example by using JJ made with a higher superconducting gap material we could try emitting radiation at THz frequencies, where no coherent source is available. It may also be interesting to study different kind of quantum conductors such as superconducting quantum point contacts, yielding more complex interaction with the environment.

Chapter 2

Interaction of a dc-biased Josephson junction and its environment

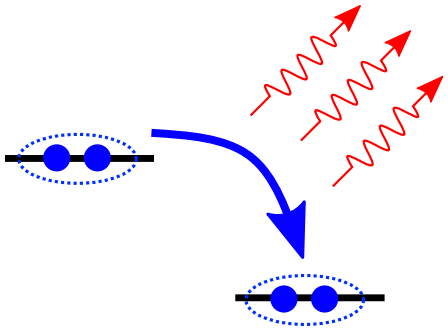

All the experiments presented in this work make use of the same system: **a small Josephson junction** put out-of-equilibrium by a **dc-voltage bias** and embedded in an **electromagnetic environment**. We first describe the Josephson junction, and explain why it is important to take into account the back-action of its embedding circuit. We present the $P(E)$ theory which describes how in the limit of a weak tunnel coupling charges can tunnel incoherently through the insulating barrier that defines the junction, while exchanging electromagnetic excitations with the rest of the circuit, and predict the associated tunnel current and photon emission rates.

We then discuss in which sense this incoherent Cooper-pair tunneling differs from the usual ac-Josephson effect, and present two earlier experiments performed to test this physical description of the system. We discuss the results of the second experiment, where both aspects of this phenomenon, current and microwave radiation, were measured for the first time simultaneously. These results prompt the idea that a dc-biased Josephson junction can be used to create quantum states of light, with a mechanism fundamentally different from the ones exploited in other microwave quantum optics experiments.

2.1 Transport through tunnel junctions

Charges can cross a tunnel junction between two conductors by quantum tunneling and give rise to a *tunnel current*. We derive here the I(V) characteristic of dc-voltage biased junctions from a microscopic picture, treating first the case of a normal junction and then of a superconducting one. This description is semi-classical as we consider an ideal voltage bias, without taking into account the effect of voltage fluctuations.

What is a tunnel junction?

A tunnel junction consists of two pieces of conducting materials which are separated by a very thin insulating layer, with a thickness of the order of the nanometer. In conventional electronics, this is the geometrical layout of a parallel plate capacitor. In a classical microscopic picture, charge carriers in the conductors cannot cross the potential barrier of the insulating layer. We would then expect a junction to behave as an open circuit for low frequencies, that cannot allow a dc-current.

On the other hand, we know from quantum mechanics that a charge carrier incoming to the barrier is described by a propagative wave packet, which fades out exponentially in the insulating region if the particle energy is lower than the barrier height. If this layer is thin enough, this evanescent wave can propagate again on the other side of the barrier. There is then a finite probability for the charge to be found in the other electrode of the junction: this is the phenomenon of **quantum tunneling** (Fig.2.1).

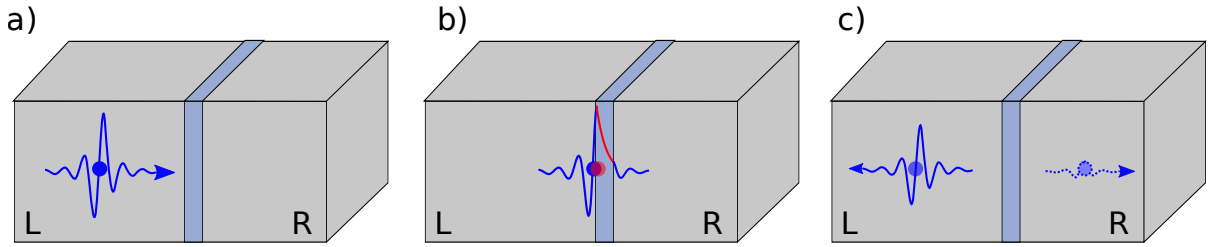

Figure 2.1: Schematic representation of a charge in a conductor incoming to a tunnel junction (a) and crossing it through quantum tunneling (b). Although the wave packet is exponentially vanishing in the insulating region, there is a finite probability of finding the particle in the other electrode (c).

Tunnel current in normal-metal junctions

The thickness of the insulating layer being generally much shorter than the electronic phase coherence length, we can describe the transport properties of a tunnel junction using the **scattering approach** [14][16]. Consider that the left and right electrodes (labelled L and R) of the junction are connected to electronic reservoirs, feeding them with electron waves propagating in independent 1D ballistic channels. The number of these channels is estimated as $N \simeq k_F^2 A/\pi^2$, with k_F the Fermi wave-vector and A the area of the junction: it is of the order of $10^5 - 10^6$ for typical nano-fabricated metallic tunnel junctions.

In the language of second quantization, we describe incoming electrons in a single spin-polarized channel of the left electrode (L) with the field operator

$$\psi_L^a(x,t) = \int_0^\infty \frac{e^{ik_L x}}{\sqrt{2\pi}} a_{k_L} dk_L, \tag{2.1}$$

where a_{k_L} is the annihilation operator for an electron of momentum $\hbar k_L$. The associated forward charge current is

$$I_L^a(x,t) = \frac{e\hbar}{im^*} Re[(\psi_L^a)^\dagger \nabla \psi_L^a] \tag{2.2}$$

with m^* the electron effective mass. This equation is valid only in the case of a perfectly transmitting scatterer. In the most general case, one has to also include the reflected electron in the field operator. The total current for spin polarization σ then includes the electron waves going away from the junction, described by annihilation operators b_{k_L}

$$I_L^\sigma(x,t) = \frac{e\hbar}{im^*} Re[(\psi_L^a)^\dagger \nabla \psi_L^a - (\psi_L^b)^\dagger \nabla \psi_L^b]. \tag{2.3}$$

We consider here a non-magnetic barrier that cannot flip the spin of scattered electrons. We then simply include the other spin polarization carried by the same channel as a factor of 2 in the total current:

$$I_L^{tot}(x,t) = I_L^\sigma(x,t) + I_L^{\bar{\sigma}}(x,t) = \frac{2e\hbar}{im^*} Re[(\psi_L^a)^\dagger \nabla \psi_L^a - (\psi_L^b)^\dagger \nabla \psi_L^b]. \tag{2.4}$$

We now switch to a representation of the operators as a function of the energy of the electrons: $\epsilon_L = \hbar^2 k_L^2 / 2m^*$. The current is then expressed as integrals over ϵ_L instead of k_L. We make here another approximation: we consider temperatures and bias voltages small compared to the Fermi energy: $k_B T, eV \ll E_F^L, E_F^R$. All excitations stay close to the Fermi surface, such that we can use a linearized version of the energy dispersion relation. The current is then simply

$$I_L^{tot}(x,t) = \frac{2e}{h} \int d\epsilon d\eta e^{i[(k_\epsilon - k_\eta)x - (\eta - \epsilon)t/\hbar]}, [a_L^\dagger(\eta) a_L(\epsilon) - b_L^\dagger(\eta) b_L(\epsilon)], \tag{2.5}$$

where we suppressed terms oscillating with $(k_\epsilon + k_\eta)x - (\eta + \epsilon)t/\hbar$ as they involve frequencies of the order of the Fermi energy, i.e much higher than $(k_B T, eV)$ or than the frequency range we can access experimentally.

Now we assume that the tunnel coupling between L and R is weak, such that it does not perturb much the electronic states in the electrodes: we can still describe them with the initial $\psi(x,t)$ operators. Its only action is a linear mixing of the states, such that we can express the outgoing mode operators $b_{L(R)}$ as a linear combination of the a_L's and the a_R's. Finally, if the electrochemical potential difference between the two reservoirs is small (compared to the Fermi energy or the potential barrier height), the tunneling is elastic such that we can write the scattering relation

$$\begin{vmatrix} b_L(\epsilon) \\ b_R(\epsilon) \end{vmatrix} = \begin{vmatrix} r(\epsilon) & t(\epsilon) \\ t'(\epsilon) & r'(\epsilon) \end{vmatrix} \times \begin{vmatrix} a_L(\epsilon) \\ a_R(\epsilon) \end{vmatrix}. \tag{2.6}$$

We can then express the current as a function of the $a_{L(R)}$ operators only and the transmission probabilities $T(\epsilon) = t^*(\epsilon) t(\epsilon)$. The incoming modes from the reservoirs are in a thermal state, such that their occupation is given by

$$\langle a_{L(R)}^\dagger(\epsilon) a_{L(R)}(\eta) \rangle = f_{L(R)}(\epsilon) \delta(\epsilon - \eta), \tag{2.7}$$

where $f_{L(R)}$ is the Fermi distribution in the $L(R)$ reservoir. The statistical average of the current from L to R is then

$$\langle I \rangle = \frac{2e}{h} \int T(\epsilon)[f_L(\epsilon) - f_R(\epsilon)]d\epsilon. \tag{2.8}$$

Suppose the two leads at the same temperature. We can set their electrochemical potential difference by applying a voltage bias V to the junction, effectively shifting one Fermi level with respect to the other by eV. If eV is small compared to the Fermi energy, then the transmission probability can be considered energy-independent in the integration range ($T(\epsilon) = T$) and we get for the contribution of this channel to the current:

$$\langle I \rangle = \frac{2e}{h} T \int [f_L(\epsilon) - f_R(\epsilon)]d\epsilon = \frac{2e}{h} T \times eV = T\frac{2e^2}{h}V. \tag{2.9}$$

Here $T \times 2e^2/h$ is the resulting conductance for a single 1D channel, with $2e^2/h \simeq 77.5\mu S \simeq (12.9k\Omega)^{-1}$. For a normal metal tunnel junction, the density of states in each electrode is flat around the Fermi level on the scale of eV, such that if we sum the independent contribution of the N channels we simply get for the total current

$$\langle I_{tot} \rangle = \sum_{i=0}^{N} T_i \frac{2e^2}{h} V = G_T V, \tag{2.10}$$

where the *tunnel conductance* $G_T = (2e^2/h)\sum T_i$ is the total conductance of the junction. The average transmission of the channels being of the order of 10^{-6} in junctions fabricated using standard techniques, we will study tunnel resistances in the range of a few kilo-ohms.

We see that even if the transport properties of a tunnel junction arise from a phenomenon which is exclusively quantum, in the simple case we considered it has the same I(V) characteristic as an ohmic conductor (Fig.2.2.b).

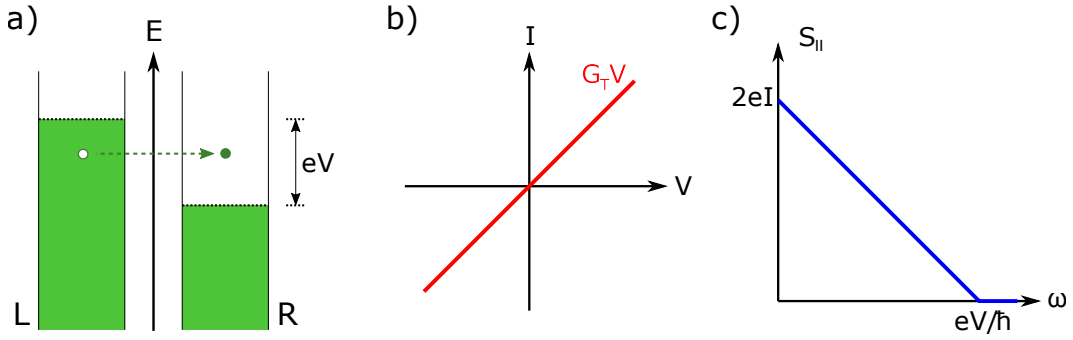

Figure 2.2: a) Schematic energy bands in a metallic tunnel junction at zero temperature. A bias voltage V shifts the two Fermi levels by eV. Irreversible elastic tunneling occurs when an electron jumps from an occupied state to an empty one. b) I(V) characteristic of a metallic tunnel junction. c) Current shot-noise $S_{II}(\omega)$ of a tunnel junction at zero temperature.

Tunnel-current noise

The difference between a tunnel junction and a classical resistor may be seen in more elaborate quantities, such as the current-noise spectral density $S_{II}(\omega) = \int \langle I(t)I(t+$

$\tau)\rangle e^{i\omega\tau}d\tau$ [15][40], which can also be computed in the scattering formalism [41]. A classical resistor presents only the Johnson-Nyquist noise coming from the thermal excitation of charges, which vanishes at zero temperature. In contrast a tunnel junction also shows a *shot-noise* contribution, which results from the discreteness of charge transfer through the junction.

The zero-frequency noise is proportional to the variance of the current $I(t)$, averaged over a long time. In the tunnel limit the charges cross the barrier independently, resulting in a Poissonian distribution $p(n)$ of the number of tunneling events n in a given time interval τ, with $\langle I\rangle = en/\tau$. The variance of a Poisson process being equal to its mean, the low frequency current noise is $S_{II}(\omega \simeq 0) = 2e\langle I\rangle$, known as Schottky noise [22].

Noise at high frequency is created when an excited electron in the leads falls back to the Fermi level. After tunneling, the maximum excess energy of an excited electron is eV, such that at frequencies higher than $eV/\hbar$ the noise is zero (Fig.2.2.c). The noise at a finite frequency ω lower than $eV/\hbar$ reads at zero temperature: $S_{II}(\omega) = 2(e\langle I\rangle - G_T\hbar\omega) = 2G_T(eV - \hbar\omega)$.

Superconducting tunnel junctions

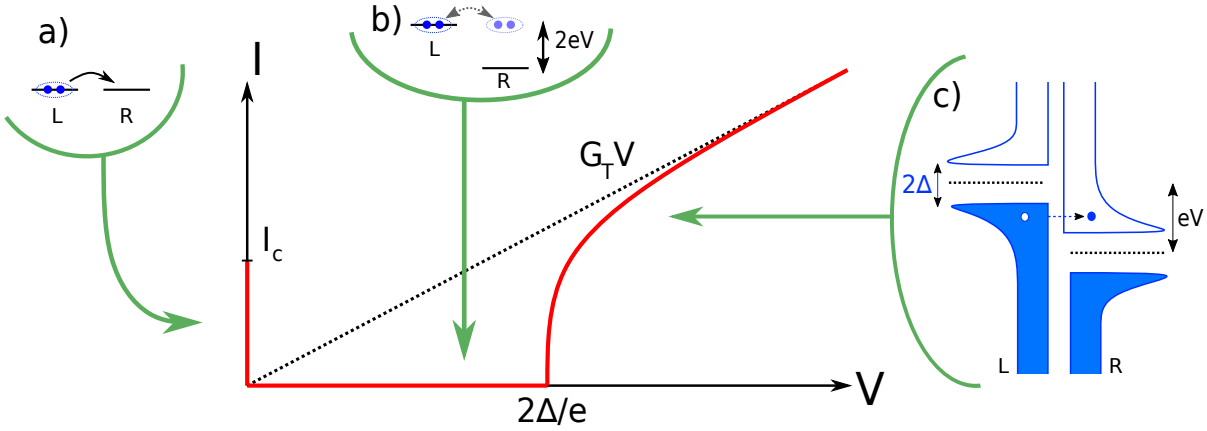

Figure 2.3: The three branches of the I(V) of a superconducting tunnel junction: a) At zero bias, the supercurrent results from the elastic transfer of Cooper pairs from one BCS condensate to the other. b) At $V \neq 0$, the irreversible transfer of Cooper pairs is prohibited: $\langle I\rangle = 0$. c) Above the gap voltage, normal quasiparticles can tunnel, as in a normal junction.

Josephson junctions, which are tunnel junctions between two superconductors, present a more complex behaviour. Recall that in a superconductor, both *Cooper pairs* [42] of charge $2e$ and normal quasi-particles can contribute to the current.

As seen before (Fig.2.2.a), the tunneling of a normal charge involves the creation of a hole-like excitation in the first electrode, and of an electron-like quasiparticle in the second electrode. In a standard BCS superconductor [43], the quasiparticle density of state presents a gap 2Δ around the Fermi energy (Fig.2.3.c). At low temperature, tunneling of quasiparticles can thus only occur if $eV > 2\Delta$. Below this *gap voltage*[1] they cannot contribute to the tunnel current: $I_{qp}(V < 2\Delta/e) = 0$. Right at $V = 2\Delta/e$, the sharp edge of the density of states gives a strongly non-linear I(V). Far above the gap voltage,

[1] for standard Aluminum junctions, $\Delta \simeq 200\ \mu eV \simeq h\times 50$ GHz.

one recovers asymptotically an ohmic behaviour with the *normal state conductance* of the junction G_T (Fig.2.3.c).

The Cooper pairs which reside at the Fermi level on each side of the junction may also contribute to the current, albeit in a non-trivial way. In 1962, Brian Josephson derived the equations which rule this tunnel current [1]:

$$I(t) = I_c \sin(\hat{\phi}(t)), \tag{2.11}$$

$$\hat{\phi}(t) = \frac{2e}{\hbar} \int_{-\infty}^{t} V(\tau) d\tau. \tag{2.12}$$

Here $\hat{\phi}$ is the **superconducting phase difference** across the junction. In a BCS superconductor, a phonon-mediated electron-electron interaction leads to the pairing of electrons close to the Fermi level, which condense to a ground state below a critical temperature [43]. These Cooper pairs are all described by a single macroscopic wave function, and all share the same phase $\hat{\phi}$. This phase is a quantum operator, it may not have a single well-defined value. As an example, a superconducting island with a fixed number of Cooper pairs is in a coherent superposition of all phase values from 0 to 2π.

The **first Josephson equation**(2.11) tells us that a phase difference between the two electrodes of the junction gives rise to a current of Cooper pairs. The scattering approach reveals that this current is carried by **Andreev bound states** (ABS) [44] localized close to the barrier, resulting from the coherent reflexion of quasiparticles at energies below the gap [45]. Each spin-degenerate channel gives rise to a pair of ABS at energy $\pm E_i$ with:

$$E_i = \Delta \sqrt{1 - T_i \sin^2(\hat{\phi}/2)}. \tag{2.13}$$

If we stay at a voltage bias and a temperature well below the gap energy, all the ABS are in their ground state of energy $-E_i$. In the tunnel junction limit of many channels with very weak transmissions, the phase-dependent part of the total energy writes:

$$\hat{H}_J = -\frac{\Delta G_T h}{8e^2} \cos(\hat{\phi}) = -E_J \cos(\hat{\phi}), \tag{2.14}$$

which is called the *Josephson Hamiltonian* [46]. Working from $\hat{H}_J(\hat{\phi})$ one can prove that the number of Cooper pairs having crossed the junction $\hat{N}$ is also a quantum operator, conjugated to $\hat{\phi}$ with $[\hat{\phi}, \hat{N}] = i$ [2]. $\hat{\phi}$ is thus the generator of translations in the $\hat{N}$ manifold, such that:

$$H_J = -E_J \frac{e^{i\hat{\phi}} + e^{-i\hat{\phi}}}{2} = -\frac{E_J}{2} \sum |N+1\rangle\langle N| + |N\rangle\langle N+1|. \tag{2.15}$$

Thus $\hat{H}_J$ couples states with different number of Cooper pairs having crossed the barrier. The **Josephson energy** E_J gives the strength of the tunnel coupling between the two electrodes.

The total current carried by the ABS ground state is given by the current-phase relation:

$$I(\hat{\phi}) = \frac{2e}{\hbar} \frac{dH_J}{d\hat{\phi}}, \tag{2.16}$$

which leads to (2.11) with $I_c = \frac{2e}{\hbar} E_J = \frac{\pi}{2e} \Delta G_T$ the **critical current** of the junction.

The **second Josephson equation**(2.12) describes the evolution of the phase difference $\hat{\phi}$. We know that the wave function of a single particle of charge q moving in an electromagnetic field from x_a to x_b acquires a phase $\frac{q}{\hbar}\int_{x_a}^{x_b}\vec{A}\cdot d\vec{x}$, where $\vec{A}$ is the 4-vector potential. In an electrical circuit, we can gauge away the 3-vector component such that this phase is actually just given by the integral of the scalar potential, i.e the voltage difference $V(x_b)-V(x_a)$ [2]. In superconducting circuits, this phase is accumulated coherently by all the Cooper pairs of the condensate. The evolution with time of $\hat{\phi}$ is ruled by the voltage drop V on the junction. This phase is thus akin to a magnetic flux: if the junction is put in a loop geometry, the value of $\hat{\phi}$ can be set by threading a magnetic field through the loop, through Lenz-Faraday law of induction.

Supercurrent in a dc-biased Josephson junction

Now that we know how the Cooper pair current depends on the phase and how to define this phase, we can complete the I(V) characteristic of the junction below the gap voltage $2\Delta/e$ (Fig.2.3). In this first description of Josephson junctions we will neglect quantum effects other than tunneling and treat the phase as a classical quantity: $\hat{\phi}\to\phi$.

As soon as there is a finite voltage drop $V\neq 0$ on the junction, $\phi(t)=\phi(0)+2eVt/\hbar$ winds up at a rate $\omega_J=2eV/\hbar$, called the **Josephson frequency**. The current $I(t)=I_c\sin\phi(t)$ is then oscillating at ω_J, giving in average *zero dc-current*.

We get a dc-current only if the phase is kept constant, so at *zero dc-bias* (Fig.2.3.a). The resulting current has a value between $-I_c$ and $+I_c$, set by the integral of the voltage $V(t)$ on the junction. This **supercurrent** is dissipation-less: the Joule power dissipated in the junction $P=\langle V(t)I(t)\rangle$ is always zero.

This is because the BCS condensate is a ground state: there is no such thing as an excited Cooper pair. In a single-particle picture, if a Cooper pair from L tunnels elastically while a finite bias voltage is applied, there is no state in R to accommodate it, as it lands $2eV$ above the Fermi level. This process cannot lead to a net charge transfer (Fig.2.3.b). On the other hand at $V=0$ Cooper pairs can tunnel irreversibly as the two condensates in L and R do not have a fixed number of particles.

The non-linear Josephson inductance

Contrary to a normal tunnel junction, a Josephson junction biased below the gap voltage does not behave as a resistor. As it links the evolution of the current I to the applied voltage V, it is actually an *inductor*. To see it better, let us take the derivative with respect to time of equation(2.11):

$$\frac{dI}{dt}=I_c\frac{2e}{\hbar}V\cos(\phi). \tag{2.17}$$

That we may put in a more familiar form:

$$V=\frac{\hbar}{2eI_c}\frac{1}{\cos(\phi)}\frac{dI}{dt}=L(\phi)\frac{dI}{dt}. \tag{2.18}$$

Here $L(\phi)=L_J/\cos(\phi)$, where L_J is called by analogy the **Josephson inductance**. For small excursions of ϕ around a fixed value, the junction behaves effectively as a linear

inductance with a value $L_J/\cos(\phi)$. By tuning the phase close to $\pi/2$, this inductance can be made arbitrary high, prompting its use in some electrical circuits as a tunable *super-inductance* [47]. Surprisingly, this inductance can also be negative! [2]

But more generally, because of the $\cos(\phi)$ term, the junction response to an applied voltage is highly non-linear. This dissipation-free non-linearity comes from the quantum Hamiltonian of the junction, which means that it can **preserve quantum coherence**.

This property has turned the Josephson junction into a much versatile tool for the engineering of quantum devices. Among many are the superconducting quantum bits such as the Cooper Pair Box and its variant the transmon qubit, or the fluxonium qubit, which use Josephson junctions as non-linear inductors to induce anharmonicity in a LC oscillator.

These devices can then be operated as effective two-level systems, as a single-tone probe can only induce coherent transitions between the first two levels of the resonator. Josephson junctions are also a the heart of many devices used in microwave quantum optics, such as quantum-limited amplifiers [3][5][4], 3 and 4-wave mixers [6][7], or single-photon detectors [10][8][9]. In this way, any electrical device which take advantage of this type of non-linearity could in principle be brought down to the quantum regime by implementing it with Josephson junctions[2].

2.2 Interaction of a dc-biased Josephson junction and its environment

This simple picture of a tunnel junction under a perfect voltage bias is inaccurate as soon as we consider a practical implementation of the biasing circuit [48][49]. Any electrical component with a non-zero impedance yields voltage fluctuations that make it impossible to impose a purely dc voltage on the junction. This voltage noise leads to random phase fluctuations that can impact the tunnel current through the Josephson equations. However what may seem like an electrical engineering problem turns out to be connected to the rich physics of out-of-equilibrium, open quantum systems: in a dc-biased Josephson junction subject to voltage fluctuations, Cooper-pair can tunnel inelastically and exchange energy with the electromagnetic environment modes [31].

Electromagnetic environment of a Josephson junction

While discussing the I(V) characteristic of a tunnel junction, we had in mind the kind of minimalist experimental apparatus depicted in Fig.2.4.a): a voltage source **V** directly connected to the terminals of the junction, in series with an ammeter Ⓐ.

In a more realistic setup, the junction would be placed inside some cryogenic enclosure to keep it a very low temperature, typically well below 1K. To connect it to the electronic devices at room temperature without bringing too much heat, we would need some length of resistive wire, that would also be somewhat inductive. The junction would be fabricated on a microchip, and connected through bonding pads. To be consistent we should then

[2]Disclaimer: this may be much easier said than done.

include in the circuit a model of the internal resistances of the voltage source and ammeter, the inductance and resistance of the wires, the stray capacitance between the bonding pads, the geometric capacitance of the junction itself... (Fig.2.4.b)

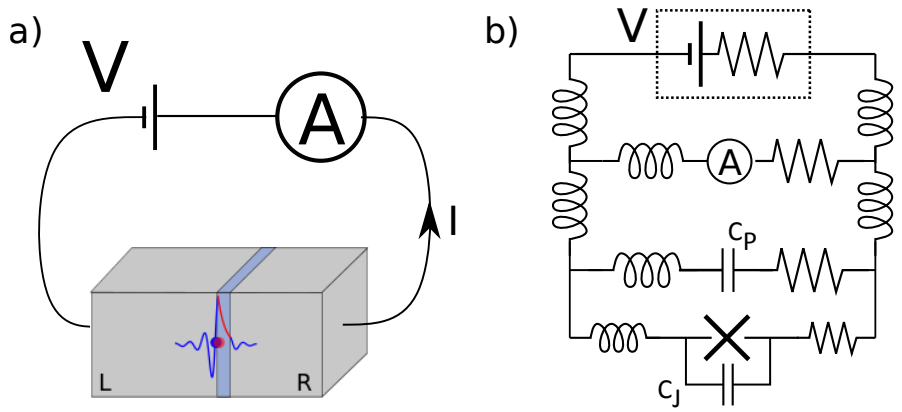

Figure 2.4: a) Ideal tunnel junction I(V) measurement setup. b) Model of a more realistic version including the internal voltage source resistance, the inductance of the dissipative leads going to the Josephson junction (represented here and after by a × symbol), the parasitic shunt capacitances of the bondings pads C_P and the geometric capacitance of the junction C_J.

All these electric components present some voltage noise at their terminals [50]. We know from the fluctuation-dissipation theoremthat at equilibrium, the voltage noise generated by an isolated dipole is proportional to the real part of its impedance [51]. The thermal noise spectral density was derived by Nyquist in 1927 [52]:

$$S_{VV}(\omega) = \int \langle V(t)V(t+\tau)\rangle e^{i\omega\tau} d\tau = 4Re[Z(\omega)]\frac{\hbar\omega}{e^{\beta\hbar\omega}-1} \tag{2.19}$$

In the low frequency limit $\hbar\omega \ll k_B T$, the noise is proportional to the temperature T of the dipole: $S_{VV}(\omega) \simeq 4k_B T Re[Z(\omega)]$. Above $k_B T/\hbar$ this thermal noise is exponentially suppressed, as it is the analogue of black-body radiation for electrical dipoles. A dilution refrigerator can typically bring a sample down to 15 mK, such that this frequency cut-off happens near $\sim$ 300 MHz.

In the high frequency range zero-point fluctuations of quantum origin start to be relevant, with a spectral density given by: $S_{VV}^{ZPF}(\omega) = 2Re[Z(\omega)]\hbar\omega$. It is well known that one cannot extract energy from these vacuum fluctuations. However a dc-biased Josephson junction is a non-linear out-of-equilibrium system, that is sensitive to them, so we will have to take them into account.

Simplifications and hypotheses about the circuit

When dipoles are combined as in our model of a biasing circuit, voltage fluctuations add up for series elements and are divided in parallel associations. We can use standard Thévenin-Norton conversions to cast all these elements as a single frequency-dependent impedance $Z(\omega)$, which constitutes the electromagnetic environment of the junction (Fig.2.5).

How much of its voltage noise falls on the junction? First of all, we know that the tunnel element in the junction is always in parallel of some capacitor, which is at least

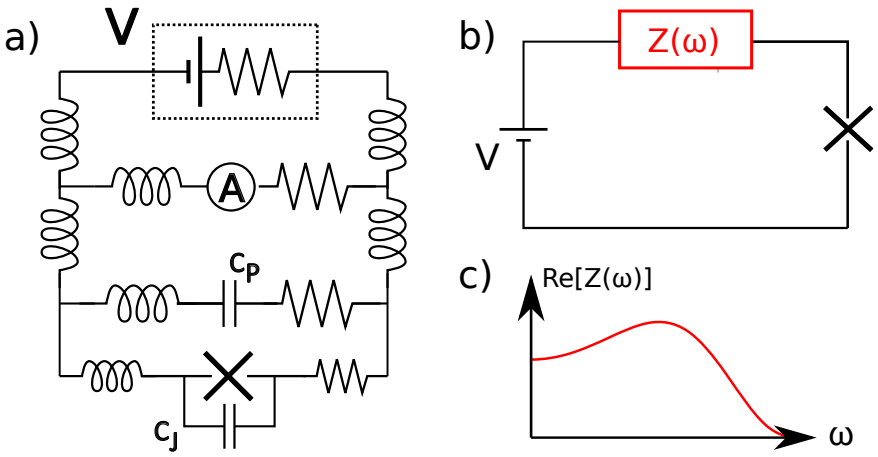

Figure 2.5: a) The complex biasing circuit of figure 2.4 can be cast through Thévenin-Norton transformations into a simpler one. b) This equivalent circuit consists of a perfect voltage source biasing the junction in series with a frequency-dependent impedance $Z(\omega)$ c) What the real part of the impedance seen by the junction may look like: it is non-zero at dc, there is a RC cut-off at high frequency and there may be resonances in between.

the geometric capacitance between the two electrodes C_J. As seen by the junction, this capacitance shorts the impedance of the rest of the circuit: $Z(\omega \to \infty) \to 0$. Thus at high frequencies the voltage noise is shunted and is never seen by the junction. A very rough order of magnitude for impedance in circuits is 100 Ω and C_J is at least a few femtoFarads, such that the RC_J cut-off is at most in the 100 GHz range, similar to the gap energy.

At lower frequencies, we need to worry about the impedance of the tunnel element itself. We have seen that below the gap voltage, a Josephson junction can be seen as a non-linear inductor with $L(\phi) = L_J/\cos(\phi)$. In the presence of voltage noise, which results in a random motion of the phase, it can become very difficult to define the value of its equivalent impedance. However we can say that in general, the **dynamical admittance** of the junction scales **at least** like its critical current I_c.

This can be seen intuitively in some limit cases. Far above the gap voltage, the junction behaves as a normal-metal junction with conductance $G_T = 2eI_c/\pi\Delta$. At zero bias, i.e fixed phase, the junction is an inductor, with admittance $\propto 1/L_J = 2eI_c\cos(\phi)/\hbar$. More generally, the real part of the admittance of a tunnel element can be linked through Rogovin-Scalapino relation to its dc-conductance [53]:

$$Re[Y(V,\omega)] = q\frac{I(V+\hbar\omega/q) - I(V-\hbar\omega/q)}{2\hbar\omega}, \tag{2.20}$$

where $q = 2e$ for the contribution of Cooper pairs to the current and $q = e$ for quasiparticles. If $I_c = 0$, there is no Josephson effect, i.e no tunnel-current of Cooper pairs. It is then safe to say that below the gap voltage, if we go the infinitesimal coupling limit $I_c \to 0$, the tunnel element is an **open circuit** with **zero admittance**. Then all the voltage fluctuations $S_{VV}(\omega)$ from $Z(\omega)$ falls right on the electrodes of the junction.

Note also that at finite applied bias V, the Josephson inductance tends to average to zero in a time $\sim \hbar/2eV$ as we have: $\langle L_J[\phi(t)]\rangle \propto \langle 1/\cos(2eVt/\hbar)\rangle = 0$, which makes defining its admittance much easier.

In this spirit and to simplify the problem, we will study **small Josephson junctions** under a **dc-voltage bias** and in the presence of an arbitrary **electromagnetic environment**, which acts as a bath of voltage fluctuations. Indeed a small junction (area $\sim 100 \times 100$ nm^2) has at the same time a small geometric capacitance and a low critical current. Thus it cannot shunt away all the voltage noise coming from the environment. At high frequencies ($\gtrsim 1$ GHz) this noise consists of vacuum fluctuations, that can prompt new phenomena in the junction. It is then necessary to promote the phase variable ϕ to a proper quantum operator $\hat{\phi}$, to account for the zero-point fluctuations (ZPF). Our treatment will be Hamiltonian, and will be perturbative in I_c (that we assumed small) to second order.

A Hamiltonian description of the environment

Voltage noise arise from the real part of the impedance of $Z(\omega)$, i.e its dissipative part. At first sight it seems impossible to provide a Hamiltonian treatment of the problem, as dissipation plays a key role in it. However we can decompose the degrees of freedom of the environmental bath as a set of fictitious harmonic oscillators coupled linearly to the junction, whose dynamics can be treated exactly. In the limit of a great number of these fictitious modes, this model effectively implements a dissipative coupling between the junction and its environment: this is known as the Caldeira-Leggett model [54].

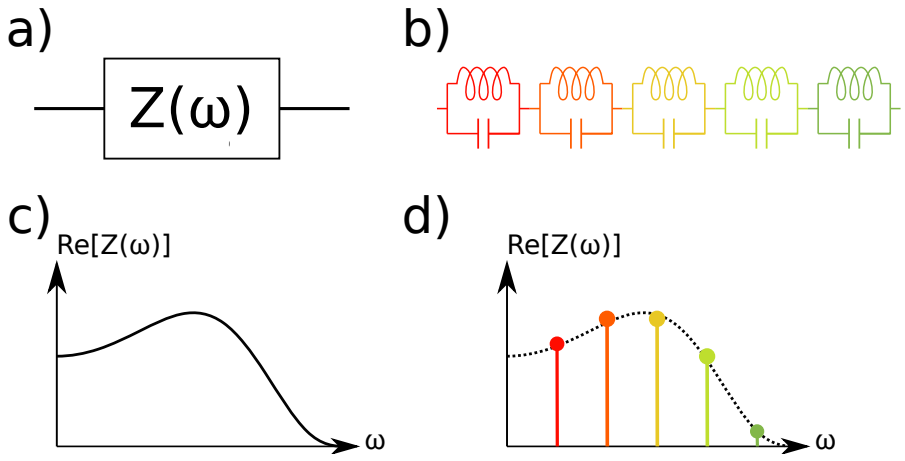

Figure 2.6: a) A linear impedance $Z(\omega)$ models the environment of the junction. b) It can be replaced in the circuit by a collection of LC modes of various frequencies and impedances. c) The real part of $Z(\omega)$ has some frequency dependence. d) Real part of the impedance of the LC modes. An infinite number of LCs can model any $Z(\omega)$.

The environment is described by an impedance $Z(\omega)$ at a finite temperature. We divide the frequency axis in some number of bins, and associate a LC resonator to each bin. The values of L and C are chosen such that it can effectively replace $Z(\omega)$ in each frequency bin (Fig.2.6).

The Hamiltonian describing the environmental bath is the sum of the Hamiltonians of all the modes in the decomposition. Let us start by defining the Hamiltonian of an electrical oscillator. The average energy stored in a LC resonator is classically given by:

$$\langle E \rangle = C\frac{\langle V^2 \rangle}{2} + L\frac{\langle I^2 \rangle}{2} \tag{2.21}$$

$$= \frac{\langle Q^2 \rangle}{2C} + \frac{\langle \Phi^2 \rangle}{2L}, \tag{2.22}$$

where we switched from the standard variables of electrical engineering, the voltage V across the capacitor C and the current I through the inductance L, to the ones that are more convenient in quantum mechanics: the charge $Q = \int I(t)dt$ accumulated on the plates of C and the magnetic flux $\Phi = \int V(t)dt$ through the loops of L [2]. We replace these classical variables with quantum operators who follow the commutation relation:

$$Q \to \hat{Q},\ \Phi \to \hat{\Phi},\ [\hat{\Phi}, \hat{Q}] = i\hbar. \tag{2.23}$$

We then follow with the procedure of canonical quantization and introduce the creation and annihilation operators $\hat{a}^\dagger$ and $\hat{a}$ through:

$$\hat{\Phi} = \sqrt{\frac{\hbar Z_c}{2}}(\hat{a}e^{-i\omega t} + \hat{a}^\dagger e^{+i\omega t}),\ \hat{Q} = \sqrt{\frac{\hbar}{2Z_c}}\frac{\hat{a}e^{-i\omega t} - \hat{a}^\dagger e^{+i\omega t}}{i}, \tag{2.24}$$

where $Z_c = \sqrt{L/C}$ is the characteristic impedance of the resonator and $\omega = 1/\sqrt{LC}$ its resonance frequency. The non-hermitian operators $\hat{a}$ and $\hat{a}^\dagger$ follow the bosonic commutation relation: $[\hat{a}, \hat{a}^\dagger] = 1$. The harmonic oscillator Hamiltonian then reads:

$$\hat{H} = \hbar\omega\left(\hat{a}^\dagger\hat{a} + \frac{1}{2}\right). \tag{2.25}$$

As a consequence of the quantization procedure, the energy eigenstates of the resonator are states where it contains a half-integer $(n+1/2)$ number of quanta of energy $\hbar\omega$. These are quanta of electromagnetic energy stored as magnetic field through the inductance L and electric field between the plates of C.

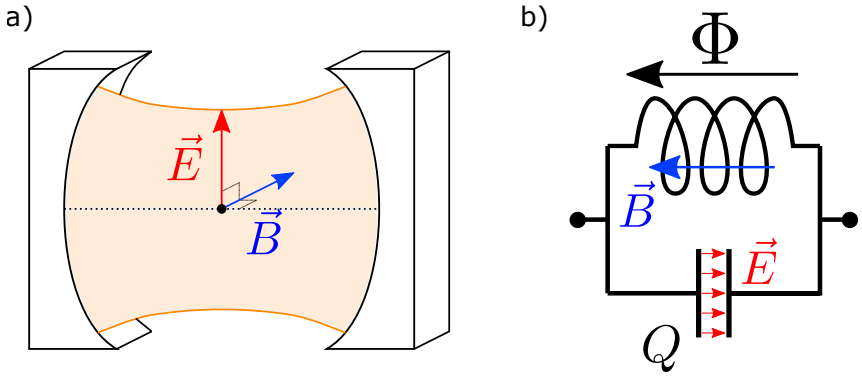

Figure 2.7: Comparison of electromagnetic cavities in the visible range (a) and in microwave circuits (b). a) Two spherical mirrors define a Fabry-Pérot cavity. The electric field and the magnetic field of a given mode form a single degree of freedom, which can be quantized and yield two conjugated quantities. b) In a LC circuit, the magnetic field through the coil and the electric field between the plates of the capacitor are also conjugated. It is however more practical to work with the magnetic flux Φ and the charge through the capacitor Q.

These quanta have been known for quite some time in condensed matter physics as **surface plasmons**. Indeed in a conductor the macroscopic observables such as voltage,

current, and charge result from the continuous displacement of the electronic fluid with respect to the underlying ionic lattice, which behaves as a plasma. However it has become customary to describe microwave fields in superconducting circuits as made of **photons**, in particular since the advent of circuit-QED [11] - even though these photons have no polarization, i.e spin degree of freedom. In this work where we have quantum optics experiments in mind we will stick to the latter term.

Commentary on the charge tunneling operator

From the commutation relation (2.23) we see that the magnetic flux operator $\hat{\Phi}$ generates translation in the manifold of charge states:

$$e^{-iq\hat{\Phi}/\hbar}|Q\rangle = |Q+q\rangle. \tag{2.26}$$

This magnetic flux, which is the integral of the voltage, is proportional to the phase difference across the dipole:

$$\hat{\phi} = \frac{2e}{\hbar}\hat{\Phi}. \tag{2.27}$$

We can know understand better the role of the Josephson Halmiltonian (2.14): under the action of the $e^{i\hat{\phi}}$ operator, two true electrons are taken from one electrode of the junction and put in the other one, increasing its charge by $-2e$. The current I is proportional to the difference of forward and backward tunneling rates, hence it reads: $I = 2eE_J(e^{i\hat{\phi}} - e^{-i\hat{\phi}})/2i\hbar = (2e/\hbar)\sin(\hat{\phi})$.

In a circuit of finite impedance, there can also be a dynamical response of the environment to this sudden charge increase, that may prompt new tunneling mechanisms: this is the framework of the $P(E)$ theory [31].

The P(E) theory of a dc-biased Josephson junction

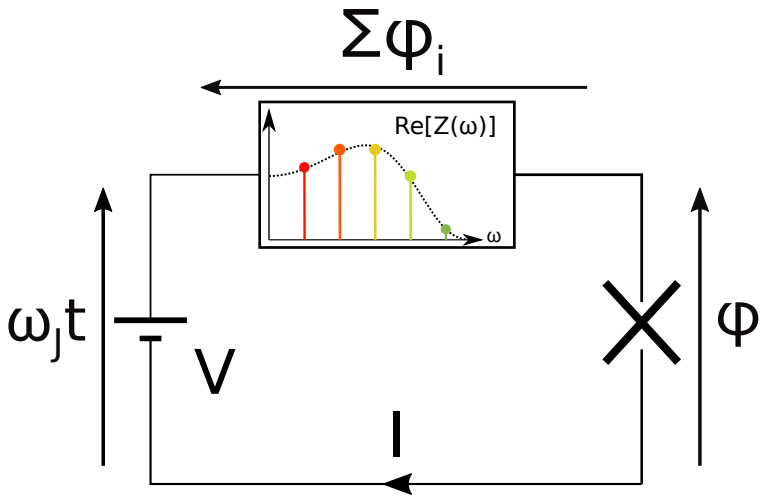

Figure 2.8: The phase ϕ across the junction is the difference of the phase bias imposed by V and the phase across the environment impedance.

We consider the circuit of figure 2.8 which represents a Josephson junction coupled to an arbitrary linear electromagnetic environment. We decompose $Z(\omega)$ as a sum of N

LC oscillators, with a set of resonance frequencies ω_i, characteristic impedances Z_c^i and equilibrium thermal occupation $n_i = (e^{\beta\hbar\omega_i} - 1)^{-1}$. The tunnel coupling being weak, we make the approximation that the Hamiltonian of the system is simply the sum of the Josephson Hamiltonian (2.14) and the Hamiltonians of all the modes:

$$H = -E_j \cos\hat{\phi} + \sum_i \hbar\omega_i \left(\hat{a}_i^\dagger \hat{a}_i + \frac{1}{2}\right). \tag{2.28}$$

We can compute the average dc-current across the junction by using second-order perturbation theory in H on $\hat{I}$:

$$\hat{I}(t) = I_0(t) + o(H) \tag{2.29}$$

$$\hat{I}(t) - I_0(t) = I_1(t) + o(H^2). \tag{2.30}$$

In the absence of tunnel coupling, the average of the first order term vanishes: $\langle I_0(t)\rangle = 0$. We then have:

$$\langle I_1(t)\rangle = \left\langle \frac{-i}{\hbar}\int_{-\infty}^{t} dt'[H(t'), I_0(t)]\right\rangle \tag{2.31}$$

$$= \frac{-i}{\hbar}\int_{-\infty}^{t} dt'\langle[-E_J\cos\hat{\phi}(t'), I_c\sin\hat{\phi}(t)]\rangle \tag{2.32}$$

$$= \frac{2ieE_J^2}{\hbar^2}\int_{-\infty}^{0} dt'\langle[\cos\hat{\phi}(t'), \sin\hat{\phi}(0)]\rangle \tag{2.33}$$

$$= \frac{eE_J^2}{2\hbar^2}\int_{-\infty}^{0} dt'\langle e^{i\hat{\phi}(t')}e^{-i\hat{\phi}(0)} - e^{-i\hat{\phi}(t')}e^{i\hat{\phi}(0)}\rangle + \text{h.c.} \tag{2.34}$$

$$= \frac{eE_J^2}{2\hbar^2}\int_{-\infty}^{+\infty} dt'\langle e^{i\hat{\phi}(t')}e^{-i\hat{\phi}(0)}\rangle - \langle e^{-i\hat{\phi}(t')}e^{i\hat{\phi}(0)}\rangle, \tag{2.35}$$

where we have removed the terms of the form $e^{i\hat{\phi}(t')}e^{i\hat{\phi}(0)}$ as they average to zero in the absence of a phase reference at finite bias V. In the last line the first term in brackets correspond to forward tunneling (the charge increases by $2e$) and the second term is backward tunneling: the net current is the difference of these two contributions.

To evaluate these correlators, we need to compute the phase correlation function. From Kirchhoff laws, we know that the voltage drop on the junction is the difference between the voltage bias V set by the source and the voltage drop across the environment impedance $Z(\omega)$ (Fig.2.8). For the superconducting phase difference $\hat{\phi}(t)$, we thus have after integration:

$$\hat{\phi}(t) - \hat{\phi}(0) = \omega_J t - \sum_i \sqrt{\frac{2e^2 Z_c^i}{\hbar}}(\hat{a}_i e^{-i\omega_i t} + \hat{a}_i^\dagger e^{+i\omega_i t}), \tag{2.36}$$

where we introduced again the Josephson frequency $\omega_J = 2eV/\hbar$. We can subtract from the value of the phase the deterministic evolution coming from the applied voltage V:

$$\langle e^{i\hat{\phi}(t)}e^{-i\hat{\phi}(0)}\rangle = e^{i\omega_J t}\langle e^{i\tilde{\phi}(t)}e^{-i\tilde{\phi}(0)}\rangle, \tag{2.37}$$

where $\tilde{\phi}(t) = \hat{\phi}(t) - \omega_J t$ describes only the phase fluctuations coming from the environment. This last correlator may be calculated if we suppose that E_J is so weak that the

environment stays close to thermal equilibrium, even after a tunneling event. Then $\tilde{\phi}$ is the sum of the phases of a collection of oscillators at thermal equilibrium, i.e the sum of a collection of gaussian variables. It is then itself gaussian, and a generalized Wick theorem gives:

$$\langle e^{i\tilde{\phi}(t)}e^{-i\tilde{\phi}(0)}\rangle = e^{\langle[\tilde{\phi}(t)-\tilde{\phi}(0)]\tilde{\phi}(0)\rangle} = e^{J(t)}, \tag{2.38}$$

where we introduced $J(t)$ the phase-phase correlation function. As there are no correlations between the fluctuations in different frequency bands, i.e associated to different fictitious LC oscillators, we can compute the $\tilde{\phi}(t)$ correlation functions at equilibrium:

$$\langle\tilde{\phi}(t)\tilde{\phi}(0)\rangle = \sum_i \langle\phi_i(t)\phi_i(0)\rangle = \sum_i \frac{4\pi e^2 Z_c^i}{h}(2\langle n_i\rangle + 1)e^{-i\omega_i t}. \tag{2.39}$$

We now express the LC parameters of the i-th oscillator in function of $Re[Z(\omega)]$, and go to the continuum limit $N \to \infty$:

$$\langle\tilde{\phi}(t)\tilde{\phi}(0)\rangle = 2\int_{-\infty}^{+\infty} \frac{d\omega}{\omega}\frac{Re[Z(\omega)]}{R_Q}\frac{e^{-i\omega t}}{1-e^{-\beta\hbar\omega}}, \tag{2.40}$$

where the superconducting quantum of impedance $R_Q = h/4e^2$ gives the natural scale of impedance to which we should compare $Re[Z(\omega)]$ to see if phase fluctuations matter or not.

The correlation function $J(t)$ is finally expressed as:

$$J(t) = \langle\tilde{\phi}(t)\tilde{\phi}(0)\rangle - \langle\tilde{\phi}(0)\tilde{\phi}(0)\rangle \tag{2.41}$$

$$= 2\int_0^{+\infty} \frac{d\omega}{\omega}\frac{Re[Z(\omega)]}{R_Q}\left\{\coth\left(\frac{\beta\hbar\omega}{2}\right)[\cos(\omega t)-1] - i\sin(\omega t)\right\}. \tag{2.42}$$

The tunnel current $\langle I(t)\rangle$ is linked to the Fourier transform of $e^{J(t)}$, usually called $P(E)$:

$$P(E) = \frac{1}{h}\int_{-\infty}^{+\infty} e^{iEt/h}e^{J(t)}dt. \tag{2.43}$$

We finally have:

$$\langle I(t)\rangle = I_{dc} = \frac{\pi e E_J^2}{\hbar}(P(2eV) - P(-2eV)). \tag{2.44}$$

Interpretation of the $P(E)$ result

We have expressed the current through a dc-biased Josephson junction with the help of a function $P(E)$, linked to the phase-phase correlation function. To interpret physically our result, let us have a look at the properties of this function in simple limit cases. First of all, $P(E)$ respects the detailed balance:

$$P(-E) = P(E)e^{-\beta E}. \tag{2.45}$$

Such that a zero temperature, we have $P(E) = 0$ for $E < 0$. In the case of an environment with a low impedance compared to R_Q at every frequency, we can develop $e^{J(t)} \simeq 1 + J(t)$ and find:

$$P(E)_{\{T=0, Re[Z]\ll R_Q\}} \simeq \left(\frac{2}{E}\frac{Re[Z(E/\hbar)]}{R_Q} + \delta(E)\right)e^{J(\infty)}, \tag{2.46}$$

which leads to:

$$I_{dc}(V) \simeq \frac{\pi e E_J^2}{\hbar} P(2eV) \simeq \frac{\pi E_J^2 e^{J(\infty)}}{\hbar V} \frac{Re[Z(2eV/\hbar)]}{R_Q}. \tag{2.47}$$

The work provided by the voltage source for each tunneling charge is $2eV$, such that the total power dissipated by the flow of this dc-current is:

$$P = V \times I_{dc} = \frac{\pi E_J^2 e^{J(\infty)}}{\hbar} \frac{Re[Z(\omega_J)]}{R_Q} = \frac{I_c^2 e^{J(\infty)} Re[Z(\omega_J)]}{2}. \tag{2.48}$$

This coincides with the ac-power dissipated by a current of amplitude $I_c e^{J(\infty)/2}$ injected into $Z(\omega_J)$. This ac-current is the oscillating part of the tunnel current resulting from the constant bias V, with an amplitude reduced by $e^{J(\infty)/2}$ [3]. The power needed to maintain this ac-current is provided by the dc-voltage source, *via* the tunneling of charges through the junction. Thus we can get an irreversible current by an inelastic process, where **each Cooper pair creates one photon in the environment** at frequency $2eV/\hbar$ (Fig.2.9).

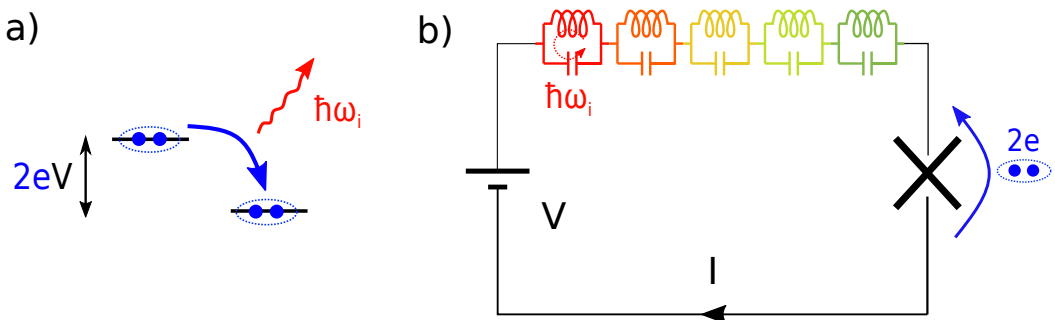

Figure 2.9: a) If $2eV = \hbar\omega_i$, a Cooper pair can tunnel inelastically and create one photon at frequency ω_i. b) There is then a dc-current flowing in the circuit, associated to the dissipation of ac-power in the environment.

The amplitude of this ac-current being fixed, the dc-current is directly proportional to $Re[Z(\omega_J)]$, i.e to how dissipative the environment is at frequency $2eV/\hbar$.

More generally, the $P(E)$ function can be understood as the probability density for a single Cooper pair of exchanging the energy E with the environment. The non-linearity coming from the expansion of $e^{i\tilde{\phi}(t)}$ means that multi-photonic processes can also occur. Two-photon processes can be predicted by expanding $e^{J(t)}$ to second order:

$$I_{dc}(V) \simeq \frac{\pi E_J^2 e^{J(\infty)}}{\hbar V} \left(\frac{Re[Z(\omega_J)]}{R_Q} + \int d\omega \frac{Re[Z(\omega_J - \omega)]}{R_Q \times (\omega_J - \omega)} \frac{Re[Z(\omega)]}{R_Q} \right). \tag{2.49}$$

We can interpret the second term on the right as a mechanism where $2eV$ is split between one photon emitted at frequency ω and a second photon at $\omega_J - \omega$, such that the total energy is conserved. As $Re[Z(\omega)]$ contains a continuum of frequency, there is an infinite number of frequency pairs that respect this relation and thus infinitely many possible ways of creating photon pairs. The probability associated to each process is weighted by the product $\frac{Re[Z(\omega_J-\omega)]}{R_Q \times (\omega_J-\omega)} \frac{Re[Z(\omega)]}{R_Q}$.

[3] The meaning of this factor will become clearer later on.

A n-th order expansion of $e^{J(t)}$ would show n-photon processes, whose magnitude is again of order n in $\frac{Re[Z]}{R_Q}$, so less and less probable as n increases in this low impedance hypothesis.

$P(E)$ is not restricted to weak effects. More generally, $P(E > 0)$ describes photon emission by the junction while $P(E < 0)$ is the probability for photon absorption. Equation(2.44) tells us that for a finite bias $V \neq 0$, we will have forward tunneling only if the excess energy $2eV$ of a single Cooper pair can be dissipated in the environment, and back-ward tunneling (giving a negative contribution to the current) if modes in the environment can give away $2eV$.

Limitations and hypotheses of the $P(E)$ theory

We have derived analytical predictions for $P(E)$ in the simple case of zero temperature and a low impedance at every frequency. That last condition may be somewhat relaxed: in equation (2.42) $Re[Z(\omega)]$ is divided by $R_Q \times \omega$, such that if $Re[Z(\omega)]$ is comparable to R_Q but only in a frequency window $\Delta\omega$ smaller than ω, then their integrated ratio is small compared to 1 and we may still expand $e^{J(t)}$ to first order only[4].

At a finite temperature, it is still possible to derive simple predictions for the dynamics of the system. We can distinguish between the modes at frequencies well below the thermal cut-off ($\omega \ll k_B T/\hbar$), where $P(-\hbar\omega) \simeq P(\hbar\omega)$ such that photon absorption and emission are equiprobable, which give in average zero contribution to the dc-current; and the modes at high frequencies ($\omega \gg k_B T/\hbar$), which are empty at equilibrium and thus can only absorb photons from the junction and give rise to a net dc-current. The first ones have high occupation numbers, so they are deep in the classical regime, meanwhile the others can be considered in the quantum regime. Modes at intermediate frequencies require a more elaborate treatment, with e.g the numerical calculation of their $P(E)$ function, but we see that setting $2eV > k_B T$ puts us in a regime where single photon processes are simple to understand as only forward processes can happen.

The $P(E)$ theory is perturbative in the Josephson Hamiltonian, as we had to suppose that E_J was "small enough" to compute the tunnel current. The higher order terms in Ej remain much smaller than the first order one that we have derived if $E_J P(E) \ll 1$. By multiplying both sides of this inequality by E_J, we see that this condition holds if the inelastic tunnel current (of order $E_J^2 P(2eV)$) stays small compared to $I_c \propto E_J$.

Finally, in the very simple model we used we did not explicitly include dissipation in the collection of LC modes. In theory turning on the inelastic tunneling process should fill the mode at frequency ω_J with an ever increasing number of photons, one for each tunneling Cooper pair (plus all the other frequencies where multi-photon processes can put energy). In practice there is of course some dissipation in the environment, which keeps the number of photons finite. A further condition for the validity of the above calculation is that this number should be close enough to the equilibrium value to leave the fluctuations of the phase across the junction unaffected. We then treat cases where once a photon is created, the mode gets empty rapidly, before another Cooper pair tunnels. In a situation where this condition would not be respected, we can expect that photon absorption from the environment to the junction becomes relevant, and changes the tunneling dynamics.

[4] this would be the case for a mode with a high quality factor.

The semi-classical ac-Josephson effect

In the first section of this chapter, we explained that if we apply a dc-bias V on the junction, it gives rise to an ac-current $I(t)$ at frequency $\omega_J = 2eV/\hbar$: this is called the **ac-Josephson effect**. In that case the junction acts as a perfect dc-ac converter.

Suppose that we consider again the circuit of Fig.2.8 but decide to treat it classically, i.e consider that the phase ϕ is not a quantum variable but simply a quantity proportional to the integral of a classical voltage. Such an approach would be justified for a very low-impedance environment. The tunnel current $I = I_c \sin(\phi)$ through the junction is still coupled to the impedance of the environment simply because they are in series in this electrical circuit (Fig.2.8). Let us derive the behaviour of this circuit at increasing order in $I_c \propto E_J$:

At zero-th order in I_c, there is no tunnel current:

$$I \simeq I^0 = 0. \tag{2.50}$$

If the impedance at low frequency of the environment is zero (which we will suppose for simplicity), the voltage provided by the source drops on the junction such that:

$$V_J^0 = V. \tag{2.51}$$

To first order in I_c, the current through the circuit is then:

$$I^1(t) = I_c \sin(\phi^0(t)) = I_c \sin(\omega_J t), \tag{2.52}$$

where we choose $\phi(0) = 0$ for simplicity. The expression for $\omega_J = 2eV/\hbar$ looks deeply quantum as it involves $\hbar$, however in a fully classical picture we **cannot** interpret this as the result of microscopic processes, where one tunneling Cooper pair creates one photon. Here $2e/\hbar$ is simply the *dc-ac ratio* of our non-linear element.

The ac-current $I^1(t)$ is injected in $Z(\omega)$, which then presents an oscillating voltage drop at its terminals which reads:

$$V_e^1(t) = I_c \times \{Re[Z(\omega_J)] \sin(\omega_J t) + Im[Z(\omega_J)] \cos(\omega_J t)\}. \tag{2.53}$$

There is then an additional voltage drop on the junction:

$$V_J^1 = -V_e^1(t), \tag{2.54}$$

which gives another phase term after integration:

$$\phi^1(t) = I_c \times \{Re[Z(\omega_J)] \cos(\omega_J t) - Im[Z(\omega_J)] \sin(\omega_J t)\}/V. \tag{2.55}$$

If $|\phi^1| \ll \pi$, we have:

$$\sin(\phi^0 + \phi^1) = \sin(\phi^0)\cos(\phi^1) + \cos(\phi^0)\sin(\phi^1) \tag{2.56}$$

$$\simeq \sin(\phi^0) + \cos(\phi^0) \times \phi^1, \tag{2.57}$$

which holds if $|Z(\omega_J)| \times I_c \ll \pi V$, i.e if the voltage drop coming from the oscillating tunnel current is small compared to the applied bias voltage V.

The current at second order is then:

$$I^{(2)}(t) = I_c^2 \cos(\omega_J t)\{Re[Z] \cos(\omega_J t) - Im[Z] \sin(\omega_J t)\}/V. \tag{2.58}$$

The time average of $I^{(2)}(t)$ gives the value of the dc-current to second order:

$$I_{dc} \simeq \langle I^{(2)}(t) \rangle = I_c^2 Re[Z(\omega_J)]/2V. \tag{2.59}$$

Comparison with the $P(E)$ theory prediction

A semi-classical treatment of the {junction+environment} system also predicts a finite dc-current I if the environment is dissipative at the frequency $2eV/\hbar$. This result may be compared with the $P(E)$ prediction (2.47) which was derived under the same hypothesis of a low impedance environment:

$$I_{dc}^{P(E)} = \frac{\pi E_J^2 e^{J(\infty)}}{\hbar V} \frac{Re[Z(2eV/\hbar)}{R_Q} = I_c^2 e^{J(\infty)} Re[Z(\omega_J)]/2V \tag{2.60}$$

Surprisingly, these two expressions that were derived using widely different formalisms match very well. They only differ by the term $e^{J(\infty)}$, which can be computed through:

$$\begin{aligned} J(\infty) &= \lim_{t\to\infty} \langle [\tilde{\phi}(t) - \tilde{\phi}(0)]\tilde{\phi}(0)\rangle & (2.61)\\ &= -\langle \tilde{\phi}(0)^2 \rangle & (2.62)\\ &= -\sum_i \frac{4\pi e^2 Z_c^i}{h} (2\langle n_i \rangle + 1) & (2.63)\\ &= -2\int_{-\infty}^{+\infty} \frac{d\omega}{\omega} \frac{Re[Z(\omega)]}{R_Q} \frac{1}{1-e^{-\beta\hbar\omega}} & (2.64) \end{aligned}$$

With $\langle \tilde{\phi}(\infty)\tilde{\phi}(0)\rangle = 0$ as correlations vanish at infinite time difference. We can interpret $I_c^* = I_c e^{-\langle\tilde{\phi}^2\rangle/2}$ as a **renormalized critical current**, that is reduced by the phase fluctuations from the environment. A fully classical treatment of the ac-Josephson effect in the presence of a finite temperature impedance would also show some reduction of the current, as the phase gets blurred by thermal agitation. However $P(E)$ predicts that this renormalization occurs even at zero temperature, where all the modes of the environment are empty. They then contribute to the phase noise through their **zero-point fluctuations**, which of course cannot be derived in a classical treatment of the junction.

These phase zero-point fluctuations turn out to also be needed to explain the **multi-photon emission** we derived through $P(E)$. If we take to higher orders in I_c our calculation of the ac-Josephson effect, we will get additional contributions to the dc-current, that are associated to the dissipation of ac-current at harmonics of the frequency ω_J, i.e at frequencies $\omega_k = k \times \omega_J$ such that $\hbar\omega_k = k \times 2eV$. In a semi-classical interpretation, we would say that k Cooper pairs tunneling together create one single photon at ω_k. These co-tunneling processes were not considered in $P(E)$, as we stayed to second order in I_c. By contrast, $P(E)$ predicts multi-photon processes, i.e emission at **subharmonics** of the Josephson frequency that cannot be derived classically at zero temperature. These processes are prompted by the zero point fluctuations of the phase coming from the environment, and are as such of a quantum nature.

Remark: when is single-charge tunneling relevant?

The first works on Josephson junction-based circuits were free of most of these considerations, as they used "big" junctions, with areas of the order of a fraction of a square

millimetre and relatively high critical currents, in quite low-impedance circuits. These big junctions have at the same time a small Josephson inductance and relatively high geometric capacitance, which mean that they can easily screen the voltage fluctuations coming from the environment[5]. From a dynamics point of view, this coincides with the junction having a high Josephson energy and a low electrostatic charging energy $E_C = e^2/2C$, such that the phase behaves as a classical variable, while the excess charging energy associated with the tunneling of Cooper pairs does not perturb the circuit.

On the other hand, nanoscale junctions present a different kind of physics. These junctions cannot shunt away the environmental phase fluctuations. This equilibrium phase noise consists mostly of thermal fluctuations up to frequency $k_B T/\hbar$, but also of quantum zero-point fluctuations, that become relevant at higher frequencies. These fluctuations also scale as the impedance of the environment, so a small junction in series with high impedances will be particularly sensitive to their effect and may display non-trivial dynamics at frequencies above the thermal cut-off. At the same time a high impedance environment can react strongly to the tunnel current, and may give a strong counteraction to the dynamics of the junction.

Finally, in small normal junctions connected to high impedance circuits, single-electron tunneling can also couple to electromagnetic modes. Indeed after one tunneling event the charge on one electrode changes by e, which can be described by the action of the operator $e^{-ie\Phi\hbar}$. One has also to take into account the kinetic degree of freedom of quasiparticles, which make the calculation more involved. The $P(E)$ theory was developed in the 1990's to describe small normal-metal junctions, where phase fluctuations from the environment result in a *reduction* of the conductance of the junction. This phenomenon is called Dynamical Coulomb Blockade (DCB) [31]. Here we used the same tools to predict a closely related phenomenon, the apparition of inelastic tunneling processes in Josephson junctions resulting in a dc-current below the gap voltage, that we will call Incoherent Cooper-Pair Tunneling (ICPT) [55].

2.3 Experimental observations of ICPT

As mentioned earlier, the tools of the $P(E)$ theory have been developed in the 1990's in order to describe the $I(V)$ of small dc-biased junctions. The first experiments focused on the case of a normal tunnel junction in series with an ohmic resistance R, and showed a reduction of the differential conductance of the junction for values of R comparable to the normal quantum of impedance $R_K = h/e^2$, which plays the same role in normal junction as R_Q does in Josephson junctions.

Another way of generating strong $P(E)$ effects in the $I(V)$ is to introduce resonances in the environment of the junction. The real part of the impedance at the resonant frequency can reach very high values, of the order of R_Q, making $P(E)$ effects more prominent. It also gives a clearer picture of where are created the photons emitted by tunneling charges: as excitations of the resonant mode.

These resonances can be engineered by microfabricating lumped-element resonators close

[5]Furthermore in low-impedance circuits the effective capacitance C_{eff} of the junction is renormalized to a much higher value than C_{geo}.

to the junction. However to be above the thermal frequency cut-off and probe quantum effects, one needs to study the emission of photons at GHz frequencies, where microfabrication becomes more involved. At these high frequencies it is natural to resort to distributed circuits, where the resonances between segments of microwave transmission lines can implement well-defined modes. It also makes possible guiding the photons created by the junction out of the chip, e.g to some detector.

This approach was implemented in two different experiments that we will describe now. The first one aimed a probing the effect of a transmission line on the $I(V)$ of a small superconducting tunnel junction. It validated the mechanism of single-photon emission by inelastic Cooper pair tunneling [32]. The second experiment, based on a similar setup, also collected the microwave photons emitted by the Josephson junction, probing for the first time the photonic side of ICPT [33].

2.3.1 Observation of ICPT in the dc-current

Enhancing $Re[Z(\omega)]$ with $\lambda/4$ resonators

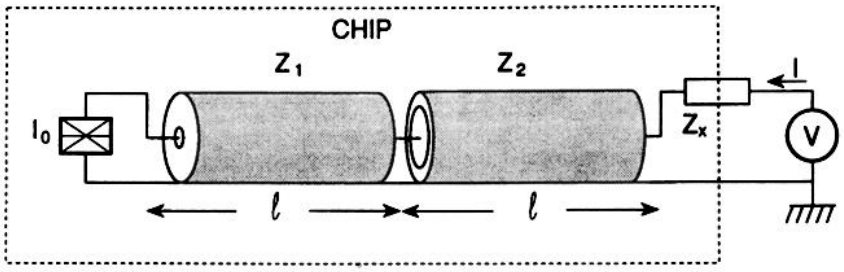

Figure 2.10: Circuit used by Holst et al. for the 1994 experiment. An ultrasmall Josephson junction (box symbol ⊠) is connected to a voltage source through two segments of transmission line built on-chip.

The sample used by Holst *et al* in 1994 [32] is represented on figure 2.10. Two ultrasmall Al/AlOx/Al junctions, put in parallel in a loop, form a Superconduting QUantum Interference Device (SQUID). Well below its self-resonance frequency the SQUID behaves as a single Josephson junction, whose critical current I_c can be tuned by threading a magnetic field Φ through the loop, with $I_c(\Phi) \simeq I_c \times |\cos(e\Phi/\hbar)|$. This equivalent junction has a rather small area of 60×60 nm^2, resulting in a small geometric capacitance $C_J \simeq 1.5$ fF, a high normal state tunnel resistance R_T, and a small critical current I_c.

The junction is shunted to ground on one side, and biased on the other side by a voltage source through a load impedance which is modelled as a resistor of $Z_x \simeq 110\ \Omega$, and two short segments of CPW transmission lines with wave impedances $Z_1 \simeq 100\ \Omega$ and $Z_2 \simeq 28\ \Omega$ respectively. The environment of the junction is then given by Z_x, transformed by resonances in Z_1 and Z_2, and shunted by the parallel association with C_J.

We recall in figure 2.11 the effect of a segment of transmission line on a given load impedance (see appendix C for a detailed derivation). The sample from Fig.2.10 presents modes with impedance $\simeq 1.4$ kΩ at resonance and a full-width at half maximum (FWHM) of $\simeq 2$ GHz. The fundamental resonance occurs at $\omega_r = 2\pi \times 22$ GHz, where the

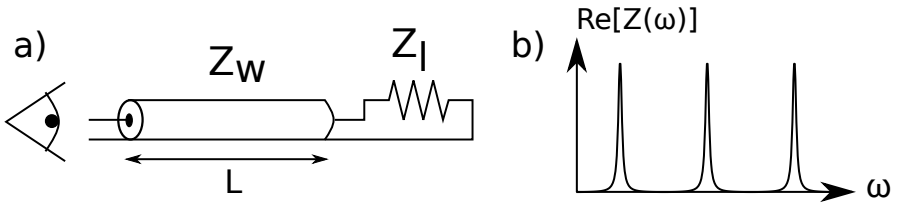

Figure 2.11: a) The impedance Z_l seen through some length L of transmission line Z_w shows resonances. b) If $Z_w > Z_l$, these resonances happens at odd multiples of the fundamental resonant frequency. The impedance on top of the resonance is Z_w^2/Z_l, and the quality factor is $Q = \pi Z_w/4Z_l$.

impedance given by the parasitic capacitance of the junction is $(jC_J\omega_r)^{-1} \simeq j \times 4.8$ kΩ. Thus C_J cannot shunt efficiently the voltage fluctuations coming from $Re[Z(\omega)]$, and we expect to detect ICPT in the dc-current.

Peaks in the I(V) below the gap voltage

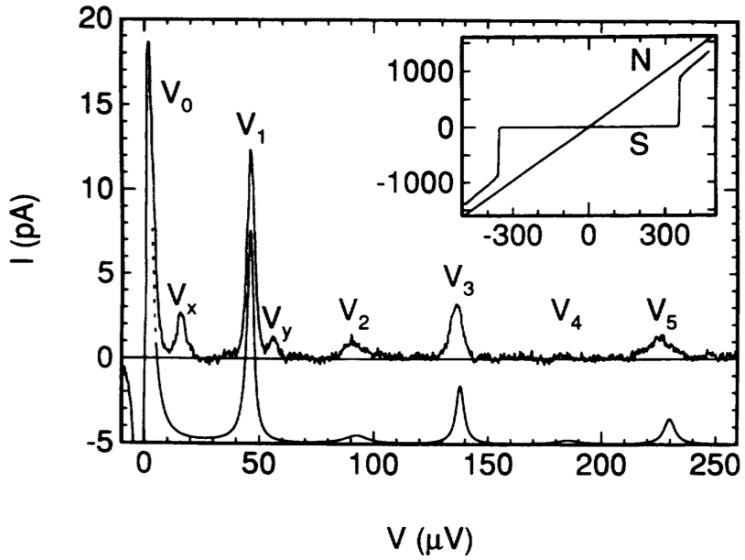

Figure 2.12: Experimental I(V) of the sample, with the $P(E)$ prediction shifted down by 5 pA for clarity. Inset: the I(V) in a wider voltage range and a much bigger current scale, measured with the junction either in the superconducting state (S), or driven normal by the application of a 1 T static magnetic field (N). Figure taken from Holst et al., PRL 1994.

The figure 2.12 presents some results of the experiment under the form of I(V) curves, taken with the sample placed in a dilution refrigerator with base temperature 22 mK. In the small inset on the upper right are the large-scale I(V)s of the junction in the superconducting and normal states (reached by applying a 1 T magnetic field to the sample). The normal state curve gives access to the tunnel resistance of the junction: $R_T \simeq 305$ kΩ. The superconducting data shows the tunneling of quasiparticles for bias above the gap voltage $2\Delta/e \simeq 358$ μV. We can estimate the critical current of the junction with the Ambegaokar-Baratoff formula [56]: $I_c = \pi\Delta/2R_T \simeq 0.92$ nA.

The rest of the figure shows peaks in the superconducting I(V) at voltages below the gap, that we understand this way:

At **zero bias** (V_0) is the supercurrent peak associated to elastic tunneling. From our discussion of part 1.1 we would expect it to go up to $I_c = 920$ pA. In practice it is always quite hard to measure directly I_c, as low frequency voltage noise changes the value of the phase ϕ during the measurement. The finite width of this peak comes from the interplay with the low-frequency impedance of the biasing circuit. Like the authors of the paper, we will not comment on it any more.

At a bias voltage V_1 corresponding to $\mathbf{2eV_1} = \hbar\omega_\mathbf{r}$ we see a finite dc-current through the junction, which results from the inelastic tunneling of Cooper pairs. The height of this peak matches quite well the value predicted by $P(E)$ for a low impedance environment: $I = I_c^2 Re[Z(\omega_r)]/2V \simeq 13$ pA. The width of this peak is also in agreement with the quality factor of the mode. Note that the dc-current stays always *much smaller than the critical current of the junction*, which is a necessary condition for the $P(E)$ result to hold.

At a bias **twice higher** V_2 there is a much smaller and broader peak. The authors attribute it also to single-photon processes, where light is emitted in a low-impedance parasitic $\lambda/2$ resonance at frequency $2 \times \omega_r$. One may argue that 2-photon processes are also visible here, as the measured current is somewhat higher than the single-photon prediction $I^{(1)}$. However the accuracy of the measurement is not high enough to confirm the existence of these processes, which are anyways expected to be small compared to the V_1 resonance in this low-impedance circuit.

At biases V_3, V_4, V_5 are similar one-photon resonances, where light is emitted in resonances at frequency $\mathbf{3} \times \omega_\mathbf{r}, \mathbf{4} \times \omega_\mathbf{r}, \mathbf{5} \times \omega_\mathbf{r}$ respectively. The height of these peaks decrease with increasing frequency, which can be understood from (2.47). First of all, at fixed impedance and tunnel coupling I_c, there is a $1/V \propto 1/\omega$ dependence in the ICPT current. Second, with increasing frequency the admittance of the junction capacitance $jC_J\omega$ gets higher: it is able to screen more efficiently the voltage fluctuations coming from the environment.

All these peaks are reproduced nicely by the $P(E)$ prediction, which only use as fitting parameter the load impedance Z_x and the high-frequency resistive losses in the CPWs, which broaden the V_3 and V_5 peaks compared to V_1 (Fig.2.12).

The additional peaks at V_x and V_y are attributed by the authors to parasitic resonances on the chip.

A definitive confirmation of the ICPT mechanism?

Even though these results compare nicely with a $P(E)$ prediction, which also describe well data taken in the DCB regime of single-electron tunneling, the authors themselves note that a semi-classical theory based on the ac-Josephson effect predicts the same 1-photon peaks. The two main features of ICPT that we described earlier, namely the **renormalization of** I_c by zero-point fluctuations and the existence of **multi-photonic processes**, cannot be confirmed by this experiment.

To probe the first effect, one would need to compare the measured current to the one predicted using the Ambegaokar-Baratoff formula. However in this relatively low-impedance circuit the renormalization of the critical current is of the order of a few percents, which

is smaller than the uncertainty on R_T, Δ or the $Re[Z(\omega)]$ seen by the junction, such that this comparison cannot be done here.

2-photon processes are maybe responsible for the slightly enhanced current at bias V_2, however once again the environment of the junction is not known well-enough to make the subtraction of the 1-photon contribution accurately. To discriminate between processes where light is emitted as one photon of frequency $2 \times \omega_r$ or 2 photons at frequency ω_r, the measure of the dc-current is not enough: one need to also **detect the photons emitted by the junction**.

In spite of these limitations, this experiment was the first one to prove that a small-enough junction would be sensitive to the high-frequency voltage fluctuations from its environment, and that quantitative predictions could be made if the impedance seen by the junction is well-known. It was thus the basis for another experiment performed 17 years later that aimed at probing the photonic (or "bright") side of ICPT as well.

2.3.2 The Bright Side of Coulomb Bockade

As mentioned earlier, one of the perks of using distributed elements to implement modes is that it makes it possible to collect the light emitted by ICPT and guide it towards a detector. This however comes at the cost of making the experiment more complex, as the constraints of the low frequency electrical engineering needed to measure accurately the I(V) of the junction are at odds with the standards of microwave power measurements. We describe here the ideas guiding the high-frequency design of such experiments.

Processing microwave photons

We gave a simple physical picture of the photon-creation process in figure 2.9: in this model circuit, the tunnel current through the junction is directly injected in an array of LC modes.

However this set of fictitious LC resonators is merely an effective model describing an arbitrary impedance $Z(\omega)$. In the Holst 1994 experiment, $Z(\omega)$ is given by the load impedance Z_x, quarter-wavelength transformed to Z_w^2/Z_x at the resonance frequencies of the Z_w transmission line. At the bias $V = \hbar\omega_r/2e$, ICPT is prompted by the vacuum voltage fluctuations coming to the junction at frequency ω_R, with $S_{VV}(\omega_r) = 2\hbar\omega_R Z_w^2/Z_x$. The electromagnetic excitations are then created as an ac-voltage drop at the input of the transmission line. These propagate in the line until the load impedance Z_x, where they are dissipated as Joule power with the **emission power** $P^{em} = \langle V_{ac}(t)^2\rangle/Z_x$ (Fig.2.13.a).

Thus the load impedance where the dissipation finally occurs does not need to be directly connected to the junction. We can also envision a situation where the output of Z_w is an arbitrarily long line of wave impedance equal to Z_x, terminated by a matched resistor. This does not change the impedance seen by the junction, nor the equilibrium phase fluctuations prompting ICPT. However it allows the routing of the emitted photons in the line from the sample to room temperature, where they can be detected.

Measuring the emission power

One very direct way of detecting these photons could then be to measure the voltage drop on the load resistor, in particular its ac-component at frequency ω_r. This is very unpractical to do, as digitizing voltages as such high frequencies is out of reach of most commercially available acquisition cards.

Recall also that in an experiment, the sample is kept at very low temperature in a cryogenic enclosure, but the electronics used to measure it is at room temperature. At T=300 K, the occupation number for modes in the few GHz range is of the order of $k_BT/\hbar\omega_r \sim 10^3$, such that there is a considerable background of thermal photons in the measurement lines. To stay in the assumptions of the $P(E)$ theory one need to keep the number of photons emitted by the junction sufficiently lower than 1 photon per mode, i.e much lower than the background thermal occupation. More over, the connection between the sample and the detector needs to be resistive enough to forbid heat transfer from room temperature to the cold stage. This in turn causes a strong attenuation of the emitted power (of the order of 10-20 dB), such that the signal to noise ratio of a direct detection technique would be extremely low and make the experiment impossible (Fig.2.13.b).

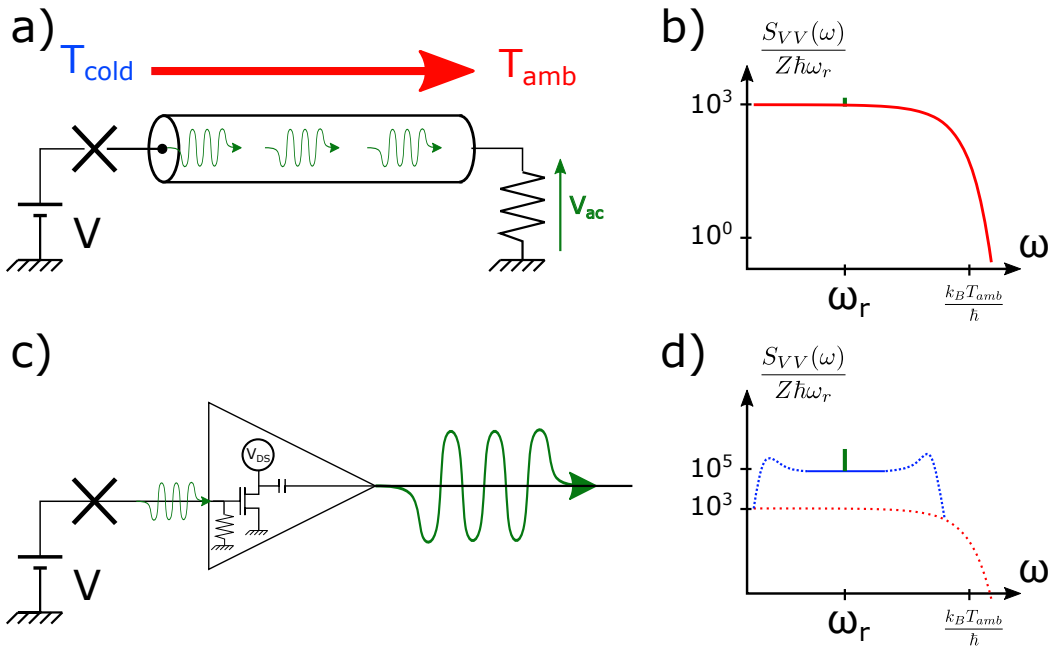

Figure 2.13: a) Schematics of a direct power detection setup. ICPT in the dc-bias Josephson junction creates excitations in the transmission line (in green), which propagate until they are dissipated in a load impedance Z_x, placed at room temperature T_{amb}. b) Typical log-log plot of the spectral density of the power dissipated in Z_x, in units of $\hbar\omega_r$. Its consists mostly of thermal Johnson-Nyquist noise (in red), which is orders of magnitude bigger than the signal from the junction (in green, exaggerated many times). c) Schematics of a setup able to amplify the signal with a cryogenic HEMT before detection. d) Log-log PSD plot of the Johnson-Nyquist noise of the detector at T_{amb} (in red), with the amplified noise of the HEMT (in blue) and the amplified signal from the junction (in green). In a frequency window around ω_r, the noise of the amplifier can be of the order of the noise of a T_{cold} impedance.

It is then necessary to rely on cryogenic low-noise microwave amplifiers, such as the commercially available HEMTs. These devices can collect weak voltage signals at their input and amplify them (Fig.2.13.c). In their operating frequency band they can give up to a G=40 dB gain to the signal power, while adding a parasitic noise equivalent to

the thermal noise of a resistor at a temperature of a few Kelvins. These devices need to be impedance matched to ensure that all the input signal is amplified and none of it reflects back to the sample. The standard at microwaves frequencies for impedances is $Z_0 = 50\ \Omega$. The ouput of the amplifier thus consists of microwave signals with the Power Spectral Density (PSD): $S_P(\omega) = G \times (k_B T_N + Z_0 S_{II}(\omega))$, where $S_{II}(\omega)$ is the current noise emitted by the junction towards Z_0 and T_N is called the *noise temperature* of the amplifier.

The amplified signals can be brought up to room temperature for further amplification. If we cascade two amplifiers 1 and 2, the output PSD of 2 reads: $S_P^{(2)}(\omega) = G^{(2)} \times (k_B T_N^{(2)} + G^{(1)} \times (k_B T_N^{(1)} + Z_0 S_{II}(\omega)))$. If we design the chain of amplification such that $G^{(1)} T_N^{(1)} \gg T_N^{(2)}$, then the signal to noise ratio is dominated by the low noise of the first cryogenic amplifier. In this way one can overcome the 300 K temperature of the final detector (Fig.2.13.d).

As we are not yet interested in the coherence properties of the photons emitted by the junction, we don't really need to access the full $V(t)$ dependence. We can detect the emission of photons by measuring the power emitted by the junction, which reads: $P^{em} = \int d\omega Z_0 S_{II}(\omega) = \hbar\omega_r \Gamma_{ph}$, where Γ_{ph} is the photon emission rate. This power can be extracted by a square-law detector, which is a diode with a non-linear I(V) terminated by a RC circuit. Near 0 this I(V) is approximately quadratic, such that the voltage at the output of the detector is directly proportional to $\langle V(t)^2 \rangle \propto P^{em}$.

The Bright Side experiment: measuring Cooper pair tunneling rates as well as photon emission rates

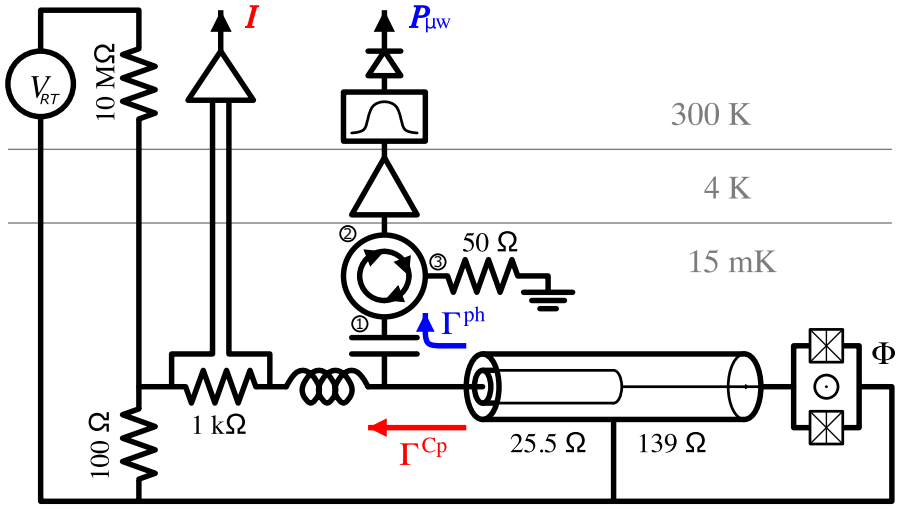

Figure 2.14: Generic setup used in the 2011 experiment. A bias tee allows to measure the dc-current of Cooper pairs Γ_{Cp} as well as collecting the microwave power Γ_{ph} emitted into an amplification chain.

The figure 2.14 shows a simplified version of the experimental setup used by Hofheinz and coworkers in 2011 [33]. It includes a SQUID, acting as a single Josephson junction tunable by an external flux Φ, connected to a bias circuit through two segments of CPWs, implementing $\lambda/4$ modes with fundamental resonance frequency $\nu_0 \simeq \times 6$ GHz[6]. Between

[6]The higher order $\lambda/4$ modes thus occur at 18 GHz, 30 GHz, and so on.

the chip and the rest of the circuit is a bias-tee, which is a 3-port microwave device which can separate the dc and the ac components of signals on the input port onto two separate output ports. It is schematized by an inductor and a capacitor connected to the sample, which is also a good model of its equivalent impedance.

On the low frequency part of the circuit there is a voltage source V_{RT} at room temperature, in series with two resistors of respectively 10 MΩ and 100 Ω. As the conductance of the junction is negligible compared to $(100\ \Omega)^{-1}$, the voltage at the low temperature resistor is $V \simeq V_{RT} \times 10^{-5}$. This allows setting precisely the value of the voltage bias on the junction $V_J \simeq V$. Measuring the voltage across the 1 kOhm resistance on the inductive part of the bias-tee allows accessing the dc current I and thus the rate of tunneling of Cooper pairs $\Gamma_{Cp} = I/2e$.

The high frequency port of the bias-tee is connected to a HEMT cryogenic amplifier, with a noise temperature of $T_N = 3.5$ K. In between the sample and the amplifier are a set of cryogenic circulators (only one represented). This 3-port microwave device contains transmission lines running over a magnetic substrate. Wave propagation is thus chiral in the circulator, such that interferences can be engineered to route all the signals coming from port 1 to port 2 only, and as well for the signals from port 2 to port 3 and those from port 3 to port 1 (following the arrow symbols). Circulators are used here to protect the sample from the voltage noise coming from the amplifier. Indeed from its input the HEMT behaves as a 50 Ω circulator at temperature T_N, which thus radiates Johnson-Nyquist noise. Without the circulator this "hot" noise would go straight to the junction, and give a finite occupation to the GHz modes of the environment. The circulator roots this noise to a matched 50 Ω load which is thermalized at the fridge base temperature. The load absorbs about 98% of this incoming power and radiates only vacuum fluctuations as it is kept around 20 mK$\ll h\nu_0/k_B$. Using several circulators helps in absorbing all of the parasitic amplifier noise.

The output of the HEMT amplifier is routed to room temperature, where it is further amplified (not shown) and finally filtered in a frequency window of 2 GHz centered on ν_0. The filtered signals are sent to a fast diode. The diode output voltage is proportional to the total power out of the amplification chain, which consists mostly of the first cryogenic amplifier noise, the comparatively much smaller noise added by the other amplifiers, and the weak signal from the sample.

At $V = 0$, as the temperature is much below $h\nu_0/k_B$, we know that the junction does not emit photons in the measurement frequency window. We consider this the **OFF** state of the sample, where $\Gamma_{ph} = 0$. By contrast at $V \neq 0$ the junction is in the **ON** state, as it may radiate power. As the noise added by the amplifiers do not depend on the state of the sample, we can extract the contribution of ICPT by performing relative **ON/OFF** measurements of the power detected by the diode, and hence access the photon emission rate $\Gamma_{ph} = P^{em}/h\nu_0$[7].

This setup makes it possible to measure at the same time Γ_{Cp} and Γ_{ph}, i.e the dc and ac aspects of ICPT, for a Josephson junction with a well controlled environment.

Note that all the microwave electronics used here is designed to work only in the so-called C band (4-8 GHz). Hence only the photons emitted in the first $\lambda/4$ mode at 6 GHZ can

[7] As this measurement is relative, we know Γ_{ph} up to the global gain of the amplification chain, that we can calibrate *in situ* (see appendix B).

be detected.

Photon rates and Cooper pair rates

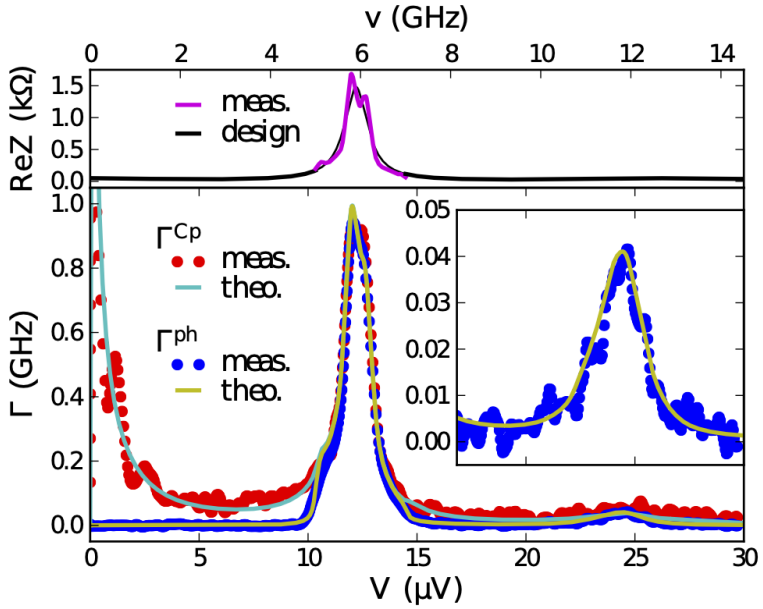

Figure 2.15: On the upper part: $Re[Z(\omega)]$ of the environment seen by the junction, calibrated *in situ* in the frequency band accessible for measurement 5-7 GHz. Main graph: measured Cooper pair tunneling rates (red points) and photon emission rates (blue points) as a function of bias voltage V. Only the photons emitted at the resonator frequency 6 GHz are detected. The $P(E)$ theory predictions for dc-current (cyan line) and microwave power (yellow line) use the measured $Re[Z(\nu)]$, and the electronic temperature $T_{el} = 60$ mK and E_J=5.1 μV as fit parameters.

The figure 2.15 presents some results of the experiment. On the upper graph is the real part of the impedance of the environment, as seen from the junction. The black line is the results of microwaves simulation, showing a mode at $\nu_0 \simeq 6$ GHz[8] with $Q \simeq 9$ which reaches $\simeq 1.5$ kΩ at maximum. The pink line shows the experimental $Re[Z(\nu)]$, reconstructed from shot-noise measurement (see appendix B for details about the procedure), which confirms the presence of the mode. The deviation to a pure Lorentzian shape is attributed to parasitic reflections in the microwave chain.

The lower part of the figure is a graph showing Γ_{Cp} and Γ_{ph} as a function of the bias voltage V, for a given value of $I_c(\Phi)$. At low bias, Γ_{Cp} shows again the $V = 0$ supercurrent peak, broaden by the interplay with low frequency modes of the circuit. Around $V = 12$ μV, corresponding to a Josephson frequency $\nu_J \simeq \nu_0$, there is a current peak, whose shape reproduces the shape of the mode, i.e $\Gamma_{Cp}(V)$ follows $Re[Z(2eV/\hbar)]$. Around $V = 24$ μV is a much broader and weaker current peak, that corresponds to the $V2$ peak of the Holst experiment.

By contrast with the dc-current which is non-zero even at low bias, we don't expect to see any photon emission from the sample below $V = h\nu_0/2e$. This is reflected in the $\Gamma_{ph}(V)$ curve, which is zero until 10 $\mu V = h/2e \times 5$ GHz, which corresponds to the lower

[8] To be consistent with the authors we switch to a description of frequencies ν_k in [GHz], instead of the ω_r in [2π GHz] we used before.

edge of the frequency detection window. Around 12 μV we see a peak in $\Gamma_{ph}(V)$, which follows again the variation of $Re[Z(2eV/\hbar)]$ and whose amplitude agrees with $\Gamma_{Cp}(V)$ within 5%. The agreement between these two rates and their V dependence confirms the intuitive picture we had in mind, where in average **one Cooper pair creates one photon**, albeit without discriminating between ICPT and the semi-classical ac-Josephson effect 2.2.

Finally, the most important feature of the figure is the small peak in $\Gamma_{ph}(V)$ that occurs around 24 μV (magnified in the inset), that coincides with the broad peak in $\Gamma_{Cp}(V)$. Recall that at this bias value, each Cooper pair has to spend the energy $2eV = 2h\nu_0$ to tunnel irreversibly, and that we only detect the photons emitted at frequency ν_0. The peak in $\Gamma_{ph}(V)$ thus proves the existence of 2-photon processes, where **each Cooper pair creates two photons**. At low temperature, these processes cannot be explained by a semi-classical theory, and are therefore a clear experimental confirmation of the ICPT mechanism of irreversible tunneling prompted by vacuum fluctuations.

The small ratio of the 2-photon to the 1-photon peak can be explained by the quite low value of the impedance of the mode. From equation (2.49), we see that the dc-current associated to 1-photon emission when biased at $V_0 = h\nu_0/2e$ is:

$$I^{(1)} = \frac{\pi {E_J^*}^2}{\hbar V} \times \frac{Re[Z(\nu_0)]}{R_Q}, \tag{2.65}$$

where we denoted $E_J^* = E_J e^{-J(\infty)/2}$ the renormalized value of the Josephson energy. When biased at $2V_0$, the contribution of the 2-photon process to the current is:

$$I^{(2)} = \frac{\pi {E_J^*}^2}{\hbar \times 2V} \times \int d\nu \frac{Re[Z(2\nu_0 - \nu)]}{2\nu_0 - \nu} \frac{Re[Z(\nu)]}{{R_Q}^2}, \tag{2.66}$$

where the integral is taken only over the width of the resonance. If its quality factor is high enough, the $2\nu_0 - \nu$ denominator may be approximated by ν_0, with an error of order Q^{-2}. The integral becomes a convolution product of $Re[Z(\nu)]$ times itself. We now approximate $Re[Z(\nu)]$ by a Lorentzian function, for which this integral is analytical, and obtain:

$$\frac{I^{(2)}}{I^{(1)}} = \frac{\pi Z_c}{4R_Q} \simeq \frac{Z_c}{8216.5\ \Omega}. \tag{2.67}$$

With $Z_c = (2/\pi) \int d\nu Re[Z(\nu)]/\nu$ the characteristic impedance of the resonator. For a $\lambda/4$ mode, we have $Z_c = 4Z_w/\pi \simeq 160\ \Omega$ in this experiment. The ratio of 2-photon to 1-photon current peaks is then of the order of $\sim 2\%$. Meanwhile, as on $2V_0$ we have $\Gamma_{ph} = 2\Gamma_{Cp}$, the 2-photon microwave power peak is $\sim 4\%$ smaller than the 1-photon one, which is close to the measured value (FIG.2.15).

Note that the Γ_{Cp} peak around 24 μV is approximately twice larger than the Γ_{ph} peak, which means that there are also other processes contributing to the dc-current (most probably 1-photon processes where light is emitted at $2\nu_0$, i.e outside of the detection window). Note also that the exact value of the critical current of the junction during the experiment cannot be assessed exactly, except at the zero-frustration point of the SQUID $\Phi = 0$. From the 1-photon peak in figure 2.15, we can estimate its value during the measurement from (2.47) as: $I_c(\Phi) = \sqrt{2h\nu_0\Gamma_{ph}/Re[Z(\nu_0)]} \simeq 20$ nA, while the dc-current is $I = 2e\Gamma_{Cp} \simeq 0.3$ nA, which confirms the validity of $P(E)$.

Two-mode processes at higher bias voltage

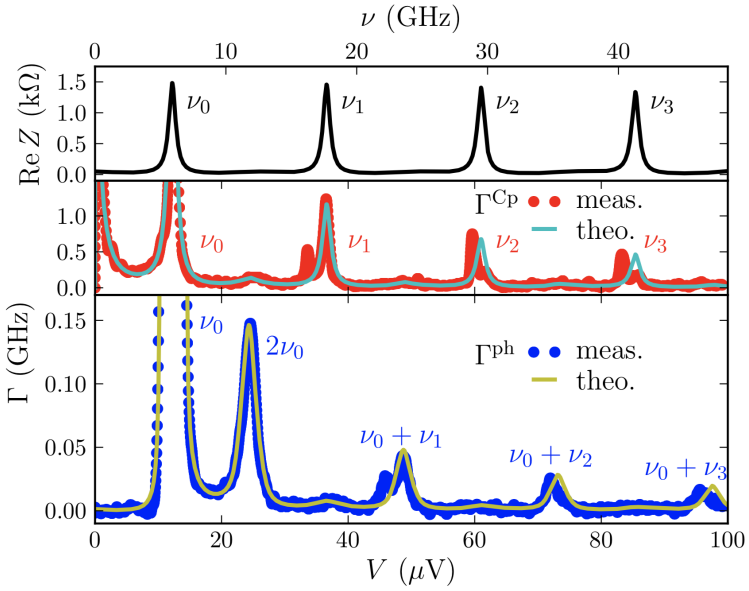

Figure 2.16: Results of the experiment at higher bias. The upper graph shows $Re[Z(\nu)]$ as it was designed, with harmonics of the $\lambda/4$ resonance at frequencies $\nu_k = (2k+1)\nu_0$. To these modes correspond 1-photon peaks in Γ_{Cp}, at bias voltages $V = h\nu_k/2e$. We see 2-photon peaks in Γ_{ph}, at voltages $V = h(\nu_k+\nu_0)/2e$.

The figure 2.16 shows the same type of data as figure 2.15 in a wider voltage range. The critical current $I_c(\Phi)$ of the SQUID was also tuned to a higher value, in order to increase the size of 2-photon processes, while staying in the domain where $P(E)$ is valid[9].

The Cooper pair tunneling rates shows a series of narrow peaks at regular positions, which may be mapped to 1-photon processes where light is emitted in the harmonics of the $\lambda/4$ mode (similar to the V_3 and V_5 peaks in Holst experiment). As such they happen at bias voltages $V_k = (2k+1)h\nu_0/2e$. In between these narrow peaks are broader and weaker resonances at even multiples of $h\nu_0/2e$. As in the previous experiment, the measurement of dc-current alone doesn't allow to distinguish the contributions of single and two photon processes.

This uncertainty is resolved when looking at the $\Gamma_{ph}(V)$ data. We see narrow peaks in the photon emission rates, which correspond to processes where one Cooper pair emits at the same time one photon at ν_0 and a second one in a harmonic mode at ν_k. These peaks prove that the junction can emit light in *two different modes at the same time*, in a process similar to **non-degenerate parametric down-conversion**.

The confirmation of these two distinct-photons emission mechanism immediately raises the question of the quantum coherence between the two modes: is the junction creating entangled photon pairs? This investigation has been a major part of the work presented in this thesis.

Entanglement (when it exists) manifest itself as non-classical correlations between quantities measured independently in the two modes, as they share a common degree of freedom. By using the power detection setup in a more refined manner, the authors of the article

[9] As for a given $Re[Z(\nu_J)]$ the dc-current scales as $(I_c)^2$, when increasing I_c there may be a point where $I_{dc} > I_c$ and $P(E)$ breaks.

have been able to study the **spectral properties** of the light emitted by the junction, and identify a potential *shared degree of freedom*, which we later turned into a proper **entanglement witness**.

Spectral properties of the emitted light

A heterodyne technique can be used to detect the power emitted in a narrow frequency window $\delta\nu$. To do so, the signals right out of the microwave amplification chain are mixed with a so-called *local oscillator* (LO), which is a sinusoidal signal at frequency ν_{LO} generated by a room-temperature radio-frequency source.

The PSD of the signal after mixing is then $S_P(\nu-\nu_{LO})+S_P(\nu+\nu_{LO})$, where the negative frequencies correspond to signals that have been aliased (i.e folded back onto positive frequencies). A low-pass filter with a cut-off frequency $\delta\nu/2$ then selects only low-frequency terms, such that the output power is $\int_{\nu_{LO}-\delta\nu/2}^{\nu_{LO}+\delta\nu/2} S_P(\nu)d\nu \simeq S_P(\nu_{LO}) \times \delta\nu$.

By scanning ν_{LO}, it is then possible to reconstruct the emission spectrum $S_P^{em}(\nu)$ of the power radiated by the junction, and divide it by $h\nu$ to obtain the photon emission rate density $\gamma(\nu)$. The results of this experiment are presented in figure 2.17, where the voltage bias was also scanned to explore the 1-photon and 2-photon resonance of the ν_0 mode.

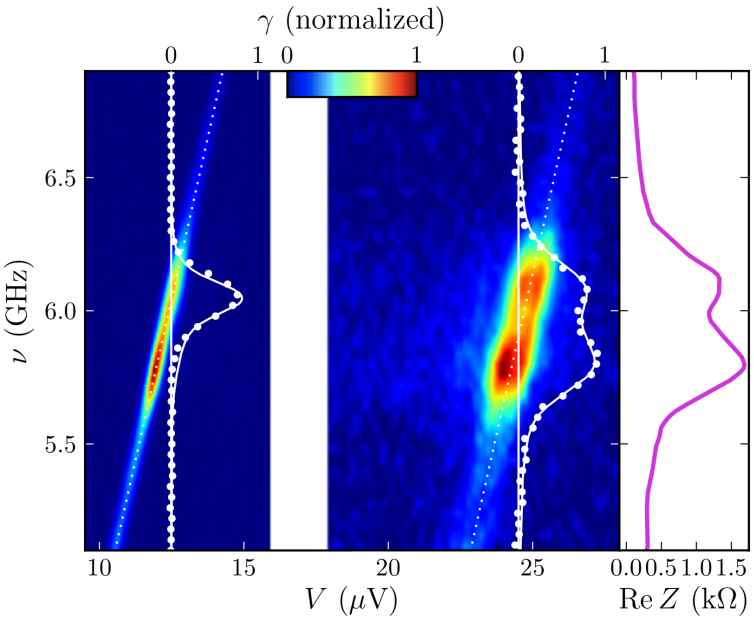

Figure 2.17: Emission rate density $\gamma(\nu)$ map in the 5 to 7 GHz range as a function of bias V. Spectra were taken for different E_Js and normalized by the maximum γ. On the left part, the bias is swept across the 1-photon resonance. On the middle map it crosses the 2-photon peak. The white points show cuts along the two white lines, at 12.5 μV and 24.5 μV. The right part shows a graph of $Re[Z(\nu)]$ in the same frequency range. The $P(E)$ prediction for the spectra (2.73) and (2.75) are plotted as white lines.

On the 1-photon emission map we see narrow emission spectra, whose maximum follows the $2eV = h\nu$ line (white dots). The amplitude of the maximum is also modulated by $Re[Z(\nu)]$ (shown in the right part of the figure), in accordance with equation 2.47. At fixed voltage, a cut through the map along the frequencies reveal the shape of the emission

line. It is approximately Lorentzian, with a width of around 150 MHz, i.e much narrower than the FWHM of the resonator ($\nu_0/Q \simeq 670$ MHz).

Similarly the 2-photon emission maximum follows the $2eV = 2h\nu$ line (white dots). However there the emission spectrum is much broader: near $2eV = 2h\nu_0$, it resembles the shape of the resonator (see cut at 24.5 μV), with a similar width $\simeq 600$ MHz.

P(E) description of the emission spectrum

As explained by the authors, these results are well reproduced by an extension of the $P(E)$ theory. We described the PSD emitted by the junction into the detector as $S_P(\nu) = \hbar\nu\gamma(\nu)$, where $\gamma(\nu)$ is the spectral density of the photon emission rate (i.e the "number of photons per travelling mode"). This may also be written as the Joule power dissipated by the tunnel current I in the impedance of the environment, which plays the role of the "detector": $S_P(\nu) = 2Re[Z(\nu)]S_{II}(\nu)$. The current noise density is the Fourier transform of the current-current correlator:

$$S_{II}(\nu) = \int_{-\infty}^{+\infty} \langle I(t)I(0)\rangle e^{i2\pi\nu t} dt. \tag{2.68}$$

Like the tunnel current itself, this correlator can be written with the charge tunneling operator:

$$\langle I(t)I(0)\rangle = \frac{e^2 E_J}{\hbar^2}\left(\langle e^{i\phi(t)}e^{-i\phi(0)}\rangle + \langle e^{-i\phi(t)}e^{i\phi(0)}\rangle\right), \tag{2.69}$$

where in the absence of a phase reference we again kept only the terms involving phase differences. These terms can be expressed with the help of the phase correlator $J(t)$:

$$\langle e^{\pm i\phi(t)}e^{\mp i\phi(0)}\rangle = e^{\pm i2eVt/\hbar}\langle e^{\pm i\hat{\phi}(t)}e^{\mp i\hat{\phi}(0)}\rangle \tag{2.70}$$

$$= e^{\pm i2eVt/\hbar}e^{J(t)}. \tag{2.71}$$

Thus the current noise can also be expressed with the $P(E)$ function, as:

$$S_{II}(\nu) = \frac{2\pi e^2 E_J^2}{\hbar}\left(P(2eV - h\nu) + P(-2eV - h\nu)\right). \tag{2.72}$$

This expression leads to a simple physical picture of the current noise through the junction. The first $P(E)$ term corresponds to emission processes, where photons are created by ICPT. The second term indicates photon absorption by the junction, i.e processes where one Cooper pair absorbs the energy $2eV + h\nu$, to be able to retro-tunnel (climbing the potential difference $2eV$) while emitting a photon at frequency ν. These absorption processes are negligible as soon as the environment of the junction is cold enough, thus empty of photons at frequencies $\sim 2eV$.

Note that the expression for the tunnel current (2.44) involved the difference of two $P(E)$ functions, which were associated to currents flowing in opposite directions. If $P(2eV) \simeq P(-2eV)$, there is in average zero current through the junction. On the other hand both forward and backward tunneling contribute to the current noise (2.72).

Going back to the shape of emission spectra, we see that the PSD around ν_J on the 1-photon peak $2eV = h\nu_0$ is directly an image of $P(E)$ around $E = 0$, modulated by

$Re[Z(\nu)]$:

$$S_P(\nu) = 2\pi^2 E_J^2 \frac{Re[Z(\nu)]}{R_Q} P(2eV - h\nu). \tag{2.73}$$

As the width of the mode is much wider than D/h, the $Re[Z(\nu)]$ dependence of the emission spectrum can be neglected: we have $S_P(\nu) \propto P(h\nu_0 - h\nu)$.

At very low energy, we cannot use the zero temperature expression 2.46 for $P(E)$ that we developed before. The continuum of low frequency modes with diverging thermal occupation near $\nu \simeq 0$ act like a bath of voltage fluctuations with a white noise spectrum, resulting in Brownian dynamics of the superconducting phase ϕ. In the limiting case where the RC cut-off of the environment impedance happens after the thermal cut-off of the modes occupation, i.e if the impedance is ohmic and "flat" up to $k_B T/h$, the interaction between ϕ and this bath can be treated exactly [57]. $P(E)$ is then a Lorentzian function near zero [58]:

$$P(E \sim 0) = \frac{D/\pi}{D^2 + E^2}, \tag{2.74}$$

with a FWHM $2D \simeq 4k_B T Re[Z(\nu = 0)]/R_Q$, where T is the temperature of the low frequency modes. The exact setup used in the Bright Side experiment is a bit more complex than a simple constant resistance [33]. A more accurate model for the circuit including both lumped and distributed elements leads to an average impedance seen by the junction between 0 and 4 GHz of around 65 Ω. Fitting the 150 MHz width of the 1-photon spectrum with the formula for D leads to an effective temperature around 55 mK, in good agreement with an independent calibration of the electronic temperature of the sample $T_{el} = 60$ mK±10 mK.

This non-zero width of the emission spectrum can be understood as the result of processes where the junction exchanges energy both with the mode at ν_0 and with the low frequency continuum. This spectrum is symmetric around ν_0 as the junction is absorbing and emitting energy into the continuum with equal probability, as $P(E) \simeq P(-E)$ for $E \ll k_B T$. However the experiment is carried over timescales much longer than the period of these modes, such that photon absorption and emission are averaged and cannot be resolved. It is more instructive to consider that the low frequency modes act like some source of voltage noise on V, leading to a widening of the $\delta(E)$ in (2.46). We could alternatively consider that the bias voltage V is perfectly noiseless but that we are changing its value during the measurement, leading to a broadening of the emission line.

The $P(E)$ expression of $S_P(\nu)$ also reproduces accurately the 2-photon measurements. Here the bias is set around $2eV = h\nu_0$, such that $S_P(\nu)$ reproduces the variation of $P(E \simeq h\nu_0)$. We can use the $Re[Z(E/h)]$ expansion of $P(E)$ to get the emission rate density $\gamma(\nu) = S_P(\nu)/h\nu$:

$$\gamma(\nu) \simeq \frac{(2\pi E_J)^2}{h^2} \times \frac{Re[Z(\nu)]}{R_Q \times \nu} \times \frac{Re[Z(2\nu_0 - \nu)]}{R_Q \times (2\nu_0 - \nu)}. \tag{2.75}$$

The emission rate density is symmetric around $2eV/2h = \nu_0$, reflecting the fact that photons are created by pairs. Indeed if we consider a single tunneling event, the energy $2eV$ ceded by the voltage source can be converted into any photon pair (ν_a, ν_b) whose sum of frequencies matches $2eV/h$. The probability of emitting a single photon at ν scaling as $Re[Z(\nu)]$, a particular pair process probability scales as $Re[Z(\nu_a)] \times Re[Z(\nu_b)]$.

When biased at $2eV = 2h\nu_0$, the shape of the PSD is thus the product of the profile of $Re[Z(\nu)]$ times its mirrored image around ν_0, $Re[Z(2\nu_0 - \nu)]$, resulting in a FWHM slightly lower than the width of the resonator itself. The $P(E)$ predictions for the 1 and 2-photon process is plotted on Fig.2.17 on top of the measured spectra (white lines), using the $Re[Z(\nu)]$ deducted from shot-noise measurements. The only fitting parameters are the effective temperature for the 1-photon spectra, and the Josephson energy E_J for both processes. The expression for the PSD, integrated over the detection frequency range, is also plotted on figure 2.15 and figure 2.16 (yellow lines), over the measured emitted microwave power, as well as is the prediction for the dc-current on top of the measured current (cyan lines), using the same set of fitting parameters (T_{el} and E_J).

The very good agreement between the predicted and measured emission spectra, photon creation rates and Cooper pair tunneling rates is a definitive proof that the $P(E)$ theory describes accurately the interaction between the Josephson junction and the electromagnetic modes in its environment.

2.4 Conclusions and open questions

Rates and statistics

These two experiments validate the idea that engineering the environment of a small dc-biased Josephson junction prompts the emission of light by an inelastic mechanism, which is fundamentally quantum as it relies on zero-point phase fluctuations. In the limit of low Josephson energy ICPT is well described by the $P(E)$ theory, which predicts intriguing effects such as the emission of multiple photons by a single tunneling charge.

However one should note that we have only derived predictions about average quantities, such as the value of the dc-current $\langle I(t) \rangle$ or the radiated ac-power $P = \hbar\omega_r\Gamma$. Such observables alone are not enough to prove that exactly one Cooper pair has created exactly a given number of photons. The microscopic nature of the photon emission process can only be definitely proven by looking at more elaborate quantities, such as the **statistics of the emitted light**.

On one hand, as the tunneling events happen in a random way and are rare enough to be considered independent, we expect the light emitted by the $2eV = k\hbar\omega_r$ process to consist of independent packets of exactly k photons. Such light would present a non-classical granular aspect that can be described by antibunching statistics, which is usually characteristic of fermions, and can be used as a resource in many quantum information protocols or fundamental tests of quantum mechanics. Two-photon states, in particular entangled photon pairs, are also often critical for quantum communication experiments.

On the other hand, we know that in the low impedance limit the 1-photon processes also emerge in a semi-classical treatment of the ac-Josephson effect. In that case the junction acts as a classical ac-current source, which can only create the so called coherent states of light, displaying classical statistics.

The investigation of the precise nature of these statistics require a more complete theoretical treatment, which could be done by identifying the right current correlators describing

the photon statistics and calculating them within P(E). This is however very cumbersome, and we will see that better approaches are available.

Back-action of the populated modes

Another limitation of the $P(E)$ theory is that it supposes that the environment of the junction stays close to equilibrium. In practice, the mode where the photons are created fills up at a rate Γ. Its stationary occupation number $\bar{n}$ is then the ratio of this rate to its energy leak rate $\kappa = \omega_r/Q$. As Γ is proportional to the inelastic current, the hypothesis that $\bar{n}$ stays close to zero is related to the main condition for $P(E)$ to hold, which is that the dc-current stays small compared to I_c. This condition also appears in our derivation of the ac-Josephson effect, as we had to suppose that $Re[Z(\omega_J)] \times I_c \ll \pi V$ in order to linearize the $\sin(\phi^{(1)}(t))$ term.

There is however a different impact of the population of the mode on the tunneling rate that manifests itself only in ICPT, and not in the semi-classical picture of the effect. Even if E_J is kept sufficiently small that $\bar{n} \ll 1$, and the average phase correlation function stays close to its equilibrium form, the granularity of charge transfer in a tunneling event means that right after one charge has tunneled, there is the **sudden creation of one photon** in the mode. Even if the photon dissipates quickly out of the resonator, on some timescale the environment cannot be considered to be empty and the instantaneous phase correlations can be strongly perturbed. What is the impact of these fast fluctuations on the ICPT mechanism, and when do they matter?

The understanding of these processes require a more complete description of the system, keeping track of the state of the modes themselves. Our field of study then shifts from the description of transport properties of a quantum conductor connected to a bath of modes, to the study of the Quantum ElectroDynamics between a Josephson junction and microwave resonators, where we will focus on the properties of the emitted light.

Discussion: quantum microwave sources

The QED of a Josephson junction coupled to microwave resonators

Mapping to the atomic QED

A small dc-biased Josephson junction is an out-of-equilibrium quantum conductor that can exchange energy with the modes of its environment upon the incoherent transfer of single Cooper pairs. These modes couple with the junction through their voltage fluctuations. Empty modes display zero-point fluctuations, which can trigger the emission of photons in the mode. The junction can also absorb photons from modes with a finite occupation number, e.g. of thermal origin, allowing for the retro-tunneling of charges.

In the limit of vanishing tunnel coupling E_J, the $P(E)$ theory predicts the strength of these various mechanisms. It is determined by the real part of the impedance of the circuit $Re[Z(\omega)]$, which gives the amplitude of the equilibrium voltage fluctuations. $P(E)$ is thus limited to situations where the modes stay close to their equilibrium state.

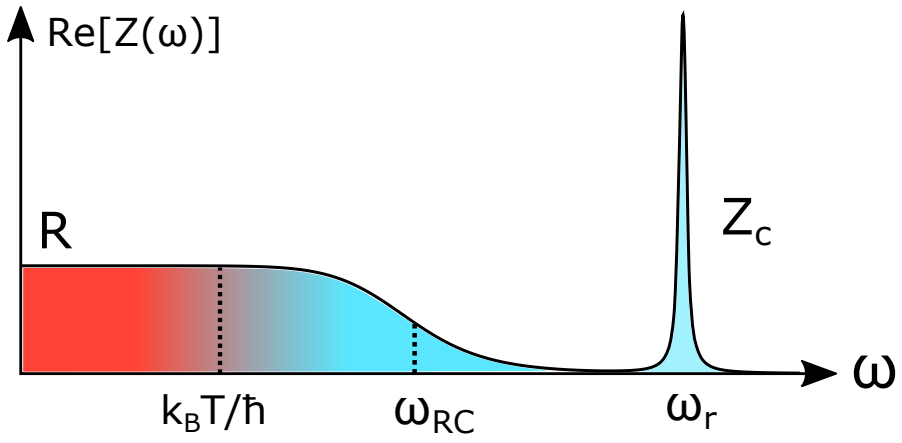

Figure 2.18: Environment of a dc-biased Josephson junction: near zero frequency is a continuum of states with high thermal population, while at ω_r is a mode of characteristic impedance Z_c in the vacuum state. Color-coded is the thermal occupation of modes, which drops to zero above $k_BT/\hbar$.

Figure 2.18 illustrates the kind of environment seen by the junction in the first experiments designed to detect ICPT, either by measuring tunneling rates or photon emission.

Applying a precise value of voltage to a cold sample without bringing too much heat from the room-temperature circuitry requires setting a finite resistance R at dc. This resistance is eventually shunted above some frequency ω_{RC}, either by some experimental filtering scheme, or simply by the geometric capacitance of the junction itself. Below ω_{RC} the environment $Re[Z(\omega)]$ thus consists of a continuum of modes, with thermal occupation that gets arbitrarily high at low frequency. At high frequency resonances can be engineered, that manifest as peaks in $Re[Z(\omega)]$ reaching values of the order of $R_Q \simeq 6.45$ kΩ.

These resonances have a finite width, due to internal losses and/or to the coupling to an external measurement circuit. Thus each resonance defines a continuum of modes in its frequency window. However if its quality factor Q is high enough, it can be treated for all purposes as a single mode of radiation at frequency ω_r [59], with the amplitude of the field varying on the relatively long timescale $\tau = Q/\omega_r$ called the *lifetime* of the mode.

Still, the finite width of the resonator shows up in the predictions of multi-photonic processes, e.g. in the emission rate for the 2-photon processes:

$$\Gamma^{2eV=2\hbar\omega_r} = \frac{\pi^2 E_J^{*2}}{2h^2\omega_r} \times \int d\omega \frac{Re[Z(2\omega_r-\omega)]}{2\omega_r-\omega}\frac{Re[Z(\omega)]}{{R_Q}^2}. \tag{2.76}$$

$\Gamma^{2eV=2\hbar\omega_r}$ writes as a sum over all the photon-pair creation processes that can happen in the bandwidth of the resonator. In the case of a high Q mode, this integral may be simplified, yielding:

$$\Gamma^{2eV=2\hbar\omega_r} = \frac{E_J^{*2}}{\hbar^2\kappa}\frac{r^2}{2}, \tag{2.77}$$

where $\kappa = \omega_r/Q$ is the energy leak rate of the mode, and $r = \pi Z_c/R_Q$ is its normalized characteristic impedance, with $Z_c = \frac{2}{\pi}\int \frac{d\omega}{\omega} Re[Z(\omega)]$. This is again a way of describing all the frequencies in the bandwidth of the resonator as a single mode of radiation. Z_c is then the typical impedance of the modes in the continuum.

More generally, the emission rate for the k-photon process has a simple expression, involving the same parameters (see appendix D for a derivation) :

$$\Gamma^{2eV=k\hbar\omega_r} = \frac{E_J^{*2}}{\hbar^2\kappa}\frac{r^k}{k!}. \tag{2.78}$$

The factor r is a coupling parameter, given by the size of zero-point fluctuations of the phase across the resonator: $\langle 0|\hat{\phi}^2|0\rangle = r$. If one describes the resonance as a LC mode, it is also equal to the ratio of the charging energy of a single Cooper pair on C to the energy of a single photon in the resonator: $E_C/\hbar\omega_r = (2e^2/C)/(\hbar/\sqrt{LC}) = \pi\sqrt{L/C}/(h/4e^2) = \pi Z_c/R_Q = r$.

At $r \ll 1$, the ZPF of $\hat{\phi}$ associated to the mode are small, such that it cannot trigger ICPT easily. Correlatively, the change of electrostatic energy in the resonator upon the tunneling of a single charge is small compared to the energy of one photon. Thus the junction cannot excite the mode easily. On the other hand, a mode with a high characteristic impedance couples efficiently to the junction, and can display multi-photonic processes more easily.

Based on these considerations, as well as the r-dependence of (2.78), it is natural to call r the **fine structure constant** of the interaction between the Josephson junction and the

mode. This establishes a parallel between the physics of a quantum coherent conductor coupled to modes in a circuit, and the Quantum ElectroDynamics (QED) of an atom interacting with electromagnetic radiation. The dc-biased junction plays the role of an atom kept out of equilibrium, that emits photons in the empty high frequency modes of its environment.

The thermally populated low-frequency continuum does not really require this QED description, given that these modes can be described classically. Their influence can be described by the addition of some voltage noise δV on V, which spreads the zero-energy peak of $P(E)$, as in (2.74). This is equivalent to blurring the energy levels of the atom in a QED setting, thus widening the emission line and inducing a finite phase coherence time for the emitted radiation.

Josephson photonics QED experiments

We test extensively this analogy with QED by performing the equivalent of quantum optics experiments in the microwave domain, where we measure the properties of the field radiated by a junction embedded in a controlled environment. First, we play with the interpretation of r as a fine structure constant by studying a circuit with a mode in the regime of **strong coupling QED**, with $r \sim 1$. This situation is far away from the standard QED regime, where the natural structure constant $\alpha \simeq 1/137 \ll 1$, and as such can create more easily non-gaussian states of light. We prove that the radiation emitted by the junction in the mode is deeply quantum, displaying in the low photon emission limit **antibunching statistics**, contrasting with the natural tendency of bosonic particles to bunch together [36]. We also measure the emission of up to six photons upon a single Cooper pair transfer, a result to be contrasted with the state of the art in quantum optics which is two-photon parametric down-conversion, recently pushed to three-photon processes in a circuit-QED setup [60]. Finally, we measure accurately the **renormalization of the Josephson energy** of the junction by the sizeable phase vacuum fluctuations from the mode ($E_J^* = E_J e^{-\frac{J(\infty)}{2}}$), confirming another prediction of the $P(E)$ theory.

In a second set of experiments, we study the **emission of entangled photon pairs** into a two-mode environment. We use modes with different frequencies but similar small impedances, to stay in the regime $r \ll 1$ where the states of light should stay gaussian and the entanglement is easier to describe. We prove that in this situation, the Josephson junction can implement a **two-mode-squeezing Hamiltonian**. This generates non-local correlations between the fields of the two modes, as well as between the two beams of radiation leaking out of the resonators. We detect the entanglement between the two emitted fields, and prove that their coherence time is essentially limited by the voltage noise on the junction. We are able to reduce strongly the decoherence rate by actively cooling down the low-frequency continuum of modes from their base temperature of 21 mK down to about 2 mK, using the same Josephson junction that is creating the entanglement as a cold low-frequency admittance.

These different results prove that the simple system of a dc-biased Josephson junction provides bright source of non-classical light, and hints that it could manipulate coherently the quantum state of microwave modes. It could potentially be useful in some quantum information protocols, as well as for solid-state experiments, as it can perform

spectroscopy at arbitrary frequencies. These concepts could also be extended to the THz range, by creating Josephson junction from materials with a higher superconducting gap [55].

Chapter 3

Strong-coupling of a Josephson junction to a single mode

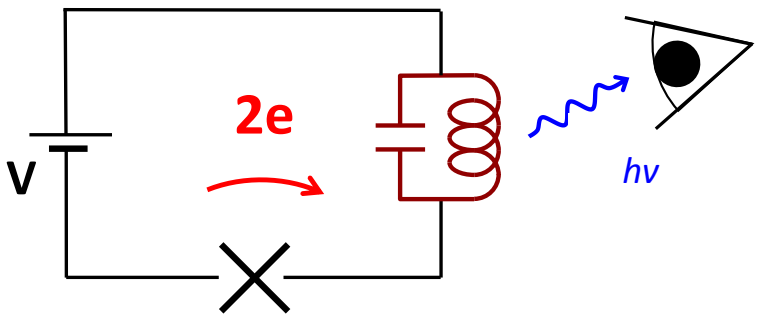

The coupling between a dc-biased Josephson junction and a single mode with a high characteristic impedance Z_c yields a situation with no direct equivalent in atomic QED, as the fine-structure constant $r = \pi Z_c/R_Q$ can be made of the order of 1. The light-matter interaction is then considerably modified compared to the weakly-coupled regime: if a charge emits a photon, the back-action of the photon on the charge is large enough to modify its dynamics.

In an out-of-equilibrium system like a dc-biased junction, which continuously emits light, this leads to non-classical correlations between two successive photon emission processes. In particular for $r \sim 2$ the creation of a first photon can prohibit the emission of a second one, which results in the emission of a beam of light with well-separated, or **antibunched**, photons.

A first experiment aiming at proving this effect was carried out by Chloé Rolland during her PhD research [35]. She managed to fabricate a simple in the strong-coupling regime $r \simeq 1$, and used power-correlation measurements to prove the antibunching of emitted photons. However incurable parasitic signals plagued the measurements and forbade a fully quantitative comparison of her results to theoretical predictions.

During this PhD work, we developed a new measurement scheme, based on the linear detection of field quadratures instead of power measurements. We could then measure different observables, such as the moments and correlation functions of both the anti-bunched photons and the parasitic signals. After identification and careful subtraction

of the unwanted parasitic terms, we ended up with a much improved accuracy in our measurements, allowing us to fully charaterize the sample and its environment.

We then present quantitative results for the measurement of the antibunching for different occupation numbers of the mode, in good agreement with numerical simulations [36]. As all parameters of the experiment are measured independently, there are no adjustable parameters in the simulations. This proves the validity of our modelling of the system, which implements a simple and bright single-photon source.

3.1 Strong-coupling QED: from non-linear dynamics to antibunched photons

Preamble: strong-coupling versus strong-driving

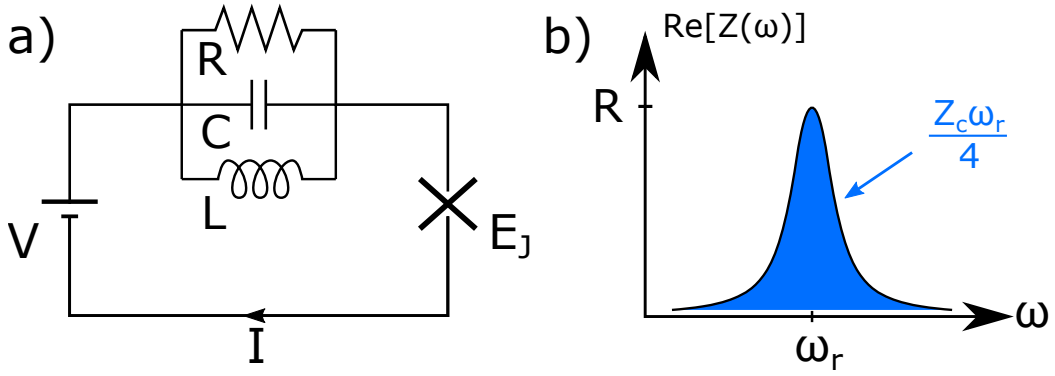

Figure 3.1: a) Model circuit: a Josephson junction with energy E_J is dc-biased by a voltage source V through a RLC resonator with frequency $\omega_r = 1/\sqrt{LC}$, characteristic impedance $Z_c = \sqrt{L/C}$ and quality factor $Q = R/Z_c$. b) $Re[Z(\omega)]$ of the environment of the junction. Z_c is proportional to its integral.

Consider the circuit of figure 3.1, assumed to be at zero temperature. When the bias voltage V matches the resonance condition $2eV = k\hbar\omega_r$, Cooper pairs can tunnel inelastically through the Josephson junction while creating k photons in the resonator, at a rate:

$$\Gamma^{ph} = k\Gamma^{2e} = k\frac{\pi {E_J}^2}{2\hbar}P(2eV) = \frac{E_J^{*2}}{\hbar^2}\frac{Q}{\omega_r}\frac{r^k}{k!}, \tag{3.1}$$

with $r = \pi Z_c/R_Q$ the coupling constant of the mode to the junction. In this very simple circuit the renormalized Josephson energy is $E_J^* = E_J e^{-\Delta\hat{\phi}_r^2/2} = E_J e^{-r/2}$, with $\Delta\hat{\phi}_r^2 = \langle 0|\hat{\phi}_r^2|0\rangle$ the ZPF of the phase across the resonator.

We insist on the difference between the regime of **strong driving** of the mode by the tunnel current, and the regime of **strong coupling** of the mode to the junction. Both result from the back-action of the field in the resonator onto the junction, leading to a reduction of the emission rate. However the strong driving regime already appears in a classical treatment of the dynamics of the circuit, whereas strong coupling is defined after considering multi-photonic emission processes, triggered at zero temperature by ZPF of quantum origin.

How strongly can the junction drive the mode?

The distinction between these two concepts already shows up for the single photon processes, $k = 1$. The stationary rate in (3.1) is the product of a term characterizing the junction, ${E_J}^2$, and one describing the ability of the environment to accomodate the energy $2eV$: $P(2eV) = 2e^{-r}rQ/\pi\hbar\omega_r = e^{-r}Re[Z(\omega_r)]/R_Q\hbar\omega_r$ for 1-photon processes.

Suppose that $r \lesssim 1$ such that the influence of the e^{-r} term can be neglected. Then the resonator characteristics enter in (3.1) only through $Re[Z(\omega_r)] = QZ_c$. It seems then

that at fixed E_J, one could always increase the emission rate by playing either on Z_c or on Q.

However the dynamics of the system are not the same if Z_c is high and Q is low or if Z_c is low and Q high. For a higher Q, the leak rate of the mode is smaller, and its average occupation number $\bar{n} = \Gamma^{ph}/\kappa$ at a given emission rate is larger. As the mode is populated its phase fluctuations $\Delta\hat{\phi}_r^2 = r(2\bar{n}+1)$ differ from their equilibrium value, eventually breaking an essential assumption of $P(E)$ theory.

Let us derive the value of $\bar{n}$ where this breakdown occur. The $P(E)$ theory is only valid when $E_J P(2eV) \ll 1$. Correlatively the semi-classical ac-Josephson 2.2 effect assumes that $Re[Z(\omega_r)]I_c \ll \pi V$, with:

$$\frac{Re[Z(\omega_r)]}{\pi V} \times I_c = \frac{Re[Z(\omega_r)]}{\pi\hbar\omega_r/2e} \times \frac{2eE_J}{\hbar} = P(2eV)E_J, \tag{3.2}$$

so that the two conditions are actually equivalent. Indeed, they both mean that the voltage drop across the environment stays small compared to the dc voltage bias on the junction.

If this condition is not met, the non-linearity of the Josephson current-phase relation has to be taken to next order. This leads to more complex emission processes, involving co-tunneling of several Cooper pairs at the same time. This effect reduces the tunneling rate, both in the classical and quantum theory (see appendix J in [61]). Because it appears in a classical treatment of the system, this effect cannot lead to the creation of a state of light with non-classical properties.

By inserting $E_J P(E) \ll 1$ in (3.1), one finds that the dc-current needs to stay small compared to the critical current of the junction:

$$I_{dc} = 2e\Gamma^{2e} = \frac{\pi E_J I_c}{2} P(2eV) \ll \frac{\pi}{2} I_c, \tag{3.3}$$

which hold in particular if:

$$\Gamma \ll \frac{\kappa}{r}, \tag{3.4}$$

with $\kappa = \omega_r/Q$ the decay rate of the resonator. The breakdown occurs when the average photon number in the mode $\bar{n} = \Gamma/\kappa$ is of the order of $1/r$. In practice, one can avoid this **strong-driving regime** by tuning down E_J so that $r\bar{n} \ll 1$. This weak-driving regime is analogous to the Lamb-Dicke condition in ion trapping experiments [62]. In the same way, for a k-photon process, one needs to ensure $r^k\bar{n} \ll 1$.

By contrast, the **strong-coupling regime** $r \sim 1$ is defined entirely by the properties of the resonator, as it amounts to $Z_c \sim R_Q/\pi \simeq 2.05$ kΩ, but no assumption on E_J or $\bar{n}$ needs to be made. In this regime, even if the average occupation number $\bar{n}$ is small compared to 1, the vacuum phase noise $\Delta\hat{\phi}_r^2 \sim 1$ itself is large enough to reduce the tunneling rate. This can be proven by a more complete treatment of the circuit, taking also into account the dynamics of the state of the mode in the resonator. Note that despite a similar name, this has nothing to do with the strong-coupling regime of cavity-QED experiments, which occurs when the coupling between an atom and the field in a cavity is larger than the inverse lifetime of either one.

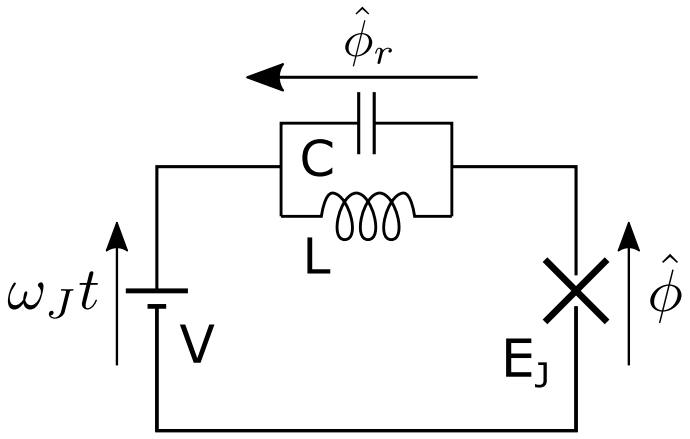

Figure 3.2: A dc-biased Josephson junction coupled to a single LC mode, with notations for the phase operators across each element of the circuit.

Dynamics of a single mode driven by a Josephson junction

As in the derivation of the $P(E)$ theory, the Hamiltonian for a Josephson junction coupled to a single mode (Fig.3.2) is:

$$H = \hbar\omega_r \left(\hat{a}^\dagger \hat{a} + \frac{1}{2}\right) - E_J \cos(\hat{\phi}), \tag{3.5}$$

with $\hat{a}$ ($\hat{a}^\dagger$) the annihilation (creation) operator of the mode. The phase operator $\hat{\phi}$ is proportional to the integral of the voltage drop across the junction (2.12). Following Kirchhoff's law, this voltage is the difference between the dc voltage bias V imposed by the voltage source and the voltage across the resonator. The phase across the junction is thus:

$$\hat{\phi} = \frac{2eVt}{\hbar} - \hat{\phi}_r \tag{3.6}$$

$$= \omega_J t - i\sqrt{r}(\hat{a}^\dagger e^{+i\omega_r t} - \hat{a}e^{-i\omega_r t}), \tag{3.7}$$

with the Josephson frequency: $2eV/\hbar = \omega_J$. The expansion of the cos term in the time-dependent Hamiltonian yields an infinite series of terms that couple the tunnel current to the field in the resonator $\hat{\phi}_r = i\sqrt{r}(\hat{a}^\dagger e^{+i\omega_r t} - \hat{a}e^{-i\omega_r t})$. To compute this expansion, we recall that the Josephson term can also be written:

$$-E_J \cos(\hat{\phi}) = -E_J \frac{e^{i\hat{\phi}} + e^{-i\hat{\phi}}}{2} = \frac{-E_J}{2} e^{i\hat{\phi}} + \text{h.c.} \tag{3.8}$$

We then use a special case of the Baker-Campbell-Hausdorff formula, which states that:

$$e^{\hat{A}} e^{\hat{B}} = e^{\hat{A}+\hat{B}+[\hat{A},\hat{B}]/2}, \tag{3.9}$$

iff the operators $\hat{A}, \hat{B}$ commute with their commutator $[\hat{A}, \hat{B}]$ [63]. First, this means that we can extract the linear evolution term $\omega_J t$ out of the exponential:

$$e^{i\hat{\phi}} = e^{i\omega_J t} e^{\sqrt{r}(\hat{a}^\dagger e^{+i\omega_r t} - \hat{a}e^{-i\omega_r t})}. \tag{3.10}$$

Second, as $[\hat{a}, \hat{a}^\dagger] = 1$, we have for $\lambda \in \mathbb{C}$:

$$e^{\lambda\hat{a}^\dagger + \lambda^*\hat{a}} = e^{-|\lambda|^2/2} e^{\lambda\hat{a}^\dagger} e^{\lambda^*\hat{a}}, \tag{3.11}$$

such that after mapping $\hat{H}$ to the frame rotating at ω_r in order to get rid of the $\hbar\omega_r\left(\hat{a}^\dagger\hat{a}+\frac{1}{2}\right)$ term, the Hamiltonian reads:

$$\hat{H}_{\omega_r} = \frac{-E_J e^{-r/2}}{2} e^{i\omega_J t} e^{\sqrt{r}\hat{a}^\dagger e^{+i\omega_r t}} e^{-\sqrt{r}\hat{a}e^{-i\omega_r t}} + \text{h.c.} \tag{3.12}$$

We note here that the renormalized Josephson energy $E_J^* = E_J e^{-r/2}$ naturally appears as a consequence of the **non-commutativity of $\hat{a}$ and $\hat{a}^\dagger$**. In the $P(E)$ theory, this renormalization is due to the vacuum fluctuations of the phase across the resonator.

A straightforward expansion of the exponential operators yields now:

$$\hat{H}_{\omega_r} = \frac{-E_J^*}{2} e^{i\omega_J t}\left(\sum_{l=0}^{\infty}\frac{(\sqrt{r}\hat{a}^\dagger)^l}{l!}e^{+il\omega_r t}\right)\left(\sum_{m=0}^{\infty}\frac{(-\sqrt{r}\hat{a})^m}{m!}e^{-im\omega_r t}\right) + \text{h.c.} \tag{3.13}$$

This Hamiltonian contains infinitely many terms oscillating at frequencies $\omega_J + q\omega_r$ with $q \in \mathbb{Z}$. We are interested only in the stationary state of the system, so we neglect all terms oscillating faster than the decay rate of the mode, as they effectively average to zero in the rotating frame. Close to a resonance condition $2eV = k\hbar\omega_r$, we only keep terms such that $k + l - m = 0$:

$$\hat{H}_{RWA}^{(k)} = \frac{-E_J^*}{2}\sum_{l=0}^{\infty}(-1)^{l+k}(\sqrt{r})^{2l+k}\frac{(\hat{a}^\dagger)^l}{l!}\frac{\hat{a}^{l+k}}{(l+k)!} + \text{h.c.} \tag{3.14}$$

This Rotating Wave Approximation (RWA) holds if the quality factor of the mode is high enough and if the driving strength $E_J/\hbar$ stays small compared to the frequency of the mode [64].

Dynamics in a low-impedance environment

It is already instructive to consider the low impedance case ($r \ll 1$). To leading order in r one obtains:

$$\hat{H}_{RWA}^{(k)} \simeq \frac{-E_J^*}{2k!}(-\sqrt{r})^k(\hat{a}^k + (\hat{a}^\dagger)^k). \tag{3.15}$$

This Hamiltonian describes a coherent k-photon drive. For $k = 1$, the resonance condition of the ac-Josephson effect 2.2, the junction drives linearly the mode:

$$\hat{H}_{RWA}^{(1)} \simeq \frac{E_J^*}{2}\sqrt{r}(\hat{a} + \hat{a}^\dagger), \tag{3.16}$$

creating a coherent state $|\alpha\rangle$ in the mode with amplitude $\alpha = E_J^*\sqrt{r}/\hbar\kappa$.

For $k \neq 1$, this Hamiltonian creates a non-trivial state of light. The stationary photon emission rate may still be computed through Fermi's Golden Rule, leading to (3.1) with $\Gamma^{ph} \propto {E_J^*}^2 r^k/k!$ at the $k-$photon resonance.

Note that as for $r \ll 1$ we always have $E_J P(E) \ll 1$, it is natural that we recover the $P(E)$ result to leading order in r.

Taking into account the next order term in r yields:

$$\hat{H}^{(k)}_{RWA} \simeq \frac{-E^*_J}{2k!}(-\sqrt{r})^k \left\{ \left(1 - \frac{r\hat{a}^\dagger\hat{a}}{k+1}\right)\hat{a}^k + (\hat{a}^\dagger)^k \left(1 - \frac{r\hat{a}^\dagger\hat{a}}{k+1}\right)\right\}. \tag{3.17}$$

The k-photon drive is now dressed by the operator $\left(1 - \frac{r\hat{a}^\dagger\hat{a}}{k+1}\right)$. This additional term reduces the driving amplitude, and hence the photon emission rate. For a low impedance $r \ll 1$, its effect can be neglected if $\langle r\hat{a}^\dagger\hat{a}\rangle = r\bar{n} \ll (k+1)$. At $k = 1$ this coincides with the condition for the system to stay away from the strong driving regime.

Full treatment of the non-linearity for an arbitrary impedance

For an arbitrary high value of the coupling parameter r, the fact that the average photon number $\bar{n}$ is small compared to $1/r$ is not enough to ensure that the RWA Hamiltonian reduces to a simple linear drive. From a dynamical point of view, immediately after a Cooper pair has tunneled, k photons are created in the mode, so that the instantaneous expectation value of $r\hat{a}^\dagger\hat{a}$ is $\sim rk$ (for a k-photon process). Then the effect of higher order terms cannot be neglected as they are comparable to the first order one, leading to complex non-linear dynamics with a stationary state hard to predict in the general case.

Such strong non linearities lead to non-classical dynamics of the emitted radiation: in 2013, Gramich and coworkers computed the statistics of the charge transport through the junction, as well as those of the photon emission, for one-photon processes $\omega_J \simeq \omega_r$ [34]. They expressed the Hamiltonian (3.14) as a linear drive $(\hat{a}^\dagger + \hat{a})$ dressed by a Bessel function of $2\sqrt{r\hat{a}^\dagger\hat{a}}$, and wrote a master equation describing the evolution of the density operator of the whole system $\hat{\rho}$ [65][66]:

$$\dot{\hat{\rho}} = -\frac{i}{\hbar}[\hat{H}^{(1)}_{RWA}, \hat{\rho}] + \frac{\kappa}{2}\mathcal{L}[\hat{a}, \hat{\rho}] + \frac{\gamma_J}{2}\mathcal{L}[\hat{N}, \hat{\rho}], \tag{3.18}$$

where as in 2.1 $\hat{N}$ counts the number of charges having crossed the junction. In addition to the Hamiltonian drive, this Lindblad equation contains the dissipator $\frac{\kappa}{2}\mathcal{L}[\hat{a}, \hat{\rho}]$ that describes the leakage of photons into the measurement line at a rate κ, and the dissipator $\frac{\gamma_J}{2}\mathcal{L}[\hat{N}, \hat{\rho}]$ which is due to the dc voltage noise on the junction. Here γ_J is a heuristic dephasing rate of the Josephson frequency, proportional to the width of the zero energy peak in $P(E)$ (2.74). Its influence on the dynamics is negligible as long as $\gamma_J \ll \kappa$.

Solving this master equation, the authors of [34] were able to retrieve the results of the $P(E)$ theory in the limit of vanishing Josephson energy. In the opposite limit of low impedance and high E_J, the system ends up in classical stationary orbits, also predicted by the exact treatment of the ac-Josephson effect 2.2.

The full strong coupling regime $r \sim 1$ with arbitrary E_J has to be solved numerically. However in the limit of low E_J, an analytical computation already shows that non-classical anti-correlations appear in the statistics of the emitted radiation [34].

The importance of the precise value of the coupling r appears when re-writing the Hamiltonian (3.14) directly in the Fock basis [67], as shown by Souquet and Clerk in [68]:

$$\hat{H}^{(1)}_{RWA} = \frac{-E_J^*}{2} \sum_{n=0}^{\infty} \left(h^{RWA}_{n+1,n} |n+1\rangle\langle n| + \text{h.c.} \right), \tag{3.19}$$

with the matrix elements:

$$h^{RWA}_{n+1,n} = \langle n+1 | e^{i\hat{\phi}} | n \rangle = \frac{\sqrt{r}}{\sqrt{n+1}} L_n^1(r), \tag{3.20}$$

where $L_n^1(r)$ is a generalized Laguerre polynomial. The first four of these polynomials are plotted as a function of r in figure 3.3.

In a charge basis picture, $|h^{RWA}_{n+1,n}|^2$ is a measure of the overlap between the $|n\rangle$ state displaced by $2e$ under the action of the $e^{i\hat{\phi}}$ operator and the $|n+1\rangle$ state (Fig.3.4.b). Following Fermi's Golden Rule, the transition rate from $|n\rangle$ to $|n+1\rangle$ is proportional to this overlap.

Let us look at particular values of some of these polynomials. $L_n^1(0)$ is simply $n+1$, so that for a low-impedance mode ($r \ll 1$):

$$\sum_{n=0}^{\infty} h^{RWA}_{n+1,n} |n+1\rangle\langle n| \sim \sqrt{r}\hat{a}^\dagger. \tag{3.21}$$

Then (3.19) reduces to a simple linear drive of the resonator, and we recover our results of 2.2 in the case of a low impedance environment.

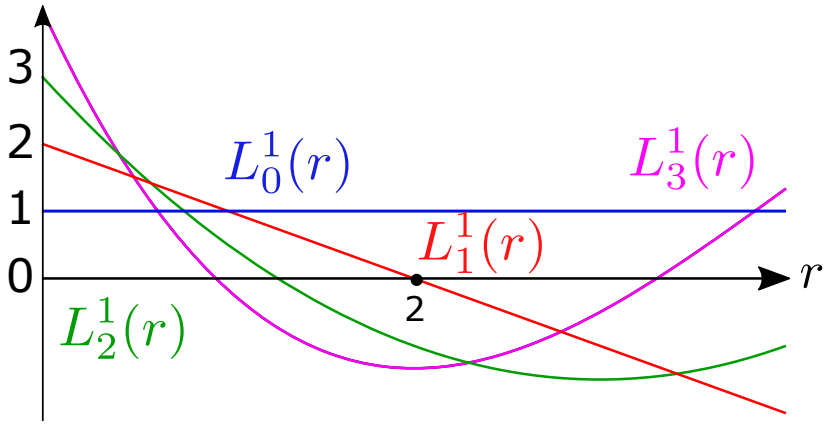

Figure 3.3: Generalized Laguerre polynomials $L_n^1(r)$ for $n \in [0,3]$, which appear in (3.20). The $|2\rangle\langle 1|$ matrix element of $\hat{H}^{(1)}_{RWA}$ is proportional to $L_1^1(r)$, which vanishes for $r = 2$.

$L_0^1(r)$ is simply equal to 1, such that for an arbitrary r value transitions from the vacuum to an occupied state are always possible. Higher order polynomials do depend on r, such that transitions between some of the Fock states may be inhibited or enhanced. Then the Hamiltonian (3.19) departs frankly from a linear drive and may lead to non-trivial dynamics. Even more interestingly the Laguerre polynomials have roots for $r > 0$, so that some transitions may be forbidden.

In particular $L_1^1(2) = 0$ (Fig.3.3), so that for $r = 2$ the system can never be driven from the $|1\rangle$ to the $|2\rangle$ Fock state. This precise r value generates an interesting photon blockade mechanism : starting with an empty resonator, a single photon is created as soon as a

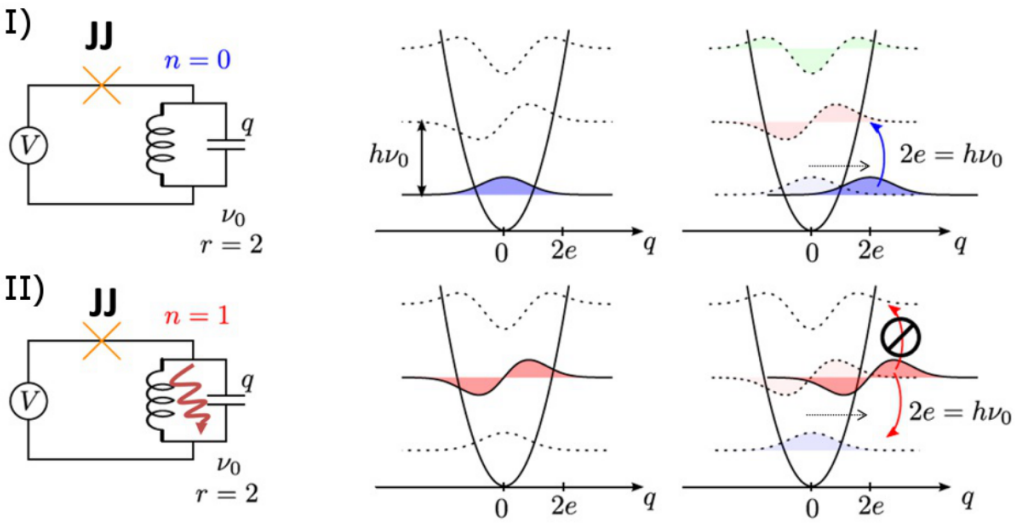

Figure 3.4: Frank-Condon blockade of the emission of a second photon after a first one has already been created, that occurs for $r = 2$.

Cooper pair tunnels. Then as long as the photon is present in the mode, no further tunneling is possible, as the transition to a state with two photons is impossible.

In the absence of dissipation, the system undergoes Rabi oscillations between the $|0\rangle$ and $|1\rangle$ states, with the junction coherently absorbing and re-emitting a single photon in the mode. In practice $\kappa \neq 0$, due e.g. to coupling to a transmission line, so that the photon eventually decays. Then Cooper pair tunneling is possible again and another single photon is created, restarting the blockade mechanism. The stationary occupation number results from the balance between the photon filling rate and the decay rate κ, and follows (3.1) in the limit of low E_J.

Characterization of single photons

This dynamics results in the creation of photons which are somewhat detached from one another, as opposed to the natural tendency of bosons to bunch together. The radiation leaking outside of the resonator then consists of **single photons**, and displays properties which can not exist in a classical description of light [69].

Single-photons are characterised by their **second-order coherence function** [64]:

$$g^{(2)}(t, t+\tau) = \frac{\langle \hat{a}^\dagger(t)\hat{a}^\dagger(t+\tau)\hat{a}(t+\tau)\hat{a}(t)\rangle}{\langle \hat{a}^\dagger(t)\hat{a}(t)\rangle\langle \hat{a}^\dagger(t+\tau)\hat{a}(t+\tau)\rangle}, \tag{3.22}$$

which is the normalized probability of detecting two photons in the same mode, at times t and $t+\tau$. As such $g^{(2)}$ gives the fringe contrast in some intensity-interferometry experiments [70]. In the case of a stationary state of light, the ensemble average can be taken as a time average over t, leading to:

$$g^{(2)}(\tau) = \frac{\langle \hat{a}^\dagger(0)\hat{a}^\dagger(\tau)\hat{a}(\tau)\hat{a}(0)\rangle}{\langle \hat{a}^\dagger\hat{a}\rangle^2}. \tag{3.23}$$

To highlight the importance of this correlation function in quantum optics, let us start by reviewing its properties in the classical case. Replacing the $\hat{a}(t)$ operator by the classical

field amplitude $a(t)$, we can reorder (3.23) without taking into account commutation relations, leading to:

$$g^{(2)}_{\text{class.}}(\tau) = \frac{\langle a^*(0)a^*(\tau)a(\tau)a(0)\rangle}{\langle a^*a\rangle^2} = \frac{\langle |a(0)|^2|a(\tau)|^2\rangle}{\langle |a|\rangle^2}. \tag{3.24}$$

The classical version of $g^{(2)}(\tau)$ can be linked to the auto-correlation function of the power radiated by the resonator $P(t) = \hbar\omega_r\kappa|a(t)|^2$:

$$g^{(2)}_{\text{class.}}(\tau) = \frac{\langle P(0)P(\tau)\rangle}{\langle P\rangle^2} \tag{3.25}$$

$$\Rightarrow g^{(2)}_{\text{class.}}(0) = \frac{\Delta P^2}{\langle P\rangle^2} + 1 > 1. \tag{3.26}$$

The classical power $P(t)$ is a real number, so that it verifies:

$$P(0)^2 + P(t)^2 - 2P(0)P(t) = (P(0) - P(t))^2 \geq 0 \tag{3.27}$$

$$\Rightarrow \; P(0)^2 + P(t)^2 \geq 2P(0)P(t) \tag{3.28}$$

$$\Rightarrow \; \langle P^2\rangle \geq \langle P(0)P(t)\rangle, \tag{3.29}$$

i.e the fluctuations of the power in a classical beam of light are always larger than the power correlation at two different times. This leads to the inequality:

$$g^{(2)}_{\text{class.}}(0) \geq g^{(2)}_{\text{class.}}(\tau). \tag{3.30}$$

Interpreting this result in a semi-classical picture, we would say that photons tend to bunch together.

The situation is much different if one takes into account the quantum nature of light, by keeping track of the commutation relation of $\hat{a}$ and $\hat{a}^\dagger$ in the calculations. In that case the inequalities (3.26) and (3.30) no longer need to hold for all fields. When $g^{(2)}(\tau) > g^{(2)}(0)$, light is said to be **antibunched**, because it means that photons (counted by the $\hat{a}^\dagger\hat{a}$ operator) tend to be well-separated in the beam (Fig.3.5).

The value of $g^{(2)}(0)$ is related to the variance of the emitted power. Due to the granular nature of light, even a quasi-classical coherent state displays some fluctuations of its intensity, with a **Poissonian** distribution of the number of photons detected in a given time-window, leading to $g^{(2)}(0) = 1$. Some other quasi-classical states, such as the thermal states of light, display **super-Poissonian** statistics with $g^{(2)}(0) > 1$, meaning that they present more intensity noise than the classical minimum. On the other hand states with $g^{(2)}(0) < 1$, said to be **sub-Poissonian**, show less noise than the classical limit, and are therefore useful for some metrology or quantum information protocols.

Pure **Fock states**, which are deeply quantum states of light containing an exact number of photons, produce the best example of sub-Poissonian light, with $g^{(2)}(0) = 1 - 1/n$ for the n-photon state.

In an experimental setting, one is more often confronted with **mixed states** of light. The blockade mechanism may partially fail due to imperfections in the sample, meddling the single photons with higher number states. Such an incoherent mixture of different states is described by a *density operator*:

$$\rho = \sum_{n\in\mathbb{N}} \sqrt{p_n}|n\rangle\langle n| + \sum_{k\neq l} c_{kl}|k\rangle\langle l| \tag{3.31}$$

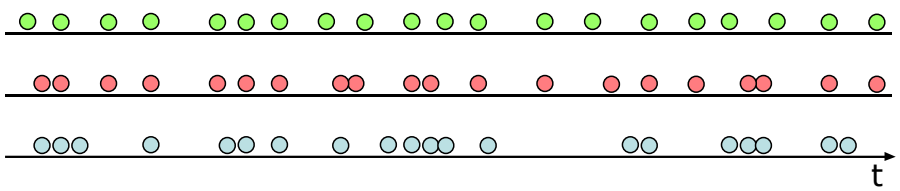

Figure 3.5: Schematic picture of the photons in a beam of light displaying (from top to bottom) anti-bunching, classical and bunchings statistics.

with p_n the probability of finding n photons in the beam. We then have:

$$\langle \hat{a}^\dagger \hat{a} \rangle_\rho = \sum_{n\in\mathbb{N}} p_n \langle n|\hat{a}^\dagger \hat{a}|n\rangle = \sum_{n\in\mathbb{N}} p_n n, \tag{3.32}$$

$$\langle \hat{a}^\dagger \hat{a}^\dagger \hat{a}\hat{a} \rangle_\rho = \sum_{n\in\mathbb{N}} p_n \langle n|\hat{a}^\dagger \hat{a}^\dagger \hat{a}\hat{a}|n\rangle = \sum_{n\in\mathbb{N}} p_n n(n-1). \tag{3.33}$$

A value of $g^{(2)}(0)$ below $1/2$ can only be obtained if $p_1 \neq 0$, and is regarded as a sufficient proof that the light consists of single photons [71]. A more precise bound on the ratio of single photon to multi-photonic emission is given by:

$$\frac{p_1}{\sum_{n\geq 2} p_n} \geq 2 \times \left(\frac{1}{\bar{n} g^{(2)}(0)} - 1 \right). \tag{3.34}$$

Generating single photons with a high-impedance resonator

In the limit of low E_J and low occupation number $\bar{n}$, the only states of the resonator with a non-vanishing occupation probability are the $|0\rangle, |1\rangle$ and $|2\rangle$ Fock states. Then a simple rate model is sufficient to predict the dynamics of a Josephson junction coupled to a single mode [72]. The second order coherence function is found to be:

$$g^{(2)}(\tau) = \left(1 - \frac{r}{2} e^{-\frac{\kappa\tau}{2}}\right)^2. \tag{3.35}$$

Remarkably, the statistics of the light depends only on the value of the coupling parameter r. If $r < 4$ we see that the photons are antibunched and sub-Poissonian, as $g^{(2)}(0) < g^{(2)}(\tau) \leq 1$ for $\tau \neq 0$. For r close to 2, $g^{(2)}(0) < 1/2$, such that the emitted light has a single-photon character, even if the transition to higher Fock states of the resonator is not totally suppressed. For $r = 2$ we find $g^{(2)}(0) = 0$, as the $|1\rangle \to |2\rangle$ transition is perfectly blocked and the emitted light consists only of a mixture of vacuum and the single photon state, with perfect sub-Poissonian statistics.

Surprisingly, light containing either one or zero photon has less intensity fluctuations than a quasi-classical coherent state with a well defined amplitude. The value $g^{(2)}(0)$ is a conditional probability: it gives the probability of finding two photons in a mode, provided that (at least) one photon has been detected.

Still it is possible to create non-classical states of light using ICPT in a circuit including a mode with a high-enough impedance. To prove the antibunching of these photons, we

designed an experiment where a small SQUID is coupled to a microwave resonator with very high impedance $Z_c \sim 2$ kΩ such that $r \sim 1$. At low-enough $E_J(\Phi)$ dc-biasing it on the one-photon resonance, it can only emit single photons in the mode, which escape before a new photon is created. By detecting the radiation leaking out of the resonator and performing correlation measurements, we proved that this device emits antibunched photons [36].

Remark: comparison with circuit-QED single photon sources

Potential applications for single-photon sources in the microwave domain [73][12] motivated pioneering circuit-QED experiments [74][75]. In these experiments, a superconducting qubit is excited from its ground state by a classical microwave pulse. The qubit is then tuned to be resonant with a microwave cavity at a different frequency, resulting in the spontaneous emission of exactly one photon in the cavity. Such a source displays good antibunching, with $g^{(2)}(0) \simeq 0$, but with relatively low photon emission rates, up to about 10^6 photons per second.

The photon emission rate is limited by the quality factor of the qubit, which need to be high enough to ensure that no unwanted transitions to higher energy states occur. This is an important practical difference with the ICPT single-photon source, where there are no limits on the decay rate of the mode. Superconducting qbits are also typically limited to the 4-8 GHz bandwidth, due to the constraints of microwave engineering and signal processing. By contrast ICPT could be implemented in junctions made out of materials with large superconducting gaps, allowing the creation of quantum states of light at higher frequencies [55].

These two schemes also differ by their modes of operations. The qubit scheme amounts to the linear driving of a non-linear oscillator, while in ICPT the resonator **stays linear** (the energy spacing between levels is always $\hbar\omega_r$) but is subject to a **non-linear drive**, that turns off as soon as a single photon is created in the mode.

There are thus practical and fundamental reasons to validate our *dissipation engineering* approach to the generation of quantum radiation, starting by the creation of single photons.

3.2 Implementation of the strong-coupling regime between a Josephson junction and a single mode

The conception and realisation of the first circuit including a dc-biased Josephson junction in series with a microwave mode in the strong-coupling regime was the work of Chloé Rolland during her PhD research [35]. She designed and fabricating a coil resonator with a characteristic impedance $Z_C \sim 2$ kΩ, so that it was coupled to a Josephson junction in the regime $r \sim 1$. We recall here the main challenges of the design of this sample.

High impedance microwave resonator

Microwave resonators can be designed using either lumped or distributed elements. **Distributed circuits** include the $\lambda/4$ resonators we described in 2.3.1, where impedance mismatches between segments of transmission line create Fabry-Pérot resonances. Cascading several segments of TL allow to shape the $Re[Z(\omega)]$ of the resonator. However the characteristic impedance of the mode is approximately given by the wave impedance of the segment closest to the junction, and cannot be increased by adding more segments.

The wave impedance of a CPW line is of the order of $Z_w \sim 100$ Ω in standard electronics. It can be increased by making the inner conductor thinner, and the ground planes farther apart, but with a limited margin for improvements, as Z_w scales approximately like the log of the ratio of these two dimensions. Moreover, the gap between the two ground planes must be kept small compared to the wavelength of the radiation to prevent coupling to non-CPW modes. Nanofabrication constraints ultimately set the limit on how precisely one can produce these dimensions, such that on a standard Si substrate only impedances in the 25 to 135 Ω range can be reliably designed (Fig.3.6).

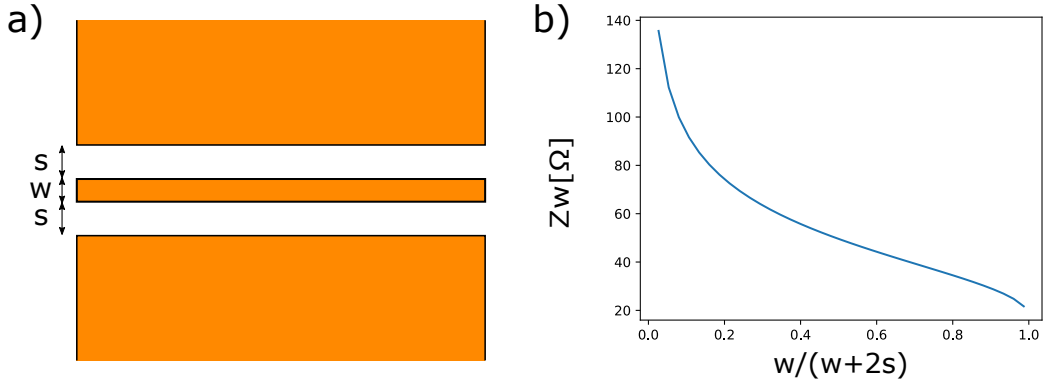

Figure 3.6: a) Schematic drawing of a CPW waveguide (metallized part in orange). b) Characteristic impedance as a function of the inner width to ground planes spacing ratio for a standard oxidized Si wafer, with a 50 nm SiO_2 capping layer.

Reaching the strong coupling regime with $Z_c \sim 2$ kΩ thus requires a more complex strategy than the one used in 2.3.2. One could boost the linear inductance of the CPW line using either a material with a high kinetic inductance, like a disordered superconductor [76], or a meta-material like a chain of SQUIDs [77]. However at the time of her PhD Chloé Rolland had in mind experiments performed to test DCB in 2D electron gases, which require high magnetic fields of the order of 1 to 10 T to be put in the Quantum

Hall regime. Such fields are incompatible with the use of superconducting waveguides, such that she resorted to a different strategy, using a **lumped element design**.

A lumped element model holds for circuit components with dimensions much less than the wavelength of propagative modes λ. At 5 GHz in a standard coaxial cable $\lambda \simeq 4$ cm, so that conductors smaller than a few hundred of microns can be considered lumped elements. In these conditions the resonator is well described by a LCR model, with a resonance frequency $\omega_r = 1/\sqrt{LC}$, a characteristic impedance $\sqrt{L/C}$ and a quality factor $Q = Z_c/R$ for a series circuit.

Aiming at $\omega_r \simeq 2\pi\times 5$ GHz, a $r = 2$ mode requires $L \simeq 130$ nH and $C \simeq 8$ fF. This value of inductance can be reached by winding a strip of metal in a coil shape. The main difficulty is actually to reduce as much as possible the capacitance of the resonator. The Josephson junction is also in parallel with its own geometrical capacitance, of the order of a few fF, so that the LCR needs to be essentially capacitance-less (Fig.3.7).

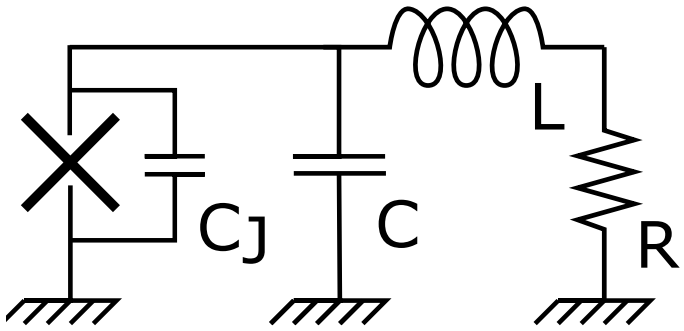

Figure 3.7: A LCR resonator is connected to the junction. The effective capacitance of the mode is the sum of the resonator capacitance C and the geometric capacitance of the junction C_J.

The solution used by Chloé Rolland was to implement the LCR as a microfabricated coil, using only C_J and the stray capacitance of the coil to generate the capacitance of the mode. Each turn of the coil has a high mutual inductance with the neighbouring turns, resulting in a high total inductance of the resonator, while keeping it compact to limit the stray capacitance to ground.

The inner pad of the coil needs to be dc coupled to the junction through a bridge supported by a dielectric brick. This brick adds some parasitic capacitance, which tends to shunt the coil. Chloé Rolland optimized the shape of the coil with the electromagnetic simulation software Sonnet to find the best dimensions, with the nanofabrication constraint of having no detail smaller than 2 μm. These simulations were needed as the resonator was not in the lumped element regime, as the total length of the coil was still of the order of 2 cm $\lesssim \lambda$.

The optimization procedure proved impossible to reliably attain $r = 2$ while respecting all the constraints of nanofabrication and microwave design, in particular due to the unavoidable stray capacitance to ground. This capacitance was reduced by choosing to fabricate the sample on a quartz substrate, with a relative dielectric constant $\epsilon_r = 4.2$ smaller than for a Si chip ($\epsilon_r = 11.8$). In the end Chloé Rolland proposed and implemented a design for a resonator reaching $r = 1$ at $\omega_r = 2\pi\times$ 5.1 GHz. She also designed an impedance adaptation at the input of the coil, to be able to reduce the quality factor of the mode down to about 30. A quality factor too high would result in

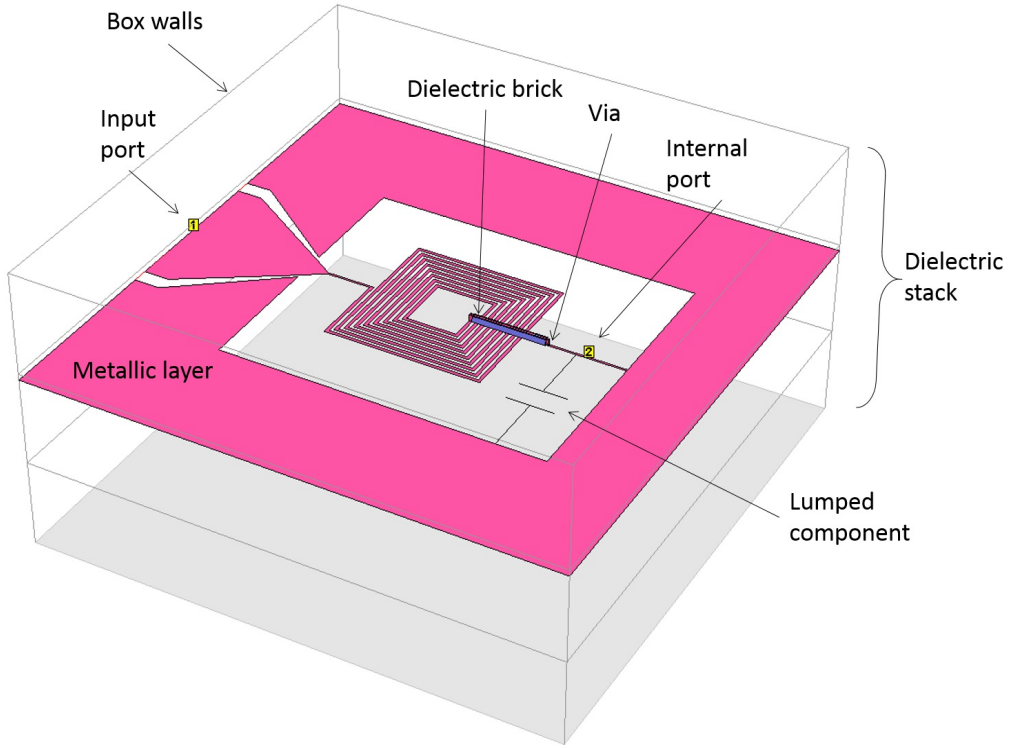

Figure 3.8: Model used in a Sonnet simulation, implementing the circuit of figure 3.7. The Josephson junction (not shown) is placed at port 2 between the ground and the coil, and is shunted by C_J, which is modelled as a lumped capacitor component of 2 fF. The coil (square in this iteration of the design) is connected to the detection chain at the input port 1, and to the junction through a bridge supported by a micron-thick dielectric bridge (taken from [35]).

a mode leak rate smaller than the dephasing rate due to voltage noise, breaking some assumptions of the theoretical predictions from 3.1.

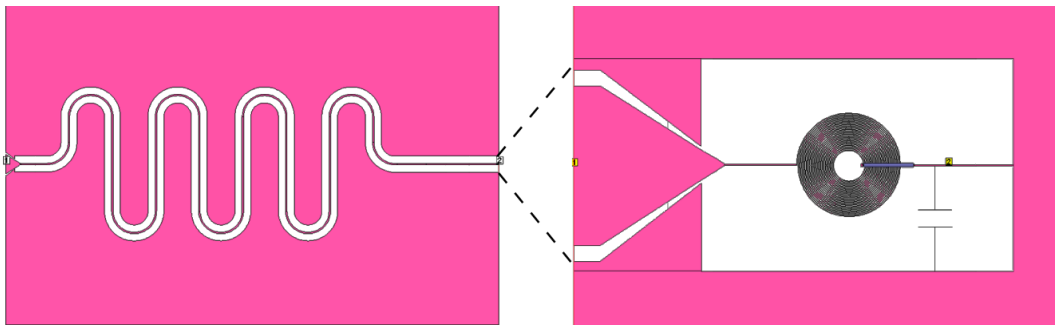

Figure 3.9: Final design for the strong-coupling resonator. A 240 μm wide coil is made with 23 turns of a 1 μm wire with 2 μm spacings between the turns. One port of the coil is connected to a 70 Ω $\lambda/4$ resonator, that raises the input impedance seen by the coil up to 100 Ω at 5 GHz. The inner pad is connected via a supported bridge to a grounded Josephson junction (taken from [35]).

Sample fabrication

We describe here the basic fabrication process of the sample. More details can be found in [35].

A 100 nm thick Niobium film is sputtered on a chip, made out of quartz to reduce its dielectric constant. Optical lithography allows to pattern the film to produce the ground planes of the chip, the inner conductor of the $\lambda/4$ resonator and the coil itself (Fig. 3.10).

A bisbenzocyclobutene layer is deposited in a second step, and etched to create the dielectric support of the bridge. An Al layer was then deposited to create the bridge connecting the inner pad of the coil to junction (Fig. 3.11).

Figure 3.10: Optical image of the whole 3 mm×10 mm chip, showing the impedance adaptation resonator (meanders in the middle) and the bonding pad on the left (taken from [35]).

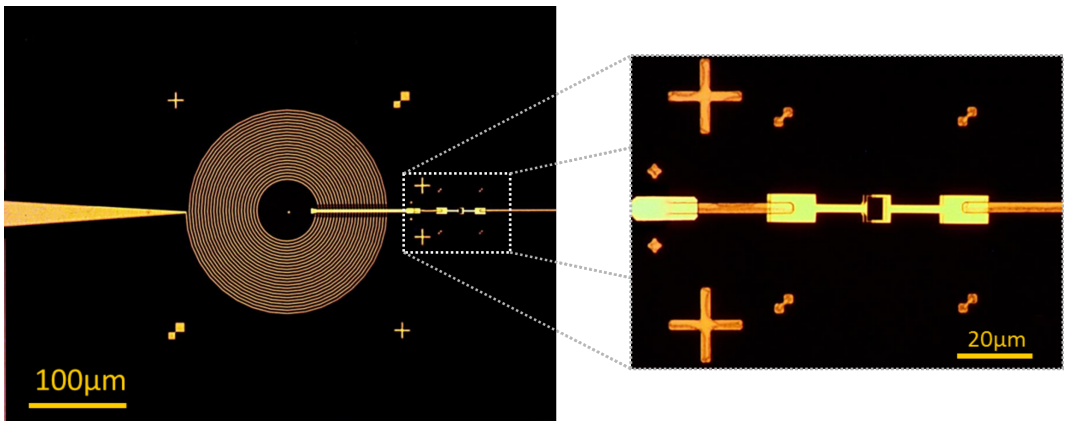

Figure 3.11: Left: microscope image of the microfabricated coil, with the bridge above the coil turns connecting to the junction on the right. Right: zoom-in on the SQUID implementing a tunable Josephson junction (taken from [35]).

The photon-emitting Josephson junction is implemented as a SQUID, with two junctions of Josephson energies E_J^A and E_J^B connected in parallel. Its effective E_J^{SQ} can be tuned by threading a magnetic flux Φ through the loop:

$$E_J^{SQ}(\Phi) = \sqrt{(E_J^A - E_J^B)^2 + 4E_J^A E_J^B \cos\left(\frac{2e\Phi}{\hbar}\right)^2} \tag{3.36}$$

With identical junctions $E_J^A = E_J^B$, E_J^{SQ} would be tunable down to zero. In practice the nanofabrication of junctions is not perfectly reproducible. Dispersion in the E_J of junctions fabricated on the same chip can be as high as 10%, in particular for very small junctions of about 100nm×100nm. In this experiment the electrodes cannot be made bigger to ensure a better reproducibility, as they would bring too much parasitic

capacitance and shunt the high impedance mode. Thus the design of the SQUID was made keeping in mind that it cannot be tuned down to less than $E_J^{min} = |E_J^A - E_J^B| \simeq (E_J^A + E_J^B)/10$.

Following (3.1), having an average occupation number $\bar{n}$ requires a Josephson energy of:

$$E_J = \hbar\kappa e^{r/2}\sqrt{\frac{\bar{n}}{r}}. \tag{3.37}$$

From Sonnet simulations [35], the FWHM of the mode is around 100 MHz, yielding $\kappa \simeq 2\pi \times 100\ \mu s^{-1}$. As $r \simeq 1$, a low-enough occupation number $\bar{n} \simeq 0.1$ requires $E_J \simeq 0.2\ \mu$eV. If this value is reached at a flux bias $2e\Phi/\hbar = \pi$, the maximum Josephson energy of the SQUID should be around 2 μeV. Using the Ambegaokar-Baratoff formula [56] yields a normal state resistance $R_N = \Delta R_Q/2E_J \simeq 300$ kΩ for an Al junction. This high resistance value would be hard to reach with standard oxidation techniques, that gives typically 300 Ω for a junction of 1 μm^2. Rolland thus decided to resort to a more complex double oxidation scheme [78]. The resulting small junctions are shown in figure 3.12.

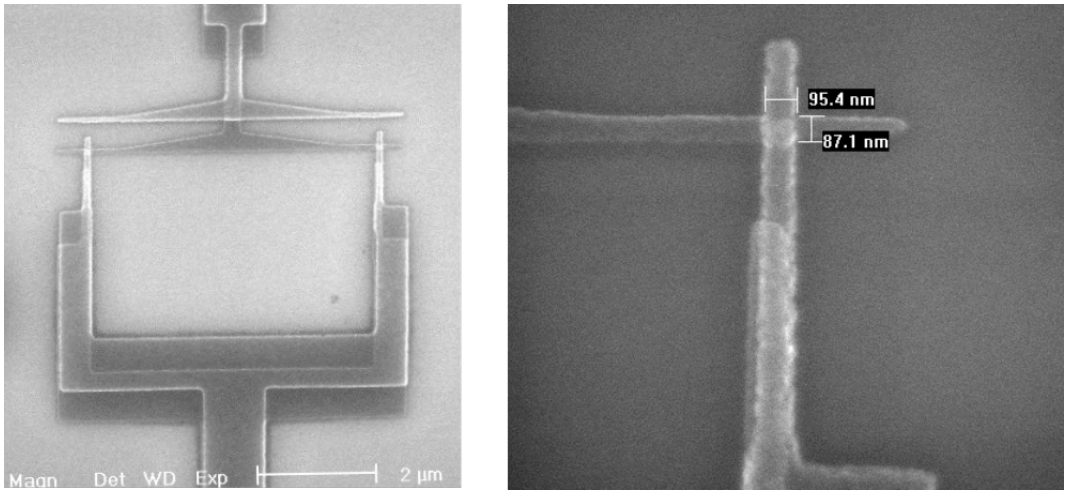

Figure 3.12: Scanning Electron Microscopy image of the nanofabricated SQUID. The two $\sim 100\times100$ nm^2 junctions are expected to add around 2 fF of geometric capacitance to the mode (taken from [35]).

3.3 Assessing the antibunching: principles of correlation measurements

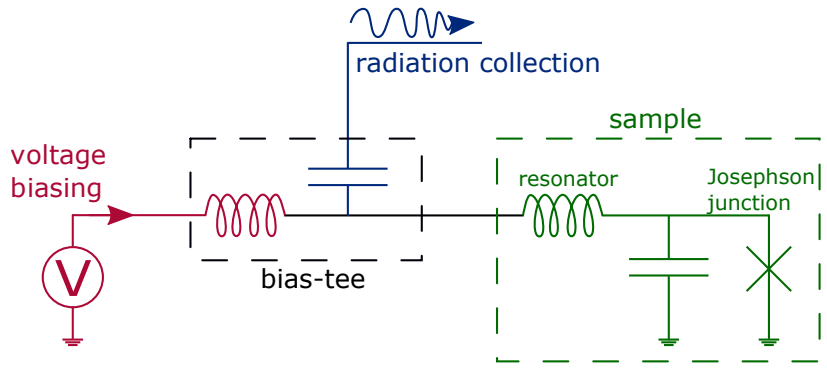

Figure 3.13: Principle of the experiment: the Josephson junction is dc-biased through the high-impedance resonator. A bias-tee at the output of the sample routes the microwave signals leaking out of the resonator towards the detection chain, while allowing the application of a precise voltage bias V (taken from [35]).

After fabrication, the strong-coupling sample is placed in the same dilution fridge that was used in the 2011 experiment 2.3.2, with a similar dc and RF setup. Here it can be biased at a precise value of voltage $V = \hbar\omega_r/2e$, where the tunneling of each Cooper pair coincides with the emission of a single photon in the measurement chain. This radiated power can be detected at room temperature after suitable amplification.

The second order coherence function $g^{(2)}(\tau)$ is generally obtained from measurements of power fluctuations in the beam of light. In our experiments this measurement is very challenging, in particular due to the very low energy of single microwave photons. The detection is notably vulnerable to parasitic correlations, which can easily flood the signal and drown it in noise.

We detail here the link between $g^{(2)}(\tau)$ and power fluctuations, and describe how its measure was first implemented by Chloé Rolland. We detail the limitations of the initial measurement scheme and the reasons why a more complete detection setup was needed. We then present a new measurement scheme, based on the *linear* detection of the emitted signals. It allows to measure arbitrary correlation functions of the field operator $\hat{a}(t)$ and prove the antibunching of the emitted photons.

3.3.1 Obtaining $g^{(2)}(\tau)$ from intensity correlations

We explain here how the coherence function (3.23) can be retrieved from measurements of light intensity fluctuations.

The original Hanbury Brown-Twiss experiment

Interferometry experiments have been used for a long time to study the properties of light. Notably the wave nature of light was demonstrated by Young in 1801, using a double-slit setup. In this classic experiment, monochromatic light from a point-like source is

diffracted by two slits separated by a distance d. Light waves scattered by the two slits interfere on an observation screen, yielding intensity fringes which can be used to infer the wavelength of the light.

Consider the case of a source which is not point-like. Here each point of the source generates a similar fringe pattern, shifted from the others. The intensity fringes are then blurred, yielding a lesser contrast of the interference figure. Note that this does not require that all points of the source emit light coherently.

Michelson proposed and successfully built a *stellar interferometer*, which used this phenomenon to accurately determine the angular diameter of stars [79]. Figure 3.14 shows the working principle of his interferometer under the form of a Young slits experiment. Here the visibility of the interference figure decreases with the spacing of the slits d, which can be used to estimate the diameter of the star.

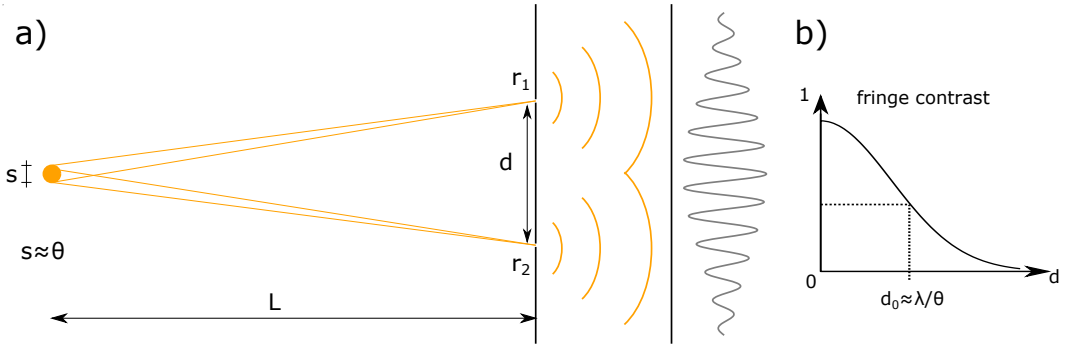

Figure 3.14: a) Schematics of a Michelson-like stellar interferometer. A star with angular diameter θ illuminates a Young slits setup. The spacing of the fringes is linked to the wavelength of the light, while their visibility (b) depends on θ and the spacing of the slits d.

The complex fringes pattern results from the superposition of the beams diffracted at points $\vec{r}_1$ and $\vec{r}_2$. If we consider that the incident light is carried by a single mode $\hat{a}(\vec{r},t)$, the intensity on the screen at a given point $\vec{r}$ is proportional to the field correlation function $Re[\langle\hat{a}^\dagger(\vec{r}-\vec{r}_1)\hat{a}(\vec{r}-\vec{r}_2)\rangle]$. Equivalently, one could study the coherence properties of light at different points in time instead of different locations. Figure 3.15 shows a Mach-Zehnder interferometer, which can yield the real part of the first order coherence function:

$$g^{(1)}(\tau) = \frac{\langle\hat{a}^\dagger(t)\hat{a}(t+\tau)\rangle}{\langle\hat{a}^\dagger\hat{a}\rangle}. \tag{3.38}$$

Here also the typical decay timescale in $g^{(1)}(\tau)$ can be related to the diameter of the light source.

First implementations of the Michelson stellar interferometer were limited to the study of large and bright celestial objects, as it soon appeared that fluctuations in the refractive index of the atmosphere tend to destroy the phase coherence between the two beams of light. To overcome this problem, Hanbury Brown and Twiss (HBT) developped in 1956 a new type of stellar interferometer [70] based on *intensity interferometry*.

In their experiment, the fluctuating intensity of light $I(\vec{r},t) = \hat{a}^\dagger\hat{a}(\vec{r},t)$ was first detected at $\vec{r}_1$ and $\vec{r}_2$. They then studied the correlation of $I(\vec{r}_1,t)$ and $I(\vec{r}_2,t)$ as a function of the spacing $|\vec{r}_1 - \vec{r}_2|$, which can once again be linked to the size of the ligth source. Their results sparked a controversy in the optics community, as non-zero correlations can only

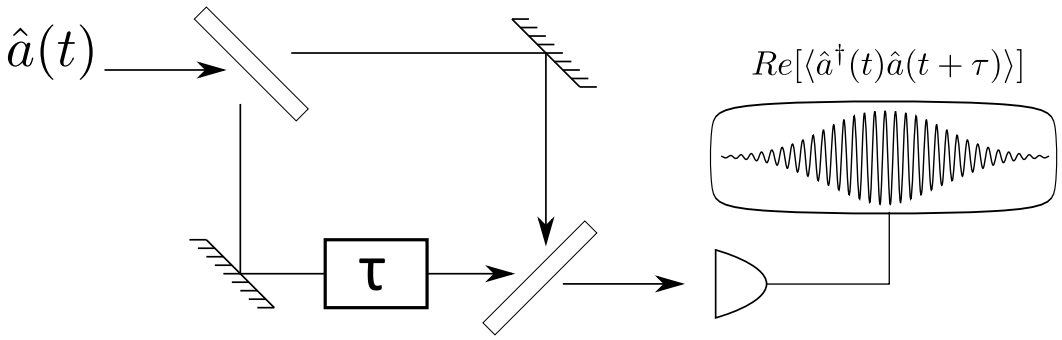

Figure 3.15: Mach-Zehnder interferometer. The incoming field $\hat{a}(t)$ is split onto two different paths by a beamsplitter. The traversal time of the two paths differ by a certain delay τ. When recombined the two beams interfere, with a fringe contrast proportional to $Re[g^{(1)}(\tau)]$.

occur if pairs of photons are detected exactly at the same time at $\vec{r}_1$ and $\vec{r}_2$. This kind of non-locality was not fully accepted at that time, and it took a long stream of fruitful results from HBT experiments (in the visible range as well as in radio-astronomy) to clarify and consolidate our understanding of quantum optics.

Like the Michelson interferometer, the HBT experiment can be adapted to yield the time-domain correlation function $\langle \hat{a}^\dagger(t)\hat{a}^\dagger(t+\tau)\hat{a}(t+\tau)\hat{a}(t)\rangle$ (Fig.3.16). One can thus access not only the spatial extent of the source, but also the statistical properties of light itself.

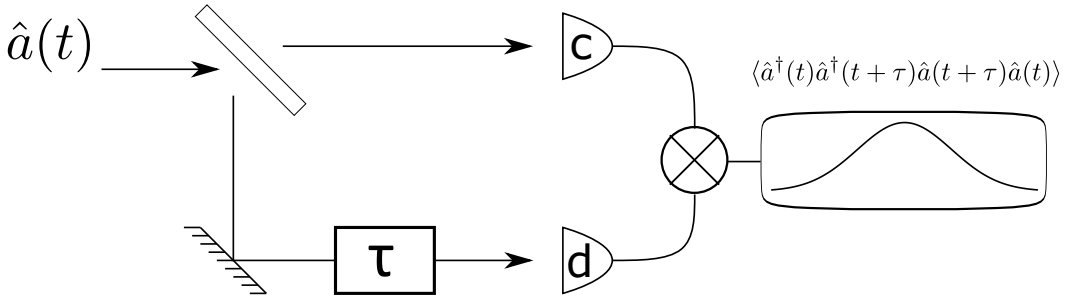

Figure 3.16: Hanbury Brown-Twiss (HBT) interferometer. The field $\hat{a}(t)$ is split onto two different paths. The intensity of the two beams is measured by two photo-counters. The product of the two photo-currents is $\propto g^{(2)}(\tau)$.

The link between intensity correlations and photon statistics is clear in the case of an incident stream of single photons. The beam splitter randomly distributes the photons over the two paths, so that the two photo-counters can never detect a photon at the same time. The coincidence rate is then $\langle I_c(t)I_d(t+\tau)\rangle = 0$, in good accordance with the expected $g^{(2)}(0) = 0$.

To justify why the measured correlation function is exactly $g^{(2)}(\tau)$, we need a more complete model of quantum interferometry. First, we show that the splitting stage is necessary to the experiment. If one detect the intensity of light at a single point a and compute its auto-correlation, it yields:

$$\langle I^a(t)I^a(t+\tau)\rangle = \langle \hat{a}^\dagger\hat{a}(t)\hat{a}^\dagger\hat{a}(t+\tau)\rangle, \tag{3.39}$$

which is **NOT** proportional to $g^{(2)}(\tau)$, as in general $\hat{a}(t)$ does not commute with $\hat{a}^\dagger(t+\tau)$.

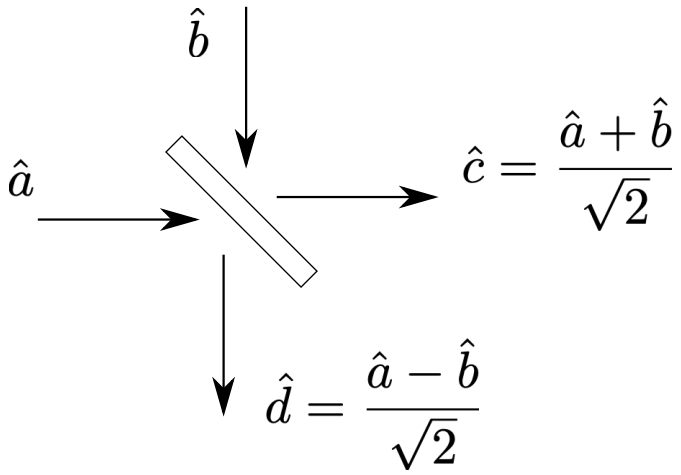

Figure 3.17: A beamsplitter couples linearly four modes of radiation: two incoming $\hat{a}, \hat{b}$ and two outgoing $\hat{c}, \hat{d}$.

On the other hand, inserting a beamsplitter generates two new modes of radiation $\hat{c}$ and $\hat{d}$ (Fig.3.17), which are linearly coupled to $\hat{a}$ by a scattering relation of the form:

$$\begin{vmatrix} \hat{c} \\ \hat{d} \end{vmatrix} = \frac{1}{\sqrt{2}} \begin{vmatrix} 1 & 1 \\ 1 & -1 \end{vmatrix} \times \begin{vmatrix} \hat{a} \\ \hat{b} \end{vmatrix}. \tag{3.40}$$

Here $\hat{b}$ describes a bosonic mode, incoming on the fourth port of the beamsplitter. One need to take it into account to yield correct commutation relations for $\hat{c}$ and $\hat{d}$:

$$[\hat{c}, \hat{c}^\dagger] = \frac{1}{2}\Big([\hat{a}, \hat{a}^\dagger] + [\hat{b}, \hat{b}^\dagger]\Big) = 1 = [\hat{d}, \hat{d}^\dagger]. \tag{3.41}$$

After splitting the photons travel in independent paths, so that they can be measured separately. This independence stems from:

$$[\hat{c}, \hat{d}^\dagger] = \frac{1}{2}\Big([\hat{a}, \hat{a}^\dagger] - [\hat{b}, \hat{b}^\dagger]\Big) = 0. \tag{3.42}$$

Then the correlation function measured in the HBT setup (Fig.3.16) can be put under the form:

$$\langle I^c(t) I^d(t+\tau)\rangle = \langle \hat{c}^\dagger(t)\hat{c}(t)\hat{d}^\dagger(t+\tau)\hat{d}(t+\tau)\rangle \tag{3.43}$$

$$= \langle \hat{c}^\dagger(t)\hat{d}^\dagger(t+\tau)\hat{d}(t+\tau)\hat{c}(t)\rangle, \tag{3.44}$$

as $\hat{c}$ commutes with both $\hat{d}$ and $\hat{d}^\dagger$, yielding:

$$\langle I^c(t) I^d(t+\tau)\rangle \propto \langle \hat{a}^\dagger(t)\hat{a}^\dagger(t+\tau)\hat{a}(t+\tau)\hat{a}(t)\rangle + \langle \hat{b}^\dagger(t)\hat{b}^\dagger(t+\tau)\hat{b}(t+\tau)\hat{b}(t)\rangle, \tag{3.45}$$

as the $\hat{a}$ and $\hat{b}$ modes are not correlated, and finally:

$$\langle I^c(t) I^d(t+\tau)\rangle \propto \langle \hat{a}^\dagger(t)\hat{a}^\dagger(t+\tau)a(t+\tau)\hat{a}(t)\rangle \tag{3.46}$$

$$\Rightarrow g^{(2)}(\tau) = \frac{\langle I^c(t) I^d(t+\tau)\rangle}{\langle I^c(t)\rangle\langle I^d(t+\tau)\rangle} \tag{3.47}$$

if the $\hat{b}$ mode is in the vacuum state. This last assumption is easily verified in visible range quantum optics by shielding the fourth port of the beamsplitter from parasitic background photons.

HBT in the microwave domain

In circuit quantum optics the basic principle of the HBT scheme can be implemented, albeit with some quirks due to the specificities of microwave measurements.

Photo-counters are not readily available at such low frequencies. Power measurements can be performed by square-law detectors 2.3.2. The voltage V_{det} at the output of the detector is proportional to the square of the incoming microwave field:

$$V_{det} \propto (\hat{a}e^{-i\omega t} + \hat{a}^\dagger e^{+i\omega t})^2, \tag{3.48}$$

where $\hat{a}$ is not the annihilation operator for a cavity mode, but for a propagating mode of the transmission line leading to the detector. The quantization of such modes is reviewed in [80]. In particular their operators fulfil different commutation relations, namely $[\hat{a}(t), \hat{a}^\dagger(t')] = \delta(t'-t)$. $\langle \hat{a}^\dagger \hat{a} \rangle$ is not a photon number, but rather the photon flux for mode a in units of s^{-1}.

The very high frequency terms at 2ω in (3.48) are removed by low-pass filtering, yielding for the slowly varying part of the diode output:

$$\langle V_{det} \rangle_T \propto \hat{a}\hat{a}^\dagger + \hat{a}^\dagger \hat{a} = 2(\hat{a}^\dagger \hat{a}) + 1, \tag{3.49}$$

where the average $\langle ... \rangle_T$ has been taken over one period $T = 2\pi/\omega$. V_{det} is proportional to the power in the mode: $P_a = \hbar\omega(\hat{a}^\dagger\hat{a} + 1/2)$, and not to the photon flux $\hat{a}^\dagger\hat{a}$. By removing the dc component of V_{det} one can access the fluctuating part of the emission power:

$$V_{det}(t) - \langle V_{det} \rangle \propto \delta P_a(t) = P_a(t) - \overline{P_a}, \tag{3.50}$$

with the average power $\overline{P_a} = \langle P_a \rangle$. In this way the vacuum noise $\hbar\omega/2$ as well as all uncontrolled dc offsets on V_{det} can be removed. Following the original HBT scheme by splitting the incoming power onto two different detection lines, $g^{(2)}(\tau)$ can be obtained by correlating the power fluctuations $\delta P_c, \delta P_d$ at the output of two different diodes (Fig.3.18):

$$g^{(2)}(\tau) = \frac{\langle \delta P_c(t) \delta P_d(t+\tau) \rangle}{\overline{P_c}\ \overline{P_d}} + 1 \tag{3.51}$$

as:

$$\begin{aligned} \langle \delta P_c(t) \delta P_d(t') \rangle &= \langle (P_c(t) - \overline{P_c})(P_d(t') - \overline{P_d}) \rangle & (3.52)\\ &= \langle P_c(t) P_d(t') \rangle - \langle P_c(t) \overline{P_d} \rangle - \langle P_d(t') \overline{P_c} \rangle + \overline{P_c}\ \overline{P_d} & (3.53)\\ &= \langle P_c(t) P_d(t') \rangle - \overline{P_c}\ \overline{P_d}. & (3.54) \end{aligned}$$

The physical implementation of a beamsplitter in the microwave domain is made with a hybrid coupler (Fig.3.18). In this four-port device, propagating waves interfere so that all the power incoming on one port is split evenly onto two output ports (provided they are matched with the appropriate line impedance).

Another specificity of circuit quantum optics is the need to amplify the signals before detection. The diode measures then not only the junction's emission power P_a, but also some parasitic noise power P_N added by the amplifier itself, so that the power flowing out of the amplifier reads:

$$P_T(t) = G \times (P_a(t) + P_N(t)). \tag{3.55}$$

In the single photon experiment, the signal-to-noise ratio (SNR) $\bar{P}_N/\bar{P}_a$ is bound to be very low. The average signal power is given by: $\bar{P}_a = \bar{n}\hbar\omega_r\kappa$, while the average noise power is: $\bar{P}_N = k_B T_N \Delta_f$, with T_N the noise temperature of the amplifier and Δ_f the acquisition bandwidth. Commercial HEMTs have $T_N \sim 5$ K, which is already 20 times larger than the energy of a single photon form the sample: $h\times 5$ GHz $\simeq k_B \times 0.25$ K. Recall that the theory predicts $g^{(2)}(\tau) \simeq (1 - \frac{r}{2}e^{-\kappa\tau})^2$. To resolve fluctuations of the power on a time scale of κ^{-1} requires a bandwidth $\Delta_f \simeq \kappa$, so that:

$$\text{SNR} = \frac{\bar{n}\hbar\omega_r\kappa}{k_B T_N \Delta_f} =\simeq \frac{\bar{n}}{20}. \tag{3.56}$$

The photon-blockade mechanism requires $\bar{n} \ll 1$. A safe value $\bar{n} \simeq 0.05$ then yields a SNR of the order of 1/400. This means that the fluctuations of any signal we detect are always dominated by the noise from the amplifier, with dire consequences on the averaging time required by the measurement.

The amplifier noise can also be detrimental to our accuracy when computing correlation functions. As an example, suppose that we compute the auto-correlation of the total power fluctuations at the output of the amplifier:

$$\langle \delta P_T(t)\delta P_T(t+\tau)\rangle = G^2(\langle \delta P_a(t)\delta P_a(t+\tau)\rangle + \langle \delta P_N(t)\delta P_N(t+\tau)\rangle), \tag{3.57}$$

where we assumed that $P_N(t)$ is uncorrelated with $P_a(t)$, so that $\langle \delta P_a(t)\delta P_N(t')\rangle = 0$. We can try to subtract the unwanted $\langle \delta P_N \delta P_N\rangle$ term by ON/OFF measurements. However the OFF value is here much greater than the difference between ON and OFF, as:

$$\langle \delta P_N \delta P_N\rangle \simeq \bar{P}_N^2 \sim (400)^2 \times \bar{P}_a^2 \sim (400)^2 \times \langle \delta P_a \delta P_a\rangle. \tag{3.58}$$

It would practically impossible to measure an observable drowned in a noise $\sim 10^5$ larger. Luckily a classical signal processing trick allows us to reduce greatly the OFF value. Recall that the full HBT setup requires us to split the signal onto two separate lines. If we amplify the signals **after** the splitting stage, then the correlation function yields:

$$\langle \delta P_c(t)\delta P_d(t+\tau)\rangle + \langle \delta P_{N_c}(t)\delta P_{N_d}(t+\tau)\rangle, \tag{3.59}$$

where $P_{N_c}(t), P_{N_d}(t')$ are independent noise powers added by the two separate amplifiers (Fig.3.18). The correlation between these two parasitic noises is expected to be practically zero, such that the measurement correctly gives the $g^{(2)}(\tau)$ function of the signal only. This comes at the cost of dividing by 2 the signal power incoming onto on the amplifiers, reducing furthermore the SNR.

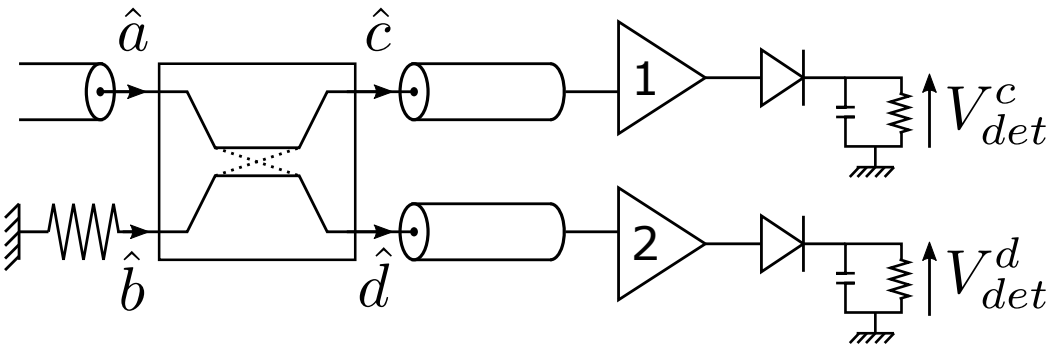

Figure 3.18: HBT setup for weak microwaves signals. The signal mode a, travelling in a coaxial cable, impinges on a 3dB-coupler, whose second input port is matched to a cold 50 Ω load. This load radiates vacuum noise carried by a mode b, which mixes with a to give two output modes c and d. The split signals are amplified by separate HEMTs (1) and (2), with nominally independent noises, and detected by two different diodes. The cross-correlation of the fluctuating part of the output voltages V^c_{det} and V^d_{det} gives access to the $g^{(2)}(\tau)$ function of the a mode.

Preliminary results from the PhD of Chloé Rolland

Following these principles, the microwave HBT setup was implemented by Chloé Rolland during her PhD research and allowed her to measure for the first time the antibunching of the photons emitted by the junction [35]. However, remaining parasitic correlations between the two measurement channels forbade a fully quantitative comparison of her results to the theoretical predictions of [34]. Using a new detection setup based on *linear measurements*, we were able to find the origins of these unwanted correlations and subtract them from the $g^{(2)}(\tau)$ function.

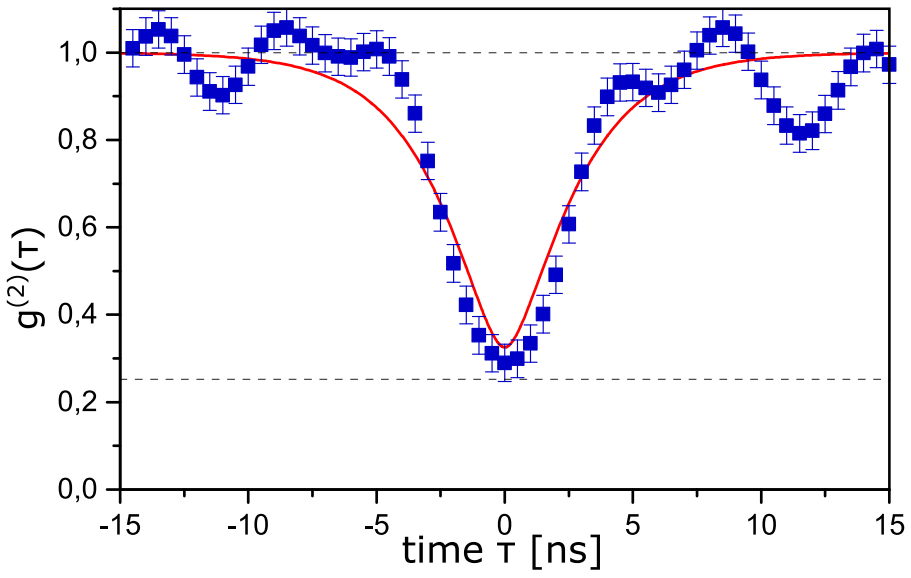

Figure 3.19: Results from the 2016 experiment. Values of $g^{(2)}(\tau)$ measured *via* power fluctuation correlations (blue squares) on top of the theoretical prediction of [34]: $g^{(2)}(\tau) = (1 - re^{-\kappa\tau}/2)^2$, with a fitted $r = 1$ and $\kappa = 1$ ns^{-1}. The error bars indicate half the statistical standard deviation, $\sigma/2$ (taken from [35]).

The measurement of $g^{(2)}(\tau)$ from [35] shows a dip near $\tau = 0$, going down to about 0.3 with a standard deviation of 0.2. These numbers alone indicate the antibunched character of the photons emitted by the junction. However one can also see some parasitic oscillations

on top of the expected $g^{(2)}(\tau)$. Far away from $\tau = 0$, where one should have $g^{(2)}(\tau) = 1$, it actually oscillates between about 0.85 and 1.05, with a period comparable to the lifetime of the resonator κ^{-1}. It is therefore quite difficult to be sure of the exact value of $g^{(2)}(0)$ and compare it with the theoretical prediction.

The origin of these unwanted oscillations appears when considering a fully quantum model of the signal processing. We explained earlier how an amplifier always adds some noise power $k_B T_N$ on top of the input signals. As shown by Caves in [81], this noise is a fundamental property of the linear amplification process. It is carried by an additional mode $\hat{h}$ that enforce the adequate commutation relation of the output mode. The amplifier scattering relation can be cast under the general form:

$$\hat{b} = \sqrt{G}\hat{a} + \sqrt{G-1}\hat{h}^\dagger. \tag{3.60}$$

The noise mode fulfils the standard bosonic commutation relation $[\hat{h}, \hat{h}^\dagger] = 1$, and is supposed to be independent from the input signal mode $\hat{a}$. This is a safe assumption, as it originates from the inner mechanism of the amplifier and is always present, even in the absence of an input signal. The dagger symbol on $\hat{h}^\dagger$ may look weird, but is actually required to ensure that $\hat{b}$ fulfils the correct commutation relation:

$$[\hat{b}, \hat{b}^\dagger] = G[\hat{a}, \hat{a}^\dagger] + (G-1)[\hat{h}^\dagger, \hat{h}] = G - (G-1) = 1. \tag{3.61}$$

The average photon number in the output mode is then:

$$\langle \hat{b}^\dagger \hat{b} \rangle = G\langle \hat{a}^\dagger \hat{a} \rangle + (G-1)\langle \hat{h}\hat{h}^\dagger \rangle = G\langle \hat{a}^\dagger \hat{a} \rangle + (G-1)(\langle \hat{h}^\dagger \hat{h} \rangle + 1). \tag{3.62}$$

In an ideal *quantum-limited* amplifier, the $\hat{h}^\dagger$ mode in the vacuum state: $\langle \hat{h}^\dagger \hat{h} \rangle = 0$. Note that the quantum-limited amplifier still adds some noise to the signal, which amounts in the $G \gg 1$ limit to the usual claim of an additional "half photon per mode" as referred to the input power. More often $\hat{h}^\dagger$ is in a thermal state, with an occupation number $n_B(T_N) = \frac{1}{\exp(\frac{\hbar\omega}{k_B T_N})-1}$.

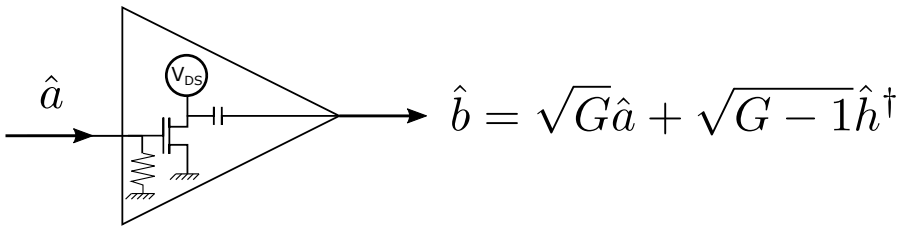

Figure 3.20: Quantum model of a linear amplifier, as described by [81]. The amplified signals are carried by an output mode $\hat{b}$, which also includes noise contribution from a mode $\hat{h}^\dagger$. The details and physical origin of $\hat{h}^\dagger$ depend on the specific implementation of the amplifier (here thermal noise from an internal resistance).

With this model at hand, let us come back to the expression for the correlation of separately amplified signals, as in the setup of figure 3.18. To simplify a bit the reasoning, suppose that we can detect photon numbers at the output of HEMTs (1) and (2), instead of relying on power fluctuations. Then the **instantaneous** photon number on channel 1 reads:

$$G\hat{c}^\dagger \hat{c} + (G-1)\hat{h}_1 \hat{h}_1^\dagger + \sqrt{G(G-1)}(\hat{c}\hat{h}_1 + \hat{c}^\dagger \hat{h}_1^\dagger), \tag{3.63}$$

and on channel 2:

$$G\hat{d}^\dagger\hat{d} + (G-1)\hat{h}_2\hat{h}_2^\dagger + \sqrt{G(G-1)}(\hat{d}\hat{h}_2 + \hat{d}^\dagger\hat{h}_2^\dagger), \tag{3.64}$$

with $\hat{h}_x^\dagger$ the noise mode of amplifier (x). We insist that even if the last term averages to zero, it gives a non null contribution to the fluctuations of the detected photon number. When correlating the intensities measured on channel (1) and (2), one gets:

$$G^2\langle\hat{c}^\dagger\hat{c}d^\dagger\hat{d}\rangle + (G-1)^2\langle\hat{h}_1\hat{h}_1^\dagger\hat{h}_2\hat{h}_2^\dagger\rangle + G(G-1)(\langle\hat{c}^\dagger\hat{d}\rangle\langle\hat{h}_1^\dagger\hat{h}_2\rangle + \langle\hat{d}^\dagger\hat{c}\rangle\langle\hat{h}_2^\dagger\hat{h}_1\rangle), \tag{3.65}$$

where we kept only terms that do not average immediately to zero. As an example, $\langle\hat{h}_1\hat{h}_2\rangle = 0$ as we do not expect phase coherence from the thermal noise of the amplifiers.

The first parasitic term in this correlator, $\langle\hat{h}_1\hat{h}_1^\dagger\hat{h}_2\hat{h}_2^\dagger\rangle$, is present even in the absence of input signal from the sample, i.e if $\langle\hat{a}^\dagger\hat{a}\rangle = 0$. Thus it can safely be removed by ON/OFF measurements, the OFF state being reached by putting the bias voltage on the sample to zero 2.3.2. On the contrary, the $\langle\hat{h}_x^\dagger\hat{h}_y\rangle$ terms are present only if $\langle\hat{a}^\dagger\hat{a}\rangle \neq 0$ and cannot be removed easily.

It was assumed in [35] that the two amplifier noise modes were independent enough so that their correlations could be neglected. In practice, the isolation between the two measurement lines is finite, and is found to be at best of about -33 dB. The parasitic correlations between the two lines are then of the order of:

$$|\langle\hat{h}_1^\dagger\hat{h}_2\rangle| \simeq 5\times10^{-4}\bar{P}_{N_c}\bar{P}_{N_d} \sim 0.2\times\langle\delta P_c\delta P_d\rangle, \tag{3.66}$$

so that they were responsible for the parasitic oscillations in figure 3.19.

The only way to remove these oscillations is to measure separately these noise correlators, and to subtract them from the measurements. As these terms arise from amplitude correlations between the two lines, they cannot be obtained using intensity detectors. Following the pioneering work of [82], we developed a scheme based on the *linear* detection of the microwave field, instead of the measurement of power fluctuations. This allowed us to remove virtually all parasitic contributions to the $g^{(2)}(\tau)$ and characterize finely this single-photon source.

3.3.2 Linear detection of the field

Complex envelope of the signals

In the experiment we are describing, the signal to be detected is the microwave voltage generated by the sample, which reads:

$$V_{ac}(t) = V_0(\hat{a}e^{-i\omega t} + \hat{a}^\dagger e^{+i\omega t}) = 2V_0 Re[\hat{a}e^{-i\omega t}], \tag{3.67}$$

with $V_0 = \sqrt{Z_w\hbar}$ the ZPF spectral density of voltage in the transmission line of impedance Z_w. It can be seen as a carrier wave $e^{-i\omega t}$ modulated by a slowly varying envelope $\hat{a}$. This fast oscillating signal is out of reach of standard Analog to Digital converters (ADC), which sample at up to a few GSamples/second.

The situation is even worse in visible range quantum optics, where the field carrier frequency is in the 300 THz range. However techniques have been developed to access the slowly varying envelope of the signal, which contains all the information about the field. Through a non-linear process, one may multiply the voltage signal with a well-known oscillating wave, provided by a so-called *local oscillator* (LO). This reference signal is a macroscopic quantity, described by a classical field $V_{LO}(be^{-i\omega_{LO}t} + b^*e^{+i\omega_{LO}t})$. Their product yields:

$$V_{mix} \propto V_0(\hat{a}e^{-i\omega t} + \hat{a}^\dagger e^{+i\omega t}) \times V_{LO}(be^{-i\omega_{LO}t} + b^*e^{+i\omega_{LO}t}). \tag{3.68}$$

The local frequency is chosen to be close to the signal frequency: $\omega_{LO} = \omega + \delta\omega$. The low-pass filtered mixing signal, which can be readily detected, reads:

$$V_{mix,LP} \propto Re[\hat{a}b^*e^{i\delta\omega t}]. \tag{3.69}$$

If $\omega_{LO} = \omega$, the measured voltage is simply $Re[\hat{a}b^*]$. By tuning the phase of the LO $\phi_{LO} = \arg(b)$ with respect to the signal carrier wave, one can access either of the **quadratures** of the signal:

$$V_{hom} \propto Re[\hat{a}e^{-i\phi_{LO}}] = \cos(\phi_{LO})\hat{X} + \sin(\phi_{LO})\hat{P}, \tag{3.70}$$

with $\hat{a} = \hat{X} + i\hat{P}$. This kind of measurement is called a *homodyne detection* of the field. From their definition, it is clear that $\hat{X}$ and $\hat{P}$ contain all the information on $\hat{a}$. They are also quantum conjugated operators, with the commutation relation: $[\hat{X}, \hat{P}] = i/2$. As such, they cannot be measured independently at the same time with an arbitrary precision, which is manifest in the expression (3.70).

At microwave frequencies, the mixing operation is readily implemented *via* voltage-rectifying diodes, implementing an IQ mixer. In the visible range, homodyning requires to split the signal and the LO over two different beams, detect the light intensity in each beam and then subtract their photo-currents (Fig.3.21). The current difference indeed yields:

$$I_c - I_d \propto (\hat{a} + \hat{b})^\dagger(\hat{a} + \hat{b}) - (\hat{a} - \hat{b})^\dagger(\hat{a} - \hat{b}) \propto Re[\langle \hat{a}\hat{b}^\dagger \rangle]. \tag{3.71}$$

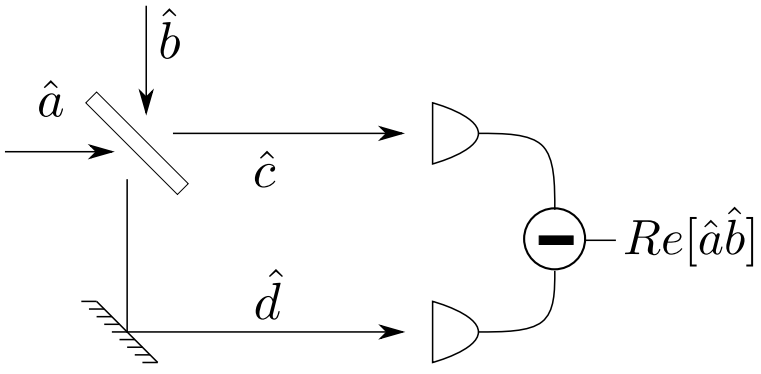

Figure 3.21: Homodyne detection scheme in visible range quantum optics.

The case where $\omega_{LO} \neq \omega$ is called *heterodyne detection*. Then the output signal is still oscillating in time, with:

$$V_{het}(t) \propto Re[\hat{a}e^{-i(\delta\omega t + \phi_{LO})}] = \cos(\delta\omega t + \phi_{LO})\hat{X} + \sin(\delta\omega t + \phi_{LO})\hat{P}. \tag{3.72}$$

In essence, this could be seen as homodyne detection where the phase of the LO is continuously varied to measure successively $\hat{X}$ then $\hat{P}$.

The signal quadratures evolve on a time scale of the order of the resonator lifetime κ^{-1}. If $\delta\omega > \kappa$, it seems that one could detect the heterodyne signal fast enough to measure both $\hat{X}$ and $\hat{P}$ at the same time, which is impossible as they are quantum conjugated observables. A complete model of heterodyne detection lifts this paradox (Fig.3.22):

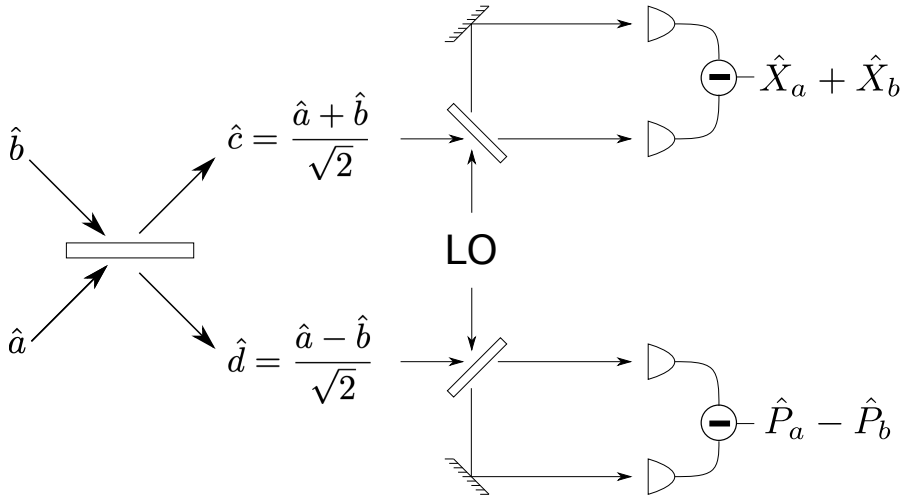

Figure 3.22: Heterodyne detection scheme in visible range quantum optics.

In the visible range, measuring $\hat{X}$ and $\hat{P}$ at the same time actually requires two different homodyne interferometers. The input signal $\hat{a}$ then necessarily needs to be split over two different beams, to create two copies of it ($\hat{c}$ and $\hat{d}$). As shown in figure 3.17, the beamsplitter actually mixes $\hat{a}$ with another mode $\hat{b}$, which adds at least vacuum fluctuations to measurements of $\hat{c}$ and $\hat{d}$.

Thanks to this fourth mode, one can measure the $\hat{X}$ quadrature on $\hat{c}$ and the $\hat{P}$ quadrature on $\hat{d}$ at the same time with arbitrary precision. These measurements can be combined in a single **complex envelope** $\hat{S} = \hat{X}_c + i\hat{P}_d$. The fact that $\hat{S}$ is a complex quantity does not forbid it from being an observable, as: $[\hat{S}, \hat{S}^\dagger] = 0$ [82].

Due to the presence of the $\hat{b}$ mode, a measurement of $\hat{S}$ is **not** equal to a measurement of $\hat{a}$. Indeed: $\hat{S} \propto \hat{X}_a + \hat{X}_b + i\hat{P}_a - i\hat{P}_b = \hat{a} + \hat{b}^\dagger$. Each measurement of $\hat{S}$ is thus a measurement of $\hat{a}$ **blurred** by the signals from $\hat{b}^\dagger$, which contains at least the vacuum level of noise.

Note that in the microwave domain, the $\hat{b}^\dagger$ mode corresponds to the idler signal of the mixer, which is also always present.

The added $\hat{b}^\dagger$ noise is a necessity of the measurement of the quantum variable $\hat{a}$. All gedanken experiments aiming at removing it fail eventually. For example, at low enough frequency, one could imagine digitizing directly the signals from the $\hat{a}$ mode. Without the splitting (or mixing) step, one does not need to include a beamsplitter's fourth port mode. However voltage measurement require the choice of some load impedance Z_l, across which the voltage drop can be detected. Following Nyquist [52], Z_l itself radiates some noise, that gets picked up by the voltage detector. Thus the measured voltage also includes an added noise term, for the consistency of quantum mechanics.

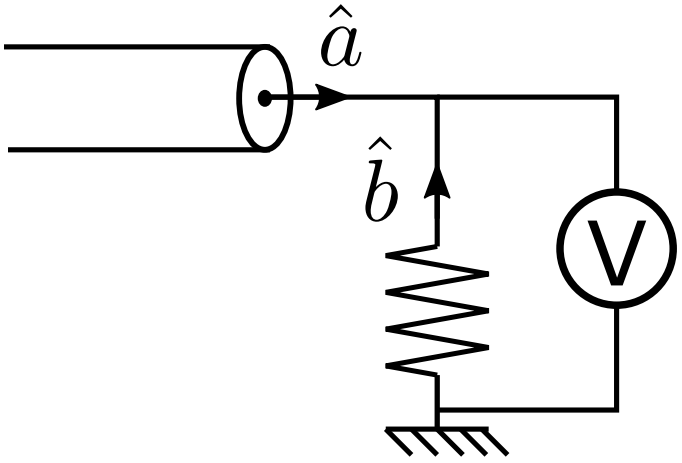

Figure 3.23: Gedanken experiment: measuring directly the fast voltage drop resulting from photons impinging on a load resistor. Even if the voltmeter is fast enough it will not detect $\hat{a}$, but a combination of $\hat{a}$ and an added noise term $\hat{b}^\dagger$.

Correlation functions from linear measurements

Arbitrary correlation functions of $\hat{a}$ can be computed from linear measurements. After suitable linear detection, we record time traces of the complex envelope $\hat{S}(t) = \sqrt{F}\left(\hat{a}(t) + \hat{b}^\dagger(t)\right)$, where $\sqrt{F}$ is some experimental conversion factor. $\hat{b}^\dagger$ describes the noise added by the heterodyne technique, which may not be quantum limited (i.e containing only vacuum fluctuations). We can compute:

$$S^\dagger(t)S(t') = F\left(a^\dagger(t)a(t') + b(t)b^\dagger(t') + a^\dagger(t)b^\dagger(t') + b(t)a(t')\right), \tag{3.73}$$

where we removed the hat notation on operators for readability. We can assume that $\hat{b}^\dagger$ is independent of the signal $\hat{a}$, so that $\langle b(t)a(t')\rangle = \langle b(t)\rangle\langle a(t')\rangle$. It is also safe to assume that the added noise is gaussian distributed. Then the only non-zero correlators are the ones of the form $\langle\prod b^\dagger(t_i)\prod b(t_j)\rangle$, with the same number of annihilation and creation operators. In particular here $\langle b(t)\rangle = \langle b^\dagger(t)\rangle = 0$. The auto-correlation function of $\hat{S}$ finally reads:

$$\langle S^\dagger(t)S(t')\rangle = F\langle a^\dagger(t)a(t')\rangle + F\langle b(t)b^\dagger(t')\rangle. \tag{3.74}$$

Because we took care to write this correlator in the *normal order*, the a mode contribution vanishes if it is in the vacuum state, i.e $\langle a^\dagger a\rangle = 0$. Once again we can reach this OFF state in an experiment by setting the bias on the sample to zero. Then we have:

$$\langle S^\dagger(t)S(t')\rangle_{ON} = F\langle a^\dagger(t)a(t')\rangle + F\langle b(t)b^\dagger(t')\rangle \tag{3.75}$$

$$\langle S^\dagger(t)S(t')\rangle_{OFF} = F\langle b(t)b^\dagger(t')\rangle \tag{3.76}$$

$$\Rightarrow \langle a^\dagger(t)a(t')\rangle = F^{-1}\left(\langle S^\dagger(t)S(t')\rangle_{ON} - \langle S^\dagger(t)S(t')\rangle_{OFF}\right), \tag{3.77}$$

such that the first order coherence function of the signal can be obtained by a normalized combination of ON and OFF measurements:

$$g^{(1)}(\tau) = \frac{\langle\hat{a}^\dagger(0)\hat{a}(\tau)\rangle}{\langle\hat{a}^\dagger\hat{a}\rangle} = \frac{\langle S^\dagger(0)S(\tau)\rangle_{ON/OFF}}{\langle S^\dagger S\rangle_{ON/OFF}}, \tag{3.78}$$

where we introduced the shorthand notation $\langle X\rangle_{ON/OFF} = \langle X\rangle_{ON} - \langle X\rangle_{OFF}$. Once the peculiar nature of quantum signals has been taken into account by including the

non-trivial commutation relations, this procedure is nothing more than standard signal processing, used to recover the statistical properties of a signal corrupted by an unwanted noise.

More generally, we know from probability theory that the distribution function of the sum $Z = X + Y$ of two independent random variables is the convolution product of the two original distribution functions of X and Y. The n-th moment of Z, $\langle Z^n \rangle$, is then a bilinear combination of all the moments of X and Y of order $\leq n$. If the $\langle Y^k \rangle$ are known separately, the statistical properties of X can be estimated by measuring the moments of Z up to desired order and inverting iteratively the convolution. The same goes for generic correlation functions $\langle \prod X(t_i) \rangle$, of which the moments are a special case.

In particular, we have:

$$\begin{aligned}\langle S^\dagger(0)S^\dagger(\tau)S(\tau)S(0)\rangle =& F^2\big(\langle a^\dagger(0)a^\dagger(\tau)a(\tau)a(0)\rangle + \langle b(0)b(\tau)b^\dagger(\tau)b^\dagger(0)\rangle \\ &+ \langle a^\dagger(0)a(0)\rangle\langle b(\tau)b^\dagger(\tau)\rangle + \langle a^\dagger(\tau)a(\tau)\rangle\langle b(0)b^\dagger(0)\rangle \\ &+ \langle a^\dagger(0)a(\tau)\rangle\langle b(\tau)b^\dagger(0)\rangle + \langle a^\dagger(\tau)a(0)\rangle\langle b(0)b^\dagger(\tau)\rangle\big) \end{aligned} \tag{3.79}$$

$$\begin{aligned}=& F^2\big(\bar{n}^2 g^{(2)}(\tau) + \langle b(0)b(\tau)b^\dagger(\tau)b^\dagger(0)\rangle + 2\bar{n}\langle bb^\dagger\rangle \\ &+ \bar{n}(g^{(1)}(\tau)\langle b(\tau)b^\dagger(0)\rangle + g^{(1)}(-\tau)\langle b(0)b^\dagger(\tau)\rangle)\big), \end{aligned} \tag{3.80}$$

such that $g^{(2)}(\tau)$ can be extracted from a combination of measurements of $\langle S^\dagger(0)S(\tau)\rangle$ and $\langle S^\dagger(0)S^\dagger(\tau)S(\tau)S(0)\rangle$, in the ON and OFF states:

$$\begin{aligned}g^{(2)}(\tau) =& \frac{\langle S^\dagger(0)S^\dagger(\tau)S(\tau)S(0)\rangle_{ON/OFF}}{(\langle S^\dagger S\rangle_{ON/OFF})^2} - \Bigg[2 \times \frac{\langle S^\dagger S\rangle_{OFF}}{\langle S^\dagger S\rangle_{ON/OFF}} \\ &+ g^{(1)}(\tau)\frac{\langle S^\dagger(0)S(-\tau)\rangle_{OFF}}{\langle S^\dagger S\rangle_{ON/OFF}} + g^{(1)}(-\tau)\frac{\langle S^\dagger(0)S(\tau)\rangle_{OFF}}{\langle S^\dagger S\rangle_{ON/OFF}}\Bigg]. \end{aligned} \tag{3.81}$$

If the assumption of a gaussian noise with no phase reference is not verified, there are more terms in the expression of the $S(t)$ correlators. These terms can always also be removed by more complex ON/OFF combinations. Experimentally it is sufficient to check that $\langle b^\dagger \rangle \propto \langle S \rangle_{OFF} = 0$ to validate this hypothesis.

In practice, how easily are subtracted the unwanted terms between brackets in (3.81)? This depends on the nature of the $\hat{b}^\dagger$ mode, and its average population. True heterodyne detection in visible range optics can be quantum-limited in the limit where the LO mode contains a large number of photons. In microwave optics, the experiment is actually limited by the noise added by the amplification stage. Using the expression from figure 3.20 for the field operator at the output of the amplifier, the complex envelope actually reads:

$$\hat{S} = \sqrt{F}(\sqrt{G}\hat{a} + \sqrt{G-1}\hat{h}^\dagger + \hat{b}^\dagger). \tag{3.82}$$

Now, as these two noise arise from different processes (and even separate parts of the experiment), they are uncorrelated: $\langle \hat{h}^\dagger \hat{b} \rangle = \langle \hat{h}\hat{b} \rangle = 0$. When computing correlation functions of $\hat{S}$, there are more parasitic terms to consider, but which can always be grouped together as arising from an effective "total noise" mode $\sqrt{G-1}\hat{h}^\dagger + \hat{b}^\dagger$. The results we derived earlier, in particular the expression of $g^{(2)}(\tau)$ as a function of $\hat{S}$ (3.81), are unchanged.

This "total noise" mode can be considered to be at thermal equilibrium with an effective temperature $\simeq T_N$, as $(G-1)\langle\hat{h}^\dagger\hat{h}\rangle \gg \langle\hat{b}^\dagger\hat{b}\rangle$. Then its contribution to the $\hat{S}$ correlators is much larger than the desired correlation function from the signal mode $\hat{a}$. As such, $\langle\hat{S}^\dagger\hat{S}\rangle_{OFF} \propto n_B(T_N) \sim 10^3 \times \langle\hat{a}^\dagger\hat{a}\rangle \propto \langle\hat{S}^\dagger\hat{S}\rangle_{ON/OFF}$, making the contrast of the measurement quite poor.

As noted before, this very low SNR is even more detrimental to the measurement of power correlations: $\langle\hat{S}^\dagger\hat{S}^\dagger\hat{S}\hat{S}\rangle_{OFF} \propto 2\,(n_B(T_N))^2 \sim 10^6 \times \langle\hat{a}^\dagger a^\dagger\hat{a}\hat{a}\rangle$. Even if unwanted terms average to a value that can be subtracted by ON/OFF measurements, it is so large that it requires a lot of averaging to make this subtraction finely enough to recover properly the $\hat{a}$ correlators. In particular, measuring $\langle\hat{S}^\dagger\hat{S}^\dagger\hat{S}\hat{S}\rangle_{OFF}$ with a 1 part in 10^7 accuracy, in order to have a $\sim 10\%$ resolution on $\langle\hat{a}^\dagger\hat{a}^\dagger\hat{a}\hat{a}\rangle$, requires of the order of 10^{14} measurements (as the added noise is gaussian distributed). The value of $\langle\hat{S}^\dagger\hat{S}^\dagger\hat{S}\hat{S}\rangle_{OFF}$ depends on T_N, which actually fluctuates during an experiment, on timescales shorter than the measurement time $\sim 10^{14}/f_s \simeq 30$ hours.

However using a HBT-like setup allows to rely on cross-correlations of the signals, which average to a much smaller value than auto-correlations. By using this linear detection scheme with the setup of 3.18, we have been able to make a quantitative measurement of all the parasitic noise contribution to the correlators and properly extract the $g^{(2)}(\tau)$ function of the emitted photons.

Microwave HBT setup with linear detection

We present in figure 3.24 the noise model of a microwave HBT experiment, including linear detection of the field amplitudes instead of the measurement of power fluctuations:

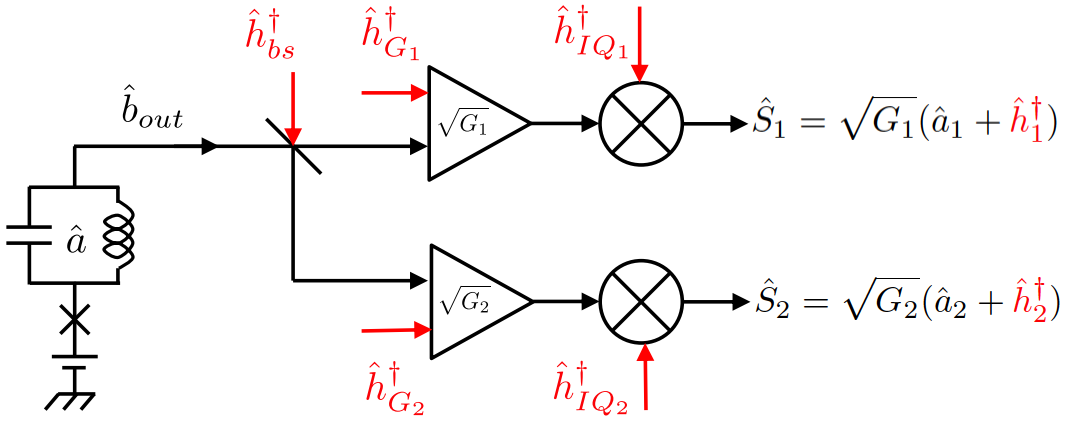

Figure 3.24: Noise model of the microwave HBT experiment with linear detection.

To be fully consistent, we stress the distinction between the $\hat{a}$ mode describing the field inside the resonator (with $[\hat{a},\hat{a}^\dagger]=1$) and the propagating mode $\hat{b}_{out}$, with $[\hat{b}_{out}(t),\hat{b}^\dagger_{out}(t')] = \delta(t'-t)$. The local $\hat{a}$ operator is the one whose stationary state can be efficiently simulated by the master equation approach of [34], while the $\hat{b}_{out}(t)$ operators are the ones that can be detected. The antibunching prediction applies to both, as: $\langle\hat{b}^\dagger_{out}\hat{b}^\dagger_{out}\hat{b}_{out}\hat{b}_{out}\rangle = \kappa^2\langle\hat{a}^\dagger\hat{a}^\dagger\hat{a}\hat{a}\rangle$, so that: $g^{(2)}_a(\tau) = g^{(2)}_{b_{out}}(\tau)$.

The $\hat{b}_{out}$ fields is routed to a beamsplitter and mixed with a mode $\hat{h}^\dagger_{bs}$. This mode carries the equilibrium noise radiated by the cold 50 Ω load on the fourt port of the hybrid coupler (Fig.3.18). Thus it can be considered in the vacuum state: $\langle \hat{h}^\dagger_{bs}\hat{h}_{bs}\rangle \sim 0$.

The several amplification stages of the experiment are modelled by a single amplifier on each channel (1) and (2), that amplifies the signal power by $G_{1/2}$ while mixing it with a noise mode $\hat{h}^\dagger_{G_{1/2}}$. These modes carry the main contribution to the total noise on the signal, with $\langle \hat{h}^\dagger_{G_{1/2}}\hat{h}_{G_{1/2}}\rangle = n_B(T_{N_{1/2}})$.

The final heterodyne detection on each channel adds a demodulation noise $\hat{h}^\dagger_{IQ_{1/2}}$, whose contribution is small compared to the amplifiers' noise. We represent it here for consistency.

To sum up, we consider that the experimental records of complex envelopes on the two channels read: $\hat{S}_{1/2}(t) = \sqrt{G_{1/2}}\left(\hat{a}_{1/2}(t) + h^\dagger_{1/2}(t)\right)$, where $\hat{a}_{1/2}(t) \propto b_{out}(t - t_{1/2})$ includes the potential time delay between the two lines, and $\hat{h}^\dagger_{1/2}$ represent all the noises added by the different signal processing steps.

Splitting the signals before amplification decreases the SNR by 2. However there are benefits of having two distinct measurement lines, which already appear in the computation of the first order coherence function. As in the single channel case, $g^{(1)}(\tau)$ can be extracted from the autocorrelation of a single complex envelope:

$$g^{(1)}(\tau) = \frac{\langle S^\dagger_x(0)S_x(\tau)\rangle_{ON/OFF}}{\langle S^\dagger_x S_x\rangle_{ON/OFF}}, \tag{3.83}$$

with $x \in \{1, 2\}$. Using this ON/OFF technique essentially requires to subtract two numbers of order 10^3 from one another, to obtain a number ~ 1. The contrast of this direct technique is quite bad, and slight drifts in the noise temperature of the amplifiers can easily ruin the measurement. By contrast, the cross correlation of the two complex envelopes yields:

$$X(\tau) = \langle S^\dagger_1(0)S_2(\tau)\rangle = \sqrt{G_1G_2}\left(\langle a^\dagger_1(0)a_2(\tau)\rangle + \langle h_1(0)h^\dagger_2(\tau)\rangle\right), \tag{3.84}$$

so that:

$$g^{(1)}(\tau) = \frac{X(\tau)_{ON/OFF}}{X(0)_{ON/OFF}}. \tag{3.85}$$

If the two measurement chains are well isolated, the OFF term $\langle h_1(0)h^\dagger_2(\tau)\rangle$ is small, and the contrast is much better. The amplitude of the OFF term is experimentally found to be about 30 dB lower than the autocorrelation of the amplifiers' noise, so about of the same order of magnitude as the signal power in the low occupation limit $\bar{n} \sim 0.1$.

The parasitic coupling between $\hat{h}_1$ and $\hat{h}_2$ can be modelled by a linear scattering relation, of the form:

$$\hat{h}_x \to \sqrt{1-\alpha}\hat{h}_x + \sqrt{\alpha}\hat{h}_y, \tag{3.86}$$

where $|\alpha| \sim 10^{-3}$ is the finite isolation between the two lines. α is in general a complex number, whose phase depends on the way the lines are coupled. In particular if there is an unwanted coupling between the two lines through a path of length L_{xy}, noise $\hat{h}_x$ leaking

to the (y) line acquires a relative phase $\delta_{xy} = \omega L_{xy}/c$, with c the celerity of signals. Then $S_1^\dagger S_2$ is a complex number, contrary to the auto-correlation $S_x^\dagger S_x$.

This is true both for the average value $\langle S_1^\dagger S_2 \rangle$, but also for the instantaneous $S_1^\dagger(t) S_2(t)$, which is a complex noise with a random phase. On the other hand the desired correlator $\langle a_1^\dagger a_2 \rangle$ averages to a real number[1]. To enhance the recovery of a real signal from a complex background noise, one one can take only the real part of the measurement, increasing the signal to noise ratio by 2. Any relative phase between the two detection channels can be compensated numerically if needed. For $\tau \neq 0$ $g^{(1)}(\tau)$ is a complex number, albeit with a well-defined phase contrary to $S_1^\dagger(t) S_2(t+\tau)$, so this intrinsic noise rejection also occurs.

Note that the instantaneous noise on $S_1^\dagger(t) S_2(t)$ is still given by $\sqrt{T_{N_1} T_{N_2}}$, even if the final value $\langle S_1^\dagger S_2 \rangle$ is much smaller than $\langle S_x^\dagger S_x \rangle$. This means that the SNR did not increase, and the number of averaging needed to extract the signal from the noisy measurements is still large. Cross-correlations simply make the OFF value to be subtracted much smaller, so the accuracy of the measurement is increased.

Accurate $g^{(2)}(\tau)$ measurement from two complex envelopes

They are $2^4 = 16$ ways of correlating complex envelopes to yield a measurement of $g^{(2)}(\tau)$. We have already seen that the choice of observables like $\langle S_x^\dagger S_x^\dagger S_x S_x \rangle$ is quite bad, as the ON/OFF value is much smaller than the OFF value. The only sensible choice is a combination where the noise of an amplifier is never directly auto-correlated.

First, one can compute the instantaneous power in the lines from: $P_x(t) = S_x^\dagger(t) S_x(t)$, and use power-correlations as in the 2016 experiment (Fig.3.18):

$$\begin{aligned} g^{(2)}_{pw}(\tau) = & \frac{\langle P_1(0) P_2(\tau) \rangle_{ON/OFF}}{\langle P_1 \rangle_{ON/OFF} \langle P_2 \rangle_{ON/OFF}} - \left[\frac{\langle P_1 \rangle_{OFF}}{\langle P_1 \rangle_{ON/OFF}} + \frac{\langle P_2 \rangle_{OFF}}{\langle P_2 \rangle_{ON/OFF}} \right. \\ & \left. + \frac{X(\tau)_{ON/OFF} X^\dagger(\tau)_{OFF}}{\langle P_1 \rangle_{ON/OFF} \langle P_2 \rangle_{ON/OFF}} + \frac{X^\dagger(\tau)_{ON/OFF} X(\tau)_{OFF}}{\langle P_1 \rangle_{ON/OFF} \langle P_2 \rangle_{ON/OFF}} \right]. \end{aligned} \tag{3.87}$$

Here the benefit of using linear detection lies in the inclusion of the last two terms, which carry $X_{OFF}(\tau)$. They were responsible for the ripples in figure 3.19 and could not be suppressed by a scheme based on power detection. This method does not yield the intrinsic complex noise rejection, as here all quantities are real numbers.

Second, one can compute the cross-signal power $C(t) = S_1^\dagger(t) S_2(t)$, which is a complex number proportional to the instantaneous $\sqrt{P_1 P_2}(t)$. In a record of $C(t)$, the $a^\dagger a(t)$ contribution is real, while the contribution of the background noise is a complex number with a random phase. Computing the auto-correlation function of $C(t)$, $\langle C^\dagger(0) C(\tau) \rangle$, would rectify this random phase and the noise would pile up on top of the signal. It is

[1] or to a complex number if the delay between the two lines $t_2 - t_1$ is not compensated for, but with a deterministic phase.

much more interesting to use $\langle C(0)C(\tau)\rangle$, which yields:

$$g^{(2)}_{cs}(\tau) = \frac{\langle C(0)C(\tau)\rangle_{ON/OFF}}{\langle C\rangle^2_{ON/OFF}} - \left[2 \times \frac{\langle C\rangle_{OFF}}{\langle C\rangle_{ON/OFF}} + \frac{X(\tau)_{ON/OFF}X(-\tau)_{OFF}}{\langle C\rangle^2_{ON/OFF}} + \frac{X(-\tau)_{ON/OFF}X(\tau)_{OFF}}{\langle C\rangle^2_{ON/OFF}}\right]. \tag{3.88}$$

Here, all the values to be subtracted are small, while the $g^{(2)}_{pw}(\tau)$ expression includes terms $\frac{\langle P_x\rangle_{OFF}}{\langle P_x\rangle_{ON/OFF}} \sim 10^3$. The parasitic contributions are also complex while the desired $g^{(2)}_{cs}(\tau)$ is purely real, such that the SNR can be increased by 2 by taking only the real part of all records.

It should be noted that this technique requires the precise compensation of all time delays between the two lines. Indeed, if $t_2 - t_1 \geq \kappa^{-1}$, then the correlation between the two channels is lost and $\langle C(t)\rangle = 0$. This is not a problem for the power correlation method, where a time delay simply shifts the $\tau = 0$ point for $P_1(0)P_2(\tau)$.

In practice, we compute both versions of $g^2(2)(\tau)$, (3.87) and (3.88), using the same numerical records of complex envelopes. The comparison of the two results, which carry uncorrelated noises, increases again the accuracy of the measurement.

3.4 Setup of the experiment: cold-stage circuit, microwave collection chain, numerical data acquisition and treatment

3.4.1 Low-temperature circuit

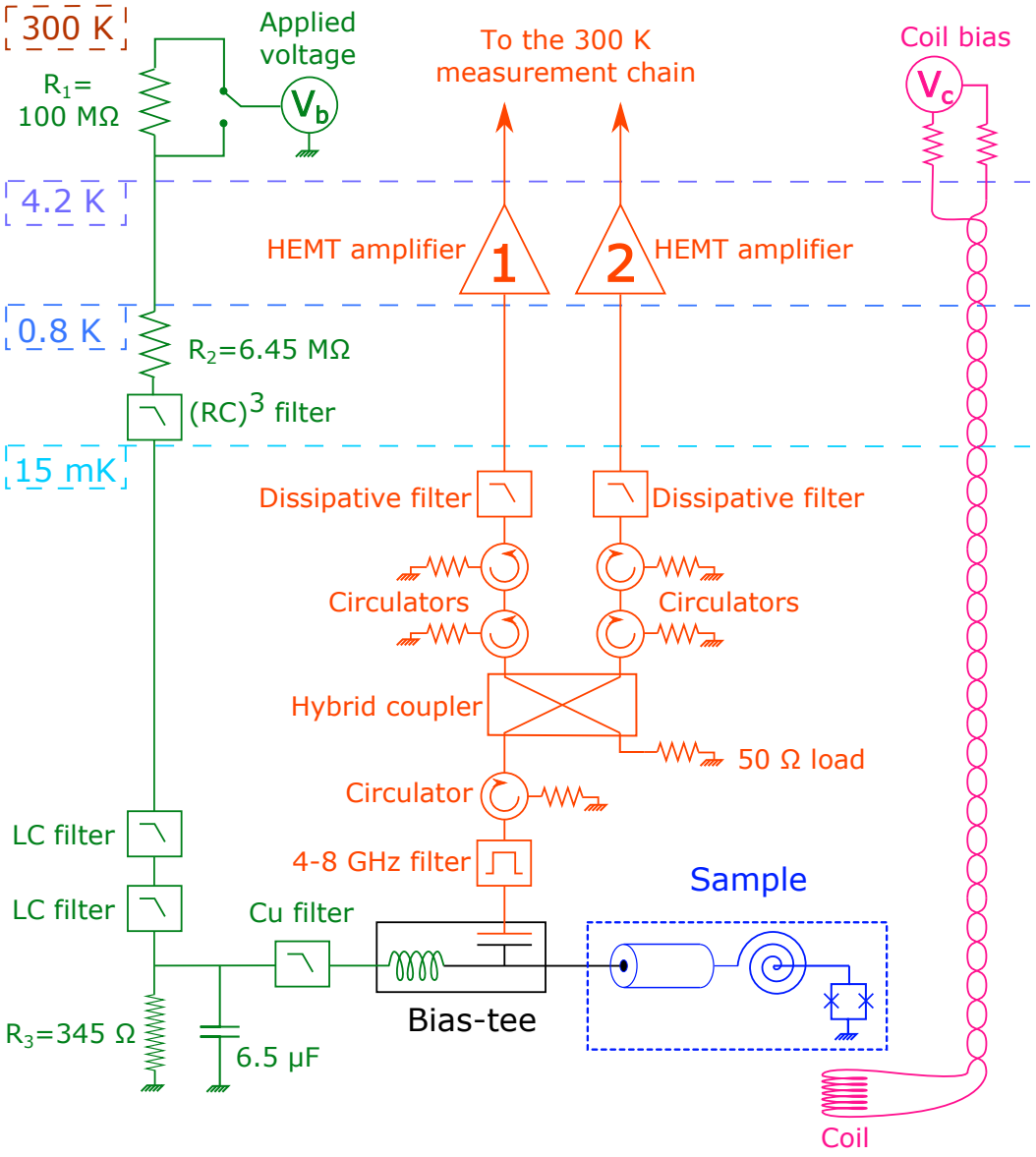

Figure 3.25: Setup used in the experiment. At the cold stage of a dilution fridge, the strong-coupling sample (dark blue) is connected through a bias-tee to a dc-voltage bias line (green) and to a RF collection line (dark orange). The microwave signals are split over two distinct amplification lines (1) and (2). A current-biased superconducting coil (pink) placed under the sample allows the application of a small magnetic field through the SQUID.

Figure 3.25 shows the setup used in our strong-coupling experiment. The **sample** (shown in dark blue) is placed at the coldest stage of a homemade wet dilution fridge, with a base temperature of 15 mK. It includes a SQUID, which is connected on one side to the cold ground of the fridge, and to the other side to a high-impedance coil resonator and a CPW

segment. The CPW segment increases the impedance seen by the resonator, reducing its quality factor.

The chip is connected to a SHF BT45 **bias-tee** (in black), whose properties were characterized separately in a 4.2 K helium dewar. Microwave reflectometry measurements show that at low temperature, the bias-tee behaves approximately as the association of an inductance L_{BT} and a capacitance C_{BT}, with:

$$L_{BT} \simeq 120\ \mu\text{H}, C_{BT} \simeq 42\ \text{nF}, \tag{3.89}$$

yielding a self-resonance frequency $1/2\pi\sqrt{L_{BT}C_{BT}} \simeq 71$ kHz at cryogenic temperatures. At this frequency, the bias-tee implements a parasitic resonant mode, with an impedance $\sqrt{L_{BT}/C_{BT}} \simeq 54\ \Omega$.

Well below this frequency, C_{BT} behaves as an open so that the sample is connected only to the **dc-voltage bias line** (in green). A voltage V_b is applied by a low-noise **Yokogawa 7651** dc source at the top of the bias line. V_b can be set from 0 to 32 V with a 10^{-4} accuracy. The bias line includes a $\mathbf{R_1}$**= 100 MΩ resistor** at room temperature. This resistor is in series with a $\mathbf{R_2}$**= 6.5 MΩ resistor** anchored at the still stage of the fridge, thermalizing it at around 0.8 K. The bias line is finally in series with the parallel association of the sample (through the bias tee), and a **homemade winded resistor** $\mathbf{R_3}$**=345** Ω placed at 15 mK.

As the tunnel resistance of the SQUID is of the order of $\sim$ 200 kΩ, the admittance of the sample is always small compared to $(345\ \Omega)^{-1}$. Thus all the current injected by the Yokogawa flows through R_3, and the sample is effectively voltage biased. The current in the bias line reads $V_b/(R_1 + R_2 + R_3)$, so the voltage drop V across R_3 is $R_3V_b/(R_1 + R_2 + R_3)$. The division ratio of the line is then $\simeq 3 \times 10^5$, which allows us to apply precisely a voltage in the μV range across the SQUID.

Note that as depicted on the figure, R_1 can easily be short-circuited to reduce the division ratio to $\simeq 2 \times 10^4$. This enables applying a much higher bias on the sample, of the order of 8 times the gap voltage Δ/e. At this high bias value the junction behaves from a microwave point of view as a resistor R_N at an effective temperature $eV/2k_B$. In this *shot-noise regime*, we can use the emission noise of the junction to calibrate the gain of the amplification chain (see appendixB).

The division ratio also reduces the impact of spurious voltage noise from the room temperature Yokogawa. To further decrease the noise on the sample, a number of filters are inserted in the line. Right after R_2 three **homemade** *RC* **lowpass filters** ($R = 2$ kΩ and C = 1 nF) are cascaded, giving a -60 dB/decade roll-off after the cut-off frequency $\simeq 80$ kHz. At the input of R_3 are **two commercial** *LC* **filters** (Murata NFE61PT472C1H9L and NFM60R00T220T1), which attenuate noise up to about 1 GHz. R_3 itself is a distributed *RC* filter, as it was made by winding up 3.5 meters of ISAOHM resistive wire around a copper rod. Its total capacitance to the ground is efficient to thermalize electrons in the wire at the base temperature of the fridge. In addition, R_3 is in parallel with **two Murata HSSC Si capacitors** of 3.3 μF[2], implementing another *RC* filter with a frequency cut-off of about 70 Hz. All these different types of low-pass filters are needed as they all eventually get shorted at sufficiently high frequencies. A **Cu powder filter** is finally inserted right before the bias-tee. At low frequency it forms a *RC* filter ($R = 0.3$

[2]yielding a total 6.5 fF at low temperature.

Ω and $C = 350$ pF) with a 1 GHz cut-off frequency. At high frequency (few GHz range), it becomes a very efficient microwave absorber thanks to the skin effect in the powder grains [83].

Far above 71 kHz L_{BT} blocks the bias line, so that the sample is connected only to the **RF line** (in dark orange). This line collects the photons leaking out of the resonator and splits them over two distinct measurement chains (1) and (2), which include distinct **low-noise HEMT amplifiers** (LNF LNC4_8C on channel (1) and LNC4_8A on channel (2)), thermalized to liquid helium temperature. These amplifiers provide a gain of about 40 dB in the 4 to 8 GHz range, with an added noise temperature $T_N \simeq 2.5$ K according to specifications.

These amplifiers radiate noise back onto the sample. If their input impedance is matched to $Z = 50\ \Omega$, they radiate approximately $k_B T_N$ in their operating band. Outside of the 4-8 GHz band, they may give much more noise (in particular at high frequencies). If sent directly to the sample, this noise would populate the resonator with a population around $n_B(T_N) \simeq 10$, ruining the antibunching of the emitted photons.

To suppress this noise, a number of filters and circulators are inserted between the amplifiers and the sample. Right before the amplifiers we put **dissipative filters** (Marki FX0109), which dissipate all noise out of the 1-9 GHz band. As they are thermalized at the base temperature of the fridge, they only absorb noise power from the amplifiers, and do not shine anything back to their input, which could lead to saturation of the amplifiers.

Circulators (Quinstar QCY) are used to route noise in the 4-8 GHz band towards **cold 50 Ω loads**, which absorb the incoming noise and only reemit vacuum fluctuations. In practice they have a finite efficiency, due to imperfect impedance matching. They still provide at least 17d B on attenuation of the amplifiers' noise. Putting 3 circulators in series allows for a comfortable 50 dB reduction of this parasitic noise power.

The beamsplitter is implemented by a **hybrid coupler** (Pulsar QS2-05-463/2S). Its fourth port is connected to a cold 50 Ω load, so that it only mixes the sample's signals with vacuum fluctuations. Finally, a **4-8 GHz cavity filter** (Microtronics BPC 50403) rejects all remaining noise outside of its frequency window.

When matched with a 50 Ω line, this filter presents an input impedance of 50 Ω in the 4 to 8 GHz band, and $\leq 1\ \Omega$ out of the band. Thus the remaining thermal voltage noise seen by the sample is mostly shunted to ground, as $Re[Z(\omega \leq k_B T/\hbar)] \simeq 1\ \Omega$. Recall that following (2.74), the voltage noise on the junction is directly linked to the $P(E)$ function, which is peaked at $E = 0$ with a width of the order of:

$$4k_B T \frac{Re[Z(\omega \leq k_B T/\hbar)]}{R_Q} \sim 2e \times 0.5 \text{ nV} \sim h \times 0.25 \text{ MHz}, \tag{3.90}$$

which should also correspond to the spectral width of the emitted radiation.

Finally, a **small superconducting coil** (in pink) is current-biased by a low-noise room temperature voltage source V_c. This allows to thread a magnetic flux Φ through the SQUID, tuning E_J. The currents leads of the coil are twisted, which makes it immune to electromagnetic interferences and sufficiently noise-less for the experiment.

3.4.2 Room-temperature chain

The outputs of the amplifiers (1) and (2) are routed towards two similar room temperature signal processing chains, depicted in figure 3.26:

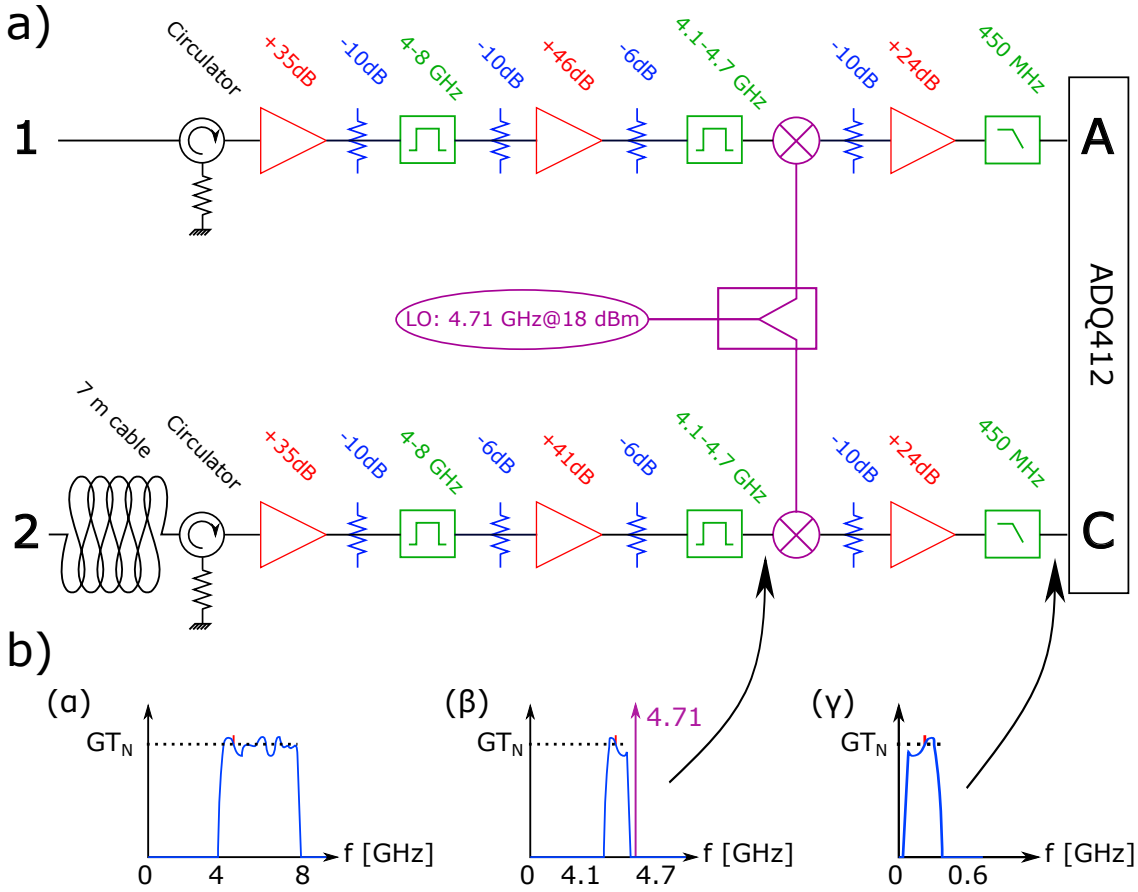

Figure 3.26: a) Room-temperature processing chain. Microwave signals from the (1) and (2) channels are amplified, filtered, mixed down to the 0-600 MHz band and routed towards a fast acquisition card. Circulators and attenuators remove unwanted reflections of the amplifiers noise. b) PSD at different points of the chain. (α) Input signals consist mostly of the flat $G \times T_N$ noise of the HEMT amplifier in the 4-8 GHz band, modulated by parasitic microwave reflections (in blue). The sample's signals (in red) are much smaller than T_N, and reside only in a narrow frequency band. (β) The 4.1-4.7 GHz filter reject all noise outside of the 600 MHz wide measurement band. (γ) After heterodyning at 4.71 GHz, the transposed signals reside in the low frequency 0-600 MHz band.

A **7 m-long cable** is inserted at input of channel (2). It adds a $\simeq$ 35 ns delay to signal propagating on this channel with respect to the other. This delay is corrected for numerically during the data acquisition. This procedure removes virtually all room-temperature crosstalk, which proved dominant in the 2016 experiment. However this trick cannot remove the parasitic crosstalk inside the fridge.

A **circulator** a the input of each chain protects the cryogenic HEMT from the noise radiated by the first amplifiers of the chain. This **first amplifier** (Miteq AFS3-040080-09-CR-4) has a gain of about 35 dB. Its noise temperature is around 70 K, so that the SNR is still determined by the 2.5 K+40dB of the HEMT amplifier.

It is followed by a **10 dB attenuator**, a **4-8 GHz bandpass filter**, another **10 dB attenuator** and a **second amplifier** (Miteq AFD5-040080-23). This amplifier yields 46

dB of gain [3], with a noise temperature around 200 K. The bandpass filter helps rejecting all unwanted noise out of the measurement band. The attenuators are used to suppress parasitic reflections in the chain due to impedance mismatches, and to avoid saturation of the next amplifier.

The second amplifier is followed by a **6 dB attenuator**, a narrower **4.1-4.7 GHz bandpass filter** (Microtronics BPC 18898 and an **IQ mixer** (Hittite HMC-C009). The mixer down-converts the signals to a lower frequency bands, by multiplying them with a **LO signal at** $f_H = 4.71$ **GHz**, provided by a RF source (Rhode & Schwarz SMR20). The heterodyning frequency is chosen just outside of the 4.1-4.7 GHz band, so that no aliasing occurs. Note that because we are heterodyning "from above", the downconverted signals are $\propto Re[(\hat{X}_a - i\hat{P}_a)e^{-i\omega t}]$ instead of $\propto Re[(\hat{X}_a + i\hat{P}_a)e^{-i\omega t}]$. As the antibunching of the photons does not require a phase reference, this is of no consequence.

The down converted signals are attenuated by **10 dB** before amplification by a **dc-1 GHz amplifier** with +24dB gain, filtering by a **lowpass filter** (Minicircuits BLP450+) and final detection by a **fast acquisition card** (ADQ412), sampling on two channels A and C at $f_S = 1.25$ GSamples/s.

3.4.3 Numerical data processing

In Fourier space, this sampling rate yields an acquisition bandwidth of $f_S/2 = 612.5$ MHz. The last filter of the chain has a nominal cutoff frequency of 450 MHz, but in practice presents a quite slow roll-off, effectively attenuating the signals only above ~ 600 MHz. This is enough to avoid aliasing of the amplifier's noise that would reduce even more the SNR. This heterodyne method gives us access to the signals emitted by the sample in the $[f_H - f_S/2; f_H] =$ band.

Recall that there is no phase reference in the experiment, as the creation of antibunched photons does not rely on a pump tone. Then we cannot synchronize the detection of the signals with a clock. Our acquisition method is rather based on the principles of noise measurement. Schematically, we acquire some length of signal, compute its PSD numerically and store it, then repeat the measurement and average all the outputs. In the absence of phase reference the PSD is the proper quantity to average, contrary to triggered experiments where one can average complex Fourier components (or quadratures) of the signal.

We then take advantage of the Wiener-Khinchin theorem, which links correlation functions in the time domain to power spectra in the frequency domain:

$$\mathbb{F}[\langle f^*(t)g(t+\tau)\rangle_t](\omega) = (\mathbb{F}[f(\tau)])^*(\omega) \times \mathbb{F}[g(\tau)](\omega), \tag{3.91}$$

with $f(t), g(t)$ complex valued functions, $\mathbb{F}[f(\tau)]$ the Fourier transform of f with respect to τ, and where the average $\langle ...\rangle_t$ is taken over t. This means that to measure $\langle S_1^\dagger(t)S_2^\dagger(t+\tau)\rangle$, we simply needs to compute the Fourier transform of $S_1^\dagger(t)$ and $S_2^\dagger(t)$, multiply them together and average the result.

Going to Fourier space also allows us to extract easily both quadratures of the signal. The microwave voltage detected by the acquisition card reads: $V(t) = Re[S(t)e^{-i\omega_0 t}] =$

[3] only 41 dB on channel (2).

$X(t)\cos(\omega_0 t) + P(t)\sin(\omega_0 t)$. Here $\omega_0 = \omega - 2\pi f_H$ is the center frequency of the signals after heterodyning. If the measurement band is wider than the frequency support of $X(t)$ and $P(t)$ (which is of the order of κ), then the analytical signal $S(t) = X(t) + iP(t)$ can be accurately reconstructed from $V(t)$.

To do so, we compute the numerical Hilbert transform of $V(t)$:

$$\mathbb{H}[V](t) = \int_{-\infty}^{+\infty} \frac{V(t')}{t - t'} \frac{dt'}{\pi} = X(t)\sin\omega_0 t - P(t)\cos\omega_0 t, \tag{3.92}$$

which holds iff: $\mathbb{F}[X](\omega > \frac{f_S}{4}) = \mathbb{F}[P](\omega > \frac{f_S}{4}) = 0$. Then:

$$V(t) + i\mathbb{H}[V](t) = S(t)e^{-i\omega_0 t}. \tag{3.93}$$

Now the convolution product in (3.92) can be written as a product in Fourier space, where (3.93) reads:

$$\mathbb{F}[S](\omega + \omega_0) = \mathbb{F}[V](\omega) + i\mathbb{F}[V](\omega) \times \mathbb{F}\left[\frac{1}{t}\right](\omega) \tag{3.94}$$

$$\Rightarrow F[S](\omega) = \mathbb{F}[V](\omega - \omega_0) \times \Theta(\omega - \omega_0), \tag{3.95}$$

with $\Theta(\omega)$ the Heaviside function. The procedure to get $S(t)e^{-i\omega_0 t}$ is then to acquire some length of signal, compute its Fourier transform, set to zero all the components with negative frequencies, and invert the Fourier transform (Fig.3.27).

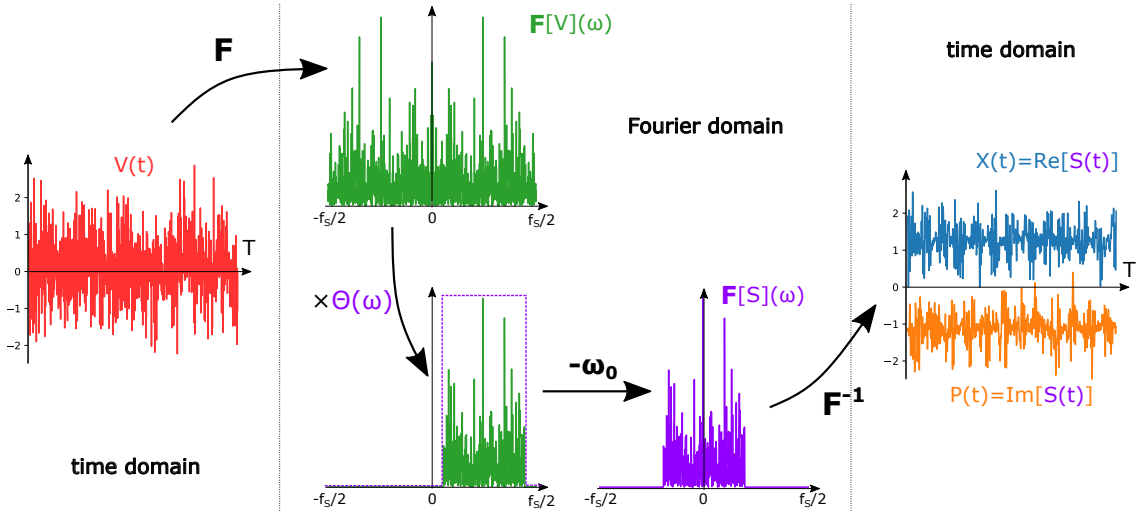

Figure 3.27: Principle of the numerical demodulation scheme. Starting from a time record of down-converted voltages $V(t)$ (in red), we compute its Fourier transform $\mathbb{F}[V](\omega)$ (absolute value plotted in green). We then set to zero all components of the Fourier transform with negative frequencies, and shift it by ω_0. This yields the Fourier transform of the complex envelope with respect to ω_0 (in purple). Going back to the time domain, we obtain $S(t)$, whose real and imaginary parts (blue and orange, shifted for readibility) are the $X(t)$ and $P(t)$ quadratures.

This procedure yields the correct result only if the spectrum of $S(t)$ lies exactly in the heterodyning window. In practice we enforce this condition by multiplying $\mathbb{F}[V](\omega)$ by a filter function narrower than $\Theta(\omega)$. We use a 12^{th} order Butterworth filter with 50 MHz and 575 MHz cutoff frequencies, which provides maximum flatness in its passband.

Let us illustrate our procedure on a specific example: we start by recording time traces of the two voltages $V_1(t)$ and $V_2(t)$, compute their discrete Fourier transforms and suppress all negative frequencies (Fig.3.27). We average the product $(F[V_1])^*(\omega) \times \mathbb{F}[V_2](\omega)$ and interpret it as the Fourier transform of $\langle S_1^\dagger(0)S_2(\tau)\rangle$, yielding the first order coherence function. In parallel to this, we shift $\mathbb{F}[V_x](\omega)\times\Theta(\omega)$ by $-\omega_0$, then bring it back to the time domain to yield $S_x(t)$. Then we compute the product $S_1^\dagger(t)S_2(t)$ to obtain the cross-signal power, bring it to Fourier domain, and square it to yield $\mathbb{F}[\langle S_1^\dagger(0)S_1^\dagger(\tau)S_2(\tau)S_2(0)\rangle](\omega)$. We average that last quantity and obtain the second order coherence function after correct subtraction of unwanted terms.

This method allows us to get any correlation function such as $g^{(1)}(\tau)$ and $g^{(2)}(\tau)$, as well as the power spectral densities $|\mathbb{F}[S_1](\omega)|^2$ and $|\mathbb{F}[S_2](\omega)|^2$, both in the ON and the OFF states.

Note finally that the numerical Fourier transform assumes the periodicity of the signal over the acquisition time T. Thus our procedure yields the correct correlation functions only if T is longer than the coherence time of the signals. Otherwise unwanted correlations between $S(t)$ and $S(t+T)$ would ruin the procedure. In practice, the prediction of [34] indicates a correlation timescale of $\kappa^{-1} \sim 1$ ns for the antibunched photons. We use a comfortable $T = 1024\ f_S^{-1}$, i.e 1024 points per chunk of data. This is more than enough to compute power fluctuations, and allows us to resolve the spectral properties of the radiation, which vary on a 1 MHz scale.

3.5 Results in the strong-coupling regime

3.5.1 Power spectral density measurements

In the spirit of our measurement scheme, the PSD of the signals emitted by the sample is computed as the Fourier transform of the first order correlation function: $\langle \hat{a}^\dagger(0)\hat{a}(\tau)\rangle = \bar{n} \times g^{(1)}(\tau)$. There are three ways of obtaining it from the two complex envelopes $\hat{S}_1(t) = \sqrt{G_1}\left(\hat{a}(t) + \hat{h}_1^\dagger(t)\right)$ and $\hat{S}_2(t) = \sqrt{G_2}\left(\hat{a}(t) + \hat{h}_2^\dagger(t)\right)$. One can use either the auto-correlation of the signals from one channel:

$$\langle \hat{a}^\dagger(0)\hat{a}(\tau)\rangle = \frac{\langle \hat{S}_1^\dagger(0)\hat{S}_1(\tau)\rangle_{ON/OFF}}{|G_1|} = \frac{\langle \hat{S}_2^\dagger(0)\hat{S}_2(\tau)\rangle_{ON/OFF}}{|G_2|}, \tag{3.96}$$

or the cross-correlation of two signals:

$$\langle \hat{a}^\dagger(0)\hat{a}(\tau)\rangle = \frac{\langle \hat{S}_1^\dagger(0)\hat{S}_2(\tau)\rangle_{ON/OFF}}{\sqrt{G_1^* G_2}}. \tag{3.97}$$

Recall here that the effective gains $\sqrt{G_1}, \sqrt{G_2}$ describe the action of the entire acquisition chain, with cascaded amplifiers, attenuators, parasitic impedance mismatches, and the numerical compensation of delays between the two channels. They are unknown complex functions of ω - as a time delay τ amounts to multiplication by $e^{-i\omega\tau}$ in the frequency-domain. They also slowly drift over time as the temperature of the room-temperature amplifiers is not maintained constant.

The Fourier transform of the auto-correlators yields the power spectra:

$$\mathrm{Sp}_1(\omega) = \mathbb{F}[\langle \hat{S}_1^\dagger(0)\hat{S}_1(\tau)\rangle](\omega) = |G_1(\omega)|\left(\langle \hat{a}^\dagger(\omega)\hat{a}(\omega)\rangle + n_B(T_{N_1})\right) \tag{3.98}$$

$$\mathrm{Sp}_2(\omega) = \mathbb{F}[\langle \hat{S}_2^\dagger(0)\hat{S}_2(\tau)\rangle](\omega) = |G_2(\omega)|\left(\langle \hat{a}^\dagger(\omega)\hat{a}(\omega)\rangle + n_B(T_{N_2})\right), \tag{3.99}$$

with the effective noise temperatures T_{N_1}, T_{N_2} such that $\langle \hat{h}_x(\omega)\hat{h}_x^\dagger(\omega)\rangle = n_B(T_{N_x})$. The cross-correlator yields the cross-spectrum:

$$\mathrm{Cr}(\omega) = \mathbb{F}[\langle \hat{S}_1^\dagger(0)\hat{S}_2(\tau)\rangle](\omega) = \sqrt{G_1^* G_2}(\omega)\left(\langle \hat{a}^\dagger(\omega)\hat{a}(\omega)\rangle + \alpha(\omega) n_B(T_{N_c})\right), \tag{3.100}$$

with $T_{N_c} = \sqrt{T_{N_1} T_{N_2}}$. Here the complex coefficient $\alpha(\omega)$ from (3.86) models the parasitic coupling between the two lines, with $|\alpha| \ll 1$.

To remove the unknown gains $G_1(\omega), G_2(\omega)$, we normalize all spectrum data by the OFF value of the power spectra, which read $|G_1(\omega)| n_B(T_{N_1})$ and $|G_2(\omega)| n_B(T_{N_2})$. More precisely, we use:

$$\frac{\mathrm{Sp}_1(\omega)_{ON/OFF}}{\mathrm{Sp}_1(\omega)_{OFF}}, \frac{\mathrm{Sp}_2(\omega)_{ON/OFF}}{\mathrm{Sp}_2(\omega)_{OFF}}, \text{ and } \frac{|\mathrm{Cr}(\omega)_{ON/OFF}|}{\sqrt{\mathrm{Sp}_1(\omega)_{OFF}\mathrm{Sp}_2(\omega)_{OFF}}} \tag{3.101}$$

to obtain the PSD in units of $n_B(T_{N_x})$, which can be calibrated using the junction biased well above the gap as a calibrated noise source (see appendix B). To be insensitive to the slow drift of the gains, we alternate between ON and OFF measurements with a period of typically 5 minutes. Integrating the emission spectrum over frequencies finally give the photon emission rate and, if κ is known, the average occupation of the resonator.

With these tools at hand, we measure spectra in various conditions of bias voltage and Josephson energy. This allows us to calibrate all the properties of the sample and the cryogenic setup *in situ*, so that we can fully characterize our single-photon source, and compare measurements of correlation functions to the theoretical predictions with no adjustable parameters.

Noise spectra in the OFF state: gain calibration

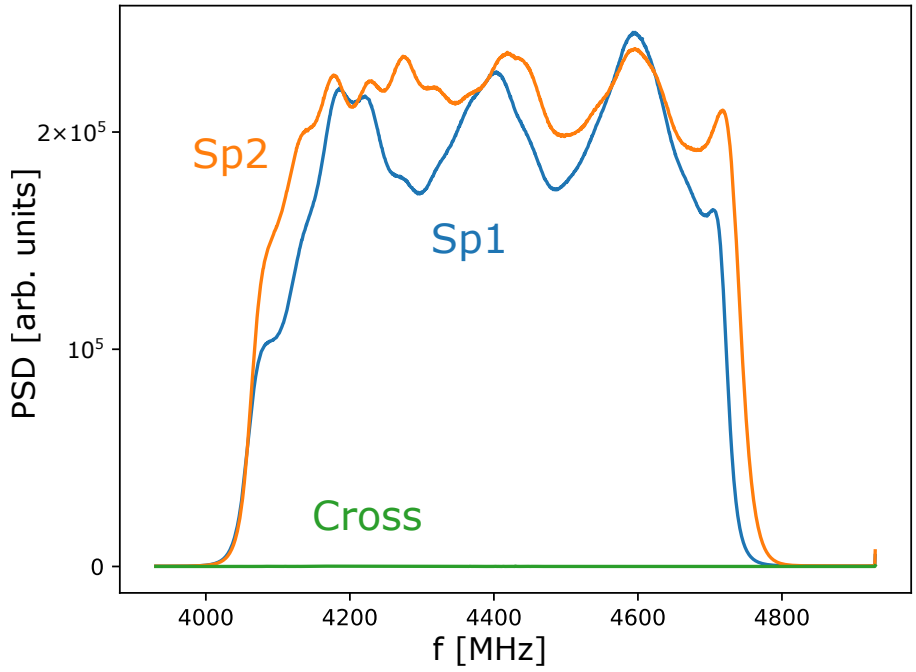

Figure 3.28: Spectra in the OFF state of the experiment, in arbitrary units.

Figure 3.28 shows the power spectra measured in the OFF state of the experiment, reached by setting $V_b = 0$. Here the heterodyne frequency was set to 4930 MHz, the acquisition rate increased up to 2 GSamples/s and the last lowpass filter removed (Fig.3.26). This in order to detect the signals in a wider frequency range and check that no important features were missed in the narrower filtering scheme used later for correlation measurements.

PSDs are expressed in arbitrary units, proportional to the $\mathrm{mV}^2/\mathrm{Hz}$ detected by the acquisition card. In the OFF state $\mathrm{Sp}_x(\omega)$ is equal to the gain of the x chain, $G_x(\omega)$, times the spectral density of the noise radiated by the HEMT amplifier, $n_B(T_{N_x})$. As the two amplification chains are nominally identical, they have similar noise temperatures and overall gain. The shape of $\mathrm{Sp}_x(\omega)$ is sculpted by the 4.1-4.7 GHz bandpass filter. Additional ripples come from imperfect impedance matching in the chains, resulting in parasitic microwave reflections. The sharp peak at 4930 MHz actually comes from a dc-offset on the acquisition card, and is of no consequence.

The cross-spectrum $\mathrm{Cr}(\omega)$ is found to be much smaller than the direct power spectra. A log-scale representation (Fig.3.29) shows that it is non-zero, but still 2000 times smaller than Sp_1 and Sp_2. This means that the isolation between the two channels is finite, and of the order of -33dB. $\mathrm{Cr}(\omega)$ also shows the shape of the 4.1-4.7 GHz filter, proving that

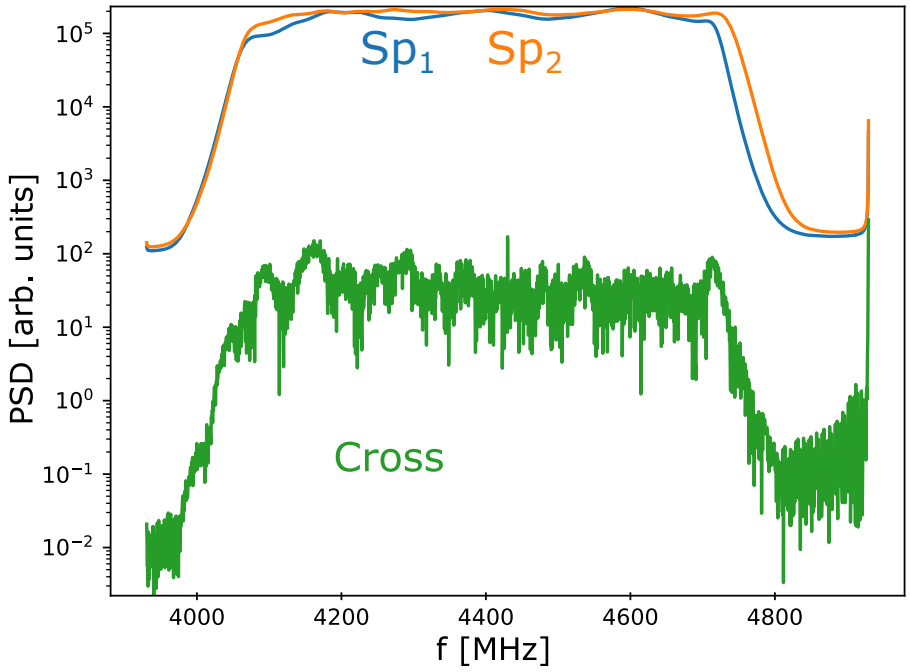

Figure 3.29: Spectra displayed in logarithmic scale. The Cross-spectrum is non-zero, but still 3 orders of magnitude lower than the amplifiers' noise.

the parasitic coupling occurs somewhere in the analog amplification chain, and not at the level of the acquisition card.

Calibration of noise temperatures in the shot-noise regime

We now remove the R_1 =100 MΩ resistor from the room-temperature circuit (Fig.3.25) and apply 32 V to the voltage-bias line. The voltage drop on the sample is then of the order of $\simeq$ 1.5 mV, which is about 8 times the gap voltage $\Delta/e \sim 200$ μV. The junction is then in the *shot-noise regime*, where it behaves from the microwave point of view as a hot resistor R_N with an effective temperature $(eV - \hbar\omega)/2k_B$. It can then be used as a calibrated current source to determine the gain of the microwave chain (see appendixB).

The shot-noise radiated by the junction is filtered by the on-chip resonator. The PSD of the sample's emission noise, $S_p^S(\omega)$, is then a peak centered at the resonator frequency, with a comparable quality factor. This radiated power piles up on top of the amplifiers noise before amplification and detection by the acquisition card.

We present the measured spectra in Figure 3.30. $\mathrm{Sp}_1(\omega)$ and $\mathrm{Sp}_2(\omega)$ show the sample's emission power, distorted by the ripples of the gains $G_1(\omega), G_2(\omega)$ and with the sizeable background noise from Sp_1^{OFF}, Sp_2^{OFF} (see figure 3.28). By contrast the background value is negligible in the $\mathrm{Cr}(\omega)$ curve, albeit ripples in $G_1(\omega), G_2(\omega)$ still distort the signals.

We remove the noise background, the ripples, as well as the slow drift of the gains, by computing normalized spectra as in (3.101). The PSDs are then expressed in units of the amplifiers' background noise $n_B(T_{N_x})$, see figure 3.31.

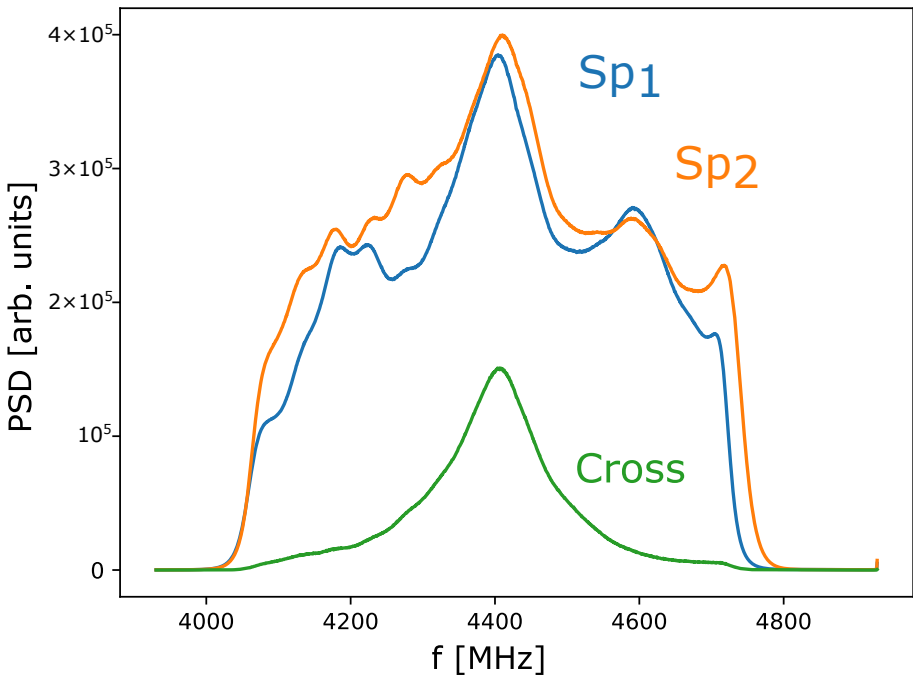

Figure 3.30: Spectra taken with the junction biased far above the gap voltage.

When dividing by the OFF PSDs, the part of the spectra which lie out of the bandpass filter gives unreliable results, as we are basically dividing by zero. Thus we do not consider as real the artefacts that appear below 4.1 GHz and above 4.7 GHz. The emission spectrum then looks approximately like a Lorentzian peak. The peak is narrower in Sp_2 than in Sp_1. We attribute this difference to microwave reflections that occur between the sample and the cryogenic amplifiers, yielding ripples in the transmission of the chain. In other words, the hybrid coupler is not exactly balanced and transmits a bit more power to channel 1 than to channel 2 at some frequencies. The peaks on the two channels still reach the same value of about $0.65 \times n_B(T_{N_x})$, indicating that the two amplifiers have approximately equal noise temperatures.

As expected the Cross-spectrum looks like the average of Sp_1 and Sp_2. To compute the total power emitted by the sample, we use both the Cross and the average $(Sp_1+Sp_2)/2$, which yield the same results within the accuracy of our measurements.

Fitting the central part of the emission peak with a Lorentzian function yields a resonance frequency of $\omega_r/2\pi = 4406$ MHZ and a FWHM of $\Delta F_{sn} = 158.3$ MHz. As detailed in Appendix B this does not correspond to the width of the resonator itself, but rather to approximately $1 + Z_0/R_N$ times this width, with $Z_0 = Re[Z(\omega_r)]$ and R_N the normal state resistance of the SQUID. The resonance frequency ω_r is smaller than what was designed during the sample's fabrication, which we attribute to an underestimated stray capacitance to ground.

The tunnel resistance was measured in a separate experiment, where we dipped the sample in a liquid He dewar. At 4.2 K, the niobium part of the sample is superconducting, so that we measure the dc-resistance of the Al bridge in series with the tunnel junction. Given the experimental uncertainties and the unknown value of the bridge's resistance, we find:

$$R_N = 222 \pm 3 \text{ k}\Omega. \tag{3.102}$$

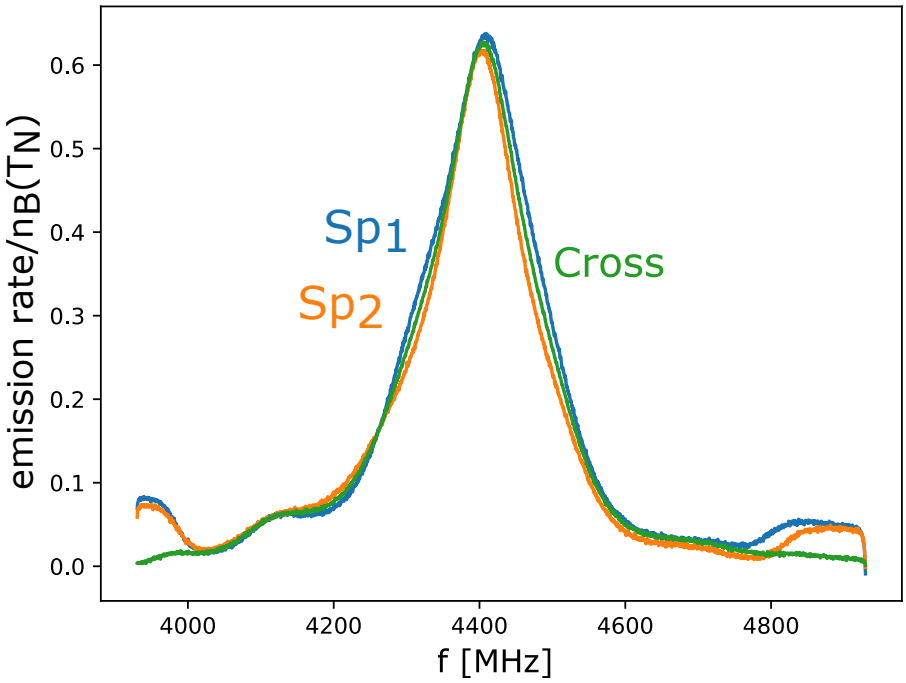

Figure 3.31: Normalized spectra far above the gap voltage. These can be seen either as true power spectral densities in units of the HEMTs noise power, or as photon emission rate spectra in units of the occupation number of the amplifiers noise mode: $\langle \hat{a}^\dagger(\omega)\hat{a}(\omega)\rangle / n_B(T_{N_x})$.

We also have access to the frequency dependence of $Re[Z(\omega)]$ as seen by the junction, through the measurement presented in 3.5.1. We find a FWHM of the resonator of $\Delta F = 120.3$ MHz. The peak impedance of the resonator is then:

$$Z_0 = Re[Z(\omega_r)] = R_N \times \frac{\Delta F_{sn} - \Delta F}{\Delta F} = 70 \pm 1 \text{ k}\Omega. \tag{3.103}$$

The microwave coupling factor between the junction in the shot-noise regime and the resonator is then:

$$C_0 = 1 - \left| \frac{R_N - Z_0}{R_N + Z_0} \right|^2 = 0.729 \pm 0.005, \tag{3.104}$$

which enter in the expression of the PSD radiated into the measurement line far above the gap voltage:

$$SP(\omega) = \frac{eV - \hbar\omega}{2} \times \frac{C_0}{1 + 4\left(\frac{\omega - \omega_r}{2\pi \Delta F_{sn}}\right)^2}. \tag{3.105}$$

For the sake of consistency, we also tried to use the same scheme without assuming that $Re[Z(\omega)]$ is exactly a Lorentzian function. To do so, we computed $Im[Z(\omega)]$ by taking the numerical Hilbert transform of its real part, assuming a $(\omega - \omega_r)^{-1}$ decay outside of the measurement window. Then we fitted the spectra to (B.2), in order to extract the value of the coupling factor. We found $C_0 = 0.740 \pm 0.005$, which is consistent with the previous approximate result.

Next, we scan the applied voltage V_b from 7 to 32 V and plot the integral of the normalized Cross spectrum as a function of the applied bias V_b (Fig.3.32). This yields the total photon emission rate $\Gamma = \langle \hat{a}^\dagger \hat{a} \rangle$ in units of $n_B(T_{N_C})$, with $T_{N_C} = \sqrt{T_{N_1} T_{N_2}}$ the effective noise temperature. Far above the gap voltage $V = 2\Delta/e \simeq 360$ μV, which we expect to

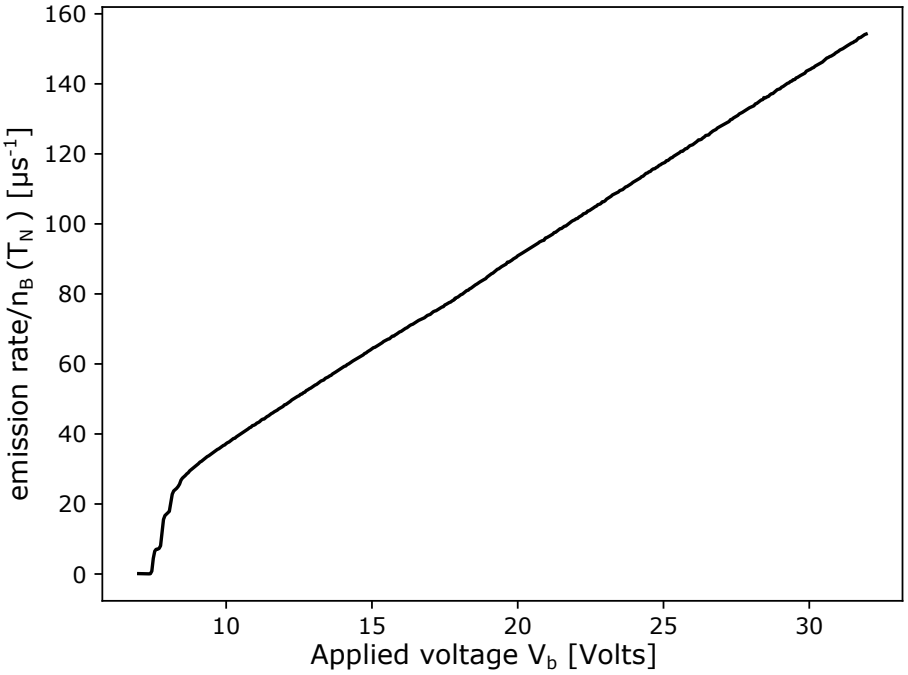

Figure 3.32: Photon emission rate in the shot-noise regime as a function of the applied voltage.

correspond to $V_b \sim 8$ V at the top of the bias line, the emission noise increase linearly with $V \propto V_b$. Below the gap voltage, quasiparticles cannot tunnel and their current noise is zero. Around $V = 2\Delta/e$, the current is a non-linear function of the bias voltage, which in the case of a junction in a low impedance environment can be computed from the shape of the BCS density of quasiparticles [31].

We tried to fit (3.105) to the measured total power (or, with similar results, to the PSD at the top of the resonator $S_P(\omega_r)$). This requires knowing quite well the voltage division ratio that links V_b to V. The fit was not so good, as the slope of $\Gamma(V)$ is actually increasing with applied voltage (this can be seen as a kink in the curve of figure 3.32 around $V_b = 20$ V). The absolute calibration of the gain and of the amplifiers' noise temperature that we could extract were also about 40% off compared to what we found using a different calibration method, described in paragraph 3.5.1.

Later on, we understood that the $R_2 = 6.5$ MΩ resistor that defines the voltage division bridge was actually heating up when a too large voltage was applied onto it, changing the value of the division ratio V_b/V during the voltage scan. Even worse, the amount of heating depends on the duration of the measurement, as the temperature of the resistor keeps increasing while a large V_b is applied. To mitigate this effect, we resorted to use the data taken right above the gap voltage (around V_b= 7 V) where heating is supposedly less important.

The emission rate shows regularly spaced steps with unequal heights (Fig.3.33). An extension of the $P(E)$ theory to the emission noise of normal conductors [84] links dS_P/dV to $P(E)$. We compute numerically the voltage derivative of the photon emission rate (blue curve), and interpret its peaks as the mark of inelastic tunneling of quasiparticles. More precisely, the k-th peak corresponds to the inelastic emission of $(k-1)$ photon per quasiparticle. Note that the $k = 0$ peak does not appear in ICPT as elastic tunneling of Cooper pairs is forbidden as soon as $V \neq 0$.

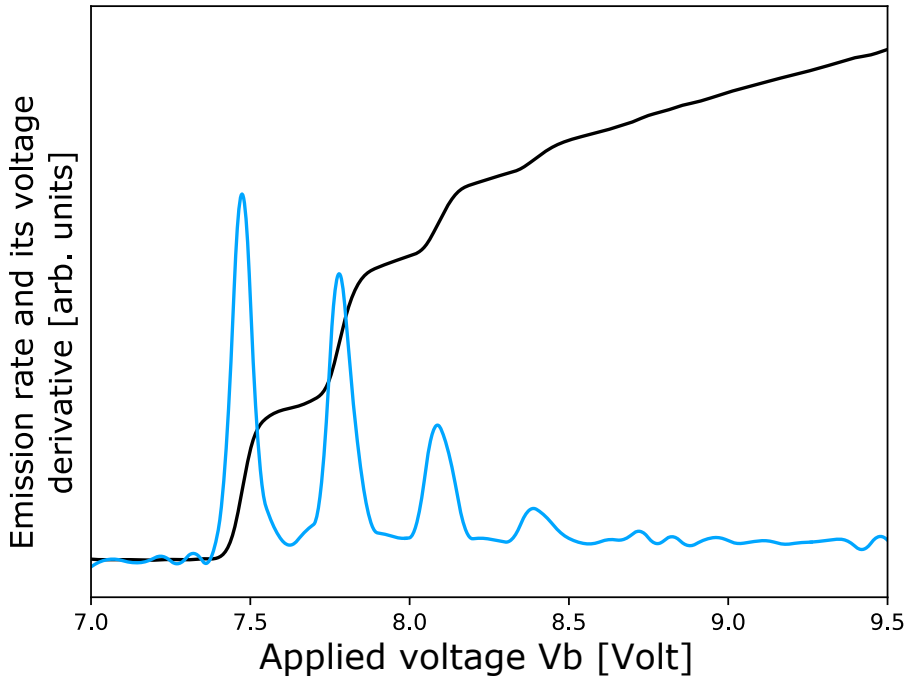

Figure 3.33: Photon emission rate and its voltage derivative.

Coulomb blockade effects are harder to trigger in normal conductors, as the natural scale of impedance is $R_K = h/e^2 = 4 \times R_Q$. The presence of inelastic $k \neq 0$ peaks is a strong indication that the photon emission occurs in a high impedance mode, namely the 4.4 GHz resonator. We thus assume that the peaks are separated by a bias voltage $\Delta V = \hbar\omega_r/e = 18.22\ \mu$V, yielding an absolute calibration of the division ratio:

$$\frac{V_b}{V} = \frac{R_2^{heated} + R_3}{R_3} = 16\ 560 \pm 50, \tag{3.106}$$

which corresponds to a decreased resistance $R_2^{heated} = 4.8\ \mathrm{M}\Omega$, close to its room-temperature value. We can now extract the value of the superconducting gap of the Al junction, which corresponds to the position of the elastic peak (see figure 3.33) minus $\hbar\omega_r/e$:

$$\Delta = 213 \pm 1\ \mu\mathrm{eV}, \tag{3.107}$$

This value, which is higher than the bulk gap of 180 μeV, is typical of thin film Al junctions. From the measurements of Δ and of R_N we can use Ambegaokar-Baratoff formula [56] to estimate the Josephson energy of the junction in the absence of $P(E)$ renormalization:

$$E_J^{AB} = \frac{\Delta R_Q}{2R_N} = 3.10 \pm 0.06\ \mu\mathrm{eV}. \tag{3.108}$$

We did not try to fit exactly the shape of the dS_P/dV curve, as the population of the resonator on the second peak is already of the order of $\bar{n} \sim 2$ photons. Then the full $P(E)$ is not applicable, as stimulated emission process increase the emission rate. Still we can be confident that the spacing of the peaks is $\hbar\omega_r/e$.

Next, we used an extension of Rogovin-Scalapino formula [53] to compute the dynamical response of the junction. Due to the strong non-linearity in the transport around the

gap voltage, the real part of the admittance of the junction is actually larger near the gap. This changes the value of the microwave coupling factor of the junction to the resonator, as R_N in (3.104) needs to be replaced by the full admittance of the junction $Z_{SIS}(\omega, V)$. We chose to fit (3.32) to the data in a voltage range around $V_b = 10$ V, where inelastic processes are negligible. The full modelling yields a correction of about 10% to the emission rate.

In the end, we could perform a quantitative fit and express the emission rates in absolute units. As we normalize all spectra by their OFF value to remove the fluctuating overall gain of the acquisition chain, this amounts to calibrating precisely the noise temperature of the HEMT amplifiers. We thus found:

$$T_{N_1} = 13.5 \pm 0.7 \text{ K} \tag{3.109}$$
$$T_{N_2} = 14.1 \pm 0.7 \text{ K} \tag{3.110}$$
$$\rightarrow T_{N_C} = 13.8 \pm 0.7 \text{ K} \tag{3.111}$$
$$\Rightarrow n_B(T_{N_C}) = 65.4 \pm 3.3 \text{ photons.} \tag{3.112}$$

The $\sim 5\%$ uncertainty comes from inaccuracies in the modelling of the junction's admittance. With the value of $n_B(T_N)$ at hand, we can know express all photon emission rate in true units of photons/s, and the emission rate spectral densities in photons/s/Hz.

This noise temperature is much larger than the nominal temperature specified by the manufacturers of the amplifiers, $T_N^{nom} \simeq 2.5$ K. This comes from all the attenuation between the sample and the input of the HEMTs. As an example, the beam splitter already divides the sample's power over two lines. The T_N we determined is actually the effective noise temperature as seen from the sample. We can then estimate the amount of losses in the acquisition chain:

$$\text{Losses} \simeq \frac{T_N}{T_N^{nom}} = 7.4 \text{ dB}. \tag{3.113}$$

Given that the hybrid coupler already yields 3 dB of attenuation, the remaining 4.4 dB can be attributed to dissipation in the microwave components inserted between the sample and the HEMTs - in particular the circulators and the dissipative filters, which yield about 1 dB of attenuation each.

We also use shot-noise measurement to estimate the remaining thermal occupation of the resonator. Similarly to inelastic emission processes above the gap voltage, **inelastic absorption processes** can occur, where quasiparticles tunnel while absorbing one photon from the resonator. For a voltage bias such that $2\Delta \leq eV < 2\Delta + \hbar\omega_r$, only these absorption processes allow the tunneling of quasiparticles with enough excess energy to emit shot-noise at $\hbar\omega_r$.

We measured finely the emission rate around $2\Delta/e$ and did not detect any such processes. Given our experimental accuracy, this means that the population of the mode is below 1%, or accordingly that the temperature of the resonator is **below $\simeq$ 50 mK**.

Emission map in the ICPT regime

We insert the R_1 =100 MΩ resistor in the bias line to increase the voltage division ratio V_b/V, and hence our precision on the bias voltage V. We now scan V across the single

photon emission peak of ICPT, around $2eV = \hbar\omega$. We detect the spectra in a frequency window covering the bandpass filter, from 4086 MHz to 4708 MHz (see figure 3.34).

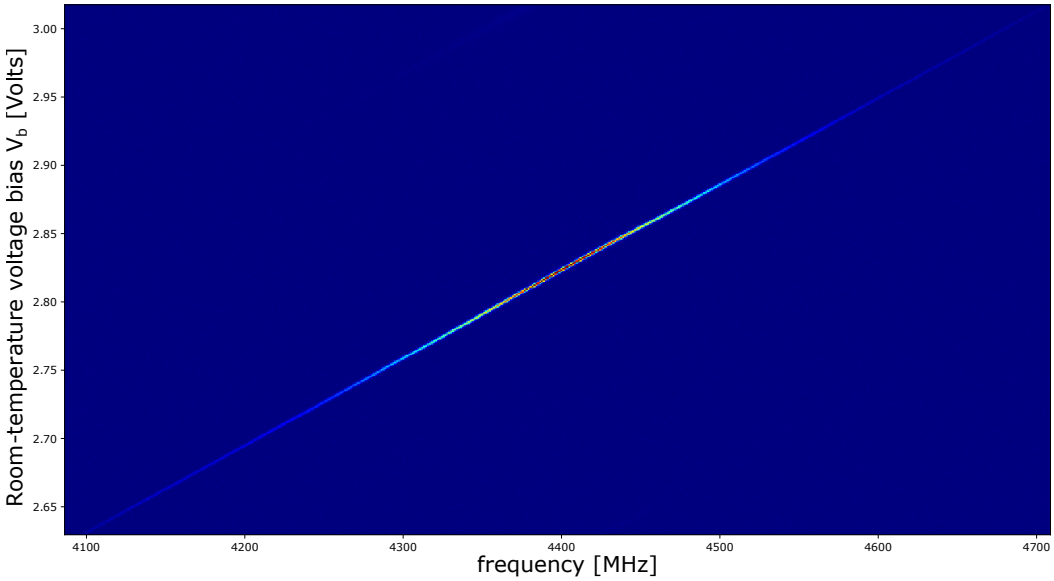

Figure 3.34: Map of the normalized Cross-spectrum as a function of voltage bias.

The spectra are taken at a value of $E_J(\Phi)$ small enough that the population of the mode stays $\ll 1$, so that expression (2.73) from $P(E)$ theory is valid.

The map from figure 3.34 shows a narrow emission peak which follows the $2eV = \hbar\omega$ line. Fitting the slope of this line, we can recover the value of the voltage division ratio:

$$\frac{V_b}{V} = \frac{2e}{\hbar}\frac{dV_b}{d\omega} = 309\ 700 \pm 50 = \frac{R_1 + R_2 + R_3}{R_3}. \tag{3.114}$$

Using a different map taken without the R_1 resistor, we can also fit the ratio $\frac{R_2+R_3}{R_3}$ in a situation where the voltage on R_2 is small enough to avoid spurious heating. Then we can accurately determine the low temperature value of both R_2= 6.45 MΩ and R_3 = 345 Ω, as they are given in figure 3.25.

Emission at a given frequency as a function of voltage bias

We take a cut through the map at a fixed frequency $\omega_r/2\pi = 4406$ MHz (Fig.3.35). This yields $S_P(\omega_r, V)$, which is directly proportional to $P(2eV - \hbar\omega_r)$. Here $P(E - \hbar\omega_r)$ is a narrow peak with a gaussian shape. It is not exactly centered on $\hbar\omega_r$, which we attribute to a remaining $\simeq -20$ nV offset of thermal origin, occurring somewhere in the bias line or between the ground plane of the sample and the ground of the fridge. This was confirmed by setting the bias voltage to negative values, as the offset stayed negative. Note that all spectra shown here are shifted by this offset.

Fitting the gaussian peak yields a FWHM of 6.24 nV, which is larger than the $\sim$ 0.5 nV we expected in (3.90). Recall that the cavity filter in 3.25 has an input impedance of about 1 Ω from dc to 4 GHz. Thus it shunts most of the voltage noise seen by the junction, and contributes to the width of $P(E)$ following (2.74). However this is only true far above the $\omega_{BT} = 2\pi\times$71 kHz cut-off frequency of the bias-tee. At lower frequencies the

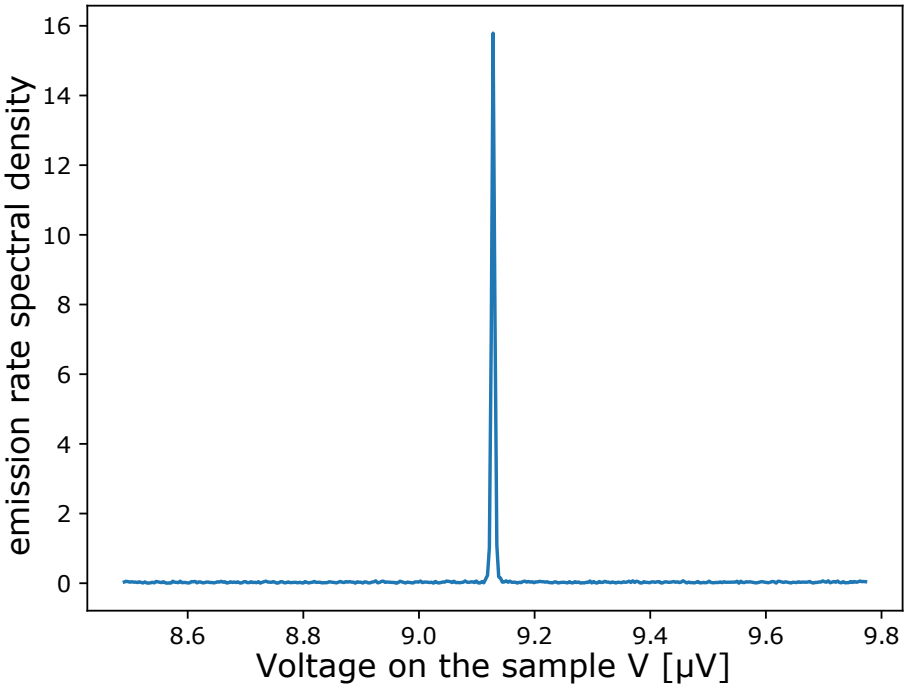

Figure 3.35: Cut through the 2D map at fixed frequency, along the voltage axis.

junction sees the impedance of the bias-line as well as the parasitic mode of the bias-tee itself (Fig.3.36).

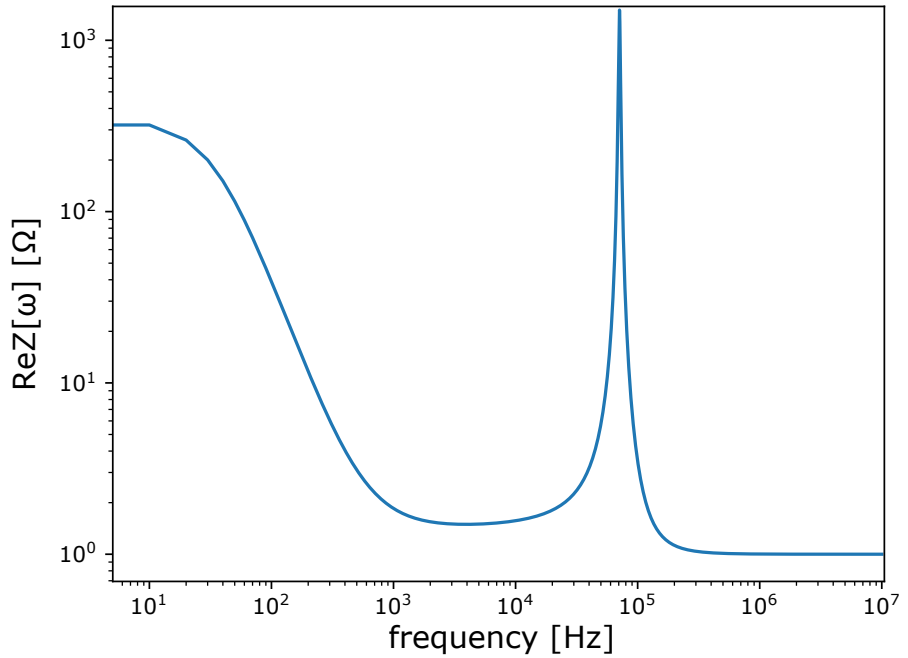

Figure 3.36: Model for the low-frequency impedance seen of the environment. R_3 gives the dc resistance of the bias line. It gets shunted above 70 Hz by the 6.6 μF capacitance put in parallel. At 71 kHz lies the self resonance of the bias-tee, with a 53 Ω impedance and a quality factor of the order of 30. At higher frequencies the cavity filter shunts the impedance to about 1 Ω.

The impact of this environment on the junction cannot be modelled as in [58], which assumes a constant impedance up to $k_B T/\hbar$. Given that these low-frequency modes are deeply in the classical regime, the semi-classical description from [85] applies.

Spectra are measured by digitizing signals at a rate f_S =1.25 GSamples/s and computing their Fourier transform on 1024 points. The effective acquisition time is thus $T_{meas} = 1024/f_S$= 819.2 ns. The dynamics of modes below $1/T_{meas} \sim 1$ MHz is frozen during the acquisition of one chunk of data, so that they do not contribute to the spreading of the emission line. However they add a random dc-offset on the junction between two measurements.

When averaging many measurements to obtain the spectra of figure 3.34, we are summing incoherently the impact of these voltage offsets. The situation is equivalent to having a perfectly defined voltage bias V, whose value would be changed at random **between** each measurement. Compare this with the effect of high-frequency noise, that was described in 2.3.2 as a random change of V **during** the acquisition.

We now use the fact that the full $P(E)$ function can be written as the convolution product of a "low-frequency" $P'(E)$ and a "high-frequency" $P''(E)$ [85]. We assume that the high frequency contribution is given by our initial estimate of ~ 0.5 nV, using (3.90). Then the spreading of $P(E)$ around $E = 0$ comes almost exclusively from the low-frequency noise. In particular the gaussian shape of $P(E)$ results from the gaussian distribution of (low-frequency) voltage on the junction. The FWHM of the peak in figure 3.35 can be converted in a standard deviation:

$$\frac{1}{2e} \times \frac{FWHM_{P(E)}}{2\sqrt{2\ln(2)}} = \sigma_V = 2.65 \text{ nv}. \tag{3.115}$$

We subtract from σ_V the high-frequency contribution:

$$\sigma_V^{\text{low freq}} = \sqrt{(\sigma_V)^2 - (\sigma_V^{\text{high freq}})^2} \simeq 2.6 \text{ nv}. \tag{3.116}$$

We attribute this noise mainly to the thermal occupation of the modes below $1/T_{meas}$, so that:

$$\sigma_V^{\text{low freq}} = \sqrt{\int_0^{1/T_{meas}} S_{VV}(\omega) d\omega}. \tag{3.117}$$

The dominant contribution to the low-frequency Johnson-Nyquist noise comes from the **bias-tee self resonance**:

$$\int_0^{1/T_{meas}} S_{VV}(\omega) d\omega = \int_0^{1/T_{meas}} 4k_B T Re[Z(\omega)] d\omega \simeq \frac{k_B T}{C_{BT}}. \tag{3.118}$$

We can fit this expression and obtain the temperature of the mode:

$$T = 20 \pm 1 \text{ mK}. \tag{3.119}$$

The uncertainty comes mostly from the value of C_{BT}. This temperature value agrees quite well with the bulk temperature of the fridge of 15 mK. It is lower than the electronic temperature $T_e = 55$ mK that was determined in the 2011 experiment, which we attribute to a better thermalization of the electrons in the coiled resistor R_3 and a better low-frequency filtering. In particular, using multiple filtering stages on the bias line, with high-order filters, is crucial to cut off all the voltage noise from room-temperature electronics.

Stokes/AntiStokes processes with a parasitic mode

Very faint emission lines parallel to the main $2eV = \hbar\omega$ are barely visible on figure 3.34. They can be discerned by re-plotting the emission map with a logarithmic colorscale (Fig.3.37):

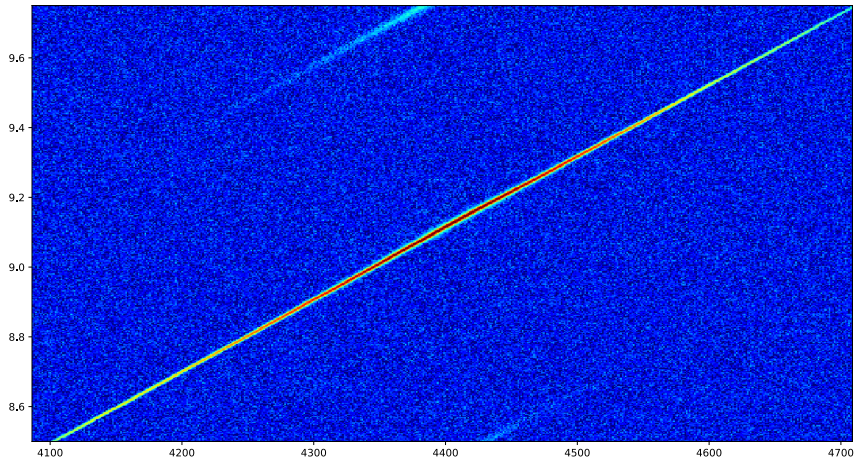

Figure 3.37: 2d-map of the logarithm of the emission spectra.

These emission lines seem to follow $Re[Z(\omega)]$, as does the main single-photon peak. The line occurring at higher biases is also brighter than the other one, with emission rates about twice higher.

We interpret these as the mark of 2-photon emission processes, where for bias voltage $V = \hbar(\omega \pm \omega_p)/2e$, one photon is emitted at ω and one photon is emitted/absorbed from a parasitic mode at frequency ω_p, in processes that we refer to as Stokes/Anti-Stokes.

From the shift of the lines we deduce $\omega_p = 2\pi \times 325$ MHz. We found out that this mode originates from a $\lambda/4$ resonance between the 50 Ω line going from the junction to the rf setup. At frequencies below 4 GHz the cavity filter presents an input impedance of about 1 Ω, so that this impedance mismatch generates the parasitic resonance. This hypothesis was tested by changing the length of wires going from the sample to the bias-tee, and checking that the frequency of the parasitic mode changed accordingly.

At such low frequency, this mode is populated by about 1 photon at cryogenic temperatures. This is why it can give energy to the tunneling Cooper pairs in the Anti-Stokes processes. A perfectly cold mode would allow only for emission processes.

We can measure this occupation number n_p by comparing the strength of the emission and absorption peaks. From $P(E)$ theory, we expect the Anti-Stokes process to scale like r_P, while the Stokes process scales like $r_p(n_p + 1)$ due to stimulated emission, with r_p the coupling factor of the mode to the junction.

As these emission lines are so weak, we integrate the spectra over a bandwidth of about 18 MHz. As we explored a limited voltage range during the experiment, we do not have access to both peak measured in the same frequency band. We thus agglomerate the data

taken at two different frequencies, and plot them on the same graph after renormalization by the area of the single-photon peak (Fig.3.38).

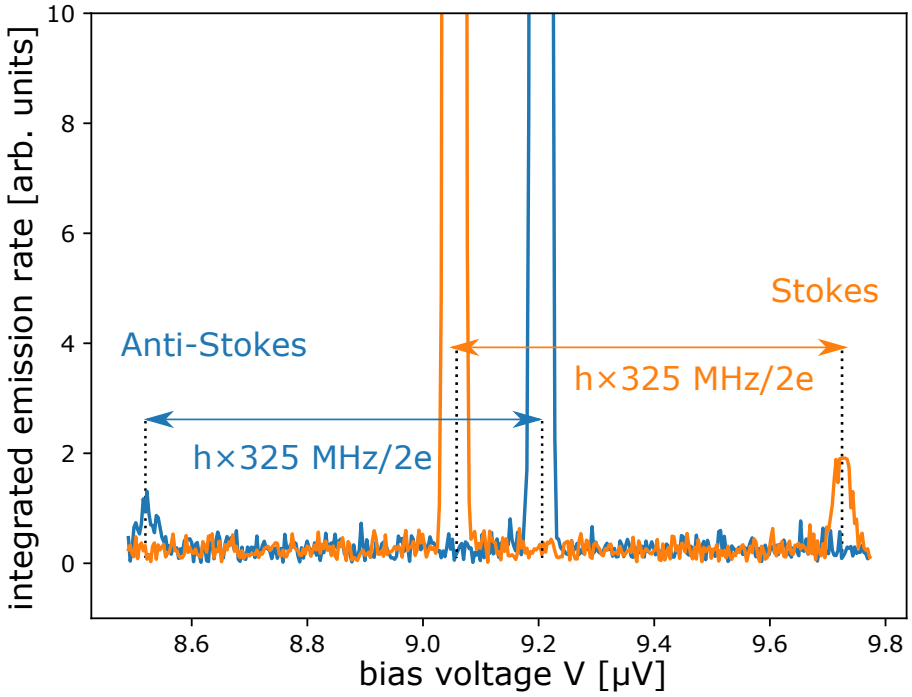

Figure 3.38: Rescaled Stokes and Anti-Stokes emission peaks.

The ratio of the area under these two peaks is 2.3 ± 0.2, which yields an occupation number of the mode:

$$n_p = \frac{1}{2.3 - 1} = 0.8 \pm 0.1, \tag{3.120}$$

corresponding to an equilibrium temperature of:

$$T_p = 19 \pm 2 \text{ mK}. \tag{3.121}$$

This temperature agrees quite well with the temperature of low-frequency modes (≤ 100 kHz) that we estimated above. Together with the upper bond for the 4.4 GHz resonator temperature we measured in 3.5.1, this is a strong indication that every part of the experimental setup is well thermalized, close to the fridge base temperature.

Finally we estimate the impedance of the parasitic mode by comparing the area under the Anti-Stokes peak to the main single-photon peak, which yields r_p. We find $Z_c \simeq 85 \pm 8\ \Omega$, in reasonable agreement with the $(4/\pi) \times 50\ \Omega \simeq 65\ \Omega$ we would expect for a $\lambda/4$ resonance.

Emission spectra as a function of bias voltage

We consider a cut in the 2d map at fixed bias V_b such that the emission peak falls at the resonator center frequency (Fig.3.39).

Here $S_P(\omega)$ is given by the product of $Re[Z(\omega)]$ and $P(2eV - \hbar\omega)$. $P(E)$ has a narrow width $\simeq 2e\times$ 6 nV$\simeq h\times$ 3 MHz, while the FWHM of the mode is expected to be ~ 100

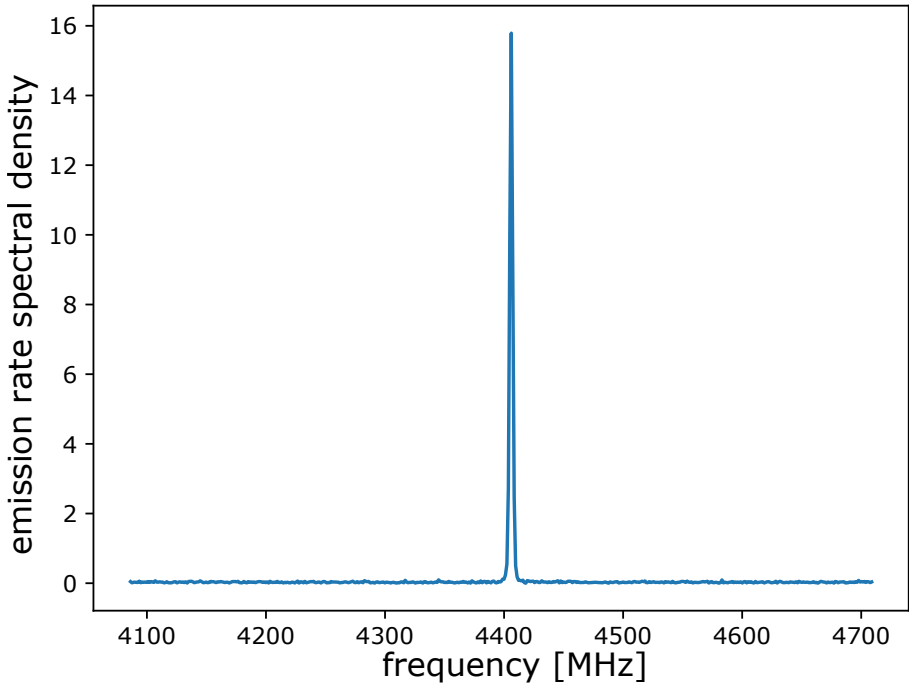

Figure 3.39: Cut through the 2D map at fixed bias voltage, along the frequency axis.

MHz. Thus $Re[Z(\omega)]$ is flat on the scale of variation of $P(2eV - \hbar\omega)$, and the spectrum also appears as a narrow gaussian peak.

The width of the gaussian curve can be translated into a standard deviation of the Josephson frequency $\sigma_f = 1.28$ MHz, which is equal to $2e/h$ times the voltage standard deviation σ_V determined earlier. We can interpret emission spectra as histograms of the Josephson frequency f_J, and hence of the voltage $V = hf_J/2e$ drop on the junction. We put this fact to use when investigating the origin of low-frequency voltage noise, see Appendix E.

We repeat the fit procedure while scanning the bias across the resonator. The fit parameters are the amplitude of the gaussian peak, its width $2\sqrt{2\ln(2)}\sigma_f$ and its position f_J, which corresponds to the Josephson frequency $2eV/h$. The results are presented in figure 3.40:

In **panel a)** are the values of the Josephson frequency fitted on each cut of the 2d-map, as a function of the bias on the sample: $f_J(V)$. A linear regression $f_J = A \times V + B$ yields the value of the dc-offset on the junction bias voltage B=-20 nV, as well a the precise value of the voltage division ratio $hf_J/2eV_b =$. Close to the center frequency of the resonator, the value of f_J departs slightly from the $2eV = \hbar\omega$ line, with a maximum deviation of about 2.5 MHz at the maximum of emission.

This slight deviation is easily understood: as soon as the junction emits photons at a rate Γ, it also allows for a dc-current $I_{dc} = 2e\Gamma$. This current is injected in the bias resistor R_3, where it creates an additional voltage drop: $\delta V = -2e\Gamma R_3$. This leads to a shift of the Josephson frequency which depends on known parameters:

$$\delta f_J = \frac{2e\delta V}{h} = \frac{-R_3}{R_Q} \times \Gamma \simeq -\frac{\Gamma}{18.7}. \tag{3.122}$$

This frequency shift provides an independent determination of the emission rate, as de-

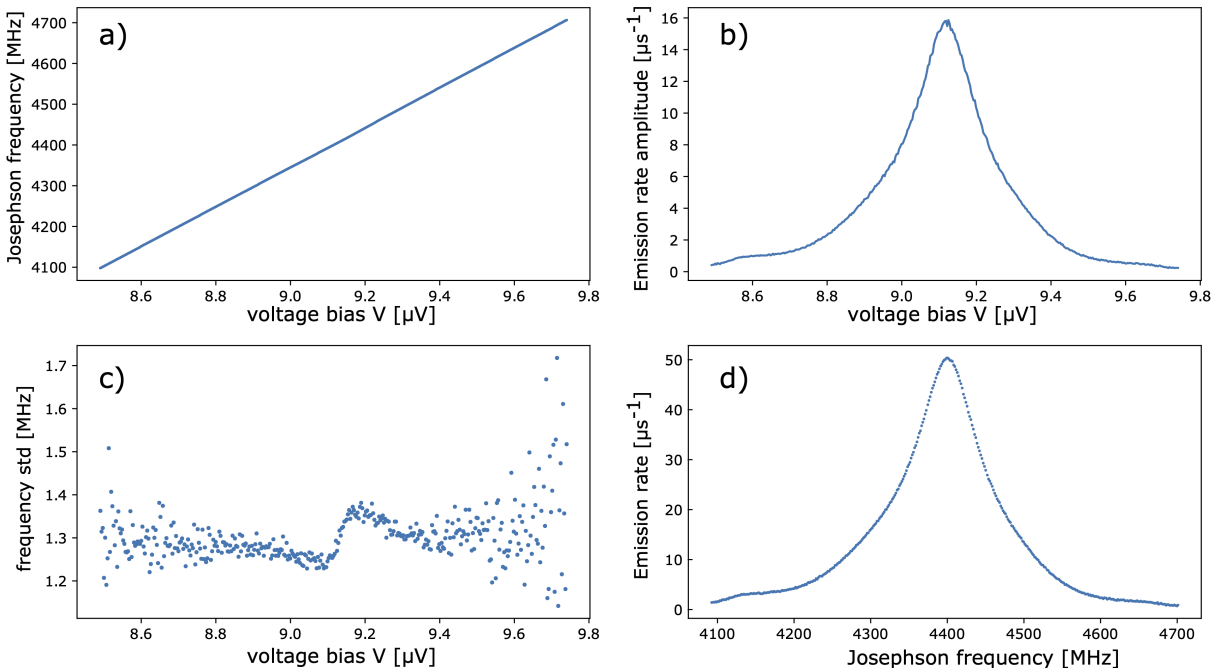

Figure 3.40: Results of the gaussian fits of spectra from figure 3.34. As a function of the bias voltage V, panel a), b) and c) show the fitted Josephson frequencies, peak amplitudes and standard deviations. Panel d) combines results of the fits to display the emission rate (proportional to $Re[Z(2eV/h)]$ as a function of the Josephson frequency.

tailed in 3.5.1.

Panel b) shows the fitted amplitudes of the gaussian peak as a function of V. As V_b is scanned across the resonator, the amplitude of the emitted power follows approximately the shape of the resonator's impedance $Re[Z(\omega)]$. The correspondence between the two is not exact, first because as we saw f_J strays away from $A \times V + B$ as soon as there is some photon emission, and second because the width of the emission peak changes during the scan.

Panel c) shows the variation of the standard deviation of the Josephson frequency, $\sigma_f(V)$. It varies non-monotonously: starting from a value around 1.3 MHz, it decreases steadily to about 1.25 MHz at the resonance frequency, increases to 1.4 MHz as ω_J crosses the resonator frequency ω_r, before decreasing again to about 1.3 MHz.

We attributed most of the peak's width to low-frequency noise of thermal origin. A *monotonous* change of σ_f with time could be interpreted as a drift of the setup temperature, e.g. when starting the experiment it typically takes about 1 week for all the circuit components to cool down to 15 mK. We also saw increases of σ_f in situations where the mixing chamber was heating up. However this particular emission map was taken 1 month after the beginning of the run, when all the experiment was already well thermalized. This behavior of $\sigma_f(V)$ was reproduced in other experimental runs, in different samples with resonators at various frequencies.

We understand this phenomenon as **active cooling/heating of the low-frequency modes** by the Josephson junction's own admittance. On general grounds, the small-signal admittance of a tunnel junction can be linked to its dc $\bar{I}(V)$ characteristic [84]:

$$Re[Y_J(\omega, V)] = e\frac{\bar{I}(V + \frac{\hbar\omega}{2e}) - \bar{I}(V - \frac{\hbar\omega}{2e})}{\hbar\omega}. \tag{3.123}$$

The junction is biased around $V = \hbar\omega_r/2e$ with ω_r much higher than the frequency of the thermal noise, so that we may use the usual form:

$$Re[Y_J(\omega \to 0, V)] \simeq \frac{d\bar{I}}{dV}(V). \tag{3.124}$$

As we scan the bias voltage across the resonator, the dc current is proportional to $Re[Z(\omega)]$. Its voltage derivative is thus positive below ω_r and negative above ω_r. The real part of the admittance of the junction follows the same trend (Fig.3.41).

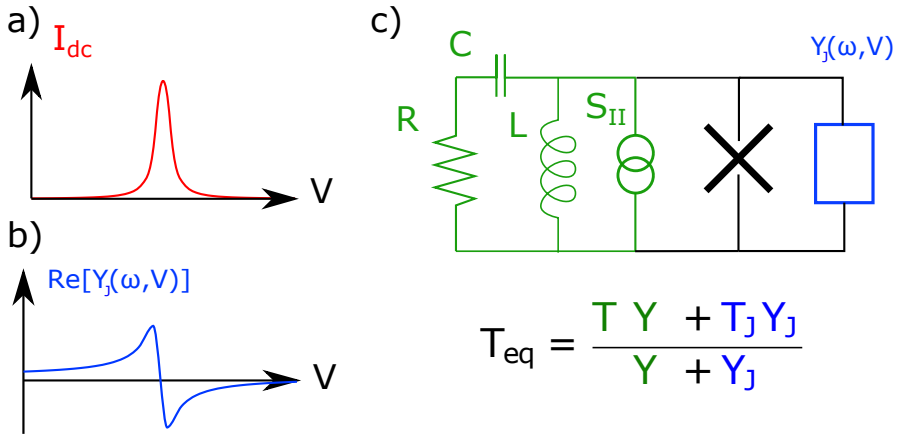

Figure 3.41: a) I(V) of the junction connected to a high frequency mode, showing a single-photon ICPT peak. b) The real part of the low-frequency admittance of the junction is proportional to the voltage derivative of the tunnel current. c) Model for the low frequency part of the circuit. The junction is connected in parallel with a RLC mode at finite temperature (in green), which presents the low-frequency current noise S_{II}. The finite admittance of the junction (in blue) shunts part of this thermal noise, effectively reducing the RLC temperature for $V < \hbar\omega_r/2e$ and heating it for $V > \hbar\omega_r/2e$.

This admittance is in parallel with the tunnel element and the environment of the junction $Re[Z(\omega)]$. We estimate its effective temperature T_J through the low-frequency shot-noise of Cooper pairs, which reads:

$$S_{II}(\omega \to 0) = 4e\bar{I} = 4k_B T_J Re[Y_J(\omega \to 0)] \tag{3.125}$$

From (3.124), we estimate the value of $Re[Y_J(\omega \to 0)]$, so that:

$$k_B T_J \simeq e\bar{I}\left(\frac{d\bar{I}}{dV}\right)^{-1} \tag{3.126}$$

On the single-photon resonance, $\bar{I}(V) \propto P(2eV) \propto Re[Z(2eV/\hbar)]$, we finally have:

$$k_B T_J \simeq \frac{P(E)}{2}\left(\frac{dP}{dE}\right)^{-1} \simeq \frac{\hbar}{2}Re[Z(\omega_J)]\left(\frac{dRe[Z]}{d\omega}\right)^{-1}. \tag{3.127}$$

From an analytical expression of $Re[Z(\omega)]$, we estimate the maximum effective temperature of the junction to be $T_J^{max} \simeq \hbar\kappa/4k_B \simeq 1.5$ mK. Thus it stays always much below the fridge temperature. This admittance acts as a cold current divider, and decrease the

thermal current noise from the environment when it is positive (below ω_r) (Fig.3.41). This is equivalent to reducing the temperature of the bias-tee, hence the decrease of σ_f.

When $f_J(V)$ matches the mode resonance frequency the admittance is zero, so that the junction is not shielded anymore from the environment and we have access to the intrinsic voltage noise of the experiment. Finally above ω_r the admittance of the junction is **negative**, such that it acts as an amplifier for low-frequency modes and **increases** the temperature of the low-frequency modes (Fig.3.41).

This mechanism was studied more in detail in a later series of experiments 4.42 which showed that the cooling power of the junction scales with its Josephson energy, and that it is maximal when the voltage derivative of the dc-current is the largest, in accordance with our model.

At a given voltage bias V, the total photon emission rate can be computed from the amplitude of the gaussian fit and its width $2\sqrt{2\ln(2)}\sigma_f$. It is plotted in **panel d)** in true units of photons per second, as a function of the Josephson frequency f_J. As $\sigma_f(V)$ is always much smaller than the scale of variation of $Re[Z(\omega)]$, this emission rate is directly proportional to $Re[Z(2eV)/\hbar)]$:

$$\Gamma(V) = \int \frac{S_P(\omega, V)}{\hbar\omega} d\omega \tag{3.128}$$

$$\propto \int Re[Z(\omega)]P(2eV - \hbar\omega)d\omega \tag{3.129}$$

$$\propto Re[Z(2eV/\hbar)] \times \int P(E)dE, \tag{3.130}$$

where the last integral is taken only over the zero-energy peak of $P(E)$. Thus this subplot is a proper image of the $Re[Z(\omega)]$ of the environment of the junction, in some undetermined units. It looks approximately Lorentzian, with odd shoulders under 4.15 GHz and above 4.6 GHz that we attribute to unreliable fits out of the 8.7-9.5 μV bias range.

$Re[Z(\omega)]$ itself can be fitted, yielding a quite good agreement to a Lorentzian shape with a center frequency of 4406 MHz and a FWHM of 120.3 MHz. The photon leak rate is thus $\kappa \simeq 756\ \mu s^{-1}$. The resonator lifetime $\kappa^{-1} \simeq 1.3$ ns is larger than the 1 ns estimated in [35]. We attribute this discrepancy to a parasitic resonance of the microwave setup that was present at that time, and that widened the resonator shape.

As detailed in 3.5.1, we can compare this curve to the PSDs measured in shot-noise regime to yield an absolute calibration of $Re[Z(\omega)]$ in Ohms, as displayed in figure 3.42.

This data shows that the sample indeed includes a mode with a very high characteristic impedance. We estimate its value by computing an extrapolation of $Re[Z(\omega)]$ out of the measurement band, assuming a Lorentzian decay $\propto (\omega - \omega_r)^{-1}$, and using the formula:

$$Z_c = \frac{2}{\pi}\int_0^\infty \frac{Re[Z(\omega)]}{\omega_r} d\omega \simeq 1970 \pm 60\ \Omega \tag{3.131}$$

$$\Rightarrow r \simeq 0.96 \pm 0.03. \tag{3.132}$$

The mode is thus in the strong-coupling regime with the junction. Here the uncertainty comes mostly from the extrapolation of $Re[Z(\omega)]$ out of the measurement band. Note

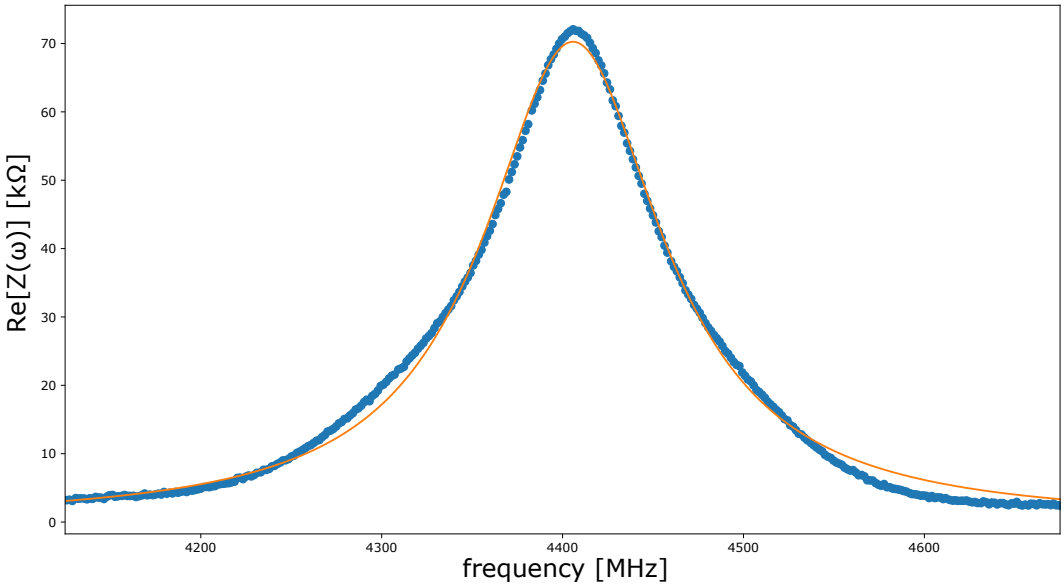

Figure 3.42: Real part of the impedance seen by the junction (blue points), plotted with Lorentzian best fit (orange curve).

that due to Kramers-Kronig relation, this is equivalent to using $Im[Z(\omega_r)]$. Such a high-impedance value should lead to strong antibunching of the emitted radiation, with $g^{(2)}(0) = (1 - r/2)^2 \simeq 0.27$.

Scanning E_J with the applied magnetic flux Φ

The emission map from figure 3.34 was taken at a very low Josephson energy $E_J(\Phi)$, to ensure that the sample stayed in the regime of validity of $P(E)$. At the highest emission rate $\Gamma = 51$ Mphotons/s the mode occupation number is $\bar{n} = 0.067$, so that $r\bar{n} \ll 1$ and the effect of strong-driving could be neglected. We now measure spectra at a fixed voltage bias $V = (h/2e)\times 4410$ MHz while sweeping the applied magnetic field Φ.

Figure 3.43 shows spectra taken while scanning one period of the $E_J(\Phi) = E_J^0|\cos(e\Phi/\hbar)|$ curve. When Φ equals half a flux quantum $(h/2e)$, the SQUID is at full frustration: $E_J \simeq 0$ and the emission line is practically invisible. It then lies at $f_J = 4410$ MHz.

When increasing E_J, the amplitude of the emission peak increases, following the $P(E)$ prediction of $\Gamma \propto E_J^2$. At the same time the position of the peak shifts towards lower frequencies, due to the finite dc-current injected by the junction into the bias resistor R_3. This frequency shifts is directly proportional to the current, and hence to the photon emission rate: $\delta f_J = -(R_3/R_Q) \times \Gamma \simeq -\Gamma/18.7$.

Near zero flux, the color plot shows that the amplitude of the peak stops increasing, and even decreases slightly while the total emission rate keeps increasing, as shown by the shift of the emission frequency.

Cuts through the map at different flux biases show that the shape of the peak indeed changes as E_J is varied (Fig.3.44). At low E_J, the peak has a narrow width $\sigma_f \simeq 1.3$ MHz. At higher emission rates a sizeable pedestal appears, with a width of the order of 100 MHz. The gaussian peak eventually saturates, while the pedestal keeps growing.

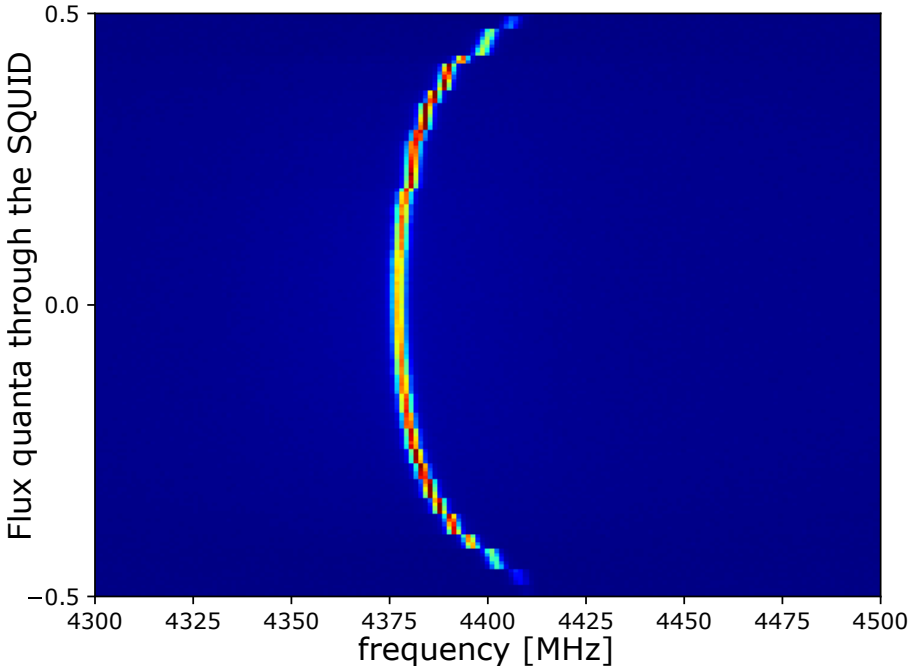

Figure 3.43: Spectra taken while sweeping the magnetic flux at fixed bias $V = (h/2e)\times 4410$ MHz.

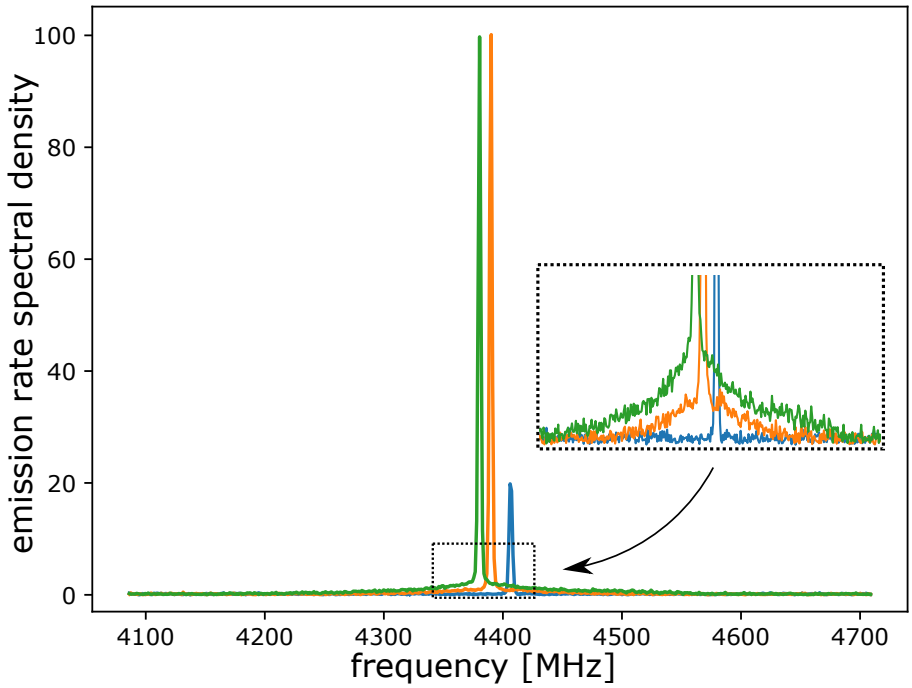

Figure 3.44: Spectra taken at three increasing values of E_J (blue, orange and green curves). The inset shows a zoom-in on the peak's pedestal, which keep increasing with E_J while the peak amplitude saturates.

By fitting the narrow gaussian peak, we can separate the contributions of the main peak and of the pedestal to the total emission rate. These contributions are plotted as a function of the applied flux bias Φ on figure 3.45. $E_J(\Phi)$ decreases from its maximum value as Φ is swept from 0 to half a flux quanta, then re-increases.

Jumps in the emission rates are visible as Φ is continuously swept. We attribute these to

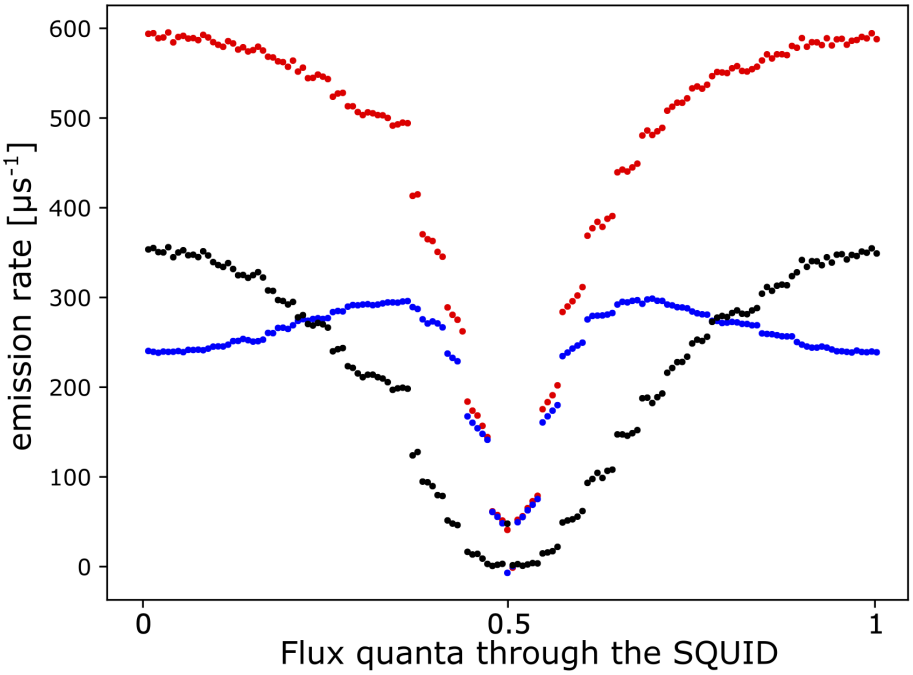

Figure 3.45: Contribution of the main gaussian peak (blue) and of its pedestal (black) to the total emission rate (red), as a function of the applied flux bias.

spurious vortex depinning in the ground plane of the sample. The Φ scale on the figure thus does not coincide exactly with the true flux through the SQUID. The area of the gaussian peak (in blue) departs from the $|\cos(e\Phi/\hbar)|^2$ prediction of $P(E)$. It saturates at about 300 Mphotons/s, and even decreases as $E_J(\Phi)$ is increased. We understand this behavior as the signature of the strong-driving regime, where the back-action of the field in the resonator reduces tunneling rates.

On the other hand the pedestal contribution (in black) increases more slowly at first, but does not saturate. It even surpasses the main peak contribution. Fitting these curves is quite hard due to the flux jumps, but its seems that the pedestal area scales as E_J^4.

From this behavior and from the width of the pedestal which coincide approximately with the FWHM of the resonator, we infer that this pedestal arises from **co-tunneling** processes, where two Cooper pairs tunnel at the same time and create photon pairs in the resonator. We expect this kind of phenomena to occur for high value of E_J. There are neglected in the $P(E)$ theory, which assumes that E_J is low enough so that the tunnel Hamiltonian can be taken up to second order only. The emission of a single photon by co-tunneling Cooper pairs was recently studied in [86].

Higher order processes generate new processes including the co-tunneling of Cooper pairs. These are then expected to scale as E_J^4. Note that in the semi-classical theory of the ac-Josephson effect 2.2, similar contribution to the photon emission and tunneling rates can be derived by taking to next order the phase drop across the junction.

As we did not measure $E_J(\Phi)$ during the flux sweep, we test our hypothesis by plotting the pedestal contribution as a function of the main peak area (Fig.3.46):

As the main peak eventually deviates from the E_J^2 law, the comparison makes sense only for low emission rates. We can still fit a quadratic function for $\Gamma \leq 200$ Mphotons/s, with

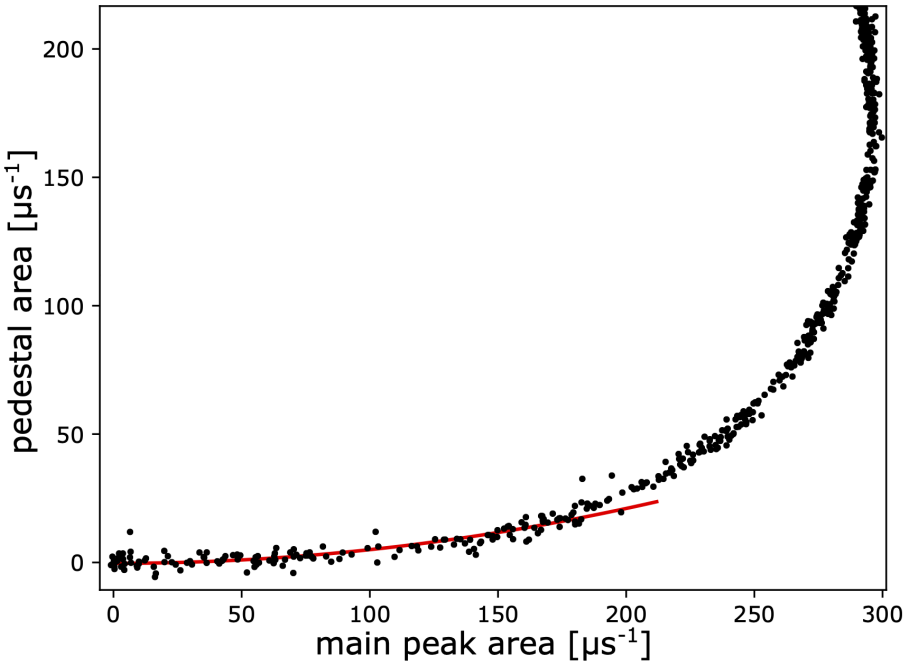

Figure 3.46: Contribution of the pedestal to the emission rate, as a function of the main peak area (in black), with quadratic fit (red), fitted for $\Gamma < 200$ MHz. As for low emission rates the main peak scales as E_J^2, this indicates that the pedestal area scales as E_J^4.

quite good agreement. We consider this an indication of the validity of our co-tunneling hypothesis.

Finally, we can plot the emission rate as a function of the frequency shift (Fig.3.47). We show again the separate contributions of the main peak (in blue) and of the pedestal (in black) to the total rate (in red). Again we see the saturation of the gaussian peak area, while the pedestal contribution is always growing. The total emission rate is a linear function of the frequency shift for Γ from 0 to 600 Mphotons/s, which validates our model of a voltage drop on the bias resistor. We can fit the slope of this curve to extract R_3=350 Ω, which agrees well with the value determined from the slope of the $f_J(V_b)$ curve.

Alternatively, we can consider that we are sure of the value of R_3, and use the frequency shift to determine the absolute emission rate. This amounts to a different calibration of the HEMT noise temperature. We thus find:

$$T_N = 14.0 \text{ K}, \tag{3.133}$$

which differs from the value determined earlier by about 1.5%. Note that in our reasoning, we assumed that the additional voltage drop on the bias resistor came only from the current associated with the emission of photons inside the resonator. In other words, if there were processes where light can be emitted outside of our detection window, we would see a larger frequency shift. In this experiment the 4.4 GHz resonator is coupled so strongly to the junction that all others processes are negligible, hence the good agreement.

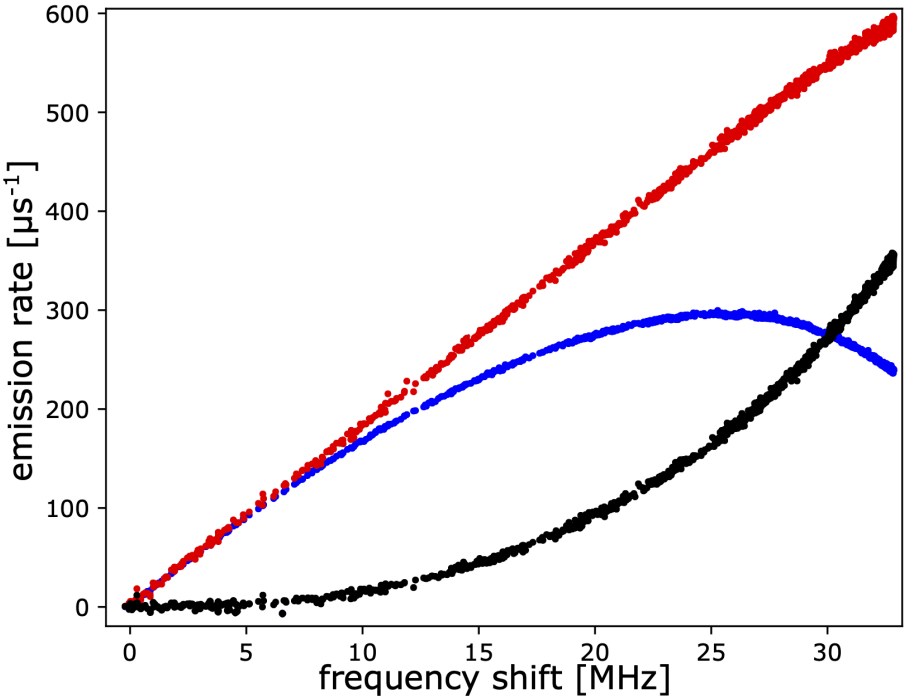

Figure 3.47: Emission rate as a function of the frequency shift.

Determination of the renormalized Josephson energy

Finally, we perform a E_J scan while the junction is biased to a higher voltage value, such that the Josephson frequency lies in the upper tail of the resonator, at $\omega_e = 2\pi \times 5535$ MHz. Then the impedance of the environment is much lower, and we expect to avoid the saturation due to strong-driving effects.

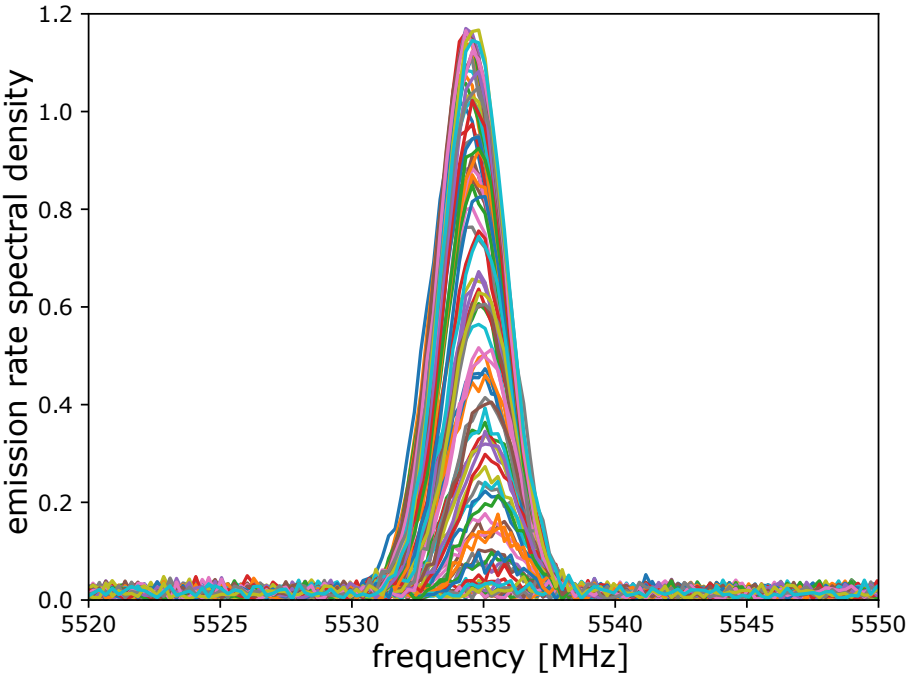

Figure 3.48: Emission spectra taken outside of the resonator while sweeping E_J.

These spectra display a very small frequency shift even at maximum E_J, which indicates that the photon emission rate stays small (Fig.3.48). The E_J^4 pedestal is not detectable, as it is dwarfed by the main gaussian peak which does not saturate. We can then fit each spectra with a gaussian function, and plot the emission rate as a function of the applied flux bias (Fig3.49).

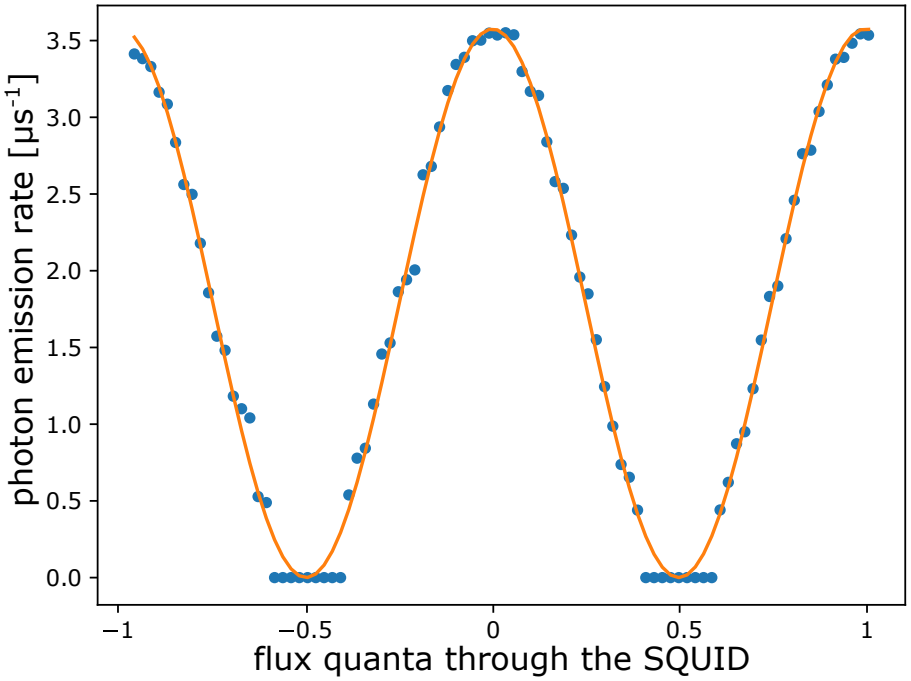

Figure 3.49: Emission rate as a function of the applied flux bias.

A simple sine function fits the data with a good agreement, despite the presence of flux jumps and the failure of the gaussian fit procedure for low E_J. We use this as a confirmation that the emission rate does not saturate, and that it follows E_J^2 even at $\Phi = 0$. The maximum emission rate is then:

$$\Gamma(\Phi = 0) = 3.55 \pm 0.05 \text{ Mphotons/s}. \tag{3.134}$$

This emission rate can be related to the value of E_J^* at zero frustration of the SQUID:

$$\Gamma(E_J) = \frac{2\pi^2 (E_J^*)^2}{\hbar\omega_e} \frac{Re[Z(\omega_e)]}{R_Q}. \tag{3.135}$$

Next, we scan the bias voltage above the gap voltage and detect the power emitted at ω_e (Fig.3.50):

As the impedance is much smaller than R_N, we directly have (see appendixB):

$$\frac{dS_P(\omega_e)}{dV} = 2e \frac{Re[Z(\omega_e)]}{R_N}. \tag{3.136}$$

Eliminating the unknown $Re[Z(\omega_e)]$ between (3.135) and (3.136) yields the renormalized Josephson energy:

$$E_J^* = 1.84 \pm 0.03 \ \mu\text{eV}, \tag{3.137}$$

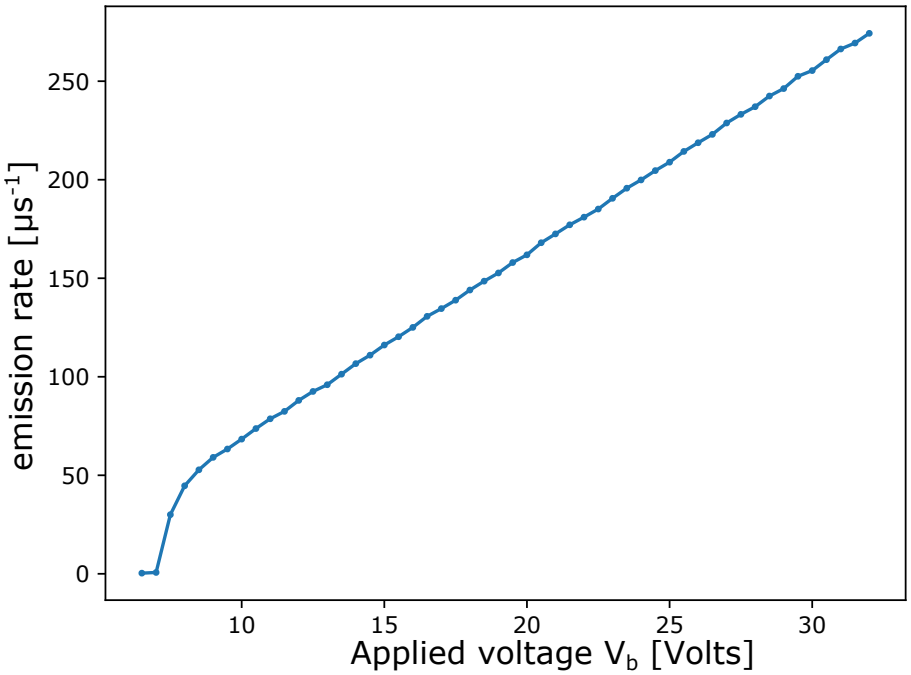

Figure 3.50: Emission rate as a function of the applied voltage V_b.

in very good agreement with the Ambegaokar-Baratoff value $E_J^{AB} = 3.1\ \mu$eV renormalized by the phase fluctuations coming from the 4.4 GHz resonator and the 325 MHz parasitic resonance:

$$\Delta\hat{\phi}^2 = \sum_{\text{mode } i} r_i \times (2\bar{n}_i + 1) \simeq 0.96 + 0.04 \times (2 * 0.8 + 1) \simeq 1.07 \tag{3.138}$$

$$\Rightarrow E_J^* = E_J^{AB} \times e^{-\Delta\hat{\phi}^2/2} = 1.82 \pm 0.04\ \mu\text{eV}. \tag{3.139}$$

3.5.2 Correlation function measurements

We now turn to the investigation of time-domain properties of the photons emitted by the junction, revealed by the measurement of correlation functions. The first order coherence function $g^{(1)}(\tau)$ (3.38) is linked to the phase coherence of the light, a wave-like property, while the second order coherence function $g^{(2)}(\tau)$ (3.23) reveals the statistics of photons themselves. We first use our linear detection procedure on the shot-noise emitted by the sample when biased far above the gap voltage and recover the usual properties of thermal light. Our aim is to demonstrate that below the gap, on the ICPT single-photon resonance, the light displays antibunching statistics at low occupation number. This antibunching gets gradually washed away as we increase the emission rate.

First test of our procedure: the correlation functions of shot-noise

Biased far above the gap voltage, the Josephson junction behaves as a source of current noise $S_{II}(\omega) = 2(e\bar{I} - R_N^{-1}\hbar\omega)$. This shot-noise results from a large number of independent tunneling events, where each quasi-particle emits a photon at a random frequency between 0 and $eV/\hbar$. Following the central limit theorem, the total finite-frequency current is

a gaussian random variable, with the same statistical properties as equilibrium thermal noise. Slight deviations from pure gaussian fluctuations arise from the discrete, Poissonian statistics of independent quasiparticles tunneling, but are completely negligible in our experiment.

This almost white noise filtered by the on-chip resonator, is collected in a frequency window given by approximately the FWHM of the resonator. Since filtering does not change the properties of a gaussian noise, we expect to measure thermal-like coherence functions, characterized by the relation [64]:

$$g^{(2)}(\tau) = 1 + |g^{(1)}(\tau)|^2 \tag{3.140}$$

$$\Rightarrow g^{(2)}(0) = 2. \tag{3.141}$$

The first order coherence function (3.38) is simply the Fourier transform of the spectrum, normalized to 1. When computing correlation functions we filter digitally the signals (Fig.3.27), so that we miss some part of the spectra. Moreover, we do not compensate for the analog filtering that occurs during amplification, i.e the ripples that can be seen in figure (3.28). We thus only have access to distorted versions of the correlation functions.

We test all our correlation procedure by applying a high voltage $V_b = 32$ V, so that the bias voltage $V \simeq 2$ mV$\simeq 10\Delta/e$. Then the resonator is populated by about $\bar{n} \simeq 14$ photons. This makes the measurements and their interpretation easier, as we do not expect to see Coulomb Blockade effects from the high-impedance mode, and the shot-noise power is comparable to the HEMTs noise power, making the parasitic correlations negligible.

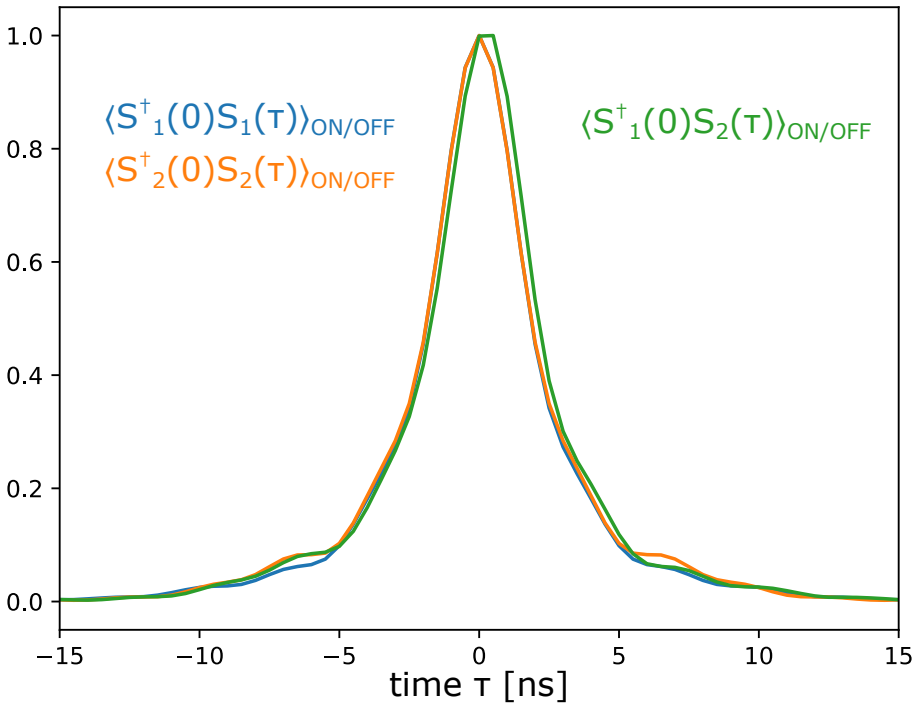

Figure 3.51: Absolute value of $g^{(1)}(\tau)$ computed from the spectra of figure 3.30.

We plot in figure 3.51 the three versions of $|g^{(1)}(\tau)|$ computed from the three spectra of

figure 3.30, using the same color code. Lorentzian emission spectra would yield exponentially decaying $|g^{(1)}(\tau)|$ function. In our experiment the $Re[Z(\omega)]$ of the resonator is not exactly Lorentzian, and neither are the shot-noise spectra. Thus the $|g^{(1)}(\tau)|$ functions are cusped at $\tau = 0$. Still we can estimate a decay time constant $\simeq 2$ ns, as expected from the 158.3 MHz width of the spectra. This is not the same as the FWHM of the resonator, because of the frequency-dependent microwave coupling factor between the junction and the resonator.

There are minor differences between $\langle S_1^\dagger(0)S_1(\tau)\rangle$ and $\langle S_2^\dagger(0)S_2(\tau)\rangle$, as the corresponding spectra where not exactly equal. They are both peaked at $\tau = 0$ and symmetric with respect to $\tau \to -\tau$, as expected for the Fourier transform of real spectra.

On the other hand the correlation function yielded by the cross-spectrum is offset from $\tau = 0$ by about 0.25 ns, and is non-symmetrical. This is because the $\langle S_1^\dagger(0)S_2(\tau)\rangle$ correlator is sensitive to time-delays between the two channels, which where not fully compensated in this particular measurement.

Just as we have three ways of evaluating emission spectra $S_P(\omega) = \langle \hat{a}^\dagger(\omega)\hat{a}(\omega)\rangle$, there are three different ways of computing the instantaneous power radiated by the sample $P_a(t) = \langle \hat{a}^\dagger(t)\hat{a}(t)\rangle$. We can take the modulus squared of a complex envelope:

$$P_x(t) = |S_x(t)|^2 \propto P_a(t) + P_{N_x}(t) \tag{3.142}$$

to obtain the total power carried over channel (x), which then includes the noise power added by the HEMT. We can also compute the *cross-signal power*:

$$C(t) = S_1^\dagger(t)S_2(t) \propto P_a(t) + P_{N_c}(t), \tag{3.143}$$

where the background cross-noise power $P_{N_c}(t)$ is a random complex number, with an average value 2000 times smaller than $\bar{P}_{N_x}$ (Fig.3.29).

From these instantaneous powers, we compute two different versions of the $g^{(2)}(\tau)$ function (Fig.3.52).

The *power-power* correlator $\langle P_1(t)P_2(t+\tau)\rangle$ yields, after subtraction of unwanted contributions, a real function (black curve). This correlator is sensitive to delays between the two measurement lines, so that it is centered on $\tau = 0.25$ ns, like $\langle S_1^\dagger(0)S_2(\tau)\rangle$ (see figure 3.51). It goes up to $g_{pw}^{(2)}(0) = 2.001$, with a statistical error of $\sigma = 8 \times 10^{-4}$. We compute this uncertainty by dividing the original raw data in many chunks, computing coherence functions on each chunk, then averaging them and estimating the statistical dispersions on each time value of $g^{(2)}(\tau)$. In particular, we found that **the uncertainty is not the same for all τ values**: it is twice higher at $\tau = 0$ that at $\tau \geq \kappa^{-1}$.

This comes from the gaussian statistics of the HEMT noise, which dominates the instantaneous measurement. Basically, the experimental variance of the $g^{(2)}(\tau)$ function we compute is set by the $g^{(4)}(\tau)$ function of the HEMT noise, which is four times higher at $\tau = 0$ than at $\tau \to \infty$. This results in twice larger error bars at $\tau = 0$ on all the measurements presented in this work (in contrast with figure 3.19 from 2016, where this effect was not taken into account).

The second version of $g^{(2)}(\tau)$ (red curve), computed from the cross-signal power $\langle C(0)C(\tau)\rangle$, is symmetric with respect to $\tau = 0$. Note that while $\langle C(0)C(\tau)\rangle$ is a complex function, with a certain phase, the normalized version used in (3.88) is real (with a remaining

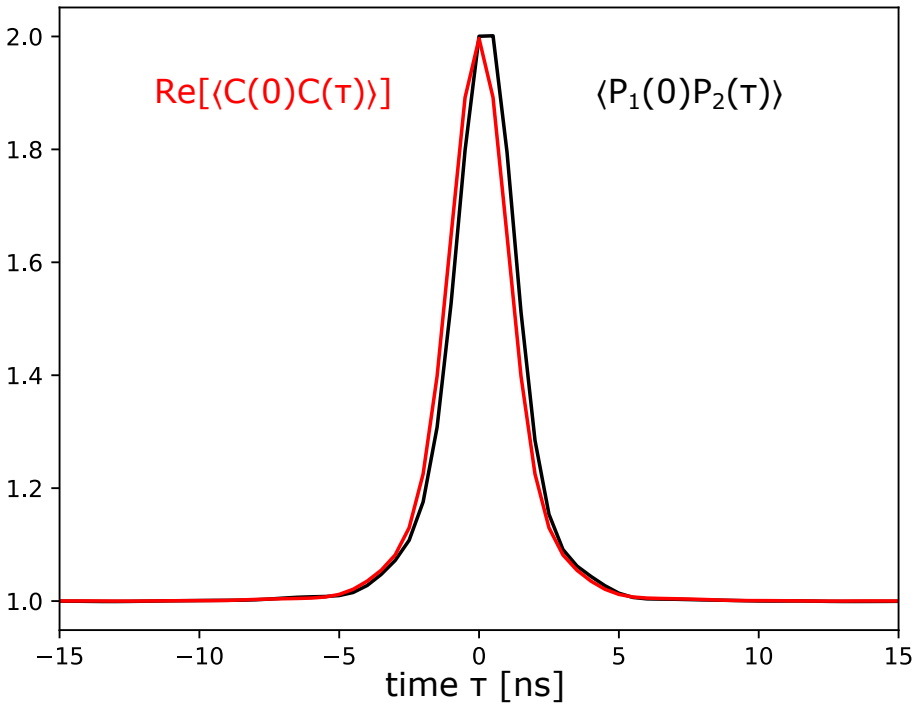

Figure 3.52: Second order coherence functions computed either from (3.87) (black curve) or (3.88) (red curve).

imaginary part that comes only from measurement noise). Thus we can take only the real part of (3.88), and end up with error bars which are $\sqrt{2}$ smaller than for the (3.87) expression.

However, the $\langle C(0)C(\tau)\rangle$ correlator is decreased by any spurious time delay between the two channels, as $|\langle S_1^\dagger(t)S_2(t+\tau)\rangle| \leq |\langle S_1^\dagger S_2\rangle|$. In the end, we measure $g_{cs}^{(2)}(0) = 1.995 \pm 0.0006$, i.e we have less statistical error than using $g_{pp}^{(2)}(\tau)$, but uncompensated delays between the two lines distort the correlation function so that $g_{cs}^{(2)}(0) \neq 2$.

In other words, we have two different ways of evaluating $g^{(2)}(\tau)$. One is in the spirit of the original HBT experiment, as we correlate true power fluctuations measured over two channels. The second scheme involves the complex cross-signal, and can only be implemented by detection of the signal quadratures. It yields a better statistical uncertainty, as the parasitic terms to be subtracted are smaller. It also provides intrinsic noise rejection, as the uncorrelated amplifiers' noise fluctuates randomly in the complex plane, while the signal correlators are purely real. These advantages are counterbalanced by an undesirable sensitivity to time delays between the two channels, so that the procedure can miss some correlations and yield the wrong value of correlators. This effect is however quite small, as a delay of 0.25 ns on signals with a correlation time of 2 ns yields a 0.25% underestimation of $g^{(2)}(0)$.

We also checked the equality of $|g^{(1)}(\tau)|^2 + 1$ and $g^{(2)}(\tau)$ for shot-noise radiation, confirming the gaussian statistics of the signals. As the correlators are either sensitive or insensitive to time delays between the lines, we find that:

$$g_{cs}^{(2)}(\tau) = 1 + g_{pw}^{(1)}(\tau) \tag{3.144}$$

$$g_{pw}^{(2)}(\tau) = 1 + g_{cs}^{(1)}(\tau), \tag{3.145}$$

up to the experimental uncertainty on the $g^{(2)}(\tau)$ correlators.

Antibunching on the single-photon resonance at low E_J

We set the bias voltage so that $\omega_J = 2\pi \times 4407$ MHz and lower E_J until there are $\bar{n} \leq 0.1$ photons in average in the resonator. At this lowest E_J value, we measured spectra and correlations functions in two successive runs of 60 and 120 hours respectively (about 7.5 days of continuous measurement).

During the first part of the run, we alternated between ON and OFF measurement every 2.5 minutes. We then decided to reduce the time devoted to OFF correlators. Because they describe the stationary noise from the amplifiers, we can average them over all the duration of the experiment, where we scanned different values of E_J. This is a way to improve the duty cycle of the measurement. In the last 5 days, we thus measured 2.5 minutes in the ON state for each 30 seconds spent in the OFF state.

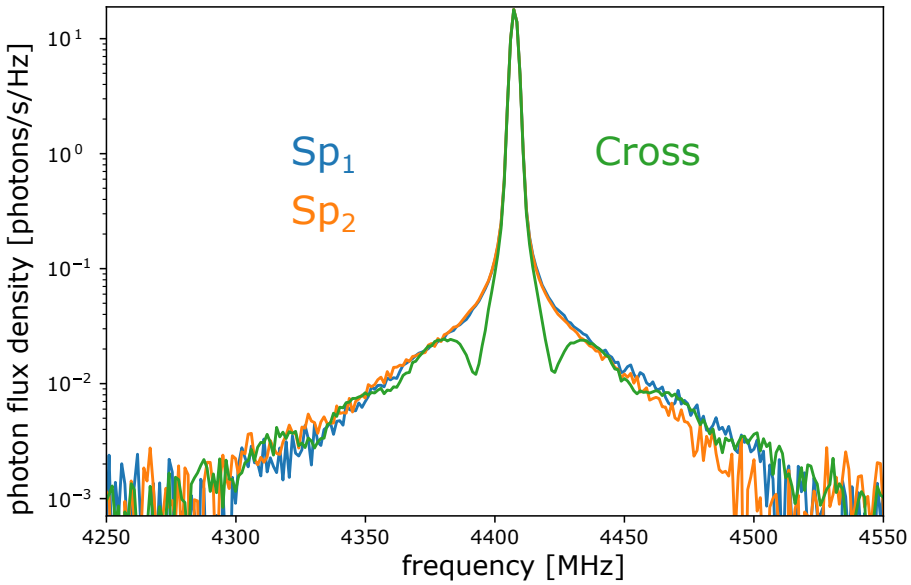

Figure 3.53: Emission spectra at low E_J on the single-photon resonance.

Figure 3.53 shows the spectra measured using either the true PSDs from channel (1) and (2), or the cross-spectrum. Again it shows a narrow gaussian peak, with a much wider and weaker pedestal. We attribute this pedestal to co-tunneling events, whose amplitude scales as E_J^4. The cross-spectrum shows weird shoulders approximately 35 MHz below and above the gaussian peak, which do not appear in Sp_1 and Sp_2. We attribute them to parasitic microwave reflexions in the setup between the hybrid coupler and the HEMTs.

During this week-long measurement, we acquire close to 2800 spectra at the same value of E_J. We fit each of them with a gaussian shape to study the stability of the emitted radiation. We plot the results in figure 3.54 as a function of time (only the data points taken during the last 5 days are shown).

The Josephson frequency drifts away from 4407 MHz, due to random changes between the sample electrical ground and the voltage source ground. It changes by at most 600 kHz over the course of one day, which amounts to a shift of about 1.2 nV. The impact on the

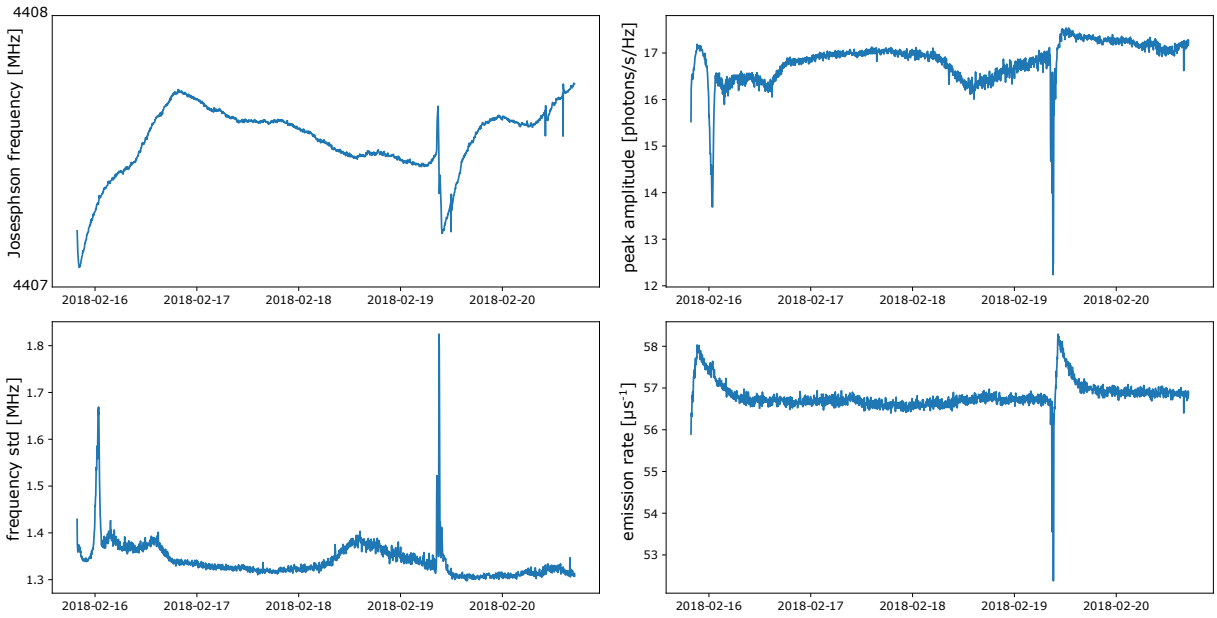

Figure 3.54: Results of the fits of the emission peak, as a function of time during the second run.

statistics of the radiation is completely negligible, as 600 kHz≪120 MHz, the resonator FWHM. The amplitude of the peak and its width σ_J are approximately constant, except for two sharp spikes. These events coincide with refillings of the liquid He cold bath of the fridge. During He transfers we perturb the experiment, as we bump into the fridge with the transfer line. This generates vibrations, which wiggle the flux bias coil placed below the sample and change E_J. The sample goes slowly back to its initial state after these perturbations, which may indicate that we also heat up the cold stage during the transfer. In definitive, the emission rate is remarkably steady, and we conclude that we can safely average altogether all the correlators measured over the course of the run. We also extract the average population of the resonator $\bar{n} = 0.075 \ll 1$, so that the radiation should display antibunching, as predicted in 3.1.

From the spectra of figure 3.53, we can compute the $g^{(1)}(\tau)$ function of the signals. Here the delays between the two lines were finely compensated, so that we can use either the Sp_x or the cross-spectrum without any difference. We plot $g^{(1)}(\tau)$ on figure 3.55, along with the OFF contribution $\langle S_1^\dagger(0)S_2(\tau)\rangle/\bar{n}$, which is needed for the computation of $g^{(2)}(\tau)$.

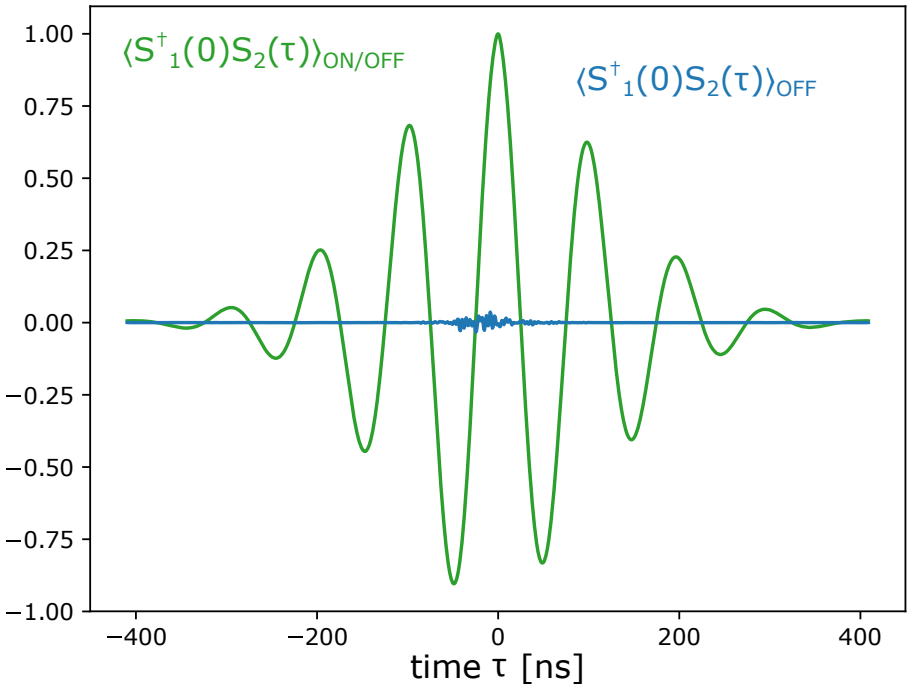

Figure 3.55: Real part of the normalized first order correlators. The ON/OFF correlator yields the $g^{(1)}(\tau)$ function of the signals (in green). The OFF correlator shows the parasitic coupling between the two channels (in blue).

The $g^{(1)}(\tau)$ functions is oscillating at the Josephson frequency, brought back to 300 MHz by the heterodyning procedure. Its envelope is a gaussian function with a width given by σ_t =120 ns. This indicates that the phase coherence time of the light is relatively long, about 100 times larger than the resonator lifetime κ^{-1}= 1.33 ns. In classical physics, this would be the characteristics of a coherent light source, and we would expect the electric field to behaves as a sine function.

However investigation of the statistics of the photons, through the measurement of the $g^{(2)}(\tau)$ function, reveals the granular nature of single photons. Figure 3.56 shows the power-power correlators in the ON and OFF states, normalized by $\bar{n}^2$.

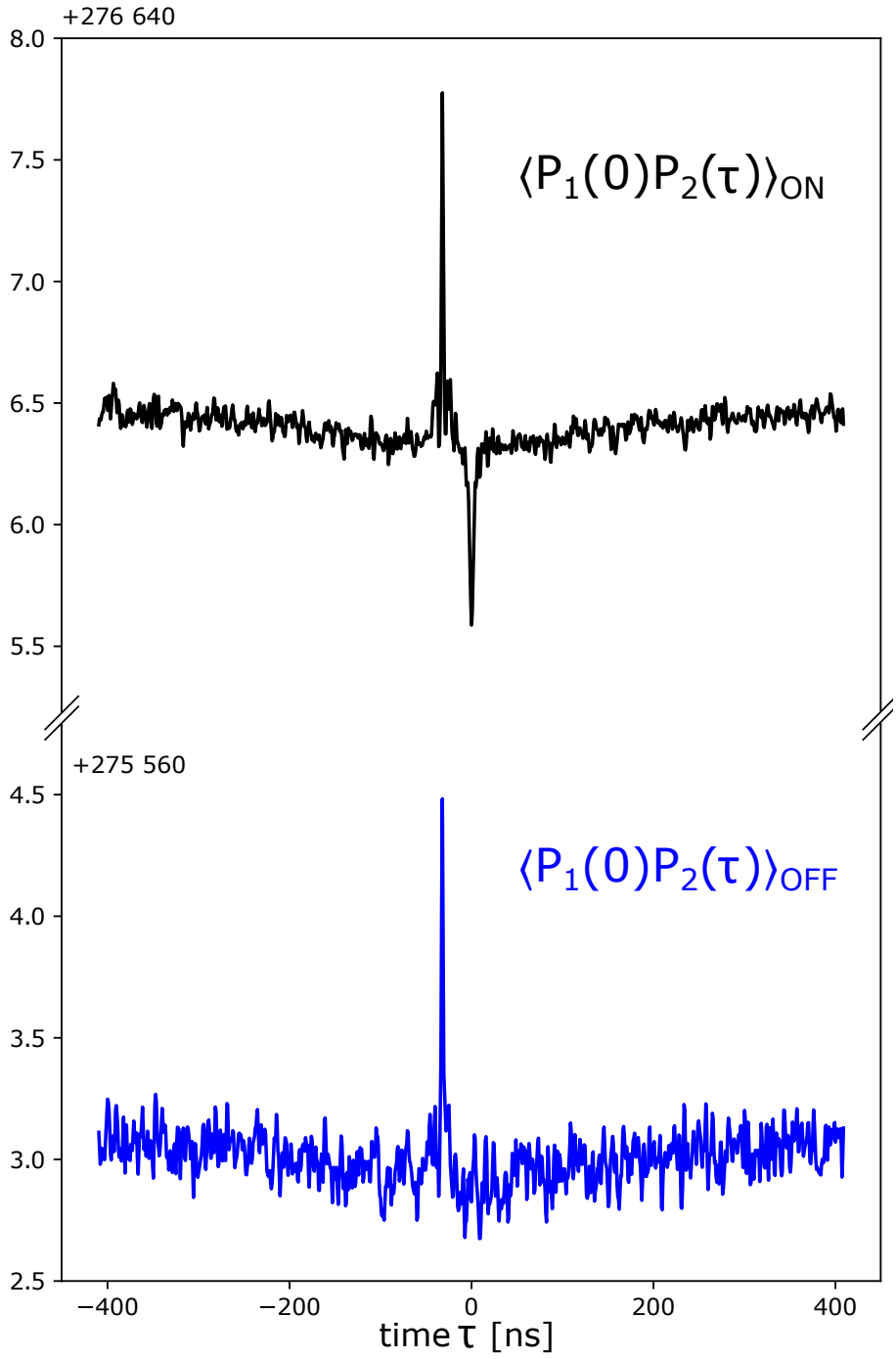

Figure 3.56: Normalized power-power correlators in the ON (black curve) and OFF (blue curve) states.

The offset value of the normalized OFF correlator is a measurement of $P_{N_1}P_{N_2}$ in units of the mode occupation number $\bar{n}^2$. Its square root yields the value of the SNR: $1/\sqrt{275560} \simeq 1/525$ at this low photon number. The positive correlation peak at $\tau = -32$ ns reveals the parasitic coupling between the two lines that occurs in the room-temperature setup, after the $\simeq 7$ m long delay line (see Fig.3.26).
In the ON correlator, the antibunching of the photons emitted by the junction manifests as a dip near $\tau = 0$ on top of the background correlations. The offset value is also higher by $P_{N_1} + P_{N_2}$. The fluctuations of the correlators far away from $\tau = 0$ indicate the statistical error on the measurement. It is $\sqrt{5}$ larger in the OFF state due a five time shorter

averaging time. Recall that we finalley averaged together the OFF data points taken over the course of the experiment, to yield a much less noisier OFF value.

We combine all the measured correlators following (3.81) to obtain $g^{(2)}_{pp}(\tau)$ (Fig.3.57):

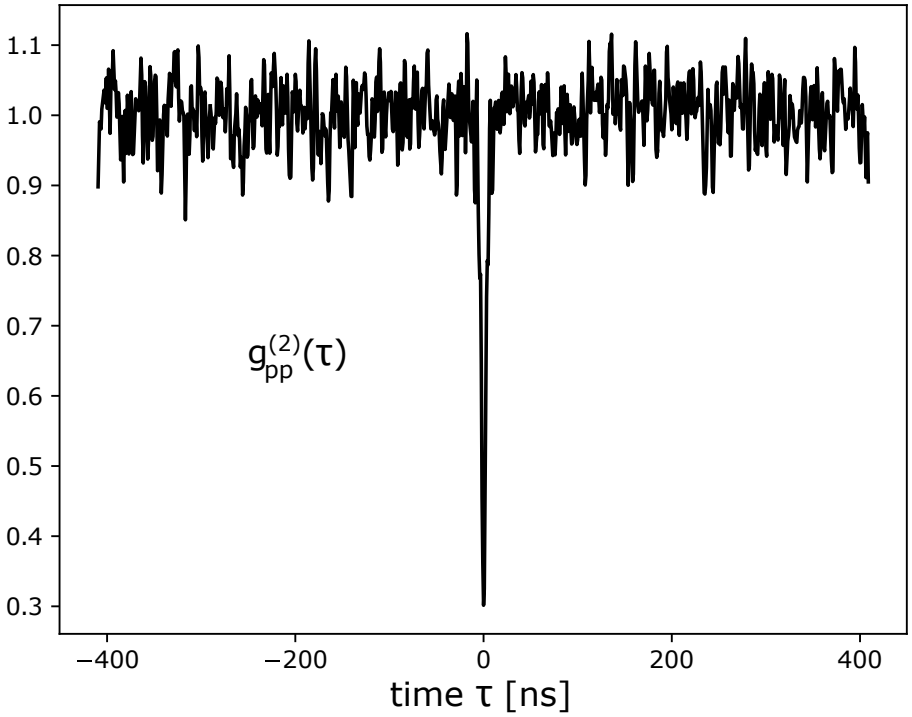

Figure 3.57: Second order coherence function $g^{(2)}_{pp}(\tau)$, measured through power-power correlations.

This correlation function is an estimation of the $g^{(2)}(\tau)$ function of the antibunched photons, deduced from power fluctuations measurement. It is nominally equal to the correlator measured in 2016 (Fig.3.19) through true power detection, albeit with the parasitic oscillations suppressed.

To increase our accuracy on the determination of $g^{(2)}(\tau)$, we use a complementary correlator, based on the detection of the cross-signal power $C(t) = S_1^\dagger(t)S_2(t)$. We plot in figure 3.58 the real part of the cross-signal correlators:

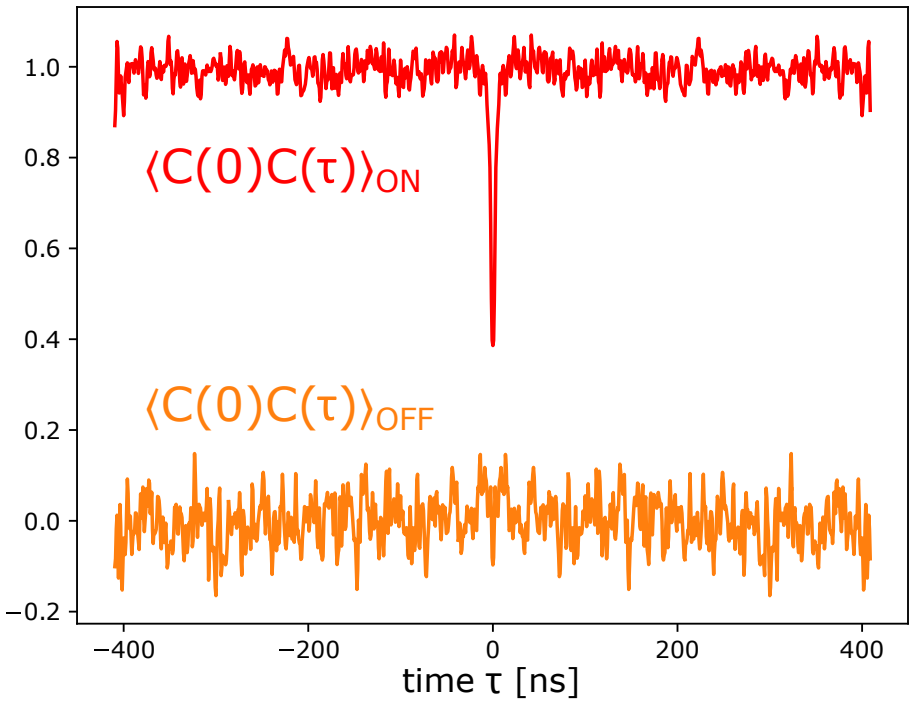

Figure 3.58: Real part of the normalized cross-signal correlators in the ON (red curve) and OFF (orange curve) states.

The offset value of the OFF correlator is here practically zero for all times τ. This comes from the 32 ns delay between the two channels introduced at room-temperature, which suppresses all parasitic correlations between the background noises of the two lines. The ON correlator displays anticorrelations near $\tau = 0$, proof of the antibunching. Again we combine these two correlators with the first order ones (Fig.3.55) to yield $g_{cs}^{(2)}(\tau)$ (Fig.3.59):

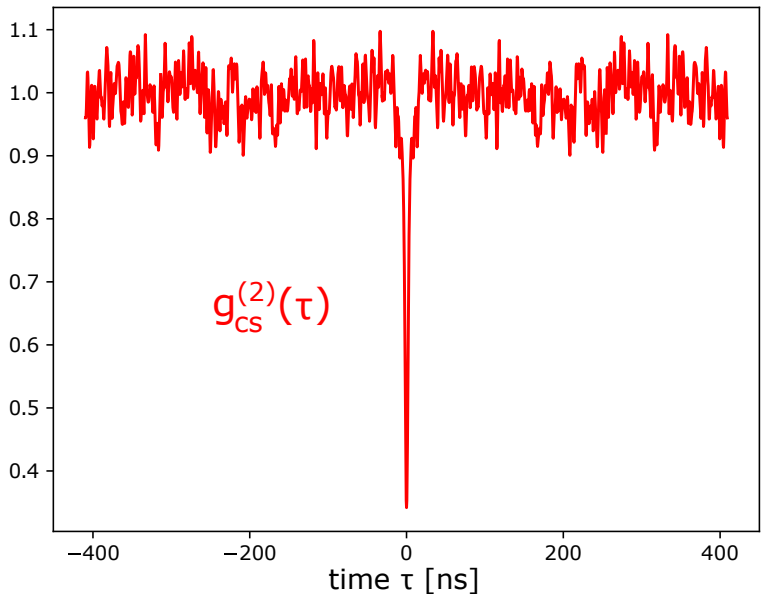

Figure 3.59: Second order coherence function $g_{cs}^{(2)}(\tau)$, measured through cross-signal correlations.

The statistical error on $g_{cs}^{(2)}(\tau)$ is $\sqrt{2}$ smaller than on $g_{pp}^{(2)}(\tau)$, as the noise on $C(t)$ is spread

uniformly on the complex plane, while the final correlator is real. We increase again our accuracy by averaging together these two versions of $g^{(2)}(\tau)$ (Fig.3.60):

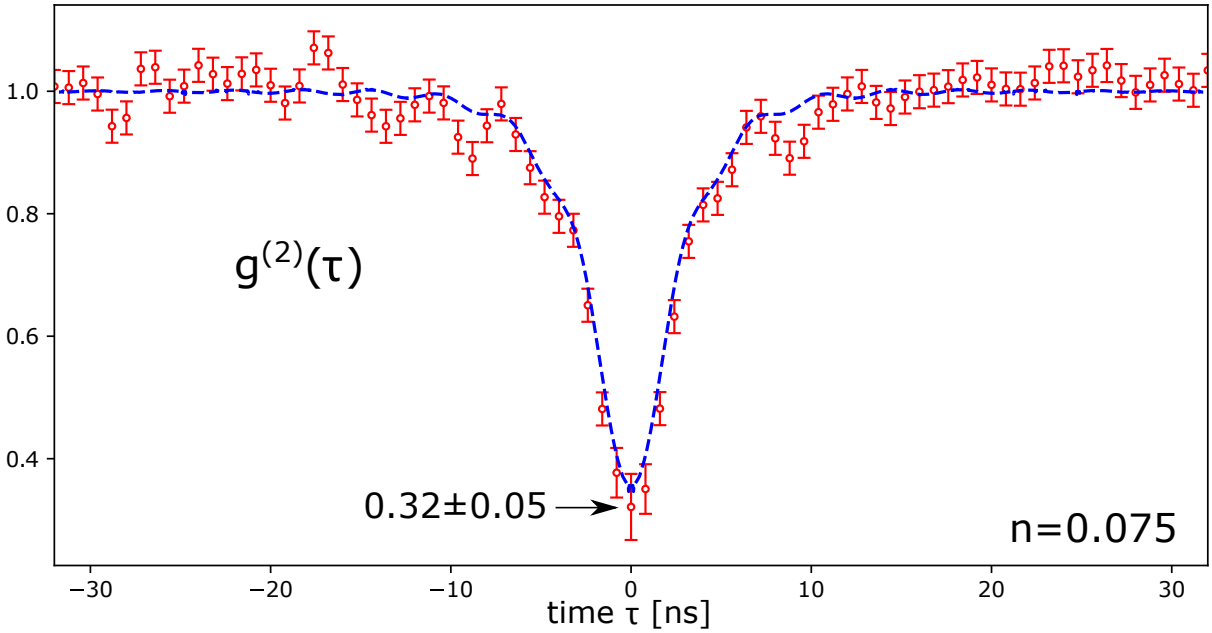

Figure 3.60: Final $g^{(2)}(\tau)$ obtained by the average of the $g^{(2)}_{pp}(\tau)$ and $g^{(2)}_{cs}(\tau)$ (red points), plotted with the result of numerical simulations (blue curve).

The final $g^{(2)}(\tau)$ function at $\bar{n} = 0.075$ displays strong antibunching of the emitted photons, with sub-Poissonian statistics as $g^{(2)}(0) = 0.32 \pm 0.05$. This is larger that the $(1 - r/2)^2 \simeq 0.27$ value predicted by the theory [34] at vanishing occupation number. We attribute this discrepancy mainly to the finite bandwidth used to digitize the signals, and to the finite value of $\bar{n}$. As described in [82], a finite acquisition window distorts the correlation function in time-domain. The effect of the filters we used in the experiment on the signals can be simulated through extensive numerical simulations [87]. The simulated correlation function agrees well with the experimentally measured one [36].

This good agreement validates our model of the system. The radiation emitted by the junction in the low E_J limit displays both antibunching and sub-Poissonian statistics. Interestingly, the relevant timescale in the $g^{(2)}(\tau)$ function is the resonator lifetime $\kappa^{-1} \simeq 1.3$ ns, while the $g^{(1)}(\tau)$ function indicates a long phase coherence time $\sigma_t \simeq 120$ ns. We interpret this as an illustration of wave-particle duality. When measuring emission spectra, we detect what looks like a very weak coherent signal $\hat{a}(t) \sim \sqrt{\bar{n}} e^{-i\omega_J t}$, with a slowly drifting frequency. When computing the second order coherence function, we gain information about the instantaneous power fluctuations $P(t) \propto \hat{a}^\dagger \hat{a}(t)$. We find that $P(t)$ fluctuates on a much shorter timescale than $\hat{a}(t)$, which is classically incompatible with the picture of a quiet continuous wave, but possible in a quantum picture of light.

This long phase coherence time also suggests that the single photons emitted by the junction could be used in interferometry experiments requiring indistinguishable photons.

Sub-Poissonian photons at higher emission rates

Using the same procedure, we measured $g^{(2)}(\tau)$ functions at larger emission rates, up to about $\bar{n} \simeq 0.9$ where the emitted power saturates (Fig.3.61). While the photons are still antibunched, there is a reduction of the sub-Poissonian character of their statistics, with $g^{(2)}(0)$ tending towards 1 when increasing $\bar{n}$.

We attribute the progressive loss of the single-photon character of the emission to the imperfect blockade mechanism that occurs at $r \simeq 1$. As the transition to higher occupation levels of the mode is not fully blocked, there is still a probability for the resonator to contain more than one photon. These transitions are still reduced as $g^{(2)}(0) < 1$, which proves that the radiation is non-classical.

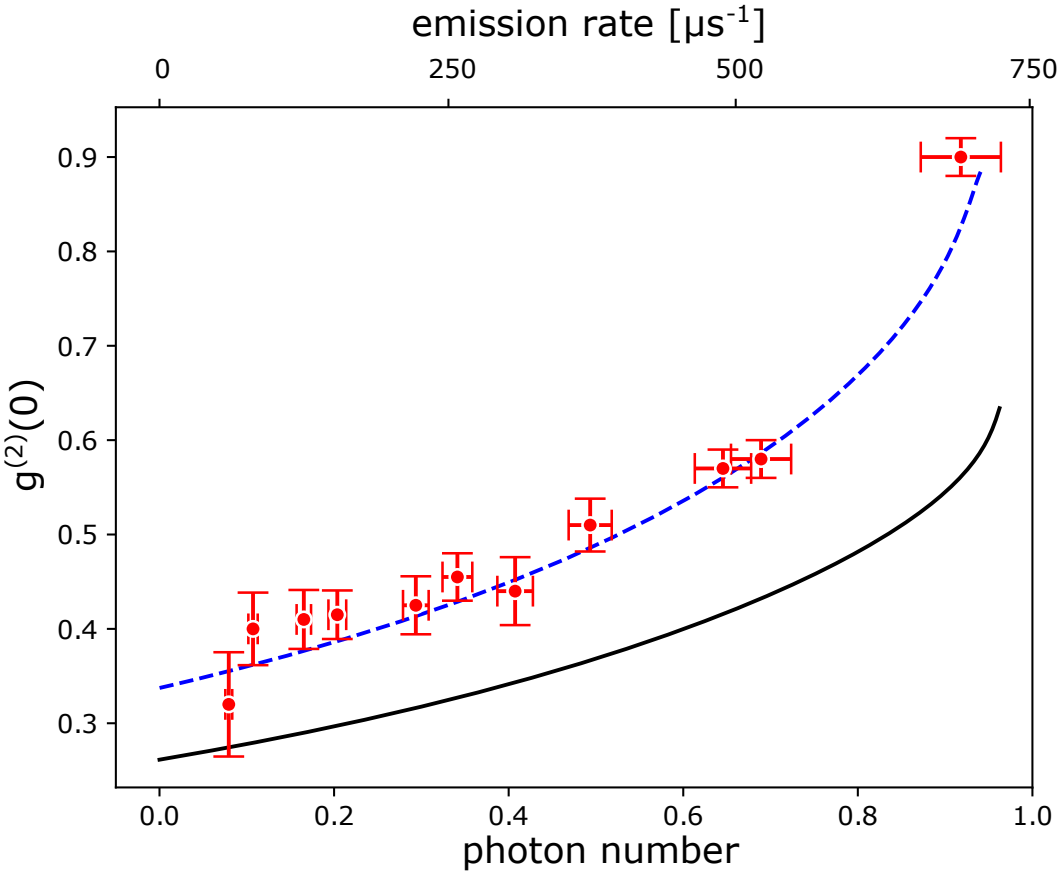

Figure 3.61: Values of $g^{(2)}(0)$ for increasing occupation number and emission rate. The vertical error bars on the experimental data (red points) reflect the statistical error on the measurement. The horizontal error bars reflect the uncertainty on the gain of the amplification chain. The result of numerical simulations of the system is plotted in black. The effect of filtering of the signals can be included in the simulations (dashed blue curve), revealing a good agreement with the measurements.

The shape of $g^{(2)}(\tau)$ itself changes at very high emission rate. We show in figure 3.62 the function measured at $\bar{n} = 0.9$. There are additional ripples on the sides of the $\tau = 0$ dip. We attribute them to the coherent exchange of energy between tunneling Cooper pairs and the cavity field, i.e Rabbi oscillations. These occur when $\bar{n} \times r \sim 1$, so that the field in the resonator is big enough to impact the tunneling events.

These results demonstrate that a small dc-biased Josephson junction in a high-impedance environment can be a bright source of non-classical radiation. The single-photon character

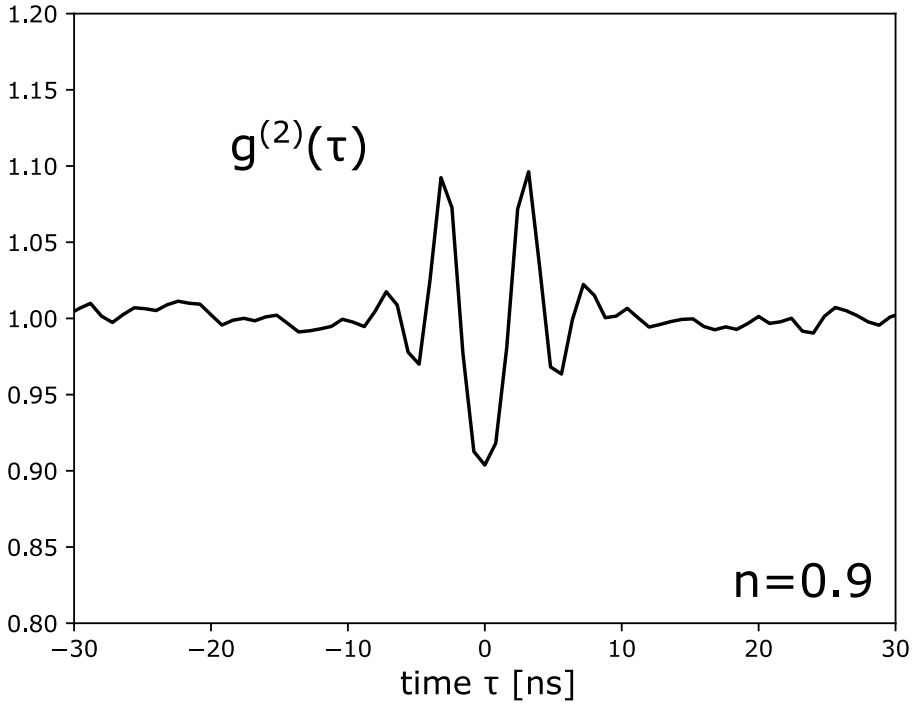

Figure 3.62: Second order coherence function at the highest emission rate, where $\bar{n} = 0.9$. We attribute the ripples to Rabbi oscillations between the cavity field and the tunneling Cooper pairs.

demonstrated here is not perfect as $g^{(2)}(0) > 0$, due to an insufficiently high impedance $r \simeq 1$. A better source could be implemented by reaching the regime of perfect photon blockade $r = 2$, using a different technology. The emission of single photons could also be triggered by pulsing the Josephson energy $E_J(\Phi)$, leading to the emission of exactly one single photon on demand. This on-demand mechanism was successfully implemented in another single-photon source based on ICPT [88]. In this experiment, the blockade mechanism resulted not from large ZPF phase fluctuations coming from a high impedance mode, but from the charging dynamics of a large on-chip resistor in series with the junction.

3.6 Conclusions and outlooks

We have developed a measurement setup and signal processing tools to investigate the properties of the radiation emitted by a dc-biased Josephson junction. Below the gap voltage the junction emits photons through Incoherent Cooper Pair Tunneling (ICPT) processes: each pair transfer distributes the energy $2eV$ in the modes of the environment, as described by the $P(E)$ perturbative theory. Above the gap voltage, quasiparticle tunneling takes place and the junction behaves as a source of shot-noise current (cf Appendix.B). In both cases the properties of the emitted radiation depend on the impedance $Re[Z(\omega)]$ of the environment of the junction, and on the occupation of its modes.

By measuring emission spectra at different values of voltage bias V and flux applied through the SQUID Φ, we can characterize accurately the sample and its environment. We calibrate *in situ* the gain and the noise power of the microwave amplification chains, as well as the spurious parasitic coupling between the two lines. We measure $Re[Z(\omega)]$ as seen by the junction in the 4-8 GHz range, and prove that it is strongly coupled with $r = 0.96$ to a single mode with vanishing thermal occupation. Thanks to the efficient filtering of the bias line, the small emission frequency jitter on the single-photon resonance is only limited by the thermal occupation of the low-frequency modes of the environment. We find that the Josephson energy is renormalized by the quantum phase fluctuations across the environment impedance, as predicted by the $P(E)$ theory.

Measurements of the second order correlation functions of the outgoing microwave field shed light on its statistics. In the shot-noise emission regime, the classical photon bunching statistics of thermal light is found, with $g^{(2)}(0) = 2$. In the ICPT emission regime, photons emitted in the high-impedance mode display non-classical sub-Poissonian statistics as well as antibunching, with $g^{(2)}(0) = 0.32 \pm 0.05$. Perfect antibunching with $g^{(2)}(0) = 0$ is not reached due to residual transitions to higher occupation states that occur at $r < 2$. Numerical simulations with no free parameter reproduce well our results, in particular the impact of the finite acquisition bandwidth on correlation functions.

Potential applications in quantum information processing would require a perfect on-demand source of single photons. The quality of the antibunching could be improved by fabricating a resonator with a higher impedance, that would be tunable to reach the exact value $r = 2$ that ensures $g^{(2)}(0) = 0$. On-demand emission could be triggered by controlling the resonance condition for single-photon emission on a short timescale, by tuning either the bias voltage V or the Josephson energy of the SQUID.

Experiments requiring undistinguishable single photons in a row could also be considered, as the phase coherence time of the emitted radiation $\sigma_t \simeq 120$ ns is much longer than the resonator lifetime $\kappa^{-1} \simeq 1.3$ ns. This feature illustrates strikingly the wave-particle duality of light, as revealed by complementary correlation measurements: on one hand, the first order coherence function $g^{(1)}(\tau)$ shows that the phase of the emitted radiation, inherited from the superconducting phase difference across the junction $\phi(t) = \int 2eV(t')dt'/\hbar$, is well-defined over a long coherence time. On the other hand, the $g^{(2)}(\tau)$ function indicates that the photon flux $\hat{a}^\dagger\hat{a}(t)$ fluctuates strongly on a a short timescale, as proven by the observed antibunching of the photons. Both aspects are not contradictory, this is just the quantum nature of light.

This long, albeit finite phase coherence time is not crucial to the production of anti-

bunched photons, which only requires $\sigma_t \leq \kappa^{-1}$. Nevertheless, one can wonder if the lack of a proper phase reference because of low-frequency modes with thermal occupation $\gg 1$, precludes any experiment relying on quantum coherence. We have proved this conjecture false in another set of experiments where we detect the creation of entangled light beams by a junction placed in series with two microwave modes, as described in the following chapter.

Chapter 4

Emission of entangled beams of light by inelastic Cooper-pair tunneling

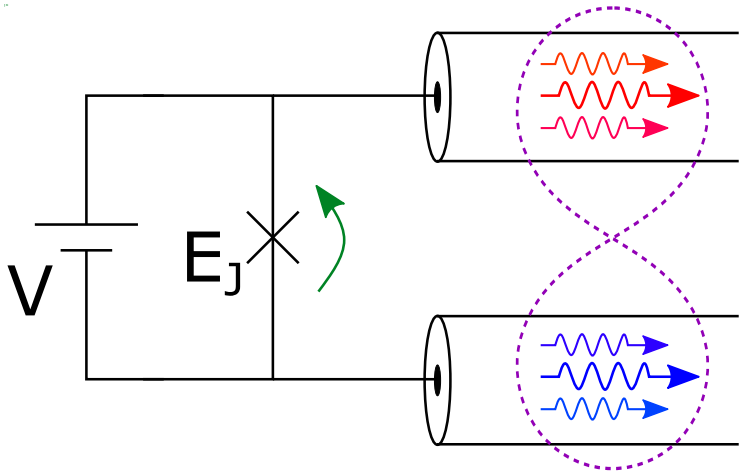

From the emission of non-classical photon pairs to the measurement of their entanglement

The energy $2eV$ transferred from the voltage bias to the rest of the circuit upon the inelastic tunneling of a Cooper pair can be split between different modes of the environment, creating multiple photons at once. This process generates quantum correlations between the photons created, as found in optics for the photons produced by parametric down-conversion. It is natural to wonder if the resulting multipartite state of light can present non-classical properties, such as entanglement or non-local features.

An earlier experiment performed by our team [39][38] considered a Josephson junction in series with two microwave resonators with distinct frequencies ω_a, ω_b. When biased at $2eV = \hbar(\omega_a + \omega_b)$ the junction emits photon pairs, with one photon being created in each resonator. Non-classical correlations between the photon emission rates at the two frequencies were measured. This result confirms that the photons are created by pairs, and then leak independently in the measurement lines. This experiment, although proving the non-classical character of the emitted radiation, did not demonstrate the entanglement of the outgoing modes.

We build on this experiment to probe the entanglement of the two outgoing microwave fields. Using our linear detection setup, we measure non-classical phase correlations between the two beams. This proves not only that the photons are created by pair at the same time, but also that their field quadratures share a non-local phase, inherited from the superconducting phase across the junction ϕ. After the two photons have left the resonators, this phase is imprinted in the subsequent photon pairs. This leads to the continuous creation of two entangled beams of light.

We prove that the decoherence of the two entangled beams stems from the slow dephasing of ϕ, which itself comes mostly from thermal low-frequency voltage noise on the junction. Furthermore, we actively cool down these low-frequency modes to reduce their voltage noise, increasing by more than a factor 3 the coherence time of the entangled beams. This cooling mechanism relies on the absorption of low-frequency photons by the junction itself through ICPT, at the same time as it is emitting entangled photons.

4.1 Entanglement of photon pairs created by ICPT

4.1.1 Choice of the system and its non-classical observables

In this experiment, we investigate the coherent emission of photon pairs by a Josephson junction placed in an environment including two low-impedance modes, with $r \ll 1$. We describe here the reasons that motivate the choice of this system.

From $P(E)$ theory to coherent k-photon drives

Non-trivial correlations between different modes appear naturally in the multi-photon processes predicted by the $P(E)$ theory. When biased at a dc-voltage $V = \hbar\omega_J/2e$, the spectral density of light $S_P(\omega)$ emitted by a Josephson junction is the sum of distinct contributions $S_P^{(k)}(\omega)$, associated to the different k-photon processes. The first-order term $S_P^{(1)}(\omega) \propto Re[Z(\omega)]$ describes the emission of one photon for each tunneling Cooper pair. The 2-photon processes yield:

$$\begin{aligned} S_P^{(2)}(\omega) &\propto Re[Z(\omega)] \times P(2eV - \hbar\omega) \\ &\propto Re[Z(\omega)] \times Re[Z(\omega_J - \omega)]. \end{aligned} \tag{4.1}$$

In particular $S_P^{(2)}(\omega) = S_P^{(2)}(\omega_J - \omega)$, which indicates that photons are created with symmetric emission around $\omega_J/2$. This yields correlations between modes of the electromagnetic field at different frequencies: if we detect a photon in a mode at ω, there should also be a photon at the mirror frequency $\omega_J - \omega$, created by the same tunneling event.

Higher order terms generate inter-frequencies correlations, that do not allow for such a simple interpretation. As an example the 3-photon processes give:

$$S_P^{(3)}(\omega) \propto Re[Z(\omega)] \times \int Re[Z(\omega')]Re[Z(\omega_J - (\omega + \omega'))]d\omega'. \tag{4.2}$$

Detection of a photon at ω is accompanied with beatings of the total photon flux at frequency $\omega_J - \omega$, an effect which is harder to demonstrate experimentally.

The $P(E)$ theory alone cannot predict the quantum state of light created by ICPT. Understanding these correlations require a more complete treatment of the system, including a description of the state of the modes, whereas the $P(E)$ theory assumes them to stay in a trivial thermal state. We will thus present a more sophisticated treatment of the emitted light, using the so called input-output formalism.

As in 3.2, we start by writing a Hamiltonian for the simple system consisting of a dc-biased Josephson junction and a **single** resonator with frequency ω_r and impedance r. At bias voltage $2eV = k \times \hbar\omega_r$, the effective Hamiltonian in the rotating frame of the resonator mode reads:

$$\hat{H}_{RWA}^{(k)} \simeq \frac{-E_J^*}{2k!}(-\sqrt{r})^k \left(\sum_i \frac{(-r\hat{a}^\dagger\hat{a})^i k!}{(k+1)!} \times \hat{a}^k + (\hat{a}^\dagger)^k \times \sum_i \frac{(-r\hat{a}^\dagger\hat{a})^i k!}{(k+1)!} \right) \tag{4.3}$$

This expression emphasises the action of the junction on the resonator: it implements a coherent k-photon drive $\hat{a}^k + (\hat{a}^\dagger)^k$, with a driving strength set by $E_J^* \sqrt{r}^k$, dressed by non-linearities proportional to $r\hat{a}^\dagger\hat{a}$.

Coherent k-photon drives with $k \neq 1$ also appear in some quantum optics experiments, e.g in parametric down-conversion processes. They can generate states of light with intriguing properties [89]. Starting from a mode in the vacuum state $|0\rangle$, a k-photon drive creates a **coherent superposition** of the $|i \times k\rangle$ Fock states, with $i \in \mathbb{N}$. Due to interferences between the quadratures probability distribution of the different Fock states, the resulting state displays an odd phase portrait, see figure 4.1.

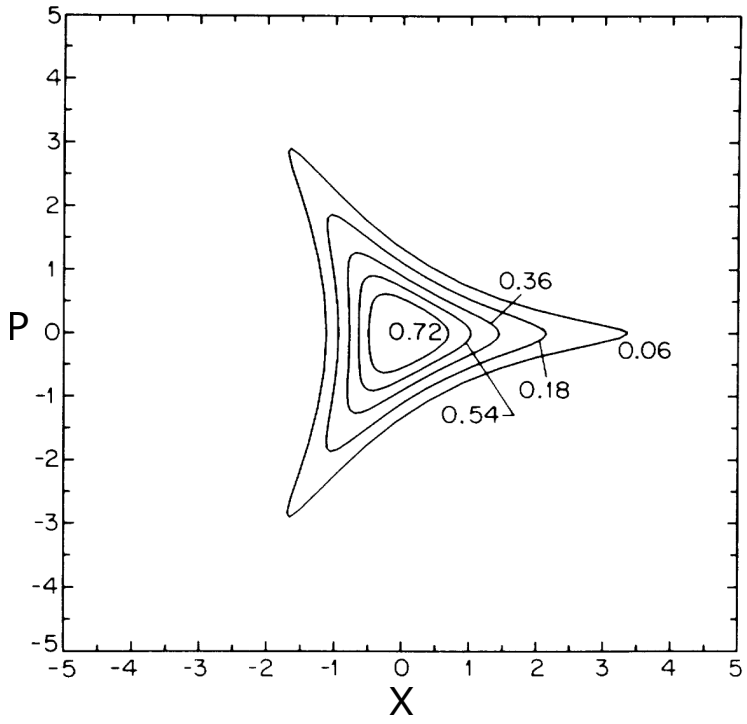

Figure 4.1: Probability contours for joint measurements of field quadratures X and P of a generalized squeezed state, created by the action of a 3-photon drive on an empty mode (taken from [89]).

The issues of non-Gaussianity

For $k \geq 3$, the distribution of quadratures of the state is *non-gaussian*, i.e it cannot be written as a product of gaussian functions of $X = \hat{a}+\hat{a}^\dagger$ and $P = i(\hat{a}^\dagger - \hat{a})$. Such states are intrinsically quantum, and are a resource for quantum information protocols [90][91][92]. Characterizing their coherence properties requires the measurement of high-order correlation functions, of the form $\langle(\hat{a}^\dagger)^m(\hat{a})^n\rangle$ with $m + n \geq 6$.

Could we demonstrate the creation of this type of states using ICPT? In our experiments, the signal-to-noise ratio is dominated by the amplifier noise power, with a $SNR \sim 1/50$ at a mode occupation number $\bar{n} = 1$. The number of acquisitions required for the precise measurement of $\langle(\hat{a}^\dagger)^m(\hat{a})^n\rangle$ scales as $(1/SNR)^{m+n}$, which becomes very large for high-order correlators. It would thus be harder for us to detect strongly non-gaussian states of light.

By contrast, a pure 2-photon drive creates **gaussian states**, which are fully characterized by their correlation functions up to order $m + n = 4$ only [93]. We should be able to measure these with the same procedure that we used for the measurement of $g^{(1)}(\tau)$ and $g^{(2)}(\tau)$ functions, so that we will focus on the emission of **photon pairs** only.

Note that as soon as the drive is not exactly of the form $\hat{a}^2 + (\hat{a}^\dagger)^2$, the stationary light state may show non-Gaussian features. In the Hamiltonian 4.3, the coherent drive is dressed by non-linear terms, which depend on the occupation state of the resonator. These describe a coherent back-action of the population of the mode onto the junction. This effect adds a non-linearity to the k-photon drive, creating a more complex stationary state of the resonator. In general this state is non-gaussian, resulting in e.g the emission of antibunched k-uplets of photons.

Measurement of correlation functions up to order 4 are enough to reveal the statistics of the emitted light, but not to determine the coherence properties of non-gaussian states. To avoid this non-gaussianity and keep measurement times reasonably short, our experiment is in the **low-coupling regime** $r \ll 1$. Then we expect back-action of the cavity field onto the junction to stay small, as long as $r\bar{n} \ll 1$.

Properties of a single mode in a two-photon coherent state

The stationary state of a mode driven coherently by a 2-photon drive is a coherent superposition of all the even-numbered Fock states. It is better known as a **quantum-squeezed state**, due to the asymmetric distribution of its field quadratures [94].

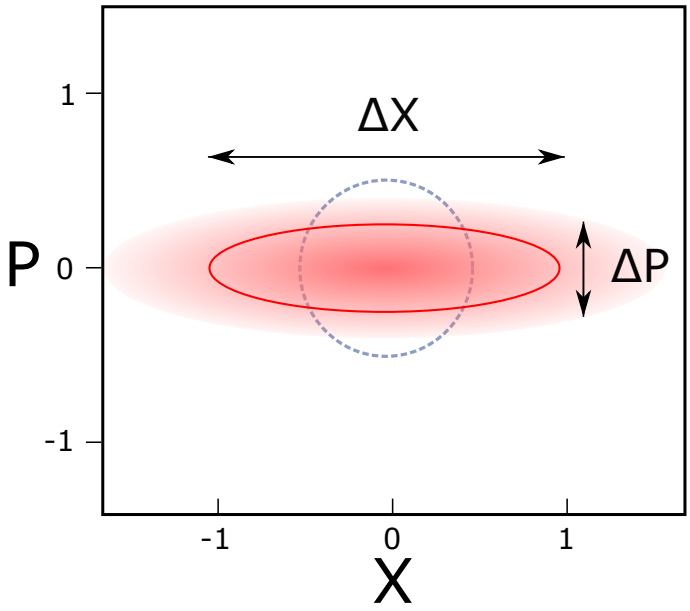

Figure 4.2: Probability distribution for the quadratures of a quantum squeezed state (red cloud). The standard deviation (red line) of X/P is larger/smaller than for the vacuum state (dashed gray).

The properties of this state of light are best described through its wavefunction in the quadrature basis. The wavefunction in the $X_\theta = e^{-i\theta}\hat{a} + e^{+i\theta}\hat{a}^\dagger$ basis is obtained by integrating the Wigner quasiprobability distribution of the mode over the orthogonal

quadrature $X_{\theta+\pi/2}$ [65]. A mode in the vacuum state has a radially symmetric wavefunction (Fig.4.2):

$$\psi_{|0\rangle}(X_\theta) = \psi_{|0\rangle}(X) = \left(\frac{2}{\pi}\right)^{1/4} e^{-X^2}. \tag{4.4}$$

The variance of any quadrature for the vacuum state is equal to $\Delta X_\theta^2 = \Delta X^2 = 1/4$. This state reaches the lower bound of the Heisenberg inequality for quadratures:

$$\Delta X_\theta \times \Delta X_{\theta+\pi/2} \geq \frac{1}{4}. \tag{4.5}$$

By contrast, a squeezed state of light displays uneven variance of its quadratures: $\Delta X_\theta^2 \neq \Delta X_{\theta+\pi/2}^2$. In particular, a 2-photon drive acting on the vacuum state generates a *squeezed vacuum*, with quadrature wavefunctions of the form:

$$\psi_{sq}(X) = \left(\frac{2}{\pi}\right)^{1/4} e^{-\left(\frac{X}{R}\right)^2}, \ \psi_{sq}(P) = \left(\frac{2}{\pi}\right)^{1/4} e^{-(RP)^2}. \tag{4.6}$$

For $R > 1$, the variance of the P quadrature is smaller than its value in the vacuum state: $\Delta P_{sq}^2 = 1/4R^2 = \langle 0|P^2|0\rangle/R^2$ (Fig.4.2). Surprisingly, there is less noise on P in this state of the mode than in the vacuum state. This is a purely quantum property, that cannot arise in a classical theory of light. Squeezed vacuum states can be used in high-precision interferometry measurements, as they allow to increase the SNR of a homodyne measurement beyond the standard quantum limit [95]. They could bring great advances in various domains such as the detection of gravitational waves [96] or electron spin resonance experiments at the single-spin limit[97].

To ensure (4.5), the orthogonal quadrature X displays amplified fluctuations with respect to the vacuum state: $\Delta X_{sq}^2 = R^2/4 = R^2 \times \langle 0|X^2|0\rangle$ (Fig.4.2). As $\Delta X_{sq}^2 \neq \Delta P_{sq}^2$, the squeezed state shows a preferential phase orientation. This phase is defined with respect to a **phase reference**, set by the driving field. In particular the state (4.6) is created by turning on an interaction Hamiltonian $H_{sq} \propto \hat{a}^2 + (\hat{a}^\dagger)^2$ at time $t = 0$. Another interaction of the form $H'_{sq} \propto i(\hat{a}^2 - (\hat{a}^\dagger)^2)$ would create a squeezed state in the orthogonal orientation, where the X quadrature is squeezed below the vacuum level and the P quadrature is anti-squeezed. The quadrature angle showing the smallest variance is called the *squeezing angle*.

In practice, effective squeezing interactions are typically realized through a three-photon process, where a pump field at frequency $2\omega_r$ drives a non-linear element [94]. The non-linear element acts as a frequency converter, continuously absorbing one photon from the pump and adding one photon pair to the mode. The squeezing angle is thus set by the phase of the pump field (Fig.4.3). The pump can then be used as a phase reference for homodyne measurements of the squeezed mode, or its application in a quantum protocol.

Blurring of single-mode squeezing in the absence of a phase reference

Measuring quantum squeezing requires knowing at which angle lies the squeezed quadrature, as well as being able to follow spurious drifts of the squeezing angle during the measuring time. In typical experiments the pump field provides a control of this angle,

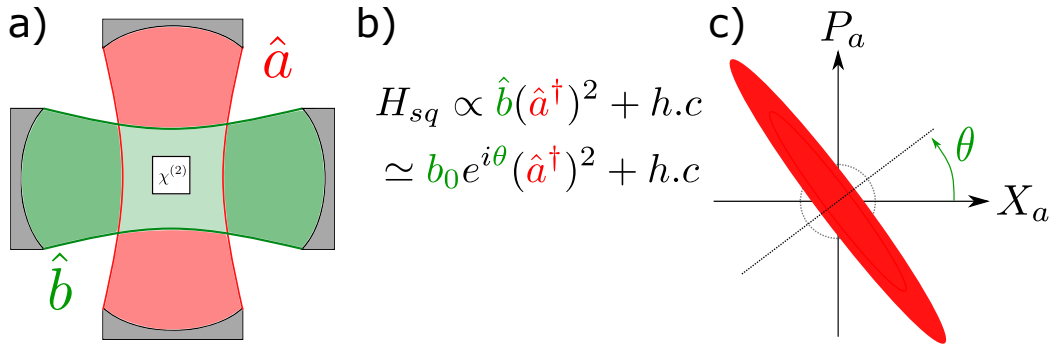

Figure 4.3: a) Typical setup for the generation of a squeezed vacuum state. A pump mode b (in green), prepared in a bright coherent state, is coupled to mode a (in red) by a $\chi^{(2)}$-type crystal (black box). b) The effective Hamiltonian of the system is proportional to $\hat{b}(\hat{a}^\dagger)^2 + h.c$. As b is kept in a quasi-classical coherent state, $\hat{b} \simeq \langle \hat{b} \rangle = b_0 e^{i\theta}$. c) The squeezing angle θ is then set by the phase of the pump mode.

which can be corrected for if the dephasing is slow enough. Furthermore, the pump field is often also used as a phase reference for the homodyne detection of quadratures, so that random drifts of the pump phase drop out in the final measured observables.

The situation is much different if we consider a squeezing experiment based on ICPT. In the simple model of the interaction between a dc-biased junction and a single low-impedance mode, setting the bias voltage on the junction such that $2eV = \hbar\omega_r$ implements an effective squeezing Hamiltonian:

$$\hat{H}^{(2)}_{RWA} \simeq \frac{-E_J^*}{2} r e^{-i\omega_J t}(\hat{a}^\dagger e^{+i\omega_r t})^2 + h.c = \frac{-E_J^*}{2} r(\hat{a}^\dagger)^2 + h.c \tag{4.7}$$

As there is no coherent pump field here, the squeezing angle is simply set by the time $t = 0$ at which the bias voltage is suddenly applied.

Given the bias line is heavily filtered, with a RC time of a few ms, the moment at which the squeezing interaction is turned on is not known, nor is the squeezing angle θ. This is the the analogue of the unknown propagation time of a microwave pump along a pump line of unknown length.

If this angle was kept constant, this problem could be circumvented by sweeping the phase of the homodyne detection until we measure a minimum of quadrature noise. However in our experimental setup the junction is also coupled to a continuum of low-frequency modes, which add thermal voltage noise to the voltage bias[1]. As the modes carrying this noise are much slower than any timescale of the interaction between the junction and the resonator, their impact can be modelled by replacing ω_J in (4.7) by $\omega_J(t) = 2eV/\hbar + \delta\omega$, with $\delta\omega$ a centered Gaussian random variable. Then:

$$\hat{H}^{(2)}_{RWA} \simeq \frac{-E_J^*}{2} r e^{-i\delta\omega \times t}(\hat{a}^\dagger)^2 + h.c, \tag{4.8}$$

so that the squeezing angle $\theta = \int_0^t \delta\omega(t')dt'$ drifts randomly over time [98] (Fig.4.4).

It should be noted that the stationary linewidth $\sigma_f \simeq 1.3$ MHz is **not** equal to the rate at which the squeezing angle dephases. From our results of the antibunching experiment

[1] as we have seen in 3.5,this $\sigma_V \simeq 2.6$ nV noise yields a stationary spectral width of the Josephson frequency $\sigma_f \simeq 1.3$ MHz

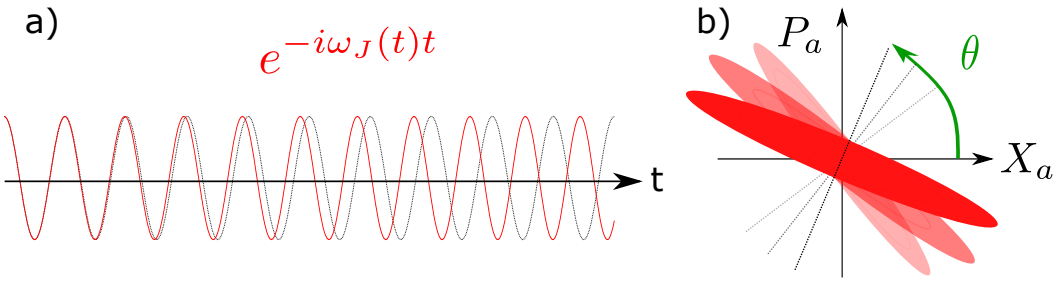

Figure 4.4: a) Due to thermal voltage noise on the junction, the Josephson frequency ω_J fluctuates randomly. The $e^{-i\omega_J(t)t}$ driving term (real part in red) in the squeezing Hamiltonian (4.8) dephases slowly with respect to a pure sinusoidal tone (dashed grey). b) The squeezing angle θ drifts randomly with time, making a direct measurement of quantum squeezing impossible.

3.5, we found that most of the voltage noise comes from a single mode of the bias setup, around $\omega_{BT} = 2\pi\times 71$ kHz $\simeq (2\ \mu\text{s})^{-1}$. On a time scale much shorter than 2 μs, the voltage noise from this mode is frozen so θ is approximately kept constant.

There are two possible ways we could try to detect directly single-mode quantum squeezing in our setup. We could either measure quadrature variance with less than 2 μs of averaging, letting the squeezing angle drift at random between measurements. This would require a much better SNR that our current one, which could be reached using wide-band quantum-limited amplifier instead of our commercial HEMTs. We could also try to measure on the fly the value of $\delta\omega(t)$, by detecting the low-frequency voltage fluctuations across the junction, and compensating the homodyning frequency accordingly.

Both strategies would require considerable technical developments, with limited new insights on the physics of quantum conductors coupled to radiation. We decided to study the creation of **two-mode squeezed states**, and prove that they could yield non-local correlations even in the absence of a stationary phase reference.

Two-mode squeezed states

An intriguing non-local state of light is created by a **two-mode drive** of the form $\hat{a}\hat{b}+\hat{a}^\dagger\hat{b}^\dagger$, which drives coherently two different modes a and b at the same time. Acting on two cavities initially in the vacuum state, this drive creates a **two-mode squeezed vacuum**, with the bipartite wavefunction [99]:

$$\psi_{TMSV}(X_a, X_b) = \sqrt{\frac{2}{\pi}} e^{-\left(\frac{X_a+X_b}{\sqrt{2}R}\right)^2} e^{-\left(R\frac{X_a-X_b}{\sqrt{2}}\right)^2}. \tag{4.9}$$

By tracing over the state of mode b, the statistical properties of a alone can be computed. Like in the vacuum state, the distribution of a quadratures are independent of the angle:

$$\Delta X^2_{a,\theta} = \Delta X^2_a = \frac{R^2 + R^{-2}}{8}. \tag{4.10}$$

For $R > 1$, this gaussian state always presents more fluctuations than the vacuum state, with an occupation number $\bar{n} = (R^2 + R^{-2} - 2)/2 \neq 0$. In fact, it can be shown that the a field presents the statistics of a thermal state at temperature $k_B T = \hbar\omega_a/2\ln(\frac{R^2+1}{R^2-1})$, with $g^{(2)}(0) = 2$. Tracing over a leads to similar properties for the b mode.

However, joint measurement of quadratures from the two modes reveal non-classical features. From (4.9), it can be seen that a linear combination of X_a and X_b presents a variance below the vacuum level:

$$\Delta\left(\frac{X_a - X_b}{\sqrt{2}}\right)^2 = \frac{1}{4R^2}, \tag{4.11}$$

while:

$$\langle 0|_a \otimes \langle 0|_b \left(\frac{X_a - X_b}{\sqrt{2}}\right)^2 |0\rangle_a \otimes |0\rangle_b = \frac{\langle 0|X_a^2|0\rangle + \langle 0|X_b^2|0\rangle}{2} = \frac{1}{4}. \tag{4.12}$$

which follows from the independence of X_a and X_b when the two modes are in the vacuum state. Conversely, the symmetric combination $X_a + X_b$ shows an increased variance in the two-mode squeezed state:

$$\Delta\left(\frac{X_a + X_b}{\sqrt{2}}\right)^2 = \frac{R^2}{4} = R^2 \times \langle 0|_a \otimes \langle 0|_b \left(\frac{X_a + X_b}{\sqrt{2}}\right)^2 |0\rangle_a \otimes |0\rangle_b. \tag{4.13}$$

This state then still obeys the Heisenberg inequality for joint quadrature measurements. The reduction of the variance of $X_a - X_b$ means that X_a and X_b are correlated, i.e they tend to have the same value when measured at the same time, see figure 4.5. The wavefunction in the P_a, P_b basis, which can be computed from (4.9), reveals that P_a and P_b are anti-correlated, with: $\Delta\left(\frac{P_a+P_b}{\sqrt{2}}\right)^2 = \Delta\left(\frac{X_a-X_b}{\sqrt{2}}\right)^2$.

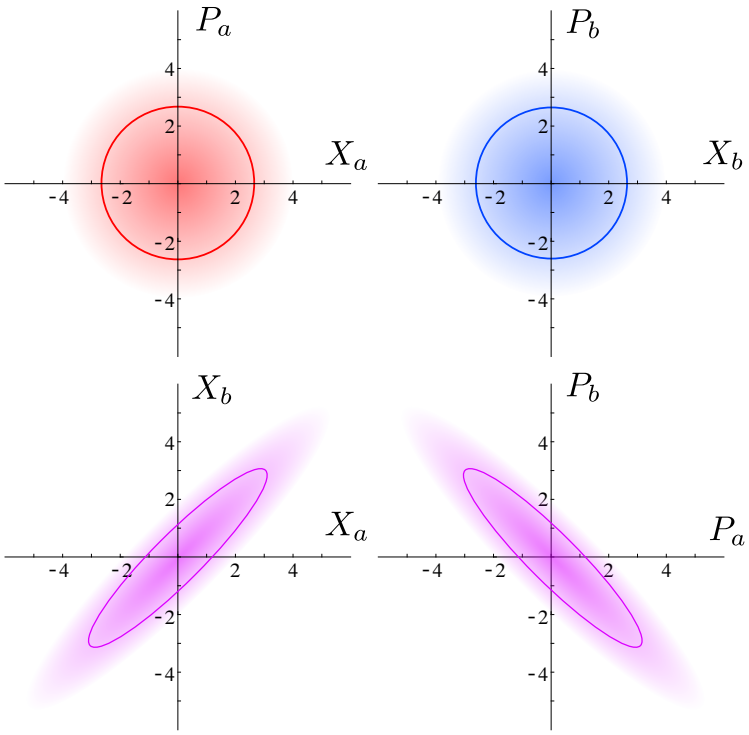

Figure 4.5: Wavefunctions of a two-mode squeezed vacuum (TMSV) with squeezing angle $\theta = 0$, in different pairs of quadrature bases. In the X_a, P_a basis, the TMSV shows no preferential orientation, and more noise than the vacuum state (not pictured). Same goes in the X_b, P_b basis. Wavefunctions in composite bases show correlations between X_a and X_b, and anti-correlations between P_a and P_b.

In the limit of infinite squeezing $R \to \infty$, joint measurement on the two modes show perfect (anti)correlations: $X_a = X_b$ and $P_a = -P_b$. At the same time, quadratures

measured separately have no well-defined value: $\Delta X_a^2 = \Delta P_a^2 = \Delta X_b^2 = \Delta P_b^2 \to \infty$. This kind of bipartite state can be considered in the more general framework of the EPR paradox [100], the first thought experiment to pinpoint the existence of entanglement in quantum physics.

Non-local properties of two-mode squeezed states can be put to use in quantum information and quantum communication protocols [101][93]. They have been performed experimentally in quantum optics setup since 1985 [102], and more recently at microwave frequencies using circuits based on Josephson non-linear elements [103][37].

In these experiments, three modes of radiation a, b, c are coupled by a non-linear element, with an effective Hamiltonian $H_{tmsq} \propto \hat{a}^\dagger \hat{b}^\dagger \hat{c} + h.c$. The $\hat{c}$ mode is put in a bright coherent state, so that $\hat{c} \simeq \langle \hat{c} \rangle = c_0 e^{i\theta}$. $H_{tmsq} \simeq c_0 e^{i\theta} \hat{a}^\dagger \hat{b}^\dagger + h.c$ then implements a two-mode drive of $\hat{a}$ and $\hat{b}$. The driving strength is set by the occupation number $\langle \hat{c}^\dagger \hat{c} \rangle = c_0^2$ of the pump mode, while its phase sets the **two-mode squeezing angle** θ.

In the single-mode case, the value of θ indicates directly which quadrature has a variance below the vacuum level. The situation is a bit different for two-mode squeezing, as **any quadrature combination of the form $X_a^\phi - X_b^{\theta-\phi}$ displays a reduced variance**, for $\phi \in [0, 2\pi]$[2]. In other words, local states of the $\hat{a}$ and $\hat{b}$ fields do not have a preferential phase orientation, but they share a hidden, non-local phase. Measuring two-mode squeezing below the vacuum level still requires knowing the value of θ.

Two-mode non-classical correlations through ICPT

A coherent two-mode drive can be implemented by putting a Josephson junction in series with two different resonators at frequencies ω_a, ω_b and setting a voltage bias $2eV = \hbar(\omega_a + \omega_b)$, such that each tunneling Cooper pair creates one photon in each mode (Fig.4.6).

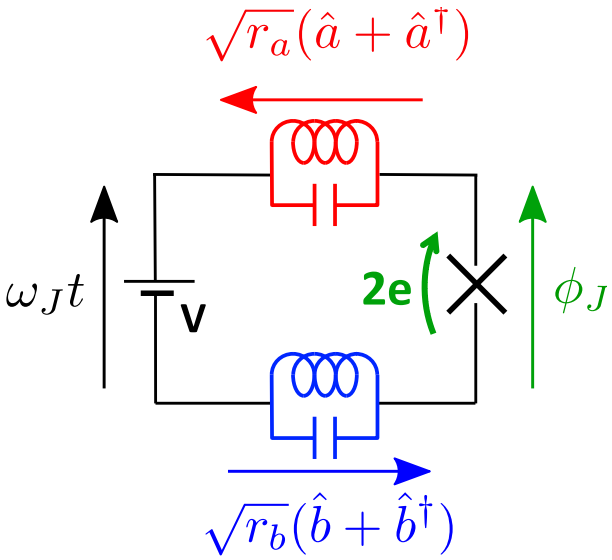

Figure 4.6: A two-mode ICPT circuit implements two-mode squeezing, with the bias voltage V set on the photon-pair resonance $2eV = \hbar(\omega_a + \omega_b)$ at $t = 0$.

[2]This is what defines the squeezing angle.

The junction is coupled to both modes at the same time, as its phase difference $\hat{\phi}$ now reads:

$$\hat{\phi} = \frac{2eV}{\hbar}t - \sqrt{r_a}(\hat{a}e^{-i\omega_a t} + \hat{a}^\dagger e^{+i\omega_a t}) - \sqrt{r_b}(\hat{b}e^{-i\omega_b t} + \hat{b}^\dagger e^{+i\omega_b t}). \tag{4.14}$$

Expanding the Josephson Hamiltonian $-E_J\cos(\hat{\phi})$ in the frame rotating at ω_J, one obtains the effective Hamiltonian:

$$\hat{H}_{RWA}^{(a+b)} = -E_J^* Re\left[e^{+i\omega_J t}\sum_{k=0}^{\infty}\frac{(r_a\hat{a}^\dagger\hat{a}\times r_b\hat{b}^\dagger\hat{b})^k}{[k!\times(k+1)!]^2}\sqrt{r_a r_b}\hat{a}\hat{b}e^{-i\omega_a t}e^{-i\omega_b t}\right], \tag{4.15}$$

which implements a coherent two-mode driving of the a and b resonators dressed by non linear terms proportional to $r_a\hat{a}^\dagger\hat{a}r_b\hat{b}^\dagger\hat{b}$. For low impedances $r_a, r_b \ll 1$ and small enough occupation numbers $\langle\hat{a}^\dagger\hat{a}\rangle \ll r_a^{-1}$, $\langle\hat{b}^\dagger\hat{b}\rangle \ll r_b^{-1}$, we can effectively neglect the non-linearities and obtain a true two-mode squeezing Hamiltonian:

$$\hat{H}_{TMS}^{(a+b)} = -E_J^*\sqrt{r_a r_b}e^{-i\omega_J t}(\hat{a}^\dagger e^{+i\omega_a t})(b^\dagger e^{+i\omega_b t}) + h.c = -E_J^*\sqrt{r_a r_b}e^{-i\delta\omega t}a^\dagger b^\dagger + h.c, \tag{4.16}$$

The driving strength is set by $E_J^*\sqrt{r_a r_b}$, and the squeezing angle by the time $t = 0$ at which the voltage bias is tuned on resonance. In this simple thought experiment, we consider that the bias voltage is turned off after some time, such that the number of photons created in the modes stay finite.

As in the single-mode squeezing case, thermal noise $\delta V(t)$ from the low-frequency modes of a real setup yields a continuous drifting of the squeezing angle $\theta(t) = \int_0^t 2e\delta V(t')dt'/\hbar$. In our experiment, this dephasing blurs the two-mode squeezing on a timescale ~ 2 μs, precluding the direct observation of squeezing below the vacuum level using longer measurement times.

However, some non-classical properties of the two-mode squeezed state can survive despite the absence of a stationary squeezing angle. Indeed the simultaneous creation of photons in the two modes generates non-classical correlations between their respective photon numbers $n_a = \hat{a}^\dagger\hat{a}, n_b = \hat{b}^\dagger\hat{b}$. These correlations manifest when writing the pure TMSV state in the joint Fock state basis [99]:

$$|\psi\rangle_{TMSV} = \frac{1}{\cosh r}\sum_{n=0}^{\infty}\left(e^{i\theta}\tanh(r)\right)^n|n\rangle_a|n\rangle_b, \tag{4.17}$$

where $r = \ln(R)$ is the *squeezing parameter*. This expression highlights the entanglement between the two modes: even though the exact photon number of each cavity is not well defined, with $\Delta n_{a/b}^2 = n_{a/b}(n_{a/b}+1) \neq 0$, simultaneous measurements of n_a and n_b would always yield the same value. This *amplitude-squeezing* can be characterized by the noise reduction factor (NRF) [104]:

$$\text{NRF} = \frac{\Delta(n_a - n_b)^2}{\langle n_a + n_b\rangle}. \tag{4.18}$$

For independent coherent states of the modes, NRF = 1. A value below 1 is a proof of non-classical correlations between the populations of the modes. For pure two-mode squeezing, $n_a = n_b$ such that NRF = 0.

When averaging over many copies of this state with random phase θ, the coherence between different components of the Fock basis wash out, but the occupation probabilities

$p_k = |\langle n|\psi\rangle_{TMSV}|^2$ at a given time remain unchanged. In particular it should still be possible to detect non-classical photon number correlations between the two modes. This motivated the first experiment to probe the non-classical emission of photon pairs by ICPT [39].

4.1.2 Photon pairs emitted by ICPT: from non-classicality to entanglement

First measurements of non-classical photon number correlations

During his PhD research in Saclay, Olivier Parlavecchio [38] designed an experiment to study the joint statistics of photon pairs emitted by a dc-biased Josephson junction in a two-mode environment (Fig.4.7). Measuring the covariance of n_a, n_b inside the cavities would require a complex scheme, e.g using dispersively coupled qubits for readout. It is simpler to let the photons leak out of the modes and relate their statistics to the measurement of correlation functions, in the spirit of the antibunching experiment (see 3.13).

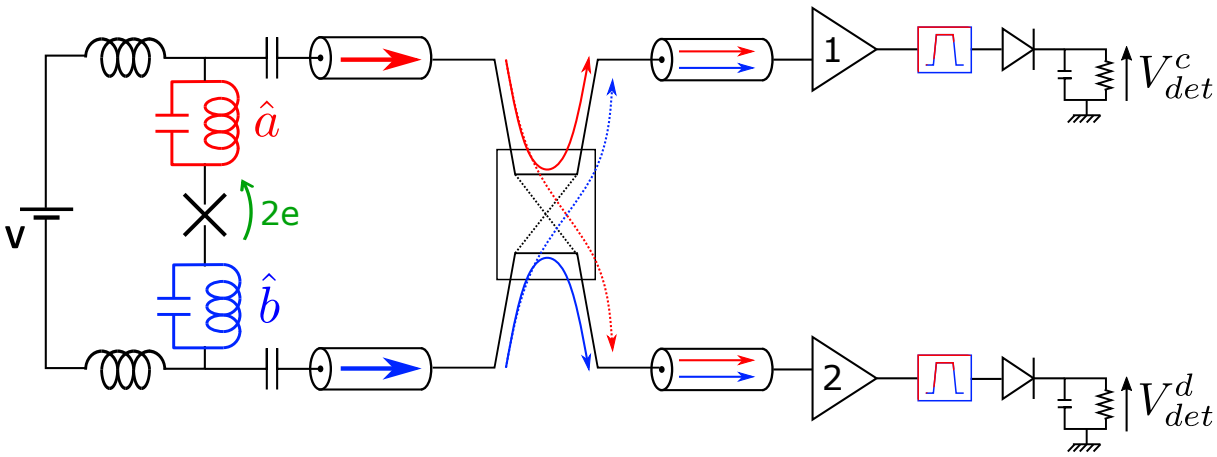

Figure 4.7: Schematic microwave setup for the detection of emission power correlations between the two resonators. When $2eV = \hbar(\omega_a + \omega_b)$, the junction creates photon pairs in the a and b modes. These photons leak into two detection lines, which implement the microwave version of a HBT experiment. By inserting after the amplifiers bandpass filters centered around ω_a (ω_b), the correlation of $V^c_{det}(0)$ and $V^d_{det}(\tau)$ yields $g^{(2)}_{a(b)}(\tau)$. Setting one filter at ω_a and the other one at ω_b yields $g^{(2)}_{ab}(\tau)$.

Each resonator is connected to a bias tee, with the rf port feeding one port of a beamsplitter. Like in the microwave HBT setup of figure 3.18, detecting the correlated power fluctuations at the outputs c, d of the beam splitter gives access to the second order coherence function of the emitted photons. At first sight, one would need to use two different HBT setups (including two beamsplitters, four amplifiers and four power detectors) to measure both $g^{(2)}_a(\tau) = \frac{\langle \hat{a}^\dagger(0)\hat{a}^\dagger(\tau)\hat{a}(\tau)\hat{a}(0)\rangle}{n_a^2}$ and $g^{(2)}_b(\tau) = \frac{\langle \hat{b}^\dagger(0)\hat{b}^\dagger(\tau)\hat{b}(\tau)\hat{b}(0)\rangle}{n_b^2}$. In practice, one can route the a and b signals to the two inputs of a single beamsplitter, and use filtering at room temperature to detect either power fluctuations at ω_a or at ω_b. The beams recombining in figure 4.7 do **not** yield interferences of the a and b photons, as they belong to different frequency bands.

Correlations between the populations of the a and b modes can also be detected by setting on one line a filter centered around ω_a, and on the other line a filter centered around ω_b. In this configuration, the correlation of power fluctuations detected on the two lines at the same time yields:

$$1 + \frac{\langle \delta P_1(0) \delta P_2(\tau) \rangle_{ON/OFF}}{\langle P_1 \rangle_{ON/OFF} \langle P_2 \rangle_{ON/OFF}} = \frac{\langle \hat{a}^\dagger(0)\hat{a}(0)\hat{b}^\dagger(\tau)\hat{b}(\tau) \rangle}{\bar{n}_a \bar{n}_b} = g^{(2)}_{ab}(\tau). \tag{4.19}$$

Auto- and cross-correlation functions of the leaking photons are linked to the NRF of the cavities state through [39]:

$$\begin{aligned} \mathrm{NRF} &= 1 + \frac{\bar{n}_a^2 g_a^{(2)}(0) + \bar{n}_b^2 g_b^{(2)}(0) - 2\bar{n}_a \bar{n}_b g_{ab}^{(2)}(0)}{\bar{n}_a + \bar{n}_b} \\ &= 1 + \bar{n} \frac{g_a^{(2)}(0) + g_b^{(2)}(0) - 2g_{ab}^{(2)}(0)}{2} \end{aligned} \tag{4.20}$$

for equal populations of the modes $\bar{n}_a = \bar{n}_b = n$. In this particular case, a classical bound on the NRF can be derived from the Cauchy-Schwarz inequality applied to n_a, n_b:

$$\begin{aligned} & 2\langle n_a n_b \rangle \leq \langle n_a^2 \rangle + \langle n_b^2 \rangle \\ \Rightarrow\ & 2g_{ab}^{(2)}(0) \leq g_a^{(2)}(0) + g_b^{(2)}(0) \\ \Rightarrow\ & \mathrm{NRF} \geq 1, \end{aligned} \tag{4.21}$$

where the first inequality is only valid if n_a, n_b are scalars and not quantum operators, i.e for classical states of light. Breaking the inequality, or equivalently measuring a NRF<1, is then a sign of non-classicality of the radiation, in the sense that the Glauber-Sudarshan P function of the two modes is non-positive.

Figure 4.8 shows the results of the experiment [39]. The $g_a^{(2)}(\tau)$ and $g_b^{(2)}(\tau)$ (not displayed) functions prove the bunching and super-Poissonian statistics of the radiation, with $g_a^{(2)}(0) \simeq g_b^{(2)}(0) \simeq 2$ as predicted for gaussian states of light. By contrast the cross-correlation coherence function $g_{ab}^{(2)}(\tau)$ proves the correlated emission of photons in the two modes, with $g_{ab}^{(2)}(0) \geq 2$.

Zero-time values of these three correlation functions are plotted as a function of the emission rate $\Gamma = \bar{n}\kappa$, tuned by threading a flux Φ trough the SQUID. The NRF, computed following expression (4.20), is also shown on the figure. Within its statistical deviation it is found to be constant, with $\mathrm{NRF} \simeq 0.7 < 1$. This proves that the photon numbers n_a, n_b are more correlated than what is possible for classical observables, reflecting the photon-pair creation processes.

As the NRF is found to be approximately constant, by inverting (4.20) one gets:

$$g_{ab}^{(2)}(0) = \frac{g_a^{(2)}(0) + g_b^{(2)}(0)}{2} + \frac{1 - \mathrm{NRF}}{\bar{n}} \simeq 2 + \frac{0.3}{\bar{n}}. \tag{4.22}$$

The $1/\bar{n}$ divergence of $g_{ab}^{(2)}(0)$ is visible on figure 4.8. At low occupation numbers, the correlated fluctuations of n_a and n_b are relatively more important. At higher photon numbers, Poissonian shot-noise overcomes these correlations.

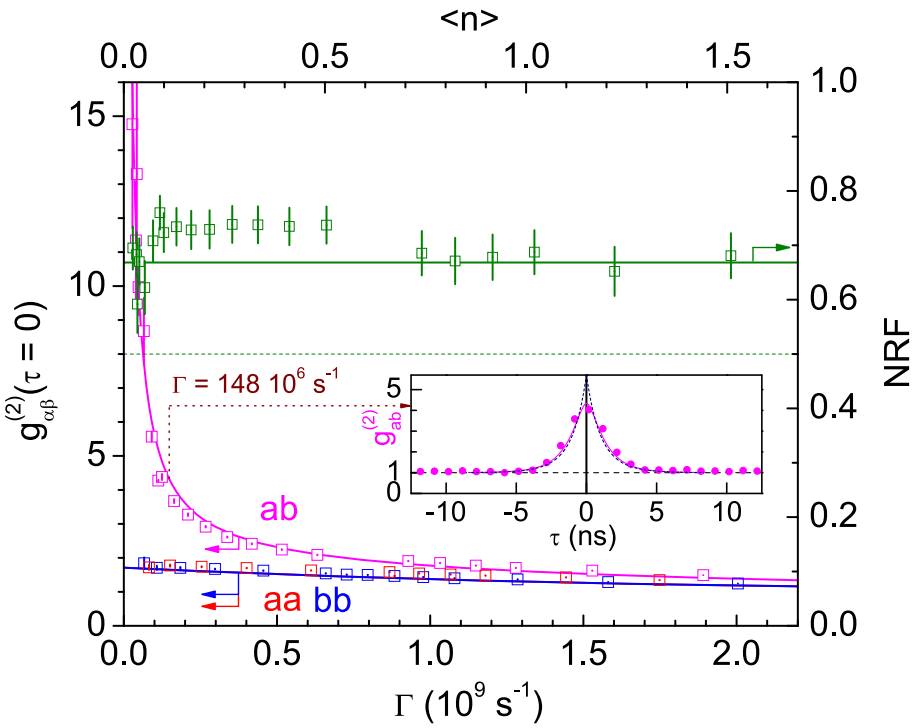

Figure 4.8: Results of the photon-pair experiment. Insert: $g^{(2)}_{ab}(\tau)$ correlation function for $\bar{n} \simeq 0.11$, with measured data points (pink points) and numerical simulations, for a zero (dashed black) of finite (pink line) response time of the quadratic detectors. Main frame: photon number correlators $g^{(2)}_a(0)$ (red dots), $g^{(2)}_b(0)$ (blue dots) and $g^{(2)}_{ab}(0)$ (pink dots) as a function of the pair emission rate Γ and of the mean occupation of the cavities $\bar{n}$. From these values the NRF is computed according to (4.20). Data points are plotted along the results are numerical simulations (full lines) (taken from [39]).

All these results are well described by an analytical theory and numerical simulations [104][105]. At low driving $E_J \to 0$ (with $\bar{n} \to 0$), the value of $g^{(2)}_a(0)$ is given by:

$$g^{(2)}_a(0) = 2\left(1 - \frac{r_a}{2}\right)^2 \left(1 - \frac{5}{8}r_b + \frac{r_b^2}{8}\right) \simeq 1.79, \tag{4.23}$$

and a similar result for $g^{(2)}_b(0)$. This value lower than 2 reflects the reduction of tunneling due to phase vacuum noise from the resonators, it is similar in essence to the antibunching described in the previous chapter. Numerical simulations are needed to compute the value of $g^{(2)}_{a/b}(0)$ at finite emission rates. It is found that the increased phase fluctuations due to the occupation of the modes, reduce even more the tunneling rates. This lowers the correlation between subsequent photon creation processes, leading to $g^{(2)}_{a/b}(0) \to 1$ as $\bar{n} \to \infty$.

Time-domain simulations reproduce well the measured correlation functions. The inset in figure 4.8 shows the measured cross-correlator $g^{(2)}_{ab}(\tau)$ at a given $\bar{n} \simeq 0.11$, along with its numerical simulation. The 0.4 ns response time of the quadratic detectors is responsible for a reduction of $g^{(2)}_{ab}(0)$, from its predicted value $\simeq 6.5$ down to a measured $\simeq 4$. Following (4.20), this leads to an increase of the measured NRF from 0.5 to 0.7. We comment later on the value predicted for infinitely fast detectors NRF $= 1/2$, as opposed to the NRF $= 0$ expected in 4.1.1. The effect of a finite response time is consistent all over the range of measured data, from $\bar{n} \simeq 0.03$ up to 1.5.

Another key ingredient for the description of photon-detection statistics is the coupling of

the cavities to the measurement lines. First of all, this coupling sets the leak rate κ of the resonators, also known as the inverse cavity lifetime. This timescale appears as the decay constant in the population correlators, see the inset of figure 4.8. For auto-correlators $g^{(2)}_{a/b}(\tau)$, this means that $c\kappa^{-1}$ is the typical length of a wavepacket propagating in the lines, i.e the "length" of a photon. In the case of $g^{(2)}_{ab}(\tau)$, κ^{-1} is also the typical timescale over which the fluctuations of the a and b emission rates are correlated. Thus there are no number correlations between two successive photon-detection events.

Second, this coupling dictates the dynamics of the field inside the cavity. The master equation formalism of [104] highlights that the resonator field $\hat{a}(t)$ (resp. $\hat{b}(t)$) is continuously driven by the two-mode squeezing Hamiltonian while leaking in the transmission line, as described by a Lindblad operator $\mathcal{L}[\hat{a}]$ (resp. $\mathcal{L}[\hat{b}]$). The photons are created by pairs, but then leak independently from the resonators. Because of their independent leaks, the correlation of the cavities occupations is only partial. This leads to a reduction of the NRF *for the cavities*, down to NRF = 0.5.

Non-local properties of the propagating radiation

We presented the results of [39] within the same perspective used by the authors, which does not make a distinction between the states of the cavity modes and the state of the outgoing radiation. As the photon emission rate $\Gamma_x = \kappa_x \bar{n}_x$ is simply proportional to the occupation number $\bar{n}_x$ of cavity x, measuring correlation of the emitted powers is equivalent to measuring correlations of the two resonators photon numbers. However the link between the cavity modes and the propagating modes is more complicated for other observables, such as the field quadratures.

The input-output formalism [59] allows to describe more comprehensively the emission of photons in the measurement lines. In this picture, the evolution of the fields $\hat{a}(t)$ and $\hat{b}(t)$ is governed both by the coherent two-mode drive and by the injection of random noise carried by the incoming mode operators $\hat{a}_{in}(\omega)$ and $\hat{b}_{in}(\omega)$. Both the cavity field and the incoming field are linked to the outgoing field by the input-output relations:

$$\sqrt{\kappa}\hat{a}(t) = \hat{a}_{in}(t) + \hat{a}_{out}(t) = \int_0^\infty \left(\hat{a}_{in}(\omega) + \hat{a}_{out}(\omega)\right) \times e^{-i\omega t}\frac{d\omega}{2\pi} \tag{4.24}$$

$$\sqrt{\kappa}\hat{b}(t) = \hat{b}_{in}(t) + \hat{b}_{out}(t) = \int_0^\infty \left(\hat{b}_{in}(\omega) + \hat{b}_{out}(\omega)\right) \times e^{-i\omega t}\frac{d\omega}{2\pi}. \tag{4.25}$$

As we detail in a later section 4.1.3, pairs of outgoing modes display perfect photon number correlations, with $\Delta(\hat{a}^\dagger_{out}\hat{a}_{out}(\omega) - \hat{b}^\dagger_{out}\hat{b}_{out}(\omega_J - \omega))^2 = 0$, leading to a NRF = 0 **for this pair of modes at ω and $\omega_J - \omega$.**

We have here a novel picture of the partial correlation between n_a and n_b: the cavities are continuously leaking perfectly correlated photon pairs in the lines at a rate κ, while absorbing uncorrelated vacuum noises at the same rate κ. Their photon numbers are thus in average only 50% correlated, yielding a NRF = 1/2.

In essence, the master equation formalism describes only the cavity states, and tells us that half of the correlations have been lost. The input-output formalism tells us exactly where did these non-classical correlations go: they travel in the line, away from the cavities. Most importantly, as the photons do not interact once they have been emitted,

their state stops evolving, and their non-classicality is preserved along their journey - until they are eventually detected.

What about the non-local phase correlations of two-mode squeezed states? The two cavities do not display measurable squeezing below the vacuum level, as their squeezing angle θ drifts continuously due to low-frequency voltage noise. However once photons have left the cavities, they are decoupled from this voltage noise and conserve their squeezing angle. We thus expect the propagating modes to display a form of phase coherence, revealing their entanglement.

The nature of this entanglement appears in a naive setp-by-step picture of the photon pair emission process. Consider that at $t = 0$ a photon pair is created, displaying perfect two-mode squeezing correlations. After a typical time κ^{-1} the two photons have independently left their respective cavities. While propagating they keep track of the shared phase $\theta(t)$, accessible through joint measurements of the $\hat{a}_{out}$ and $\hat{b}_{out}$ modes (Fig.4.9).

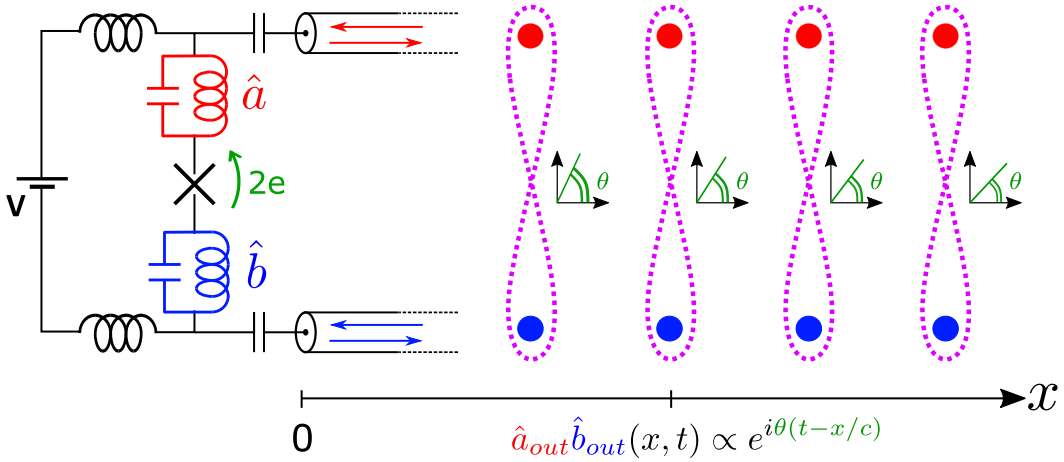

Figure 4.9: Simplified picture of the emission of entangled photon pairs. The dc-biased Josephson junction squeezes vacuum incoming from the transmission lines at frequencies ω_a, ω_b and reemit a non-local state of light, pictured here as entangled photons (colored dots). At position x on the propagation line, squeezing manifests as non-local correlations, with $\hat{a}_{out}\hat{b}_{out}(x,t) \propto e^{i\theta(t-x/c)}$. The squeezing angle $\theta(x,t)$ is given by the phase $\phi(t - x/c)$ on the junction. Successive photon pairs, emitted on a timescale shorter than the phase coherence time σ_t, have approximately the same squeezing angle.

If the dephasing is slow enough compared to the rates at which photons leave the cavities, then we expect the next pair of emitted photons to display a very close value of θ. There are then correlations not only between photon pairs at different frequencies, but also between successive photon pairs emitted over a time equal to the inverse dephasing rate $\sigma_t \simeq 2\ \mu$s. As light is continuously emitted by the cavities, this leads to the creation of two correlated beams of light (Fig.4.9).

This picture is a bit too naive because the Hamiltonian (4.16) does not write naturally in the basis of discrete photon number states. It rather acts like a smooth drive of the fields $\hat{a}(t), \hat{b}(t)$. We should then rather think of continuous amplitudes $\hat{a}_{out}(t), \hat{b}_{out}(t)$ carrying a field of non-local phase $\theta(t)$, rather than in terms of single photons with individual quadrature phases. This is because a low-impedance environment does not promote the granularity of light. Only observables sensitive to the statistics of light, like the $g^{(2)}(\tau)$ functions, reveal the short timescale associated with photon wavepackets.

This new point of view helps us understanding the squeezing angle $\theta(t)$ not as a property

of ponctual measurements of the quadratures, but rather as pertaining to the propagating fields $\hat{a}_{out}(t), \hat{b}_{out}(t)$. In particular we can link its value to the argument of the complex observable $\langle \hat{a}_{out}\hat{b}_{out}(t)\rangle$. We start by noting that if:

$$\arg(\langle \hat{a}\hat{b}\rangle) = \theta, \tag{4.26}$$

then:

$$\langle \hat{a}e^{-i\theta}\hat{b}\rangle \in \mathbb{R}. \tag{4.27}$$

We rewrite this expression using the quadratures with $\hat{a} = X_a + iX_{a,\frac{\pi}{2}}, \hat{b} = X_b + iX_{b,\frac{\pi}{2}}$:

$$\langle \hat{a}e^{-i\theta}\hat{b}\rangle = \langle X_a X_{b,\theta} - X_{a,\frac{\pi}{2}} X_{b,\frac{\pi}{2}+\theta}\rangle + i\langle X_a X_{b,\frac{\pi}{2}+\theta} - X_{a,\frac{\pi}{2}} X_{b,\theta}\rangle. \tag{4.28}$$

From (4.27), we know that the last term is zero. The first term can be linked to the variance of linear combinations of a, b quadratures:

$$\Delta\left(\frac{X_a \pm X_{b,\theta}}{\sqrt{2}}\right)^2 = \frac{\Delta X_a^2 + \Delta X_{b,\theta}^2}{2} \pm \langle X_a X_{b,\theta}\rangle \tag{4.29}$$

$$\Delta\left(\frac{X_{a,\frac{\pi}{2}} \pm X_{b,\frac{\pi}{2}+\theta}}{\sqrt{2}}\right)^2 = \frac{\Delta X_{a,\frac{\pi}{2}}^2 + \Delta X_{b,\frac{\pi}{2}+\theta}^2}{2} \pm \langle X_{a,\frac{\pi}{2}} X_{b,\frac{\pi}{2}+\theta}\rangle. \tag{4.30}$$

For a pure two-mode squeezed state, the right choice of quadrature phase θ and $\pm$ sign of the linear combination reveals squeezing below the vacuum level. This means that the squeezing angle θ of a and b appears directly in the phase of $\langle \hat{a}\ \hat{b}\rangle$.

This phase is simply the sum of the phases of $\hat{a}$ and $\hat{b}$. In the meantime the phases of a and b alone are random, with $\langle \hat{a}\rangle = \langle \hat{b}\rangle = 0$. This is the essence of the non-local entanglement of the two fields: if we were to measure the local phases of the signals $\arg(\langle \hat{a}\rangle), \arg(\langle \hat{b}\rangle)$, we would find only random noise, averaging to zero, while a joint measurement would yield always the same value for the sum of the phases: θ.

If the phase across the junction was fixed, the sum of the phases of the two emitted fields would stay constant through time. The finite coherence time of $\theta(t)$ leads to a finite coherence length of the two propagating beams of figure 4.9. This means that we cannot measure and average the sum of the phases of $\hat{a}_{out}(t), \hat{b}_{out}(t)$ longer than the θ coherence time, as it averages down to zero. However, we can build a correlation function that reveals the existence of these phase correlations over a finite time:

$$g_\phi^{(2)}(\tau) = \frac{\langle \hat{a}_{out}^\dagger \hat{b}_{out}^\dagger(x,t)\hat{a}_{out}\hat{b}_{out}(x-c\tau,t)\rangle}{\langle \hat{a}_{out}^\dagger \hat{a}_{out}\rangle\langle \hat{b}_{out}^\dagger \hat{b}_{out}\rangle} = \frac{\langle \hat{a}_{out}^\dagger \hat{b}_{out}^\dagger(t)\hat{a}_{out}\hat{b}_{out}(t+\tau)\rangle}{\langle \hat{a}_{out}^\dagger \hat{a}_{out}\rangle\langle \hat{b}_{out}^\dagger \hat{b}_{out}\rangle}, \tag{4.31}$$

where we used the invariance of the field through propagation to map observables taken at different positions into a measurement of the same observable at different times. The input-output relations link this correlator to the field inside the cavities:

$$g_\phi^{(2)}(\tau) = \frac{\langle \hat{a}^\dagger \hat{b}^\dagger(t)\hat{a}\hat{b}(t+\tau)\rangle}{\langle \hat{a}^\dagger \hat{a}\rangle\langle \hat{b}^\dagger \hat{b}\rangle}. \tag{4.32}$$

Contrary to the value of the squeezing angle or the $\langle \hat{a}\hat{b}\rangle$ correlator, $g_\phi^{(2)}$ does not average to zero when θ drifts randomly. Consider two times values t_1, t_2 such that $|t_2 - t_1| \gg \sigma_t$,

i.e separated by such a long time that $\theta(t_1)$ and $\theta(t_2)$ are completely uncorrelated. Then for short times $\tau \ll \sigma_t$:

$$\hat{a}^\dagger\hat{b}^\dagger(t_1)\hat{a}\hat{b}(t_1+\tau) \propto e^{-i\delta\omega(t_1)\times t_1} e^{i\delta(t_1+\tau)\times(t_1+\tau)} \simeq e^{i\delta\omega(t_1)\times\tau}, \tag{4.33}$$

while:

$$\hat{a}^\dagger\hat{b}^\dagger(t_2)\hat{a}\hat{b}(t_2+\tau) \propto e^{i\delta\omega(t_2)\times\tau}. \tag{4.34}$$

Averaged together, these two measurements of $\hat{a}^\dagger\hat{b}^\dagger(t)\hat{a}\hat{b}(t+\tau)$ yield constructive interferences for $\tau \leq \langle\delta\omega\rangle^{-1} \simeq 125$ ns. By looking at a higher order correlation function, including a conjugated $a^\dagger\hat{b}^\dagger(t)$ term, we are compensating for the phase drift between times t_1 and t_2. In a sense $a^\dagger\hat{b}^\dagger(t)$ is used as a local phase reference to demodulate $\hat{a}\hat{b}(t+\tau)$. We then expect $g^{(2)}_\phi(\tau)$ to average to a finite value, despite the drifting of the squeezing angle during the measurement.

Link with the Franson two-photon interferometer

The phase correlation function $g^{(2)}_\phi(\tau)$ appeared for the first time in the description of a new type of two-photon interferometer [106] due to Franson. In a Franson interferometer, the light source is an atom with three energy levels g, e, f, with $E_f > E_e > E_g$, where $E_i = \langle i|\hat{H}|i\rangle$ is the energy of the i state (Fig.4.10). These states also have different lifetimes, with the e level being much more short-lived than the f and g levels: $\tau_e \ll \tau_f, \tau_g$. Following Heisenberg uncertainty principle, this implies that the energy of the atom in the e state is less defined than in the f and g levels: $\Delta E_e \simeq \hbar/\tau_e \gg \Delta E_f, \Delta E_g$.

The experiment starts with the atom in the doubly excited state f. In a typical time τ_f, it relaxes to state e while emitting a first photon at frequency $\omega_{fe} = (E_f - E_e)/\hbar$. After a much shorter time τ_e, the atom emits a second photon at $\omega_{eg} = (E_e - E_g)/\hbar$ while relaxing to the ground state g. The two photons are then in a time-frequency entangled state: because both f and g are long-lived, the total energy released by the atom $E_f - E_g$ is well-defined. On the other hand the energy of each photon is less well-defined: $\Delta(E_f - E_e)^2 \simeq \Delta(E_e - E_g)^2 \simeq \Delta E_e^2 \gg \Delta(E_f - E_g)^2$.

In this situation, the frequency of each photon is ill-defined, while their sum is well-known. As the atom relaxes in a coherent process, the two propagating photons are in an entangled EPR state, where only a shared observable (the sum of their frequencies) has a physical meaning, while local measurements of ω_{fe} and ω_{eg} yield random results.

This non-local frequency entanglement is mirrored by a time-domain entanglement: because f is long-lived, there is a considerable uncertainty on the exact moment at which the first photon is emitted. However we know that the second photon is emitted immediately after, as $\tau_e \ll \tau_f$. Each photon is then in a highly delocalized state, with a position uncertainty of the order of $\Delta x^{(1)} \simeq c \times \tau_f$. But immediately after one photon has been detected, the position of the second one is instantly known with a precision of $\Delta x^{(2)} \simeq c \times \tau_e \ll \Delta x^{(1)}$. The complementarity of entanglement between conjugated variables (such as time and energy, or position and momentum) is again a feature of EPR states.

In the original experiment proposal by Franson, each photon is routed towards an imbalanced Mach-Zehnder interferometer (MZI) (Fig.4.10). The difference of length D

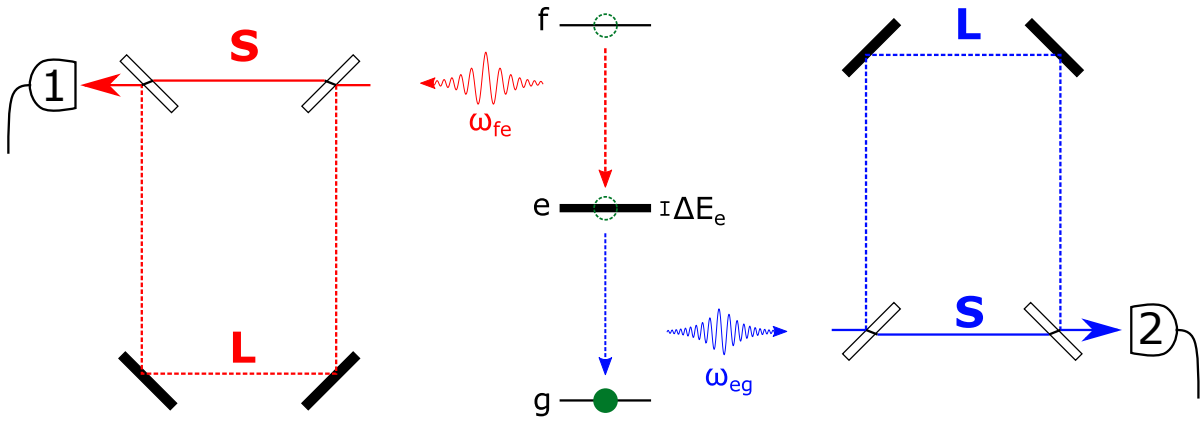

Figure 4.10: Original Franson experiment. An atom (green dot) undergoes a relaxation cascade, emitting successively two photons (red and blue wavepackets). Each photon is routed towards an unbalanced Mach-Zehnder interferometer. The imbalance of the short (S) and long (L) paths is larger than the one-photon coherence length. Nevertheless, coincidences of the detection rates at photo-counters (1) and (2) reveal non-classical two-photon coherence.

between the short (S) and long (L) paths yields as time delay $\tau = D/c$, chosen such that: $\tau_e \ll \tau \ll \tau_f$. Consider the first photon from the emitted pair, carried by a propagating mode $\hat{a}(x,t)$. Its wavefunction at the detector is the sum of two probability amplitudes, associated with the photon travelling either through the short or the long path:

$$\hat{a}(x = x_{\mathrm{det}_1}, t) = \frac{\hat{a}_S(t) + \hat{a}_L(t)}{\sqrt{2}} = \frac{\hat{a}e^{-i\omega_{fe}t} + \hat{a}e^{-i\omega_{fe}(t-\tau)}}{\sqrt{2}} \tag{4.35}$$

The (L) amplitude shows an additional phase factor, due to a longer propagation time. As $\Delta\omega_{fe} \simeq 1/\tau_e \gg 1/\tau$, this phase fluctuates randomly, so that there are no stationary interferences of the two amplitudes. The final detection rate at photocounter (1) reads:

$$p^{(1)} = \langle \hat{a}^\dagger \hat{a}(x_{\mathrm{det}_1}, t)\rangle = \frac{\langle \hat{a}_S^\dagger \hat{a}_S(t)\rangle + \langle \hat{a}_L^\dagger \hat{a}_L(t)\rangle}{2} = \langle \hat{a}^\dagger \hat{a}\rangle. \tag{4.36}$$

The condition $\tau_e \ll \tau$ hence ensures that there is no single-photon coherence in the MZI. Same goes for the second photon at ω_{eg}, carried by a mode $\hat{b}$.

If the two photocounters "click" at different moments, it means that the two photons took different paths: one went in the short arm, and the other in the long arm of its MZI. These events are discarded as they do not lead to quantum interference. On the contrary if the two detectors register a photon at the same time, it means that the two photons made the same choice. Now as $\tau \ll \tau_f \simeq \Delta x_1/c$, events where the pair travelled through both short or both long arms are indistinguishable. The photon pair detection rate is then:

$$\begin{aligned} p^{(1)\&(2)} &= \langle \hat{a}^\dagger \hat{a}(x_{\mathrm{det}_1}, t)\hat{b}^\dagger \hat{b}(x_{\mathrm{det}_2}, t)\rangle \\ &= \frac{\langle \hat{a}_S^\dagger \hat{a}_S \hat{b}_S^\dagger \hat{b}_S\rangle}{4} + \frac{\langle \hat{a}_L^\dagger \hat{a}_L \hat{b}_L^\dagger \hat{b}_L\rangle}{4} + \frac{\langle \hat{a}_L^\dagger \hat{a}_S \hat{b}_L^\dagger \hat{b}_S\rangle}{4} + \frac{\langle \hat{a}_S^\dagger \hat{a}_L \hat{b}_S^\dagger \hat{b}_L\rangle}{4} \\ &= \left[\frac{\langle \hat{a}^\dagger \hat{a}\hat{b}^\dagger \hat{b}\rangle}{4} + \frac{\langle \hat{a}^\dagger(t-\tau)\hat{a}(t)\hat{b}^\dagger(t-\tau)\hat{b}(t)\rangle}{4}\right] + \text{h.c.} \end{aligned} \tag{4.37}$$

The second term is the $g_\phi^{(2)}(\tau)$ 2-photon phase coherence function (4.32). It leads to interferences in the coincidence count, which can be either reduced or enhanced compared

to the coincidence count for photons emitted independently:

$$p^{(1)\&(2)} = \langle \hat{a}^\dagger \hat{a} \hat{b}^\dagger \hat{b} \rangle \times \frac{1 + \cos\left((\omega_{fe} + \omega_{eg}) \times \tau\right)}{2} \tag{4.38}$$

The Franson interferometer illustrates how a bipartite system can exhibit two-photon coherence effect, in settings where there is no single-photon coherence. Franson advocated it as a tool to study the non-locality of quantum mechanics, as a change of the length D_1 of interferometer (1) should affect instantly the coincidence count at interferometer (2). Despite his affirmation, it is still up to debate wether or not this kind of experiment could show a violation of Bell's inequalities [107].

Entanglement witness for correlated beams of light

In the ICPT experiment that we are considering, the entangled subsystems are not single photons but rather continuous beams of light. As discussed before, the Wigner function of two-mode squeezed state is a gaussian function of the quadratures X_a, P_a, X_b, P_b. It is always positive, and as such can never lead to a violation of Bell's inequality.

Nevertheless, we learn from the Franson experiment that the entanglement of the a and b mode can also be expressed as a non-local relation for the instantaneous frequencies of the propagating wavepackets. We can link this relation to the ICPT mechanism for 2-photon processes. Each tunneling event generates electromagnetic excitations in the environment of the junction with a total energy $2eV$. In the 2-photon case, this energy can be shared among a continuum of pairs of modes.

The $P(E)$ theory yields the emission rate spectral density (4.1), which is a quantity averaged over many tunneling events. The equality $S_P^{(2)}(\omega) = S_P^{(2)}(\omega_J - \omega)$ indicates that photons tend to be created by pairs, with $\langle \hat{a}^\dagger_{out} \hat{a}_{out}(\omega) \rangle = \langle \hat{b}^\dagger_{out} \hat{b}_{out}(\omega_J - \omega) \rangle$, but tells nothing about the coherence between these photon pairs. A more complete treatment (detailed in section 4.1.3) shows that the coherent 2-mode drive actually creates a **quantum superposition** of all the photon pair states of the outgoing radiation whose sum of frequency is equal to ω_J.

The instantaneous fields $\hat{a}_{out}(t) = \int_0^\infty \hat{a}_{out}(\omega) \times e^{-i\omega t} \frac{d\omega}{2\pi}$ and $\hat{b}_{out}(t) = \int_0^\infty \hat{b}_{out}(\omega) \times e^{-i\omega t} \frac{d\omega}{2\pi}$ thus have an ill-defined frequency. On the other hand the sum of their instantaneous frequency is much better defined, as: $\langle \hat{a}_{out} \hat{b}_{out}(t) \rangle \propto e^{-i\omega_J t}$. This works because all frequency components of $\hat{a}_{out}$ and $\hat{b}_{out}(t)$ agree on the values of ω_J and of the squeezing angle θ.

Furthermore, the Franson experiment teaches us that entanglement between the two fields is characterized by having two-photon coherence in the absence of single-photon coherence. The long-lived value of the sum of frequencies of the two fields is revealed within the phase correlation function $g_\phi^{(2)}(\tau)$(4.32). The short phase coherence time of each field (or, in other terms, its large frequency uncertainty) appears in the population $g^{(2)}(\tau)$ functions, which indicate fluctuations of the emission rates on the short timescale κ^{-1} (see the inset of figure 4.8).

These two kinds of correlation functions can be combined to yield an **entanglement**

witness for the two beams. Following the work of [108], the inequality:

$$|\langle A_1 A_2 B_1 B_2\rangle_{\text{sep.}}|^2 \leq \langle A_1 A_1^\dagger B_2^\dagger B_2\rangle_{\text{sep.}} \times \langle A_2^\dagger A_2 B_1 B_1^\dagger\rangle_{\text{sep.}} \tag{4.39}$$

is valid for all **separable states** of a bipartite system $\{a \otimes b\}$, where the operators A_i (resp. B_i) act only on subsystem a (resp. b). For two beams of light in a separable state, we can thus write:

$$\begin{gathered} |\langle \hat{a}_{out}^\dagger(x_1,t)\hat{a}_{out}(x_2,t)\hat{b}_{out}^\dagger(x_1,t)\hat{b}_{out}(x_2,t)\rangle_{\text{sep.}}|^2 \\ \leq \\ \langle \hat{a}_{out}^\dagger\hat{a}_{out}(x_1,t)\hat{b}_{out}^\dagger\hat{b}_{out}(x_2,t)\rangle_{\text{sep.}} \times \langle \hat{a}_{out}^\dagger\hat{a}_{out}(x_2,t)\hat{b}_{out}^\dagger\hat{b}_{out}(x_1,t)\rangle_{\text{sep.}}. \end{gathered} \tag{4.40}$$

This expression means that for separable states, the correlation between the sum of the phases of the fields measured at two different points of space (x_1, x_2) is smaller than the correlation between the populations of the two beams, taken at these points. As in (4.31), we can map the position difference $x_2 - x_1$ onto a time delay $\tau = (x_2 - x_1)/c$, yielding after normalization:

$$|g_\phi^{(2)}(\tau)_{\text{sep.}}|^2 \leq g_{ab}^{(2)}(\tau)_{\text{sep.}} \times g_{ab}^{(2)}(-\tau)_{\text{sep.}}. \tag{4.41}$$

As this inequality is true for any separable state, its violation provides an entanglement witness.

Probing the entanglement of the two beams

In which conditions could the two beams of light violate this inequality? As $g_\phi^{(2)}(0) = g_{ab}^{(2)}(0)$, the two correlators have the same value at $\tau = 0$. We know that in our experiment, $g_{ab}^{(2)}(\tau)$ decays to 1 in a typical time κ^{-1}. We also expect $g_\phi^{(2)}(\tau)$ to display the long-lived phase correlations between the two beams, with a phase coherence time $\sim \langle\delta\omega\rangle^{-1} \simeq 125$ ns. If this dephasing rate $\langle\delta\omega\rangle$ is smaller than the decay time of the resonators, then correlation functions measured on the two beams should break the inequality, proving their entanglement.

In other words, the two beams are entangled if the emitted photons leave the cavities before having lost their shared phase θ. This constrains both the value of the voltage noise in the experiment (which yields the dephasing rate), and the design of the two cavities (which should have short enough lifetimes).

We thus aim to prove that the two beams are entangled by measuring a violation of (4.41), using the same kind of sample as in [39] and our new linear detection setup.

The main difference between our system and true TMSV is that due to a slow dephasing of the squeezing angle, we can only prove the entanglement of a slice of length $L \sim c/\langle\delta\omega\rangle$ of the two beams. Photon pairs which are more than L apart in the beam do not agree on the value of θ (or equivalently ω_J), and do not yield a violation of (4.41).

Note also that the entanglement witness deduced from (4.39) does not apply to the state of the cavities, as it requires the operators A_1 and A_2 (resp. B_1 and B_2) to be independent. This is true for the propagating operators $\hat{a}_{out}^\dagger(x_1,t)$ and $\hat{a}_{out}(x_2,t)$ (resp. $\hat{b}_{out}^\dagger(x_1,t)$ and $\hat{b}_{out}(x_2,t)$), but not for the cavity operators, which evolve non-trivially under the Hamiltonian (4.16).

The stationary state of the cavities is indeed hard to describe. Their Wigner function is approximately the Wigner of TMSV, averaged over all values of θ. This state is *a priori* non-gaussian, so that we lack the tools to describe simply its properties. We then resort to numerical simulations to predict and interpret the values of observables.

Moreover, we know from the results of figure 4.8 that non-linear terms in the driving strength, due to the finite impedance of the resonators, make even the propagating modes depart from pure gaussianity. This is manifest in the value of $g_a^{(2)}(0), g_b^{(2)}(0) \neq 2$. However these deviations are small at moderate occupation numbers of the cavities, and more importantly they do not affect the validity of our entanglement witness, which applies to **any** state of the outgoing modes, Gaussian or not.

To complete the predictions of numerical simulations for the cavities, we derived an analytical scattering model for the propagating modes, assuming pure two-mode squeezing and perfectly gaussian states. This simple model helps us interpreting our results at low emission rates, and allow for an independent calibration of some parameters of the experiment. It also allows us to estimate the amount of instantaneous entanglement between the cavities, and to propose a value for the entanglement rate in this experiment.

4.1.3 Scattering model for a pure two-mode squeezer

We present here a simple scattering model that describes the generation of entangled beams by a pure two-mode squeezing Hamiltonian, i.e in the absence of any non-idealities such as higher-order non-linearities. Our treatment is based on the work of [7] (Chapter 5). We use the same tools (Langevin equation for the cavities fields, scattering approach...) to describe the properties of the radiation emitted by the junction, adapting it to our own implementation of the squeezing Hamiltonian. A similar work was done in [109], although not in the context of the generation of two-mode squeezing.

Scattering coefficients from the input-output model and Langevin equations

In this model, the dc-biased Josephson junction is seen as a non-degenerate parametric amplifier, which absorbs the vacuum noise incoming from the transmission lines and reflects two photons at ω_a, ω_b. The energy needed to create these photons is taken directly from the dc bias upon the inelastic tunneling of a Cooper pair. The main feature of this amplifier is its use of a **dc pump** rather than a microwave tone at $\omega_p = \omega_a + \omega_b$.

The resonance condition $2eV = \hbar(\omega_a + \omega_b)$ yields the effective Hamiltonian (4.16), valid for small modes impedances $r_a, r_b \ll 1$ and low-enough cavity occupation numbers, so that $r_a n_a, r_b n_b \ll 1$. Even in the absence of voltage noise ($\delta\omega = 0$), the bias voltage may be detuned from the sum of frequencies of the two modes. We thus consider here the more general Hamiltonian:

$$\hat{H} = -E_J^* \sqrt{r_a r_b} e^{-i\omega_J t} (\hat{a}^\dagger e^{+i\omega_a t})(\hat{b}^\dagger e^{+i\omega_b t}) + h.c = -E_J^* \sqrt{r_a r_b} e^{-i\Delta t} \hat{a}^\dagger \hat{b}^\dagger + h.c, \qquad (4.42)$$

with the detuning $\Delta = \omega_J - (\omega_a + \omega_b)$.

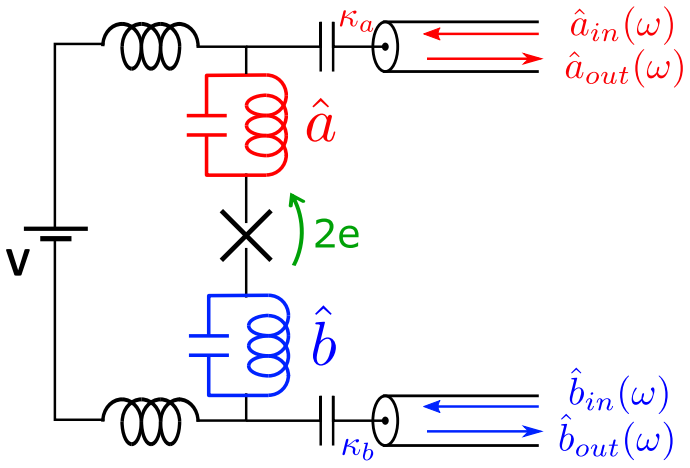

Figure 4.11: Input-output model for the two-resonator experiment. The a (b) cavity is driven by the effective Hamiltonian (4.16), is subject to incoming vacuum noise from the transmission line at frequency ω_a (ω_b), and re-emits photons in the line.

In closed systems, the time evolution of an operator $\hat{O}(t)$ under $\hat{H}$ is set by the Heisenberg equation of motion:

$$\frac{d\hat{O}}{dt} = \frac{i}{\hbar}[\hat{H}, \hat{O}]. \tag{4.43}$$

For open systems, this equation can be modified to include coupling to the environment. The evolution of the cavity fields is then given by the quantum Langevin equations:

$$\frac{d\hat{a}}{dt} = \frac{i}{\hbar}[\hat{H}, \hat{a}] - \frac{\kappa_a}{2}\hat{a} + \sqrt{\kappa}_a \hat{a}_{in} \tag{4.44}$$

$$\frac{d\hat{b}}{dt} = \frac{i}{\hbar}[\hat{H}, \hat{b}] - \frac{\kappa_b}{2}\hat{b} + \sqrt{\kappa}_b \hat{b}_{in}, \tag{4.45}$$

where the $-\frac{\kappa_a}{2}\hat{a}$ term models the leaking of the field out of resonator a at a rate κ_a, while $\sqrt{\kappa}_a \hat{a}_{in}$ describes the incoming vacuum noise from the transmission line. This non-conservative equation of motion can be derived in a Hamiltonian setting, by modelling the environment as an infinite collection of harmonic oscillators $\{\hat{a}_{in}(\omega)\}$ linearly coupled to $\hat{a}$. Tracing out the environment degrees of freedom yields (4.44). This treatment of the dissipative coupling to the environment is similar to the Caldeira-Leggett model used in the derivation of the $P(E)$ theory.

The Hamiltonian $\hat{H}$ yields the commutator:

$$\begin{aligned}
[\hat{H}, \hat{a}] &= \left[\frac{-E_J^*\sqrt{r_a r_b}}{2}(e^{-i\Delta t}\hat{a}^\dagger\hat{b}^\dagger + e^{+i\Delta t}\hat{a}\hat{b}), \hat{a}\right] \\
&= \frac{-E_J^*\sqrt{r_a r_b}}{2} e^{-i\Delta t} \times [\hat{a}^\dagger, \hat{a}] \times \hat{b}^\dagger \\
&= \frac{E_J^*\sqrt{r_a r_b}}{2} e^{-i\Delta t}\hat{b}^\dagger
\end{aligned} \tag{4.46}$$

and similarly:

$$[\hat{H}, \hat{b}] = \frac{E_J^*\sqrt{r_a r_b}}{2} e^{-i\Delta t}\hat{a}^\dagger, \tag{4.47}$$

so that the Langevin equations are coupled linear differential equations:

$$\frac{d\hat{a}}{dt} = \frac{i}{\hbar}\frac{E_J^*\sqrt{r_a r_b}}{2}e^{-i\Delta t}\hat{b}^\dagger - \frac{\kappa_a}{2}\hat{a} + \sqrt{\kappa}_a\hat{a}_{in} \tag{4.48}$$

$$\frac{d\hat{b}}{dt} = \frac{i}{\hbar}\frac{E_J^*\sqrt{r_a r_b}}{2}e^{-i\Delta t}\hat{a}^\dagger - \frac{\kappa_b}{2}\hat{b} + \sqrt{\kappa}_b\hat{b}_{in}. \tag{4.49}$$

The effective Hamiltonian $\hat{H}$ being written in the reference frame of the cavities, it does not include the EM fields energy term $\hbar\omega_a\hat{a}^\dagger\hat{a} + \hbar\omega_b\hat{b}^\dagger\hat{b}$. In the laboratory frame of reference, the fields write $\hat{a}(t)e^{-i\omega_a t} + \hat{a}^\dagger(t)e^{+i\omega_a t}$ and $\hat{b}(t)e^{-i\omega_b t} + \hat{b}^\dagger(t)e^{+i\omega_b t}$. We define the Fourier decomposition of the fields as:

$$\hat{a}(t)e^{-i\omega_a t} = \int_0^\infty a(\omega)e^{-i\omega t}\frac{d\omega}{2\pi} \Rightarrow a(\omega) = \int \hat{a}(t)e^{i(\omega-\omega_a)t}dt, \tag{4.50}$$

$$\hat{b}(t)e^{-i\omega_b t} = \int_0^\infty b(\omega')e^{-i\omega' t}\frac{d\omega'}{2\pi} \Rightarrow b(\omega') = \int \hat{b}(t)e^{i(\omega'-\omega_b)t}dt. \tag{4.51}$$

The Langevin equations write in Fourier space:

$$-i(\omega-\omega_a)a(\omega) = \frac{i}{\hbar}\frac{E_J^*\sqrt{r_a r_b}}{2}b^\dagger\big(\omega_b + \Delta - (\omega-\omega_a)\big) - \frac{\kappa_a}{2}a(\omega) + \sqrt{\kappa_a}a_{in}(\omega) \tag{4.52}$$

$$-i(\omega'-\omega_b)b(\omega') = \frac{i}{\hbar}\frac{E_J^*\sqrt{r_a r_b}}{2}a^\dagger\big(\omega_a + \Delta - (\omega'-\omega_b)\big) - \frac{\kappa_b}{2}b(\omega') + \sqrt{\kappa_b}b_{in}(\omega'). \tag{4.53}$$

We introduce the dimensionless variable:

$$\beta = \frac{E_J^*\sqrt{r_a r_b}}{\hbar\sqrt{\kappa_a\kappa_b}}. \tag{4.54}$$

which plays the role of the reduced pump amplitude of the parametric amplifier. We rewrite the system of equations, taking the complex conjugate of the second one, as:

$$0 = \left[i(\omega-\omega_a) - \frac{\kappa_a}{2}\right]a(\omega) + \frac{i\beta}{2}\sqrt{\kappa_a\kappa_b}b^\dagger(\omega_J-\omega) + \sqrt{\kappa_a}a_{in}(\omega) \tag{4.55}$$

$$0 = \left[i(\omega'-\omega_b) + \frac{\kappa_b}{2}\right]b^\dagger(\omega') + \frac{i\beta}{2}\sqrt{\kappa_a\kappa_b}a(\omega_J-\omega') - \sqrt{\kappa_b}b_{in}^\dagger(\omega') \tag{4.56}$$

We aim to eliminate the $b^\dagger(\omega_J-\omega)$ term from the expression of $a(\omega)$. For the rest of this section we set $\omega' = \omega_J - \omega$. We also introduce reduced frequencies:

$$\delta_a = 2\frac{\omega-\omega_a}{\kappa_a}, \delta_b = 2\frac{\omega'-\omega_b}{\kappa_b}, \tag{4.57}$$

We then have:

$$0 = (i\delta_a - 1)a(\omega) + i\beta\sqrt{\frac{\kappa_b}{\kappa_a}}b^\dagger(\omega') + \frac{2}{\sqrt{\kappa_a}}a_{in}(\omega) \tag{4.58}$$

$$0 = (i\delta_b + 1)b^\dagger(\omega') + i\beta\sqrt{\frac{\kappa_a}{\kappa_b}}a(\omega) - \frac{2}{\sqrt{\kappa_b}}b_{in}^\dagger(\omega'), \tag{4.59}$$

so that:

$$(1 - i\delta_a)a(\omega) = i\beta\sqrt{\frac{\kappa_b}{\kappa_a}}b^\dagger(\omega') + \frac{2}{\sqrt{\kappa_a}}a_{in}(\omega) \tag{4.60}$$

$$\begin{aligned}\Rightarrow (1 - i\delta_a)(1 + i\delta_b)a(\omega) &= (1 + i\delta_b)\left[i\beta\sqrt{\frac{\kappa_b}{\kappa_a}}b^\dagger(\omega') + \frac{2}{\sqrt{\kappa_a}}a_{in}(\omega)\right] \\ &= \beta^2 a(\omega) + \frac{2i\beta}{\sqrt{\kappa_a}}b_{in}^\dagger(\omega') + (1 + i\delta_b)\frac{2}{\sqrt{\kappa_a}}a_{in}(\omega)\end{aligned} \tag{4.61}$$

$$\Rightarrow \left((1 - i\delta_a)(1 + i\delta_b) - \beta^2\right)a(\omega) = \frac{2i\beta}{\sqrt{\kappa_a}}b_{in}^\dagger(\omega') + (1 + i\delta_b)\frac{2}{\sqrt{\kappa_a}}a_{in}(\omega), \tag{4.62}$$

where we used (4.59) to substitute $b^\dagger(\omega')$ in (4.61). Now the Fourier component $a(\omega)$ of the cavity field operator $\hat{a}(t)$ depends only on the incoming fields $a_{in}(\omega)$ and $b_{in}^\dagger(\omega')$. A similar expression can be obtained for $b(\omega')$:

$$\left((1 - i\delta_b)(1 + i\delta_a) - \beta^2\right)b(\omega') = \frac{2i\beta}{\sqrt{\kappa_b}}a_{in}^\dagger(\omega) + (1 + i\delta_a)\frac{2}{\sqrt{\kappa_b}}b_{in}(\omega'). \tag{4.63}$$

Let us discuss this result. In the absence of tunnel coupling through the junction, $E_J^* = 0$ so that $\beta = 0$. Then we have the decoupled equations:

$$\sqrt{\kappa_a}a(\omega) = \frac{2}{1 - 2i\frac{\omega - \omega_a}{\kappa_a}}a_{in}(\omega) \tag{4.64}$$

$$\sqrt{\kappa_b}b(\omega') = \frac{2}{1 - 2i\frac{\omega' - \omega_b}{\kappa_b}}b_{in}(\omega'). \tag{4.65}$$

The field inside cavity a is simply given by the incoming field $a_{in}(\omega)$ times a transmission factor $\frac{2}{\sqrt{\kappa_a} - 2i\frac{\omega - \omega_a}{\sqrt{\kappa_a}}}$. This is what we expect for a resonator connected at the output of a transmission line. If the $a_{in}(\omega)$ operators carry only vacuum noise, then $\hat{a}(t) = \int_0^\infty a(\omega)e^{-i(\omega - \omega_a)t}\frac{d\omega}{2\pi}$ is also in the vacuum state:

$$\langle\hat{a}^\dagger\hat{a}\rangle = \int_0^\infty \langle a^\dagger a(\omega)\rangle\frac{d\omega}{2\pi} = \int_0^\infty \left|\frac{2}{\sqrt{\kappa_a} - 2i\frac{\omega - \omega_a}{\sqrt{\kappa_a}}}\right|^2 \langle a_{in}^\dagger a_{in}(\omega)\rangle\frac{d\omega}{2\pi} = 0, \tag{4.66}$$

and similarly for $\hat{b}(t)$. On the other hand as soon as $E_J^* \neq 0$, $a(\omega)$ depends also on the field incoming from the b transmission line at frequency ω', while $b(\omega')$ becomes dependent on $a_{in}(\omega')$. There are thus correlations between the fields in the two cavities, associated with the creation of photons in the resonators **even if** $a_{in}(\omega)$ **and** $b_{in}(\omega')$ **are in the vacuum state**:

$$\langle a^\dagger a(\omega)\rangle \propto \langle b_{in}b_{in}^\dagger(\omega')\rangle = 1 + \langle b_{in}^\dagger b_{in}(\omega')\rangle \neq 0 \tag{4.67}$$

$$\Rightarrow \langle\hat{a}^\dagger\hat{a}\rangle = \int_0^\infty \langle a^\dagger a(\omega)\rangle\frac{d\omega}{2\pi} \neq 0, \tag{4.68}$$

and similarly for $\hat{b}(t)$. In this picture, the vacuum noise carried by $a_{in}(\omega)$ and $b_{in}(\omega')$ impinging on the junction prompts the inelastic tunneling of Cooper pairs and correlated emission of photons in the two modes at the same time. These photons eventually leave the cavities, feeding the transmission lines with signals carried by the output modes

$a_{out}(\omega), b_{out}(\omega')$. To describe the state of these modes, we now write the input-output relations [59] in the frequency domain:

$$\sqrt{\kappa}a(\omega) = a_{in}(\omega) + a_{out}(\omega) \Rightarrow a_{out}(\omega) = \sqrt{\kappa}a(\omega) - a_{in}(\omega) \tag{4.69}$$

$$\sqrt{\kappa}b(\omega) = b_{in}(\omega) + b_{out}(\omega) \Rightarrow b_{out}(\omega) = \sqrt{\kappa}b(\omega) - b_{in}(\omega). \tag{4.70}$$

We can finally write a scattering relation for the output operators as a function of the input operators:

$$\begin{bmatrix} a_{out}(\omega) \\ b^{\dagger}_{out}(\omega') \end{bmatrix} = \begin{bmatrix} \mu_a(\omega) & \nu_a(\omega) \\ \nu^*_b(\omega') & \mu^*_b(\omega') \end{bmatrix} \times \begin{bmatrix} a_{in}(\omega) \\ b^{\dagger}_{in}(\omega') \end{bmatrix}, \tag{4.71}$$

with the scattering coefficients:

$$\mu_a(\omega) = \frac{(1+i\delta_a)(1+i\delta_b)+\beta^2}{(1-i\delta_a)(1+i\delta_b)-\beta^2}, \tag{4.72}$$

$$\mu^*_b(\omega') = \frac{(1-i\delta_a)(1-i\delta_b)+\beta^2}{(1-i\delta_a)(1+i\delta_b)-\beta^2}, \tag{4.73}$$

$$\nu_a(\omega) = \frac{2i\beta}{(1-i\delta_a)(1+i\delta_b)-\beta^2}, \tag{4.74}$$

$$\nu^*_b(\omega') = \frac{-2i\beta}{(1-i\delta_a)(1+i\delta_b)-\beta^2}. \tag{4.75}$$

Gain and emission spectra of the non-degenerate parametric amplifier

The scattering formalism above is reminiscent of the Caves model of a quantum linear amplifier [81]. Incoming signals carried by $a_{in}(\omega)$ are reflected by the junction as $a_{out}(\omega) = \mu_a(\omega)a_{in}(\omega) + \nu_a(\omega)b^{\dagger}_{in}(\omega')$. The coefficient $\mu_a(\omega)$ is the *amplitude gain* of this parametric amplifier, $\nu_a(\omega)$ is the *cross-gain* and $b^{\dagger}_{in}(\omega')$ is the *idler mode*. The idler is responsible for the unavoidable noise added by the amplification process. If $b^{\dagger}_{in}(\omega')$ is in the vacuum state, then the amplifier is quantum-limited.

In a similar fashion $b_{out}(\omega')$ is an amplified version of $b_{in}(\omega')$, where $a_{in}(\omega)$ plays the role of the idler. As the $a_{out}(\omega)$ and $b_{out}(\omega')$ inhabit different frequency bands and separate transmission lines, the amplifier is said to be spatially and temporally **non-degenerate**. This means that the modes never overlap, and can thus demonstrate non-local entanglement.

The **power gains** $G_a(\omega) = |\mu_a(\omega)|^2$ and $G_b(\omega') = |\mu_b(\omega')|^2$ depend on the decay rate of the resonators κ_a, κ_b, the detuning Δ, and the reduced pump amplitude β.

In the simple case of zero detuning $\Delta = 0$, the on-resonance gain is:

$$G_a(\omega_a) = G_b(\omega_b) = G(\beta) = \left(\frac{1+\beta^2}{1-\beta^2}\right)^2, \tag{4.76}$$

which diverges for $\beta \to \beta^{\circ} = 1$. This limit sets the threshold of the parametric transition of the amplifier, where the driving strength $E^*_J\sqrt{r_a r_b}$ overcomes the decay rate $\sqrt{\kappa_a \kappa_b}$. The parameter $C = \beta^2$ is also known as the *cooperativity* of the amplifier.

At a finite detuning $\Delta \neq 0$, the divergence arises for a higher pump strength [110]:

$$\beta^{\circ}(\Delta) = \sqrt{1 + \left(\frac{2\Delta}{\kappa_a + \kappa_b}\right)^2}. \tag{4.77}$$

In the limit of $\beta \simeq \beta^{\circ}$, the gains have approximately a Lorentzian shape, with a 3dB-bandwidth given by:

$$\Delta\Omega_G(\beta) \simeq \frac{2\kappa_a\kappa_b}{\kappa_a + \kappa_b} \times \frac{1-\beta^2}{1+\beta^2} = \frac{\kappa_{eff}}{\sqrt{G(\beta)}}, \tag{4.78}$$

with the effective decay rate $\kappa_{eff} = \frac{2\kappa_a\kappa_b}{\kappa_a+\kappa_b}$. This is the well-known constant amplitude gain×bandwidth product rule for amplifiers.

The **photon emission spectral density** is given by:

$$\begin{aligned}
\gamma_a(\omega) &= \langle a^{\dagger}_{out} a_{out}(\omega)\rangle \\
&= |\mu_a(\omega)|^2 \langle a^{\dagger}_{in} a_{in}(\omega)\rangle + |\nu_a(\omega)|^2 \langle b_{in} b^{\dagger}_{in}(\omega')\rangle \\
&= |\mu_a(\omega)|^2 \langle a^{\dagger}_{in} a_{in}(\omega)\rangle + |\nu_a(\omega)|^2 \left(\langle b^{\dagger}_{in} b_{in}(\omega')\rangle + 1\right),
\end{aligned} \tag{4.79}$$

$$\gamma_b(\omega') = |\mu_b(\omega')|^2 \langle b^{\dagger}_{in} b_{in}(\omega')\rangle + |\nu_b(\omega')|^2 \left(\langle a^{\dagger}_{in} a_{in}(\omega)\rangle + 1\right). \tag{4.80}$$

Even if $a_{in}(\omega)$ and $b_{in}(\omega')$ are in the vacuum state, the junction radiates light, with:

$$\gamma_a(\omega) = |\nu_a(\omega)|^2 = |\mu_a(\omega)|^2 - 1 = G_a(\omega) - 1, \tag{4.81}$$

$$\gamma_b(\omega') = |\nu_b(\omega')|^2 = |\mu_b(\omega')|^2 - 1 = G_b(\omega') - 1. \tag{4.82}$$

where the last equality follows from the symplectic character of the scattering matrix. Thus in the limit of high gain $\beta \simeq \beta^{\circ}$, the emission spectral density follows closely the power gain, with a FWHM given by the 3dB-bandwidth of the gain (Fig.4.12.b). In the weak pumping limit $\beta \ll 1$, the gain is approximately constant $G(\omega) \simeq 1$, i.e the junction simply reflects incoming signals without amplification. In this limit, the shape of the emission PSD is:

$$\gamma_a(\omega) = |\nu_a(\omega)|^2 \simeq \frac{4\beta^2}{(1+\delta_a^2)(1+\delta_b^2)} = \frac{(2\pi E_J^*)^2}{\hbar\omega_a \hbar\omega_b} \frac{Re[Z(\omega)]}{R_Q} \frac{Re[Z(\omega_J - \omega)]}{R_Q}, \tag{4.83}$$

which coincides with the $P(E)$ expression (2.75) for high quality factors of the modes and small detuning. The emission spectra then have the shape of a Lorentzian function squared, with a FWHM $\kappa' \simeq \sqrt{\sqrt{2}-1}\kappa_{eff}$ (Fig.4.12.a).

To illustrate this behaviour, we plot in figure 4.12 the power gain and emission spectra around ω_a in the simple case of symmetric cavities $\kappa_a = \kappa_b$ and zero detuning, for two different values of β.

The integral of the emission spectra yields the total photon pair emission rate Γ:

$$\Gamma = \int \gamma_a(\omega) d\omega = \int \gamma_b(\omega') d\omega'. \tag{4.84}$$

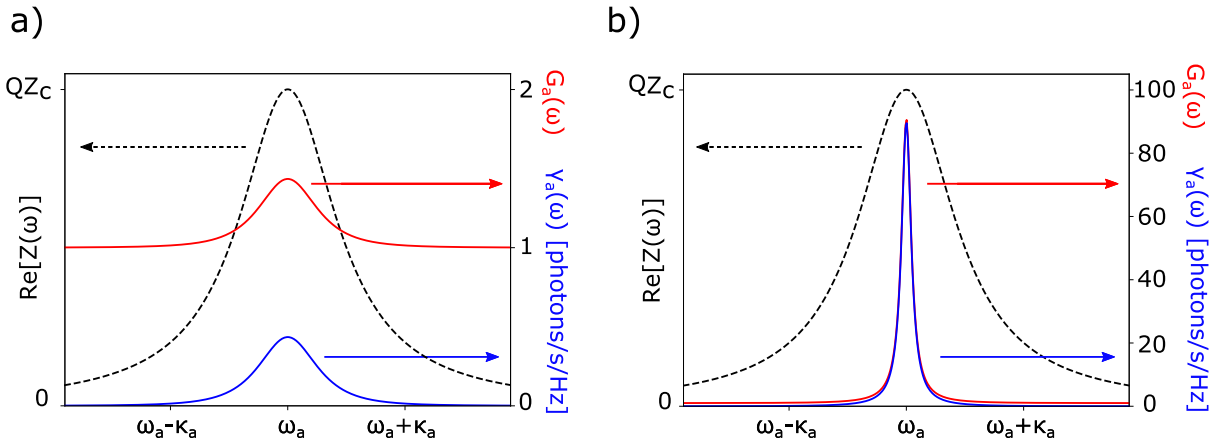

Figure 4.12: a) Power gain $G_a(\omega)$ (red curve) and photon emission spectral density $\gamma_a(\omega)$ (blue curve) for a pump strength $\beta = 0.3$, with zero detuning and equal leak rates of the cavities, plotted along the $Re[Z(\omega)]$ of the environment (dashed black). At this low pump value, the emission spectra follow the prediction of the $P(E)$ theory, with a FWHM $\sqrt{\sqrt{2}-1}\kappa_a \simeq 0.64\times\kappa_a$. b) Same curves for a high pumping strength $\beta = 0.9$. The emission spectrum is much narrower, with a FWHM$\simeq \kappa_a/\sqrt{G_a(\omega_a)} \simeq \kappa_a/10$. The gain $G_b(\omega')$ and emission spectra $\gamma_(\omega')$ around ω_b have a similar behaviour.

which yields:

$$\Gamma = \frac{\kappa_{eff}\beta^2}{2\left(1-\beta^2+\left(\frac{2\Delta}{\kappa_a+\kappa_b}\right)^2\right)} = \frac{\kappa_{eff}\beta^2}{2(\beta^{\circ 2}-\beta^2)}. \tag{4.85}$$

From this rate we can compute the occupation number of the two cavities:

$$\bar{n}_a = \langle \hat{a}^\dagger \hat{a} \rangle = \frac{\Gamma}{\kappa_a} = \frac{\beta^2}{(1+\frac{\kappa_a}{\kappa_a})(\beta^{\circ 2}-\beta^2)} \tag{4.86}$$

$$\bar{n}_b = \langle \hat{b}^\dagger \hat{b} \rangle = \frac{\Gamma}{\kappa_b} = \frac{\beta^2}{(1+\frac{\kappa_b}{\kappa_a})(\beta^{\circ 2}-\beta^2)}. \tag{4.87}$$

Like the power gain, the occupation numbers diverge at the threshold of the parametric transition $\beta \to \beta^\circ$. Note that while the emission rates $\bar{n}_a\kappa_a$ and $\bar{n}_b\kappa_b$ are always equal, the population of the two cavities differ if $\kappa_a \neq \kappa_b$.

Two-mode squeezing

When the incoming modes $a_{in}(\omega), b_{in}(\omega')$ are in the vacuum state, the non-degenerate parametric amplifier squeezes the cavity field and re-emit two-mode squeezed vacuum over the outgoing modes $a_{out}(\omega), b_{out}(\omega')$. The degree of squeezing depends on the value of the scattering coefficients.

By redefining the phase origin for the field operators at every frequency, the scattering matrix can be put under the simpler form:

$$\begin{bmatrix} a_{out}(\omega) \\ b^\dagger_{out}(\omega') \end{bmatrix} = \begin{bmatrix} \cosh(r[\omega]) & e^{i\theta[\omega]}\sinh(r[\omega]) \\ e^{-i\theta[\omega']}\sinh(r[\omega']) & \cosh(r[\omega']) \end{bmatrix} \times \begin{bmatrix} a_{in}(\omega) \\ b^\dagger_{in}(\omega') \end{bmatrix}. \tag{4.88}$$

Then one has:

$$a_{out}(\omega) \pm e^{i\theta[\omega]} b^\dagger_{out}(\omega') = e^{\pm r[\omega]} \times \left(a_{in}(\omega) \pm e^{i\theta[\omega]} b^\dagger_{in}(\omega')\right). \tag{4.89}$$

Taking the real part of both sides yields:

$$X_a^{out}(\omega) \pm X_{b,\theta[\omega]}^{out}(\omega') = e^{\pm r[\omega]} \times \left(X_a^{in}(\omega) \pm X_{b,\theta[\omega]}^{in}(\omega')\right), \tag{4.90}$$

The variance of the asymmetric combination $X_a^{out}(\omega) - X_{b,\theta[\omega]}^{out}(\omega')$ is then squeezed below the vacuum level by a factor $e^{2r[\omega]}$, while the symmetric combination $X_a^{out}(\omega) + X_{b,\theta[\omega]}^{out}(\omega')$ is anti-squeezed.

The squeezing parameter $r[\omega]$ and the squeezing angle $\theta[\omega]$ depend on the frequency ω. As $\gamma_a(\omega) = |\nu_a(\omega)|^2 = \sinh(r[\omega])^2$, $r[\omega]$ can be linked to the emission spectra:

$$r[\omega] = \sinh^{-1}(\sqrt{\gamma_a(\omega)}) = \ln(\sqrt{\gamma_a(\omega)+1} + \sqrt{\gamma_a(\omega)}). \tag{4.91}$$

The spectral density of squeezing is thus higher where the emission rate is the strongest, i.e on resonance for $\Delta = 0$. We then have $r[\omega_a] = \ln\left(\frac{1+\beta}{1-\beta}\right)$. Away from the resonance, where the gain $G(\omega)$ drops to 1, the squeezing vanishes.

As the emission rate diverges as $\beta \to \beta^\circ$, the degree of squeezing could in theory be made arbitrary large. In practice, non-idealities such as higher-order non-linearities of the Hamiltonian limit the degree of squeezing. In the case of the dc-biased junction, we estimate that non-linear terms in the Hamiltonian (4.3) are the main limitations to the maximum squeezing. These terms become relevant as soon as $\bar{n}_a \sim 1/r_a$. A typical $Z_c = 100\ \Omega$ resonator yields $r_a \simeq 0.05$, so $\bar{n}_a$ should be kept well below 20, or equivalently $G_a(\omega)$ well below 38 dB[3].

For symmetric cavities $\kappa_a = \kappa_b$, we have $\beta^2 = \frac{2\bar{n}_a}{1+2\bar{n}_a}$. The emission rate on resonance is then $\gamma_a(\omega_a) = 8\bar{n}_a(1+2\bar{n}_a)$. A conservative $\bar{n}_a = 2$ (with $G_a(\omega_a) \simeq 19$) leads to $\gamma_a = 80$ photons/s/Hz, and a degree of squeezing $r[\omega_a]$= 25 dB. This number could be increased by fabricating very low-impedance resonators.

By contrast, the degree of squeezing inside the cavities is limited to at most 3 dB [65]. This can be understood as a consequence of the simple input-output balance: even if the output field is infinitely squeezed, with a null variance, there is still trivial vacuum noise incoming to the cavity. The variance of the quadratures for the cavity fields is then only reduced to half the vacuum value.

Entanglement of the two-mode squeezed state

Two-mode squeezing is a manifestation of the entanglement between the modes, which can be quantified both for the cavity modes and the outgoing modes.

The logarithmic negativity (log-neg) has been proposed as a quantitative measure of the entanglement between two systems [111]. It is defined as the logarithm of the trace norm of the partially transposed density operator of the total system:

$$E_N(\rho) = \log(||\rho^{T_a}||_1) = \log(||\rho^{T_b}||_1). \tag{4.92}$$

For entangled 2-level systems (qubits), the base-2 logarithm ($\log_2$) is typically used in the definition of E_N. The log-neg is then expressed in units of entangled bits (e-bits). For

[3] In practice, if one aim to maximize the gain of this device, Z_c could easily be decreased by a factor of about 10. The constraint on the gain is then $G_a(\omega) \ll 58$ dB

continuous variables such as the electromagnetic field, it is more natural to work with the natural logarithm (ln): E_N is then expressed in e-nats, with ln(2) e-nat = 1 e-bit. It is an upper bound of the distillable entanglement, i.e the usefulness of the TMSV source for quantum information protocols [101][93].

For a pure two-mode squeezed state, E_N can be computed from the covariance matrix of the two modes [93]. We map these covariances to field operators, yielding [112]:

$$E_N[A,B] = -\ln(1 + \langle A^\dagger A\rangle + \langle B^\dagger B\rangle - \sqrt{(\langle A^\dagger A\rangle - \langle B^\dagger B\rangle)^2 - 4|\langle AB\rangle|^2}), \tag{4.93}$$

where A and B stand for the field operators of two modes, being either output modes $a_{out}(\omega), b_{out}(\omega')$ or cavity modes $\hat{a}(t), \hat{b}(t)$. It can be proven that $E_N[A,B]$ is also linked to the squeezing parameter r_{AB}, with:

$$E_N[A,B] = 2r_{AB}. \tag{4.94}$$

For a pair of *propagating modes* $a_{out}(\omega), b_{out}(\omega')$, (4.93) yields a **spectral density of log-neg**:

$$E_N[\omega,\omega'] = -\ln(1+\gamma_a(\omega)+\gamma_b(\omega') - \sqrt{(\gamma_a(\omega)-\gamma_b(\omega'))^2 - 4|\langle a_{out}(\omega)b_{out}(\omega')\rangle|^2}). \tag{4.95}$$

From the scattering matrix, we compute:

$$|\langle a_{out}(\omega)b_{out}(\omega')\rangle|^2 = |\mu_a(\omega)|^2|\nu_b(\omega)|^2 = (\gamma_a(\omega)+1)\gamma_b(\omega'). \tag{4.96}$$

As $\gamma_a(\omega) = \gamma_b(\omega')$ we get:

$$E_N[\omega] = -\ln(1 + 2\gamma_a(\omega) - 2\sqrt{(\gamma_a(\omega)+1)\gamma_a(\omega)}). \tag{4.97}$$

Assuming perfect two-mode squeezing, $E_N[\omega]$ could in principle be estimated from a measurement of the emission spectra $\gamma_a(\omega)$. Of course this would be a very crude estimation, as any non-idealities such as thermal occupation of the incoming modes, or losses in the microwave cables carrying the signals, reduce the quantum efficiency of this device.

For zero detuning, the maximum value of $E_N[\omega]$ is:

$$E_N[\omega_a] = 2r[\omega_a] = 2\ln\left(\frac{1+\beta}{1-\beta}\right). \tag{4.98}$$

It can be arbitrary large as the pumping strength approaches the threshold $\beta \to \beta^\circ$.

The amount of entanglement *inside the cavities* follows a different trend:

$$E_N^{cav} = -\ln(1 + \bar{n}_a + \bar{n}_b - \sqrt{(\bar{n}_a - \bar{n}_b)^2 + 4|\langle \hat{a}\hat{b}\rangle|^2}). \tag{4.99}$$

The last correlator can be computed either using (4.62) (4.63) and the scattering coefficients, or using the following equality:

$$|\langle \hat{a}\hat{b}\rangle|^2 = \langle \hat{a}^\dagger\hat{a}\hat{b}^\dagger\hat{b}\rangle - \langle \hat{a}^\dagger\hat{a}\rangle\langle \hat{b}^\dagger\hat{b}\rangle, \tag{4.100}$$

which is true for gaussian states of light. From the 2016 experiment 4.1.2, we know that for the cavity fields NRF = 1/2, which brings:

$$\langle \hat{a}^\dagger\hat{a}\hat{b}^\dagger\hat{b}\rangle = \bar{n}_a\bar{n}_b \times g_{ab}^{(2)}(0) = \bar{n}_a\bar{n}_b \times \left(2 + \frac{1}{\bar{n}_a + \bar{n}_b}\right), \tag{4.101}$$

so that:

$$|\langle \hat{a}\hat{b} \rangle|^2 = \bar{n}_a \bar{n}_b \times \left(1 + \frac{1}{\bar{n}_a + \bar{n}_b}\right). \tag{4.102}$$

Then we have:

$$E_N^{cav} = -\ln\left(1 + \bar{n}_a + \bar{n}_b - \sqrt{(\bar{n}_a - \bar{n}_b)^2 + 4\bar{n}_a\bar{n}_b \times \left(1 + \frac{1}{\bar{n}_a + \bar{n}_b}\right)}\right). \tag{4.103}$$

This can be expressed as a function of the pump strength and decay rates:

$$E_N^{cav} = -\ln\left(1 + \frac{\beta^2}{1-\beta^2} - \sqrt{\frac{\beta^2}{1-\beta^2}\left\{\frac{\beta^2}{1-\beta^2} + 4\frac{\kappa_a\kappa_b}{(\kappa_a+\kappa_b)^2}\right\}}\right). \tag{4.104}$$

There is a striking difference between E_N^{cav} and $E_N[\omega]$: if the cavities have very asymmetric decay rates, with e.g $\kappa_a \gg \kappa_b$, then their log-neg tends to zero, whatever the value of β. This is in contrast to $E_N[\omega]$, which can always be made arbitrary large by increasing β. In the limit $\kappa_a/\kappa_b \to \infty$ and $\beta \to \beta^\circ$, we are in a seemingly paradoxical situation where the cavities are in a separable state ($E_N^{cav} = 0$) while emitting perfectly entangled light ($E_N[\omega_a] = \infty$)!

The log-neg of the cavities is maximal in the symmetric case $\kappa_a = \kappa_b$, with:

$$E_N^{cav} = -\ln\left(1 + 2\bar{n} - 2\sqrt{\left(\bar{n} + \frac{1}{2}\right)\bar{n}}\right), \tag{4.105}$$

with $\bar{n}_a = \bar{n}_b = \bar{n}$. As $\beta \to \beta^\circ$, $\bar{n} \to \infty$, and $E_N^{cav} \to \ln(2)$ e-nats, or 1 e-bit. This is again a major difference with the entanglement of the output modes, which is unbounded. Finally the zero detuning case $\Delta = 0$ yields the simple expression:

$$E_N^{cav} = \ln(1 + \beta). \tag{4.106}$$

Defining an entanglement rate

A non-degenerate parametric amplifier is a continuous source of light in a two-mode squeezed state. It seems natural to define an **entanglement rate** to quantify the rate at which this device creates entangled photons.

In the first article describing the emission of entangled beams in the microwave range [37] (using a Josephson mixer [7]), Flurin et al. estimated this entanglement rate by multiplying the *entropy of formation* of the pair of modes $a_{out}(\omega_a), b_{out}(\omega_b)$, i.e the propagating modes with the largest entanglement, by the *dynamical bandwidth* of the power gain $G(\omega)$.

The entropy of formation E_F is an upper bound on the usable entanglement of the beams. It can be linked to the squeezing parameter:

$$\begin{aligned} E_F &= \cosh(r)^2 \times \log_2(\cosh(r)^2) - \sinh(r)^2 \times \log_2(\sinh(r)^2) \\ &= (\gamma_a + 1) \times \log_2(\gamma_a + 1) - \gamma_a \times \log_2(\gamma_a). \end{aligned} \tag{4.107}$$

It is approximately equal to E_N at large pump strength $\beta \to \beta^\circ$.

Flurin et al justify their approach by stating that the FWHM of $G(\omega)$ ($\simeq \gamma_a(\omega)$ at large pump strength) yields the inverse timescale of propagating modes. In this picture, the amplifier emits pairs of entangled wavelets containing $E_F \sim E_N[\omega_a]$ e-nats every $\Delta\Omega_G^{-1}$ seconds. Their entanglement rate is thus $E_F \times \Delta\Omega_G/2\pi$[4].

As $E_F \sim E_N[\omega_a] = 2\ln\left(\frac{1+\beta}{1-\beta}\right)$ increases with β while $\Delta\Omega_G \simeq \kappa_{eff} \times \frac{1-\beta^2}{1+\beta^2}$ decreases, this rate displays a maximum of $\simeq 0.21\ \kappa_{eff}$ e-nats/s for $\beta \simeq 0.54$. For higher pump strengths, the dynamical bandwidth reduces faster than $E_N[\omega_a]$ increases.

A more recent paper [113] suggests using the average of $E_N[\omega]$ over the emission spectra bandwidth $\Delta\Omega_E$ ($\simeq \Delta\Omega_G$ at large pump strength), instead of its maximum value $E_N[\omega_a]$. This may be a more realistic bound on the useful entanglement one can extract out of the beams, as all pairs of modes $a_{out}(\omega), b_{out}(\omega)$ do not have the same amount of log-neg (Fig.4.13.a).

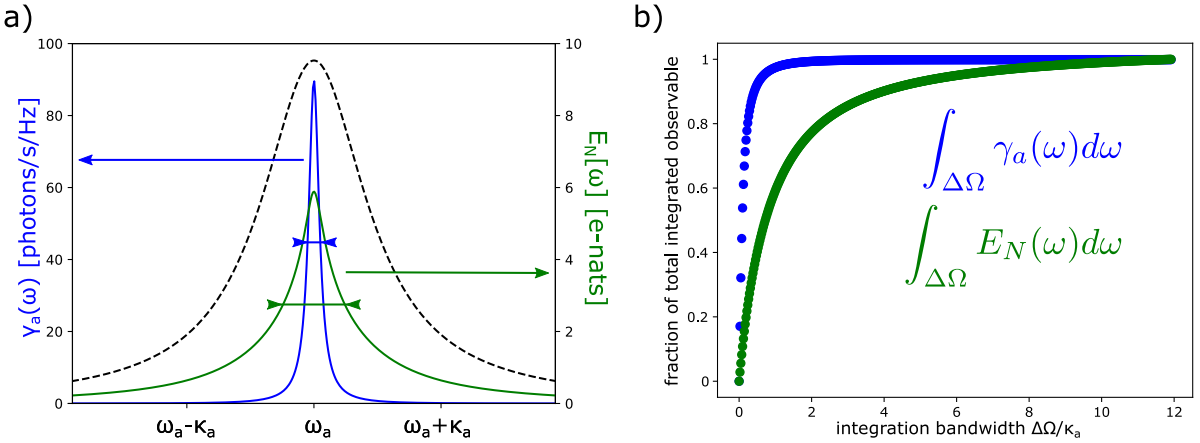

Figure 4.13: a) Emission spectrum (blue line) and log-neg spectral density (green line) for $\beta = 0.9$, plotted with $Re[Z(\omega)]$ of the environment (dashed black, same scale as figure 4.12). Here $\kappa_a = \kappa_b$ and $\Delta = 0$ for simplicity. The double-headed arrows highlight the difference of FWHM of these two curves. Flurin et al. estimate the entanglement rate by multiplying the maximum value of the log-neg, $E_N[\omega_a]$, by the FWHM of the emission spectra. The authors of [113] use the value of $E_N[\omega]$ integrated over the same FWHM. Deng et al. suggest integrating $E_N[\omega]$ over all frequencies, yielding a much larger value. b) Integrals of the emission spectra $\gamma_a(\omega)$ and the log-neg spectral density $E_N[\omega]$ over an integration bandwidth $\Delta\Omega$, for the curves of panel a). Integrating in the resonator bandwidth $\Delta\Omega = \kappa_a$ is enough to catch most of the emitted photons, but captures only about half of the total entanglement rate.

These two approaches are in a sense application-oriented, as they estimate the amount of log-neg one can extract in a practical experiment, where the measurement bandwidth is limited to typically the FWHM of the resonators. A concurrent theoretical proposal suggests a way to estimate the *total* entanglement generated by the device [112]. As the log-neg is an additive measure of entanglement, Deng et al. proposed integrating $E_N[\omega]$ over all frequencies to yield the total entanglement rate:

$$\Gamma_E = \int_0^\infty E_N[\omega] d\omega. \tag{4.108}$$

As the FWHM of $E_N[\omega]$ is larger than the FWHM of the emission rate, Γ_E is typically larger than the other estimates for the entanglement rate (Fig.4.13.b). In the simple case

[4]The use of an additional factor 2π by Flurin et al. is not justified in this wavelet picture.

of equal leak rates and zero detuning, we find:

$$\Gamma_E = \beta\kappa. \tag{4.109}$$

As $\beta \to 1$, $\Gamma_E \to \kappa$ e-nats/s. However, accessing all this entanglement requires capturing light in a very wide frequency band, larger than the resonator FWHM and typically much larger than the emission spectra (Fig.4.13). In a practical measurement, this requires opening up the acquisition bandwidth to detect non-classical correlations out of the resonance, where the emitted power is effectively zero. One may wonder what is the meaning of an entanglement measure which depends so crucially on signals carried by what is essentially modes in the vacuum state.

Finally, note that due to their different dependence on β, there is no obvious way to link the entanglement of the cavities $E_N^{cav} = \ln(1+\beta)$ to either definition of an entanglement rate.

Comparison with the Josephson mixer

The derivation above of the scattering matrix of the sample and its properties closely follows the work of Flurin [7], adapting it to the specificities of our system and adding the effect of a finite detuning Δ on the expression of the scattering coefficients.

The experiments described in [7] were performed using a Josephson mixer, which is a non-linear device where three microwave resonators a, b, c are coupled by a Josephson ring modulator [114]. The effective interaction Hamiltonian of this device depends on the electromagnetic phases across the three resonators:

$$H_{3WM} = \hbar\chi(ae^{-i\omega_a t} + a^\dagger e^{+i\omega_a t})(be^{-i\omega_b t} + b^\dagger e^{+i\omega_b t})(ce^{-i\omega_c t} + c^\dagger e^{+i\omega_c t}) \tag{4.110}$$

with $\omega_c = \omega_a + \omega_b$. The mode c is put in a bright coherent state $|c_0 e^{i\theta}\rangle$ so that $(ce^{-i\omega_c t} + c^\dagger e^{+i\omega_c t})$ can be considered as a classical variable. After expansion of this triple product, a Rotating Wave Approximation yields a two-mode squeezing Hamiltonian for modes a and b, with a pump strength set by $\hbar\chi|c_0|^2$ and a squeezing angle θ:

$$H_{TMS} = 2\hbar\chi|c_0|^2 e^{i\theta} a^\dagger b^\dagger + h.c. \tag{4.111}$$

The main limitations of this amplifier are the *exhaustion* of the Josephson non-linearity, the *depletion* of the pump and the various *spurious non-linearities*. It is instructive to see how these translate to our own ICPT amplifier.

The exhaustion of the Josephson non-linearity occurs if the amplified current I_{ac} flowing through a Josephson junction of the device is of the order of the critical current I_0 of the junction. As the emitted power in one cavity reads $P_a = \hbar\omega_a\bar{n}_a\kappa_a = QZ_cI_{ac}^2/2$, we have:

$$I_{ac} = \sqrt{\frac{2\hbar\omega_a\bar{n}\kappa_a}{QZ_c}} \ll I_0^* = \frac{2e}{\hbar}E_J^* = \frac{2e\beta\sqrt{\kappa_a\kappa_b}}{\sqrt{r_a r_b}}. \tag{4.112}$$

For symmetric cavities $\kappa_a = \kappa_b, r_a = r_b$ we find:

$$I_{ac} \ll I_0^* \Leftrightarrow r\bar{n} \ll 1 \tag{4.113}$$

which is the condition to stay far away from the strong driving regime that we derived in the previous chapter.

In the Josephson mixer, the depletion of the pump occurs if the photon emission rate becomes larger than $\langle c^\dagger c \rangle \kappa_c$. Then the population of the pump mode decreases down to zero, so that it cannot provide energy for the amplification of signals. In a dc-biased junction, the tunneling Cooper pairs play the role of the pump. The equivalent condition would be that the dc-current I_{dc} through the junction must stay small compared to I_0^*, which yields:

$$I_{dc} = 2e\Gamma = 2e\bar{n}\kappa \ll I_0^* \Leftrightarrow r\bar{n} \ll 1. \tag{4.114}$$

We find the same condition on the occupation of the cavities, which should stay small compared to $1/r$.

In all devices, the two-mode squeezing Hamiltonian is derived from a truncated expansion of the $\cos(\phi)$ Hamiltonian of a Josephson junction. Higher order terms of the expansion modify the dynamics of the system, and are generally detrimental to the quality of the squeezing (or amount of entanglement) generated by the device. In the case of the Josephson mixer, various Kerr terms (quadratic in the photon numbers $a^\dagger a, b^\dagger b, c^\dagger c$) render the resonators anharmonic. These anharmonicities limit the maximum occupation of the modes.

The full expansion of (4.3) reveals non-linearities which are not of the Kerr type: $\chi^{(2)}(a^\dagger a)^2$, but rather reminiscent of the Lamb-Dicke effect [62]: $:: ra^\dagger a(a + a^\dagger) ::$. These non-linearities can safely be neglected if $r\bar{n} \ll 1$. Note that the total absence of any Kerr terms is a unique feature of the dc-biased Josephson junction Hamiltonian. Devices used in circuit-QED experiments can be made practically Kerr-free at some operation points, at the price of an increased complexity [115][116]. They also suffer from the spurious ac-Stark shift, where the frequency of the modes depends on the population of the pump mode. In our system, the shift depends on the field inside the cavities themselves, so that we could potentially drive much harder the junction.

Remarkably, it seems that the very simple mechanism of parametric amplification by ICPT is quite robust, as a single condition $r\bar{n} \ll 1$ is enough to tame all adversary effects. An additional constraint of the design of the Josephson mixer is the stiff pump hypothesis, which requires that the leak rate of the pump mode be much larger than the leak rates of the two cavities. This limits the maximum bandwidth of the amplifier. An ICPT device does not require this condition, and may provide wideband parametric amplification at the quantum limit [117].

Remark: renormalization of the parametric transition

The simple model described here predicts a divergence of the occupation number of the cavities at the threshold of the parametric transition:

$$\bar{n} = \frac{\beta^2}{2(1-\beta^2)} \xrightarrow[\beta \to 1]{} \infty. \tag{4.115}$$

This non-physical divergence is the result of the truncation of the full Hamiltonian (4.3) to the lowest order. Non-linearities scaling as $\propto r\bar{n}$ tend to reduce the effective two-photon drive. As $\beta \to 1$, this reduction becomes more and more important, so that $\bar{n}$ never diverges.

This renormalization of the divergence is predicted to depend crucially on the coupling constant r [104]. The Fano factor of the photons is also predicted to be renormalized at the parametric transition. In this situation the non-equilibrium phase fluctuations in the environment modify the statistics of the emitted photons.

4.2 Implementation of the entanglement experiment

We use standard fabrication techniques for superconducting circuits to create a sample where a small SQUID is put in series with two microwave modes a and b at different frequencies: $\omega_a \neq \omega_b$. This sample is put at the cold stage of our dilution fridge and connected to the measurement circuitry presented in 3.4. After a careful calibration of the environment of the junction (from dc to the GHz range), it is biased on the two-photon resonance condition: $2eV = \hbar(\omega_a + \omega_b)$. We then measure correlation functions of $\hat{a}_{out}(t)$ and $\hat{b}_{out}(t)$ to prove their entanglement.

4.2.1 Design and fabrication of the sample

Constraints on sample parameters

The sample for the experiment must implement the simple circuit from figure 4.11: a small Josephson junction with Josephson energy E_J in series with two microwave resonators a and b, characterized by their normalized impedances r_a, r_b, their frequencies ω_a, ω_b and their leak rates to the detection lines κ_a, κ_b.

The resonators must have different frequencies $\omega_a \neq \omega_b$ for the junction to emit entangled photons. If $\omega_a \simeq \omega_b$, then the two-mode driving is in competition with other two-photon processes, where the two photons are created in the same resonator. The choice $\omega_a/2\pi \simeq 5$ GHz and $\omega_b/2\pi \simeq 7$ GHz put the output signals in the 4-8 GHz band, the working range of our detection setup, with a comfortable margin for safety: even a 30% error on either frequency would not bring the resonators too close to each other.

The quality factors of the modes should be high enough for the RWA to hold, with $Q_a, Q_b \gg 10$ so $\kappa_a, \kappa_b \ll 2\pi\times 500$ MHz. On the other hand, we argued that the output fields are entangled if the cavity leak rates are larger than the dephasing rate of the instantaneous squeezing angle θ. This dephasing rate was about $\sigma_f = 1.3$ MHz in our strong coupling experiment 3.5. Leak rates between $2\pi\times 50$ MHz and $2\pi\times 100$ MHz satisfy these two conditions, so that we target Q factors of the order of 50-100.

The reduced impedance of the modes $r = \frac{\pi Z_c}{R_Q}$ should be small compared to 1, to avoid non-gaussianity of the created light states. We can use conventional microwave resonator designs yielding $Z_c \sim 100\ \Omega$, corresponding to a coupling factor $r \sim 0.05$.

The Josephson junction can be implemented by a SQUID, whose effective Josephson energy $E_J(\Phi)$ is tunable by threading a magnetic flux Φ through the sample. Tuning $E_J(\Phi)$ downs to almost zero allows us to use the calibration procedure detailed in 3.5 to extract all relevant information about the sample and its environment. A SQUID with a tunnel resistance $R_N \sim 25\ \text{k}\Omega$ and a typical residual asymmetry of its junctions $\sim 10\%$ would yield a Josephson energy tunable between $E_J(0) \sim 25\ \mu$eV and $E_J(h/4e) \sim 2\ \mu$eV. This should be enough to reach a low occupation number of the cavities $\bar{n} \sim 0.1$. At the maximum value of $E_J(\Phi)$, the reduced pump strength for the parametric amplifier model is then $\beta \sim 5$, far above the parametric threshold. This allows us to explore a wide range of values of the pump strength, testing extensively our physical description of the system.

Interestingly, while our simple amplifier model predicts that the entanglement of the fields grows with the pump strength, the results of the 2016 experiment (Fig. 4.8) show that the violation of the Cauchy-Schwarz equality is more pronounced at low emission rates. It is thus useful being able to explore both the weak and strong driving regime of the experiment.

Design of the sample

All constraints on the parameters of the experiments can be fulfilled by the same kind of sample as in the 2016 experiment [39]. We thus simply used a Si chip from the same wafer, covered with a thin Nb film patterned with resonators. Each resonator is implemented as three sections of CPW transmission lines with equal lengths but different impedances Z_1, Z_2, Z_3, as indicated in the table below (Fig.4.14).

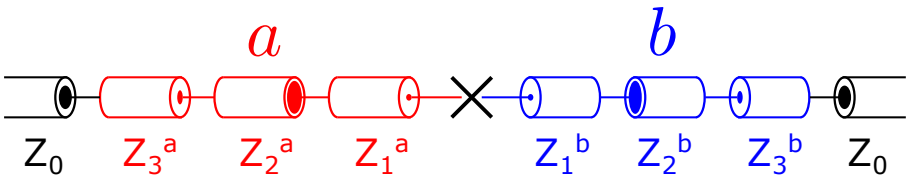

Figure 4.14: Microwave electrical model of the sample. The small Josephson junction acts as an open circuit. The segments of CPW on the left (right) side have a length such that their first $\lambda/4$ resonance occurs at ω_a (ω_b).

	Z_1	Z_2	Z_3	$\omega_r/2\pi$
resonator a	121 Ω	24 Ω	101 Ω	5.1 GHz
resonator b	121 Ω	24 Ω	121 Ω	7.0 GHz

The series combination of $\lambda/4$ resonators yield a resonance with characteristic impedance $Z_c \simeq (4/\pi) \times Z_1 \simeq 150\ \Omega$ ($r \simeq 0.07$) and a quality factor set by the impedance mismatch $Q = (\pi/4) \times Z_1/Z_L$, with $Z_L = (Z_2)^2 \times Z_0/(Z_3)^2$ and $Z_0 = 50\ \Omega$ the impedance of the measurement lines. The value of Z_3 on each side is adjusted so that the two modes have similar decay rates: $\kappa_a = \omega_a/Q_a \simeq \kappa_b = \omega_b/Q_b \simeq 800\ \mu s^{-1}$.

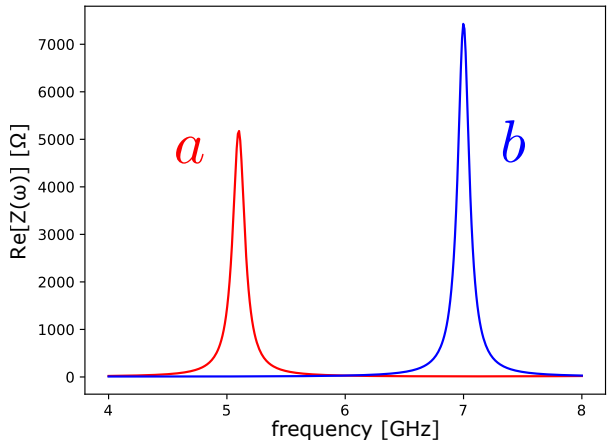

Figure 4.15: Impedance seen on each side of the junction, computed with the transmission line formula for impedance transforms [118]. The two modes at 5.1 GHz and 7.0 Ghz have similar FWHM $\simeq$ 120 MHz.

The impedance $Re[Z(\omega)]$ seen by the junction is then the sum of the impedance seen on each side. It can be computed using the transmission line formula for impedance transforms [118] (Fig.4.15). Higher Q factors could be reached by adding more cascaded $\lambda/4$ segments on each side, at the detriment of making fabrication errors more probable. Lower values of Z_c could be reached by lowering Z_1, to the detriment of the quality factor.

Fabrication

The microwave resonators were fabricated by optical lithography of a 150 nm Nb thin film, sputtered on an oxydized Si [3 mm×10 mm] chip (Fig.4.16). To fit the $\simeq$ 20 mm total length of CPW segments, these are designed with equidistant windings. Electromagnetic simulations of the CPW geometry with the finite-element analysis software Sonnet prove that these close windings do not impact at all the $\lambda/4$ resonances.

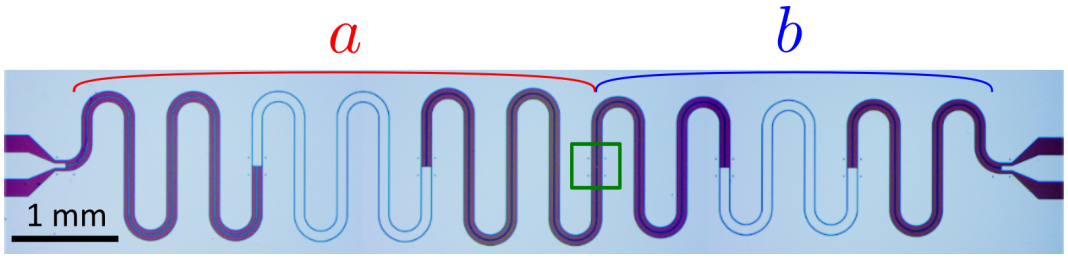

Figure 4.16: Zoom-in of an optical micrography of the sample before evaporation of the Al SQUID. The green box indicates the future position of the junction, connecting the inner conductors of the two CPWs. On each side are three cascaded $\lambda/4$ CPW segments, implementing resonators a and b. Bonding pads on each side of the chip will allow connecting the sample to the measurement circuit.

The Al/AlOx/Al SQUID was fabricated using standard electron-beam lithography and double-angle evaporation techniques, yielding junctions of about $\simeq$ 200 nm×200 nm (Fig.4.17). This small area ensures a small geometric capacitance of the squid $C_S \simeq$ 8 fF, which cannot shunt the $\simeq$ 8 kΩ impedance of the environment at the frequency $\sim$ 6 GHz of the signals we will be measuring.

As we did not want to take risks with the Josephson junction, we did not measure its dc resistance. Thus we do not know the exact value of the tunnel resistance R_N. We estimate it from room-temperature measurement of test junctions put on the same chip to $R_N \simeq 16 \pm 4$ kΩ, which yields a Josephson energy $E_J \simeq 40 \pm 10$ μeV. The value of E_J can be calibrated in situ as we will see later.

After fabrication, the sample is glued with UV-III resist to a PCB board and wire-bonded to 50 Ω transmission lines.

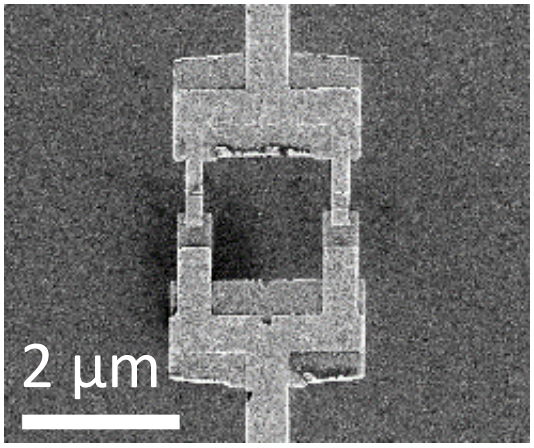

Figure 4.17: Electronic micrography image of the SQUID connected between the two resonators.

4.2.2 Cold stage setup

After fabrication, the sample is placed at the cold stage of our dilution refrigerator and connected to the measurement setup.

We use the same cold temperature setup as in the strong-coupling experiment (Fig.3.25), with minor modifications. This two-mode sample has two ports, at the output of resonators a and b. We thus add a second bias-tee to the setup, connected to ground on the dc-port and to the hybrid coupler on the rf port (Fig.4.18).

On the dc bias line, we replaced the 6.45 MΩ bias resistor by a 1 MΩ one. The previous resistor was heating up when applying voltages above $\sim$ 7 Volts, which affected its value. The new resistor has a lower resistance, such that it heats up about 6.5 times less. It is also made using a different technology, with a measured resistance change of less than 1 kΩ between room temperature and 1 K. The dc bias applied to the sample can thus be controlled much more precisely.

The soldering of the 3^{rd}-order RC filter on the bias line broke at some point in a previous run. It had became brittle due to thermal cycling. As we believed that this filter was not crucial to the reduction of noise on the voltage bias, we simply removed it entirely. This proved later to be detrimental to the voltage noise, which went up by about 40% compared to what we expected for a two-port sample.

The rest of the setup was left unchanged. As in the previous experiment, signals leaking from the sample are split by the hybrid coupler, amplified by the two HEMTs and routed towards room temperature via channels (1) and (2).

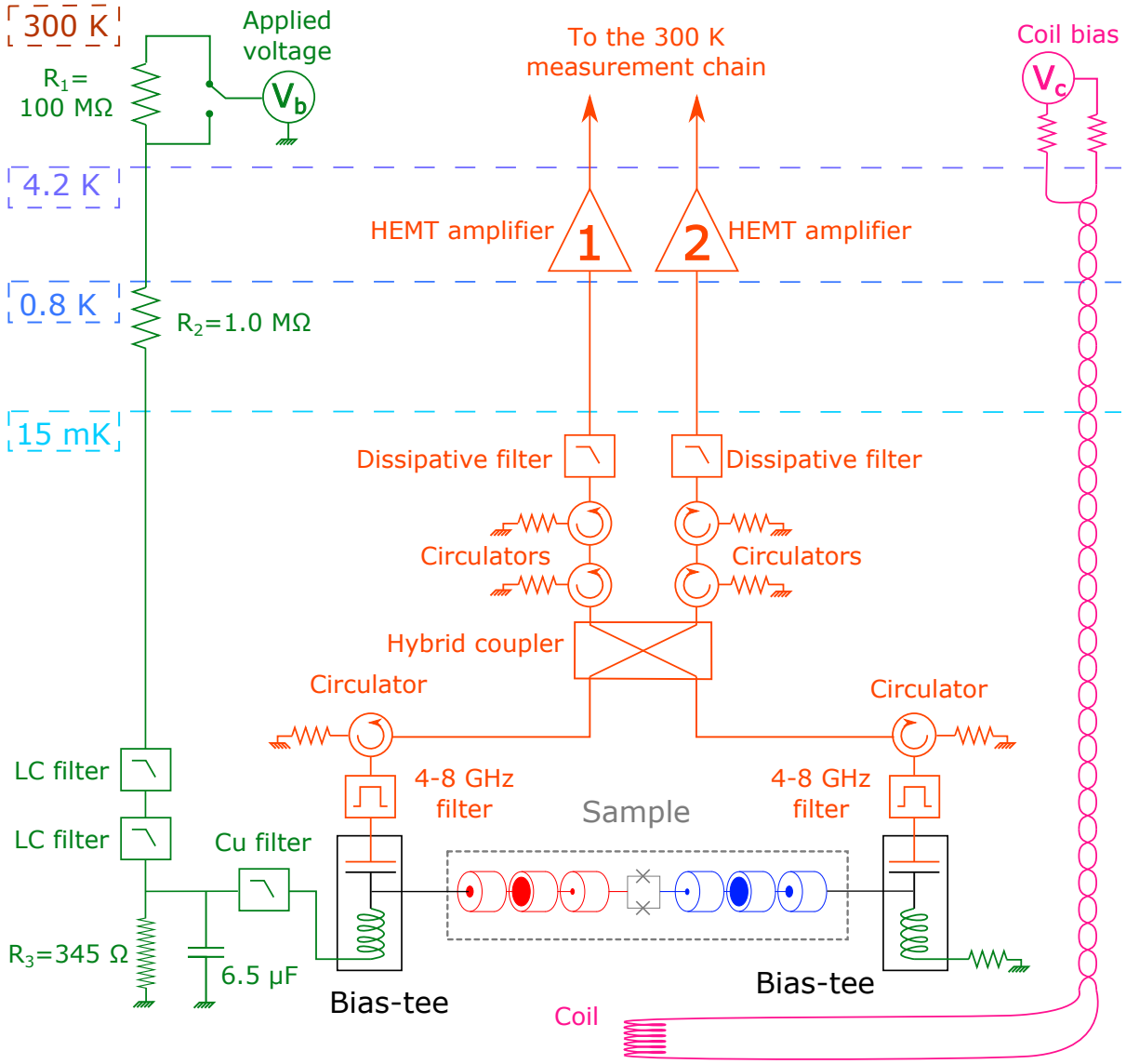

Figure 4.18: Cryogenic part of the experimental setup. A pair of bias-tees allows setting a dc-voltage bias on the sample while collecting the microwave radiation leaking out of the resonators. Signals from modes a and b are split by the hybrid coupler over the same two amplification lines. As they reside in different frequency bands (around 5.1 GHz and 7 GHz respectively), they do not interfere and can later be easily separated by bandpass filtering. A small current-biased superconducting coil placed below the sample allows tuning its Josephson energy $E_J(\Phi)$ via the applied magnetic flux Φ.

4.2.3 Room-temperature setup

Channels (1) and (2) carry microwave signals from the cryogenic circuit to the room temperature signal processing and acquisition chains. The room temperature setup (see figure 4.19) is similar to the one used in the antibunching experiment (Fig.3.26). It includes several stages of amplification and filtering of the signals, down-conversion to the dc-600 MHz range by an IQ mixer, further amplification and filtering, then detection of the voltage signals by an ADQ412 acquisition card (Fig.4.19).

The main difference with respect to the strong-coupling experiment is that we need to detect two different signals: those emitted by resonator a around $\omega_a/2\pi \simeq \times$ 5.1 GHz and those from resonator b around 7 GHz. Due to splitting by the hybrid coupler at cold temperature, both signals are carried by both channels (1) and (2). To detect them separately, we split channels (1) and (2) at room temperature, and bandpass the signals around either 5.1 GHz or 7 GHz (Fig.4.19). We use adjustable microwave filters with bandwidth ranging from 660 MHz to 700 MHz. Filtered signals are down-converted by two LO at 5.35 GHz and 7.15 GHz respectively.

Finally we use the four ports **A,B,C,D** of the acquisition card to detect down-converted signals from the two channels and two frequency bands. We use a sampling frequency of 1.25 GSamples/s, yielding a Nyquist frequency of 612.5 MHz. Numerical filtering reduces the acquisition bandwidth down to 525 MHz.

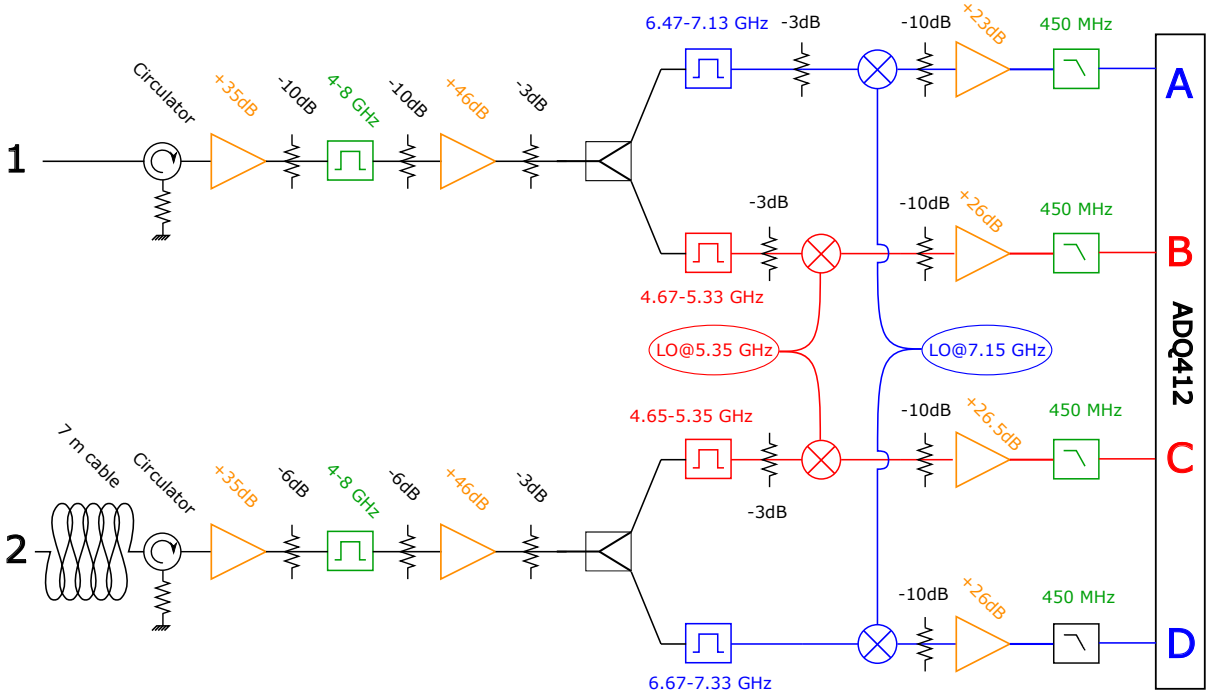

Figure 4.19: Room-temperature setup. After amplification, filtering and down-conversion, a and b signals carried by the two channels (1) and (2) are separated by bandpass filtering and detected separately on four acquisition channels. The attenuation and length of each channel is adjusted to yield balanced signal powers and propagation times.

4.2.4 Numerical computation of the correlation functions

We adapt the linear detection procedure developed in 3.4.3 to measure different correlation functions of the four propagating fields, yielding $g_a^{(2)}(\tau), g_b^{(2)}(\tau), g_{ab}^{(2)}(\tau)$ and $g_\phi^{(2)}(\tau)$ after numerical processing.

First we record chunks of microwave voltages $V_A(t)$, $V_B(t)$, $V_C(t)$, $V_D(t)$ of length 2048 (corresponding to an acquisition time $\tau_{\text{acq}} \simeq 1.64\ \mu$s) and compute their numerical Hilbert transform. This yields the complex envelopes $S_A(t)$, $S_B(t)$, $S_C(t)$, $S_D(t)$, which are observables related to the fields operators $a_{out}(t)$ and $b_{out}(t)$. We model this relation as:

$$S_A(t) = \sqrt{G_A}\big(a_{out}(t - t_A) + h_A^\dagger(t)\big) \tag{4.116}$$
$$S_B(t) = \sqrt{G_B}\big(b_{out}(t - t_B) + h_B^\dagger(t)\big) \tag{4.117}$$
$$S_C(t) = \sqrt{G_C}\big(b_{out}(t - t_C) + h_C^\dagger(t)\big) \tag{4.118}$$
$$S_D(t) = \sqrt{G_D}\big(a_{out}(t - t_D) + h_D^\dagger(t)\big), \tag{4.119}$$

where the G_i are conversion factors between the field amplitudes and the voltage detected by the acquisition card. The $h_i^\dagger(t)$ operators model all the noise terms added by the different steps of signal processing on channel i (as in figure 3.24). All delays between the channels are included in the time differences $t - t_i$, which we compensate for numerically.

The main contribution to the noise operators arise from the cryogenic HEMT amplifiers. In a given frequency band, noise operators from two different amplifiers commute: $[h_A, h_D^\dagger] = [h_B, h_C^\dagger] = 0$. Noise operators from two different frequency bands always commute, even if they originate from the same amplifier: $[h_A, h_B^\dagger] = [h_C, h_D^\dagger] = 0$. Due to the finite isolation $\simeq$-33 dB, there are parasitic correlations between the four channels.

After compensation of the different time delays, cross-correlations of signals in the same frequency band yield the first and second order correlation functions, following (3.85) and (3.88) respectively. The correlation functions which appear in the entanglement witness (4.41) are computed from cross-correlations of the signals in different frequency bands:

$$\langle a^\dagger a(0) b^\dagger b(\tau)\rangle \propto \langle S_A^\dagger S_D(0) S_B^\dagger S_C(\tau)\rangle_{ON/OFF} - \Big\{ \langle S_A^\dagger S_D\rangle_{ON/OFF}\langle S_B^\dagger S_C\rangle_{OFF} + \langle S_B^\dagger S_C\rangle_{ON/OFF}\langle S_A^\dagger S_D\rangle_{OFF} + \langle S_A^\dagger(0) S_C(\tau)\rangle_{ON/OFF}\langle S_D(0) S_B^\dagger(\tau)\rangle_{OFF} + \langle S_D(0) S_B^\dagger(\tau)\rangle_{ON/OFF}\langle S_A^\dagger(0) S_C(\tau)\rangle_{OFF} \Big\} \tag{4.120}$$

$$\langle a^\dagger b^\dagger(0) a b(\tau)\rangle \propto \langle S_A^\dagger S_B^\dagger(0) S_C S_D(\tau)\rangle_{ON/OFF} - \Big\{ \langle S_A^\dagger(0) S_D(\tau)\rangle_{ON/OFF}\langle S_B^\dagger(0) S_C(\tau)\rangle_{OFF} + \langle S_B^\dagger(0) S_C(\tau)\rangle_{ON/OFF}\langle S_A^\dagger(0) S_D(\tau)\rangle_{OFF} + \langle S_A^\dagger(0) S_C(\tau)\rangle_{ON/OFF}\langle S_B^\dagger(0) S_D(\tau)\rangle_{OFF} + S_B^\dagger(0)\langle S_D(\tau)\rangle_{ON/OFF}\langle S_A^\dagger(0) S_C(\tau)\rangle_{OFF} \Big\} \tag{4.121}$$

where the terms in brackets arise from the parasitic contribution of the amplifiers noise. After suitable normalization by $\langle S_A^\dagger S_D\rangle\langle S_B^\dagger S_C\rangle$, these expressions yield $g_{ab}^{(2)}(\tau)$ and $g_\phi^{(2)}(\tau)$.

Remark: classical interpretation of the correlators

As detailed in 3.4.3, we actually compute correlation functions of the form $C_{XY}(\tau) = \langle X^\dagger(0) Y(\tau)\rangle$ as the inverse Fourier transform of $X^\dagger(\omega)Y(\omega)$, where $X(\omega)$ and $Y(\omega)$ are the direct Fourier transform of $X(t)$ and $Y(t)$ respectively. It is instructive to consider the form the $g_{ab}^{(2)}(\tau)$ and $g_\phi^{(2)}(\tau)$ correlators take in the frequency domain.

For simplicity we consider here $\hat{a}(t)$ and $\hat{b}(t)$ not as quantum operators, but as classical complex amplitudes. We have:

$$\mathbb{F}[\langle a^\dagger a(0) b^\dagger b(\tau)\rangle](\omega) = \mathbb{F}[a^\dagger a(t)]^\dagger(\omega) \times \mathbb{F}[b^\dagger b(t)](\omega). \tag{4.122}$$

The frequency spectrum of $g_{ab}^{(2)}(\tau)$ is thus the product of the spectra of the instantaneous emission rates $a^\dagger a(t)$ and $b^\dagger b(t)$ (Fig.4.20). These emission rates fluctuate over a short timescale κ^{-1}, which is the duration of a photonic wavepacket. Hence the population correlator has a decay time of the order of κ^{-1}.

On the other hand the Fourier transform of the phase correlator is:

$$\mathbb{F}[\langle a^\dagger b^\dagger(0) a b(\tau)\rangle](\omega) = \mathbb{F}[ab(t)]^\dagger(\omega) \times \mathbb{F}[ab(t)](\omega) = |\mathbb{F}[ab(t)](\omega)|^2. \tag{4.123}$$

$\mathbb{F}[g_\phi^{(2)}(\tau)](\omega)$ is directly the PSD of the observable $ab(t) \propto e^{-i\omega_J t}$ (Fig.4.20). In the case of ideal two-mode squeezing, $\langle ab(t)\rangle$ is simply a complex number, whose argument yield the squeezing angle after demodulation. In the absence of phase diffusion $ab(t)$ is thus a **signal**, i.e a quantity which, given a phase reference, can be averaged over time to yield a better SNR.

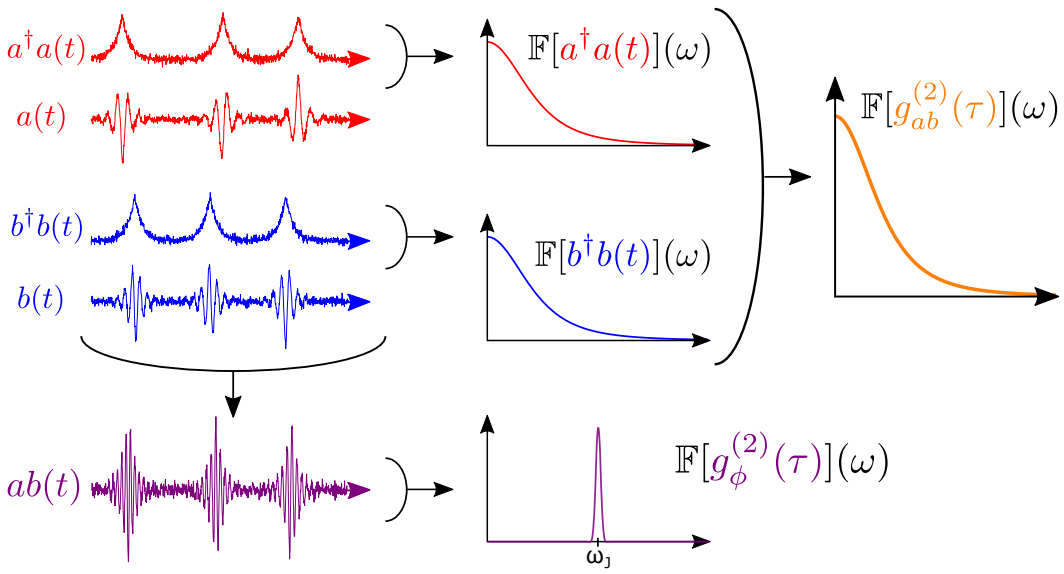

Figure 4.20: Classical model of the correlations between the a and b fields. In a classical picture, $a(t)$ and $b(t)$ are a sequence of pulses at frequency ω_a and ω_b respectively. The instantaneous intensities $a^\dagger a(t)$ and $b^\dagger b(t)$ are correlated. The spectrum of the population correlator $g^{(2)}_{ab}(\tau)$ is the product of the spectra of these intensities. The Fourier transform of the phase correlator $g^{(2)}_{\phi}(\tau)$ is the power spectral density (PSD) of the observable $ab(t)$.

In our experiment, the squeezing angle drifts slowly. Averaging $\langle ab(t)\rangle$ over a long time simply yields zero. The observable $ab(t)$ is thus not a stationary signal, but is rather akin to a **noise**, i.e a random process. Contrary to a signal, a noise cannot be averaged over arbitrary long times. It also cannot be described by its Fourier components, which all average to zero.

A random noise process $X(t)$ can however always be characterized by its PSD $S_X(\omega) = \mathbb{F}[\langle X^\dagger(0)X(t)\rangle](\omega) \neq 0$, even if $\langle \mathbb{F}[X(t)](\omega)\rangle = 0$. This is the fundamental principle behind all noise measurements.

Our detection scheme thus consists in adapting the tools of noise measurements to measure a quantity which usually requires a phase reference. Instead of detecting and averaging the squeezing angle θ, we measure the spectrum of its fluctuations. The entanglement witness then gives us a criterion which indicate wether or not the fluctuations of θ are slow enough for the two signals to stay entangled.

4.3 Two-photon emission experiment

We present in this section the results of our experiment **except** those related to the entanglement of the modes. We calibrate accurately the electromagnetic environment of the Josephson junction, measure emission spectra in the single-photon and two-photon regimes, and study the joints statistics of photon pairs. Experimental results are systematically compared to the predictions of the parametric amplifier model, highlighting the renormalization of the pump strength β due to the environment phase fluctuations.

4.3.1 Calibration of the environment of the junction

We use the same tools presented in 3.5 to calibrate precisely the environment of the junction, which consists of the on-chip microwave resonators and the lower frequency modes of the bias circuit.

Shotnoise calibrations

We put the junction in the normal quasiparticle regime (see Appendix B) by applying a voltage bias much higher than the gap voltage, and measure its emission spectra around 5.1 GHz and 7 GHz. This yields the frequency-dependent **microwave coupling factor** between the junction and the two resonators:

$$C(\omega) = 1 - \left| \frac{Z(\omega) - R_N}{Z(\omega) + R_N} \right|^2 . \tag{4.124}$$

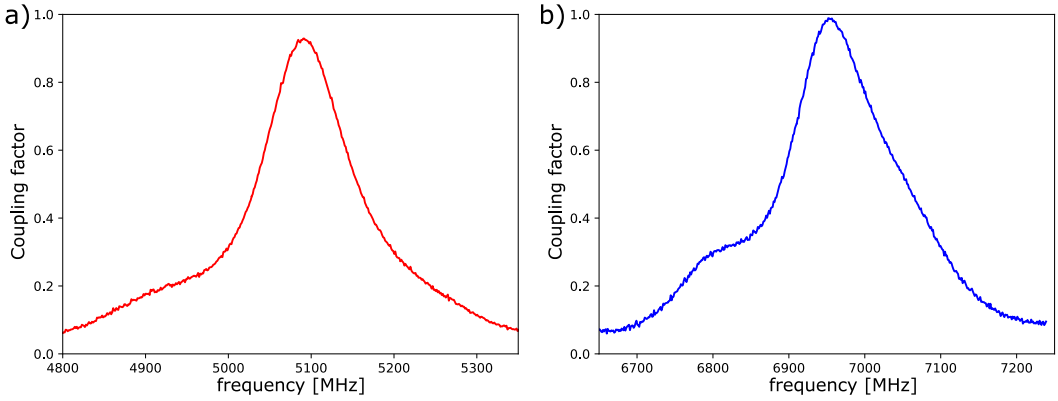

Figure 4.21: Emission spectra around ω_a (panel a) and ω_b (panel b) in shotnoise regime yield the microwave coupling factor between the junction and the resonators, as defined by (4.124).

As in 3.5, the value of $C(\omega)$ on resonance is extracted by comparing these spectra (Fig.4.21) to the $Re[Z(\omega)]$ measured in the ICPT regime. We find:

$$C(\omega_a) = 0.929 \pm 0.005 \tag{4.125}$$

$$C(\omega_b) = 0.989 \pm 0.005, \tag{4.126}$$

with the **resonance frequencies $\omega_a/2\pi$ = 5092 MHz and ω_b = 6955 MHz**. The derivative of the emitted power with respect to the bias voltage yields a calibration of

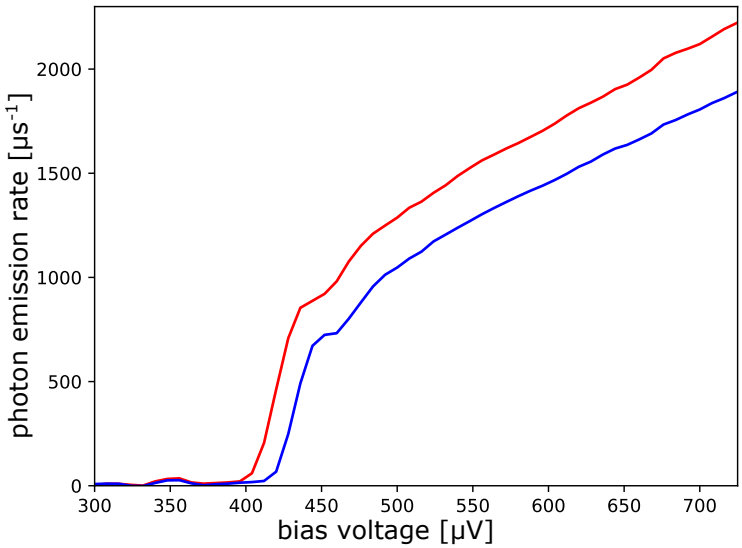

Figure 4.22: Total emission rate in the a mode (red curve) and the b mode (blue curve) as a function of the bias voltage. At bias voltage $V = (2\Delta + \hbar\omega_0)/e$ larger than the gap voltage, quasiparticles can tunnel through the junction, generating shot-noise with a spectral density $S_{II}(\omega) \neq 0$ for $\omega \leq \omega_0$. The emission power at ω_a is thus shifted by $(\omega_b - \omega_a)/e$ with respect to the emission power at ω_b.

the noise temperature of the HEMT amplifiers (1) and (2), $T_N^{(1)}$ and $T_N^{(2)}$, which we use to calibrate the gain of the microwave detection chains.

We find that these noise temperatures depend on the frequency at which we evaluate them, even within one resonance. We interpret this as an imbalance of the hybrid coupler, which instead of splitting exactly in half the incoming power, distributes a fraction $\alpha(\omega)$ on one channel and $1-\alpha(\omega)$ on the other channel. We thus resort to always using the sum of the emission spectra measured over channel (1) and channel (2), which should yield the total emission power from the sample. We find the equivalent **noise temperature**:

$$\frac{T_N^1 + T_N^2}{2} \simeq T_N = 12.4 \pm 0.6 \text{ K @ } 5.1 \text{ GHz} \tag{4.127}$$

$$= 17.4 \pm 0.9 \text{ K @ } 7 \text{ GHz}. \tag{4.128}$$

We attribute the different values of T_N at ω_a and ω_b to a larger attenuation between the sample and the HEMT amplifiers at higher frequencies, due in particular to a low pass dissipative filter meant to avoid stationary parasitic standing waves ocuring outside of the 4-8 GHz band, where the various elements of our detection are not specified.

The derivative of the total emitted power with respect to the voltage bias also allows us to pinpoint the value of the **superconducting gap**. We find:

$$\Delta = 201 \pm 2 \ \mu\text{eV}, \tag{4.129}$$

which is a typical value for Aluminum thin films. Finally we estimate the equilibrium thermal occupation of the resonators by measuring the emitted power due to inelastic absorption processes. We find an equilibrium occupation of the modes below 2×10^{-3}, which means a **temperature below 40 mK**.

Emission maps on the single-photon resonance

We scan the bias voltage V across the single-photon resonances, where one photon per tunneling Cooper pair is emitted in one mode. The emission spectrum map shows a narrow line following $2eV = \hbar\omega$. For each value of the applied voltage we fit the emission peak with a Gaussian function.

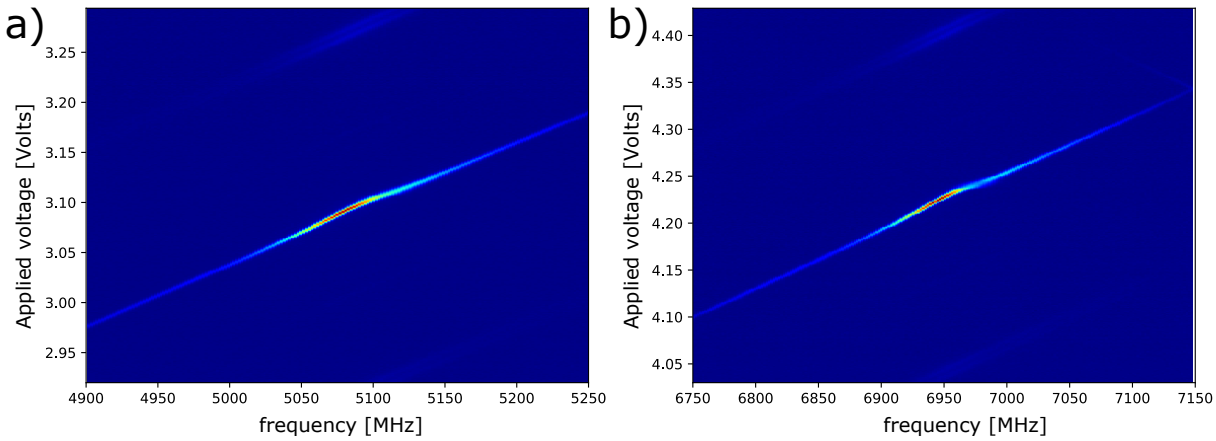

Figure 4.23: Emission maps around the $2eV = \hbar\omega_a$ (panel a) and $2eV = \hbar\omega_b$ (panel b) resonances.

The value of the Josephson frequency $\omega_J = 2eV$ as a function of the applied voltage V_b yields the voltage division ratio of the bias line. We use it to calibrate the value of the cold resistor $R_2 = 1.014 \pm 0.003$ MΩ. The bias voltage across the junction is not exactly proportional to the applied voltage, due to the finite dc-current flowing through the sample when it emits photons. This deviation yields an independent estimation of the emission rate, as in 3.5.1.

The width of the Gaussian peak σ_f varies with V, due to the mechanism described in 3.41 where the junction itself actively cools/heats up the low frequency modes of the bias line. The intrinsic width $\sigma_f = 2.6$ MHz, measured in the tail of the resonance, is twice larger than in our strong-coupling experiment.

The area under the peak yields the total emission rate, which is directly proportional to $Re[Z(\omega)]$. We compare this data with the coupling factor extracted in shotnoise regime to obtain an absolute calibration of the $Re[Z(\omega)]$ of the resonators.

As we do not know exactly the value of R_N, we have to follow a more complex procedure than in 3.5. We use the fact that the emitted power for single-photon process reads:

$$P_{em}(2eV) = \int S_P(\omega)d\omega \simeq \frac{Re[Z(\omega_J)] \times (I_0^*)^2}{2}, \tag{4.130}$$

while the critical current of the junction is linked to its normal resistance by the Ambegaokar-Baratoff relation:

$$I_0 = \frac{\pi\Delta}{2eR_N}. \tag{4.131}$$

We start by assuming that the renormalization of the critical current due to environment zero-point phase fluctuations is small: $I_0^* = I_0 \times e^{-\Delta\phi^2} \simeq I_0$. Then we combine (4.124), (4.130) and (4.131) to yield a first estimation of $Re[Z(\omega)]$ around ω_a and ω_b. We compute the characteristic impedance $Z_c = (2/\pi)\int Re[Z(\omega)]d\omega/\omega$ of the resonators, and obtain

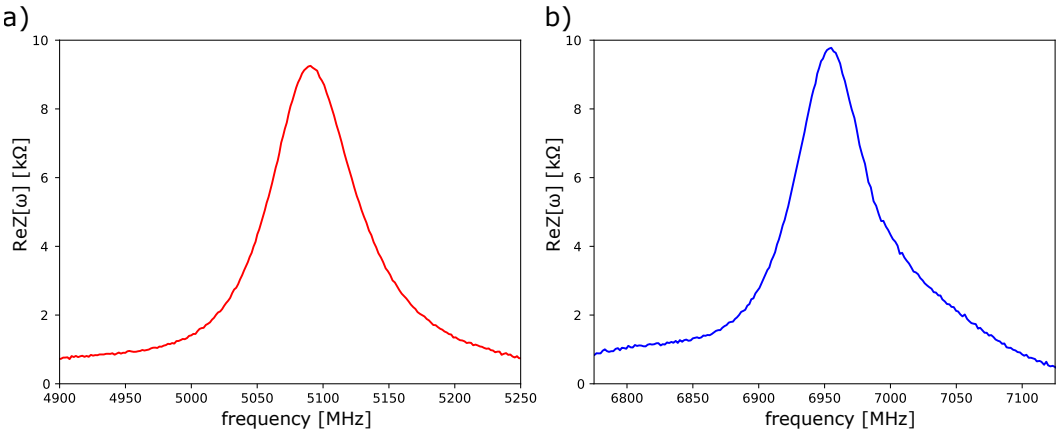

Figure 4.24: $Re[Z(\omega)]$ of the environment of the junction, showing the two microwave resonances.

an approximate value for the phase ZPF: $\Delta\Phi^2 \simeq r_a + r_b$. We use this value to estimate the value of the renormalized critical current I_0^*, and re-inject it into the calculation. After a few iterations, the procedure converges to yield the true value of $Re[Z(\omega)]$, see figure 4.24. We improve furthermore its accuracy by including in the computation of $\Delta\Phi^2$ the low frequency modes of the setup around 300 MHz and their harmonics.

The $Re[Z(\omega)]$ of the resonators are fitted with Lorentzian functions, yielding:

	$\omega_r/2\pi$	Q	κ	Z_c	r
a	5092 MHz	60.8	526.2 μs^{-1}	144.2 Ω	0.070
b	6955 MHz	97.0	450.5 μs^{-1}	125.7 Ω	0.061

This procedure also yields the normal state resistance: $R_N = 16.0 \pm 0.3$ kΩ, as well as the values of the critical current and Josephson energy:

$$I_0 = 19.7 \pm 1 \text{ nA} \rightarrow I_0^* = 15.7 \pm 0.8 \text{ nA} \tag{4.132}$$

$$E_J = 40.4 \pm 0.8 \ \mu\text{eV} \rightarrow E_J^* = 32.3 \pm 0.6 \ \mu\text{eV}. \tag{4.133}$$

The SQUID on this sample does not manifest the same hysteretic behaviour and spurious flux jumps as in the strong-coupling experiment. We are thus able to pinpoint the precise value of E_J^* that is used for each measurement. Note that the maximum value of E_J^* yields a value of $\beta = 6.6$, i.e above the parametric threshold.

Stokes and Anti-Stokes processes with 300 MHz modes

The two emission maps from figure 4.23 show faint secondary emission lines, parallel to the main $2eV = \hbar\omega$ line. The upper line at $2eV = \hbar(\omega + \omega_p)$ results from **two-photon emission processes**, where one photon is emitted at ω and one photon is created in a parasitic mode of the setup at $\omega_p \simeq 300$ MHz. The lower line at $2eV = \hbar(\omega - \omega_p)$ corresponds to **absorption processes**, where one photon is absorbed from the 300 MHz mode and one photon is emitted at ω. For both the Stokes and Anti-Stokes processes, we can only detect the light emitted at $\omega \sim \omega_{a/b}$.

We plot in figure 4.25 two spectra measured at $2eV = \hbar(\omega_\pm \omega_p)$, so that either the Stokes or Anti-Stokes peak is located at ω_a. We observe that the emission peak is actually double. These double peaks originate from $\lambda/4$ resonances of the 50 Ω cables connecting

the two sides of the sample to the bias-tees. As the length of the wound CPW resonators on the chip are not the same, these two resonances have slightly different frequencies.

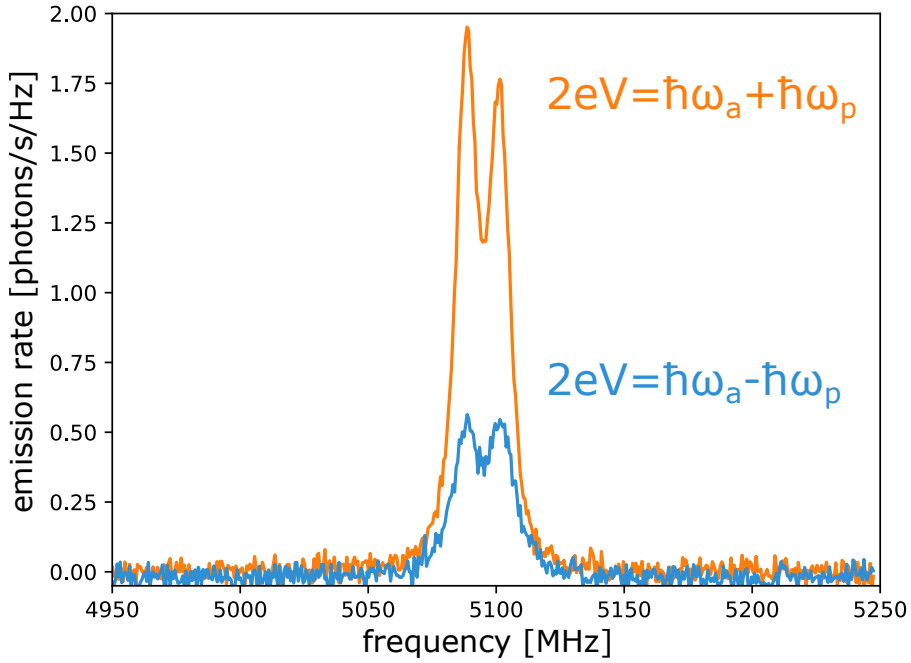

Figure 4.25: Photon emission rate spectral density measured at $2eV = \hbar(\omega_{\pm}\omega_p)$, maximizing either the Stokes process (orange curve) or the Anti-Stokes process (blue curve).

We fit the shape of the spectra as the sum of two Lorentzian functions to obtain the frequencies and quality factors of these two resonances. We also compare the area under the Anti-Stokes peaks to the emission rate due to direct single-photon processes, which yield the characteristic impedances of the modes:

	$\omega_r/2\pi$	Q	κ	Z_c	r
p_1	292 MHz	30 ± 1	61.2 ± 2 μs^{-1}	86 ± 5 Ω	0.04
p_2	307 MHz	30 ± 1	64.3 ± 2 μs^{-1}	86 ± 5 Ω	0.04

In the limit of low E_J^*, the tunneling rates follow the $P(E)$ theory. It predicts that the emission rate du to Anti-Stokes processes scales as $r_p \times \bar{n}_p$, while the Stokes processes yield a $r_p \times (\bar{n}_p + 1)$ scaling. Here the extra 1 is the mark of spontaneous emission process. If the mode is empty at equilibrium with $\bar{n}_p = 0$, absorption processes are impossible, as no energy can be extracted from the vacuum. The ratio of absorption power to emission power $\bar{n}_p/(\bar{n}_p + 1)$ allows us to extract the **equilibrium population:** $\bar{n}_p = \mathbf{0.58 \pm 0.03}$, corresponding to **a temperature of** $T = \mathbf{14.5 \pm 0.5\ mK}$. Spectra measured at ω_b yields a similar temperature.

On figure 4.25 we see that the Stokes peak corresponding to the lower frequency mode $\omega_{p_1} = 292$ MHz is larger than the peak associated to $\omega_{p_1} = 307$ MHz, while the Anti-Stokes peaks have similar height. We attribute this discrepancy to the back-action of the out-of-equilibrium phase fluctuations from the modes onto the junction.

As these modes arise from $\lambda/4$ resonances, they have higher harmonics at odd multiple of their fundamental frequency, i.e near 900 MHz, 1.5 GHz, and so on. The $(2k+1)\times\omega_p$ mode

has a characteristic impedance which is $2k+1$ times lower than ω_p. We estimate their occupation number from the temperature $T = 14.5$ mK of the fundamental resonance, and compute their contribution to the phase fluctuations on the junction. This yields a correction of a few percents on the value of E_J^*, and on the $Re[Z(\omega)]$ determined from the emission maps.

Remark: voltage noise on the junction

The value of the dc-voltage noise on the junction, $\sigma_V = h\sigma_f/2e$, was monitored repeatedly during the run by measuring the width of the Josephson radiation. It decreased continuously over the first few weeks, as all the microwave components inside the fridge were thermalizing. Its final value was $\sigma_V = 5.4$ nV, corresponding to $\sigma_f = 2.6$ MHz. This is twice higher than the equilibrium value we had in the strong-coupling experiment.

We attribute most of the low-frequency voltage noise to the parasitic LC resonance of the bias-tee at $\omega_{BT} \simeq 71$ kHz, with $Z_c \simeq 50\ \Omega$ and $\bar{n} \simeq 5000$. When putting a second bias-tee in series with the sample, their random voltage fluctuations add incoherently, increasing $\Delta V^2 = \sigma_V^2$ by 2 and hence σ_V by $\sqrt{2}$. Hence we would have expected a value of σ_V closer to 7.6 nV, and a dephasing rate σ_f of about 1.8 MHz, given that the bias-tee stays at approximately the same temperature.

This increased noise could come from a higher temperature of the bias-tees. But as we find that the 300 MHz modes are thermalized at the fridge base temperature, we estimate that the modes at ω_{BT} should also be cold.

The main difference in our dc-bias line compared to the previous experiment is the removal of the homemade $(RC)^3$ filter, which broke after thermal cycling. We thus suggest that the extra voltage noise in this experiment comes from room temperature, and that it was previously well filtered by the $(RC)^3$ filter.

4.3.2 Two-photon emission in the a and b modes

Emission map at low E_J^*

We now scan the bias voltage across the two-photon resonance $2eV = \hbar\omega_a + \hbar\omega_b$, where each tunneling Cooper pair emits one photon in mode a and one in mode b simultaneously, and measure the corresponding emission spectra (Fig.4.26). The Josephson energy is tuned down to a low value of $E_J^*(\Phi) = 2.65\ \mu$eV, which should yield a driving strength $\beta \simeq 0.54$ and a population of the modes of $\bar{n} \simeq 0.20 \ll 1$ on resonance according to (4.87), with the average population $\bar{n} = \sqrt{\bar{n}_a \bar{n}_b}$.

On panel (a) of figure 4.26, the light is mostly emitted along two intersecting lines. The first line follows $2eV = \hbar\omega + \hbar\omega_b$, the second line is fixed at $\omega = \omega_a$. This illustrates the competition between the two modes: at a finite detuning $\Delta = \omega_J - \omega_a - \omega_b$, it is more favorable for the junction to emit light on top of a resonance, rather than at $\omega_a + \Delta/2$ and $\omega_b + \Delta/2$. The same observation can be made on panel (b).

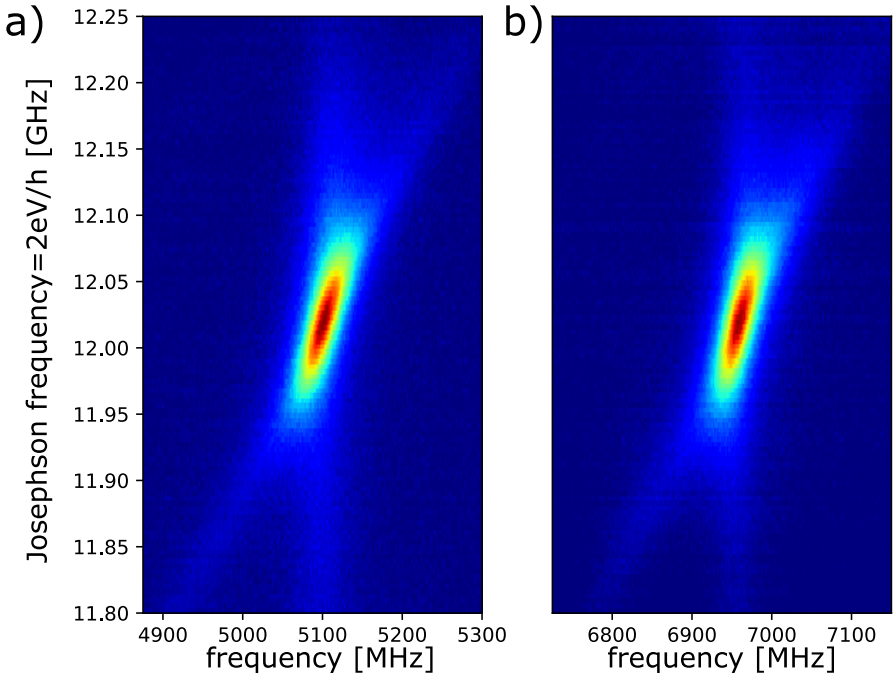

Figure 4.26: Two-photon emission map around ω_a (panel a) and ω_b (panel b).

At low E_J, the emission spectra are well described by the $P(E)$ theory, with:

$$\gamma(\omega) = \frac{S_P(\omega)}{\hbar\omega} = \frac{(2\pi E_J^*)^2}{\hbar^2} \times \frac{Re[Z(\omega)]}{R_Q \times \omega} \times \frac{Re[Z(\omega_J - \omega)]}{R_Q \times (\omega_J - \omega)}. \tag{4.134}$$

On resonance $\omega_J = \omega_a + \omega_b$, the shape of the emission spectra is thus the product of the $Re[Z(\omega)]$ of the two modes (Fig.4.27). As the modes have approximately Lorentzian shapes, we fit the spectra by a Lorentzian function squared. We find a FWHM of 72 MHz for the Lorentzian function, in good agreement with the width of the narrower resonator. This yields a FWHM of about 46 MHz for the spectra.

Note that using a more complex fit function, like the product of two Lorentzian with different widths, does not increase much the agreement of the fit, as the resonators already have similar FWHM.

Non-degenerate parametric emission at higher E_J^*

The probability of ICPT accompanied with emission of light at frequencies $\{\omega_i\}$ depends on the occupation of the modes of the environment at $\{\omega_i\}$. As soon as light is emitted, the population of the modes increases, modifying the tunneling rates, and hence the emission rate itself. We already described how in the strong-driving regime of a single mode, when $\bar{n} \sim 1/r$, the tunneling rate is decreased by the enhanced phase fluctuations of the mode. On the other hand it is known that parametric processes, such as the two-mode driving, are stimulated by the build-up of field inside the resonators, yielding enhanced emission rates. Finding the stationary state of the modes is thus a complex problem, whose solution should be self-consistent.

The perturbative $P(E)$ theory works around this issue by assuming that the stationary state of the modes stays close to the thermal equilibrium that exists in the absence of

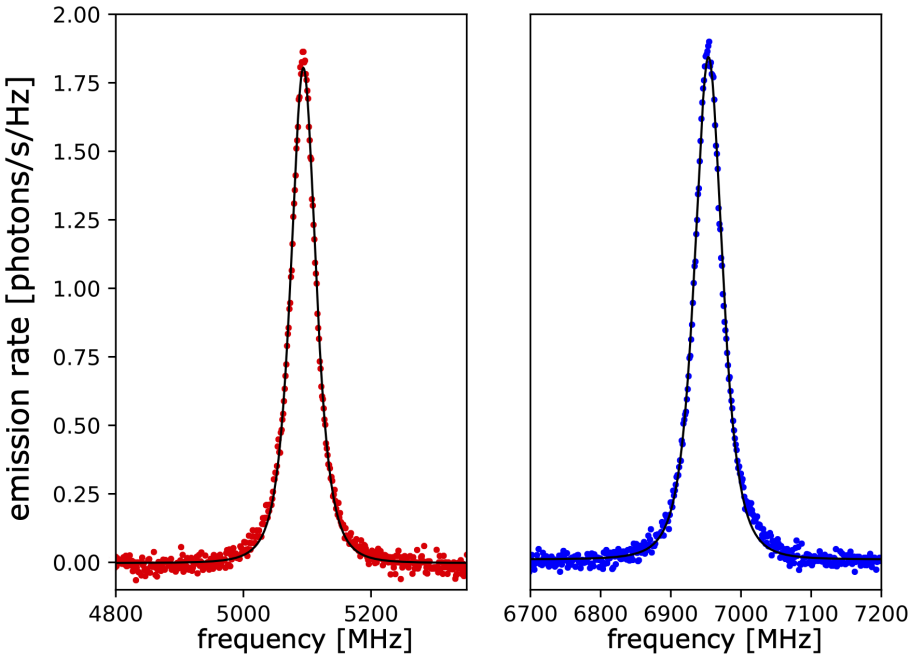

Figure 4.27: Emission spectra at a voltage bias $2eV = h\times$ 12.05 GHz. The spectra are fitted by a Lorentzian function squared, reproducing the $Re[Z(\omega)] \times Re[Z(\omega_J - \omega)]$ shape.

tunneling, i.e for $E_J^* \to 0$. This generally implies $\bar{n} \ll 1$. The self-consistency is assured by the condition that the dc and ac current through the junction stay much smaller than its critical current I_0^*.

The $P(E)$ prediction (4.134) reproduces well the shape of the emission spectra at low pumping strength β, with a FWHM $\simeq \sqrt{\sqrt{2}-1} \times \kappa_{eff} = 2\pi \times 50$ MHz[5] (Fig.4.27), as well as the emission rate $\Gamma \simeq \beta^2 \frac{\kappa_{eff}}{2}$ for $\beta^2 \ll 1$. The population of the modes is then $\bar{n} \simeq \frac{\beta^2}{2}$.

As soon as E_j^* is large enough to have a β not much smaller than 1, the $P(E)$ theory fails to predict the correct emission rate. This is manifest in the spectra of figure 4.27, where the integrated PSD yields $\Gamma = 100 \pm 5$ Mphotons/s, while $\beta^2 \frac{\kappa_{eff}}{2} \simeq 70$ Mphotons/s.

Meanwhile, our simple non-degenerate parametric amplifier model 4.1.3 captures the impact of stimulated emission from the finite occupation of the cavities. We predict the correct emission rate $\Gamma = \frac{\beta^2}{1-\beta^2}\frac{\kappa_{eff}}{2} = 99.8 \pm 5$ MPhotons/s for $\beta = 0.54$, corresponding to an occupation number $\bar{n} = 0.20 \pm 0.01$.

At larger pumping strength β, the shape of the spectra changes from a Lorentzian function squared to a true Lorentzian. At the same time it becomes narrower. This effect is visible on the four spectra of figure 4.28. Here the Josephson frequency is slightly detuned by $\Delta \simeq -10$ MHz with respect to the sum of the resonance frequencies. The value of E_J^* is increased from 3.30 μeV up to 6.88 μeV, corresponding to β ranging from 0.67 up to 1.4, i.e above the threshold for the parametric transition[6].

The evolution of the shape of spectra is also captured by the parametric amplifier model, whose dynamical bandwidth is $\Delta\Omega_G \simeq \kappa_{eff}\frac{1-\beta^2}{1+\beta^2}$. We fit the spectra of figure 4.28 with

[5] with $\kappa_{eff} = \frac{2\kappa_a\kappa_b}{\kappa_a+\kappa_b} = 485\ \mu s^{-1}$.

[6] A this finite detuning, the threshold is $\beta^\circ(\Delta) = 1.015$.

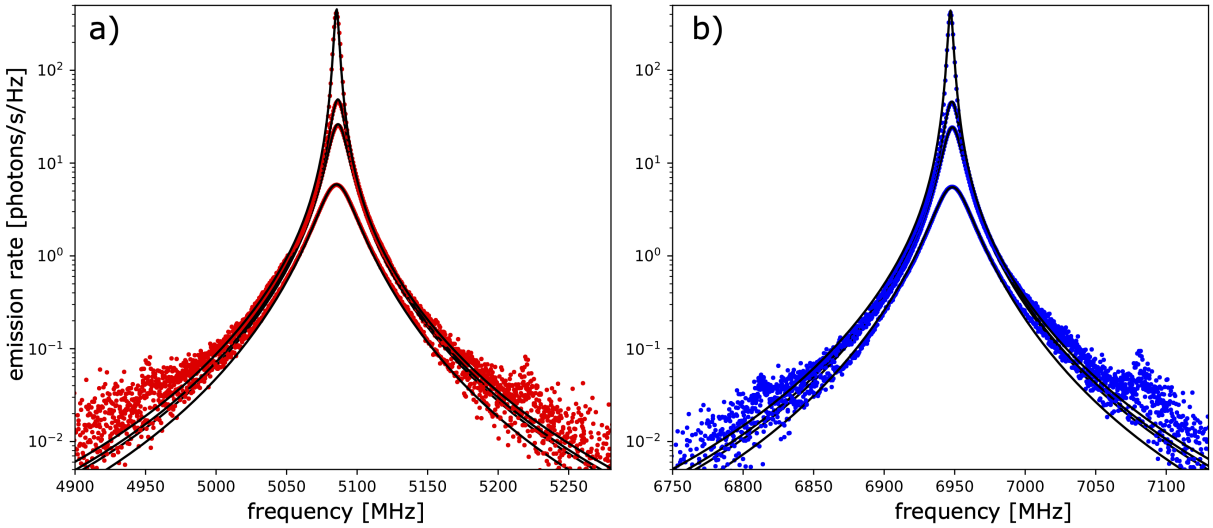

Figure 4.28: Emission spectra at a voltage bias $2eV = h\times$ 12.035 GHz and increasing pump strength β. The independent fits in panels (a) and (b) yield the same value of the detuning $\Delta \simeq -10$ MHz and of the emission rates, corresponding to $\bar{n} = 0.4$, 1.0, 1.5 and 5.0 photons respectively ($\pm$ 5%).

the expression for the PSD (4.81). In our fit procedure the resonance frequencies and leak rates of the modes are fixed, having been determined in 4.3.1. The only free parameters are the detuning Δ and the pump strength β.

These fits reproduce extremely well the emission spectra. In particular the independent fits around ω_a and ω_b yield the same value for the detuning, and equal emission rates within our accuracy $\pm$ 5%. However, the effective value of β extracted from the fit differs from the applied pump strength, being systematically lower.

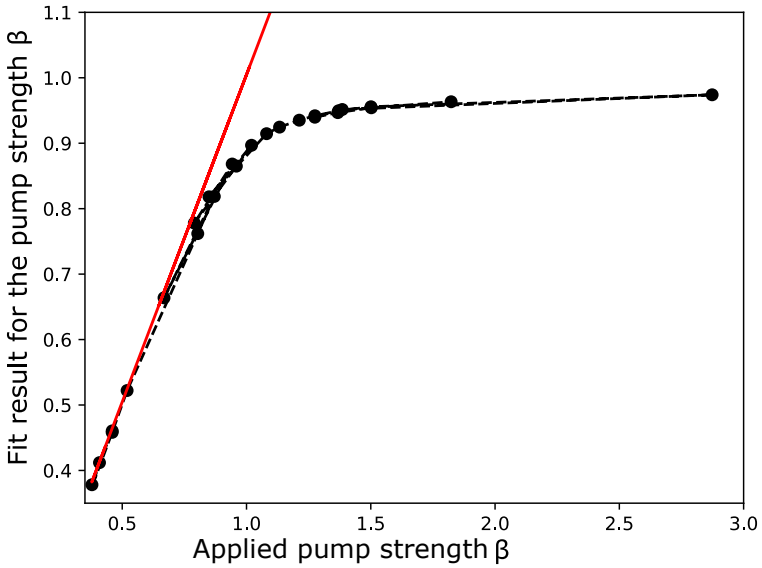

Figure 4.29: Results of the fit of 25 emission spectra, with the pump strength β varying from 0.41 to 2.87 and various values of the detuning Δ. The fitted pump strength (black dots) agrees well with the true β (red line) at low driving, but disagrees for strong driving.

We plot in figure 4.29 the result of the fit procedure applied on 25 pairs of spectra, taken with β varying from 0.41 up to 2.87 and in various conditions of detuning, ranging from Δ = -42 MHz to Δ = +7 MHz. Here we compensate for the detuning, so that $\beta^\circ = 1$ is

the parametric threshold for each point. The fits yield the correct value of β at very low driving only, when $\bar{n} \leq 1$, and disagrees strongly for strong driving.

This result illustrates the limits of our simple parametric amplifier model. As $\beta \to 1$, non-linearities of the driving Hamiltonian slow down the emission rate, so that $\bar{n}$ never diverges [104]. This means that in practice we can always increase β above the parametric threshold and measure a finite emission rate. On the other hand for small detuning Δ the fit procedure can never yield a β well above 1, hence this disagreement.

Figure 4.29 suggests that this effect is equivalent to a re-definition of the pump strength, as while the fits yield an incorrect value of β, they give the correct value for the emission rates and the right shape for the spectra. We plot in figure 4.30 the measured occupation number $\bar{n}$ as a function of β, along with the prediction of the parametric amplifier model, which illustrates the smooth renormalization of the parametric divergence.

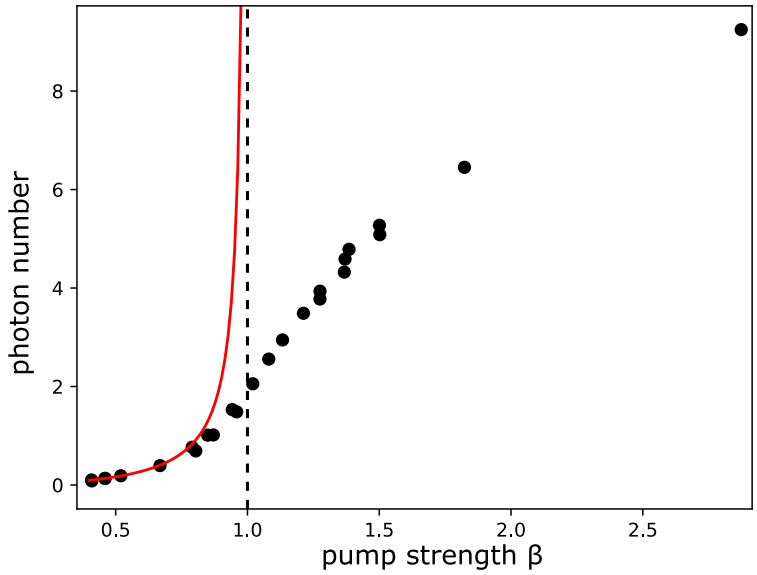

Figure 4.30: Occupation number of the cavities $\bar{n}$ as a function of the pump strength β. The measured values (black dots) agree well with the parametric amplifier model (red line) at low β. Close to the parametric transition $\beta = 1$, the simple model predicts a divergence of $\bar{n}$. In the real system.

4.3.3 Photon statistics

In the same condition of pump strength and detuning than in 4.29, we measure correlation functions of the a and b fields, revealing their non-classical statistics.

Studying the two modes separately: $g^{(2)}(\tau)$ functions and Fano factors

The simple scattering of a parametric amplifier predicts chaotic statistics for the emitted radiation, with:

$$g_a^{(2)}(0) = g_b^{(2)}(0) = 2. \tag{4.135}$$

In the simple case of equal leak rates $\kappa_a = \kappa_b$ and zero detuning, the time-dependence of the correlation functions is [119]:

$$g_a^{(2)}(\tau) = g_b^{(2)}(\tau) = 1 + e^{-\kappa|\tau|} \frac{\left(\beta \cosh(\beta\kappa|\tau|/2) + \sinh(\beta\kappa|\tau|/2)\right)^2}{\beta^2}. \tag{4.136}$$

At low driving $\beta \ll 1$, we have $g_{a/b}^{(2)}(\tau) \simeq 1 + e^{-\kappa|\tau|}$. For intermediate pump strength $g_{a/b}^{(2)}(\tau)$ is the sum of terms of the form $e^{-\kappa|\tau|}$, $e^{-(1+\beta)\kappa|\tau|}$ and $e^{-(1-\beta)\kappa|\tau|}$. As $\beta \to 1$ the exponential decay constant in the last term tends to zero, so that $g_{a/b}^{(2)}(\tau) \to 2, \forall \tau \in \mathbb{R}$.

This model is found to be too naive to describe our data, where even at low driving the back-action from the finite impedance of the resonators reduce the bunching of the emitted photons, with a zero-time value following (4.23). This is visible on panel (a) of figure 4.31, where the $g^{(2)}(\tau)$ functions have been measured at a low driving strength $\beta = 0.46$, yielding $\bar{n} = 0.13$. Their initial value are $g_a^{(2)}(0) = 1.95 \pm 0.1$ and $g_b^{(2)}(0) = 1.85 \pm 0.07$.

Furthermore, for finite occupation number $\bar{n}$, the back-action of the cavity fields onto the junction modifies the photon emission rate, yielding photon statistics closer to the one of coherent light, with $g_a^{(2)}(0), g_b^{(2)}(0) \to 1$. This is visible in panels (b) and (c) of figure 4.31, where the correlators were measured at pump strength $\beta = 0.87$ and 1.13, yielding occupation numbers of $\bar{n} = 1.0$ and 3.0 photons respectively.

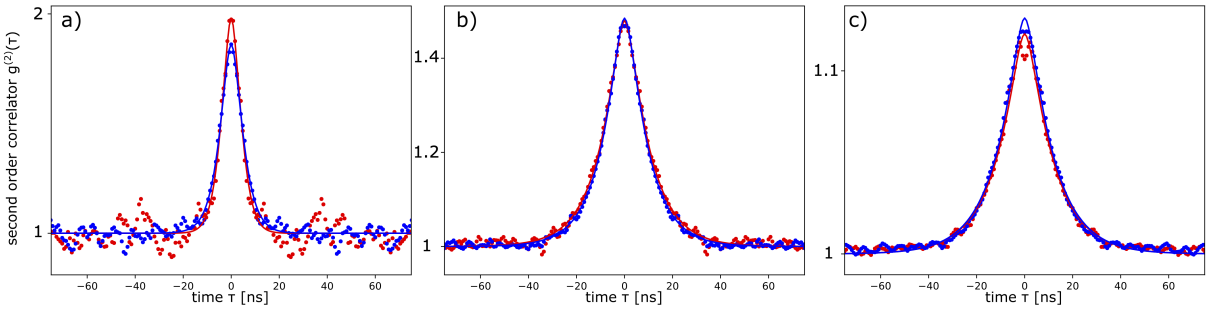

Figure 4.31: Second order coherence functions of the a (red) and b (blue) photons, measured at occupation numbers of $\bar{n} = 0.13$ (panel a), 1.0 (panel b) and 3.0 (panel c) photons, with phenomenological fits.

The zero-time value of the correlators decreases steadily from a value of about 1.8 down to 1 at high occupation numbers, which is characteristic of quasi-classical radiation. We plot in figure 4.32 the values of $g_a^{(2)}(0)$ and $g_b^{(2)}(0)$ for increasing occupation pump strength β, which illustrates this trend toward classical statistics of each mode considered separately.

We fit each correlator with a phenomenological fit function, which is a version of (4.136) with an extra parameter:

$$g_{fit}^{(2)}(\tau) = 1 + A \times e^{-\kappa|\tau|} \frac{\left(\beta \cosh(\beta\kappa|\tau|/2) + \sinh(\beta\kappa|\tau|/2)\right)^2}{\beta^2}. \tag{4.137}$$

The fit parameter $A = g^{(2)}(0) - 1$ encodes the reduced value of $g^{(2)}(0)$ with respect to the TMSV prediction of $g^{(2)}(0) = 2$. The evolution of the decay rate of the correlation functions is well reproduced by (4.137), although here again the fits yield an underestimated value of β, close to the results of figure 4.29.

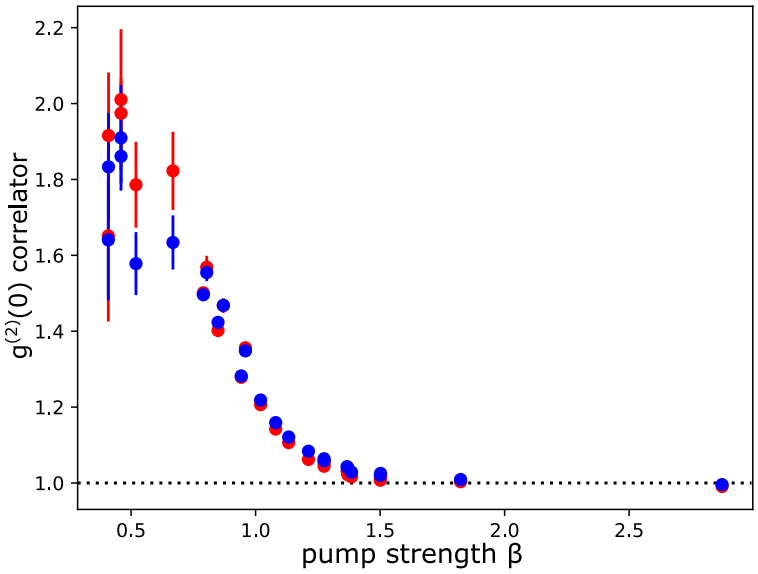

Figure 4.32: Zero-time value of the second order correlation functions $g^{(2)}(\tau)$ (red dots) and $g^{(2)}(\tau)$ (blue dots) as a function of the pump strength β.

Finally from the measurement of the $g^{(2)}(\tau)$ functions we estimate the **Fano factors** of the emitted photons, with [119]:

$$F_x = 1 + \gamma_x \int d\tau g_x^{(2)}(\tau) - 1. \tag{4.138}$$

The Fano factor is a measure of the slow fluctuations of the occupation number of the modes. Like the photon number $\bar{n}$ it is predicted to diverge at the parametric transition. For a finite impedance of the environment, this divergence is washed out by the phase fluctuations from the modes [104].

The Fano factors for the two modes are plotted in figure 4.33. F_a and F_b increase strongly from about 1.5 at low β to 8 at the parametric threshold, then decrease slowly.

Occupation numbers cross-correlations

We study the non-classical correlations between the occupation of the two modes n_a and n_b. They are characterized by the cross-correlation function $g_{ab}^{(2)}(\tau) = \frac{\langle n_a(0) n_b(\tau)\rangle}{\bar{n}_a \bar{n}_b}$. The parametric amplifier model predicts [119]:

$$g_{ab}^{(2)}(\tau) = 1 + e^{-\kappa|\tau|} \frac{\left(\cosh(\beta\kappa|\tau|/2) + \beta \sinh(\beta\kappa|\tau|/2)\right)^2}{\beta^2}. \tag{4.139}$$

The zero-time value reads: $g_{ab}^{(2)}(0) = 1 + \frac{1}{\beta^2} = 2 + \frac{1}{2\bar{n}}$, which diverges at low driving $\bar{n} \to 0$. This value also yields a NRF $= \frac{1}{2}$, i.e partial correlation between n_a and n_b.

We plot in figure 4.34 the measured $g_{ab}^{(2)}(\tau)$ cross-correlation function, for the same values of occupation numbers than in figure 4.31. The time dependence follows the same trend as the $g_{a/b}^{(2)}(\tau)$ correlators.

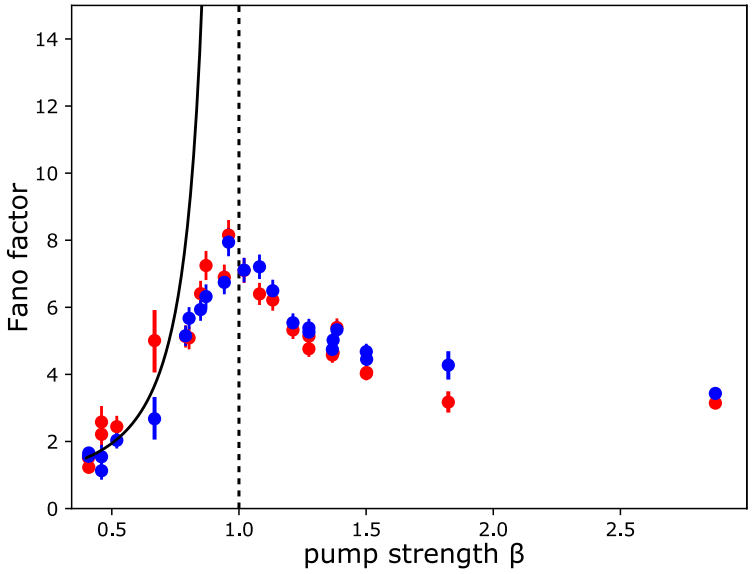

Figure 4.33: Fano factors of the a (red dots) and b (blue dots) photons as a function of the reduced pump strength. As β is increased, the Fano factors increase strongly from about 1.5 at low driving to 8 near the parametric transition threshold. Above the threshold, they decrease slowly. The parametric model prediction (black line) diverges at $\beta = 1$.

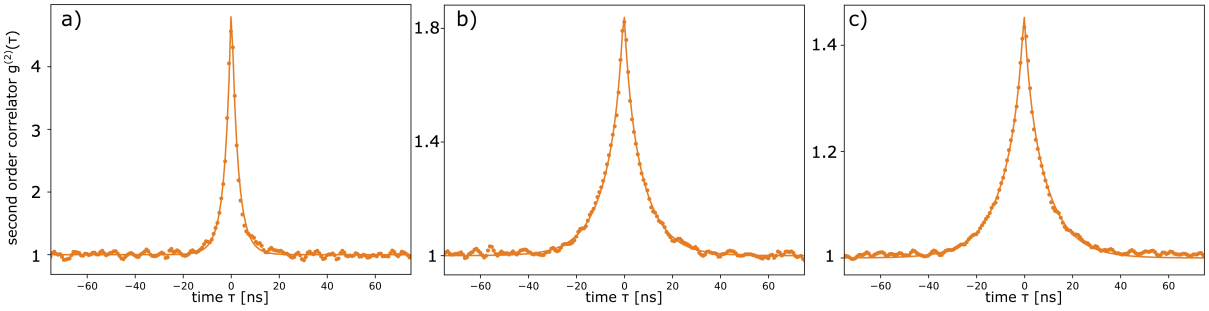

Figure 4.34: Cross-correlation function $g^{(2)}_{ab}(\tau)$, measured at occupation numbers of $\bar{n} = 0.13$ (panel a), 1.0 (panel b) and 3.0 (panel c) photons, with phenomenological fits.

At low driving, the zero-time of $g^{(2)}_{ab}(\tau)$ is much larger than 2, breaking the classical Cauchy-Schwarz inequality $g^{(2)}_{ab}(0) \leq \frac{g^{(2)}_a(0)+g^{(2)}_b(0)}{2} \leq 2$. At increasingly high pump strength, $g^{(2)}_{ab}(0)$ goes down to 1, while the decay time in $g^{(2)}_{ab}(\tau)$ decreases (Fig.4.31).

The measured correlation functions deviate once again from the predictions of the naive amplifier model, as $g^{(2)}_{ab}(0)$ goes well below 2. They are however well fitted by a phenomenological fit function:

$$g^{(2)}_{ab,fit}(\tau) = 1 + B \times e^{-\kappa|\tau-\tau_0|} \frac{\left(\cosh(\beta\kappa|\tau-\tau_0|/2) + \beta \sinh(\beta\kappa|\tau-\tau_0|/2)\right)^2}{\beta^2}, \qquad (4.140)$$

which reproduces the evolution of the decay time with increasing pump strength. The parameter B describes the deviation to the parametric model, while $\tau_0 \simeq 0.2$ ns is the uncompensated time delay between the measurement lines. The effective value of β extracted from the fits is lower than the true value, close to the results of figure 4.29.

Noise reduction factor

We plot in figure 4.35 the zero-time value of the three correlation functions $g_a^{(2)}(0)$, $g_b^{(2)}(0)$ and $g_{ab}^{(2)}(0)$ as a function of the occupation number of the cavities. The classical Cauchy-Schwarz inequality on n_a, n_b is violated in all measurements, which extends the previous results of Olivier Parlavecchio (Fig.4.8) up to high occupation numbers $\bar{n} \simeq 9$.

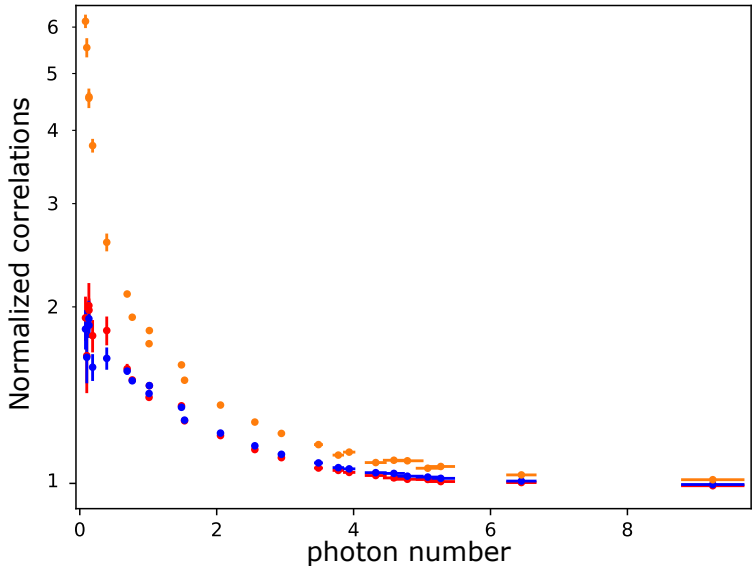

Figure 4.35: Auto and cross-correlations of the populations of the two modes. We use a log-scale on the y-axis to better display the violation of the classical inequality $g_{ab}^{(2)}(0) \leq \frac{g_a^{(2)}(0)+g_b^{(2)}(0)}{2}$ up to $\bar{n} = 9$.

The non-classicality of the radiation can be quantified by the noise reduction factor (NRF), which is computed from the measured correlation functions following (4.20). We plot its value in figure 4.36 as a function of $\bar{n}$.

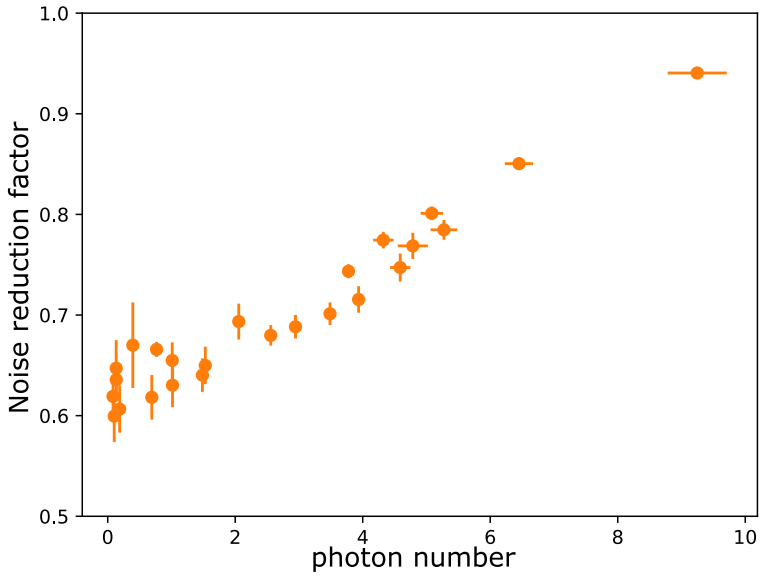

Figure 4.36: Noise reduction factor as a function of the occupation number. The value NRF≤ 1 proves the two-mode amplitude squeezing of the radiation.

At low occupation numbers, we have NRF$=0.625 \pm 0.03$. We attribute the discrepancy with the predicted value NRF$=\frac{1}{2}$ to the finite acquisition bandwidth of our experiment,

as detailed in 4.4.1. As $\bar{n}$ is increased, the NRF increases towards 1, the value for classical independent beams of light. This transition to the classical regime was not probed in the 2015 experiment by Olivier Parlavecchio and coworkers, as they stayed in a low occupation regime $\bar{n} \leq 1.5$ (Fig.4.8).

4.4 Results on the emission of entangled photons

We turn to the study of the non-classical phase correlations between the two beams, accessible through the non-local observable $ab(t)$. In our simple parametric model, its auto-correlation function reads:

$$g^{(2)}_{\phi}(\tau) = \left\{ \frac{1}{\beta^2} + e^{-\kappa|\tau|} \frac{1 + \left(\beta \cosh(\beta\kappa|\tau|/2) + \sinh(\beta\kappa|\tau|/2)\right)^2}{\beta^2} \right\} \times e^{-i\omega_J \tau}. \tag{4.141}$$

As expected its zero-time value $g^{(2)}_{\phi}(0) = \frac{1}{\beta^2} + 1 = 2 + \frac{1}{2\bar{n}}$ coincides with $g^{(2)}_{ab}(0)$. For any $\tau \neq 0$, the model predicts $|g^{(2)}_{\phi}(\tau)| > g^{(2)}_{ab}(\tau)$, i.e a violation of the Cauchy-Schwarz inequality for separable states (4.41).

4.4.1 Preliminary experiment in the heating regime

We describe here the results of a **preliminary experiment** in the low-driving regime $\beta \leq 0.63$ (yielding occupation numbers $\bar{n} \leq 0.33$), where the acquisition bandwidth was reduced from 525 MHz down to 180 MHz. This increases greatly the SNR, as all the background noise outside of the measurement bandwidth is rejected, while the signal PSD is almost entirely contained in a band of $\sim 3 \times \kappa \simeq 225$ MHz.

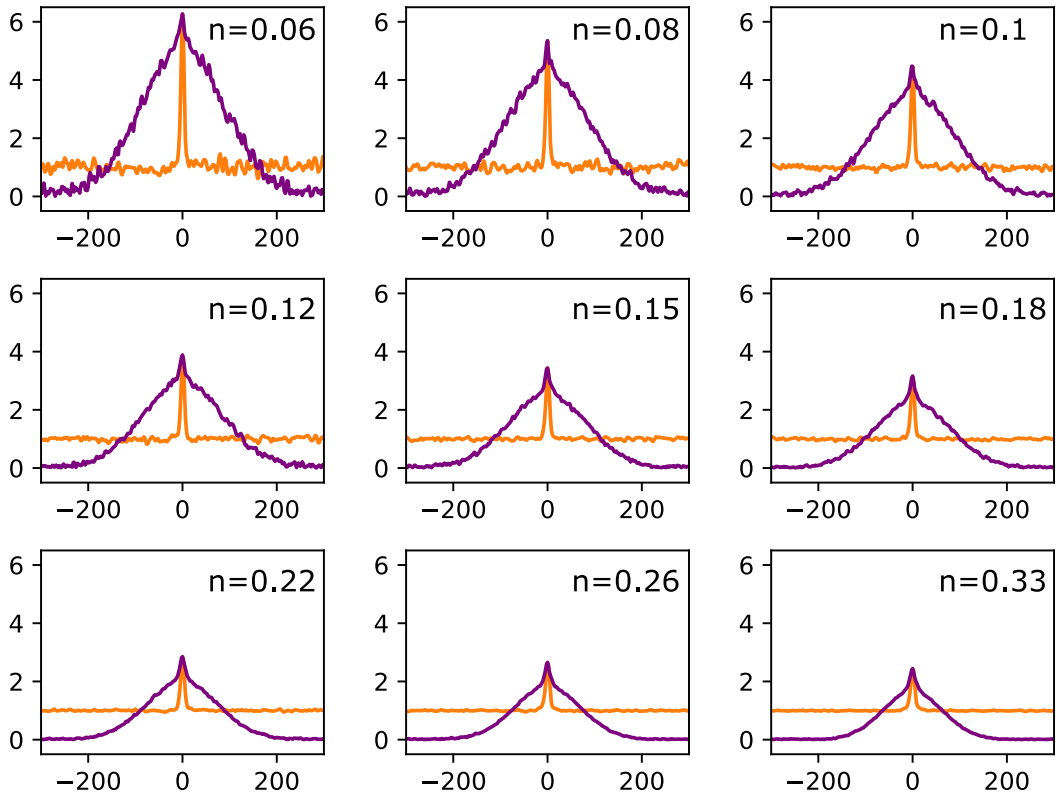

Figure 4.37: Measurement of the entanglement witness correlators $g^{(2)}_{ab}(\tau)$ (orange curves) and $|g^{(2)}_{\phi}(\tau)|$ (purple curves) as a function of time τ in nanoseconds, for $\bar{n}$ ranging from 0.06 up to 0.33.

We present in figure 4.37 the measured $g^{(2)}_{ab}(\tau)$ and $|g^{(2)}_{\phi}(\tau)|$ functions for a pump strength β between 0.32 and 0.63, yielding occupation numbers ranging from 0.06 up to 0.33. For

each set of curves, there is a time window of varying length (from about 340 ns down to 125 ns) where the phase correlator is larger than the population correlator, i.e where the inequality (4.41) is broken. This is a direct witness that in each measurement **the emitted a and b fields are entangled**.

There are noticeable differences between the measured correlators and the predictions (4.139) and (4.141) of our parametric amplifier model. The fact that the inequality is violated only over a finite time window is unexpected. At higher pump strength $\beta > 0.63$ the fields do not display entanglement, while we predicted $|g_\phi^{(2)}| - g_{ab}^{(2)} \geq \beta^{-2} - 1 > 0$ as long as $\beta \leq 1$. To understand better these phenomena, we focus on a single set of correlation functions, measured at $\beta = 0.55$ with $\bar{n} = 0.22$.

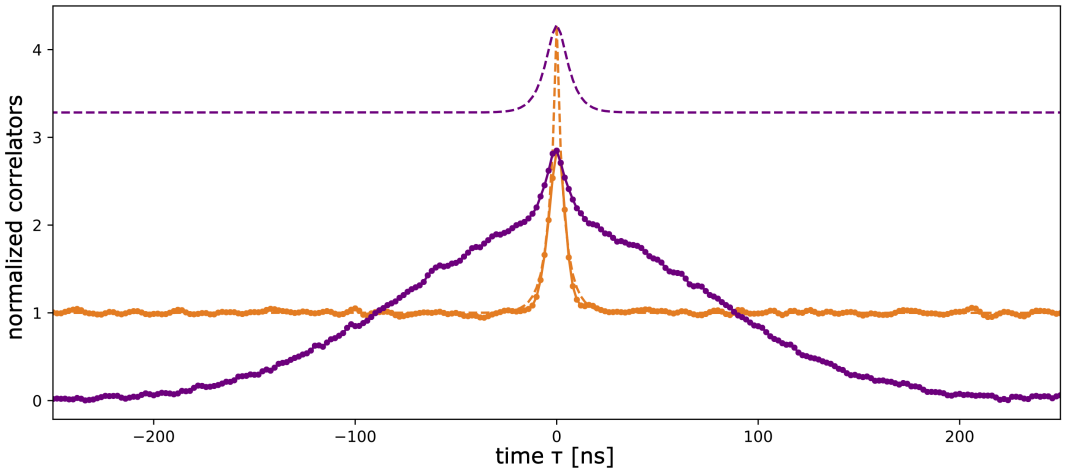

Figure 4.38: Correlation functions $g_{ab}^{(2)}(\tau)$ (orange points) and $|g_\phi^{(2)}(\tau)|$ (purple points) measured at an occupation number $\bar{n} = 0.22$, with theoretical predictions of the parametric model (dashed curves).

We plot in figure 4.38 the measured correlators, along with the predictions of (4.139) and (4.141) for this value of pump strength. Both theoretical curves start at $\tau = 0$ at a larger value ($\simeq 4.3$) than the experimental data ($\simeq 2.85$). The initial decay of both measured curves is close to the decay time of the theoretical predictions. However, while the phase correlator is predicted to tend to a finite value at long times: $|g_\phi^{(2)}(\tau \to \infty)| \to \beta^{-2}$, the measured correlator tends to zero. It is this slow decay that limits the time window over (4.41) is violated, i.e over which we can prove that the fields are entangled.

At this low pump strength, the antibunching contribution to number correlations is small but finite (Fig.4.32), with $g_{a/b}^{(2)}(0) \simeq 1.8$ instead of 2, so that we expect $g_{ab}^{(2)}(0) \simeq 4.1$ instead of 4.3. We attribute further discrepancies between predictions and measurements to two main causes that we discuss below: the finite frequency window of our detection setup and the spurious drifts of the Josephson frequency due to voltage noise.

Impact of a finite acquisition window on the correlation functions

When studying frequency-dependent quantities such as the spectral density of quadrature squeezing (4.91), it is advantageous to filter out the incoming fields $a(t) = \int a(\omega) e^{-i\omega t} d\omega/2\pi$, $b(t) = \int b(\omega') e^{-i\omega t} d\omega'/2\pi$ to select only the field components $a(\omega)$, $b(\omega_J - \omega)$ displaying the greatest amount of correlations.

On the other hand the study of time-dependent observables such as correlation functions require capturing the full time dependence of the field operators $a(t), b(t)$. Any filtering stage in the experimental data acquisition rejects a fraction of the field components, so that we miss part of the correlations. This amounts to having a finite detection efficiency, and leads to a lower value of the measured correlators compared to theoretical predictions.

When the shape of the effective filtering function $F(\omega)$ applied to the signals prior to acquisition is known, its impact on measured correlation functions can be calculated [82]. The filtered field operators read:

$$a_{filt.}(t) = \int F(\omega - \omega_a) a(\omega) e^{-i\omega t} \frac{d\omega}{2\pi} = \int F_a(t - t') a(t') dt' \tag{4.142}$$

$$b_{filt.}(t) = \int F(\omega - \omega_b) b(\omega) e^{-i\omega t} \frac{d\omega}{2\pi} = \int F_b(t - t') b(t') dt' \tag{4.143}$$

so that:

$$\begin{aligned} \langle a^\dagger_{filt.}(t_1) a_{filt.}(t_2) b^\dagger_{filt.}(t_3) b_{filt.}(t_4) \rangle =& \Big\langle \int F_a^\dagger(t_1 - t_\alpha) a^\dagger(t_\alpha) F_a(t_2 - t_\beta) a(t_\beta) \times \\ & F_b^\dagger(t_3 - t_\gamma) b^\dagger(t_\gamma) F_b(t_4 - t_\delta) b(t_\delta) dt_\alpha dt_\beta dt_\gamma dt_\delta \Big\rangle \\ =& \int \mathbb{F}(t_1, t_2, t_3, t_4) \langle a^\dagger(t_\alpha) a(t_\beta) b^\dagger(t_\gamma) b(t_\delta) \rangle d^4 t_{\alpha\beta\gamma\delta} \end{aligned} \tag{4.144}$$

The filtered correlation function can be expressed as a generalized convolution product of its unfiltered version times a multi-dimensional filter function $\mathbb{F}$. In the relevant case where two of the dummy time variables t_{1-4} are equal, the calculations require extra care due to the non-trivial commutation relations of $a(t), b(t)$.

Our theoretician collaborators at Ulm University have developed a framework to compute efficiently these convolution products, mapping it to a simpler two-dimensional integral [87]. In addition to the back-action of the finite impedance of the resonators, their simulations reproduce well the reduction of the initial value of the correlators compared to the naive parametric amplifier model due to filtering effects.

A simple, classical picture of the signals allows us to understand this reduction and how it depends on the width of the acquisition window. Consider the time-dependent part of the population correlator: $f(\tau) = g^{(2)}_{ab}(\tau) - 1$. Within our acquisition procedure, we actually measure and average its Fourier transform $\mathbb{F}[f(\tau)](\omega) = \tilde{f}(\omega)$.

In a classical picture, $\tilde{f}(\omega)$ is the product of the Fourier transforms of the instantaneous populations $n_a(t)$, $n_b(t)$ (Fig.4.20). As $f(\tau)$ is the sum of terms of the form $e^{-\kappa|\tau|}$, $e^{-(1+\beta)\kappa|\tau|}$ and $e^{-(1-\beta)\kappa|\tau|}$, its Fourier transform is the sum of Lorentzian functions with widths κ, $\kappa(1+\beta)$ and $\kappa(1-\beta)$.

Due to the slow decay of the Lorentzian function $\propto |\kappa + i\omega|^{-2}$, reconstructing exactly $f(\tau)$ would require an infinite acquisition bandwidth. In practice, an integration bandwidth $\Delta\omega = 2\pi \times \kappa$ is required to capture about 90% of $\tilde{f}(\omega)$, which amounts to losing between 5% and 10% of the correlations in $g^{(2)}_{ab}(\tau) = f(\tau) + 1$.

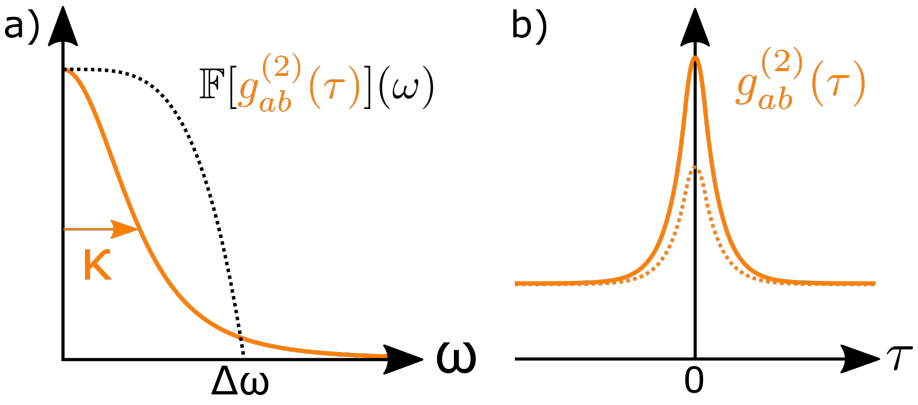

Figure 4.39: a) The Fourier transform of $g^{(2)}_{ab}(\tau)$ is a Lorentzian function of width κ at low driving $\beta \ll 1$. The bandpass filtering used in the experiment amounts to low-pass filtering $\mathbb{F}[g^{(2)}_{ab}(\tau)](\omega)$. The shape of the low-pass filter (dashed) depends on the detail of the bandpass filters. b) The measured correlator of filtered signals (dashed curve) shows less correlations than for the unfiltered fields (full curve).

In our experiments, the Nyquist frequency ω_N (equal to half the sampling rate) sets a first upper limit on the effective integration bandwidth: when digitizing signals at a rate of 1 sample every T nanoseconds, we can never detect features of the correlation functions varying on a scale smaller than T. A second stage of effective low-pass filter in the acquisition of correlation function results from the bandpass filtering of the signals $a(t), b(t)$ with filter $F(\omega)$. The low-pass cut-off frequency is approximately set by the width $\Delta\omega$ of the bandpass filters, while its shape is given by the auto-convolution product $F(\omega) \otimes F^{\dagger}(\omega')$ (Fig.4.39).

In the preliminary experiment whose results are presented in figure 4.37, the narrow bandpass filters with $\Delta\omega = 2\pi \times 180$ MHz were only about 2.5 times wider than κ. As a result we missed a considerable amount of correlations between the a and b fields, hence the reduction of the zero-time value of normalized correlation functions in figure 4.38. In later experiments we used the filtering scheme presented in figure 4.19, with $\Delta\omega = 2\pi \times 525$ MHz $\simeq 7 \times \kappa$, which is enough to capture most of the correlations.

Our finite sampling rate and measurement bandwidth impact the short-time features of correlation functions, in particular the initial decay from their zero-time value (Fig.4.38). However their long times behaviour, carried by the zero-frequency Fourier components, is not affected by filtering. The decay down to zero of $|g^{(2)}_{\phi}(\tau)|$ is actually explained by the low frequency voltage noise on the junction.

Impact of the voltage noise on the phase correlations

The Josephson frequency $\omega_J = 2eV/\hbar$ appears in the phase correlator with:

$$g^{(2)}_{\phi}(\tau, \omega_J) = |g^{(2)}_{\phi}(\tau)| \times e^{-i\omega_J \tau}. \tag{4.145}$$

Even though the entanglement witness involves only the absolute value $|g^{(2)}_{\phi}(\tau)|$, fluctuations of $\omega_J(t) = 2eV/\hbar + \delta\omega(t)$ during the acquisition and averaging of $g^{(2)}_{\phi}(\tau, \omega_J)$ lower its value.

Through the calibration of the environment of the junction and our results on the spectral width of the Josephson radiation 3.5, we developed a simple model for the low-frequency

voltage noise in our experiments. The emission spectra in the single photon regime have a Gaussian shape with a FWHM $= 2\sqrt{2\ln(2)}\sigma_\omega$, reflecting the Gaussian statistics of thermal voltage noise on the junction. The measured value $\sigma_\omega = 2\pi \times 1.3$ MHz can be quantitatively explained by attributing most of the voltage noise $\sigma_V = \hbar\sigma_\omega/2e$ to the very low frequency modes of the impedance of the environment, dominated by the spurious LC resonance of the bias-tee at 71 kHz.

When measuring correlation functions, our effective measurement repetition time is much shorter than 1/(71 kHz), so that when acquiring one chunk of data $\omega_J(t) = 2eV(t)/\hbar$ is kept constant and we truly measure $g_\phi^{(2)}(\tau, \omega_J(t))$. However when repeating many times the acquisition we average together correlators corresponding to different values of $\omega_J(t)$, taken at different values of the detuning $\Delta(t) = \omega_J(t) - \omega_a - \omega_b$. The averaged correlator reads:

$$\langle g_\phi^{(2)}(\tau)\rangle_\Delta = \int |g_\phi^{(2)}(\tau, \omega_J + \Delta)| e^{-i(\omega_J+\Delta)\tau} p(\Delta) d\Delta. \tag{4.146}$$

Here $p(\Delta)$ is the probability density function for having the value of detuning Δ during one acquisition. Following our model of purely thermal, Gaussian noise, we have:

$$p(\Delta) = \frac{1}{\sqrt{2\pi}\sigma_\omega} e^{-\frac{\Delta^2}{2\sigma_\omega^2}}. \tag{4.147}$$

As $\Delta\omega_J^2 \ll \kappa$, we can estimate the averaged correlator as:

$$\begin{aligned} \langle g_\phi^{(2)}(\tau)\rangle_\Delta &\simeq g_\phi^{(2)}(\tau, \omega_J) \int e^{-i(\omega_J+\Delta)\tau} p(\Delta) d\Delta \\ &\simeq g_\phi^{(2)}(\tau, \omega_J) \times e^{-\frac{(\sigma_\omega \tau)^2}{2}}. \end{aligned} \tag{4.148}$$

Hence the decay to zero at long times of $g_\phi^{(2)}(\tau)$ originates directly from the Gaussian noise δV. This correlator can be interpreted as the auto-correlation function of the sum of the phases of the $a(t)$ and $b(t)$ fields, which is itself equal to the squeezing angle θ. The random motion of $\theta(t)$ through time, due to thermal noise on the junction, results in a finite phase coherence time for the propagating beams.

The total voltage noise on the junction may also result from non-equilibrium events, or from the thermal occupation of modes up to $k_B T/h \simeq 400$ MHz which impact $V(t)$ faster than the measurement rate. Taking these phenomena into account would require a more complex treatment and numerical simulations. However the simple picture of slow Gaussian noise is enough to explain the bell shape of the measured phase correlators (Fig.4.37). In particular the value of the phase coherence time at low driving, obtained from a complex Gaussian fit of $g_\phi^{(2)}(\tau)$, agrees very well with the voltage noise δV deduced from single-photon spectra. We thus find that the entanglement of the a and b beams is limited only by the low-frequency thermal noise on the bias voltage, in agreement with the simple picture presented in figure 4.9.

Evolution of the phase coherence time in the preliminary experiment

To validate this picture, we fit the Fourier transform of the phase correlators from figure 4.37 with Gaussian functions. It is easier to perform these fits in the frequency domain, where the short-time features of $|g_\phi^{(2)}(\tau)|$ near $\tau = 0$ can be neglected.

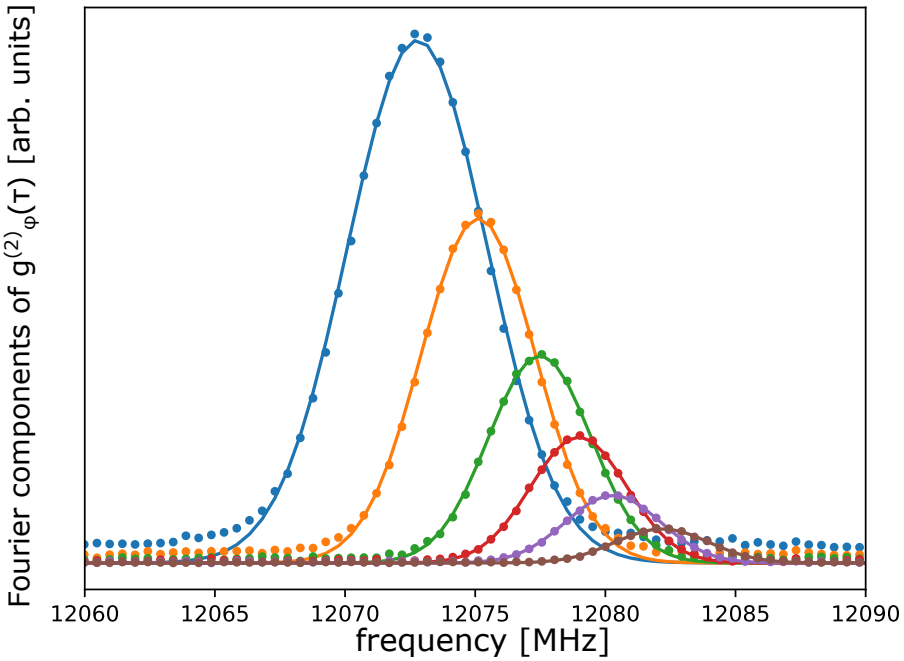

Figure 4.40: Gaussian fits of the Fourier transforms of the phase correlators, measured at occupation numbers ranging from $\bar{n} = 0.33$ (blue points and curve) down to $\bar{n} = 0.033$ (brown points and curve).

The agreement of the Gaussian fits is excellent for values of $\bar{n}$ ranging from 0.33 down to 0.033, see figure 4.40. The slight difference between the data and the fits comes from our neglecting of the short-time features of $g^{(2)}_{\phi}(\tau)|$, which adds a low pedestal to the Fourier transform.

The position of the peaks is the Josephson frequency $\omega_J = 2eV/\hbar$. As we increase the photon emission rate it is shifting from 12.082 GHz towards lower frequencies, see figure 4.41 panel (a). The width of the Gaussian peaks, which is equal to the dephasing rate σ_ω of the time-domain correlation functions, is found to be about $2\pi \times 1.8$ MHz at low occupation of the modes. It increases up to $2\pi \times 2.7$ MHz at $\bar{n} = 0.33$ (Fig.4.41.b).

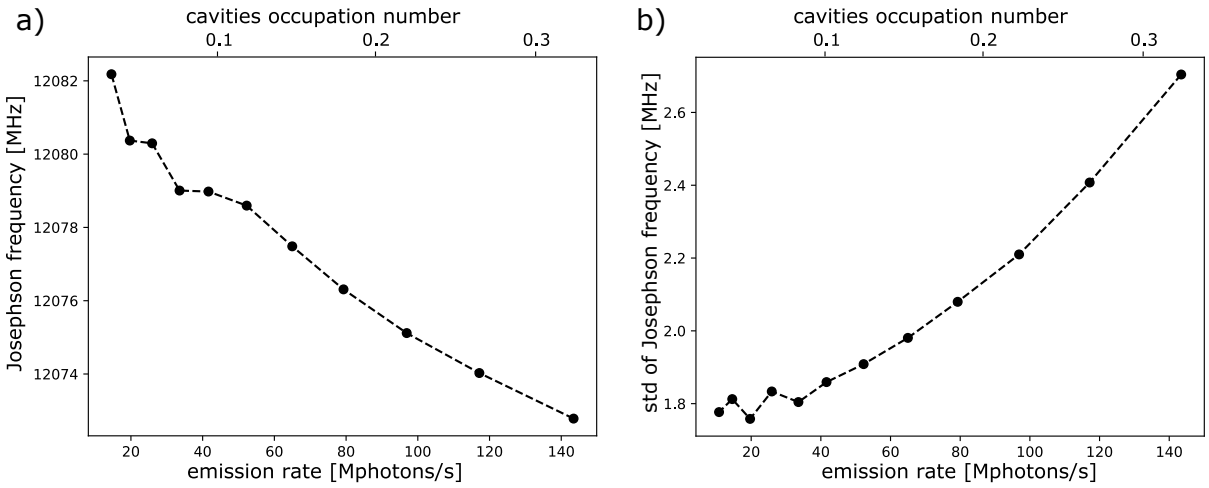

Figure 4.41: a) Josephson frequency as a function of the emission rate Γ and the occupation number $\bar{n}$. b) Standard deviation of the Josephson frequency $\sigma_\omega/2\pi$, extracted from the Gaussian fits of figure 4.40.

The **shift of the Josephson frequency** with increasing emission rate is easily under-

stood. The emission of photon pairs at a rate Γ is accompanied with the flow of a dc current $I_{dc} = 2e\Gamma$ through the junction. This dc-current is extracted from the voltage bias line, resulting in a lower voltage drop across the bias resistor R_3, see figure 4.18. Then the voltage bias on the junction shifts by $\delta V = R_3 \times 2e\Gamma$, resulting in a frequency shift $\delta\omega/2\pi = 2e \times \delta V/h = \Gamma \times R_3/R_Q \simeq \Gamma/18.7$.

As the emission rate itself depends on the value of the detuning Δ through (4.85), there may be several possible stationary states for the system. In particular if $Re[Z(\omega_J)] \ll Re[Z(\omega_J - \delta\omega)]$, the junction may either be emitting photons at $\omega_J - \delta\omega$, or fall in a "dark state" where $\Gamma \simeq 0$ and $\Delta = 0$. Jumps between the two possible states of this bi-stable system become more probable at higher bias voltage noise.

The **standard deviation of the Josephson frequency** at low driving is very close to $\sqrt{2}$ times the value we had in the strong-coupling experiment (3.5). This is exactly what we expect when adding a second bias-tee in series with the sample, as the variance of independent random variable add up. This agreement confirms furthermore our model for the low frequency noise on the bias voltage. In later experiments, the noise was higher due to the removal of a stage of lowpass filtering in the bias line.

We attribute the increase of σ_ω with Γ to the interplay between the low frequency modes and the admittance of the junction itself. From the determination of the Josephson frequency at low driving (Fig.4.41.a), we see that the bias was actually blue-shifted from the resonance condition $\omega_J = \omega_a + \omega_b = 2\pi \times 12047$ MHz by about $+2\pi \times 35$ MHz. In these conditions, the derivative of the emission rate with respect to the bias voltage is **negative**, see (4.85). The equivalent low-frequency admittance of the junction itself is also negative, see figure 3.41. Then the junction acts as a negative resistor in parallel to the low-frequency modes, i.e an **amplifier** for low-frequency voltage noise.

As these modes are in a thermal state, this amounts to increasing their temperature, from about $T_{cold} = 18$ mK at equilibrium up to $\left(\frac{2.7}{1.8}\right)^2 \times T_{cold} = 40$ mK at the highest pump strength. The bias condition $\omega_J > \omega_a + \omega_b$ thus yields a **heating regime** of the low-frequency modes.

Conclusions of the preliminary experiment in the heating regime

The increase of the dephasing rate of the phase correlators with increasing pump strength (Fig.4.37) is not an intrinsic property of the system itself, but rather of its interaction with the bias setup. The misguided choice of a bias voltage **above** the resonance condition $2eV = \hbar\omega_a + \hbar\omega_b$ results in the amplification of low-frequency voltage noise, to the detriment of the phase coherence of the emitted photons.

This heating mechanism limits the maximum emission rate of entangled photons: at high bias voltage noise δV, the probability that the system jumps to a bi-stable"dark state" increases. For the bias conditions of this experiment, this limits the maximum emission rate to $\Gamma = 0.33\kappa \simeq 150$ MPhotons/s.

Having understood this phenomenon, we went on to perform a second series of measurements, carefully keeping the bias voltage at the resonance condition $2eV = \hbar\omega_a + \hbar\omega_b$. In particular we monitored closely the value of ω_J during the experiment, compensating the bias voltage for the frequency shift at a finite emission rate.

We also decided to use wider bandpass filters, going from a 180 MHz acquisition window up to 525 MHz. This is the measurement setup that was used for all the results presented in section 4.3. With this very wide frequency band we expect to miss fewer correlations, increasing the maximum emission rate at which we detect entanglement.

4.4.2 Emission of entangled photons at equilibrium voltage noise

Determination of the bias neutral point

In order to determine the exact position of the voltage bias neutral point, i.e the value of ω_J such that the junction does not interact with the low frequency modes, we measured the $g_\phi^{(2)}(\tau)$ correlation function at different values of bias V and pump strength β.

For each curve, we fit the time constant of the gaussian decay at long times of the phase correlator, that we interpret as the dephasing rate σ_ω of the squeezing angle. The results of these fits are plotted as a function of the Josephson energy in figure 4.42.

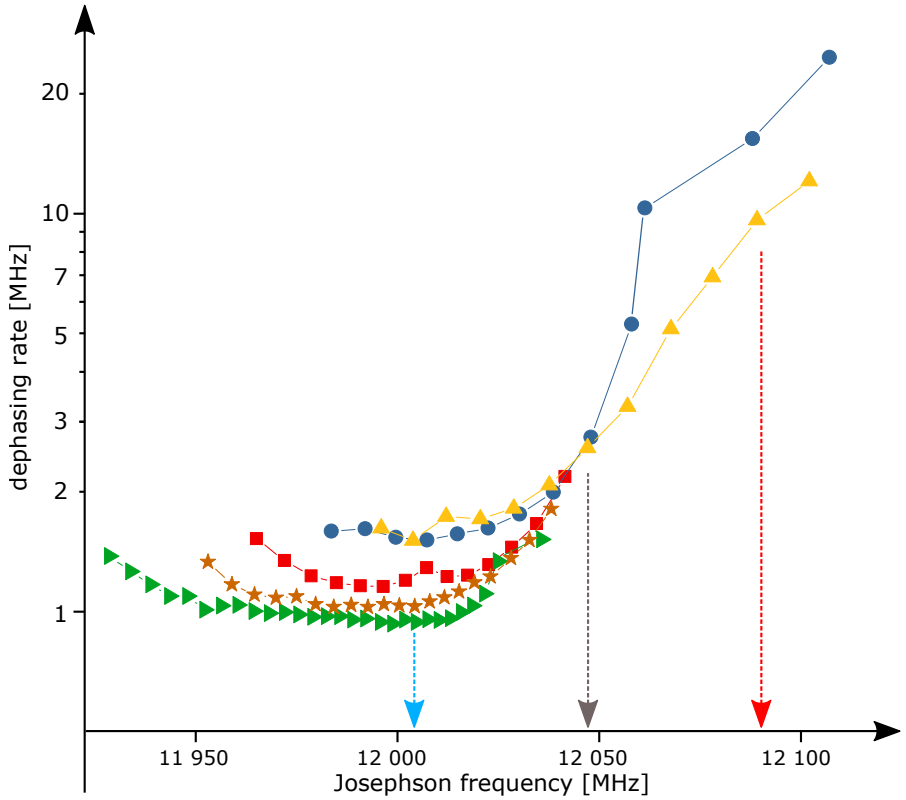

Figure 4.42: Dephasing rate $\sigma_\omega/2\pi$ of the phase correlator for different values of β, as a function of the Josephson frequency. The red arrow indicates the bias voltage used in the preliminary experiment, which lies in the heating regime. The grey arrow indicates the bias neutral point $\omega_J = \omega_a + \omega_b$. The light blue arrow points to the optimal cooling point at $\Delta = -\frac{\kappa_a+\kappa_b}{2\sqrt{3}}$.

Each curve of a given colour indicates points measured at the same value of β, with the yellow points indicating the lowest value and the green points the largest one. For each curve, we started the measurement with the bias voltage far below $\hbar(\omega_a + \omega_b)/2e$, and increased it steadily until we hit the bi-stable regime of the system, where we lose the Josephson emission. Due to the emission rate dependent frequency shift, at a given value

of voltage V the effective Josephson frequency $\omega_J = 2eV/\hbar - 2\pi\Gamma R_3/R_Q$ is not the same for all β values, so that the curves do not line up along the x axis.

We find that for all β values the curves cross approximately at the resonance condition $\omega_J = \omega_a + \omega_b$, indicated by the grey arrow, where the low frequency admittance of the junction is zero and it does not impact the voltage noise from the environment modes. This defines the **neutral point**, or non-interacting regime for the junction and low frequency modes.

Below this neutral point, the dephasing rate is reduced compared to the non-interacting value of $\sigma_\omega/2\pi \simeq 2.6$ MHz. The noise reduction is larger at higher β (compare the yellow to green curves), yielding $\sigma_\omega/2\pi \simeq 0.8$ MHz at the highest pump strength. The optimal **cooling point** (light blue arrow) is close to the value of ω_J where $\frac{d\Gamma}{d\Delta}$ is the largest, which lies at $\Delta = -\frac{\kappa_a+\kappa_b}{2\sqrt{3}} \simeq -2\pi \times 43$ MHz according to (4.85).

Above the neutral point, the dephasing rate increases steadily, corresponding to the **heating regime**, where the junction amplifies the low frequency voltage noise. At large β, the voltage noise becomes so high that the system becomes unstable and the Josephson frequency jumps out of the measurement window. The red arrow indicates the bias voltage used in the preliminary experiment, which is close the "optimal" heating point, i.e the worst possible choice to try and witness the entanglement.

In this section, we describe experiments performed close to the neutral point $\omega_J = \omega_a + \omega_b$. In these conditions we consider that the junction decouples from the low frequency modes and interact only with the a and b modes, simplifying the interpretation of our results.

Correlators at the bias neutral point

We present in figure 4.43 the witness correlators measured close to the neutral point $\omega_J \simeq \omega_a + \omega_b$. At this bias voltage, we are able to push the driving strength up to a much higher value $\beta = 1.385$, yielding an occupation number $\bar{n} = 4.8$.

Even at this very high occupation number, corresponding to an emission rate $\Gamma = 4.8\kappa \simeq 2.3$ Gphotons/s, **the emitted photons are still entangled**. Figure 4.44 shows a close zoom-in on the witness correlators near $\tau = 0$ for the $\bar{n} = 4.8$ measurement. Each point is plotted with an error bar, showing twice the statistical measurement uncertainty σ. For $\tau < 12$ ns, the inequality (4.41) is violated by as much as 20 σ.

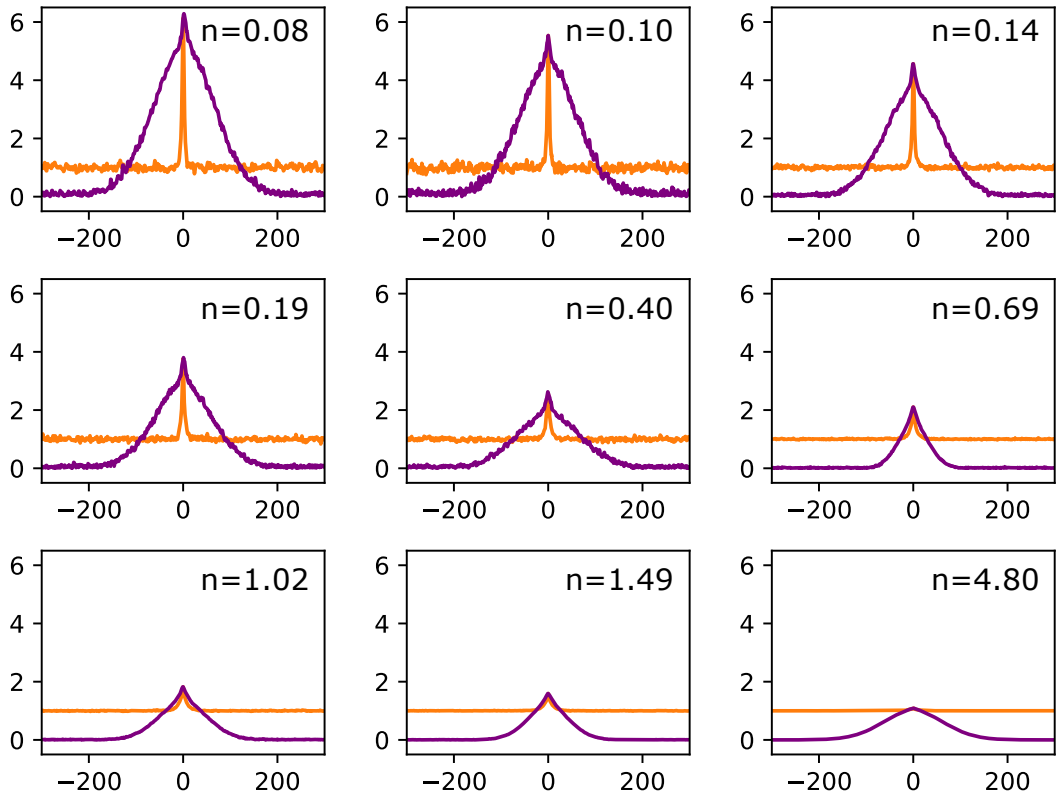

Figure 4.43: Measurement of the entanglement witness correlators $g^{(2)}_{ab}(\tau)$ (orange curves) and $|g^{(2)}_{\phi}(\tau)|$ (purple curves) as a function of time τ in nanoseconds, for $\bar{n}$ ranging from 0.08 up to 4.8.

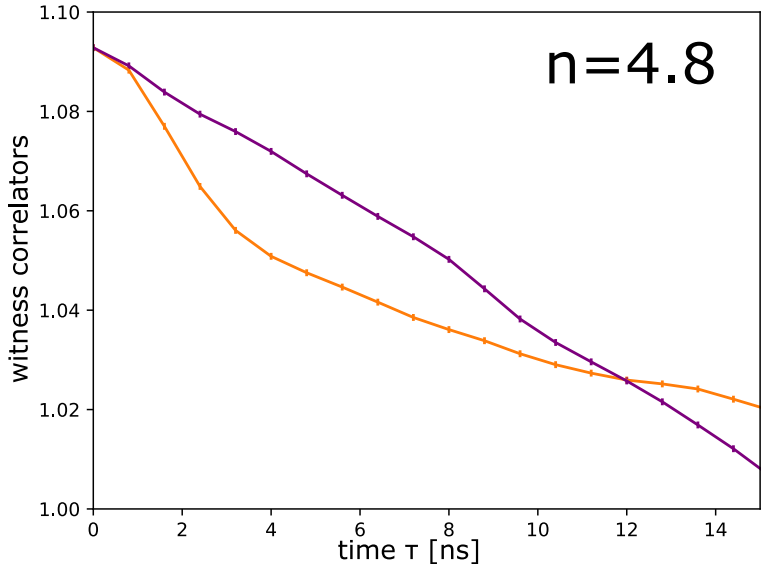

Figure 4.44: Entanglement witness correlators at $\bar{n} = 4.8$. The phase correlator (purple curve) is larger than the number correlator (orange curve) by 20 σ, which is a proof of entanglement.

The maximum emission rate where we detect entanglement is limited by the decrease of the initial value $|g^{(2)}_{\phi}(0)| = g^{(2)}_{ab}(0)$ with increasing β. This phenomenon, which is not predicted by the naive parametric model, comes from the impact of the resonators' phase fluctuations on the junction. As the occupation of the cavities grows, they reach the strong-driving regime, where the statistics of the radiation becomes close to the one of a

coherent field, with:

$$|g_\phi^{(2)}(0)| = g_{ab}^{(2)}(0) = g_a^{(2)}(0) = g_b^{(2)}(0) \xrightarrow[\bar{n}\to\infty]{} 1. \tag{4.149}$$

At the same time, the time constant in the initial decay of $|g_\phi^{(2)}(\tau)|$ and $g_{ab}^{(2)}(\tau)$ both tend to infinity, so that we cannot witness the violation of the inequality (4.41) before the Gaussian dephasing takes place.

Improvements compared to the preliminary experiment

The curves presented in figure 4.43 were measured over the course of several weeks. During this time, the value of the bias voltage noise was drifting considerably, starting at about $\sigma_\omega/2\pi = 5.5$ MHz at the beginning of the run, then cooling down progressively to an equilibrium value $\simeq 2.6$ MHz. Due to the removing of a crucial filtering stage of the bias line, this value is even higher than the amplified voltage noise measured in the heating regime (Fig.4.41).

However we could check that after these few weeks of thermalization, when the bias voltage was kept at the neutral point, the dephasing rate was consistently equal to 2.6 MHz for all β values, see figure 4.42. This value coincides with the voltage noise measured in the single photon regime, through the width of the Gaussian emission spectra.

Thanks to the wider acquisition bandwidth used in this experiment, the distortions of the measured correlators due to filtering effects are reduced. We plot in figure 4.45 the value of $g_{ab}^{(2)}(0) = |g_\phi^{(2)}(0)|$ as a function of the inverse occupation number $1/\bar{n}$ for the two experiments. Data points measured in the the preliminary experiment are in red, those taken at the neutral point are in black. Along them is the theoretical prediction for an infinite detection bandwidth: $g_{ab}^{(2)}(0) = \frac{g_a^{(2)}(0)+g_b^{(2)}(0)}{2} + \frac{1}{2\bar{n}}$, associated with NRF $= \frac{1}{2}$.

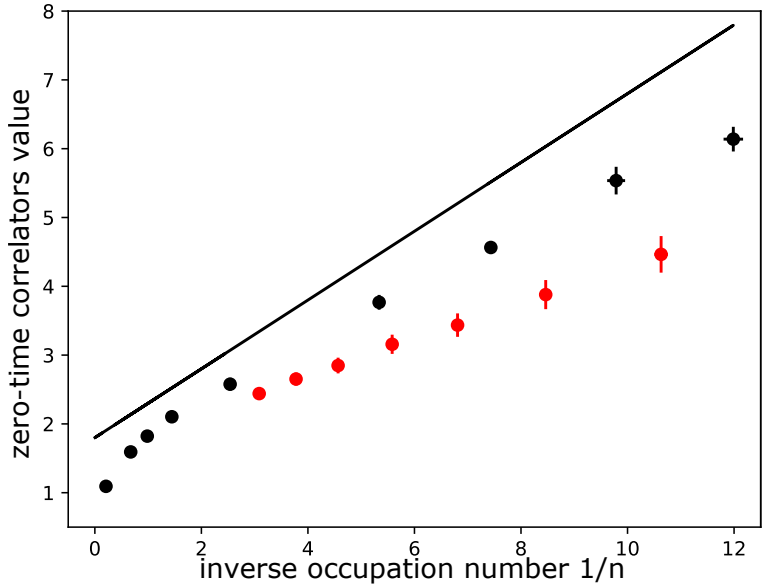

Figure 4.45: Zero-time value of the population correlators as a function of $1/\bar{n}$ for the two experiments, using either narrow filters (red points) or wide filters (black points), along with the theoretical prediction $g_{ab}^{(2)}(0) = \frac{g_a^{(2)}(0)+g_b^{(2)}(0)}{2} + \frac{1-\mathrm{NRF}}{\bar{n}}$. Fewer correlations are missed when using wider filters.

For the experiment in the heating regime, the missed correlations due to a too narrow measurement bandwidth lead to NRF = 0.72 at vanishing photon number, i.e a loss of about $\frac{0.72-0.5}{0.5} = 44\%$ of the correlations. With wider bandpass filters, we have NRF = 0.625 at low photon number (Fig.4.36), so that we miss only about 25 % of the correlations. This effect is quantitatively accounted for by numerical simulations.

Numerical simulations at the neutral point

Our theoretician collaborators from Ulm University have developed a theoretical framework and numerical tools to simulate efficiently the evolution of the cavity states under the full Hamiltonian (4.3). Within a master equation formalism, they can compute correlation functions for the cavity fields, which are linked to the measured correlation functions of propagating modes by the input-output relation.

Their approach captures the back-action of the finite impedance of the resonators onto the system's dynamics, and are then closer to the real system than our naive parametric amplifier model. They can also incorporate the impact of bandpass filtering of the signal on the correlation functions, in very good agreement with our experimental results.

However these simulations with filtering effects are quite expensive in time and numerical resources, in particular at high photon number. They are in practice limited to about $\bar{n} = 2$.

We show in figure 4.46 the results of the simulations of the phase correlator $|g_\phi^{(2)}(\tau)|$ at $\beta = 0.409$ with $\bar{n} = 0.10$, along with the measured data (purple curve). The full black curve corresponds to the ideal case of an infinite detection bandwidth and a perfect dc voltage bias, with $\sigma_\omega = 0$. Its long times value is close to the prediction of the parametric model, with: $|g_\phi^{(2)}(\infty)| = \beta^{-2} \simeq 6$. The only parameters of this simulation are the leak rates of the cavities κ_a, κ_b, their coupling constants r_a, r_b and the pump strength β, which were all determined independently. There is no adjustable parameter.

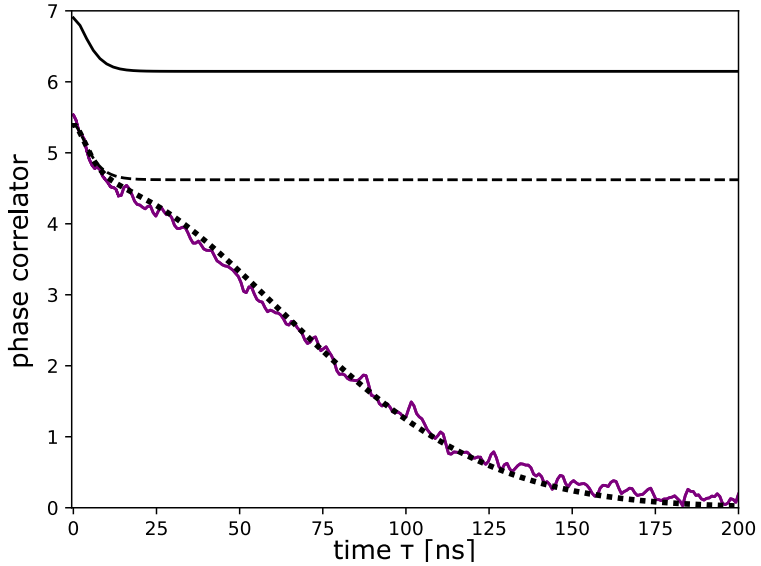

Figure 4.46: Measurement of the entanglement witness correlators $g_{ab}^{(2)}(\tau)$ (orange curves) and $|g_\phi^{(2)}(\tau)|$ (purple curves) as a function of time τ in nanoseconds, for $\bar{n}$ ranging from 0.08 up to 4.8.

The dashed curve shows the impact of filtering, still in the case of a perfect dc bias. As some of the correlations are missed due to bandpass filtering of the signals, the normalized correlator is lowered by about 1.5 compared to the unfiltered one. The initial value goes from 6.9 to about 5.4, and coincides with the $\tau = 0$ value of experimental data. The amount of missed correlations $\frac{6.9-5.4}{6.9-1} \simeq 25\%$ agrees with our previous estimate.

The dotted curve shows the impact of voltage bias noise on the correlation function. It was obtained by simulating many copies of $g_{\phi}^{(2)}(\tau)$, each with a different value of detuning Δ, then averaging them together with a Gaussian weight following (4.147). The value of σ_ω used in the averaging of simulation results was fitted from experimental data. It agrees very well with the experimental measurement of the correlator.

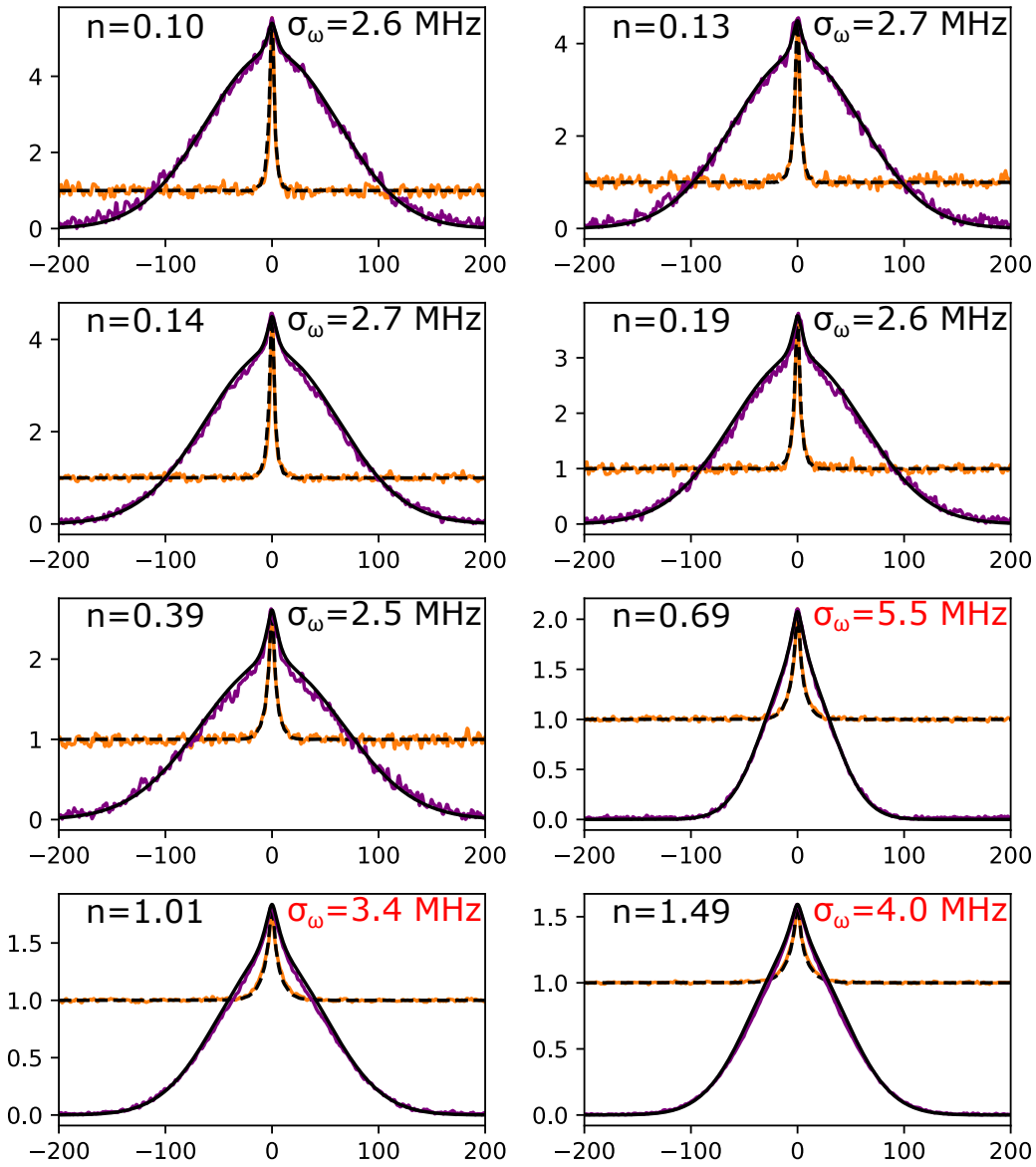

Figure 4.47: Entanglement witness plotted along numerical simulations (black curves). The only fit parameter is the voltage noise, yielding the dephasing rate σ_ω.

The same procedure is used for the simulation of the number correlator $g_{ab}^{(2)}(\tau)$, yielding similar agreement. We repeat it for all measurements at the neutral bias point (Fig.4.47),

except for the $\bar{n} = 4.8$ point which cannot be simulated in a reasonable time.

Taking into account the dc voltage noise, the simulated curve agrees very well with the measured data. Simulations captures accurately the impact of bandpass filtering, which systematic reduces the amount of correlations by about 25%. The voltage noise is consistently equal to about 2.6 MHz, except for the data measured at the beginning of the run (in red) where it is higher.

This quantitative agreement validates our description of this simple system. A dc-biased Josephson junction implements a non-degenerate parametric amplifier. When fed with vacuum fluctuations, it generates two-mode vacuum squeezing in the two resonators. The leaking fields are then entangled, sharing a non-local phase θ inherited from the superconducting phase difference of the junction. Thermal voltage noise on the bias yields a finite phase coherence for the junction, which limits the entanglement of the propagating beams. The back-action from the non-zero impedance of the resonators add non-linearities to the two-mode drive, making the light states non-gaussian.

Quantifying the amount of entanglement

Even though we cannot detect stationary entanglement of the two cavities due to slow dephasing of the squeezing angle, we can still estimate their instantaneous amount of entanglement. The log-negativity between the two cavities is given by:

$$E_N^{cav} = -\ln(1 + \bar{n}_a + \bar{n}_b - \sqrt{(\bar{n}_a - \bar{n}_b)^2 + 4|\langle ab\rangle|^2}). \tag{4.150}$$

We can measure easily the occupation numbers $\bar{n}_a, \bar{n}_b$. The value of the $|\langle ab\rangle|^2$ correlator can be estimated by the long times value of the phase correlator:

$$\langle a^\dagger b^\dagger(0) ab(\tau)\rangle \xrightarrow[\tau\to\infty]{} \langle a^\dagger b^\dagger\rangle\langle ab\rangle = |\langle ab\rangle|^2. \tag{4.151}$$

Now, all the measured $g_\phi^{(2)}(\tau)$ functions tend towards zero at long times, indicating that the stationary entanglement is zero. However we can estimate the value it would have **in the absence of voltage noise**. To do so, we simply fit the Gaussian decay of $g_\phi^{(2)}(\tau)$, and deconvolve it to estimate $|g_\phi^{(2)}(\infty)|$.

This approach is justified by the good agreement of independent numerical simulations of the system with experimental data. We also check that the deconvolved $|g_\phi^{(2)}(\infty)|$ agrees up to 2% with the result of simulations at long times.

The estimated $\log_2$ negativity is plotted in figure 4.48 (black dots). We also show the log-neg computed from the simulated density matrix, assuming or not Gaussian statistics of the modes (blue and green curves). We also plot the log-neg estimated from simulations of the signals including the impact of the bandpass filters (purple line). The estimated log-neg reaches about 0.5 e-bits for the experimental data.

The estimated log-neg is systematically lower for the experimental points compared to simulations. This discrepancy may be due to the crudeness of our modelling of the filtering, or to the sensitivity of the fit procedure to noise in the experimental data.

As our measurement of the entanglement is not frequency-resolved, we cannot estimate directly the entanglement rate. We will only give the very rough following estimate:

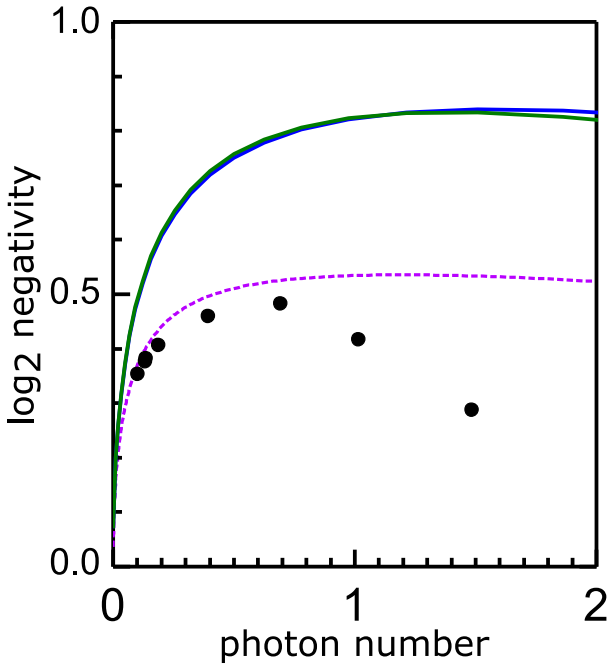

Figure 4.48: Logarithmic negativity E_N of the two cavities as a function of the photon number $\bar{n}$. The black dots are extracted from the estimated value of the $g_\phi^{(2)}(\tau)$ correlators at long times, compensating for the gaussian dephasing. The blue and green curve show the log-neg calculated from the density matrix, obtained by numerical simulations of the full Hamiltonian (4.15), assuming or not Gaussian statistics of the light. The purple curve shows the log-neg estimated from simulation of the phase correlator, including filtering effects.

at $\bar{n} = 0.69$ where we have the largest log-neg for the cavities $E_N^{cav} \simeq 0.5$ e-bits, the dynamical bandwidth of the emission spectrum is about 20 MHz. We estimate the log-neg of the propagating modes at ω_a, ω_b following (4.97) to be: $E_N[\omega_a] \simeq 6$ e-bits/s/Hz. Then the entanglement rate delivered in the emission bandwidth is $\Gamma_E \simeq 120$ Me-bits/s, one order of magnitude above current state of the art [37][113]. This very crude estimation assumes perfect quantum efficiencies both in the generation and detection of the entangled photons, which we do not claim to have in this experiment.

4.4.3 Emission of entangled photons in the cooling regime

Figure 4.47 shows that we can detect the entanglement of the beams if the dephasing rate σ_ω yielded by the voltage noise is smaller than the leak rate of the cavities κ. This dephasing rate is not intrinsic to the system itself, but to how good is the filtering of the bias line. However the junction itself can interact with the low-frequency modes of the setup, increasing or reducing the voltage noise.

In a final series of experiments, we placed the bias voltage below the resonance condition $\omega_J = \omega_a + \omega_b$, at the optimal point of the **cooling regime** (Fig.4.42), and measured the entanglement of the emitted photons. We then expect the dephasing rate to be reduced, slowing the Gaussian decay of the phase correlator and allowing us to witness the entanglement up to higher emission rates.

We plot in figure 4.49 the witness correlators measured at the same photon number $\bar{n} = 1.0$ both at the neutral point (full lines) and in the cooling regime (dashed lines). We

see that the emitted photons are still entangled in the cooling regime, as $|g_{\phi}^{(2)}(\tau)| > g_{ab}^{(2)}(\tau)$ for $|\tau| < 60$ ns. At the same time the junction is interacting with the low frequency modes and cooling them down, as the dephasing rate $\sigma_\omega/2\pi = 1.8$ MHz is lowered compared to the neutral point value $\sigma_\omega/2\pi = 3.4$ MHz.

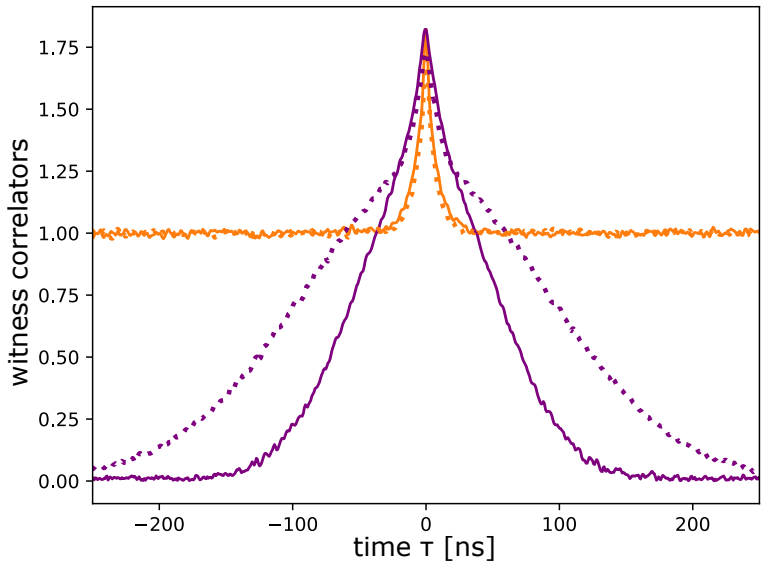

Figure 4.49: Entanglement correlators measured at $\bar{n} = 1.0$ both at the neutral point (full lines) and in the cooling regime (dashed lines). The Gaussian decay rate of the phase correlator is reduced in the cooling regime, yielding a longer entanglement time.

The persistence of entanglement in the cooling regime is remarkable. In a microscopic picture, Cooper pairs tunnel inelastically across the junction, absorbing energy from the low frequency noise while emitting entangled photon pairs in the microwave resonators. The low frequency modes are in a thermal state with occupation number $n_B \simeq 5000$, and thus deeply in the classical regime. One would naturally expect that actively coupling a quantum device to this highly excited bath should destroy any kind of quantum coherence. To the contrary, we prove that a well-tailored interaction can actually **increase** the coherence time, by reducing the dephasing rate in our entanglement witness.

The reduction of the dephasing rate has an immediate consequence on the correlators, as it extends the range over which the inequality (4.41) is broken, from $\Delta\tau = 70$ ns at the neutral point up to $\Delta\tau = 120$ ns in the cooling regime for this value of $\bar{n} = 1.0$. Following the picture we developed in figure 4.9, this time window can be converted into a coherence length $c \times \Delta\tau$ over which the two beams of light agree on the value of the squeezing angle, i.e over which they are entangled.

It should be noted that the $\tau = 0$ time value of the correlators is slightly lower in the cooling regime than at the neutral point. This effect is not predicted by the simple parametric model. It may be a mark of the classical statistics of the absorbed low-frequency noise, which pollute the entangled states and reduce their correlations. As of today numerical simulations cannot include both the dynamics of the GHz modes where the entanglement is created and of the kHz modes being cooled down, due to the vastly different timescales involved and the very large number of photons in the low frequency modes.

As the Josephson admittance of the junction is proportional to $\frac{d\Gamma}{dV}$, we expect the cooling

power of the junction to increase at higher emission rates. We plot in figure 4.50 the witness correlators measured in the cooling regime at increasing pump strengths, up to an occupation number $\bar{n} = 5.3$.

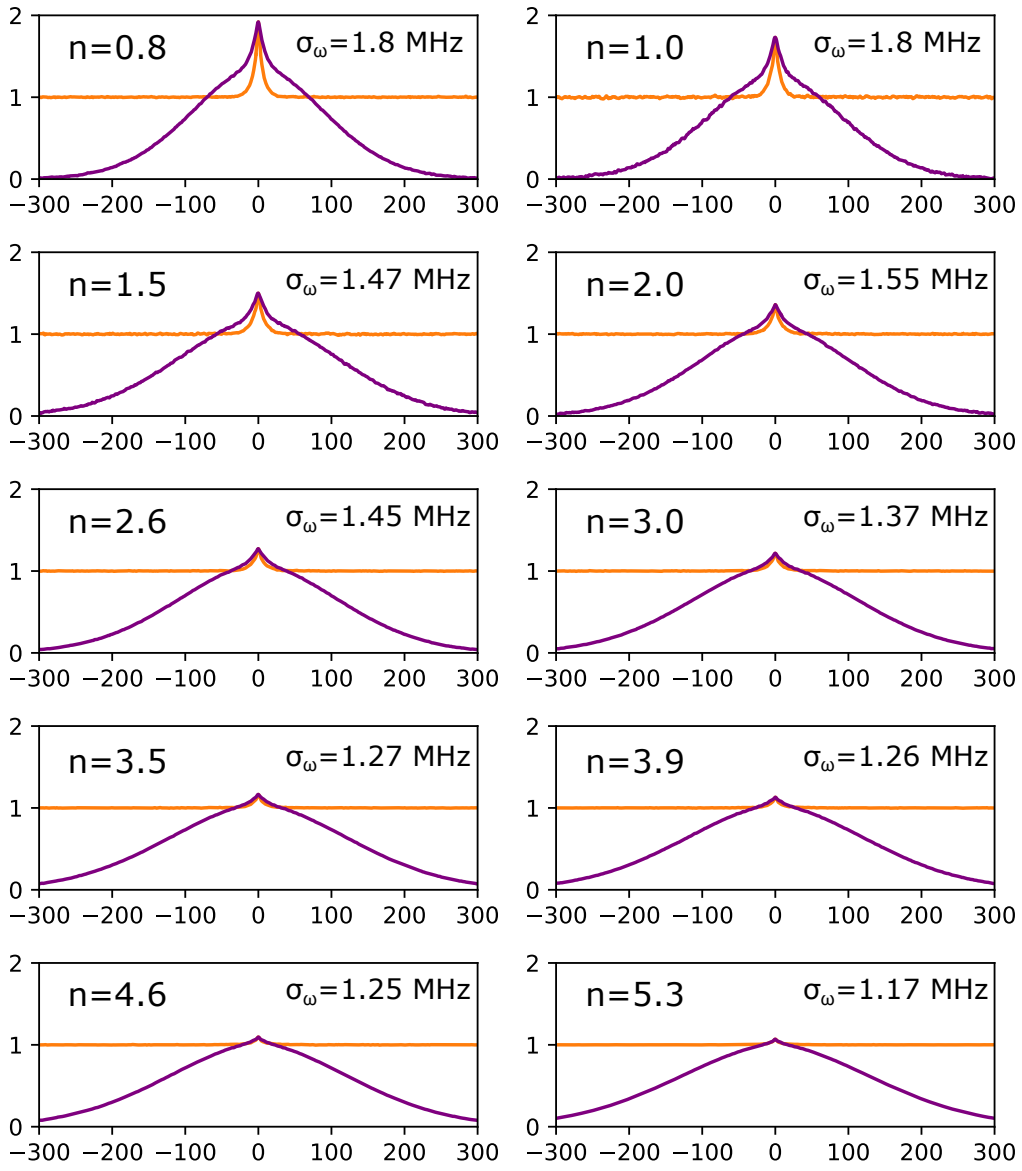

Figure 4.50: Entanglement correlators measured in the cooling regime. As the pump strength β is increased, the $\tau = 0$ value of correlators decreases down to 1. At the same time the dephasing rate σ_ω is reduced, due to cooling of the low frequency modes by the junction.

As expected, the dephasing rate σ_ω decreases steadily with increasing occupation number $\bar{n}$. At the same time, the zero-time value of correlators decreases towards 1, which limits the visibility of the entanglement witness. Up to $\bar{n} = 5.3$, corresponding to a high emission rate of 2.57 Gphotons/s, the inequality (4.41) is violated by at least 11 σ, proving the entanglement of the emitted beams.

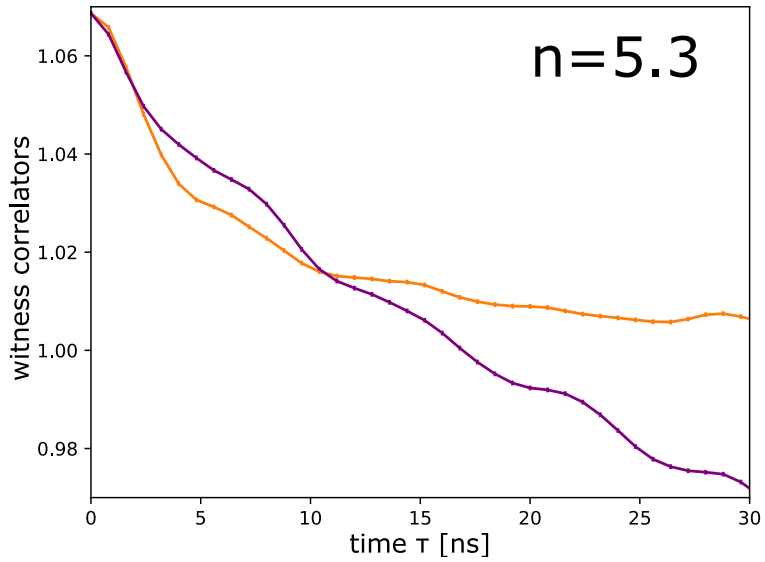

Figure 4.51: Witness correlators measured at $\bar{n} = 5.3$ in the cooling regime. The witness inequality (4.41) is violated by 11 σ, despite the presence of parasitic oscillations in the correlation functions.

However the structure of the entanglement seems to differ at high emission rates compared to what we observed at the neutral point. We plot in figure 4.51 the correlators measured at the highest occupation number $\bar{n} = 5.3$. Contrarily to what was observed in the earlier experiments, the witness inequality is not broken at very short times $\tau < 2.5$ ns, but only over a limited range 2.5 ns $< \tau <$ 10 ns. This is due to parasitic oscillations with a period $\simeq 7.5$ ns and amplitude $\simeq 10^{-3}$ that appeared on top of the correlation functions.

We show in figure 4.52 the Fourier transform of the phase correlator at a high photon number $\bar{n} = 9.25$, where the entanglement is not witnessed. In addition to the main Gaussian peak at $\omega_J/2\pi = 12.005$ GHz, it reveals the existence of secondary peaks at $\omega_J \pm \omega_P$, with $\omega_P/2\pi = 135$ MHz.

These peaks are visible in the Fourier transforms of all phase correlators measured in the cooling regime for $\bar{n} > 2$. At lower occupation number they may be present but fall below the noise floor of the measurement, so that they do not appear in the time domain correlators.

We attribute these peaks to parasitic Stokes/Anti-Stokes processes involving a mode at $\omega_P/2\pi = 135$ MHz, which contains about $n_B = 2.3$ photons at equilibrium. In a Stokes process, the junction emits three photons upon each tunneling event, in the a, b and P modes. In an Anti-Stokes process, the junction absorbs one photon from the P mode while emitting entangled photons in a and b. In both processes, the junction is also cooling down the kHz modes of the bias line by absorbing voltage noise, so that we may argue that we witness here the coherent exchange of four photons between modes at widely different frequencies.

As all these processes are coherent, the system is actually entangling together the a, b

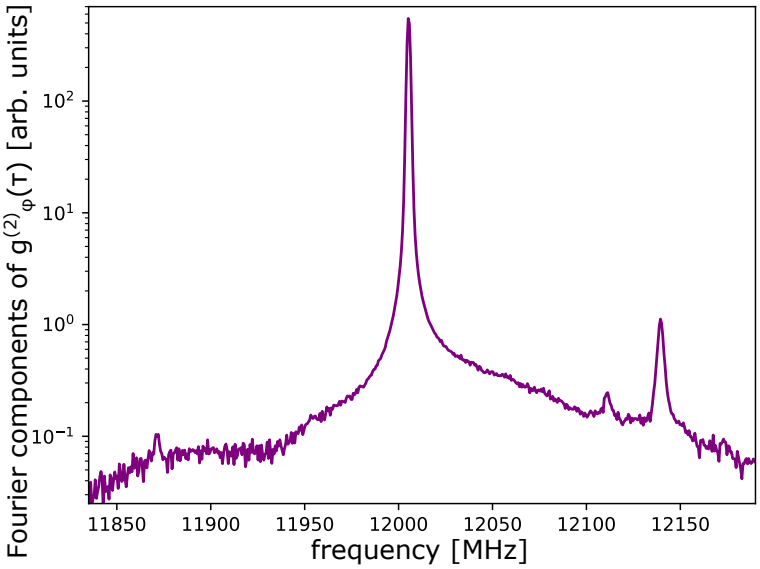

Figure 4.52: Fourier transform of the phase correlator at $\bar{n} = 9.25$. In addition to the main Gaussian peak at 12.005 GHz due to the direct emission of entangled photons, Stokes and Anti-Stokes processes are visible at 11.87 GHz and 12.14 GHz respectively, as well as a single Anti-Stoke peak at 12.11 GHz.

and P modes. The description of the stationary state of these modes is far beyond the reach of this work, although it may exhibit some intriguing features.

From a practical point of view, these oscillations reduce the visibility of the entanglement witness between the a and b modes. One could argue that in the measurements of figure 4.51, the parasitic oscillations add an uncertainty to the correlation functions, which is much bigger than the statistical error $\sigma = 8 \times 10^{-4}$. To prove the entanglement in an unambiguous manner, we reduced the bandpass filters' bandwidth down to 300 MHz, in order to reject the signals from the Stokes/Anti-Stokes processes.

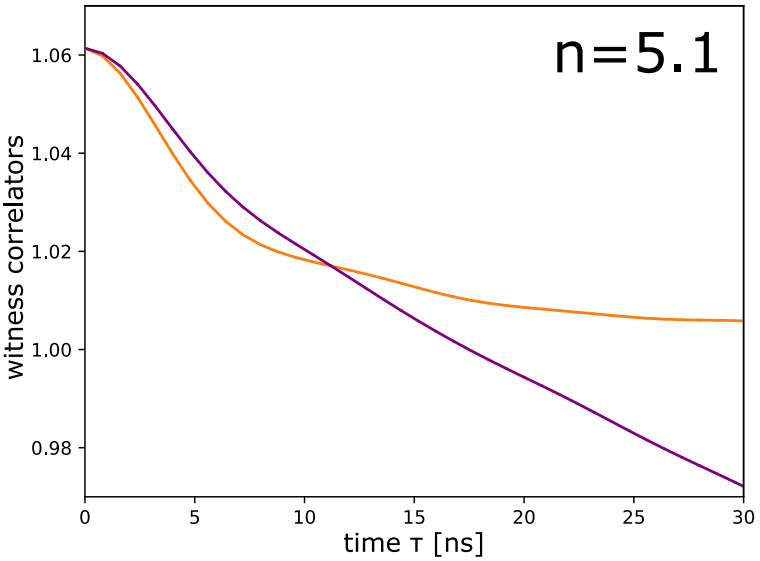

Figure 4.53: Witness correlators measured at $\bar{n} = 5.1$ with narrower filters. Parasitic oscillations in the correlation functions have been reeduced. The witness inequality (4.41) is violated by 13 σ.

The results of the experiment with narrower filters at $\bar{n} = 5.1$ is plotted in figure 4.53. The parasitic oscillations due to indirect processes have greatly decreased, such that the

entanglement can be witnessed without ambiguity. At the same time, the initial time decay of the population correlator has lengthened, due to the impact of the filters. For even narrower filtering, this time decay becomes slower than the $g_{\phi}^{(2)}(\tau)$ dephasing rate, such that the inequality is not violated anymore.

Finally we estimate once again the log-neg of the cavities from the value of the phase correlator at long times. In figure 4.54, we add the log-neg estimated in the cooling regime to the results of figure 4.48. It is non-zero up to $\bar{n} = 3.5$. Albeit the decay of E_N^{cav} with $\bar{n}$ seems to follow a lower slope in the cooling regime than at the neutral point, this does not lead to an increase of the maximum entanglement rate.

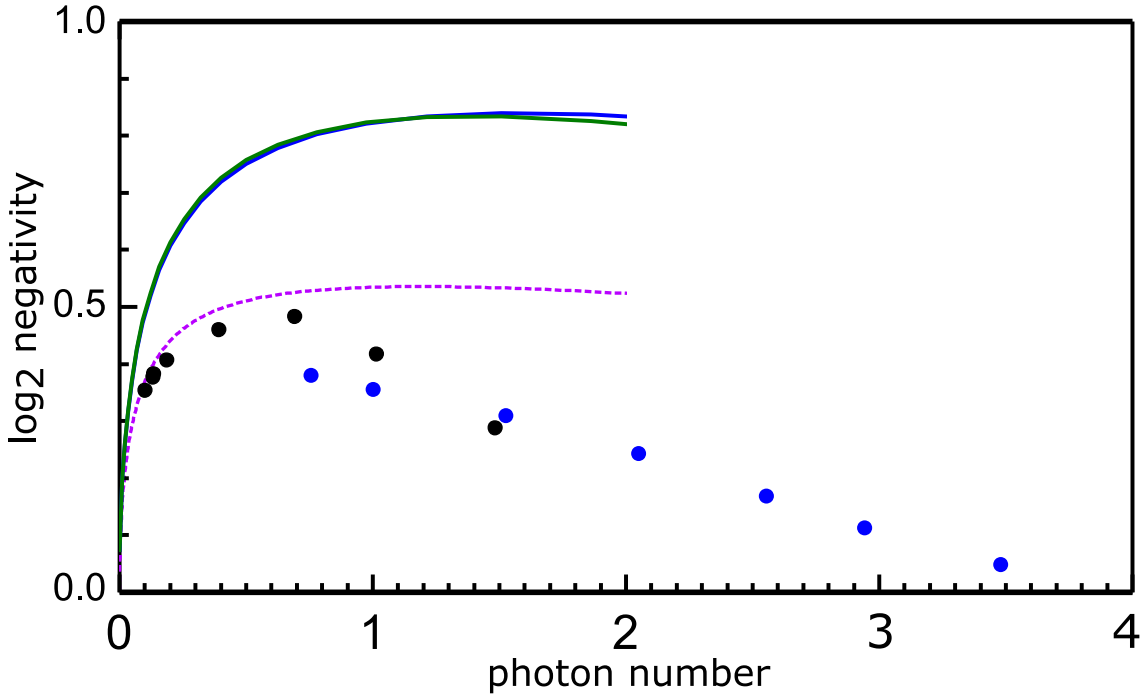

Figure 4.54: Logarithmic negativity as a function of the photon number $\bar{n}$. Experimental data measured in the cooling regime (blue dots) have been added to figure 4.48.

Dephasing rate in the cooling regime

At higher occupation number, we do not witness the entanglement anymore. There is a competition between different time scales, namely the dephasing rate σ_ω and the initial decay constant $\simeq (1-\beta)\kappa$, which gets even shorter for narrower acquisition bandwidth. The $\tau = 0$ value of the correlators also reduces down to 1 at high emission rates, so that we cannot witness the violation of 4.41 with our limited accuracy.

After heuristically optimized the filters' bandwidth, the emission rate and the averaging time, we detect unambiguous proofs of the entanglement up to $\bar{n} = 5.1$, corresponding to an emission rate $\Gamma = 2.470$ Gphotons/s. At higher emission rates, even if we do not witness the entanglement, we still measure a reduction of the dephasing rate σ_ω. We went on to study how low we could decrease it, even if it did not yield entanglement proof anymore.

Figure 4.55 shows the dephasing rate extracted from the phase correlators as a function

of the occupation number in the cooling regime (blue dots). It goes from the equilibrium value $\sigma_\omega/2\pi = 2.6$ MHz at low driving down to $\sigma_\omega/2\pi = 0.8$ MHz at high pump strength.

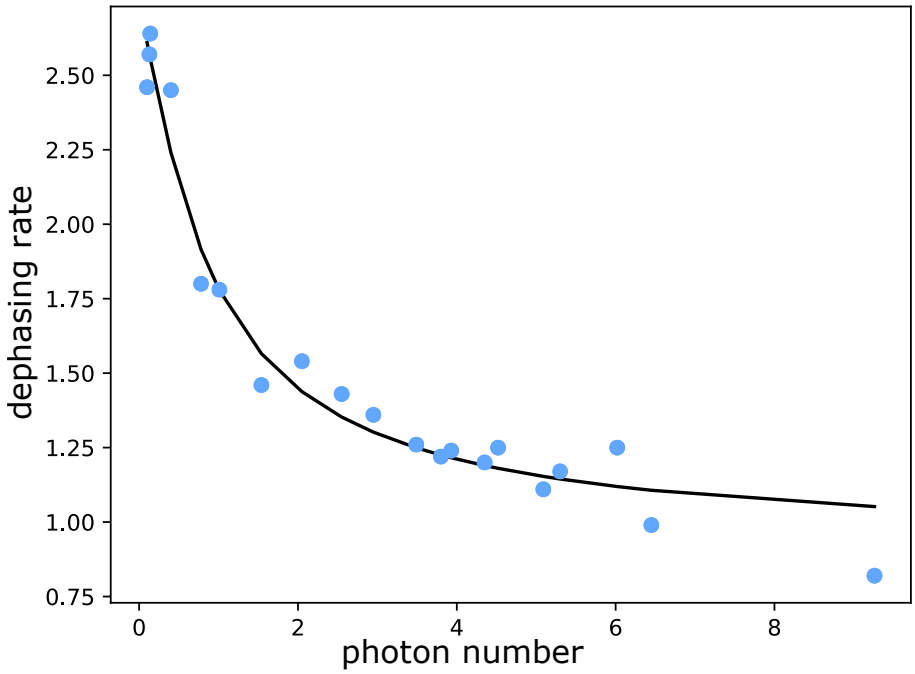

Figure 4.55: Dephasing rate measured in the cooling regime as a function of the occupation number (blue dots), along with the prediction of the Josephson admittance model (black line).

We compare this data to the prediction of our simple model for the cooling mechanism, based on the Josephson admittance of the junction (Fig.3.41). As we know the Josephson energy of the junction and the impedance of the environment at ω_a and ω_b, we can compute the equivalent admittance of the junction $Y_J(\omega)$ following Rogovin-Scalapino. We estimate the equivalent temperature T_J of the Josephson admittance through the shot-noise of Cooper pairs:

$$S_{II}(\omega \to 0) = 4Re[Y_J(\omega \to 0)]k_B T_J = 4eI_{dc}, \tag{4.152}$$

and find $T_J \leq 1$ mK for all β. The only unknown parameter of the model is the value of $Re[Z(\omega)]$ at low frequency. Making the simplifying assumption that all voltage noise is carried by the bias-tee LC mode, we simply need to know its quality factor Q, which should be somewhere between 10 and 30.

We fit the data from figure 4.55 with our simple model, having as a single adjustable parameter this quality factor. We find $Q \simeq 25$ and a very good agreement between the measured dephasing rates and our model. Our prediction holds up to $\bar{n} \simeq 7$, where $r \times \bar{n} \simeq \frac{1}{2}$. This is the onset of the strong-driving regime, where non-linearities in (4.3) become sizeable and our simple model should not apply anymore.

This very good agreement confirms furthermore our understanding of the main limiting mechanism for the entanglement of photons, which is thermal noise from the bias setup. This voltage noise can be either increased or reduced by inelastic Cooper pair tunneling, which can emit or absorb energy from the low frequency modes. In particular the temperature of these modes can be reduced down to 1/10 of its equilibrium value. We plot

in figure 4.56 the voltage noise δV^2 measured in the three experiments, normalized by its equilibrium value at $\beta = 0$. This voltage noise translates to an equivalent temperature of the low frequency modes, which can be reduced from about 20 mK down to 2 mK.

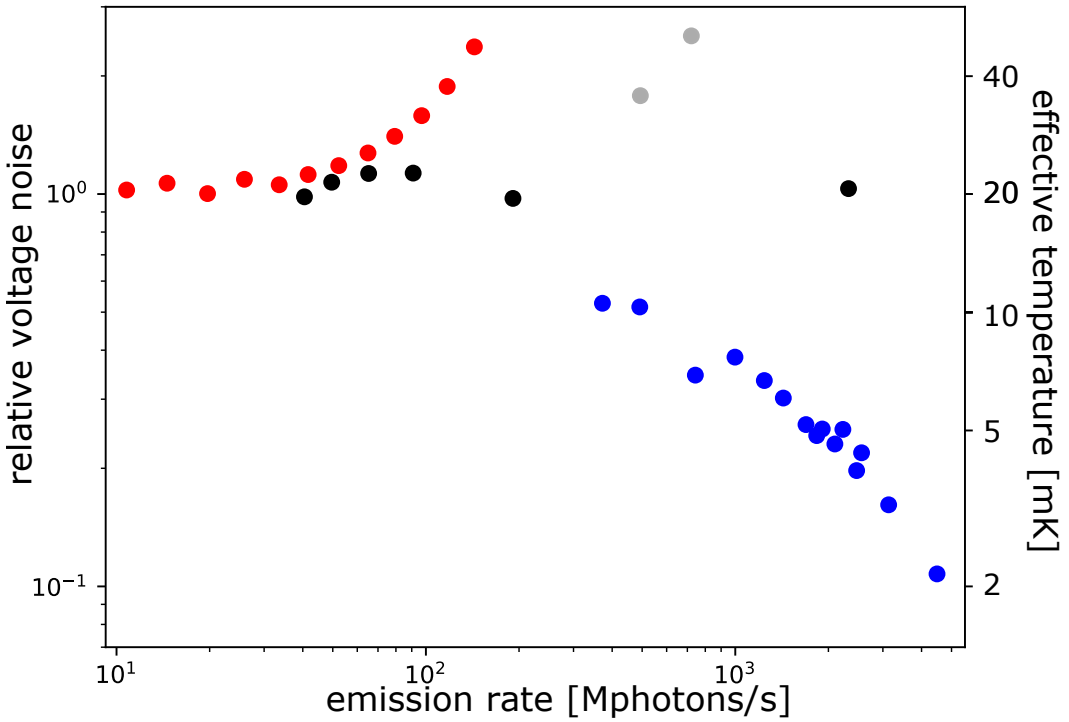

Figure 4.56: Relative voltage noise δV^2 measured in the heating regime (red dots), at the neutral point (black dots) and in the cooling regime (blue dots) as a function of the emission rate Γ. Points measured at the neutral point but in non-equilibrium conditions are indicated in grey.

4.5 Conclusions and perspectives

Our results prove that a dc-biased Josephson junction in series with two resonators a and b can generate continuous entanglement between the two light beams leaking out of the resonators. The energy needed to create this entanglement is extracted from the voltage bias in an inelastic process where for each tunneling Cooper pair, one photon is created in a and another one in b. The shared degree of freedom between the two entangled subsystems is the sum of their two instantaneous frequencies, which is fixed by the voltage difference across the junction. On the other hand the instantaneous frequency of each beam is less well-defined. In a simple picture, the two beams show 2-photon phase coherence in the absence of 1-photon phase coherence.

As the two beams propagate away from the sample they conserve these frequency correlations, even though voltage noise at the junction precludes any stationary entanglement of the two resonators. By measuring normalized correlation functions of the emitted signals we prove their entanglement. In particular the time window over which the equality 4.41 (valid for separable states) is violated indicates the length over which the two beams are entangled.

At low emission rates our results are quantitatively described using a simple two-mode squeezing Hamiltonian, with a driving strength set by the tunable Josephson energy of the junction $E_J^*(\Phi)$. At higher driving, non-linearities in the real Hamiltonian become relevant and modify the dynamics of the system, reducing coherently the driving strength and bringing the two fields closer to coherent states.

Our results are well reproduced by independent numerical simulations of the system, which captures the deviation from pure two-mode squeezing due to these non-linearities, as well as the impact of experimental bandpass filtering on the signals and of voltage noise on the phase correlations.

This voltage noise is not an intrinsic property of the system itself, but rather of its low-frequency environment. We also prove that the junction itself is able to interact with this noise. We demonstrate various regimes of this interaction, where the junction if either heating up the environment or cooling it down by absorbing photons from its modes. We use this active cooling mechanism to decrease the value of the voltage noise, improving the 2-photon phase coherence time of the entangled signals by a factor of 3.

This finite phase coherence time severely limits the relevance of our entangled photon source in the context of two mode squeezing. However it may be interesting to enhance the non-linearities by fabricating resonators with high enough impedances. Following this line of research could yield a simple source of strongly non-Gaussian entangled light beams, enabling the study of more complex states of light.

The heating/cooling mechanism in itself could be developed into a tool to either perform the spectroscopy of electromagnetic modes at arbitrary frequencies, or to cool down a system down to its quantum ground state.

Chapter 5

Conclusions of this work, preliminary experiments and perspectives

In this work, we have studied the creation of quantum states of light by inelastic Cooper-pair tunneling. We considered experiments where a small Josephson junction is dc-biased below the superconducting gap $2\Delta/e$, and embedded in a circuit with a high-enough impedance $Re[Z(\omega)]$ at microwave frequencies.

The inelastic mechanism responsible for light emission arises from the granularity of the charge $2e$ transferred upon each tunneling event. This charge displacement is described by the operator $e^{i\phi}$, where ϕ is the superconducting phase difference across the junction. If the junction is small enough, so that it has a negligible geometric capacitance and a low critical current I_0, then it cannot shunt the phase fluctuations imposed by the embedding circuit, which constitues its electromagnetic environment.

This environment can be described as a collection of bosonic modes, which display phase noise even if they are in their quantum ground state due to zero-point fluctuations (ZPF). Modes with the highest impedance exhibit the largest ZPF, with a spectral density given by: $S_{\phi\phi}(\omega) = \frac{2}{\omega}\frac{Re[Z(\omega)]}{R_Q}$. If $Re[Z(\omega)]$ cannot be neglected compared to R_Q at frequencies larger than the thermal cutoff $k_BT/\hbar$, then ϕ has to be promoted to a full quantum operator $\hat{\phi}$ and the dynamics of the junction treated accordingly.

Computing the steady state of this system is in general a complex problem, as the junction is an out-of-equilibrium quantum system which can interact with all the modes of its environment, from dc up to at least $2eV/\hbar$. These modes get populated due to photon emission by the junction, which modifies their occupation numbers and, subsequently, the amplitude of their phase ZPF.

The perturbative $P(E)$ theory

In Chapter 2, we have presented the theoretical apparatus developed in the early Nineties to predict the transport properties of small dc-biased tunnel junctions, the so-called $P(E)$ theory [31]. One of the main assumptions of this theory is that the environment is only

weakly perturbed by the photon creation/absorption processes. Its spectral density of phase fluctuations in this out-of-equilibrium situation is then still described by $Re[Z(\omega)]$, which yields the phase autocorrelation function $J(t) = \langle(\hat{\phi}(t) - \hat{\phi}(0))\hat{\phi}(0)\rangle$. The Fourier transform of $e^{J(t)}$ is the $P(E)$ function, which weighs the probability for the junction to exchange the energy E with the environment upon inelastic tunneling of a single charge.

From the knowledge of $Re[Z(\omega)]$, one can compute the $P(E)$ function, from which result the values of the dc-current I_{dc} and of the current noise $S_{II}(\omega)$ as a function of the bias voltage V. The current noise generates the emission of power in the environment of the junction, with a power spectral density (PSD)$S_P(\omega) = 2Re[Z(\omega)]S_{II}(\omega)$. It can then be checked in an auto-consistent way wether or not the photon emission rate density $\gamma(\omega) = \frac{S_P(\omega)}{\hbar\omega}$ is low enough compared to the environment intrinsic loss rate for $P(E)$ to hold.

The $P(E)$ theory is perturbative in the Josephson energy of the junction - or equivalently in its critical current. As an example, for the single-photon processes, I_0 should be at least much smaller than $V/Re[Z(\omega_J)]$, so that $I_{dc} \ll I_0$. This limits $P(E)$ to the case of low single-charge tunneling rates. On the other hand if its conditions of validity are met, this theory can deal with an arbitrary environment. The dc-current and photon emission rates can then be predicted up to arbitrary high order in $\frac{Re[Z(\omega)]}{R_Q}$, revealing multi-photon processes.

We describe two pioneering experiments [32][33], where a SQUID device with tunable Josephson energy is placed in series with microwave resonators. These resonators generate peaks in the $Re[Z(\omega)]$ seen by the junction. When E_J is tuned down low enough, the $I_{dc}(V)$ characteristic of the junction is well reproduced by a $P(E)$ calculation, showing peaks as a function of V associated to the emission of photons in modes of $Re[Z(\omega)]$. A $P(E)$ calculation also reproduces the power spectral density $S_P(\omega)$ measured in the second experiment. In particular as $S_P(\omega) \propto Re[Z(\omega)] \times P(2eV - \hbar\omega)$, the PSD measured on a single-photon resonance is linked to the low frequency modes at $E \simeq 0$, which can be treated by $P(E)$.

The PSD measured on a 2-photon resonance reveals the symmetric emission of light around the frequency $\omega_J/2$, indicating that photons are created by pairs in a process similar to parametric down-conversion. This photon-pair emission processes motivated the experiment described in Chapter 4, where we study their entanglement. This investigation requires a description of the quantum state of the light created by ICPT. This could be done by extending the formalism of $P(E)$ to describe current-current correlators of higher order, although this would be very cumbersome.

Aside from the particular case of photon-pair emission, it would be interesting in the general case to study the statistics of photons emitted by ICPT. In a simple picture, there should be a competition between the Poissonian statistics of the incoherent single-charge tunneling, and the coherent back-action of the electromagnetic field from the modes of the environment. This back-action is neglected in the frame of the $P(E)$ theory, where the environment stays close to its equilibrium state.

In Chapters 3 and 4, we introduce a different formalism to treat the questions both of the properties of the light emitted by ICPT, and of the coherent back-action of the emitted photons, going beyond the $P(E)$ theory. This allows us to build experiments where a

Josephson junction acts as a bright source of quantum radiation.

Strong-coupling of a junction to a single mode

Although the $P(E)$ theory links the transport properties of a junction to the impedance of its environment at all frequencies, the results of [33] can be reproduced using a smaller number of ingredients. In particular the tunneling rates and emission PSDs can be explained by considering only the low-frequency part of $Re[Z(\omega)]$ up to $k_BT/\hbar$, and the impedance near the resonances in the microwave range. This is a consequence of the conservation of energy: at zero temperature, the emission of a single photon of energy $\hbar\omega_J = 2eV$ depends only on $Re[Z(\omega_J)]$. At finite temperature, thermally excited modes up to $k_BT/\hbar$ may contribute to the tunneling rate, although their impact can be taken into account as a simple voltage noise δV on the voltage bias V.

In experiments where we use ICPT as a mechanism for the emission of photons, it is thus reasonable to simplify our description of the environment $Re[Z(\omega)]$, by considering only a small number of modes. The starting point of Chapter 3 is a very simple circuit, including only a voltage source V, a Josephson junction of energy E_J and a single mode, described as a LC oscillator. This simple model allows for a Hamiltonian description where the stationary state of the mode can be studied.

The amplitude of k-photon processes, that is the relative probability for a tunneling Cooper pair to create k photons at once in the mode, scales as $\frac{r^k}{k\times k!}$, where $r = \frac{\pi Z_c}{R_Q}$ is the dimensionless coupling constant between the mode and the junction, with $Z_c = \sqrt{\frac{L}{C}}$. . In the framework of the QED of conductors, r can be seen as the fine-structure constant of this interaction.

In this Hamiltonian system, we introduce dissipation in the mode by considering an effective leak rate κ, which enters in the master equation describing the evolution of the density matrix of the system. This leak rate is necessary to link this simple model to any real world experiment, where there is of course dissipation at some point. It also helps us in understanding exactly how the back-action of the cavity field on the junction impacts tunneling rates.

A finite leak rate κ induces the existence of a cavity lifetime κ^{-1}, which is the typical time over which a created photon stays in the mode. In a simple dynamical picture, we see that even if the photon emission rate is sufficiently low that the average photon number in the mode is always close to its equilibrium value, on a timescale κ^{-1} the occupation number is suddenly increased by 1 upon a tunneling event.

One may wonder in which conditions does adding a single photon to a mode modify significantly its phase fluctuations. In the equilibrium state, the phase noise from a single mode reads: $\Delta\hat{\phi}^2 = r(\bar{2}n + 1)$, with $\bar{n}$ the average occupation number. Hence a single photon added to the mode strongly modify its instantaneous phase fluctuations if this mode is strongly coupled to the junction, with $r \sim 1$.

The impact of this single added photon is more pronounced if the mode is initially in the vacuum state with $\bar{n} = 0$. In that case the probability of emitting a second photon in the mode, given that a first one is already present, is reduced by a factor of $(1 - \frac{r}{2})^2$ compared to the weak-coupling case. This coherent photon blockade leads to the emission

of antibunched photons in the mode for $r \sim 2$, with a second-order coherence function $g^{(2)}(0) = (1 - \frac{r}{2})^2$. At finite emission rates such that $\bar{n} \neq 0$, the system cannot be treated analytically. However numerical simulations reveal that the antibunching is progressively reduced as $\bar{n}$ is increased to the strong-driving regime $\bar{n} \sim 1/r$.

We test extensively these predictions in a microwave quantum optics experiment, where we measure the statistics of the light emitted by a Josephson junction coupled to a single mode in the strong-coupling regime $r = 0.96$. In this experiment, we calibrate *in situ* the environment of the sample and the gain of the microwave acquisition chain by using the junction itself as a calibrated light source, described notably by the $P(E)$ theory. Correlation functions of the microwave fields detected at room-temperature after amplification by a HBT like setup allows us to characterize the quantum properties of the emitted light.

We prove that the phase coherence properties of the photons, revealed by their $g^{(1)}(\tau)$ function, depend essentially on the amount of voltage noise added by the low-frequency modes of the setup. The phase coherence time $\sigma_\omega^{-1} \simeq 120$ ns greatly exceeds the typical timescale of intensity fluctuations, revealed by the measurement of the $g^{(2)}(\tau)$ function to be $\kappa^{-1} \simeq 1.3$ ns. These intensity fluctuations are lower than for a classically coherent beam of light, proving that the emitted photons display both antibunching and sub-Poissonian statistics. This is a manifestation of the quantum nature of light, revealing either wave-like or particle-like properties depending on the type of measurement.

Finally we test another prediction of $P(E)$ by measuring the renormalized Josephson energy of the junction $E_J^* = E_J^{-J(\infty)/2}$. This renormalization results from the equilibrium phase fluctuations from the environment, which blurry the value of $\hat{\phi}$ and effectively reduces the critical current of the junction.

Emission of entangled beams of light

Our theoretical treatment of the strong-coupling experiment differs from the $P(E)$ in that we used a simplified model for the environment of the junction. Instead of including a continuum of modes described by $Re[Z(\omega)]$, with various occupation numbers, we considered a single mode at ω_r, and summed up the impact of all the low-frequency modes as a random contribution to the voltage bias V.

This simplified model allows us to keep track of the quantum state of the mode at ω_r. In the limit of low occupation numbers, we can analytically describe the photon emission processes at arbitrary high order in r, recalling the multi-photon processes predicted by $P(E)$. There is another way of going beyond the $P(E)$ theory, which is to simplify again the problem by considering an experiment in the weak coupling regime $r \ll 1$. Then the dynamics of the system can be calculated at finite occupation number $\bar{n}$.

This is what we describe in Chapter 4, where we consider a Josephson junction put in series with two low-impedance resonators with different frequencies ω_a, ω_b. When biased on the two-mode resonance $2eV = \hbar\omega_a + \hbar\omega_b$, the effective RWA Hamiltonian of the system takes the form of a two-mode squeezing Hamiltonian $H_{TMS} \propto \hat{a}^\dagger \hat{b}^\dagger$+h.c. The next order terms in this Hamiltonian are of the form $r_a \hat{a}^\dagger \hat{a} r_b \hat{b}^\dagger \hat{b}$. Their influence may safely be neglected if the occupation numbers of the cavities stay low enough, so that: $r_a \bar{n}_a, r_b \bar{n}_b \ll 1$.

We derive a scattering model of the sample, which is described as a non-degenerate parametric amplifier with a noisy pump. The predictions of our model agree with the $P(E)$ theory in the low-driving regime $\bar{n}_a, \bar{n}_b \ll 1$. As soon as the occupation of the modes is finite, the $P(E)$ theory fails to account for the value of the photon emission rates or the shape of the emission PSDs. On the other hand our model, which takes into account the back-action of a finite occupation of the mode, agrees well with experimental data, provided that $r_a\bar{n}_a, r_b\bar{n}_b \ll 1$. However this model fails to capture the slight antibunching contribution to the light statistics inherited from the finite impedance of the resonators.

Nevertheless this simple two-mode squeezing picture helps us understands how entanglement is generated in this experiment. From $P(E)$ theory, we know that for each tunneling Cooper pair, the energy $2eV$ is ceded to the environment. On the 2-mode resonance, this energy is shared among a photon pair, created in the two resonators. It was already understood that as the emission process is coherent, each photon in the pair would be in a superposed state with an ill-defined frequency, while the sum of the two frequencies of the two photons would be well-defined. This is the type of quantum light studied in a Franson interferometer, where non-local interferences arise from the pair 2-photon phase coherence.

The simple parametric amplifier model reveals that this particle-like picture of the photon creation is not suited in a low-impedance environment. It is more instructive to consider that the junction continuously pumps energy into the two microwave fields, in a phase-coherent way. The entanglement of the fields is revealed by the measurement of the same 2-photon correlator used in the Franson experiment, which can yield an entanglement witness when compared to the $\langle n_a(0)n_b(\tau)\rangle$ correlator. These correlation functions do not show any granularity of the emitted light, i.e they do not prove that the junction is emitting entangled photon pairs. On the other hand these correlators indicate that a slice of the microwave beam at frequency ω_a is entangled with a slice of the beam at ω_b, validating this picture of a continuous entanglement of the fields.

In the two-mode squeezing model of the system, the Cooper pair condensate acts the pump field, which drives the continuous entanglement of the modes. The two-mode squeezing angle θ is fixed by the value of the superconducting phase $\hat{\phi}$ at the junction. We prove that the finite coherence time of the two emitted beams directly originates from the voltage noise on the junction, which dephases θ randomly. We proved that this dephasing rate can be reduced by cooling down the low-frequency modes of the setup.

This active cooling mechanism is activated by simply red-shifting the bias voltage on the junction. Then the junction tends to absorb low-frequency noise while emitting entangled photons, reducing the voltage noise and increasing the coherence time of the entangled beams. We proved that this mechanism can reduce the effective temperature of the modes from 20 mk down to 2 mK. However this does not increase the amount of entanglement of the cavities, computed from an estimation of their logarithmic negativity.

Preliminary experiments on the manipulation of quantum states

We have presented two experiments where a dc-biased Josephson junction is used a source of quantum microwave light. Here the modes coupled to the junction act as cold baths where the electrostatic energy $2eV$ can be dumped. Other kinds of experiment based on the ICPT mechanism can be considered, where the quantum state of light stored in a mode can be manipulated.

During this PhD research we worked on two such preliminary experiments, devoted to the manipulation of quantum light. The first one is the application of the cooling mechanism described in 3.41 to cool down a rf mode from a thermal equilibrium population of $\bar{n} \simeq 1$ down to its quantum ground state $\bar{n} \simeq 0$. We obtained results indicating a form of cooling, however their interpretation was complicated by the spurious coupling to another mode at a close frequency. At this point we did not have theoretical grounds firm enough to fully understand this experiment, so that it was discontinued.

We also designed a more complex experiment, that could yield the autonomous stabilization of the Fock state $|n = 1\rangle$ by an ICPT mechanism. This experiment was proposed by Souquet and Clerk in [68]. It is implemented by coupling a Josephson junction to two modes with well-chosen properties. The storage mode s must have a rather high quality factor $Q_s \gg 1$ and a characteristic impedance $Z_c^s = \frac{2R_Q}{\pi}$, so that it is strongly coupled to the junction with $r_s = 2$ exactly. The ancilla mode a must have a much lower quality factor $Q_a \ll Q_s$ and lie at a different frequency than s. The two modes should also have zero population at thermal equilibrium.

When the junction is voltage biased on the 2-mode resonance $2eV = \hbar\omega_s + \hbar\omega_a$, one photon is created in each mode upon the tunneling of a single Cooper pair. The two modes thus go from their initial empty state $|0\rangle_s \otimes |0\rangle_a$ to the state $|1\rangle_s \otimes |1\rangle_a$. After a short time $\frac{Q_a}{\omega_a}$ the ancilla photon has left its resonator, so that the modes end up in the state $|1\rangle_s \otimes |0\rangle_a$. In this state, both forward and backward tunneling of Cooper are blocked: on one hand, as $r = 2$ the transition from $|1\rangle_s$ to $|2\rangle_s$ by ICPT is forbidden, so no photon can be emitted. On the other hand, the absorption of photons from the modes to promote retro-tunneling is also forbidden, as it would require the energy $2eV = \hbar\omega_s + \hbar\omega_a$ to be taken from the environment and only $\hbar\omega_s$ is available.

As long as the single photon stays in the storage mode, the system is thus blocked, and the storage mode stays in the Fock state $|1\rangle_s$. After a long time $\frac{Q_s}{\omega_s}$ this single photon leaks out of the resonator, so that the system is once again in the vacuum state $|0\rangle_s \otimes |0\rangle_a$, and the mechanism starts again. What we gave here is a naive picture of the dynamics of the system, which insists on the granularity of light. Actually, as both photon creation and photon leakage are coherent processes, the Fock state $|1\rangle_s$ is continuously created and maintained in the mode, leading to its autonomous stabilization.

This mechanism utilizes dissipation engineering to stabilize a pure quantum state of light. Its simplicity is striking: once the right parameters have been set, mainly $r_s = 2$ and $2eV = \hbar\omega_s + \hbar\omega_a$, the Fock state stabilization is completely autonomous. This contrasts with usual circuit-QED experiments where complex series of fine-tuned pulses must be used to achieve similar effects.

We worked on a conceptual design of the sample, yielding a choice of the parameters $E_J, r_s, \omega_s, Q_s, r_a, \omega_a, Q_a$ that would lead the maximum fidelity of the stationary state of

the storage mode to the Fock state $|1\rangle_s$, given the experimental constraints on each of these parameters. We optimized the design of the experiment by running numerical simulations of the system's evolution, using the QuTiP library. We found out in particular that the dynamics of the system were greatly impacted by non-RWA terms in the Hamiltonian, which made the photon blockade mechanism imperfect. In the end we proposed a choice of parameters that should yield a fidelity greater than 90%.

We then worked on a practical implementation of this experiment, using microwave design tools. We propose to use a chain of densely packed SQUIDs to implement a CPW line with a very high and flux-tunable lineic inductance. A segment of this Josephson-CPW line host $\lambda/4$ modes, with a characteristic impedance that can be tuned up to $r_s = 2$. We ran numerical simulations of the microwave response of the sample, showing that we could implement the theoretical design that we had optimized earlier.

In the end we fabricated a first Fock stabilizer sample and ran a preliminary experiment. Its results proved that we had underestimated the stray capacitance to ground of the resonators, which prevented reaching the $r = 2$ regime of Fock state stabilization. This can be compensated in future design by packing more densely the SQUID array.In the future the updated design could be measured with the setup we developed for the anti-bunching experiment. In particular we propose to estimate the fidelity to Fock state $|1\rangle_s$ by measuring the $g^{(2)}(\tau)$ function of the emitted photons, which yield a lower bound on the fidelity.

Further perspectives

In this work, we have shown how the complicated interaction between a quantum conductor and its environment can be treated in a framework reminiscent of cavity-QED experiments. Provided that this environment is well-controlled and kept clean, we can map the high-frequency part of the environment to a finite number of modes, and treat the low-frequency modes as a random voltage source. In the end a Hamiltonian description of the system, combined either with a full master equation treatment, or a simpler Langevin equation for the fields, allow to predict the quantum properties of the light emitted by the junction.

We demonstrate the interest of these quantum light sources by probing the non-classical properties of the emitted photons, demonstrating antibunching and sub-Poissonian statistics in on experiment, and entanglement of propagating beams in the other. These properties are probed *via* the measurement of stationary correlation functions, as the absence of phase reference in these experiments forbid using the standard tools from circuit-QED, such as homodyne detection of the quadratures.

In the future, it may be interesting to push further the comparison to circuit-QED. By reducing the impedance of the resonators, the simulation of parametric Hamiltonians could be made more precise, allowing e.g to reach high levels of quantum squeezing. ICPT devices may hold a competitive advantage, as they exploit the Josephson non-linearity in a different way, which naturally rejects any Kerr terms in the Hamiltonian. However its seems that the harmful effect of unavoidable voltage noise would make the competition with circuit-QED very challenging.

It may also be worth it to develop ICPT-devices that could work in frequency ranges where

no coherent light is available. As an example, the ICPT mechanism may be exploited in Josephson junction made with higher-gap materials such as NbTiN (with $\Delta \sim 1$ THz), to produce quantum light sources or quantum-limited amplification in the THz range.

It may also be interesting to explore more fundamental aspects of the QED of coherent conductors. In this work we have studied a very simple kind of conductor, that cannot host any excitations or dissipate energy by itself. We also considered very simple models for the environment, including at most a few modes of radiation. The general problem of the coupling between a conductor and its environment is still ill-understood. In particular, if we consider a more complex conductor such as a QPC, then our theoretical treatment based on the expansion of the effective Josephson Hamiltonian cannot be used.

It may be interesting to start by checking to which extent the $P(E)$ theory, which hold also for normal conductors, can predict the quantum state of the emitted light. This calculation could help us work out the link between charge carriers statistics and properties of the radiation. On the applicative point of view, understanding better this interaction could lead to the design of new types of mesoscopic devices, where the coherence properties of conductors are exploited to yield novel quantum effects.

Appendix A

Résumé en français : cohérence quantique dans un conducteur électrique dissipatif hors-équilibre

Dans cette thèse, nous étudions l'interaction entre une jonction Josephson polarisée par une tension continue et les modes de son environnement électromagnétique. Nous prouvons lors de différentes expériences que ce système simple peut donner une source brillante de rayonnement micro-onde quantique.

Une première description de la jonction Josephson

Le point de départ de nos travaux est la jonction Josephson (JJ), c'est-à-dire une jonction tunnel entre deux électrodes supraconductrices (Fig.A.1). On sait que les électrons présents dans chaque électrode peuvent traverser la barrière isolante grâce à l'effet tunnel, ce qui génère un courant électrique. Cette jonction tunnel est un conducteur quantiquement coherent : la phase de la fonction d'onde des porteurs de charge est préservée après leur passage à travers la barrière.

À l'état supraconducteur, les électrons sont associés pour former des *paires de Cooper*. Ces paires d'électrons émergent d'une transition de phase analogue à la condensation de Bose-Einstein, et peuvent être décrites par une fonction d'onde macroscopique. Leur effet tunnel donne naissance à un courant, dont la valeur est donnée par l'équation de Josephson: $I = I_0 \sin(\phi)$ [1]. Ici, ϕ est la différence de phase entre les deux condensats d'électrons de chaque électrode, tandis que I_0 est une grandeur caractéristique de la jonction appelée *courant critique*.

La différence de phase ϕ est proportionnelle à l'intégrale de la différence de potentiel V aux bornes de la jonction, avec $\phi(t) = \frac{2e}{\hbar} \int V(t')dt'$. Cette phase décrivant des particules microscopiques est donc proportionnelle au flux magnétique aux bornes de la jonction, une grandeur électrique macroscopique.

L'équation de Josephson peut être réécrite pour relier la dérivée du courant I à la chute de tension V, avec : $\frac{dI}{dt} = I_0 \cos(\phi) \frac{2e}{\hbar} V$, ou de manière équivalente $V = \frac{\hbar/2e}{I_0 \cos(\phi)} \frac{dI}{dt}$. La JJ peut donc être considéré comme une inductance non linéaire valant $L_J(\phi) = \frac{\hbar/2e}{I_0 \cos(\phi)}$,

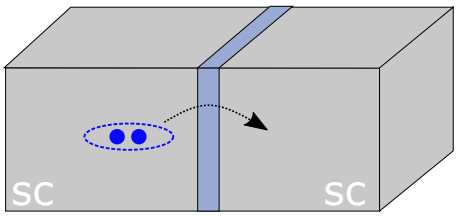

Figure A.1: Schéma d'une JJ entre deux électrodes supraconductrices (sc) (en gris). Le transport du courant à travers la jonction à basse énergie peut être décrit comme le passage par effet tunnel de paires de Cooper à travers la barrière isolante (couche bleu ardoise).

qui est intrinsèquement dépourvue de dissipation [2]. Grace à ces propriétés, les JJ sont omniprésentes dans deux domaines de recherche distincts : le traitement de l'information quantique et le transport mésoscopique.

Les jonctions Josephson dans les dispositifs d'information quantique

Lorsqu'une JJ est intégrée dans un circuit, sa non-linéarité peut être exploitée pour réaliser une application donnée, comme pour tout composant électrique. Les JJ sont particulièrement cruciales dans le domaine de l'information quantique, car leurs propriétés de cohérence et l'absence de dissipation interne les rendent aptes à la manipulation des signaux quantiques.

En guise d'exemple, on peut construire un circuit dans lequel une JJ se comporte dans une bande de fréquence donnée comme une résistance négative, de sorte qu'elle amplifie les signaux incidents. Cet amplificateur Josephson peut fonctionner à la limite quantique, en ce sens qu'il n'ajoute aux signaux amplifiés que le minimum de bruit requis par la mécanique quantique [3][4][5]. D'autres types de dispositifs à la limite quantique peuvent être conçus à partir des JJ, tels que des convertisseurs de fréquence [6][7], ou des détecteurs à photon unique [8][9][10].

La non-linéarité des JJ est également utilisée pour fabriquer des systèmes à deux niveaux, appelés atomes artificiels ou qubits. Le plus simple d'entre eux est le dipôle électrique formé par une seule JJ en parallèle avec une capacité. Ce circuit se comporte comme un résonateur LC anharmonique. La transition entre l'état fondamental et le premier état excité de cet oscillateur quantique peut être adressée de manière sélective, ce qui fait qu'il se comporte de manière effective comme un système à deux niveaux.

Les qubits à base de JJ peuvent être couplés électriquement à des résonateurs micro-ondes supraconducteurs hébergeant des modes du champ électromagnétique [11]. Leur domaine d'étude est appelé *circuit-QED*, par analogie avec les expériences de *cavity-QED* où des atomes "naturels" sont placés en cavité. La circuit-QED a permis de sonder l'interaction lumière-matière dans des régimes où la force de couplage naturelle entre électrons et photons peut être grandement augmentée, mettant en évidence de nouveaux effets physiques [12].

De plus, les qubits supraconducteurs constituent une plateforme potentielle pour le domaine naissant de l'informatique quantique, ce qui a motivé un grand nombre de propositions théoriques ainsi que des expériences de plus en plus complexes (Fig.A.2). L'effort expérimental mis en œuvre lors de ces expériences vise notamment à augmenter la durée

de cohérence de ces atomes artificiels, ainsi que la fidélité des portes logiques.

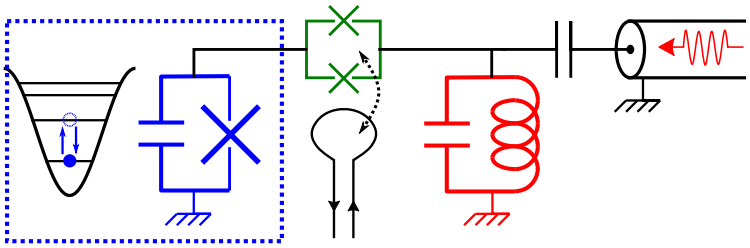

Figure A.2: Exemple de circuit supraconducteur où plusieurs JJ (symbole croix) sont utilisés pour manipuler l'information quantique. Une JJ en parallèle avec une capacité (en bleu) forme un oscillateur anharmonique. Ce qubit peut être sélectivement couplé à un résonateur électrique (en rouge) par l'intermédiaire d'un dispositif supraconducteur appelé SQUID (en vert), dont l'admittance peut être rapidement ajustée en faisant passer un flux magnétique dans la ligne de flux (boucle noire).

Ces exemples illustrent comment la cohérence quantique peut être exploitée en utilisant les JJ comme des dipôles électriques non linéaires et sans dissipation. Le succès de ces expériences repose notamment sur un découplage contrôlé entre une JJ et son environnement. Dans ces conditions, les mécanismes microscopique à l'œuvre au coeur de la jonction peuvent être ignorés, et il est possible de les considérer uniquement du point de vue de l'ingénierie quantique [13].

A rebours de ce point de vue, nous détaillons dans cette thèse des expériences où la jonction est directement reliée à un circuit de polarisation continue. Dans cette situation, la jonction peut être vue comme le lien entre deux réservoirs électroniques hors d'équilibre, permettant le passage d'un courant continu et dissipatif. Ces expériences relient les circuits supraconducteurs à un domaine de recherche plus ancien, la physique des conducteurs mésoscopiques.

Transport quantique dans le régime mésoscopique

Un conducteur cohérent est un conducteur électrique suffisamment petit pour que la phase de la fonction d'onde des électrons soit préservée pendant leur transmission. Le transport électrique à travers ces systèmes doit alors être décrit par la diffusion d'ondes électroniques à travers l'échantillon, ouvrant la possibilité d'interférences quantiques.

Les premières expériences de transport électrique quantique se sont intéressées à la mise en évidence des effets d'interférences électroniques sur les grandeurs observables les plus facilement accessibles, tels que la conductance électrique en courant continu. Le transport cohérent a été étudié dans une grande variété de conducteurs mésoscopiques : les jonctions Josephson, mais aussi les jonctions tunnel normales entre deux électrodes métalliques, les jonctions p-n dans les semi-conducteurs, des jonctions plus exotiques où la barrière est elle-même semi-conductrice, magnétique ou présentant une forte interaction spin-orbite, les gaz électroniques 2D qui peuvent être structurés pour former des boîtes quantiques ou bien des contacts ponctuels quantiques...

Les résultats de ces expériences sont bien compris dans le cadre de l'approche dite de Landauer-Büttiker (LB), où le transfert de charge par des conducteurs quantiques est probabiliste [14][15][16]. En raison de la granularité de la charge, ce caractère probabiliste induit un bruit de courant d'origine purement quantique. L'observation de ce bruit de

grenaille a été l'une des plus importantes confirmations expérimentales de l'approche LB [17][18].

Les expériences ultérieures incluent l'application d'une polarisation en tension alternative. Si la fréquence ω de la polarisation en courant alternatif est suffisamment élevée pour que $\hbar\omega$ soit supérieure à l'énergie thermique k_BT, des singularités apparaissent dans la densité spectrale de bruit électrique à basse fréquence $S_{II}(0) = \langle I^2\rangle - \langle I\rangle^2$ à la tension $V = k\hbar\omega/e$. C'est une indication de l'effet tunnel photo-assisté, où la transmission d'un électron à travers l'échantillon est accompagnée de l'absorption de k quanta d'énergie valant $\hbar\omega$ [19][20][21].

Du bruit électrique au rayonnement micro-onde

Le bruit en courant à fréquence finie $S_{II}(\omega) = \int \langle I(t)I(t+\tau)\rangle e^{i\omega\tau}dt$ est une observable qui fournit également des informations précieuses sur le système étudié [16]. En général, les fluctuations de courant dans le conducteur peuvent être captées par les modes électromagnétiques de l'environnement, où elles sont dissipées sous forme de *bruit d'émission* (Fig.A.3). Si cet environnement n'est pas dans son état fondamental, il peut également transférer de l'énergie au conducteur par ce mécanisme. $S_{II}(\omega)$ est alors aussi relié à l'absorption de lumière par le conducteur.

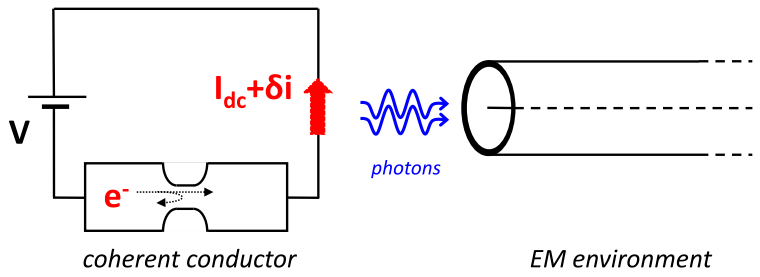

Figure A.3: Schéma d'un conducteur cohérent (représenté ici comme une constriction dans un guide d'onde électronique) mis hors équilibre par une tension continue de polarisation V. Le courant I circulant dans le circuit est formé d'une composante continue I_{dc}, due au transfert irréversible des charges dans le conducteur, et d'une composante fluctuante δI de densité spectrale $S_{II}(\omega)$, due à la granularité de la charge dans le cas du bruit de grenaille. Ce bruit en courant peut être capté par des modes dans l'environnement électromagnétique, ce qui entraîne l'émission de photons par le conducteur.

Le *bruit de grenaille* dû au passage incohérent des charges à travers une jonction tunnel hors équilibre [22] est l'exemple le plus simple de ce type de rayonnement. En raison de la très faible probabilité de transmission à travers la barrière tunnel, chaque événement tunnel est aléatoire et non corrélé avec les évènements précédents et suivants. Le courant I résultant de ce grand nombre d'événements indépendants présente des fluctuations qui peuvent être caractérisées par la densité spectrale de bruit $S_{II}(\omega)$.

Supposons que l'on connecte une impédance $Z(\omega)$ à température nulle en parallèle avec une jonction polarisée en tension, afin de capter ce bruit de courant et de mesurer sa valeur. Dans une image microscopique simple, les électrons qui passent par effet tunnel élastique de l'électrode source à l'électrode drain se retrouvent avec un excès d'énergie eV, qui est dissipé dans le réservoir du drain. La partie de cette énergie qui est dissipée dans $Z(\omega)$ peut être interprétée comme l'émission de photons $\hbar\omega$ par la jonction tunnel dans l'environnement. De manière étonante, comme chaque électron tunnel porte une

énergie qui est au maximum de eV, il ne peut jamais émettre de photons à une fréquence supérieure à $eV/\hbar$, ce qui entraîne que $S_{II}(\omega > 2eV/\hbar) = 0$ [16][23].

Ce premier exemple relie les propriétés des charges microscopiques à une grandeur macroscopique : la puissance dissipée par effet Joule dans une impédance externe. Il établit également un lien entre le transport de charges à travers un conducteur et l'émission de lumière dans son environnement, c'est-à-dire qu'il met en évidence le lien entre l'électronique et l'optique dans les conducteurs cohérents quantiques.

L'électrodynamique quantique des conducteurs cohérents

Nous avons donné une présentation simplifiée de la manière dont la JJ est considérée pour la circuit-QED ainsi que pour le transport mésoscopique : soit comme un dipôle électrique non linéaire utilisé pour le traitement quantique de l'information, soit comme un conducteur cohérent accueillant des processus microscopiques. Dans les deux domaines, l'interaction des JJ avec le champ électromagnétique est également considérée, mais une fois encore avec des points de vue très différents.

En circuit-QED, il est typique d'utiliser un champ micro-onde classiquement cohérent pour préparer un système quantique dans un état donné, ou bien pour lire son état après manipulation. Les signaux réfléchis ont une relation de phase fixe par rapport aux signaux incidents, de sorte qu'ils peuvent être détectés de manière synchrone, par exemple par détection homodyne. Le rayonnement émis par un dispositif quantique peut également être constitué de lumière quantique, c'est-à-dire d'états de la lumière qui ne peuvent être décrits par l'optique classique : on peut citer les photons uniques, les états de Fock de la cavité, la création d'un vide comprimé ou *quantum squeezed vacuum* ... ayant des applications dans le traitement de l'information quantique. Pout tous ces différents exemples, il est clair que la lumière doit être considérée comme un **signal**, c'est-à-dire une onde cohérente dont la détection repose sur une référence de phase bien connue.

En revanche, pour les expériences de transport mésoscopique que nous avons évoquées plus haut, la lumière est considérée comme un bruit électrique, sans qu'aucune attention particulière ne soit accordée à sa cohérence classique. Pour le transport photo-assisté, il n'y a pas de lien simple entre l'état de la lumière incident sur le conducteur et les grandeurs électriques observables. Dans le cas du rayonnement de shot-noise, la seule grandeur prédite par la théorie de la diffusion du transport d'électrons est la densité spectrale de la lumière émise $S_P(\omega) = 2Re[Z(\omega)]S_{II}(\omega)$. Les propriétés de la lumière elle-même, telles que ses statistiques ou l'existence d'une forme quelconque de cohérence quantique, ne sont généralement pas prises en compte, car cela nécessiterait un appareil théorique beaucoup plus complexe. En l'absence de cohérence, la lumière échangée entre un conducteur et les modes de son environnement est considérée comme un **bruit** plutôt que comme un signal.

L'unification de ces deux points de vue, qui permettrait d'obtenir une image cohérente de l'interaction entre la lumière quantique et les degrés de liberté microscopiques d'un conducteur, est le point central de l'**électrodynamique quantique des conducteurs**. Dans cette approche, on peut commencer par étudier un conducteur cohérent, éventuellement hors équilibre, et introduire l'interaction entre les charges et la lumière. L'inclusion d'une description quantique de la lumière révèle les propriétés de cohérence de cette inter-

action. En particulier, il a été prouvé que le **transport dissipatif** à travers le conducteur peut entraîner la création d'**états non classiques de la lumière** [24][25][26][27][28]. Il a également été suggéré récemment que le couplage entre une cavité et un conducteur quantique dissipatif pouvait être utilisé pour produire des états de type "chat de Schrödinger" du champ électromagnétique [29].

Dans l'exemple du shot-noise, on peut se demander si les propriétés des particules fermioniques influent sur la lumière rayonnée, en raison du mécanisme de couplage microscopique derrière cette interaction lumière-matière. Dans le cas simple d'une jonction tunnel polarisée en courant continu, l'émission de lumière se produit lors de la relaxation incohérente des charges dans les réservoirs. Comme les photons sont créés de manière aléatoire et indépendante, la statistique des photons émis est celle du rayonnement thermique, c'est-à-dire un état classique de la lumière avec une statistique chaotique. Cependant, pour des conducteurs plus exotiques tels que les contacts de points quantiques, il a été prédit que les statistiques de Fermi des électrons peuvent être imprimées aux photons, conduisant à la création d'une lumière fortement non classique avec des statistiques sub-poissoniennes [24]. Le test expérimental de cette prédiction fait l'objet de recherches intensives, nécessitant un développement technologique poussé [30].

Dans les travaux présentés ici, nous nous concentrons sur les propriétés quantiques de la lumière émise par un mécanisme étroitement lié à l'émission du shot-noise : l'effet tunnel inélastique des paires de Cooper à travers une jonction Josephson polarisée en tension continue.

Emission de lumière dans l'environnement et effet tunnel inélastique

Dans l'image simple du rayonnement de shot-noise que nous avons donnée plus tôt, nous avons commencé par décrire l'émission de bruit de courant par le conducteur, puis nous avons expliqué comment ce bruit pouvait être capté par les modes de son environnement. Ces modes jouent un rôle passif, en ce sens qu'ils n'agissent que comme un drain où l'énergie électrostatique des charges peut être déversée. Cependant, comme un couplage va toujours dans les deux sens, on peut s'attendre à ce qu'il existe une réaction de l'environnement sur le conducteur.

Examinons de plus près le mécanisme de ce couplage dans le cas d'une jonction tunnel normale. Après qu'un électron a traversé la jonction, la charge de chaque électrode change soudainement de $\pm e$. Ce déplacement de l'état de charge du système peut être décrit par l'opérateur de décalage $e^{i\chi}$, avec χ la différence de phase des électrons à travers la jonction. Cette phase est définie par $\chi(t) = \frac{e}{\hbar}\int^t V(t')dt'$, avec V la chute de tension aux bornes de la jonction.

Une tension continue parfaitement constante entraînerait un effet tunnel élastique des charges. Cependant, dans une image plus complète du système, nous devons considérer les fluctuations de tension provenant de l'environnement de la jonction, décrit par une impédance $Z(\omega)$. Même si cet environnement est à température nulle, il présente toujours au moins les fluctuations de vide, qui ont une densité spectrale donnée par $S_{VV}(\omega) = 2Re[Z(\omega)]\hbar\omega$.

Ces fluctuations de tension à fréquence finie peuvent déclencher des mécanismes inélastiques, où les charges creusent traversent la jonction de manière inélastique tout en émet-

tant ou en absorbant des photons de l'environnement. L'énergie nécessaire pour créer (absorber) ces photons est extraite de (donnée à) la source de tension elle-même : la jonction se comporte comme un convertisseur dc/ac. La lumière émise peuple les modes de l'environnement, les plaçant hors équilibre et modifiant ainsi la valeur des fluctuations de tension. Cela soulève la question de savoir dans quelles conditions ce mécanisme inélastique existe et comment il modifie les propriétés de transport de la jonction.

Ces questions ont été abordées pour la première fois au début des années 90, avec le développement de la théorie dite $P(E)$ [31]. Ce traitement perturbateur du Hamiltonien tunnel suppose que les taux d'émission/absorption des photons sont suffisamment faibles, de sorte que l'environnement reste à chaque instant proche de l'équilibre thermique. Ainsi, la valeur des fluctuations de tension est simplement fixée par l'occupation thermique des modes de l'environnement, ainsi que par leur impédance $Z(\omega)$. Si les modes ont une occupation élevée ($kT \ll \hbar\omega$), les probabilités d'émission et d'absorption des photons sont quasi-égales, de sorte que les processus tunnels inélastiques d'absorption et d'émission se produisent à des taux similaires. En revanche, si les modes de l'environnement sont initialement vides, ils ne peuvent qu'absorber des photons et jamais en fournir, ce qui ouvre de nouveaux canaux pour le transport dissipatif à travers la jonction (Fig.A.4).

Ces processus d'émission inélastiques ont un impact significatif sur le transfert de charges à travers le conducteur lorsque l'impédance de l'environnement $Re[Z(\omega)]$ est non négligeable devant le quantum d'impédance $R_K = h/e^2 \simeq 25,8$ kΩ. Comme cet impédance est typiquement de l'ordre de l'impédance du vide $Z_0 = \sqrt{\frac{\mu_0}{\epsilon_0}} \simeq 377$ Ω, la contribution de l'effet tunnel inélastique est généralement beaucoup plus faible que celle des processus élastiques directs, tant pour la valeur du courant continu que pour celle du bruit en courant.

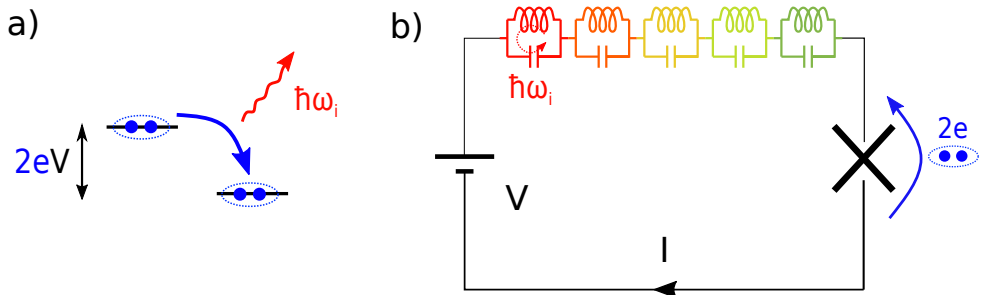

Figure A.4: a) Image schématique d'une paire de Cooper traversant inélastiquement une jonction polarisée en courant continu tout en émettant un photon d'énergie $\hbar\omega_i = 2eV$. b) L'énergie pour créer un photon dans un mode de l'environnement (représenté ici comme une collection d'oscillateurs LC) est extraite de la source de tension V.

Les effets inélastiques deviennent cependant considérables pour une jonction supraconductrice. À une tension de polarisation inférieure au gap supraconducteur $2\Delta/e$, aucune quasiparticule ne peut traverser la jonction. Les processus inélastiques sont donc le seul moyen par lequel une JJ polarisé en tension continue peut permettre le passage d'un courant continu[1]. Il s'agit d'un exemple simple de mécanisme dans lequel l'environnement d'un conducteur cohérent modifie considérablement ses propriétés de transport.

[1]De plus dans le cas de la JJ, $Re[Z(\omega)]$ doit être comparé au quantum d'impédance supraconducteur $R_Q = R_K/4$, de sorte que les processus inélastiques sont plus faciles à déclencher par rapport au cas normal.

Effet tunnel inélastique des paires de Cooper : du transport dissipatif à l'émission de lumière quantique

Les premières expériences visant à tester la théorie $P(E)$ dans le cas supraconducteur se sont concentrés sur la valeur du courant continu à travers la jonction. L'expérience de 1994 par Holst *et al* [32] a été la première à prouver que l'effet tunnel inélastique des paires de Cooper (ICPT) pouvait être exacerbé en adaptant l'environnement d'une JJ, par la création de résonances de $Re[Z(\omega)]$ aux fréquences micro-ondes. Un courant dissipatif $\bar{I}$ est alors mesuré pour des valeurs de tension de polarisation V inférieures à la tension de gap. La courbe $\bar{I}(V)$ de l'échantillon est bien reproduite par des simulations basées sur la théorie $P(E)$ et l'impédance $Re[Z(\omega)](\omega)$ du circuit en série avec la jonction. En particulier, les pics de la courbe $\bar{I}(V)$ sont associés à l'émission de photons dans les modes à l'environnement à la fréquence $2eV/\hbar$, dans des processus où toute l'énergie électrostatique $2eV$ fournie par la source de tension lors du passage d'une seule charge $2e$ par effet tunnel est convertie en photons (Fig.A.5).

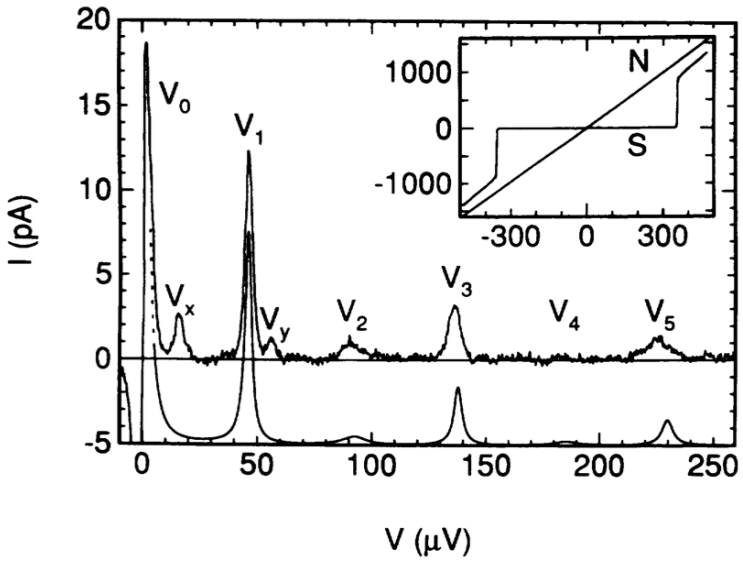

Figure A.5: I(V) expérimental mesuré en [32]. Un courant continu est mesuré en dessous de la tension de l'écart $2\Delta/2$, en raison des processus inélastiques d'effet tunnel des paires de Cooper. Chaque pic à la tension de polarisation V_i est associée à l'émission de lumière dans une résonance de l'environnement à la fréquence $2eV_i/\hbar\omega$, dans des processus où un photon est créé pour chaque paire de Cooper transférée.

Les progrès réalisés dans le domaine de l'ingénierie et de la mesure micro-ondes ont permis la détection directe de cette lumière émise lors d'une deuxième expérience pionnière en 2011 [33]. Le "versant lumineux" de l'effet tunnel inélastique des paires de Cooper a été prouvé sans ambiguïté, la mesure des taux d'émission de photons coïncidant avec les taux d'effet tunnel sur les résonances à un seul photon de la courbe I(V). Cette expérience a également prouvé l'existence des processus *multi-photoniques*, où l'énergie $2eV$ est répartie entre plusieurs photons créés en même temps (Fig.A.6).

Les résultats probants de cette expérience et les nouvelles techniques de détection de la lumière émise ont incité à proposer de nouvelles expériences, où la statistiquea des photons eux-mêmes serait mesurée. Ces expériences visent à élargir le champ de la photonique Josephson, en sortant du cadre de la théorie $P(E)$ par l'étude de l'état même de la lumière émise, dans des conditions où les photons émis peuvent modifier l'état de l'environnement et agir en retour sur le transport de courant continu.

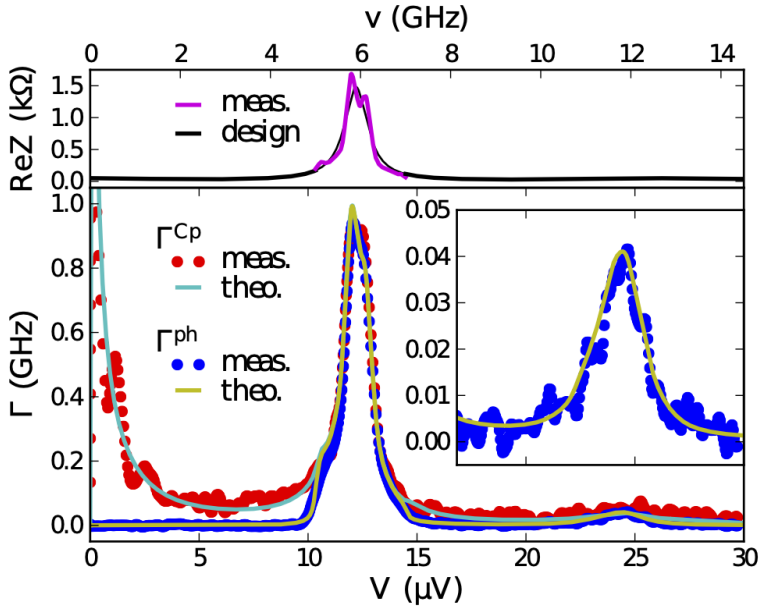

Figure A.6: Résultats de l'expérience décrite dans [33], où ont été mesurés à la fois le taux d'effet tunnel de la paire de Cooper Γ_{Cp} et le taux d'émission de photons Γ_{ph} dans un mode à $\omega_r/2\pi$ =6 GHz. Sur la résonance à 1 photon, $2eV = \hbar\omega_r$, Γ_{Cp} et Γ_{ph} coïncident. Sur la résonance à 2 photons $2eV = 2\hbar\omega_r$, la puissance d'émission à ω_r est détectée, indiquant des processus à 2 photons (encadré).

Dans ce travail, nous présentons deux expériences que nous avons menées pour étudier deux aspects complémentaires de cette physique : le régime de **couplage fort** d'une JJ à un seul mode micro-onde et l'émission de **photons intriqués** par effet tunnel inélastique.

Couplage fort d'une JJ à un mode unique

L'une des principales hypothèses de la théorie $P(E)$ est que les modes de l'environnement ne sont que faiblement perturbés par les processus inélastiques de création de photons. Un critère suffisant pour que cette condition se maintienne est que la population stationnaire des modes, résultant de l'équilibre entre la création de photons et les pertes intrinsèques des modes, reste proche de sa valeur d'équilibre $\bar{n} = n_B(T) = (e^{\frac{\hbar\omega}{k_B T}} - 1)^{-1}$.

Cette condition sur l'état stationnaire des modes garantit que les valeurs du courant continu et d'émission de photons sont correctement prédites par la théorie $P(E)$, car l'excès de population dû à l'effet tunnel inélastique ne modifie pas la probabilité de creusement de tunnels. Cependant, dans une image instantanée, juste après la création d'un photon, le mode peut être fortement déplacé de son état d'équilibre, en particulier s'il était initialement dans l'état vide. Si le mode est fortement couplé à la jonction, ce changement soudain de son occupation modifie profondément les fluctuations de tension instantanées, ce qui a un impact sur le taux d'effet tunnel de paires de Cooper.

Cette rétroaction de la lumière émise sur le taux de création de photons peut conduire à une dynamique non triviale du système. Il n'est cependant pas évident de savoir si l'état de la lumière qui en résulte présente des statistiques non classiques : même si les fluctuations de point zéro qui provoquent l'émission de photons sont par nature quantiques, l'état du vide lui-même est quasi-classique. Un traitement plus complet révèle

que l'état stationnaire des modes dépend de façon cruciale de leur force de couplage à la jonction.

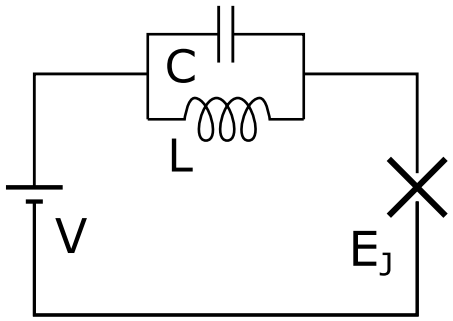

Figure A.7: Un résonateur LC hébergeant un seul mode du rayonnement est placé en série avec une source de tension continue et une JJ. Les deux dipôles sont couplés : un effet tunnel inélastique à la jonction peut être provoqué par les fluctuations de tension dans le résonateur. En même temps, le courant tunnel à travers la jonction est directement injecté dans l'oscillateur, ce qui crée des excitations dans le mode.

Dans le circuit simple comprenant une JJ et un mode unique à la fréquence ω_r (représenté par un oscillateur LC dans la figure A.7 avec $\omega_r = \sqrt{LC}^{-1}$), la constante sans dimension caractérisant leur couplage est $r = \frac{\pi Z_c}{R_Q}$, avec $Z_c = \sqrt{\frac{L}{C}}$ l'impédance caractéristique du mode. Dans le régime de couplage fort $r \sim 1$, les fluctuations de point zéro de la tension $\Delta V = \sqrt{r}\frac{\bar{\omega}_r}{2e}$ sont de la même amplitude que la tension continue V sur la résonance à photon unique $2eV = \hbar\omega_r$, où un photon est créé pour chaque effet tunnel de paire de Cooper.

ce régime de couplage fort doit produire deux effets observables sur le système [34]. Premièrement, même dans le cas d'une population moyenne proche de zéro, le taux d'effet tunnel est influencé par ses fluctuations de point zéro. Cette réduction de la probabilité d'effet tunnel apparaît dans l'énergie Josephson E_J de la jonction, qui est renormalisée par les fluctuations de phase du mode à la valeur $E_J^* = E_J e^{-\frac{r}{2}}$.

Deuxièmement, pour des faibles taux tunnel, correspondant à une faible excitation du mode telle que sa population $\bar{n}$ reste petite devant 1, des propriétés non classiques sont prévues pour la lumière émise, qui présente une statistique de dégroupement sous-poissonienne.Cet effet est caractérisée par la fonction de cohérence du second ordre de la lumière $g^{(2)}(\tau) = (1 - \frac{r}{2}e^{-\kappa|\tau|})^2$, avec κ le taux de fuite du résonateur. Cet effet résulte de la rétroaction cohérente du champ dans le résonateur sur la jonction. La présence d'un premier photon dans le mode réduit la probabilité d'en créer un deuxième, ce qui entraîne des anticorrélations dans le flux de photons émis par le résonateur (Fig.A.8).

Pour une impédance suffisamment élevée du résonateur telle que $r \sim 2$, ce simple circuit crée une **source de photons uniques**. D'un point de vue pratique, la simplicité du mécanisme de dégroupement, qui ne nécessite que de régler la tension de polarisation à $V = \frac{\hbar\omega_r}{2e}$ et l'impédance à $Z_c = \frac{2R_Q}{\pi} \simeq 4$ kΩ, pourrait le rendre utile pour des applications où des taux élevés de photons micro-ondes uniques sont recherchés. D'un point de vue fondamental, ce dispositif illustre la puissance de l'approche dite de **dissipation engineering**, où la dissipation est vue comme une ressource plutôt qu'un phénomène nuisible.

La conception d'une expérience dans le régime de couplage fort a été le projet de recherche

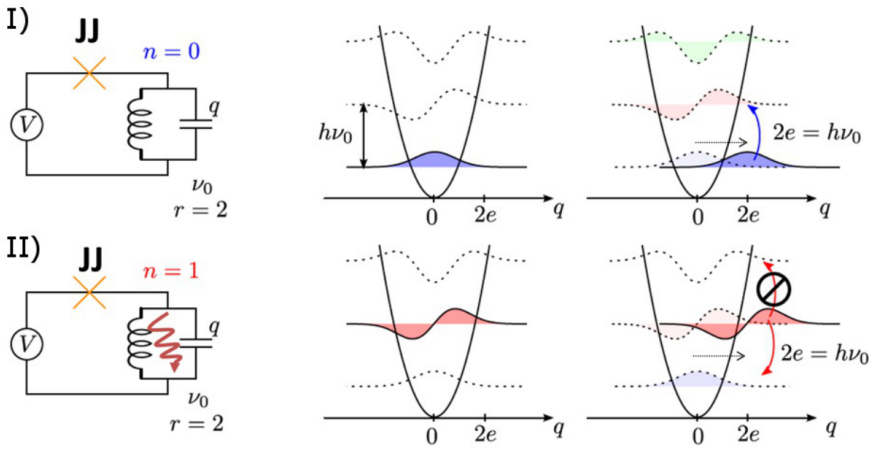

Figure A.8: Mécanisme de blocage des photons dans un mode fortement couplé à un JJ avec $r = 2$. Après qu'une seule paire de Cooper a été tunnellisée, le mode se retrouve dans son premier état excité, avec une fonction d'onde déplacée dans l'espace de charge de $q = 2e$. Cette fonction d'onde déplacée ne chevauche pas l'état excité suivant, de sorte que la création d'un deuxième photon est interdite.

de Chloé Rolland lors de son séjour doctoral dans notre équipe en 2014-2016 [35]. Elle a réussi à concevoir et à fabriquer un échantillon comprenant un mode micro-ondes avec une impédance $Z_c \simeq 2$ kΩ, fortement couplé avec un SQUID accordable en flux avec $r \simeq 1$ (Fig.A.9). En utilisant l'équivalent micro-ondes d'un interféromètre Hanbury Brown-Twiss, elle a fait des mesures préliminaires de la statistique des photons émis dans le régime de faible excitation, prouvant le dégroupement des photons. Cependant, ce dispositif de détection souffrait de couplages parasites entre les lignes de mesure, ce qui ajoutait un bruit non-négligeable aux mesures.

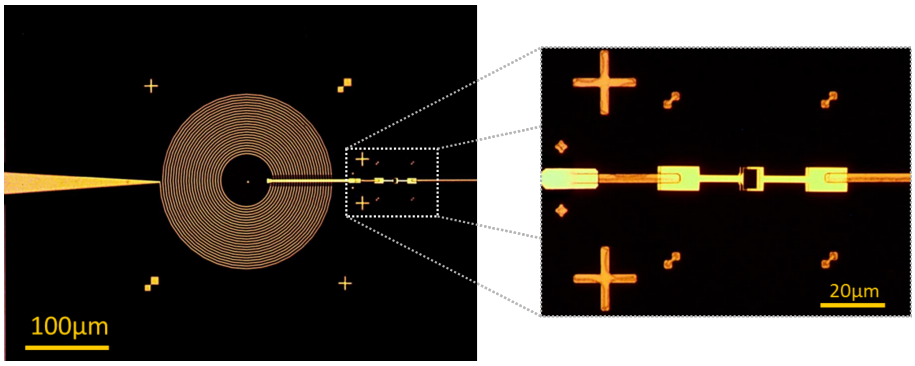

Figure A.9: Micrographie de l'échantillon fabriqué par Chloé Rolland lors de son doctorat. La bobine microfabriquée (partie gauche) implémente un résonateur en régime de couplage fort avec une JJ accordable de type SQUID (en médaillon), avec $r \simeq 1$.

Cette thèse de doctorat présente nos efforts pour développer un nouveau type de *système de détection linéaire*, permettant non seulement de mesurer la puissance rayonnée par l'échantillon, mais aussi les quadratures de ces signaux. En combinant ces quadratures de manière judicieuse, nous sommes en mesure de rejeter le bruit de fond parasite dû au couplage micro-ondes parasite des lignes, ce qui augmente considérablement notre précision dans la mesure des fonctions de corrélation des signaux. Nous pourrions ainsi mieux confirmer la mesure du dégroupement des photons émis par l'échantillon (Fig.A.10), en étudiant la transition vers un état classique du rayonnement au fur et à mesure que la population du mode augmente [36].

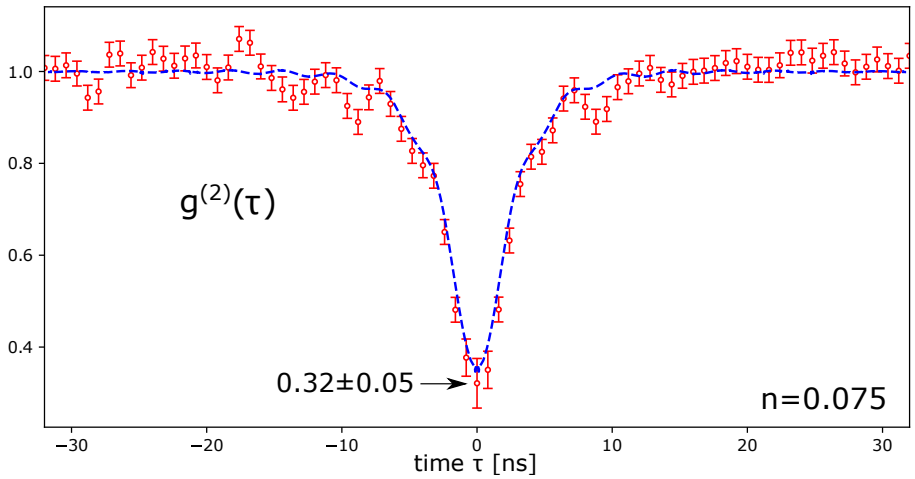

Figure A.10: Fonction de cohérence de second ordre des photons émis par l'échantillon à fort couplage à faible nombre d'occupation $n = 0,075$ du résonateur. La valeur $g^{(2)}(0) = 0.32$ prouve la statistique sub-posissonienne du photon, à un taux d'émission $\Gamma \simeq 60$ Mphotons/s.

Notre dispositif de détection linéaire nous permet également d'obtenir une bien meilleure résolution sur les propriétés spectrales de la lumière émise par la jonction, tant en régime d'effet tunnel incohérent que pour les tensions de polarisation supérieures à la tension de la jonction $2\Delta/e$, où la jonction se comporte comme une source de bruit de grenaille. En combinant ces mesures avec un modèle simple du circuit de l'échantillon, nous sommes en mesure de caractériser soigneusement l'environnement, en mesurant son impédance $Re[Z(\omega)]$ et la population de ses modes. Nous avons ainsi pu vérifier une prédiction de la théorie $P(E)$, à savoir que l'énergie Josephson effective de la jonction E_J^* est réduite par les fluctuations de phase de tous les modes de son environnement, de la gamme rf jusqu'aux fréquences micro-ondes.

Au-delà de la statistique des photons, notre dispositif de détection nous permet de mesurer des fonctions de corrélation arbitraires des photons émis par un échantillon. Nous l'avons utilisé dans une autre expérience pour prouver l'intrication de la lumière émise à deux fréquences différentes.

Faisceaux intriqués émis par effet tunnel inélastique

Les résultats de la figure 1.6 montrent que lorsque la tension de polarisation V sur une JJ vérifie $2eV = \hbar(\omega_a + \omega_b)$, avec ω_a et ω_b les fréquences de résonances dans l'environnement de la jonction, un courant continu peut circuler, grâce à des processus inélastiques où pour chaque paire de Cooper une paire de photons est créée, avec un photon dans chaque résonance (Fig. A.11).

Ce processus est similaire à la conversion paramétrique de l'optique quantique, où un photon est absorbé à partir d'un mode "pompe" à $\omega_p = \omega_a + \omega_b$ et converti de manière cohérente en une paire de photons à ω_a et ω_b via une interaction non linéaire. Selon la forme de cette interaction, la paire de photons créée peut être dans un état intriqué, partageant un degré de liberté non local (par exemple une polarisation totale égale à zéro), tandis que les mesures locales sur un seul photon de la paire donnent des résultats incohérents (par exemple une valeur de polarisation aléatoire). De tels états de paires sont couramment utilisés dans les tests de Bell de la non-localité en physique quantique.

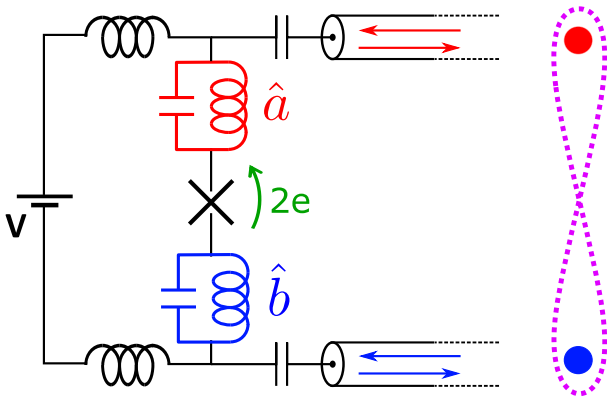

Figure A.11: Deux résonateurs aux fréquences ω_a, ω_b sont connectés à une JJ polarisé een courant continu. Lorsque $2eV = \hbar\omega_a + \hbar\omega_b$, des paires de photons intriqués sont créés par effet tunnel des paires de Cooper.

L'intrication de faisceaux de lumière micro-ondes par un dispositif Josephson a déjà prouvé qu'une conversion paramétrique pouvait être réalisée dans une expérience de circuit-QED [37]. La grandeur intriquée dans cette expérience était la somme des phases des deux champs micro-ondes, ce qui prouve la compression sous la limite quantique standard d'une combinaison linéaire de leurs quadratures. Ce résultat prouve que la non-linéarité d'un dispositif de Josephson peut être utilisée pour concevoir une excitation cohérente des deux modes. Néanmoins, il n'est pas évident de savoir si les paires de photons créées par effet tunnel inélastique présentent ou non de telles propriétés non-classiques. En effet, le mécanisme tunnel inélastique n'a pas d'équivalent direct en optique, car ici le rôle du mode de pompage cohérent est joué par les condensats supraconducteurs des deux électrodes.

La cohérence de ce système électronique macroscopique réside dans la phase de l'état fondamental supraconducteur. Cette cohérence de phase devrait en principe être héritée par les paires de photons créées par effet tunnel. Dans une jonction connectée galvaniquement, l'évolution temporelle de la différence de phase $\hat{\phi}$ est fixée par la valeur de la polarisation de tension V à travers la jonction. Dans les circuits simples dont nous avons parlé jusqu'à présent, la partie continue de la tension entraîne une augmentation linéaire de cette phase avec : $\frac{d\hat{\phi}(t)}{dt} = \frac{2eV}{\hbar}$, tandis que les fluctuations de tension à fréquence finie des modes d'environnement déclenchent les processus d'émission inélastique de photons. Dans un cadre plus réaliste, la jonction est également couplée à un continuum de modes de basse fréquence, du dc jusqu'à au moins $k_B T/\hbar \simeq 2\pi \times 400$ MHz à $T = 20$ mK. Ces modes sont dans un état thermique avec un nombre d'occupation élevé, de sorte qu'ils ajoutent un bruit aléatoire considérable à la polarisation de la tension.

Ce bruit à basse fréquence produit un déphasage aléatoire de la différence de phase supraconductrice, qui affiche un temps de cohérence très limité de quelques centaines de nanosecondes au maximum. Il semble donc que ce système dissipatif ne puisse jamais produire d'effets de cohérence quantique. Cependant, nous avons pu prouver qu'un choix judicieux d'observables pouvait prouver l'intrication de la lumière micro-onde émise par effet tunnel inélastique, même en l'absence d'une référence de phase stationnaire, à condition que l'environnement de la jonction soit soigneusement contrôlé.

Nous avons conçu une expérience à partir de celle réalisée par Olivier Parlavecchio lors

de son doctorat dans notre équipe en 2011-2014 [38] (Fig.A.12). Dans cette première expérience, une JJ est placé en série avec deux résonateurs à micro-ondes, qui crée des modes à 5 GHz et 7 GHz. L'impédance de ces résonateurs est suffisamment faible pour que les modes ne soient que faiblement couplés à la jonction avec $r \ll 1$, afin que leur occupation ne perturbe pas les taux d'effet tunnel. Sur la résonance des paires de photons $2eV = h \times 12$ Ghz, les puissances micro-ondes mesurées à la sortie des deux modes montrent des corrélations non classiques, indiquant que les photons sont effectivement créés par paires. Ce résultat valide le mécanisme de création de paires, et prouve que les deux résonateurs sont entraînés de manière cohérente par la jonction [39].

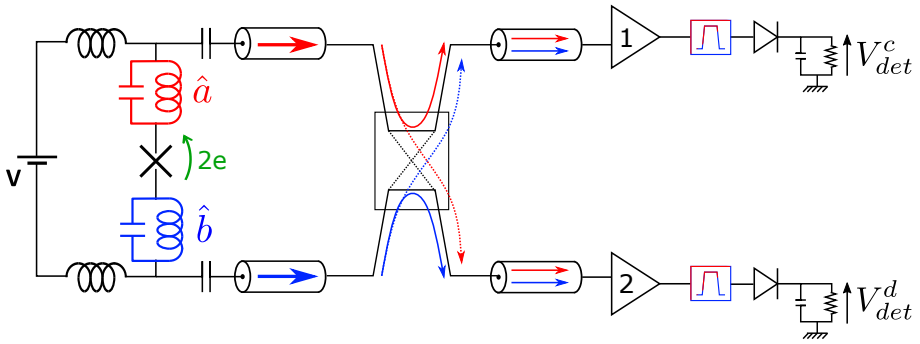

Figure A.12: Représentation schématique de la configuration utilisée pour sonder les statistiques non classiques des paires de photons émises par un JJ. La puissance micro-onde qui s'échappe à la sortie des deux modes (rouge et bleu) est détectée à température ambiante après amplification et répartition sur une installation de type HBT.

Cette expérience repose sur le fait que les corrélations de flux de photons mesurées à la sortie des résonateurs sont directement liées au nombre de photons à l'intérieur des cavités. Le lien entre les modes de propagation et les modes de la cavité peut être exprimé à l'aide du formalisme *input-output*. Avec ce formalisme, il a finalement été compris que les corrélations de phase non-locales entre les champs de la cavité sont imprimées dans les photons sortants. Ainsi, même si la différence de phase à travers la jonction est sujette au bruit local et présente un temps de cohérence limité, la lumière émise peut conserver sa cohérence à 2 photons lorsqu'elle se propage loin de l'échantillon.

Les corrélations de phase des photons émis à deux fréquences différentes peuvent être caractérisées par la violation d'une inégalité classique sur les fonctions de corrélation à 2 photons, qui fournit un *témoin d'intrication*. Dans un dispositif expérimental similaire à celui de 1.12, nous avons pu détecter cette intrication en utilisant notre dispositif de détection linéaire (Fig.A.13). Nous avons confirmé cette image simple de l'intrication des champs propageant, selon laquelle les photons restent intriqués s'ils quittent les résonateurs plus rapidement que le taux de déphasage à la jonction.

Comme ce taux de déphasage provient d'une tension à basse fréquence, il n'est pas intrinsèque à l'échantillon lui-même, mais plutôt à son circuit de mesure. Nous avons confirmé que le taux de déphasage était effectivement limité par la valeur du bruit de la tension thermique d'équilibre sur la jonction, en chauffant ou en refroidissant activement ces modes (Fig.A.14). Ce mécanisme de chauffage/refroidissement est basé sur l'effet tunnel inélastique par la même jonction qui crée les photons intriqués. Ce dernier résultat prouve qu'un système quantique dissipatif et ouvert, activement couplé à un bain dans un état profondément classique, peut encore créer une intrication observable. Le mécanisme de refroidissement lui-même pourrait être étendu pour amener les dispositifs quantiques

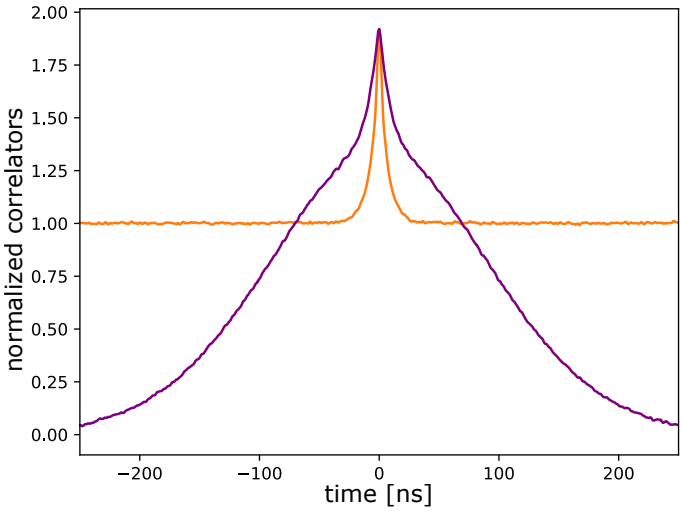

Figure A.13: Corrélateurs à 2 photons prouvant l'intrciation des champs émis. Pour des champs séparables, la fonction de corrélation de phase (en violet) est toujours plus petite que le corrélateur de population (en orange).

à leur état fondamental, ou effectuer la spectroscopie de systèmes mésoscopiques aux fréquences rf.

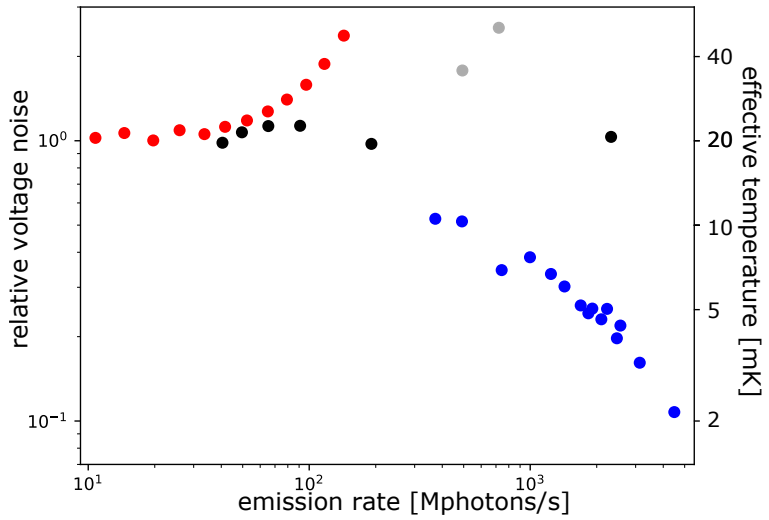

Figure A.14: Bruit relatif de tension en fonction des taux tunnel pour différentes valeurs de polarisation. La jonction peut être utilisée pour chauffer (points rouges) ou refroidir (points bleus) les modes basse fréquence de son environnement, en augmentant ou en réduisant leur bruit de tension. Cette interaction peut également être désactivée pour obtenir un régime sans interaction (points noirs).

Conclusions, expériences en cours et perspectives

Dans ce travail de doctorat, nous explorons comment les concepts et les outils de l'optique quantique peuvent être adaptés dans un cadre mésoscopique pour produire un nouveau type de sources de lumière quantique.

Dans nos expériences, nous considérons une JJ polarisée en tension continue, qui est un système quantique ouvert, hors équilibre, interagissant avec les modes de son environnement électromagnétique depuis dc jusqu'à $2eV/\hbar \sim$ quelques GHz. Nous montrons comment modéliser l'interaction avec ces modes, qui présentent des échelles de temps et des populations d'équilibre très différentes. Nous décrivons comment les modes à haute fréquence, créés par des résonateurs micro-ondes, agissent comme des cavités dans l'état vide excités par le transport inélastique à travers la jonction, tandis que les modes thermiques à basse fréquence agissent comme une source de bruit de tension aléatoire, déphasant les champs sur une échelle de temps lente.

Nous étudions deux types d'échantillons différents, un avec un seul mode dans le régime de couplage fort $r \simeq 1$ et un autre où deux modes à des fréquences différentes se couplent à la même jonction. Dans chaque expérience, nous caractérisons entièrement l'environnement de l'échantillon, en utilisant les propriétés d'émission de la jonction dans différents régimes de tension de polarisation et d'énergie Josephson. Nous mesurons ensuite des fonctions de corrélation pour prouver les propriétés non classiques de la lumière émise par effet tunnel, en étudiant la transition vers une source de lumière classique à des taux d'émission élevés.

Dans l'expérience de couplage fort, nous prouvons le caractère granulaire de la lumière émise à faible taux d'émission en mesurant le dégroupement des photons, avec une fonction de cohérence du second ordre $g^{(2)}(0) = 0,32 < 1$, la valeur pour les états classiques. Cette expérience ne repose sur aucune cohérence de phase des photons émis. Cependant, nous prouvons que notre dispositif de détection résolue en phase augmente la précision de la mesure, en rejetant le bruit de fond thermique parasite de la chaîne d'amplification. Nous mesurons également quantitativement la renormalisation de l'énergie Josephson de la jonction par les fluctuations de point zéro des modes de l'environnement.

Dans l'expérience à deux modes, nous détectons l'intrication des photons émis en prouvant leur cohérence de phase à deux photons. Nous interprétons cette intrication dans le cadre de la compression à deux modes, et nous mettons en relation les corrélations de phase des champs émis avec la dynamique de la phase supraconductrice de la jonction. Nous étudions la correction à la compression à deux modes pure due à l'impédance finie des modes, qui conduit à une rétroaction des photons émis sur la jonction. Nous étudions comment cette rétroaction produit des statistiques de plus en plus classiques des champs à taux d'émission élevé. Nous prouvons que le taux de déphasage à la jonction, qui donne le temps de cohérence de phase fini des faisceaux intriqués, provient du bruit de tension à basse fréquence du circuit de polarisation. Nous augmentons ensuite la valeur du taux maximal auquel nous détectons encore l'intrciation en refroidissant ces modes, réduisant ainsi leur bruit de tension. Ce mécanisme de refroidissement actif est basé sur l'absorption du bruit à basse fréquence par la jonction elle-même par le biais de l'effet tunnel inélastique.

Les résultats de ces deux expériences prouvent qu'une JJ polarisée en tension continue

peut créer une **source de lumière quantique micro-ondes** polyvalente, même s'elle est couplée à un continuum de modes de haute occupation thermique. L'expérience de couplage fort met en évidence l'impact des fluctuations de point zéro de l'environnement sur l'excitation du mode créé par la jonction, qui peut conduire à la création d'états de lumière fortement non-gaussiens. Dans l'expérience d'intrication à deux modes, cette non-Gaussianité réduit la fidélité de l'état lumineux par rapport à un pur état comprimé à deux modes. Cependant, cette non-Gaussianité pourrait être avantageuse pour la création d'une lumière fortement non classique, qui pourrait être utilisée dans des protocoles d'information quantique.

Nous avons également contribué à la conception d'autres expériences, qui n'ont pas encore été réalisées. La première fait suite à une proposition de mise en œuvre d'un stabilisateur autonome d'état de Fock, utilisant une jonction couplée à deux modes, dont l'un est en régime de couplage fort $r = 2$. Nous avons développé un plan pour un échantillon qui mettrait en œuvre un résonateur micro-ondes accordable en flux, permettant d'atteindre cette condition de fort couplage. Nous avons également mené une expérience préliminaire de refroidissement en bande latérale, visant à refroidir un mode rf jusqu'à son état fondamental quantique par effet tunnel inélastique. Ces expériences permettraient d'aller plus loin que la réalisation de sources de lumière quantique, vers la manipulation des états quantiques.

Dans les futures expériences, nous pourrions essayer de nous rapprocher du domaine de la circuit-QED, par exemple en ajoutant des tons cohérents micro-ondes pour verrouiller la phase des signaux émis et éliminer les problèmes liés à l'absence de référence de phase fixe. Ce type de dispositif bénéficierait alors du rejet intrinsèque des termes Kerr dans le Hamiltonien, ce qui le rendrait plus adapté aux applications à nombre de photons élevé.

Il peut également être intéressant de s'écarter franchement de la circuit-QED et d'explorer un espace de paramètres interdit aux circuits supraconducteurs typiques. Par exemple, en utilisant des JJ fabriqués avec un matériau supraconducteur à gap plus élevé, nous pourrions essayer d'émettre des radiations à des fréquences THz, là où aucune source cohérente n'est disponible. Il peut également être intéressant d'étudier différents types de conducteurs quantiques tels que les contacts supraconducteurs à points quantiques, qui permettent une interaction plus complexe avec l'environnement.

Appendix B

Shot-noise measurements and calibration

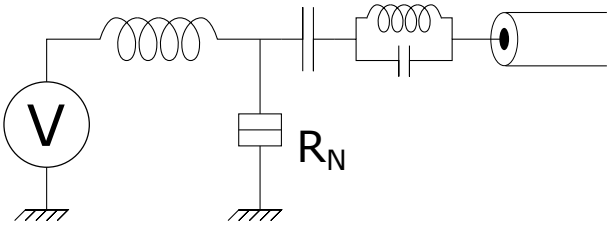

Figure B.1: Model circuit of the experiments in the shot-noise regime. Biased far above the gap voltage, the Josephson junction behaves as a normal junction with tunnel resistance R_N (box symbol). A bias-tee defines low-frequency and rf branches of the rest of the circuit, with a dc resistance $Re[Z(0)] = 0$.

The shot-noise regime is reached when applying on a Josephson junction a bias V much larger than the gap voltage $2\Delta/e$ (see figure 2.3). The transport through the junction is then dominated by normal quasiparticles, with a dc-current $\bar{I} \simeq V/R_N$.

The transfer of charges by quantum tunneling is a stochastic process. For each tunnel event, a charge $-e$ is abruptly transferred from one electrode to the other. This granularity results in the finite-frequency current noise $S_{II}(\omega) = 2(e\bar{I} - R_N^{-1}\hbar\omega)$ for $\omega < eV/\hbar$.

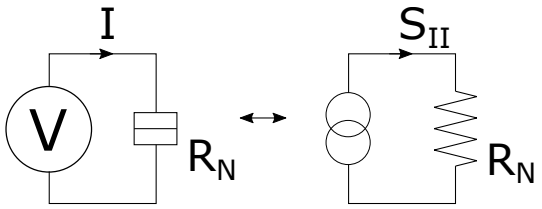

Figure B.2: A dc-biased tunnel junction give rise to a tunnel current, which includes an average value $\bar{I} = V/R_N$ as well as a noise spectral density $S_{II}(\omega)$.

If the impedance of the rest of the circuit $Re[Z(\omega)] \gg R_N$ at finite frequency, the junction can be considered isolated, as its own admittance R_N^{-1} shunts the environment. The current noise is entirely dissipated through R_N itself, heating the junction with the Joule power spectral density $S_P(\omega) = R_N \times S_{II}(\omega)$ (Fig.B.2).

On the other hand if $Re[Z(\omega)]$ is of the order of R_N or smaller, the environment can collect a part of the current noise. The circuit can be cast in a form where $Z(\omega)$ is in parallel with the junction, forming a current-divider with R_N (Fig.B.3). The junction then behaves as a current source with output impedance R_N.

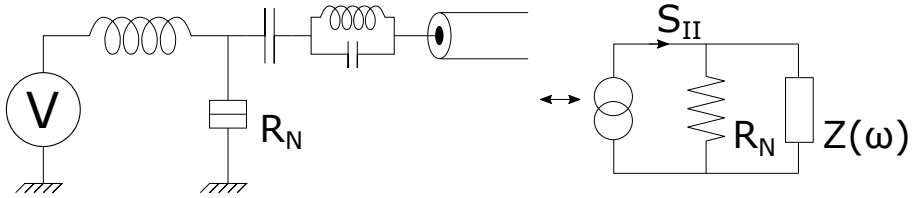

Figure B.3: At finite frequency $\omega \neq 0$ the junction behaves as a current source with an output impedance R_N, feeding the environment $Re[Z(\omega)]$.

The fraction of $S_{II}(\omega)$ radiated into the environment reads: $S_{II}(\omega) \times |R_N/(R_N + Z(\omega))|^2$. The PSD associated to this current noise is:

$$S_p(\omega) = Re[Z(\omega)] \times S_{II}(\omega) \times \left| \frac{R_N}{R_N + Z(\omega)} \right|^2 \tag{B.1}$$

$$= \frac{eV - \hbar\omega}{2} \left(1 - \left| \frac{R_N - Z(\omega)}{R_N + Z(\omega)} \right|^2 \right). \tag{B.2}$$

Perfect matching occurs when $Re[Z(\omega)] = R_N$. Then the PSD collected by the environment is $(eV - \hbar\omega)/2$. In the case of a low impedance environment $Re[Z(\omega)] \ll R_N$, we have:

$$S_p(\omega) \simeq 2(eV - \hbar\omega) \frac{Re[Z(\omega)]}{R_N}. \tag{B.3}$$

The shape of the PSD follows then $Re[Z(\omega)]$. This can be use to determine the resonance frequency ω_r and quality factor Q of a mode in the environment of the junction.

If $Re[Z(\omega)] \sim R_N$, information about a single mode can still be extracted from $S_p(\omega)$. The impedance near a resonance frequency reads:

$$Z(\omega) = \frac{Z_0}{1 + 2iQ\frac{\omega - \omega_r}{\omega_r}}, \tag{B.4}$$

Such that:

$$Re[Z(\omega)] = \frac{Z_0}{1 + 4Q^2 \left(\frac{\omega - \omega_r}{\omega_r} \right)^2}. \tag{B.5}$$

Then:

$$S_p(\omega) = \frac{eV - \hbar\omega}{2} \frac{1 - \left| \frac{R_N - Z_0}{R_N + Z_0} \right|^2}{1 + 4 \left(\frac{Q}{1 + Z_0 R_N} \right)^2 \left(\frac{\omega - \omega_r}{\omega_r} \right)^2}. \tag{B.6}$$

The shape of the PSD is still a Lorentzian, but with a quality factor divided by $1 + Z_0/R_N$. If R_N and the shape of $Re[Z(\omega)]$ are known, the absolute value of the impedance Z_0 of the mode can be computed.

If the two quality factors (shape of the mode and shape of the shot-noise PSD) are measured, the ratio Z_0/R_N can be extracted. Then we also know the coupling factor

$1 - \left|\frac{R_N - Z_0}{R_N + Z_0}\right|^2$. Finally, this allows us to calibrate the absolute gain of the microwave collection chain. The voltage derivative of the PSD, measured at the resonance frequency, reads:

$$\frac{dS_p(\omega_r)}{dV} = \frac{e}{2} \times \left(1 - \left|\frac{R_N - Z_0}{R_N + Z_0}\right|^2\right). \tag{B.7}$$

It is more convenient to use the voltage derivative that the absolute value of (B.6), at it is insensitive to potential dc-voltage offsets in the bias line and as it removes the $\hbar\omega$ component of the expression.

In our experiments we measure this voltage derivative to calibrate the photon emission rate of the samples.

Appendix C

Transmission line resonators

In a TL, electrical waves can propagate at speed v with a given ratio between the voltage amplitude $V^{\pm}(x \pm vt)$ and the current amplitude $I^{\pm}(x \pm vt)$, called the *wave impedance* Z_w of the line. This ratio is positive for waves travelling in one direction and negative for counter-propagating waves: $V^{\pm}(x \pm vt) = \pm Z_l \times I^{\pm}(x \pm vt)$. If we terminate a TL at $x = 0$ with a load impedance Z_l, we impose a boundary condition to stationary waves in the line, namely that at $x = 0$:

$$V^+(0,t) + V^-(0,t) = Z_l \times (I^+(0,t) + I^-(0,t)) \tag{C.1}$$

If $Z_w \neq Z_l$, then a wave incoming onto Z_l has to be partly reflected to ensure the boundary condition.

The interference between the reflected and incoming waves produces a certain ratio of $V(-L,t)/I(-L,t)$ at the other end of the line. As the wave vector k is proportional to the frequency of the wave, this mean that different frequencies will have different V/I ratios after a length of propagation L, or different *input impedances* as seen from $x = -L$. This can be summed up by the transmission line equation:

$$Z(\omega = kv) = Z_w \frac{Z_l + jZ_w \tan(kL)}{Z_w + jZ_l \tan(kL)} = Z_w \frac{Z_l + jZ_w \tan(\frac{\pi\omega}{2\omega_r})}{Z_w + jZ_l \tan(\frac{\pi\omega}{2\omega_r})} \tag{C.2}$$

At frequencies such that $kL = \pi/2 \pmod{2\pi}$, the $\tan(kL)$ terms diverge. If $Z_w > Z_l$, there is then a peak in $Re[Z(\omega)]$. These resonances appear for frequencies which are odd multiples of the fundamental resonant frequency $\omega_r = \pi v/2L$, whose wavelength $\lambda_r = 2\pi v/\omega_r = L/4$ is one quarter of the length of the line L: these are called **$\lambda/4$ resonances**. The impedance at the top of the peaks is then Z_w^2/Z_l, and the quality factor of the first resonance is $Q \simeq \pi Z_W/4Z_l$.

Appendix D

Multiphotonic emission rates

Here is a derivation of the tunneling rate in a dc-biased Josephson junction in series with a single mode, on the k-photon resonances $2eV = k\hbar\omega_0$. It was extracted from a note by Philippe Joyez, which was first published in the supplementary material of our antibunched photons article [36].

The spectral density of the emitted radiation is given by [33]:

$$\gamma(V,\nu) = \frac{2\mathrm{Re}[Z(\nu)]}{R_Q}\frac{\pi}{2\hbar}E_J^2 P(2eV - h\nu), \tag{D.1}$$

where $Z(\nu)$ is the impedance across the junction, R_Q is the superconducting resistance quantum $R_Q = h/4e^2$, E_J is the Josephson energy of the junction, and $P(E)$ represents the probability density for a Cooper pair tunneling across the junction to dissipate the energy E into the electromagnetic environment described by $Z(\nu)$[58]. $P(E)$ is a highly nonlinear transform of $Z(\nu)$:

$$\begin{array}{rcl} P(E) & = & \frac{1}{2\pi\hbar}\int_{-\infty}^{\infty}\exp[J(t)+iEt/\hbar]dt \\ J(t) & = & \int_{-\infty}^{+\infty}\frac{\mathrm{d}\omega}{\omega}\frac{2\mathrm{Re}Z(\omega)}{R_Q}\frac{e^{-i\omega t}-1}{1-e^{-\beta\hbar\omega}}, \end{array} \tag{D.2}$$

where $\beta = 1/k_BT$. For an LC oscillator of infinite quality factor at zero temperature, $P(E)$ is given by

$$P(E) = e^{-r}\sum_n \frac{r^n}{n!}\delta(eV - n\hbar\omega_0) \tag{D.3}$$

where $r = \pi\sqrt{\frac{L}{C}}/R_Q$ and $\omega_0 = 1/\sqrt{LC}$.

Here, we consider the case of a mode of finite linewidth, so that near the resonance the real part of the impedance can be approximated as

$$\frac{2\mathrm{Re}Z(\omega)}{R_Q} \simeq r\mathcal{L}(\omega,\omega_0,Q). \tag{D.4}$$

where

$$\mathcal{L}(\omega,\omega_0,Q) \equiv \frac{2}{\pi}\frac{Q}{1+4Q^2\left(\frac{\omega}{\omega_0}-1\right)^2}$$

denotes a Lorentzian function centered at ω_0 with a maximum value $\frac{2}{\pi}Q$ and a quality factor $Q = \frac{\omega_0}{\Delta\omega}$. Note that $\int\mathcal{L}(\omega,\omega_0,Q)d\omega = \omega_0$.

For such a finite-Q mode, we aim to get a formula similar to Eq. D.3, i.e. we look for an expansion

$$P(E) = P_0(E) + P_1(E) + P_2(E) + \ldots + P_n(E) + \ldots \tag{D.5}$$

where each $P_n(E) \propto r^n$. However, from the integral expressions (D.2), accessing the different multiphoton peaks, i.e. calculating $P(E \simeq n\hbar\omega_0)$ is not straight-forward. Such an expansion can be obtained using the so-called Minnhagen equation [58], which is an exact integral relation obeyed by $P(E)$, valid for any impedance. We first establish the Minnhagen equation starting from

$$e^{J(t)} - e^{J(\infty)} \;=\; \int_{-\infty}^{t} d\tau J'(\tau) e^{J(\tau)} \;,$$

which, using the definition (D.2) of J can be recast as

$$e^{J(t)} - e^{J(\infty)} \;=\; -i \int_{-\infty}^{+\infty} d\omega' h(\omega') \int_{-\infty}^{\infty} d\tau e^{-i\omega'\tau} e^{J(\tau)} \theta(t-\tau)$$

where θ is the Heaviside function, $h(\omega) = \frac{1}{1-e^{-\beta\hbar\omega}} \frac{2\mathrm{Re}Z(\omega)}{R_Q}$ and using the fact that $J(-\infty) = J(\infty)$. The rightmost integral being the Fourier transform of a product, we replace it by the convolution product of the Fourier transforms and use the detailed balance property of h and P to simplify the r.h.s.:

$$\begin{aligned} e^{J(t)} - e^{J(\infty)} &= -i \int_{-\infty}^{+\infty} d\omega' h(\omega') \int du \left(\pi\delta(u) + \frac{i e^{it'u}}{u} \right) P(-\omega' - u) \\ &= \int_{-\infty}^{+\infty} d\omega' h(\omega') \int du \frac{e^{itu}}{u} P(-\omega' - u). \end{aligned}$$

Finally, we take the Fourier transform on both sides and rearrange, which yields the Minnhagen equation

$$P(E) \;=\; \tfrac{\hbar}{E} \textstyle\int P(E - \hbar\omega) \frac{1}{1-e^{-\beta\hbar\omega}} \frac{2\mathrm{Re}Z(\omega)}{R_Q} d\omega + \delta(E) e^{\mathrm{Re}J(\infty)} \;. \tag{D.6}$$

At zero temperature $\frac{1}{1-e^{-\beta\hbar\omega}} \to \theta(\omega)$ and $P(E)$ is zero for negative energies, so that the Minnhagen equation is most frequently found written as

$$P(E) \;=\; \tfrac{\hbar}{E} \textstyle\int_0^E P(E - \hbar\omega) \frac{2\mathrm{Re}Z(\omega)}{R_Q} d\omega + \delta(E) e^{\mathrm{Re}J(\infty)} \;. \tag{D.7}$$

Plugging the expansion (D.5) into Eq. D.6, one immediately gets

$$\begin{aligned} P_0(E) &= \delta(E) e^{J(\infty)} \\ P_1(E) &= \frac{1}{E} \int_{-\infty}^{\infty} P_0(E - \hbar\omega) \frac{r\mathcal{L}(\omega, \omega_0, Q)}{1 - e^{-\beta\hbar\omega}} d\hbar\omega \\ &\simeq \frac{e^{J(\infty)}}{\hbar\omega_0} r\mathcal{L}\left(\frac{E}{\hbar}, \omega_0, Q\right) \end{aligned}$$

where the approximation of the last line was obtained assuming that $k_B T \ll \hbar\omega_0$ and taking the value of the denominator at $E = \hbar\omega_0$ –where $\mathcal{L}$ (and P_1) peak– which is reasonable if the Q is large enough. By repeated replacement in Eq. D.6 and with similar approximations, one systematically obtains the higher orders terms of (D.5) as shifted Lorentzians of constant Q

$$P_{n\geqslant 1}(E) \simeq e^{J(\infty)} \frac{r^n}{nn!} \frac{\mathcal{L}(E/\hbar, n\omega_0, Q)}{\hbar\omega_0}$$

whose value at each peak are

$$P_{n\geqslant 1}(E = n\hbar\omega_0) = \frac{2}{\pi} e^{J(\infty)} \frac{r^n}{nn!} \frac{Q}{\hbar\omega_0}$$

yielding a tunneling rate at the peaks

$$\Gamma_{2e}(eV = n\hbar\omega_0) = \frac{1}{\hbar} \frac{E_J^2 e^{J(\infty)}}{\hbar\omega_0} \frac{r^n}{n!} \frac{Q}{n}.$$

Note that the Cooper pair rates at different orders scale with an extra Q/n compared to the naive rates obtained from Eq. D.3.

In the main text, $E_J^2 e^{J(\infty)}$ is called E_J^{*2}. This renormalization of the Josephson energy is obtained from the zero point phase correlator

$$J(\infty) = -\langle\varphi(0)\varphi(0)\rangle = -\int_0^{+\infty} \frac{d\omega}{\omega} \frac{2\mathrm{Re}Z(\omega)}{R_Q} \coth\frac{\beta\omega}{2}$$

which in the limit of $k_B T = 0$ and for an RLC parallel resonator (it is important that $\mathrm{Re}Z(\omega \sim 0) \propto \omega^2$ for proper convergence) yields

$$J(\infty) = -\frac{Qr\left(1 + \frac{2}{\pi}\mathrm{atan}\frac{2Q^2-1}{\sqrt{4Q^2-1}}\right)}{\sqrt{4Q^2-1}} = -r\left(1 - \frac{1}{\pi Q} + \mathcal{O}\left(\frac{1}{Q^2}\right)\right),$$

in agreement with the expression $E_J^* = E_J e^{-r/2}$ used in the main text (The finite-Q correction to this renormalization is of order of 1%, beyond the precision of our measurements). In [33], E_J^{*2} was given with an approximate first-order expansion of the phase correlator valid for small phase fluctuations (and which was correct for the small r value in that paper).

Appendix E

Spectrum of low-frequency noise

In a series of different experiments, we measured the width of the emission peak as a function of the acquisition time T_{meas}. We found that the width of the peak decreases abruptly when T_{meas} goes below about 1 μs, indicating that most of the noise occurs on longer timescales:

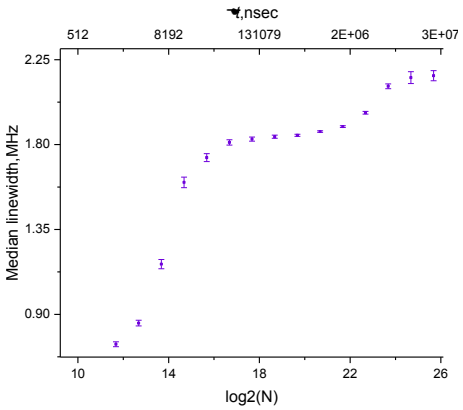

Figure E.1: Acquisition time is varied.

We also looked at fast fluctuations of the position of the peak, in and out of an integration window:

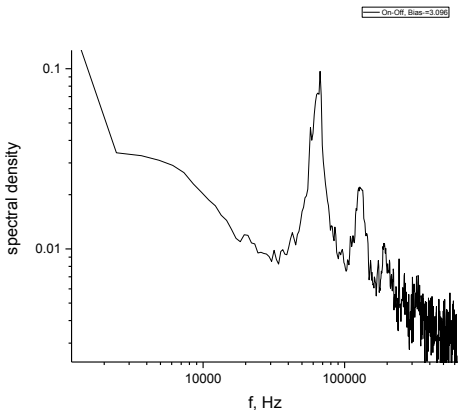

Figure E.2: F-Spectrum of peak jumps.

Here a clear peak occurs around 70 kHz, which is consists with random noise from the bias-tee mode. A harmonic appears at 140 kHz, which is an artefact of the integration method. Finally we looked at the full spectrum of the positions of the peak:

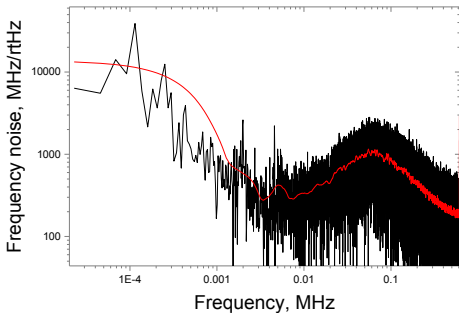

Figure E.3: F-Spectrum of peak position.

Which indicates the same peak at 70 kHz, albeit widened by the averaging.

Bibliography

[1] B. D. Josephson, "Possible new effects in superconductive tunnelling," *Physics letters*, vol. 1, no. 7, pp. 251–253, 1962.

[2] M. H. Devoret *et al.*, "Quantum fluctuations in electrical circuits," *Les Houches, Session LXIII*, vol. 7, no. 8, 1995.

[3] I. Siddiqi, R. Vijay, F. Pierre, C. Wilson, M. Metcalfe, C. Rigetti, L. Frunzio, and M. Devoret, "Rf-driven josephson bifurcation amplifier for quantum measurement," *Physical review letters*, vol. 93, no. 20, p. 207002, 2004.

[4] X. Zhou, V. Schmitt, P. Bertet, D. Vion, W. Wustmann, V. Shumeiko, and D. Esteve, "High-gain weakly nonlinear flux-modulated josephson parametric amplifier using a squid array," *Physical Review B*, vol. 89, no. 21, p. 214517, 2014.

[5] T. Yamamoto, K. Inomata, M. Watanabe, K. Matsuba, T. Miyazaki, W. D. Oliver, Y. Nakamura, and J. S. Tsai, "Flux-driven josephson parametric amplifier," *Applied Physics Letters*, vol. 93, no. 4, p. 042510, 2008.

[6] N. Bergeal, F. Schackert, M. Metcalfe, R. Vijay, V. E. Manucharyan, L. Frunzio, D. E. Prober, R. J. Schoelkopf, S. M. Girvin, and M. H. Devoret, "Phase-preserving amplification near the quantum limit with a josephson ring modulator," *Nature*, vol. 465, no. 7294, pp. 64–68, 2010.

[7] E. Flurin, *The Josephson mixer : a swiss army knife for microwave quantum optics*. Theses, Ecole normale supérieure - ENS PARIS, Dec. 2014.

[8] J.-C. Besse, S. Gasparinetti, M. C. Collodo, T. Walter, P. Kurpiers, M. Pechal, C. Eichler, and A. Wallraff, "Single-shot quantum nondemolition detection of individual itinerant microwave photons," *Physical Review X*, vol. 8, no. 2, p. 021003, 2018.

[9] R. Lescanne, S. Deléglise, E. Albertinale, U. Réglade, T. Capelle, E. Ivanov, T. Jacqmin, Z. Leghtas, and E. Flurin, "Detecting itinerant microwave photons with engineered non-linear dissipation," *arXiv preprint arXiv:1902.05102*, 2019.

[10] S. Kono, K. Koshino, Y. Tabuchi, A. Noguchi, and Y. Nakamura, "Quantum nondemolition detection of an itinerant microwave photon," *Nature Physics*, vol. 14, no. 6, p. 546, 2018.

[11] A. Blais, R.-S. Huang, A. Wallraff, S. M. Girvin, and R. J. Schoelkopf, "Cavity quantum electrodynamics for superconducting electrical circuits: An architecture for quantum computation," *Phys. Rev. A*, vol. 69, p. 062320, Jun 2004.

[12] X. Gu, A. F. Kockum, A. Miranowicz, Y.-x. Liu, and F. Nori, "Microwave photonics with superconducting quantum circuits," *Physics Reports*, vol. 718, pp. 1–102, 2017.

[13] E. Jeffrey, D. Sank, J. Mutus, T. White, J. Kelly, R. Barends, Y. Chen, Z. Chen, B. Chiaro, A. Dunsworth, *et al.*, "Fast accurate state measurement with superconducting qubits," *Physical review letters*, vol. 112, no. 19, p. 190504, 2014.

[14] R. Landauer, "Electrical transport in open and closed systems," *Zeitschrift für Physik B Condensed Matter*, vol. 68, pp. 217–228, Jun 1987.

[15] Y. Blanter and M. Büttiker, "Shot noise in mesoscopic conductors," *Physics Reports*, vol. 336, no. 1, pp. 1 – 166, 2000.

[16] T. Martin, "Noise in mesoscopic physics," *arXiv preprint cond-mat/0501208*, 2005.

[17] M. Reznikov, M. Heiblum, H. Shtrikman, and D. Mahalu, "Temporal correlation of electrons: Suppression of shot noise in a ballistic quantum point contact," *Physical Review Letters*, vol. 75, no. 18, p. 3340, 1995.

[18] A. Kumar, L. Saminadayar, D. Glattli, Y. Jin, and B. Etienne, "Experimental test of the quantum shot noise reduction theory," *Physical review letters*, vol. 76, no. 15, p. 2778, 1996.

[19] A. Kozhevnikov, R. Schoelkopf, and D. Prober, "Observation of photon-assisted noise in a diffusive normal metal–superconductor junction," *Physical Review Letters*, vol. 84, no. 15, p. 3398, 2000.

[20] L.-H. Reydellet, P. Roche, D. Glattli, B. Etienne, and Y. Jin, "Quantum partition noise of photon-created electron-hole pairs," *Physical review letters*, vol. 90, no. 17, p. 176803, 2003.

[21] M. Kapfer, P. Roulleau, M. Santin, I. Farrer, D. Ritchie, and D. Glattli, "A josephson relation for fractionally charged anyons," *Science*, vol. 363, no. 6429, pp. 846–849, 2019.

[22] W. Schottky, "Über spontane stromschwankungen in verschiedenen elektrizitätsleitern," *Annalen der Physik*, vol. 362, no. 23, pp. 541–567, 1918.

[23] G. Lesovik and R. Loosen, "On the detection of finite-frequency current fluctuations," *Journal of Experimental and Theoretical Physics Letters*, vol. 65, no. 3, pp. 295–299, 1997.

[24] C. Beenakker and H. Schomerus, "Counting statistics of photons produced by electronic shot noise," *Physical review letters*, vol. 86, no. 4, p. 700, 2001.

[25] G. Gasse, C. Lupien, and B. Reulet, "Observation of squeezing in the electron quantum shot noise of a tunnel junction," *Physical review letters*, vol. 111, no. 13, p. 136601, 2013.

[26] J.-C. Forgues, G. Gasse, C. Lupien, and B. Reulet, "Non-classical radiation emission by a coherent conductor," *Comptes Rendus Physique*, vol. 17, no. 7, pp. 718–728, 2016.

[27] C. Mora, C. Altimiras, P. Joyez, and F. Portier, "Quantum properties of the radiation emitted by a conductor in the coulomb blockade regime," *Physical Review B*, vol. 95, no. 12, p. 125311, 2017.

[28] U. C. Mendes, S. Jezouin, P. Joyez, B. Reulet, A. Blais, F. Portier, C. Mora, and C. Altimiras, "Parametric amplification and squeezing with an ac-and dc-voltage biased superconducting junction," *Physical Review Applied*, vol. 11, no. 3, p. 034035, 2019.

[29] A. Cottet and Z. Leghtas, "Theory of interactions between cavity photons induced by a mesoscopic circuit," *arXiv preprint arXiv:1910.07801*, 2019.

[30] J. Müller, *Finite frequency dynamics in correlated quantum conductors*. PhD thesis, Université Paris-Saclay, 2020.

[31] G.-L. Ingold and Y. Nazarov, *Charge Tunneling Rates in Ultrasmall Junctions*, pp. 21–107. Boston, MA: Springer US, 1992.

[32] T. Holst, D. Esteve, C. Urbina, and M. H. Devoret, "Effect of a transmission line resonator on a small capacitance tunnel junction," *Phys. Rev. Lett.*, vol. 73, pp. 3455–3458, Dec 1994.

[33] M. Hofheinz, F. Portier, Q. Baudouin, P. Joyez, D. Vion, P. Bertet, P. Roche, and D. Esteve, "Bright side of the coulomb blockade," *Phys. Rev. Lett.*, vol. 106, p. 217005, May 2011.

[34] V. Gramich, B. Kubala, S. Rohrer, and J. Ankerhold, "From coulomb-blockade to nonlinear quantum dynamics in a superconducting circuit with a resonator," *Physical review letters*, vol. 111, no. 24, p. 247002, 2013.

[35] C. Rolland, *Strong coupling Quantum electrodynamics of a voltage biased Josephson junction*. PhD thesis, Lille 1, 2016.

[36] C. Rolland, A. Peugeot, S. Dambach, M. Westig, B. Kubala, Y. Mukharsky, C. Altimiras, H. le Sueur, P. Joyez, D. Vion, *et al.*, "Antibunched photons emitted by a dc-biased josephson junction," *Physical review letters*, vol. 122, no. 18, p. 186804, 2019.

[37] E. Flurin, N. Roch, F. Mallet, M. H. Devoret, and B. Huard, "Generating entangled microwave radiation over two transmission lines," *Physical review letters*, vol. 109, no. 18, p. 183901, 2012.

[38] O. Parlavecchio, *Blocage de Coulomb dynamique: des fluctuations électroniques aux micro-ondes quantiques*. PhD thesis, Paris 6, 2015.

[39] M. Westig, B. Kubala, O. Parlavecchio, Y. Mukharsky, C. Altimiras, P. Joyez, D. Vion, P. Roche, D. Estève, M. Hofheinz, *et al.*, "Emission of nonclassical radiation by inelastic cooper pair tunneling," *Physical review letters*, vol. 119, no. 13, p. 137001, 2017.

[40] C. Beenakker, C. Schönenberger, *et al.*, "Quantum shot noise," *Physics Today*, vol. 56, no. 5, pp. 37–42, 2003.

[41] G. B. Lesovik, "Excess quantum noise in 2d ballistic point contacts," *JETP Letters*, vol. 49, no. 9, p. 592, 1989.

[42] L. N. Cooper, "Bound electron pairs in a degenerate fermi gas," *Phys. Rev.*, vol. 104, pp. 1189–1190, Nov 1956.

[43] J. Bardeen, L. N. Cooper, and J. R. Schrieffer, "Theory of superconductivity," *Physical review*, vol. 108, no. 5, p. 1175, 1957.

[44] C. Beenakker, "Transport phenomena in mesoscopic systems," *Springer Series in Solid State Sciences*, vol. 109, 1992.

[45] A. Andreev, "Thermal conductivity of the intermediate state of superconductors," *Sov. Phys. JETP*, vol. 46, no. 5, 1964.

[46] A. Barone and G. Paterno, *Physics and applications of the Josephson effect*. Wiley, 1982.

[47] V. Manucharyan, *Superinductance*. PhD thesis, Yale University, 2012.

[48] M. H. Devoret, D. Esteve, H. Grabert, G.-L. Ingold, H. Pothier, and C. Urbina, "Effect of the electromagnetic environment on the coulomb blockade in ultrasmall tunnel junctions," *Phys. Rev. Lett.*, vol. 64, pp. 1824–1827, Apr 1990.

[49] S. M. Girvin, L. I. Glazman, M. Jonson, D. R. Penn, and M. D. Stiles, "Quantum fluctuations and the single-junction coulomb blockade," *Phys. Rev. Lett.*, vol. 64, pp. 3183–3186, Jun 1990.

[50] J. B. Johnson, "Thermal agitation of electricity in conductors," *Phys. Rev.*, vol. 32, pp. 97–109, Jul 1928.

[51] H. B. Callen and T. A. Welton, "Irreversibility and generalized noise," *Phys. Rev.*, vol. 83, pp. 34–40, Jul 1951.

[52] H. Nyquist, "Thermal agitation of electric charge in conductors," *Phys. Rev.*, vol. 32, pp. 110–113, Jul 1928.

[53] D. Rogovin and D. Scalapino, "Fluctuation phenomena in tunnel junctions," *Annals of Physics*, vol. 86, no. 1, pp. 1 – 90, 1974.

[54] A. O. Caldeira and A. J. Leggett, "Influence of dissipation on quantum tunneling in macroscopic systems," *Phys. Rev. Lett.*, vol. 46, pp. 211–214, Jan 1981.

[55] A. Grimm, *Josephson photonics: Statistics of photons emitted by inelastic Cooper pair tunneling*. PhD thesis, Grenoble Alpes, 2015.

[56] V. Ambegaokar and A. Baratoff, "Tunneling between superconductors," *Physical Review Letters*, vol. 10, no. 11, p. 486, 1963.

[57] H. Grabert, G.-L. Ingold, and B. Paul, "Phase diffusion and charging effects in josephson junctions," *Europhysics Letters (EPL)*, vol. 44, pp. 360–366, nov 1998.

[58] G.-L. Ingold and H. Grabert, "Finite-temperature current-voltage characteristics of ultrasmall tunnel junctions," *Europhysics Letters (EPL)*, vol. 14, pp. 371–376, feb 1991.

[59] B. Yurke, "Input-output theory," in *Quantum Squeezing*, pp. 53–96, Springer, 2004.

[60] C. Chang, C. Sabín, P. Forn-Díaz, F. Quijandría, A. Vadiraj, I. Nsanzineza, G. Johansson, and C. Wilson, "Observation of three-photon spontaneous para-

metric downconversion in a superconducting parametric cavity," *arXiv preprint arXiv:1907.08692*, 2019.

[61] L. Bretheau, *Localized excitations in superconducting atomic contacts: probing the Andreev doublet*. PhD thesis, Ecole Polytechnique X, 2013.

[62] D. J. Wineland, C. Monroe, W. M. Itano, D. Leibfried, B. E. King, and D. M. Meekhof, "Experimental issues in coherent quantum-state manipulation of trapped atomic ions," *Journal of Research of the National Institute of Standards and Technology*, vol. 103, no. 3, p. 259, 1998.

[63] L. Mandel and E. Wolf, *Optical coherence and quantum optics*. Cambridge university press, 1995.

[64] R. Loudon, *The quantum theory of light*. OUP Oxford, 2000.

[65] D. F. Walls and G. J. Milburn, *Quantum optics*. Springer Science & Business Media, 2007.

[66] H. J. Carmichael, *Statistical methods in quantum optics 1: master equations and Fokker-Planck equations*. Springer Science & Business Media, 2013.

[67] K. E. Cahill and R. J. Glauber, "Ordered expansions in boson amplitude operators," *Physical Review*, vol. 177, no. 5, p. 1857, 1969.

[68] J.-R. Souquet and A. Clerk, "Fock-state stabilization and emission in superconducting circuits using dc-biased josephson junctions," *Physical Review A*, vol. 93, no. 6, p. 060301, 2016.

[69] K. C. Tan and H. Jeong, "Nonclassical light and metrological power: An introductory review," *AVS Quantum Science*, vol. 1, no. 1, p. 014701, 2019.

[70] R. Hanbury Brown, R. Q. Twiss, *et al.*, "Correlation between photons in two coherent beams of light," *Nature*, vol. 177, no. 4497, pp. 27–29, 1956.

[71] P. Grünwald, "What $g^{(2)} < 1/2$ tells you-and what it does not," *arXiv preprint arXiv:1711.05897*, 2017.

[72] S. Dambach, B. Kubala, V. Gramich, and J. Ankerhold, "Time-resolved statistics of nonclassical light in josephson photonics," *Physical Review B*, vol. 92, no. 5, p. 054508, 2015.

[73] Z.-L. Xiang, M. Zhang, L. Jiang, and P. Rabl, "Intracity quantum communication via thermal microwave networks," *Physical Review X*, vol. 7, no. 1, p. 011035, 2017.

[74] A. A. Houck, D. Schuster, J. Gambetta, J. Schreier, B. Johnson, J. Chow, L. Frunzio, J. Majer, M. Devoret, S. Girvin, *et al.*, "Generating single microwave photons in a circuit," *Nature*, vol. 449, no. 7160, p. 328, 2007.

[75] D. Bozyigit, C. Lang, L. Steffen, J. Fink, C. Eichler, M. Baur, R. Bianchetti, P. Leek, S. Filipp, M. Da Silva, *et al.*, "Antibunching of microwave-frequency photons observed in correlation measurements using linear detectors," *Nature Physics*, vol. 7, no. 2, p. 154, 2011.

[76] N. Samkharadze, A. Bruno, P. Scarlino, G. Zheng, D. P. DiVincenzo, L. DiCarlo, and L. Vandersypen, "High-kinetic-inductance superconducting nanowire resonators

for circuit qed in a magnetic field," *Physical Review Applied*, vol. 5, no. 4, p. 044004, 2016.

[77] P. Jung, A. V. Ustinov, and S. M. Anlage, "Progress in superconducting metamaterials," *Superconductor Science and Technology*, vol. 27, no. 7, p. 073001, 2014.

[78] T. Holmqvist, M. Meschke, and J. P. Pekola, "Double oxidation scheme for tunnel junction fabrication," *Journal of Vacuum Science & Technology B: Microelectronics and Nanometer Structures Processing, Measurement, and Phenomena*, vol. 26, no. 1, pp. 28–31, 2008.

[79] A. A. Michelson, *On the application of interference methods to astronomical measurements*, vol. 5. National Academy of Sciences, 1894.

[80] B. Yurke and J. S. Denker, "Quantum network theory," *Physical Review A*, vol. 29, no. 3, p. 1419, 1984.

[81] C. M. Caves, "Quantum limits on noise in linear amplifiers," *Physical Review D*, vol. 26, no. 8, p. 1817, 1982.

[82] M. P. da Silva, D. Bozyigit, A. Wallraff, and A. Blais, "Schemes for the observation of photon correlation functions in circuit qed with linear detectors," *Physical Review A*, vol. 82, 2010.

[83] J. M. Martinis, M. H. Devoret, and J. Clarke, "Experimental tests for the quantum behavior of a macroscopic degree of freedom: The phase difference across a josephson junction," *Physical Review B*, vol. 35, no. 10, p. 4682, 1987.

[84] O. Parlavecchio, C. Altimiras, J.-R. Souquet, P. Simon, I. Safi, P. Joyez, D. Vion, P. Roche, D. Esteve, and F. Portier, "Fluctuation-dissipation relations of a tunnel junction driven by a quantum circuit," *Physical review letters*, vol. 114, no. 12, p. 126801, 2015.

[85] G.-L. Ingold, H. Grabert, and U. Eberhardt, "Cooper-pair current through ultrasmall josephson junctions," *Phys. Rev. B*, vol. 50, pp. 395–402, Jul 1994.

[86] W. T. Morley, A. Di Marco, M. Mantovani, P. Stadler, W. Belzig, G. Rastelli, and A. D. Armour, "Theory of double cooper-pair tunneling and light emission mediated by a resonator," *arXiv preprint arXiv:1905.06194*, 2019.

[87] S. Dambach, *Josephson photonics and Josephson scanning tunneling microscopy: inelastic charge transfer across superconducting junctions.* PhD thesis, Universität Ulm, 2019.

[88] A. Grimm, F. Blanchet, R. Albert, J. Leppäkangas, S. Jebari, D. Hazra, F. Gustavo, J.-L. Thomassin, E. Dupont-Ferrier, F. Portier, and M. Hofheinz, "Bright on-demand source of antibunched microwave photons based on inelastic cooper pair tunneling," *Phys. Rev. X*, vol. 9, p. 021016, Apr 2019.

[89] S. L. Braunstein and R. I. McLachlan, "Generalized squeezing," *Physical Review A*, vol. 35, no. 4, p. 1659, 1987.

[90] S. Ghose and B. C. Sanders, "Non-gaussian states of light as an offline resource for universal continuous variable quantum information processing," in *Quantum*

Communications and Quantum Imaging III, vol. 5893, p. 58930X, International Society for Optics and Photonics, 2005.

[91] M. Gu, C. Weedbrook, N. C. Menicucci, T. C. Ralph, and P. van Loock, "Quantum computing with continuous-variable clusters," *Physical Review A*, vol. 79, no. 6, p. 062318, 2009.

[92] R. Takagi and Q. Zhuang, "Convex resource theory of non-gaussianity," *Physical Review A*, vol. 97, no. 6, p. 062337, 2018.

[93] C. Weedbrook, S. Pirandola, R. García-Patrón, N. J. Cerf, T. C. Ralph, J. H. Shapiro, and S. Lloyd, "Gaussian quantum information," *Reviews of Modern Physics*, vol. 84, no. 2, p. 621, 2012.

[94] P. D. Drummond and Z. Ficek, *Quantum squeezing*, vol. 27. Springer Science & Business Media, 2013.

[95] P. Grangier, R. Slusher, B. Yurke, and A. LaPorta, "Squeezed-light–enhanced polarization interferometer," *Physical review letters*, vol. 59, no. 19, p. 2153, 1987.

[96] L. Barsotti, J. Harms, and R. Schnabel, "Squeezed vacuum states of light for gravitational wave detectors," *Reports on Progress in Physics*, vol. 82, no. 1, p. 016905, 2018.

[97] A. Bienfait, P. Campagne-Ibarcq, A. Kiilerich, X. Zhou, S. Probst, J. Pla, T. Schenkel, D. Vion, D. Esteve, J. Morton, *et al.*, "Magnetic resonance with squeezed microwaves," *Physical Review X*, vol. 7, no. 4, p. 041011, 2017.

[98] J. Leppäkangas, G. Johansson, M. Marthaler, and M. Fogelström, "Input–output description of microwave radiation in the dynamical coulomb blockade," *New Journal of Physics*, vol. 16, no. 1, p. 015015, 2014.

[99] A. I. Lvovsky, "Squeezed light," *Photonics: Scientific Foundations, Technology and Applications*, vol. 1, pp. 121–163, 2015.

[100] A. Einstein, B. Podolsky, and N. Rosen, "Can quantum-mechanical description of physical reality be considered complete?," *Physical review*, vol. 47, no. 10, p. 777, 1935.

[101] S. L. Braunstein and P. Van Loock, "Quantum information with continuous variables," *Reviews of Modern Physics*, vol. 77, no. 2, p. 513, 2005.

[102] R. Slusher, L. Hollberg, B. Yurke, J. Mertz, and J. Valley, "Observation of squeezed states generated by four-wave mixing in an optical cavity," *Physical Review Letters*, vol. 55, no. 22, p. 2409, 1985.

[103] N. Bergeal, F. Schackert, L. Frunzio, and M. Devoret, "Two-mode correlation of microwave quantum noise generated by parametric down-conversion," *Physical review letters*, vol. 108, no. 12, p. 123902, 2012.

[104] A. D. Armour, B. Kubala, and J. Ankerhold, "Josephson photonics with a two-mode superconducting circuit," *Physical Review B*, vol. 91, no. 18, p. 184508, 2015.

[105] S. Dambach, B. Kubala, and J. Ankerhold, "Time-resolved statistics of photon pairs in two-cavity josephson photonics," *Fortschritte der Physik*, vol. 65, no. 6-8, p. 1600061, 2017.

[106] J. D. Franson, "Bell inequality for position and time," *Physical review letters*, vol. 62, no. 19, p. 2205, 1989.

[107] S. Aerts, P. Kwiat, J.-Å. Larsson, and M. Zukowski, "Two-photon franson-type experiments and local realism," *Physical review letters*, vol. 83, no. 15, p. 2872, 1999.

[108] S. Wölk, M. Huber, and O. Gühne, "Unified approach to entanglement criteria using the cauchy-schwarz and hölder inequalities," *Physical Review A*, vol. 90, no. 2, p. 022315, 2014.

[109] S. Jebari, *The inelastic Cooper pair tunneling amplifier (ICTA)*. PhD thesis, Grenoble Alpes, 2017.

[110] L. Arndt and F. Hassler, "Statistics of radiation due to nondegenerate josephson parametric down-conversion," *Physical Review B*, vol. 100, no. 1, p. 014505, 2019.

[111] G. Vidal and R. F. Werner, "Computable measure of entanglement," *Physical Review A*, vol. 65, no. 3, p. 032314, 2002.

[112] Z. J. Deng, S. J. Habraken, and F. Marquardt, "Entanglement rate for gaussian continuous variable beams," *New Journal of Physics*, vol. 18, no. 6, p. 063022, 2016.

[113] A. Rueda, W. Hease, S. Barzanjeh, and J. M. Fink, "Electro-optic entanglement source for microwave to telecom quantum state transfer," *npj Quantum Information*, vol. 5, no. 1, pp. 1–11, 2019.

[114] B. Abdo, A. Kamal, and M. Devoret, "Nondegenerate three-wave mixing with the josephson ring modulator," *Physical Review B*, vol. 87, no. 1, p. 014508, 2013.

[115] N. Frattini, U. Vool, S. Shankar, A. Narla, K. Sliwa, and M. Devoret, "3-wave mixing josephson dipole element," *Applied Physics Letters*, vol. 110, no. 22, p. 222603, 2017.

[116] T.-C. Chien, O. Lanes, C. Liu, X. Cao, P. Lu, S. Motz, G. Liu, D. Pekker, and M. Hatridge, "Multiparametric amplification and qubit measurement with a kerr-free josephson ring modulator," *arXiv preprint arXiv:1903.02102*, 2019.

[117] S. Jebari, F. Blanchet, A. Grimm, D. Hazra, R. Albert, P. Joyez, D. Vion, D. Esteve, F. Portier, and M. Hofheinz, "Near-quantum-limited amplification from inelastic cooper-pair tunnelling," *Nature Electronics*, vol. 1, no. 4, pp. 223–227, 2018.

[118] D. M. Pozar, *Microwave engineering*. John Wiley & Sons, 2009.

[119] M. Trif and P. Simon, "Photon cross-correlations emitted by a josephson junction in two microwave cavities," *Physical Review B*, vol. 92, no. 1, p. 014503, 2015.

université PARIS-SACLAY | ÉCOLE DOCTORALE Physique en l'Île-de-France (PIF)

Titre : Sources de rayonnement micro-onde quantique par effet tunnel inélastique de paires de Cooper

Mots clés : Photonique Josephson – Supraconductivité mésoscopique – Optique quantique micro-onde

Résumé : Le passage aléatoire des charges à travers une jonction tunnel génère un bruit en courant, qui peut être capté par l'environnement de la jonction où il crée des excitations électromagnétiques appelés photons. Dans cette thèse, nous démontrons qu'une jonction tunnel supraconductrice couplée à un environnement bien choisi peut implémenter une source brillante de rayonnement micro-onde quantique. L'énergie nécessaire pour créer les photons est fournie par la source de tension continue lors du passage tunnel inélastique d'une paire de Cooper à travers la jonction.

Nous détectons cette lumière émise et étudions ses propriétés avec des outils de l'optique quantique adaptés au domaine micro-onde. Nous caractérisons le dégroupement des photons émis dans un seul mode fortement couplée à une jonction, ainsi que l'intrication de paires de photons émis dans deux modes à des fréquences différentes. Outre une meilleure compréhension du couplage charge-lumière dans les conducteurs cohérents, ces travaux pourraient déboucher sur de nouvelles façons de manipuler l'information au niveau quantique.

Title: Quantum microwave sources from inelastic Cooper pair tunneling

Keywords: Josephson photonics – Mesoscopic superconductivity – Microwave quantum optics

Abstract: The probabilistic charge transfer in tunnel junctions is a source of current noise, which can be picked up by the environment of the junction where it creates electromagnetic excitations - or photons. In this thesis, we demonstrate that a superconducting tunnel junction coupled to a tailored environment can act as a bright source of quantum microwave radiation. The energy required to create photons is extracted from a DC voltage source during the inelastic tunneling of Cooper pair through the junction.

We detect this emitted light and study its properties with quantum optics tools adapted to the microwave domain. We characterize the single-photon nature of the light emitted in a single mode strongly coupled to a junction, as well as the entanglement of photon pairs emitted in two modes at different frequencies. In addition to a better understanding of the charge-light coupling in coherent conductors, this work could lead to new ways of manipulating information at the quantum level.

Université Paris-Saclay
Espace Technologique / Immeuble Discovery
Route de l'Orme aux Merisiers RD 128 / 91190 Saint-Aubin, France